

**LEVEL III**



✓ AGARD-LS-114

AGARD-LS-114

# AGARD

ADVISORY GROUP FOR AEROSPACE RESEARCH & DEVELOPMENT

7 RUE ANCELLE 92200 NEUILLY SUR SEINE FRANCE

AD A 103764

AGARD LECTURE SERIES No. 114

A063851

## Dynamic Stability Parameters

DTIC  
ELECTED  
S SEP 3 1981 D  
D

NORTH ATLANTIC TREATY ORGANIZATION



INT FILE COPY

DISTRIBUTION AND AVAILABILITY  
ON BACK COVER

DISTRIBUTION STATEMENT A

Approved for public release;  
Distribution Unlimited

81 9 02 077

14  
AGARD-LS-114

NORTH ATLANTIC TREATY ORGANIZATION  
ADVISORY GROUP FOR AEROSPACE RESEARCH AND DEVELOPMENT  
(ORGANISATION DU TRAITE DE L'ATLANTIQUE NORD)

⑨<sup>9</sup>  
AGARD Lecture Series No.114

DYNAMIC STABILITY PARAMETERS.

11  
10.404

Accession For	
NTIS GRA&I	<input checked="" type="checkbox"/>
DTIC TAB	<input type="checkbox"/>
Unannounced	<input type="checkbox"/>
Justification	
By _____	
Distribution/	
Availability Codes	
Dist	Avail and/or Special
A	

DTIC  
ELECTED  
S D SEP 3 1981  
D

DISTRIBUTION STATEMENT A  
Approved for public release;  
Distribution Unlimited

The material in this publication was assembled to support a Lecture Series under the sponsorship of the Fluid Dynamics Panel, the Consultant and Exchange Programme of AGARD and the von Kármán Institute for Fluid Dynamics presented on: 2-5 March 1981 at NASA Ames Research Center, Moffett Field, California, USA and 16-19 March 1981 at the von Kármán Institute, Rhode-Saint-Genèse, Belgium.

400043  
11

## THE MISSION OF AGARD

The mission of AGARD is to bring together the leading personalities of the NATO nations in the fields of science and technology relating to aerospace for the following purposes:

- Exchanging of scientific and technical information;
- Continuously stimulating advances in the aerospace sciences relevant to strengthening the common defence posture;
- Improving the co-operation among member nations in aerospace research and development;
- Providing scientific and technical advice and assistance to the North Atlantic Military Committee in the field of aerospace research and development;
- Rendering scientific and technical assistance, as requested, to other NATO bodies and to member nations in connection with research and development problems in the aerospace field;
- Providing assistance to member nations for the purpose of increasing their scientific and technical potential;
- Recommending effective ways for the member nations to use their research and development capabilities for the common benefit of the NATO community.

The highest authority within AGARD is the National Delegates Board consisting of officially appointed senior representatives from each member nation. The mission of AGARD is carried out through the Panels which are composed of experts appointed by the National Delegates, the Consultant and Exchange Programme and the Aerospace Applications Studies Programme. The results of AGARD work are reported to the member nations and the NATO Authorities through the AGARD series of publications of which this is one.

Participation in AGARD activities is by invitation only and is normally limited to citizens of the NATO nations.

The content of this publication has been reproduced  
directly from material supplied by AGARD or the authors.

Published May 1981

Copyright © AGARD 1981  
All Rights Reserved

ISBN 92-835-1385-1



Printed by Technical Editing and Reproduction Ltd  
Harcourt House, 7-9 Charlotte St, London, W1P 1HD

## **FOREWORD**

The advent of flight at high angles of attack has revived our interest in the dynamic stability of aircraft and missiles. This Lecture Series is intended to provide a review of the impact of high- $\alpha$  aerodynamics on dynamic stability characteristics of aerospace vehicles and to present a state-of-the-art survey of the analytical, wind-tunnel and flight-test techniques used for dynamic stability work. The programme also features a discussion of the various mathematical models used for the analysis of flight behaviour of aircraft at high angles of attack including the non-linear and time dependent formulations as well as a review of some pertinent sensitivity and simulator studies. This scope is patterned after the very successful AGARD Fluid Dynamics Panel Symposium on Dynamic Stability Parameters, which was held in Athens in the Spring of 1978. The Lecture Series is intended not only to provide suitable training and information to engineers and scientists *who wish to enter the field*, but also as a follow-on activity to the above mentioned symposium to provide a focal point for technical discussions and an opportunity to exchange views and ideas among engineers and scientists *who already work in the field* and who already may be experts in one or more parts of it. This is of particular importance since the material presented by the Lecture Series covers not less than four distinct disciplines: theoretical aerodynamics, wind-tunnel experiments, flight testing and flight mechanics. It is, of course, only through simultaneous use of all of these disciplines that a better understanding of the flight dynamics of a modern aerospace vehicle can be achieved.

The Lecture Series should also be of interest to specialists in computational fluid dynamics who may wish to be better informed about the required future applications of their techniques.

This Lecture Series is sponsored by the Fluid Dynamics Panel of AGARD and implemented by the von Kármán Institute, and will be presented in Belgium after the presentation at NASA, Ames.

**K.J.ORLIK-RÜCKEMANN**  
Lecture Series Director

## LIST OF SPEAKERS

Lecture Series Director: Dr K.J.Orlik-Rückemann  
Unsteady Aerodynamics Laboratory  
National Aeronautical Establishment  
National Research Council  
Ottawa, Ontario K1A OR6  
Canada

## SPEAKERS

Mr J.Chambers  
NASA Langley Research Center  
M/S 355  
Hampton, Virginia 23665  
USA

Dr L.E.Ericsson  
Lockheed Missiles and Space Co.  
Dept. 81-10, Building 154  
Sunnyvale, California 94086  
USA

Dr P.Hamel  
DFVLR  
Postfach 3267  
3300 Braunschweig  
Germany

Dr E.S.Hanff  
Unsteady Aerodynamics Laboratory  
National Aeronautical Establishment  
National Research Council  
Ottawa, Ontario K1A OR6  
Canada

Mr G.N.Malcolm  
NASA Ames Research Center  
M/S 227-8  
Moffett Field, California 94035  
USA

Mr C.O'Leary  
Royal Aircraft Establishment  
Aerodynamics Department  
Bedford  
UK

Dr J.Ross  
Royal Aircraft Establishment  
Aerodynamics Department  
Farnborough, Hants GU14 6TD  
UK

Dr L.Schiff  
NASA Ames Research Center  
M/S 227-8  
Moffett Field, California 94035  
USA

Dr C.P.Schneider  
Bayern Chemie  
YCH 31  
Postfach 220  
8012 Ottobrunn  
Germany

**CONTENTS**

	<b>Page</b>
<b>FOREWORD</b>	iii
<b>LIST OF SPEAKERS</b>	iv
	<b>Reference</b>
<b>AERODYNAMIC MATHEMATICAL MODELING - BASIC CONCEPTS ;</b> by M.Tobak and L.B.Schiff	1
<b>IMPACT OF HIGH-ALPHA AERODYNAMICS ON DYNAMIC STABILITY PARAMETERS OF AIRCRAFT AND MISSILES ;</b> by G.N.Malcolm	2
<b>REVIEW OF TECHNIQUES FOR DETERMINATION OF DYNAMIC STABILITY PARAMETERS IN WIND TUNNELS ;</b> by K.Orlik-Rückemann	3
<b>DIRECT FORCED-OSCILLATION TECHNIQUES FOR THE DETERMINATION OF STABILITY DERIVATIVES IN WIND-TUNNELS ;</b> by E.S.Hanff	4
<b>WIND-TUNNEL MEASUREMENT OF AERODYNAMIC DERIVATIVES USING FLEXIBLE-STING RIGS ;</b> by C.O.O'Leary	5
<b>ROTARY AND MAGNUS BALANCES ;</b> by G.N.Malcolm	6
<b>CURVED-FLOW, ROLLING FLOW AND OSCILLATORY PURE-YAWING WIND-TUNNEL TEST METHODS FOR DETERMINATION OF DYNAMIC STABILITY DERIVATIVES ;</b> by J.R.Chambers, S.B.Grafton and F.H.Lutze	7
<b>SUPPORT INTERFERENCE ;</b> by L.E.Ericsson	8
<b>APPLICATIONS OF HALF-MODEL TECHNIQUE IN DYNAMIC STABILITY TESTING ;</b> by E.S.Hanff	9
<b>DETERMINATION OF AIRCRAFT DYNAMIC STABILITY AND CONTROL PARAMETERS FROM FLIGHT TESTING ;</b> by P.G.Hamel	10
<b>ESTIMATION OF DYNAMIC STABILITY PARAMETERS FROM DROP MODEL FLIGHT TESTS ;</b> by J.R.Chambers	11
<b>ANALYTICAL DETERMINATION OF DYNAMIC STABILITY PARAMETERS ;</b> by C.P.Schneider	12
<b>AEROELASTICITY, INCLUDING DYNAMIC EFFECTS OF SEPARATED FLOW ;</b> by L.E.Ericsson	13
<b>CONTROL DERIVATIVES ;</b> by A.J.Ross	14
<b>SENSITIVITY OF AIRCRAFT MOTION TO CROSS-COUPLING AND ACCELERATION DERIVATIVES ;</b> by K.J.Orlik-Rückemann	15
<b>SOME APPLICATIONS OF AERODYNAMIC FORMULATIONS TO PROBLEMS IN AIRCRAFT DYNAMICS ;</b> by L.B.Schiff and M.Tobak	16

cont.

Reference

**APPLICATIONS OF DYNAMIC STABILITY PARAMETERS TO PROBLEMS IN  
AIRCRAFT DYNAMICS**

by J.R.Chambers, D.J.Dicarlo and J.L.Johnson, Jr

17

**APPLICATION TO MISSILE DYNAMICS**

by C.P.Schneider

18

**Appendix A – LIST OF PARTICIPANTS AT NASA AMES RESEARCH CENTER,  
MOFFETT FIELD, CALIFORNIA, USA**

A

**Appendix B – LIST OF PARTICIPANTS AT VON KARMAN INSTITUTE, RHODE-ST-GENESE,  
BELGIUM**

B

## AERODYNAMIC MATHEMATICAL MODELING - BASIC CONCEPTS

by

Murray Tobak and Lewis B. Schiff  
 Ames Research Center, NASA  
 Moffett Field, California, 94035, U.S.A.

## SUMMARY

This lecture is a review of the basic concepts involved in the mathematical modeling of the aerodynamic response of an aircraft to arbitrary maneuvers. The review leads from Bryan's original formulation through the concepts of linear aerodynamic indicial functions and superposition to the extension of these concepts into the nonlinear regime. The nonlinear generalization yields a form for the aerodynamic response that can be built up from the responses to a limited number of well-defined characteristic motions, reproducible in principle either in wind-tunnel experiments or flow-field computations. A further generalization leads to a form accommodating the discontinuous and double-valued behavior characteristic of hysteresis in the steady-state aerodynamic response.

## NOTATION

$C_x$	axial-force coefficient (along $x_B$ ), $2(\text{axial force})/\rho V^2 S$
$C_y$	side-force coefficient in the aerodynamic axis system (along $y$ ), $2(\text{side force})/\rho V^2 S$
$C_z$	normal-force coefficient in the aerodynamic axis system (along $z$ ), $2(\text{normal force})/\rho V^2 S$
$\hat{C}_y, \hat{C}_z$	side-force and normal-force coefficients in the body axis system; along $y_B, z_B$ , respectively
$C_l$	rolling-moment coefficient in the aerodynamic axis system (along $x_B$ ), $2L/\rho V^2 S l$
$C_m$	pitching-moment coefficient in the aerodynamic axis system (along $y$ ), $2M/\rho V^2 S l$
$C_n$	side-moment coefficient in the aerodynamic axis system (along $z$ ), $2N/\rho V^2 S l$
$\hat{C}_l, \hat{C}_m, \hat{C}_n$	rolling, pitching, and yawing-moment coefficients in the body axis system; along $x_B, y_B, z_B$ , respectively
$\Delta C_p$	local loading coefficient (pressure coefficient on lower surface minus pressure coefficient on upper surface), Fig. 12
$G\{\delta(\xi), \psi(\xi), \lambda(\xi), q(\xi), r(\xi)\}$	functional notation: value at $\xi = t$ of a time-dependent function which depends on all values taken by the five argument functions $\delta(\xi)$ , $\psi(\xi)$ , $\lambda(\xi)$ , $q(\xi)$ , $r(\xi)$ over the time interval $0 \leq \xi \leq t$
$g$	gravitational acceleration, Eq. (10)
$I$	aircraft polar moment of inertia, Eq. (10)
$L$	moment along longitudinal axis of body, Fig. 3
$z$	reference length
$z_{cg}$	distance along $x_B$ from center of rotation to nose, Fig. 17
$m$	aircraft mass, Eq. (10)
$M$	moment along an axis normal to the plane of the resultant angle of attack (along $y$ ), Fig. 3
$N$	moment along an axis in the plane of the resultant angle of attack (along $z$ ), Fig. 3
$p_B, q_B, r_B$	components along the $x_B, y_B, z_B$ axes, respectively, of the total angular velocity of the body axes relative to inertial space
$\dot{q}, \dot{r}$	components of angular velocity along the $\dot{y}, \dot{z}$ axes, respectively, Eq. (5)
$q, r$	components of angular velocity along the $y, z$ axes, respectively, Eq. (6)
$S$	reference area
$t$	time
$u_B, v_B, w_B$	components of flight velocity along $x_B, y_B, z_B$ axes, respectively, Fig. 3
$V$	magnitude of flight velocity vector
$x_B, y_B, z_B$	body-fixed axes, origin at mass center, $x_B$ coincident with a longitudinal axis of the body, Fig. 3

$x_B, y, z$	aerodynamic axes, origin at mass center, $x_B$ , $y$ , $z$ in the plane of the resultant angle of attack, $y$ , $z$ in the crossflow plane normal to the resultant angle-of-attack plane, Fig. 3
$x_B, \bar{y}, \bar{z}$	nonrolling axes (with respect to inertial space), origin at mass center, $\bar{y}$ , $\bar{z}$ in the crossflow plane, Fig. 3
$\alpha$	angle of attack in body axes, Eq. (7)
$\hat{\alpha}$	angle-of-attack parameter in body axis system, $w_B/V$
$\beta$	angle of sideslip in body axes, Eq. (7)
$\hat{\beta}$	angle-of-sideslip parameter in body axis system, $v_B/V$
$\gamma$	dimensionless axial component of velocity, Fig. 3 and Eq. (2)
$\delta$	magnitude of the dimensionless crossflow velocity in the aerodynamic axis system, Fig. 3 and Eq. (2)
$\epsilon$	$\tan \sigma$ , Fig. 3 and Eq. (2)
$\theta$	pitch angle of the $x_B$ axis above the horizontal, Fig. 4
$\lambda$	angular inclination from the $\bar{y}$ axis of the crossflow velocity vector, Fig. 3
$\rho$	atmospheric mass density
$\sigma$	resultant angle of attack defined by $x_B$ axis and velocity vector, Fig. 3
$\dot{\phi}$	coning rate of $x_B$ axis about the velocity vector of a body in level flight
$\dot{\psi}$	angular inclination from the $\bar{y}$ axis of the $y_B$ axis, Fig. 3 and Eq. (3)
$\psi$	angular inclination from the crossflow velocity vector of the $z_B$ axis, Fig. 3
( $\cdot$ )	$d/dt ( )$

## 1. INTRODUCTION

One of the most difficult problems facing an investigator in the field of flight dynamics is to correctly describe the relationship between the aerodynamic reactions and the motion variables in the inertial equations of motion of an aircraft. This statement remains as true today as it was fifty years ago when B. Melville Jones, in his survey article on the dynamics of the airplane,<sup>1</sup> wrote

"Given the shape of the aeroplane and the properties of the air through which it moves the air-reactions  $X$ ,  $Y$ ,  $Z$ ,  $L$ ,  $M$ ,  $N$ , depend on the motion of the aeroplane relative to the air; that is to say upon the six variables  $U$ ,  $V$ ,  $W$ ,  $P$ ,  $Q$ ,  $R$ , and their rates of change with respect to time. In practice, the principal difficulty lies in determining the relationships between  $X$ ,  $Y$ , . . . and  $U$ ,  $V$ , . . .".

In the succeeding half-century our analytical methods and computational and experimental tools have improved remarkably. Flight trajectories which then took months to compute are now computed routinely in seconds, and flow-field computations which would have taken lifetimes to finish are now completed in minutes. Experimental instrumentation, then only dreamed of, is now in common use. On the other hand, because of the corresponding remarkable improvements in performance, aircraft of today fly in speed regimes and encounter aerodynamic phenomena far removed from those encountered in the 1930s. The appearance of shock waves and three-dimensional separated flows have introduced complex nonlinear aerodynamic effects which must now be considered by the designers of modern aircraft. As has been the case in the past, the need for improved methods of analysis to account for the aerodynamic reactions on maneuvering aircraft continues apace with the aircraft's entry into new flight regimes.

The main difficulty in determining the relationship between the instantaneous aerodynamic reactions on a maneuvering aircraft and the motion variables is the fact that this relationship is not solely determined by the *instantaneous* values of the motion variables. Rather, the instantaneous aerodynamic reactions depend, in general, on all of the prior states of the motion up to the instant in question. Today, in the light of recent advances in computer technology and numerical methods for the computation of flow fields, we can already envision how the computer could be utilized to help surmount the difficult problem of accounting for time-history effects in determining the aerodynamic reactions. For example (on the assumption that it will be possible to resolve the problem of turbulence modeling in the presence of three-dimensional separated flow), we can foresee the availability of a computer capable of solving the time-dependent Reynolds-averaged form of the Navier-Stokes equations for the flow over a complete aircraft. For a specified motion, this would also determine the instantaneous aerodynamic response to the motion. The computer thus would be performing the traditional task of dynamical experiments in the wind tunnel, in principle without the limitations of physical constraints and scale effects that are always present in wind-tunnel testing. If the eventual availability of such a powerful computational tool is postulated, the question arises as to how best to employ it to determine the instantaneous aerodynamic response, not to specified motions, but to the arbitrary maneuvers of an aircraft in flight.

A straightforward approach to determining the aerodynamic response of a maneuvering aircraft would be to solve the flow-field equations simultaneously with the inertial equations of motion of the aircraft (Fig. 1). Results from these coupled computations would be complete time-histories of the aircraft motion and of the instantaneous aerodynamic response. With this approach, the aircraft motion would be specified in advance only through the choice of initial conditions. The aircraft would be free to move under the influence of the aerodynamic forces and moments, while the current state of the flow field surrounding the aircraft would be influenced by its prior states. Such an approach could be extended to include additional unsteady effects, such as aeroelastic deformation of the aircraft, or, in the related case of an ablating reentry vehicle, the close coupling between the history of the shape of the vehicle and the motion history.

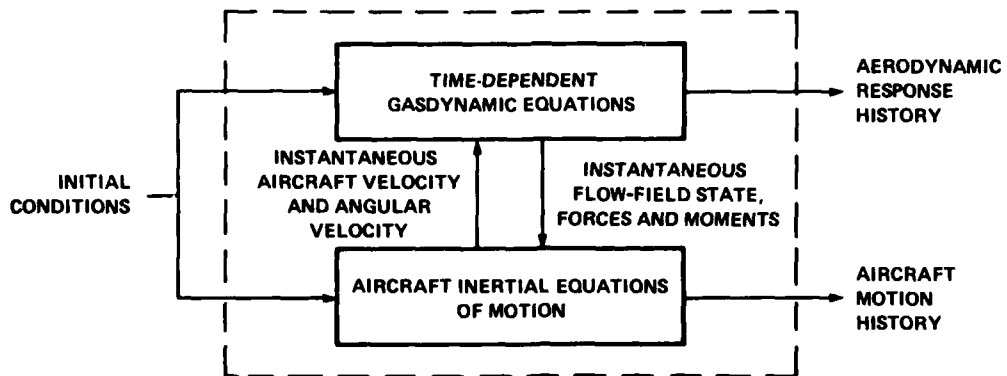


Figure 1. Coupled gasdynamic and inertial equations approach.

Although direct coupling of the gasdynamic equations and the inertial equations of motion represents, in principle, an exact approach to the problem of accounting for time-history effects, it will inevitably be a very costly approach. In general the aerodynamic reactions are nonlinear functions of the motion variables and may have a sensitive dependence on initial conditions. As a result, the aircraft may experience widely differing motion histories even when the motions originate from adjacent initial conditions. Thus, a satisfactory evaluation of the performance envelope of the aircraft may require a large number of coupled computations, one for each change in initial conditions. Further, since the motion and the aerodynamic response are linked, with the coupled-equations approach there can be no reutilization of the previously obtained aerodynamic reactions. In spite of the costs involved, closely coupled aerodynamic problems can be envisaged (notably that of the massively ablating reentry vehicle) for which adoption of the coupled-equations approach may prove to be a necessity.

For rigid aircraft of fixed shape, there is reason to believe that the interdependence between the aerodynamic reactions and the past motion can be at least partially uncoupled. Under these circumstances, mathematical "modeling" affords an alternative approach (Fig. 2) in which a principal goal is to avoid the need for coupling the inertial and gasdynamic equations. In formulating a model, one tries to specify a form for the aerodynamic response which underlies the aerodynamic responses to all motions of interest. The choice of a model implies the specification of a limited number of characteristic motions from whose responses the responses to arbitrary motions can be compounded. Thus, in principle, the aerodynamic

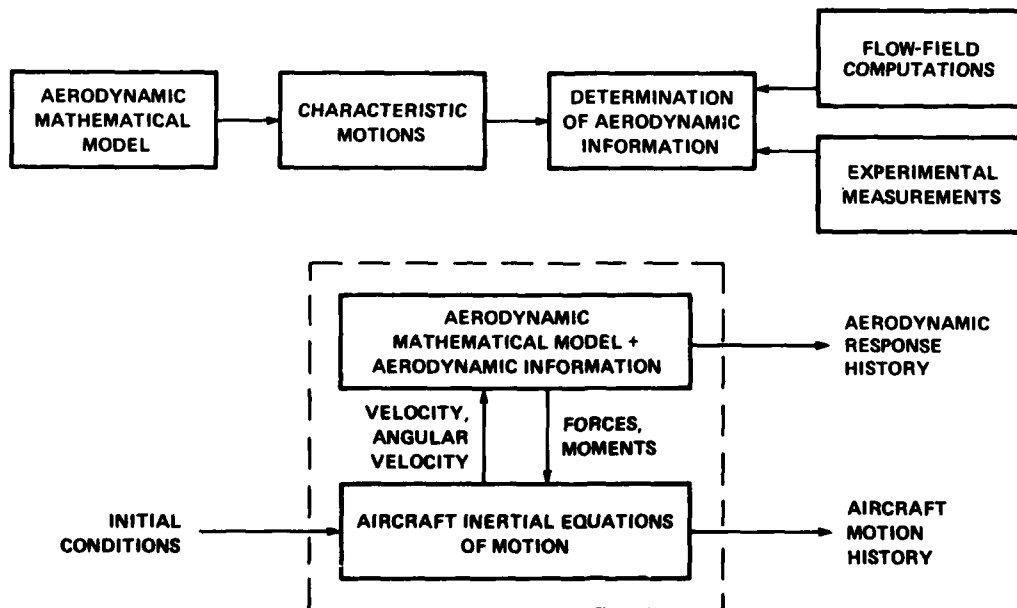


Figure 2. Aerodynamic mathematical modeling approach.

responses to the characteristic motions can be determined once and for all and then be applicable (i.e., reusable) over a wide range of motion variables and flight conditions. In view of this factor, the modeling approach would appear to be potentially less costly than the coupled-equations approach. Here, the powerful computational tool that has been postulated would be used to evaluate, via the appropriate flow-field equations, the aerodynamic responses to the set of characteristic motions specified by the model. When the forms compounded from these characteristic aerodynamic responses are inserted within the inertial equations of motion, the latter can be solved for arbitrary initial conditions without any further reference to the flow-field equations.

It emerges, then, in reply to the question as to how best to use the postulated future computer, that it should be used in conjunction with modeling so long as the economy of this approach is superior to that of the coupled-equations approach. This in turn will depend on the adequacy with which the modeling approach accommodates aerodynamic time-history effects in comparison with the exact accommodation afforded by the coupled-equations approach. Thus, the future viability of mathematical modeling hinges on the economy with which it provides an adequate treatment of time-history effects.

The two computational approaches to determining the aerodynamic response of an aircraft to an arbitrary maneuver have experimental counterparts. In the experimental analogy to the coupled-equations approach, the procedure of solving the flow-field equations would be replaced with an apparatus capable of simulating an arbitrary motion of an aircraft in a wind tunnel (at reduced frequencies typical of those of the full-scale aircraft motion) and of measuring the instantaneous aerodynamic response to the motion. A computer linked to the apparatus would solve the aircraft's equations of motion during the course of the experiment (with the instantaneous values of the aerodynamic forces and moments obtained from the wind-tunnel measurements) and thus control the motion of the apparatus. Results from such an experiment would be time histories of the aircraft motion and of the aerodynamic response. The experimental analogy of the second approach, mathematical modeling, would be to carry out experimental evaluation of the aerodynamic responses to the characteristic motions called for by the model. This is, of course, the approach conventionally employed in flight-dynamics research. In the modeling approach, given the instantaneous aerodynamic reactions specified by the mathematical model, the aircraft's equations of motion would be solved to determine the history of the aircraft's motion. In the experimental analog of the coupled-equations approach, technical difficulties, due mainly to the small size of a wind-tunnel model relative to the actual aircraft, have so far precluded the construction of an apparatus capable of simulating arbitrary aircraft motions in a wind tunnel. Thus the coupled-equations approach would appear to be useful only from the standpoint of computations. From an experimental standpoint, mathematical modeling, with the aerodynamic responses to the characteristic motions obtained from experimental measurements, is currently the only approach available.

In this lecture, we review the basic concepts involved in the mathematical modeling of the instantaneous aerodynamic response of the aircraft to an arbitrary maneuver. In the light of the previous discussion, we focus on the treatment of time-history effects, showing, via an historical account, how the subject has evolved from the original contribution of Bryan<sup>2</sup> through our own contributions.<sup>3,4</sup> In Lecture 16 (Ref. 5) we shall take up the subject again, where we investigate the applicability of the modeling concepts reviewed here. For the case of the unconstrained motions of a flap on an airfoil in transonic flow, we show that the modeling approach adequately accommodates aerodynamic time-history effects in comparison with the exact accommodation afforded by the coupled-equations approach.<sup>6</sup> We then demonstrate how our most recent formulation, which accommodates aerodynamic hysteresis phenomena, can be applied to clarify the interpretation of the results of experimental investigations of the wing-rock problem.<sup>7</sup>

## 2. COORDINATE SYSTEMS

Three coordinate systems will be used. They have a common origin at the body's mass center and a common axis  $x_B$  aligned with a longitudinal axis of the body.

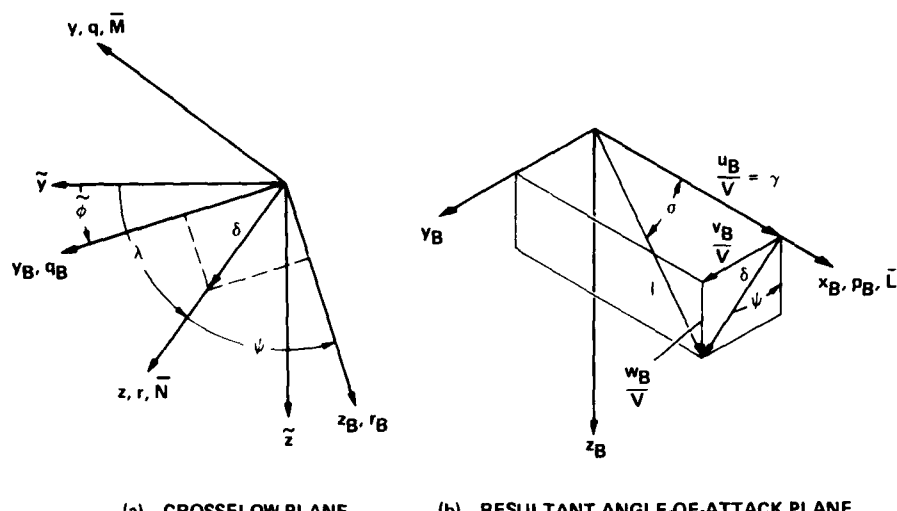
Axes  $x_B, y_B, z_B$  are body-fixed axes (Fig. 3). The flight velocity vector of magnitude  $V$  has components  $u_B, v_B, w_B$  resolved along  $x_B, y_B, z_B$ , respectively. Thus,

$$V = \sqrt{u_B^2 + v_B^2 + w_B^2} \quad (1)$$

Resultant angle of attack  $\alpha$  is defined by the flight velocity vector and the  $x_B$  axis. The plane formed by  $y_B, z_B$  is called the crossflow plane, illustrated in Fig. 3(a). The projection of a unit vector in the flight velocity direction onto the crossflow plane is a vector with magnitude  $\delta$ ; it will be called the (dimensionless) crossflow velocity vector. Reference to Fig. 3(b) gives

$$\left. \begin{aligned} \delta &= \sqrt{\left(\frac{v_B}{V}\right)^2 + \left(\frac{w_B}{V}\right)^2} = \sin \alpha \\ \gamma &= \frac{u_B}{V} = \cos \alpha \\ \epsilon &= \frac{\delta}{\gamma} = \tan \alpha \end{aligned} \right\} \quad (2)$$

The components of the body's angular velocity relative to inertial space, resolved along  $x_B, y_B, z_B$ , are  $p_B, q_B, r_B$ , respectively.



(a) CROSSFLOW PLANE (b) RESULTANT ANGLE-OF-ATTACK PLANE

Figure 3. Axes, angles, and velocity components in the crossflow and resultant angle-of-attack planes.

A second axis system  $x_B, \bar{y}, \bar{z}$  is nonrolling with respect to inertial space. Specifically, the  $x_B, \bar{y}, \bar{z}$  axes have an angular velocity with respect to inertial space whose component resolved along the  $x_B$  axis is zero, while the components resolved along  $\bar{y}, \bar{z}$  are  $\dot{q}, \dot{r}$ , respectively. The angle  $\phi$  through which the body axes have rolled at any time  $t$  can be defined relative to the nonrolling axis system as

$$\phi = \int_0^t p_B d\tau \quad (3)$$

The angular inclination  $\lambda$  of the crossflow velocity vector  $\delta$  is measured relative to the nonrolling axis system, while  $\psi$  is the angular inclination of the body axes from the crossflow velocity vector. With the aid of Fig. 3(a), the body roll rate is seen to be

$$\dot{p}_B = \dot{\lambda} + \dot{\psi} \quad (4)$$

The components  $p_B, \dot{q}, \dot{r}$  of the body's angular velocity vector resolved in the nonrolling axis system are related to those in the body axis system  $p_B, q_B, r_B$  through

$$\dot{q} + i\dot{r} = e^{i\phi}(q_B + ir_B) \quad (5)$$

Finally, an axis system  $x_B, y, z$  will be called the aerodynamic axis system. Axis  $z$  lies in the crossflow plane and is aligned with the direction of  $\delta$ ; axis  $y$  lies in the crossflow plane aligned with a direction normal to the direction of  $\delta$ . The components of the body's angular velocity resolved in the aerodynamic axis system  $p_B, q, r$  are related to those resolved in the body axis system through

$$q + ir = e^{i\psi}(q_B + ir_B) \quad (6)$$

It will be noted (cf. Fig. 3(b)) that  $\delta$  and  $\psi$  are no more than the polar coordinates of the dimensionless velocities  $w_B/V$  and  $v_B/V$  in the body axis system. Let  $w_B/V$  be called the angle-of-attack parameter  $\alpha$  and  $v_B/V$  the angle-of-sideslip parameter  $\beta$ ;  $\alpha$  and  $\beta$  are related to the standard NASA definitions of angle of attack  $\alpha$  and angle of sideslip  $\beta$  through

$$\left. \begin{aligned} \tan \alpha &= w_B/u_B = \hat{\alpha}/\gamma \\ \sin \beta &= v_B/V = \hat{\beta} \end{aligned} \right\} \quad (7)$$

and to  $\delta$  and  $\psi$  through

$$\hat{\alpha} + i\hat{\beta} = \delta e^{i\psi} \quad (8)$$

The components of the aerodynamic force coefficient resolved along the body axes  $x_B, y_B, z_B$  are  $\hat{c}_x, \hat{c}_y, \hat{c}_z$ , respectively, while the corresponding components of the aerodynamic moment coefficient (about the mass center) are  $\hat{c}_l, \hat{c}_m, \hat{c}_n$ , respectively. Analogously, the components of the force and moment coefficients resolved along the aerodynamic axes  $x_B, y, z$  are  $c_x, c_y, c_z$  and  $c_l, c_m, c_n$ , respectively. Components of the aerodynamic moment coefficient resolved in the aerodynamic axis system are related to those resolved in the body axis system through

$$\left. \begin{aligned} C_l &= \hat{C}_l \\ C_m + iC_n &= e^{i\psi} (\hat{C}_m + i\hat{C}_n) \end{aligned} \right\} \quad (9)$$

Corresponding relations between the components of the aerodynamic force coefficient are obtained by replacing  $l, m, n$  by  $X, Y, Z$ , respectively, in Eq. (9).

To completely describe the state of a six-degree-of-freedom motion of a rigid body, it is necessary to specify the velocity and angular velocity vectors of the body. These may be expressed in terms of their scalar components resolved in the body-fixed axes  $u_B, v_B, w_B, p_B, q_B, r_B$ , or equivalently by  $\dot{\alpha}, \dot{\beta}, V, p_B, q_B, r_B$ . Analogously, in the aerodynamic axis system the motion is specified by the scalar variables  $\delta, \psi, V, p_B, q, r$ , or by  $\delta, \psi, V, \lambda, q, r$ , since  $p_B$  is related to  $\psi$  and  $\lambda$  through Eq. (4). These are the principal variables on which the aerodynamic force and moment formulation must depend in general, although, as will be seen, certain simplifications are possible in special cases.

### 3. AERODYNAMIC MODELING OF PLANAR MOTIONS

In order to simplify the discussion in the following work we impose several (removable) restrictions. The aircraft is considered to be a rigid body which, for a long time prior to time zero, has been in steady flight. At time zero the aircraft begins to execute an arbitrary maneuver, during which its velocity along the flight path remains constant. During the course of the maneuver the excursions of the aircraft's altitude are small enough that atmospheric properties, such as density and temperature, can be considered constant. Hence flight-path properties such as dynamic pressure, Mach number, and Reynolds number remain constant throughout the maneuver. Under these restrictions a general motion is described in terms of variables in the body-fixed axis system by  $\dot{\alpha}, \dot{\beta}, p_B, q_B, r_B$ . In terms of variables in the aerodynamic axis system, the motion is described by  $\delta, \psi, \lambda, q, r$ .

To focus directly on the basic concepts underlying aerodynamic modeling, we first eliminate consideration of all but two of the motion variables by restricting the analysis to a general planar motion of a symmetric aircraft. The analysis is extended to a general nonplanar motion in a later section. In a planar motion  $v_B = 0, p_B = r_B = 0$  and the aerodynamic and body-fixed axes coincide. Consequently  $\psi = 0$ ,  $\delta = \dot{\alpha}$ ,  $\sigma = \alpha$ , and  $\lambda = r = 0$ . As a result of the aircraft's bilateral symmetry about the angle-of-attack plane  $C_y = \hat{C}_y = 0, C_l = \hat{C}_l = 0$ , and  $C_n = \hat{C}_n = 0$ . Thus a general planar motion referred to the body-axis system is completely described by the variables  $\dot{\alpha}$  and  $q_B$ , while in the aerodynamic axis system the motion is described by the variables  $\delta$  and  $q$ . The simplified coordinates for planar motions, described in terms of variables in the aerodynamic axis system, are illustrated in Fig. 4.

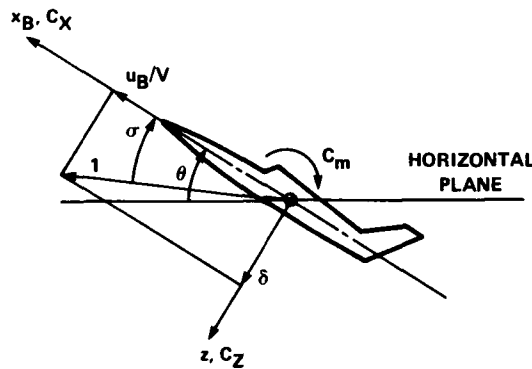


Figure 4. Aerodynamic axis system and notation for planar motion.

#### 3.1 Equations of Motion

The inertial equations governing the planar motion of the aircraft can be written with respect to an observer fixed in the body as

$$\left. \begin{aligned} \dot{\delta}(t) &= \gamma(t)q(t) + \frac{g}{V} \cos \theta(t) + \frac{\rho V^2 S}{2m} C_Z(t) \\ \dot{q}(t) &= \frac{\rho V^2 S Z}{2I} C_m(t) \end{aligned} \right\} \quad (10)$$

Equations (10) comprise a set of coupled, first-order nonlinear equations for the motion variables  $\delta$  and  $q$ . In Eqs. (10)  $\theta(t)$  denotes the instantaneous pitch angle of the aircraft's  $x_B$  axis above the horizontal reference plane (Fig. 4). If we are given knowledge of the state of the motion at a specified time instant  $t_0$ , that is, if we are given  $\delta(t_0), q(t_0)$ , and  $\theta(t_0)$ , we must be able to evaluate the right hand sides of Eqs. (10) in order to determine the state of the motion at the succeeding time instant  $t_0 + \Delta t$ . In particular, since the motion variables are specified, the only terms which remain unknown are the instantaneous normal-force and pitching-moment coefficients,  $C_Z(t)$  and  $C_m(t)$ . The specification of a form from which the instantaneous aerodynamic coefficients may be evaluated constitutes the problem of mathematical modeling.

### 3.2 Historical Development of Mathematical Modeling

Although earlier efforts of Lanchester (Ref. 8, 1908) helped focus attention on the phugoid motions of aircraft, the foundations of aerodynamic mathematical modeling, as commonly applied, originated with the work of Bryan (Ref. 2). Bryan's formulation is based on two principal assumptions: First, the instantaneous aerodynamic force and moment depend only on the instantaneous values of the motion variables (here  $\delta$  and  $q$ ). Second, the aerodynamic force and moment vary only linearly with the motion variables. Thus, the first assumption allows writing (e.g.)  $C_m(t)$  as a function

$$C_m(t) = C_m(\delta(t), q(t)) \quad (11)$$

while the second assumption allows expanding Eq. (11) in a Taylor series about a reference state  $\delta = 0$ ,  $q = 0$ , and retaining only linear terms of the expansion. In Bryan's formulation, therefore, the instantaneous aerodynamic pitching-moment coefficient would be represented as

$$C_m(t) = C_{m_0} + \delta(t) \left( \frac{\partial C_m}{\partial \delta} \right)_{\substack{q=0 \\ \delta=0}} + q(t) \frac{z}{V} \left( \frac{\partial C_m}{\partial (qz/V)} \right)_{\substack{q=0 \\ \delta=0}} \quad (12)$$

The analogous form for the instantaneous normal-force coefficient  $C_z$  is obtained by replacing  $m$  by  $z$  in Eq. (12). The dimensionless partial derivatives appearing in Eq. (12) are time-invariant quantities and are referred to as *stability derivatives*. Each of the stability derivatives is associated with a *steady* flow field from which it may be evaluated. Thus  $C_{m_\delta} \equiv \partial C_m / \partial \delta$  is the slope of the static pitching-moment coefficient curve, evaluated at  $\delta = 0$ , with  $q$  held fixed at zero. The remaining term,  $C_{m_q} \equiv \partial C_m / \partial (qz/V)$  is commonly referred to as a *rotary derivative*. It is defined as the change in the pitching-moment coefficient with pitch-rate parameter  $qz/V$ , evaluated at  $q = 0$  (with  $\delta$  held fixed at zero), that would be present in a *steady* pitching maneuver. This is the classical "whirling-arm" maneuver, in which the mass center of the aircraft describes a circle at constant rate  $q$  about a fixed point in the angle-of-attack plane. Of the two principal assumptions in Bryan's formulation, the first, that  $C_m(t)$  is a function of  $\delta(t)$  and  $q(t)$ , has by far the more serious implications. It is this assumption that makes a model based on Eq. (12) a quasi-steady model, one which is unable to acknowledge any effects that the past history of the motion may have on the instantaneous aerodynamic reactions.

In the years following the publication of Bryan's analysis, researchers in flight dynamics realized that the presence of the horizontal tail caused a significant time lag in the response of the aerodynamic pitching moment to a change in the aircraft's angle of attack. The time lag is essentially the time interval required for a change in the wing downwash, generated in response to a change in the angle of attack, to be convected downstream to the vicinity of the tail. To be precise, determination of the effect of the time lag on the aerodynamic reactions would require the solution of an unsteady flow-field problem. However, by an appropriate averaging, the main aerodynamic contribution resulting from the time lag could be determined from the tail's aerodynamic response to an equivalent steady flow (cf. Ref. 9). When applied to the slowly varying motions of aircraft this analysis results in the appearance of an aerodynamic contribution proportional to the time-rate-of-change of the angle of attack. Thus, to acknowledge the aerodynamic contribution of the tail due to time-lag effects within the quasi-steady linear moment expansion, Eq. (12) must be rewritten as

$$C_m(t) = C_{m_0} + \delta(t) C_{m_\delta} + q(t) \frac{z}{V} C_{m_q} + \dot{\delta}(t) \frac{z}{V} C_{m_\delta} \quad (13)$$

It is important to note that the addition of a term proportional to  $\dot{\delta}$ , while required on the basis of observations, violated the notion that the stability derivatives were partial derivatives, since  $\delta$  and  $\dot{\delta}$  are not independent quantities. As will be seen later, the fault lay not in the additional term, but in Bryan's first assumption that  $C_m(t)$  could be written as a function of the instantaneous motion variables. The form of Eq. (13), with its unfortunate suggestion that mathematically incorrect expansions were permissible, has been the source of considerable confusion over the intervening years.

Improvement of the aerodynamic mathematical model at this stage of its development (about 1940) was hampered by the lack of an underlying unified theory. Aerodynamic terms such as  $C_{m_\delta}$  had been added in an ad hoc manner as needed to overcome demonstrated deficiencies of the model. The unifying concept was supplied through the introduction of methods for solving the nonsteady linearized potential form of the gasdynamic equations. Investigators concerned with flutter, in particular, obtained solutions for the nonsteady flow fields of wings performing harmonic oscillations. Other researchers obtained solutions for the aerodynamic responses of wings to step changes in the motion variables, that is, for linear aerodynamic indicial responses (cf. Ref. 10 for an extensive bibliography covering both methods). Results of the computations demonstrated the existence of significant time lags in the aerodynamic harmonic and indicial responses of even isolated wings and thereby (among other things) led to the establishment of a firm theoretical basis for including a term proportional to  $\dot{\delta}$  within the aerodynamic mathematical model.

From the standpoint of mathematical modeling, exploiting the concept of a linear indicial response was an important step, since it showed how the aerodynamic response to an arbitrary motion could be generated from a small number of aerodynamic indicial responses by the use of superposition integrals. It is from this idea that the modeling approach derives its economy in the treatment of time-history effects. Further, the use of the superposition integral overcame in a concise way the principal objectionable assumption of Bryan's model, now allowing  $C_m(t)$  to depend not only on the instantaneous values of the motion variables, but also on their past values. Mathematically speaking, expressing  $C_m(t)$  in the form of the linear superposition integral was a replacement of Bryan's function by a linear functional. The idea of a functional, as it turned out later, was the key to extending the linear form into the nonlinear regime. Tobak (Ref. 11) used the indicial response concept to study the nonsteady motions of wings and

wing-tail combinations. In that work he demonstrated the equivalence between the linear indicial-response approach, when applied to slowly varying motions, and the linear stability-derivative and harmonic-response approaches. More recently, in a series of papers (Refs. 12-17), Tobak and his colleagues have used concepts from functional analysis to generalize the linear notions and extend them into the nonlinear regime. In the following sections we shall review the notion of an aerodynamic indicial response and of superposition, and show how these concepts have been extended to model the nonlinear aerodynamics of maneuvering aircraft (Refs. 14-17). Further, we discuss the types of flow-field computations or wind-tunnel measurements required to obtain the aerodynamic information specified by the models.

### 3.3 Linear Integral Aerodynamic Pitching-Moment Response

At time zero the aircraft begins a planar maneuver during which the angle-of-attack parameter  $\delta$  and the pitching velocity  $q$  vary. For brevity, attention is focused solely on the aerodynamic pitching moment. All that is said, however, will hold as well for any other of the force or moment components that may exist merely on the substitution of that component for  $C_m$ .

Consider the aerodynamic pitching-moment response to the variations in  $\delta$  and  $q$ . It is usually admissible to break the variations into a large number of small step changes (cf. Fig. 5). In response to typical step changes  $\Delta\delta$  and  $\Delta(qz/V)$  at time  $\tau$ , there is an incremental change in pitching moment  $\Delta C_m$ ; it is measured at a fixed time  $t$  subsequent to  $\tau$ . The assumption of linearity is now invoked, having, in the context of this discussion, the following meaning:  $\Delta C_m$  is said to be independent of  $\delta(\tau)$ ,  $q(\tau)$ , and on all values that these variables have taken over the course of the motion prior to time  $\tau$ . This enables writing  $\Delta C_m$  in the form

$$\Delta C_m(t) = \frac{\Delta C_m(t - \tau)}{\Delta\delta} \Delta\delta + \frac{\Delta C_m(t - \tau)}{\Delta(qz/V)} \Delta(qz/V) \quad (14)$$

The form implies that  $\Delta C_m/\Delta\delta$  and  $\Delta C_m/\Delta(qz/V)$  are derivable from solutions of linear gasdynamic equations. That they depend on elapsed time  $t - \tau$ , rather than on  $t$  and  $\tau$  separately implies that the parameters within the gasdynamic equations are independent of time. It is important to note the following distinction: the significance of the linearity assumption does not rest on the assertion that  $\Delta C_m$  is linearly dependent on  $\Delta\delta$  and  $\Delta(qz/V)$ , or that the contributions to  $\Delta C_m$  from the two increments are linearly additive. Both of these assertions are always justified whenever  $\Delta\delta$  and  $\Delta(qz/V)$  are so small that terms of  $O((\Delta\delta)^2)$ ,  $(\Delta qz/V)^2$ ,  $(\Delta\delta\Delta qz/V)$  can be neglected. The significance of the assumption lies in saying that the two ratios are independent of  $\delta$  and  $q$ . Thus, no matter how large the values of  $\delta$  and  $q$  at the origins of the steps and regardless of the history of the motion prior to the steps, the response functions  $\Delta C_m/\Delta\delta$  and  $\Delta C_m/\Delta(qz/V)$  are said to be the same functions, dependent only on  $t - \tau$ . The limits of these functions as  $\Delta\delta$  and  $\Delta(qz/V)$  approach zero

$$\left. \begin{aligned} \lim_{\Delta\delta \rightarrow 0} \frac{\Delta C_m(t - \tau)}{\Delta\delta} &= C_{m_\delta}(t - \tau) \\ \lim_{\Delta(qz/V) \rightarrow 0} \frac{\Delta C_m(t - \tau)}{\Delta(qz/V)} &= C_{m_q}(t - \tau) \end{aligned} \right\} \quad (15)$$

are called the linear indicial pitching-moment responses per unit step changes in  $\delta$  and  $qz/V$ , respectively. Every pair of steps in  $\delta$  and  $qz/V$  beginning at an instant of time prior to  $t$  has a corresponding incremental pitching-moment response (of the form of Eq. (14)) that contributes to the pitching moment at time  $t$ . The summation of these incremental responses to the steps that occur over the time interval from zero to  $t$  then gives the aerodynamic pitching-moment response at time  $t$  to the variations in  $\delta$  and  $q$ . As the indicial responses depend only on the time difference  $t - \tau$ , in the limit the summations take the form of the familiar convolution integral. The sum of the two integral contributions and the initial value of  $C_m$  then give the total pitching moment at time  $t$

$$C_m(t) = C_m(0) + \int_0^t C_{m_\delta}(\tau) \frac{d}{dt} \delta(\tau) d\tau + \frac{z}{V} \int_0^t C_{m_q}(\tau) \frac{d}{dt} q(\tau) d\tau \quad (16)$$

For constant  $V$  and within the assumption of linearity, the integral form, Eq. (16) is exact. Although the linear indicial responses are independent of the past history of the motion prior to the origin of the steps, all values of  $\delta$  and  $q$  figure within the limits of the integrals. Consequently,  $C_m$  at time  $t$  depends on the whole past of  $\delta$  and  $q$ .

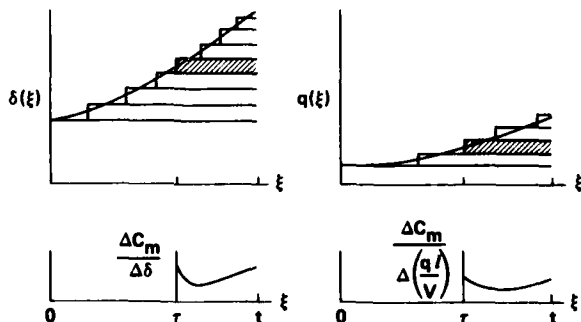


Figure 5. Summation of incremental responses.

### 3.4 Definition of a Functional

The description of  $C_m(t)$  as a function that depends on all of the past values of the argument functions  $\delta$  and  $q$  corresponds mathematically to Volterra's description of a functional (Ref. 18). If Volterra's square-bracket notation is adopted, the assertion that  $C_m(t)$  is a functional is indicated thus,

$$C_m(t) = G[\delta(\xi), q(\xi)] \quad (17)$$

where it is understood that  $\xi$  is a running variable in time, ranging over the interval zero to  $t$ .

In brief, just as an ordinary function  $f(x)$  assigns a number to each  $x$  for which it is defined, a functional  $F[y(\xi)]$  assigns a number to each function  $y(\xi)$  of the set of functions (all of which are defined in some interval  $a \leq \xi \leq b$ ) for which the functional is defined. Thus, Eq. (17) may be interpreted as follows: given any pair of functions  $\delta(\xi), q(\xi)$  out of the collection of all such pairs defined in the interval  $0 \leq \xi \leq t$ , the functional  $G$  assigns a number to  $C_m(t)$ . It is the idea of a functional, with its formal recognition of the influence of past events on present behavior, that provides the key to generalizing the linear integral form.

### 3.5 Nonlinear Aerodynamic Pitching-Moment Response

An heuristic argument will show how the most general linear form for the aerodynamic response  $C_m(t)$  to a planar motion (Eq. (16)) can be freed of the linearity assumption. A more rigorous mathematical development yielding the same result is available in Ref. 12.

Attention is directed to the incremental form for  $\Delta C_m(t)$ , Eq. (14), where the principal limitation imposed by the linearity assumption first appears. As already noted, this limitation does not hinge on the assertion that  $\Delta C_m(t)$  is linearly dependent on  $\Delta\delta$  and  $\Delta(q/V)$ , or that the two incremental contributions are linearly additive. Both of these assertions remain in force in the more general development. The limitation is simply that the indicial responses are said to be independent of the past values of  $\delta$  and  $q$ . Now, as described more precisely below, an indicial response to a step change in a motion is formed by taking a difference between the responses to two motions whose histories differ only by the step imposed on the second motion. Hence, the motions prior to the step are identical. When the difference is taken in the linear case, the influence of this identical past cancels identically. In the absence of linearity, exact cancellation of the influence of the past motion is not to be expected, so that some remnant of that influence must be evidenced in the behavior of the indicial response. That is to say, the indicial response must be a functional. The way to eliminate the limitation of the linearity assumption in Eq. (14) thus becomes clear: replace the indicial functions by functionals, themselves dependent on values of  $\delta$  and  $q$  prior to the origin of the steps. That this replacement can be rigorously justified is, in fact, the principal result of the mathematical development in Ref. 12.

If the notation already introduced for a functional is followed, the designation of the indicial responses as functionals is indicated thus,

$$\left. \begin{aligned} \lim_{\Delta\delta \rightarrow 0} \frac{\Delta C_m(t, \tau)}{\Delta\delta} &= C_{m_\delta}[\delta(\xi), q(\xi); t, \tau] \\ \lim_{\Delta(q/V) \rightarrow 0} \frac{\Delta C_m(t, \tau)}{\Delta(q/V)} &= C_{m_q}[\delta(\xi), q(\xi); t, \tau] \end{aligned} \right\} \quad (18)$$

where, as before,  $t$  is the time at which the increment  $\Delta C_m$  is measured,  $\tau$  is the time at which the steps originate, and  $\xi$  is a running variable in time over the interval zero to  $\tau$ ; that is, over the past for steps beginning at  $\xi = \tau$ .

Although the replacement of the indicial functions by functionals appears to be largely a matter of notation, the change is far-reaching and, for example, requires a more precise description of the formation of indicial responses than was necessary in the linear case. Two motions have to be considered (cf. Fig. 6). First, beginning at  $\xi = 0$ , the aircraft is made to execute the motion under study  $\delta(\xi), q(\xi)V$ . At a

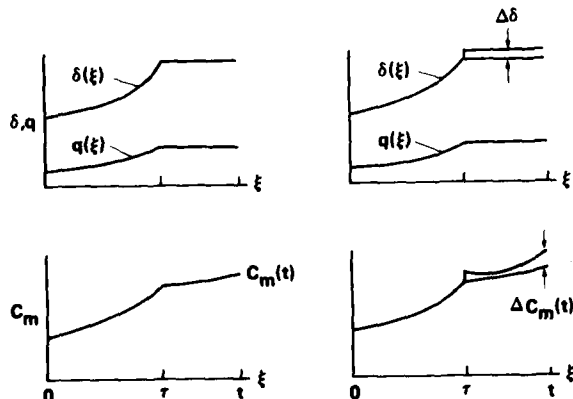


Figure 6. Formation of indicial responses.

certain time,  $\tau$ , the motion is constrained such that the values of the flight variables existent at time  $\tau$ , that is,  $\delta(\tau)$ ,  $q(\tau)z/V$  remain constant thereafter. The pitching moment corresponding to this maneuver is measured at a time  $t$ , subsequent to  $\tau$ . Second, the aircraft is made to execute precisely the same motion, beginning at  $\xi = 0$  and constrained in the same way at  $\xi = \tau$ , except that at the latter time, one of the variables  $\delta$  or  $qz/V$  is given an incremental step  $\Delta\delta$  or  $\Delta(qz/V)$  over its value at  $\xi = \tau$ . Hence, if it is  $\delta$  that is given an increment  $\Delta\delta$ , the values of the flight variables for all times subsequent to  $\tau$  are  $\delta(\tau) + \Delta\delta$  and  $q(\tau)z/V$ . The pitching moment corresponding to this maneuver is again measured at time  $t$ . The difference between the two measurements is divided by the magnitude of the incremental step  $\Delta\delta$  or  $\Delta(qz/V)$ . The limit of this ratio as the magnitude of the step approaches zero is called the indicial pitching-moment response at time  $t$  per unit step at time  $\tau$  of one of the two flight variables  $\delta$  or  $qz/V$ . As indicated in Fig. 6, since the two motions prior to  $\xi = \tau$  are identical, the ratio must be identically zero for all  $\xi < \tau$ . At  $\xi = \tau$ , a discontinuity in the ratio is permissible, reflecting the discontinuous change in one of the motion variables. For all values of  $\xi > \tau$ , the ratio must be continuous.

Formed as described above and as defined in Eq. (18), the indicial responses are suitably generalized to be free of dependence on a linearity assumption. With Eq. (18) replacing Eq. (15) in Eq. (14), the summation of incremental responses to yield an integral form for  $C_m(t)$  follows as before. The resulting generalization of Eq. (16) is

$$C_m(t) = C_m(0) + \int_0^t C_{m_\delta}[\delta(\xi), q(\xi); t, \tau] \frac{d}{d\tau} \delta(\tau) d\tau + \frac{z}{V} \int_0^t C_{m_q}[\delta(\xi), q(\xi); t, \tau] \frac{d}{d\tau} q(\tau) d\tau \quad (19)$$

Equation (19), applicable to a planar motion involving arbitrary variations in  $\delta$  and  $q$ , is believed to be of sufficient generality to provide a framework for the study of a wide variety of nonlinear aerodynamic problems. Derivation of the integral forms corresponding to motions involving more than two variables follows simply by an application of the same formalism. In the next section, simplifying approximations are introduced in Eq. (19) which make the form more practicable at the price of narrowing the classes of aerodynamic behavior that can be acknowledged within its scope.

### 3.6 Limitations and Simplification of the Nonlinear Integral Form

Conditions that flight-path properties remain constant during the motion and that the aircraft be a rigid body have been imposed at the outset. Imposing constant flight-path properties excludes from consideration the influence on motions of very large changes in flight velocity or variations in atmospheric density, such as might occur, for example, during atmospheric reentry. Omitting structural variables rules out the possibility of treating the buffeting and flutter problems, which involve interactions between the elastic airframe and random aerodynamic fluctuations. However, these limitations are not inherent in the development of the nonlinear integral form, and can be relaxed as needed. For example, upon providing for the elastic deformation of the aircraft, the nonlinear integral form can be extended to yield a framework for the treatment of flutter problems governed by nonlinear aerodynamic responses. The presence of fluctuations themselves can be acknowledged within the framework already established by adopting the notion of ensemble averaging (cf. Ref. 17). The remaining assumptions are of two main classes: first, fundamental assumptions associated with the use of functional analysis to develop the general integral form for the aerodynamic response; second, simplifying assumptions associated with the reduction of the general integral form to more practicable forms.

#### 3.6.1 Fundamental assumptions

Despite their generality, the nonlinear indicial responses defined by Eq. (18), and hence the corresponding integral form for the aerodynamic pitching moment, Eq. (19), already contain implicit assumptions that limit their applicability. These are principally that the indicial responses must exist for all values of their arguments (for  $\xi > \tau$ ) and must be unique. The nonexistence of an indicial response follows the nonexistence of its steady-state value. Thus, assuming the existence of the indicial responses for all values of their arguments (that is, for  $\xi > \tau$ ) implies the exclusion of cases in which the variation of the steady-state pitching moment with  $\delta$  (at  $q = 0$ ) becomes discontinuous in either its magnitude or slope at certain isolated values of  $\delta$ . At these points the limit of the ratio  $\Delta C_m(\infty)/\Delta\delta$ , taken as  $\Delta\delta \rightarrow 0$ , will not exist. Such cases are known to characterize certain types of stall behavior (cf. for example Ref. 19). An analogous discontinuous response of the steady-state rolling moment to variations in the roll angle  $\psi$  has been observed (Refs. 20,21) on aircraft models at angles of attack close to stall. This phenomenon is believed to be caused by an asymmetric breakdown of the leeward vortex flow. Although this aerodynamic behavior can be modeled by an appropriate addition of jump conditions at the isolated points, for simplicity consideration of such discontinuities will be withheld until Section 5.

The assumption of uniqueness implies the exclusion of cases where more than one steady-state response to the same maneuver is possible. More precisely, cases must be excluded where the steady-state responses to repetitions of the same maneuver can be multi-valued and probabilistic. An example of aerodynamic behavior that must be excluded on this basis is the steady asymmetric vortex flow above a body of revolution at large  $\delta$  when it is a matter of chance whether the vortices form a left-hand or a right-hand pattern. In Section 5 the assumptions of existence and uniqueness are redefined to permit the modeling of flight phenomena in which the steady-state values of the aerodynamic response exhibit the discontinuous, double-valued behavior characteristic of hysteresis. Given these fundamental limitations on the applicability of the general integral form for  $C_m(t)$ , Eq. (19), simplifying assumptions still need to be attached in order to reduce it to more usable forms.

#### 3.6.2 Simplifying assumptions

In the form Eq. (19) the indicial responses within the integrals are themselves functionals, depending in general on the whole past history of the motion  $\delta(\xi), q(\xi)$ . This makes the further use of the form exceedingly difficult, since the history of the motion normally is not known in advance but rather is desired as the solution of the equations of motion. Thus, when the past history is unspecified, the

functionals also are unknown beforehand. Simplification of Eq. (19) hinges on replacing the functionals by appropriate functions whose dependence on the past is denoted by a limited number of parameters rather than by continuous functions. If  $\delta(\xi), q(\xi)$  can be considered analytic functions in a neighborhood of  $\xi = \tau$  (corresponding to the most recent past for an indicial response with origin at  $\xi = \tau$ ), their histories can be reconstructed, in principle, from a knowledge of all of the coefficients of their Taylor series expansions about  $\xi = \tau$ . Thus, since  $\delta(\xi), q(\xi)$  are equally represented by the coefficients of their expansions, the functional, with its dependence on  $\delta(\xi), q(\xi)$ , can be replaced without approximation by a function which depends on all of the coefficients of the expansions of  $\delta(\xi), q(\xi)$  about  $\xi = \tau$ . The indicial response  $C_{m_\delta}$ , for example, can be expressed as

$$C_{m_\delta}[\delta(\xi), q(\xi); t, \tau] = C_{m_\delta}(t, \tau; \delta(\tau), \dot{\delta}(\tau), \dots, q(\tau), \dot{q}(\tau), \dots) \quad (20)$$

Now physical reasoning suggests that, in general, the indicial response should have "forgotten" long-past events and thus should depend mainly on events which have occurred within the most recent past. If this is assumed to be true, then so far as the effect of the past on the indicial response is concerned, the form of the past motion just prior to the origin of the step might just as well have existed for all earlier times. Hence, at most only the first few coefficients of the expansions of  $\delta(\xi), q(\xi)$  need be retained to characterize correctly the most recent past, which is all the indicial response remembers. Retaining the first two coefficients of  $\delta(\xi)$ , for example, implies matching the true past history of  $\delta$  in magnitude and slope at the origin of the step, thereby approximating  $\delta(\xi)$  by a linear function of time  $\delta(\xi) \approx \delta(\tau) - \delta(\tau)(\tau - \xi)$ . With an approximation of this order in force for both  $\delta(\xi)$  and  $q(\xi)$  in the indicial responses, the integral form replacing Eq. (19) becomes

$$\begin{aligned} C_m(t) = C_m(0) + \int_0^t C_{m_\delta}(t, \tau; \delta(\tau), \dot{\delta}(\tau), q(\tau), \dot{q}(\tau)) \frac{d}{d\tau} \delta(\tau) d\tau \\ + \frac{1}{V} \int_0^t C_{m_q}(t, \tau; \delta(\tau), \dot{\delta}(\tau), q(\tau), \dot{q}(\tau)) \frac{d}{d\tau} q(\tau) d\tau \end{aligned} \quad (21)$$

This form, while considerably more tractable than Eq. (19), is still sufficiently general to allow the treatment of motions involving rate-dependent hysteresis effects. Retaining a dependence on  $\delta(\tau)$ , for example, allows assigning different indicial responses to a step at a single pair of values  $\delta(\tau), q(\tau)$ , depending on the magnitude and sign of  $\dot{\delta}(\tau)$ . It is permissible, for example, to distinguish between indicial responses where  $\delta$  was increasing or decreasing prior to the step. Although implications of the use of Eq. (21) will not be explored further in this lecture, the equation is believed to be both tractable enough and of sufficient scope to provide a framework for the study of rapidly varying maneuvers (e.g., the rapid pull-up), where hysteresis effects governed by rate-dependent flow phenomena are known to be present in the aerodynamic response.

When rate-dependent hysteresis effects are absent, and if, additionally, the assumption of a slowly varying motion is introduced, then the dependence of the indicial responses on  $\delta(\tau), q(\tau)$  will not be significant (cf. Fig. 7). So far as the indicial responses are concerned, omitting these dependencies in Eq. (21) implies that the motion prior to the origin of the steps is being approximated by the time-invariant motion  $\delta(\xi) \approx \delta(\tau), q(\xi) \approx q(\tau)$ . The indicial responses at any value of elapsed time, now

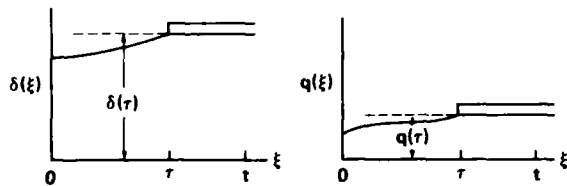


Figure 7. Slowly varying motions.

dependent only on the magnitudes of  $\delta$  and  $q$  just prior to the steps, must not only be continuous functions of  $\delta(\tau), q(\tau)$ , but henceforward also single-valued functions of  $\delta(\tau), q(\tau)$ . Further, with a given time-invariant past motion and with the already assumed constant flight-path properties, clearly an indicial response must have the same value after a given time has elapsed subsequent to the origin of a step no matter when the step occurs. That is, just as in the linear case, the indicial response must be a function of elapsed time  $t - \tau$  rather than of  $t$  and  $\tau$  separately. Finally, then, for slowly varying motions and with the additional restriction on the indicial responses of single-valuedness with respect to  $\delta(\tau), q(\tau)$ , and  $t - \tau > 0$ , a much more specific form of Eq. (19) may be written, still capable of embracing a fairly broad range of nonlinear aerodynamic problems. It is

$$C_m(t) = C_m(0) + \int_0^t C_{m_\delta}(t - \tau; \delta(\tau), q(\tau)) \frac{d}{d\tau} \delta(\tau) d\tau + \frac{1}{V} \int_0^t C_{m_q}(t - \tau; \delta(\tau), q(\tau)) \frac{d}{d\tau} q(\tau) d\tau \quad (22)$$

Although the form of Eq. (22) represents a great simplification over that of Eq. (19), the equation still includes the full linear form (Eq. (16)) as a special case. Equation (22) is the basic integral form underlying the subsequent simplified formulations.

### 3.7 Application of the Simplified Nonlinear Integral Form to Dynamic Stability Studies

Equation (22) is now applied to the study of aircraft dynamic stability. The rigid-body motions of aircraft are normally oscillatory, and moreover, the oscillations are generally of very low frequency. Several analytical benefits accrue from the latter fact. First, since the motions are slowly varying, the assumptions underlying Eq. (22) are particularly well grounded in this application. Second, Eq. (22) can be further simplified. The simplification, which in effect reduces Eq. (22) to an equation correct to the first order in frequency, parallels that realized in the linear case in the application of Eq. (16) to stability studies.<sup>11</sup>

#### 3.7.1 Stability coefficient formulation

The reduction of Eq. (22) to first order in frequency is carried out in detail so that, later, the analogous reduction of the more lengthy equations for nonplanar motions will need only to be indicated in passing. Equation (22) is first rearranged to give a more convenient form. From physical considerations, the indicial responses must approach steady-state values with increasing values of the argument  $t - \tau$ . To indicate this, the following notation is introduced (the notation parallels that of Ref. 11):

$$\left. \begin{aligned} C_{m_\delta}(t - \tau; \delta(\tau), q(\tau)) &= C_{m_\delta}(\infty; \delta(\tau), q(\tau)) - F_3(t - \tau; \delta(\tau), q(\tau)) \\ C_{m_q}(t - \tau; \delta(\tau), q(\tau)) &= C_{m_q}(\infty; \delta(\tau), q(\tau)) - F_4(t - \tau; \delta(\tau), q(\tau)) \end{aligned} \right\} \quad (23)$$

where  $C_{m_\delta}(\infty; \delta(\tau), q(\tau))$  is the rate of change with  $\delta$  of the pitching-moment coefficient that would be measured in a steady flow, evaluated at the instantaneous value of  $\delta(\tau)$  with  $q$  fixed at the instantaneous value  $q(\tau)$ . Similarly,  $C_{m_q}(\infty; \delta(\tau), q(\tau))$  is the rate of change with  $q$  of the pitching-moment coefficient that would be measured in a steady flow, evaluated at the instantaneous value  $q(\tau)$  with  $\delta$  fixed at the instantaneous value  $\delta(\tau)$ . The functions  $F_3$  and  $F_4$  are termed deficiency functions; they tend to vanish with increasing values of the argument  $t - \tau$ . When Eqs. (23) are inserted in Eq. (22), the terms involving the steady-state parameters form a perfect differential which can be immediately integrated. Thus, Eq. (22) becomes

$$\begin{aligned} C_m(t) &= C_m(\infty; \delta(t), q(t)) - \int_0^t F_3(t - \tau; \delta(\tau), q(\tau)) \frac{d}{d\tau} \delta(\tau) d\tau \\ &\quad - \frac{1}{V} \int_0^t F_4(t - \tau; \delta(\tau), q(\tau)) \frac{d}{d\tau} q(\tau) d\tau \end{aligned} \quad (24)$$

where  $C_m(\infty; \delta(t), q(t))$  is the total pitching-moment coefficient that would be measured in a steady flow with  $\delta$  fixed at the instantaneous value  $\delta(t)$  and  $q$  fixed at the instantaneous value  $q(t)$ .

Equation (24) is a form of Eq. (22) particularly amenable to approximation. We have already restricted the motion under consideration to be slowly varying when restricting the deficiency functions  $F_3$  and  $F_4$  to depend only on  $\delta(\tau)$  and  $q(\tau)$ . Let it be assumed for illustration that the angle-of-attack parameter  $\delta$  and the pitch angle  $\theta$  are essentially slowly varying harmonic oscillations about constant mean values. That is

$$\begin{aligned} \delta &\approx \delta_m + \delta_1 e^{i\omega t} \\ \theta &\approx \theta_m + \theta_1 e^{i\omega t} \end{aligned} \quad (25)$$

Clearly, since  $q = \dot{\theta}$ ,  $q$  itself will be of first order in frequency  $\omega$ . Hence  $q$  will be small for all values of time, and powers of  $q$  higher than the first will be of second and higher orders in frequency. Therefore, for any given values of  $t$  or  $\tau$ , it is permissible to expand the terms in Eq. (24) in a Taylor series about  $q = 0$  and to discard terms containing powers of  $q$  higher than the first. Terms in  $\dot{q}$  and  $\ddot{q}$  likewise may be discarded as they will be of second order in frequency. The result of the expansion is

$$C_m(t) = C_m(\infty; \delta(t), 0) + q(t) \frac{1}{V} C_{m_q}(\infty; \delta(t), 0) - \int_0^t F_3(t - \tau; \delta(\tau), 0) \frac{d}{d\tau} \delta(\tau) d\tau \quad (26)$$

Definitions of  $C_m(\infty; \delta(t), 0)$  and  $C_{m_q}(\infty; \delta(t), 0)$  follow from those given earlier with the substitution of  $q(t) = 0$ . The first two terms are clearly the nonlinear counterparts of the terms  $\delta C_{m_\delta}$  and  $(q/V)C_{m_q}$  that appear in linear analyses based on the stability derivative concept (Eq. (13)). Therefore, the integral, when also reduced to the first order in frequency, is anticipated to be the nonlinear counterpart of the term  $(\dot{\delta}/V)C_{m_\delta}$ . This reduction is taken up next.

With the change in variable  $t - \tau = \tau_1$ , the integral becomes

$$I = \int_0^t F_3(\tau_1; \delta(t - \tau_1), 0) i\omega \delta_1 e^{i\omega(t-\tau_1)} d\tau_1 \quad (27)$$

which may be rewritten

$$I = \delta(t) \int_0^t F_3(\tau_1; \delta(t - \tau_1), 0) e^{-i\omega\tau_1} d\tau_1 \quad (28)$$

Practically speaking, the deficiency function essentially vanishes after a relatively short period of time has elapsed. Let the value of  $\tau_1$  at which  $F_3$  essentially vanishes be  $t_a$ , and consider events at a time  $t$  sufficiently removed from the start of the motion that  $t > t_a$ . Then the upper limit in Eq. (28) may be replaced by  $t_a$ , whereupon, with  $\tau_1$  bounded and  $\omega$  small, the harmonic function may be expanded in powers of  $\omega$ . Since  $\delta$  is itself of first order in  $\omega$ , however, only the first term in the expansion, unity, contributes within the order of the approximation. Moreover, with respect to the parameter  $\delta(t - \tau_1)$ , a further simplification can be realized when the condition  $t > t_a$  is invoked, for then  $\delta(t - \tau_1) \approx \delta(t)$ . The integral reduces to

$$I = \frac{\dot{\delta}(t) \zeta}{V} \left( V \int_0^{t_a} F_3(\tau_1; \delta(t), 0) d\tau_1 \right) \quad (29)$$

where, as anticipated, the integral term within parentheses may be identified with  $-C_{m\delta}$ .

Hence, just as in the linear case,<sup>11</sup> to the first order in frequency  $C_{m\delta}$  is proportional to the area of the deficiency function, now, however, evaluated at and dependent on the particular value of the angle-of-attack parameter  $\delta(t)$  under consideration. The nonlinear counterpart of the linear stability derivative formulation Eq. (13) thus becomes

$$C_m(t) = C_m(\omega; \delta(t), 0) + q(t) \frac{V}{\zeta} C_{m_q}(\omega; \delta(t), 0) + \dot{\delta}(t) \frac{V}{\zeta} C_{m\delta}(\delta(t)) \quad (30)$$

where

$$C_{m\delta}(\delta(t)) = -\frac{V}{\zeta} \int_0^{t_a} F_3(\tau_1; \delta(t), 0) d\tau_1$$

### 3.7.2 Evaluation of stability coefficients

Each term in Eq. (30) is associated with a characteristic motion from which it may be determined. The term  $C_m(\omega; \delta(t), 0)$  is the pitching-moment coefficient that would be evaluated in a steady flow with the angle-of-attack parameter held fixed at a value equal to the (possibly large) instantaneous flight value  $\delta(t)$ , and with the pitch rate  $q$  held fixed at 0. The nonlinear behavior with  $\delta$  of the static aerodynamic reactions of an aircraft are basic to the behavior of the vehicle in both steady and nonsteady motion, and much effort is expended in their evaluation for a new configuration. Both experimental programs and computational programs are undertaken to obtain the static aerodynamic reactions. Experimentally, the steady flow is merely that surrounding a wind-tunnel model at fixed angle of attack. From the standpoint of computation, the time-invariance of this flow permits the elimination of the time variable from the gas-dynamic equations, and the employment of numerical techniques especially suited to the steady form of the equations.

The second term in Eq. (30),  $C_{m_q}(\omega; \delta(t), 0)$  can also be determined from a steady flow. The term is defined as the rate of change of the pitching-moment coefficient with pitch rate  $q$ , evaluated at  $q = 0$ , that would be measured in a steady flow with  $\delta$  held fixed at  $\delta(t)$ . The characteristic motion defining this flow is illustrated in Fig. 8a. Experimentally, this flow can be generated by fixing the model to the

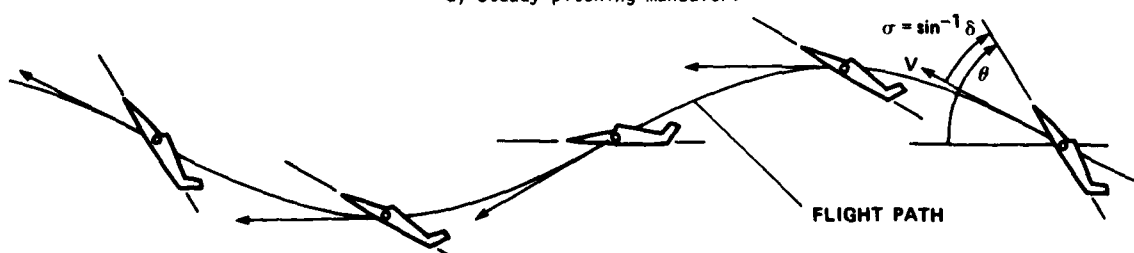
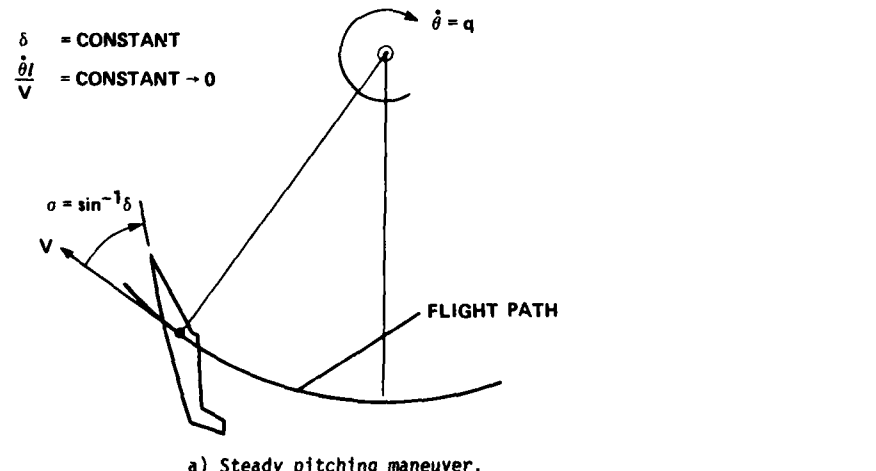


Figure 8. Definitive motions for the evaluation of  $C_{m_q}(\omega; \delta, 0)$ .

end of an arm which is caused to rotate at a fixed rate about a point. The whirling-arm experiment is rarely undertaken in view of the difficulties arising from the presence of interference between the model and its own wake. From the computational standpoint, an evaluation of  $C_{m\dot{q}}$  again can be based on a steady form of the gasdynamic equations. To an observer fixed in the moving body the flow field surrounding the aircraft in the whirling-arm maneuver is time-invariant. Consequently, it should be easy to extend the computational methods developed for solving the nonlinear flow-field problem for steady angle of attack to the steady curved-flow problem for arbitrary fixed values of  $q$ . Given a set of such solutions (all obtained at a fixed value of  $\delta$ ), taking their rate of change with respect to  $q$  at  $q = 0$  yields  $C_{m\dot{q}}(\infty; \delta(t), 0)$ .

An alternative characteristic motion from which  $C_{m\dot{q}}$  may be evaluated, one which is, in principle, more amenable to simulation in a wind-tunnel experiment, is the snaking motion illustrated in Fig. 8b. In this motion the aircraft performs a sinusoidal oscillation in pitch angle  $\theta$ , while the angle-of-attack parameter  $\delta$  remains constant. The component of the unsteady periodic aerodynamic moment response that is 90° out of phase with the time-history of the pitch angle is proportional to  $C_{m\dot{q}}(\infty; \delta, 0)$ . Experimental devices for simulating the snaking motion of an aircraft model in a wind tunnel and measuring the attendant nonsteady aerodynamic response have been constructed. Details of the devices are surveyed in the lectures of other authors within this lecture series.

The remaining term in Eq. (30),  $C_{m\ddot{\delta}}(\delta(t))$  is evaluated from an oscillations-in-plunge motion. In this motion, as illustrated in Fig. 9, the angle-of-attack parameter undergoes a small-amplitude harmonic oscillation about a mean value, which may be large. The pitch angle  $\theta$  remains constant, so that  $q = \dot{\theta} = 0$  throughout the maneuver. The unsteady aerodynamic moment response to this motion can be represented in terms of its Fourier components, one in phase and one 90° out of phase with the time-history of  $\delta$ . The component in phase with  $\delta$  is proportional to the local slope of the static pitching-moment curve; the out-of-phase component is proportional to  $C_{m\dot{\delta}}(\delta(t))$ . Experimental devices for generating the oscillations-in-plunge motion in a wind tunnel exist and are reviewed in this lecture series. The flow field generated in the oscillations-in-plunge maneuver is truly nonsteady. From the computational standpoint, simulation of this flow field for the nonlinear case would require evaluation of the full time-dependent gasdynamic equations. Such computations are not as yet feasible for fully three-dimensional flow fields. However, several computations have been carried out (e.g., Refs. 22-24) to obtain the nonsteady two-dimensional flow fields surrounding airfoils performing oscillations in plunge at transonic Mach numbers.

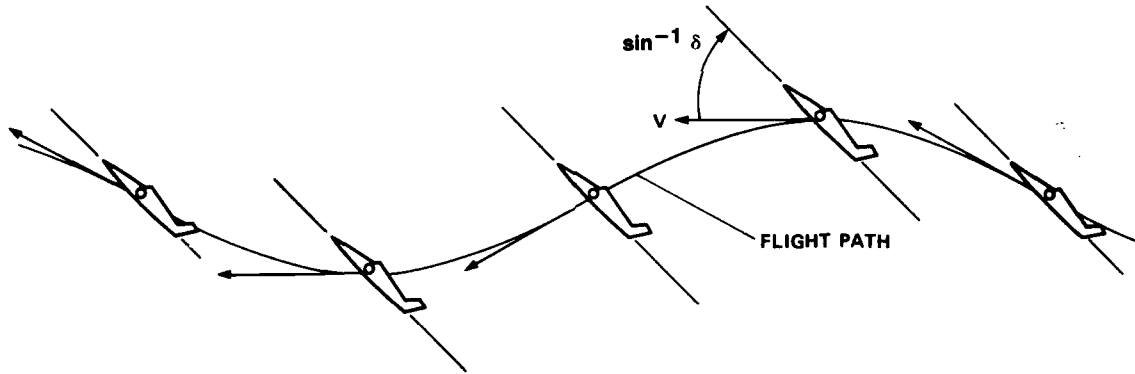


Figure 9. Oscillations-in-plunge motion defining  $C_{m\ddot{\delta}}(\delta)$ .

The need for a separate determination of  $C_{m\dot{q}}$  and  $C_{m\ddot{\delta}}$  from snaking and plunging oscillatory motions can be eliminated when the aircraft's center of mass travels in an essentially rectilinear path. In this case the unsteady contribution to the aerodynamic response can be determined from a single characteristic motion. This can be easily seen by rewriting Eq. (30) in the form

$$\begin{aligned} C_m(t) = & C_m(\infty; \delta(t), 0) + \dot{\delta}(t) \frac{L}{V} [C_{m\dot{q}}(\infty; \delta(t), 0) + \gamma C_{m\ddot{\delta}}(\delta(t))] \\ & + [\dot{q}(t) - \dot{\delta}(t)] \frac{L}{V} C_{m\dot{q}}(\infty; \delta(t), 0) \end{aligned} \quad (31)$$

The last term vanishes identically for the case of rectilinear motion ( $q = \dot{\delta}$ ) and therefore, may be neglected when the departures from a rectilinear flight path are small. The remaining nonsteady term  $(C_{m\dot{q}} + \gamma C_{m\ddot{\delta}})$  is recognized as the planar damping-in-pitch coefficient. It is determined from a characteristic motion, illustrated in Fig. 10, in which the aircraft performs small-amplitude angular oscillations in  $\sigma$  about a value of  $\delta$  held fixed at the instantaneous value  $\delta(t)$  (recall that  $\delta = \sin \sigma$ ). An experimental simulation of this motion corresponds to an oscillations-in-pitch experiment in the wind tunnel in which the model's mass center remains fixed. Computationally, the requirements for the evaluation of the combination  $(C_{m\dot{q}} + \gamma C_{m\ddot{\delta}})$  are analogous to those needed for the evaluation of  $C_{m\ddot{\delta}}$  alone.

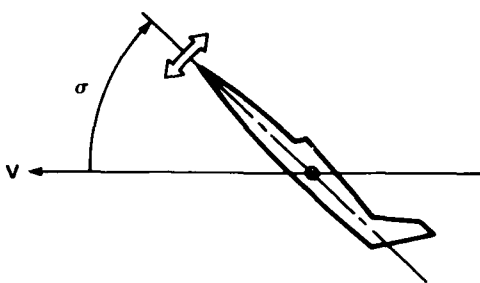


Figure 10. Oscillations-in-pitch motion defining  $C_{m_q}(\infty; \delta, 0) + \gamma C_{m_\delta}(\delta)$  for rectilinear flight paths.

### 3.7.3 Physical interpretation of $C_{m_\delta}$

Computation of the steady flow field surrounding a simple three-dimensional body, and thus of the steady nonlinear aerodynamic response, is barely attainable with the currently available electronic computers. The increased capability that will be needed to compute the nonsteady flow fields, from which the corresponding stability coefficients may be determined, awaits future technological developments. Consequently, in this section we discuss some of the physical features of the indicial response and of the integral form for  $C_{m_\delta}$  which might assist in making at least order-of-magnitude estimates of that term.

The two-dimensional wing is chosen for demonstration purposes since the important features of sound-wave propagation are easily illustrated in this case. A subsonic flight speed is specified since, for subsonic flow, many of the results for the linear indicial response do not require modification in principle and thus can be adapted to guide the drawing of a physical picture of the nonlinear indicial response. By means of these adaptations, the results may have more general bearing. Consider the boundary conditions corresponding to a step change in the angle-of-attack parameter  $\delta$  imposed at  $\tau_1 = 0$ , where the flight speed  $V$  is subsonic. Let the wing move away from a coordinate system that is fixed in space at the position of the mass center at time  $\tau_1 = 0$  where the step change in the boundary conditions occurs (cf. Fig. 11).

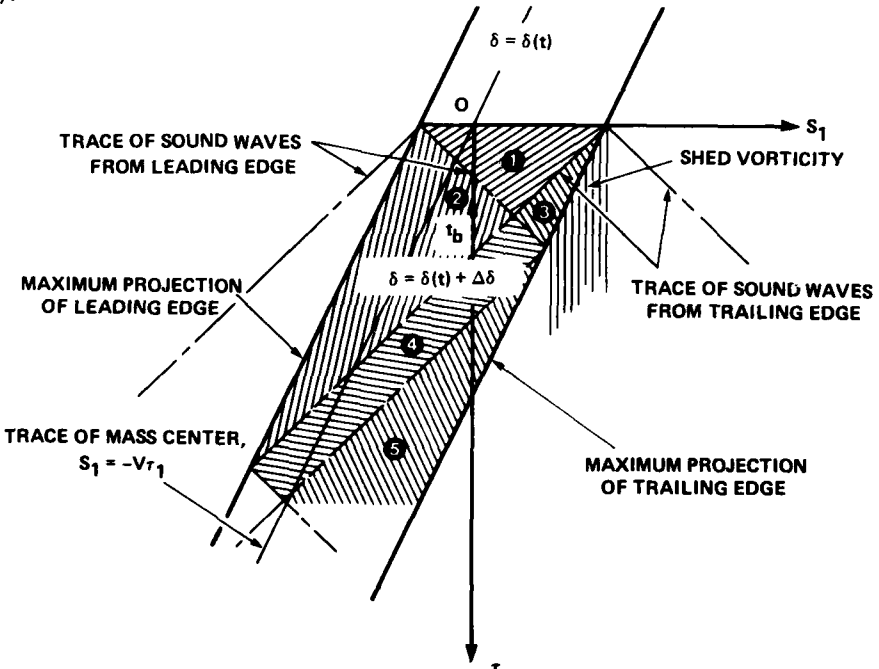


Figure 11. Boundary conditions for indicial loading.

The distance traveled by the mass center along the flight path is measured by a coordinate  $s_1$ . Since the mass center moves at constant speed, the trace of its path plotted against time  $\tau_1$  is a straight line. This is shown in Fig. 11, where the maximum projections of the leading and trailing edges are also shown, parallel to the trace of the mass center. For  $\tau_1 < 0$ , the angle-of-attack parameter  $\delta$  is constant at  $\delta(t)$ . A step change in  $\delta$  occurs at  $\tau_1 = 0$ , so that for  $\tau_1 \geq 0$ , the angle-of-attack parameter is  $\delta(t) + \Delta\delta$ . Due to the impulsive change in  $\delta$ , the loading on the wing at  $\tau_1 = 0$  also undergoes a sudden change. The physical situation at this instant corresponds essentially to that described by piston theory (cf., for example, Ref. 25), which should give a reasonably accurate estimate of the initial change in loading. Reflecting the local character of the instantaneous response, the initial change in loading is essentially constant across the chord, so that the corresponding center of pressure is located very near the mid-chord. Also at  $\tau_1 = 0$ , the sudden change in flow conditions causes disturbances to be propagated from every point on the chord line. Of particular importance are those from the leading and trailing edges. Each disturbance is propagated at the local speed of sound, so that, on a plot such as shown in Fig. 11, the

zone of its influence is bounded by projections of an approximately conic surface whose origin is the point of the disturbance. As shown in Fig. 11, traces of the waves from the edges divide the wing into a number of distinct regions. Points in region (1) have not yet been made aware of the changed conditions at the leading and trailing edges by the arrival of the sound waves, and hence the loading in this region remains essentially unchanged from that existent at  $\tau_1 = 0$  (cf. Fig. 12). This loading gradually disappears as

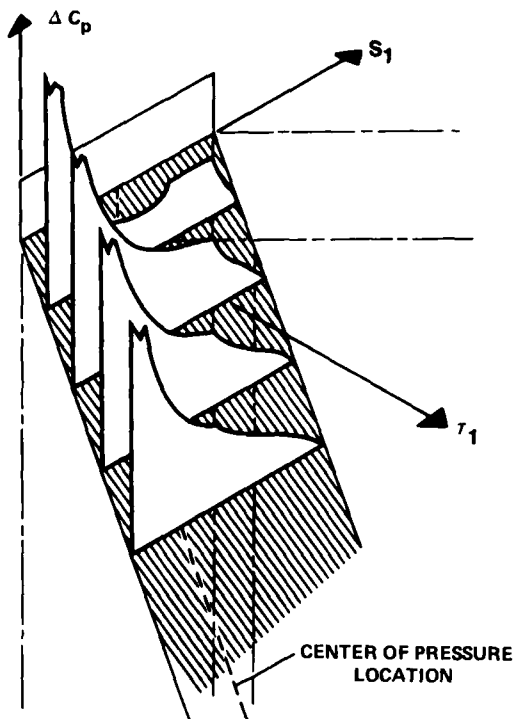


Figure 12. Indicial loading on two-dimensional wing at subsonic speed.

the propagation of the two sound waves announces the new conditions to increasing portions of the wing, and it disappears completely at  $\tau_1 = t_b$ . Points in region (2) have been made aware of new conditions at the leading edge but are as yet unaware of changed conditions at the trailing edge. The reverse is true for points in region (3). Points in region (4) have become aware of changes at both the leading and trailing edges, whereas points in region (5) in addition have become aware of the reflection from the trailing edge of the initial wave from the leading edge. Not long after the first reflection, the loading on the wing has essentially assumed the form of its ultimate steady-state loading (Fig. 12) and only its amplitude increases thereafter with increasing  $\tau_1$ , asymptotically approaching the steady-state amplitude. Therefore, as shown in Fig. 12, the center of pressure has essentially reached its steady-state position while the loading is still increasing in amplitude. The above behavior suggests breaking the indicial pitching-moment function into two separate contributions as shown in Fig. 13. The first variation represents the pitching-moment contribution of the integrated loading in region (1). Accordingly, it begins with the value  $C_{m\delta}(0; \delta(t), 0)$  and vanishes at  $\tau_1 = t_b$ . The second variation reflects the lumped contributions of the integrated loadings in the remaining regions; in conformity with the loading, its initial value is zero while its end value, essentially attained at  $\tau_1 = t_a$ , is  $C_{m\delta}(\infty; \delta(t), 0)$ . The sum of the two contributions is the indicial pitching-moment function  $C_{m\delta}(\tau_1; \delta(t), 0)$ . The end values of the two contributions are evidenced explicitly by introducing the normalized functions  $f_1$  and  $f_2$  as shown in the figure. This enables writing the indicial response in the form

$$C_{m\delta}(\tau_1; \delta(t), 0) = C_{m\delta}(0; \delta(t), 0)f_1(\tau_1; \delta(t)) + C_{m\delta}(\infty; \delta(t), 0)f_2(\tau_1; \delta(t)) \quad (32)$$

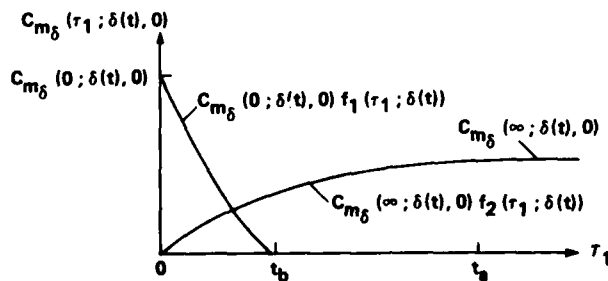


Figure 13. Breakdown of indicial response.

where  $f_1$  and  $f_2$  vary within the limits zero and unity. Then the deficiency function  $F_3$  is

$$F_3(\tau_1; \delta(t), 0) = C_{m_\delta}(\infty; \delta(t), 0) [1 - f_2(\tau_1; \delta(t))] - C_{m_\delta}(0; \delta(t), 0) f_1(\tau_1; \delta(t)) \quad (33)$$

so that the integral for  $C_{m_\delta}$  takes the form

$$\frac{1}{V} C_{m_\delta}(\delta(t)) = C_{m_\delta}(0; \delta(t), 0) \int_0^{t_b} f_1(\tau_1; \delta(t)) d\tau_1 - C_{m_\delta}(\infty; \delta(t), 0) \int_0^{t_a} [1 - f_2(\tau_1; \delta(t))] d\tau_1 \quad (34)$$

Equation (34) clearly shows the strong dependence of  $C_{m_\delta}$  on the steady-state parameter  $C_{m_\delta}(\infty; \delta(t), 0)$ . Further, the sign relation evidenced in Eq. (34) should be noted. Since the integral involving  $f_2$  normally will be positive, the equation indicates that as  $C_{m_\delta}(\infty; \delta(t), 0)$  becomes more negative (i.e., statistically more stable),  $C_{m_\delta}$  becomes more positive (i.e., dynamically more unstable).

Since  $f_1$  and  $f_2$  are normalized functions, cases are anticipated where their dependence on  $\delta$  will not be significant. For example, the process of arriving at the form Eq. (34) suggests that it might be reasonably accurate to use the linear theory as a basis for estimating  $f_1$  and  $f_2$ , in which case they would not show a dependence on  $\delta$ . In such cases, the integrals in Eq. (34) become constants. When it can be further assumed that  $C_{m_\delta}(0; \delta(t), 0)$  is also independent of  $\delta$ , the expression for  $C_{m_\delta}$  takes the simple form

$$C_{m_\delta}(\delta(t)) = A + BC_{m_\delta}(\infty; \delta(t), 0) \quad (35)$$

Despite differences in detail in the formation of the individual indicial responses, the representations of  $C_{m_\delta}$  given in Eqs. (34) and (35) should find applications to other more general categories of wings and bodies.

#### 4. NONPLANAR MOTIONS

The treatment of nonplanar motions raises the question of the role played by coupling in a nonlinear formulation. By coupling is meant the following: in the analysis of, for example, a combined pitching and yawing motion, the linearity assumption (i.e., indicial responses independent of the past motion) allows the vector decomposition of the nonplanar motion into two orthogonal planar motions, the treatment of each planar motion as though the other were absent, and finally superposition of the separate results. In the nonlinear regime, where the indicial responses depend on all the variables of the past motion, the aerodynamic response to motion in one plane clearly will be influenced by the presence of the other motion. That influence is what is meant by coupling; the role assigned to it by the nonlinear formulation is studied in the sections to follow.

For simplicity, flight-path properties, including flight velocity, are again assumed to remain constant throughout the motion, so that a general motion involves five independent variables. These are taken to be the components of the aircraft's flight velocity and angular velocity resolved either in the aerodynamic axis system ( $\delta, \psi, \lambda, q, r$ ) or in the body axis system ( $\dot{\alpha}, \dot{\beta}, p_B, q_B, r_B$ ). Having established the general integral form for the aerodynamic response to a motion involving two variables (Eq. (19)), extending it to five variables is formal and requires no additional explanation. The general integral forms are assumed to have been derived and simplified in accordance with the same simplification invoked in the analysis of the planar motions; namely, that the indicial responses within the integrals, initially functionals, have been replaced by functions dependent only on the magnitude of the past motion just prior to the origin of the steps. The analysis begins, then, with simplified integral forms analogous to the form applicable to planar motion, Eq. (22).

##### 4.1 Approximate Formulation in the Aerodynamic Axis System

As noted above, the aerodynamic force and moment components resolved in the aerodynamic axis system are assumed to depend on the five variables  $\delta, \psi, \lambda, q, r$ . For example, the pitching-moment coefficient  $C_m(t)$  is specified as a functional of the form

$$C_m(t) = G[\delta(\xi), \psi(\xi), \lambda(\xi), q(\xi), r(\xi)] \quad (36)$$

The simplified integral form analogous to that of Eq. (22) thus contains five integrals, one for each variable. The indicial functions within the integrals depend on  $t - \xi$  and the magnitudes of the five variables just prior to the origin of the steps. Just as in the planar case, the integrals can be further simplified for slowly varying motions by reducing them to forms correct to the first order in frequency, assuming that  $\delta$  and  $\psi$  may be large but that the angular rates  $\lambda, q, r$  remain small. If the procedure illustrated for the planar case (Eqs. (23)-(30)) is followed, an expansion of the integrals about  $\lambda = 0, q = 0, r = 0$  yields, to first order in the rates, a sum of stability coefficients. The result is

$$C_m(t) = C_m(\infty; \delta(t), \psi(t)) + \frac{iZ}{V} C_{m_\lambda}(\infty; \delta(t), \psi(t)) + \frac{qZ}{V} C_{m_q}(\infty; \delta(t), \psi(t)) + \frac{rZ}{V} C_{m_r}(\infty; \delta(t), \psi(t)) \\ + \frac{\dot{\delta}Z}{V} C_{m_\delta}(\delta(t), \psi(t)) + \frac{\dot{\psi}Z}{V} C_{m_\psi}(\delta(t), \psi(t)) \quad (37)$$

where, as before, the infinity symbol indicates steady flow. For brevity the zeros belonging to  $\lambda, q, r$  have been omitted. Analogous expressions for  $C_x$  and  $C_n$  and the axial-, side-, and normal-force coefficients  $C_x, C_y, C_z$  are obtained by substituting these coefficients wherever  $C_m$  appears in Eq. (37).

#### 4.2 Simplification of the Formulation in the Aerodynamic Axis System

Just as in the planar case (Eq. (31)), an additional simplification of Eq. (37) can be achieved by invoking the conditions of an almost rectilinear flight path. The conditions require, as before,  $q \approx \dot{\sigma}$ , and, in addition,  $r \approx \epsilon\lambda$ . Adding and subtracting the terms  $(\dot{\sigma}Z/V)C_{m_q}$  and  $\epsilon(\lambda Z/V)C_{m_r}$  and rewriting Eq. (37) yields

$$\begin{aligned} C_m(t) = & C_m(\infty; \delta(t), \psi(t)) + \frac{\dot{\psi}Z}{V} C_{m_\psi}(\delta(t), \psi(t)) + \frac{\dot{\sigma}Z}{V} [C_{m_q}(\infty; \delta(t), \psi(t)) + \gamma C_{m_\delta}(\delta(t), \psi(t))] \\ & + \frac{1}{Y} \frac{\dot{\lambda}Z}{V} [YC_{m_\lambda}(\infty; \delta(t), \psi(t)) + \delta C_{m_p}(\infty; \delta(t), \psi(t))] \\ & + (q - \dot{\sigma}) \frac{Z}{V} C_{m_q}(\infty; \delta(t), \psi(t)) + (r - \epsilon\lambda) \frac{Z}{V} C_{m_r}(\infty; \delta(t), \psi(t)) \end{aligned} \quad (38)$$

The last two terms vanish identically when the flight path is precisely rectilinear, and so may be neglected when departures from a rectilinear flight path are small. The remaining terms are identified by comparing them with those obtained when the flight path is precisely rectilinear, where exactly,  $q = \dot{\sigma}$ ,  $r = \dot{\delta}\phi$ ,  $\lambda = \gamma\phi$ , and  $\dot{\phi}$  is the coning rate of the longitudinal axis around the flight velocity vector. The result is

$$\left. \begin{aligned} C_{m_\sigma} &= C_{m_q} + \gamma C_{m_\delta} \\ C_{m_\phi} &= \gamma C_{m_\lambda} + \delta C_{m_p} \end{aligned} \right\} \quad (39)$$

Each of the terms in Eq. (38) is associated with a particular motion from which it may be determined. The term  $C_m(\infty; \delta(t), \psi(t))$  is the pitching-moment coefficient that would be evaluated in a steady planar motion with  $\delta$  and  $\psi$  at the fixed inclinations  $\delta = \text{const}$ ,  $\psi = \text{const}$ . The term  $C_{m_\psi}$  is the contribution to the pitching-moment coefficient due to roll oscillations that would be evaluated for small-amplitude oscillations in  $\psi$  about  $\psi = \text{const}$  with  $\delta = \text{const}$  and  $\dot{\phi}$  fixed at zero. The term  $C_{m_\sigma}$  is, as before, the contribution to the pitching-moment coefficient due to pitch oscillations that would be evaluated for small-amplitude planar oscillations in  $\sigma$  about a mean, evaluated now, however, with both  $\delta$  and  $\psi$  at the fixed inclinations  $\delta = \text{const}$ ,  $\psi = \text{const}$ . The term  $C_{m_\phi}$  is the rate of change with coning-rate parameter  $\dot{\phi}Z/V$ , evaluated at  $\dot{\phi} = 0$ , of the pitching-moment coefficient that would be determined from a steady coning motion,  $\delta = \text{const}$ ,  $\psi = \text{const}$ ,  $\dot{\phi} = \text{const}$ . Thus, coning motion emerges as one of the characteristic motions required in constructing the response to an arbitrary nonplanar motion.

In summary, with terms multiplied by  $(q - \dot{\sigma})$  and  $(r - \epsilon\lambda)$  neglected, the aerodynamic force and moment system takes the form

$$\begin{aligned} C_k(t) = & C_k(\infty; \delta(t), \psi(t)) + \frac{\dot{\psi}Z}{V} C_{k_\psi}(\delta(t), \psi(t)) \\ & + \frac{\dot{\sigma}Z}{V} C_{k_\sigma}(\delta(t), \psi(t)) + \frac{\dot{\lambda}Z}{Y} \frac{1}{V} C_{k_\lambda}(\infty; \delta(t), \psi(t)) ; \quad k = \{X, Y, Z \\ & , m, n\} \end{aligned} \quad (40)$$

Equation (40) suggests that, for nearly rectilinear flight paths, the forces and moments due to an arbitrary motion may be compounded of the contributions from four simple motions: steady resultant angle of attack, oscillations in roll and pitch at constant resultant angle of attack, and coning at constant resultant angle of attack, all at a constant inclination of the body axes from the crossflow velocity vector. The motions are illustrated schematically in Fig. 14.

#### 4.3 Approximate Formulation in the Body Axis System

The aerodynamic force and moment components resolved in the body axis system are assumed to depend on the five variables  $\hat{\alpha}$ ,  $\hat{\beta}$ ,  $p_B$ ,  $q_B$ ,  $r_B$ . For example, the pitching-moment coefficient  $\hat{C}_m(t)$  is said to be a functional of the form

$$\hat{C}_m(t) = H[\hat{\alpha}(t), \hat{\beta}(t), p_B(t), q_B(t), r_B(t)] \quad (41)$$

The reduction of the integral form based on Eq. (41) parallels those of the preceding sections. Expanded about  $p_B = 0$ ,  $q_B = 0$ ,  $r_B = 0$ , the integral form for  $\hat{C}_m(t)$  yields, to first order in the rates

$$\begin{aligned} \hat{C}_m(t) = & \hat{C}_m(\infty; \hat{\alpha}(t), \hat{\beta}(t)) + \frac{p_B Z}{V} \hat{C}_{m_{p_B}}(\infty; \hat{\alpha}(t), \hat{\beta}(t)) + \frac{q_B Z}{V} \hat{C}_{m_{q_B}}(\infty; \hat{\alpha}(t), \hat{\beta}(t)) \\ & + \frac{r_B Z}{V} \hat{C}_{m_{r_B}}(\infty; \hat{\alpha}(t), \hat{\beta}(t)) + \frac{\dot{\hat{\alpha}}Z}{V} \hat{C}_{m_{\dot{\alpha}}}(\hat{\alpha}(t), \hat{\beta}(t)) + \frac{\dot{\hat{\beta}}Z}{V} \hat{C}_{m_{\dot{\beta}}}(\hat{\alpha}(t), \hat{\beta}(t)) \end{aligned} \quad (42)$$

where the zeros belonging to  $p_B$ ,  $q_B$ ,  $r_B$  have been omitted. Analogous expressions for  $\hat{C}_x$ ,  $\hat{C}_y$ ,  $\hat{C}_z$  and the axial-, side-, and normal-force coefficients  $\hat{C}_x$ ,  $\hat{C}_y$ ,  $\hat{C}_z$  are obtained by substituting these coefficients wherever  $\hat{C}_m$  appears in Eq. (42).

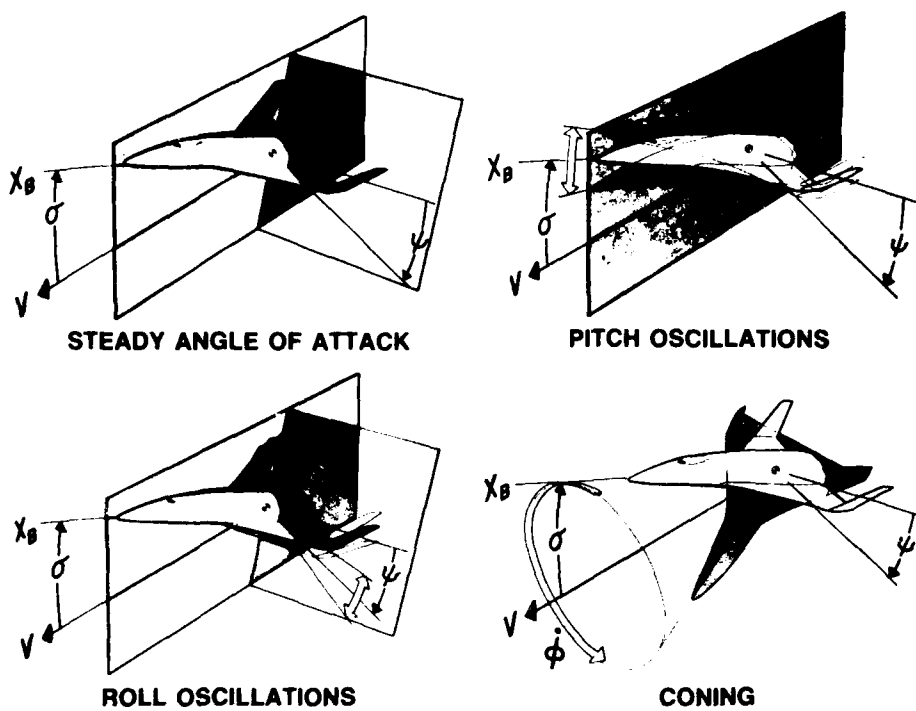


Figure 14. Characteristic motions in the aerodynamic axis system. Linear dependence on angular rates.

#### 4.4 Simplification of the Formulation in the Body Axis System

When the assumption of a nearly rectilinear flight path is justified, Eq. (42) can be simplified to yield a form analogous to that of Eq. (38) in the aerodynamic axis system. The approximate expressions for  $q_B$  and  $r_B$ , consistent with  $q \approx \dot{\alpha}$ ,  $r \approx \epsilon\dot{\lambda}$ , are

$$\left. \begin{aligned} q_B &\approx \frac{\dot{\alpha}}{V} + p_B \frac{\dot{\beta}}{V} \\ r_B &\approx -\frac{\dot{\beta}}{V} + n_B \frac{\dot{\alpha}}{V} \end{aligned} \right\} \quad (43)$$

Substituting in Eq. (42) gives

$$\begin{aligned} \hat{C}_m(t) = & \hat{C}_m(\omega; \hat{\alpha}, \hat{\beta}) + \frac{1}{V} \frac{p_B^2}{V} \left[ \gamma \hat{C}_{m_{p_B}}(\omega; \hat{\alpha}, \hat{\beta}) + \hat{\beta} \hat{C}_{m_{q_B}}(\omega; \hat{\alpha}, \hat{\beta}) + \hat{\alpha} \hat{C}_{m_{r_B}}(\omega; \hat{\alpha}, \hat{\beta}) \right] \\ & + \frac{1}{V} \frac{\dot{\alpha}^2}{V} \left[ \hat{C}_{m_{q_B}}(\omega; \hat{\alpha}, \hat{\beta}) + \gamma \hat{C}_{m_{\alpha}}(\hat{\alpha}, \hat{\beta}) \right] - \frac{1}{V} \frac{\dot{\beta}^2}{V} \left[ \hat{C}_{m_{r_B}}(\omega; \hat{\alpha}, \hat{\beta}) - \gamma \hat{C}_{m_{\beta}}(\hat{\alpha}, \hat{\beta}) \right] \end{aligned} \quad (44)$$

Again, each of the terms in Eq. (44) is associated with a particular motion from which it can be determined. The first term is the pitching-moment coefficient along  $y_B$  that would be evaluated in steady planar motion with  $\dot{\alpha}$  and  $\dot{\beta}$  at the fixed inclinations  $\hat{\alpha} = \text{const}$ ,  $\hat{\beta} = \text{const}$ . The combination of terms multiplied by  $p_B^2/V^2$  can be shown to be the rate of change with coning-rate parameter  $\dot{\phi}^2/V$ , evaluated at  $\dot{\phi} = 0$ , of the pitching-moment coefficient along  $y_B$  that would be determined from a steady coning motion  $\dot{\alpha} = \text{const}$ ,  $\dot{\beta} = \text{const}$ ,  $\dot{\phi} = \text{const}$ . The term  $(\hat{C}_{m_{q_B}} + \gamma \hat{C}_{m_{\alpha}})$  is recognized as being the contribution to the pitching-

moment coefficient measured along  $y_B$  for small-amplitude oscillations in  $\hat{\alpha}$  about  $\hat{\alpha} = \text{const}$  with  $\hat{\beta}$  held fixed at  $\hat{\beta} = \text{const}$ , that is, the planar damping-in pitch coefficient. The term  $(\hat{C}_{m_{r_B}} - \gamma \hat{C}_{m_{\beta}})$  is a

cross-coupling term, that is, the contribution to the pitching-moment coefficient measured along  $y_B$  due to small-amplitude planar oscillations in  $\hat{\beta}$  about  $\hat{\beta} = \text{const}$ , with  $\hat{\alpha}$  held fixed at  $\hat{\alpha} = \text{const}$ . This term and the analogous term in  $\hat{C}_n(t)$ ,  $(\hat{C}_{n_{q_B}} + \gamma \hat{C}_{n_{\alpha}})$  are nonlinear interaction terms that are normally excluded

in the classical aerodynamic mathematical model on the basis of symmetry arguments, and which are missed by attempts to generalize into the nonlinear aerodynamic regime linear formulations based on the principle of superposition.

In summary, for nearly rectilinear flight paths, the aerodynamic force and moment system in body axes take the form

$$\hat{C}_k(t) = \hat{C}_k(\infty; \hat{\alpha}, \hat{\beta}) + \frac{1}{\gamma} \frac{P_B^2}{V} \hat{C}_{k\phi}(\infty; \hat{\alpha}, \hat{\beta}) + \frac{1}{\gamma} \frac{\dot{\beta}^2}{V} \left[ \hat{C}_{kq_B}(\infty; \hat{\alpha}, \hat{\beta}) + \gamma \hat{C}_{k\hat{\alpha}}(\hat{\alpha}, \hat{\beta}) \right] - \frac{1}{\gamma} \frac{\dot{\beta}^2}{V} \left[ \hat{C}_{kr_B}(\infty; \hat{\alpha}, \hat{\beta}) - \gamma \hat{C}_{k\hat{\beta}}(\hat{\alpha}, \hat{\beta}) \right]; \quad k = \begin{cases} X, Y, Z \\ Z, m, n \end{cases} \quad (45)$$

In the body axis system, the four characteristic motions are steady angle of attack and sideslip, coning at constant angle of attack and sideslip, and the oscillations in pitch and in yaw at constant angles of attack and sideslip. The oscillations-in-roll motion that was required in the aerodynamic axis system is, in effect, incorporated in the oscillations in pitch and yaw motions in the body axis system. An oscillation in  $\hat{\alpha}$  with  $\hat{\beta}$  held fixed, for example, will be seen to involve an oscillation in  $\psi$ . The four motions are illustrated schematically in Fig. 15.

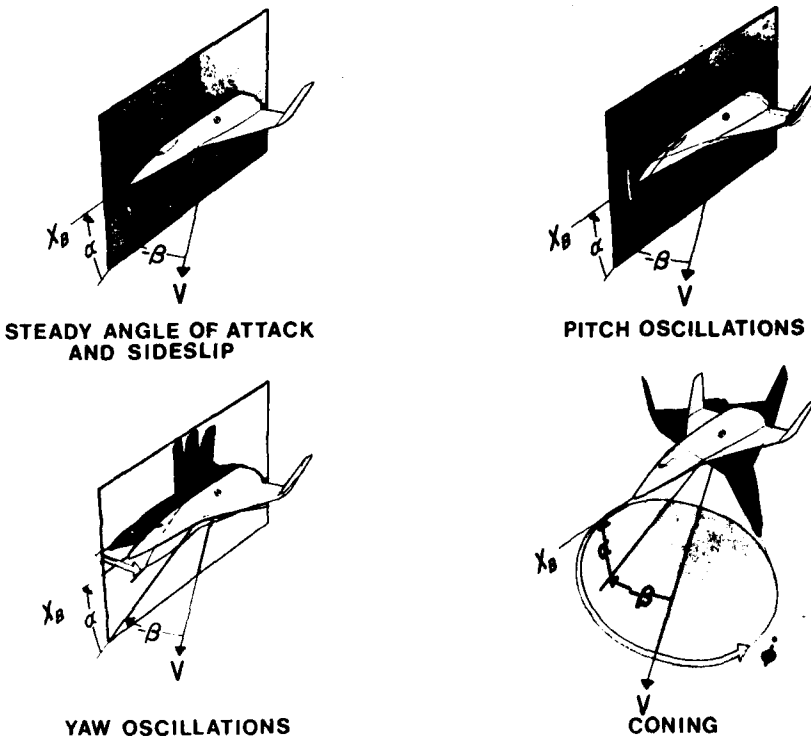


Figure 15. Characteristic motions in the body axis system. Linear dependence on angular rates.

That the nonlinear aerodynamic mathematical model Eq. (45) encompasses the conventional linear formulation for body-fixed axes and defines a complete set of characteristic motions is demonstrated by the behavior of the characteristic motions as  $\hat{\alpha}$  and  $\hat{\beta}$  both become small. In this case the oscillatory motions in pitch and yaw are merely those defining the conventional damping-in-pitch and damping-in-yaw. Also, at low angles of attack and sideslip, coning motion approximates a steady roll maneuver about the  $X_B$  body axis which defines the conventional damping-in-roll. Indeed, for  $\hat{\alpha} = \hat{\beta} = 0$  the two motions are identical and, as can be shown with the aid of Eqs. (44) and (45),  $C_{Z\phi} = C_{Zp_B}$ . Thus, according to the nonlinear aerodynamic mathematical model in the body axis system, the effects of roll-damping are contained within the aerodynamic response to coning motion.

#### 4.5 Equivalence Between Formulations in the Body and Aerodynamic Axis Systems

That Eqs. (37) and (42) and similarly that Eqs. (40) and (45) yield compatible forms may be verified by transferring  $\hat{C}_m$  and  $\hat{C}_n$  to the aerodynamic axis system by the use of Eq. (9) and then replacing the variables  $\hat{\alpha}$ ,  $\hat{\beta}$ ,  $P_B$ ,  $q_B$ ,  $r_B$  by variables in the aerodynamic axis system through the use of Eqs. (4), (6), and (8). It will be found that each coefficient in  $\hat{C}_m(t)$  and  $\hat{C}_n(t)$  can be matched with a combination of coefficients in  $\hat{C}_m(t)$  and  $\hat{C}_n(t)$  having the same multiplying variable. The matches for the coefficients in  $\hat{C}_m(t)$  yield:

$$\left. \begin{aligned} C_m(\infty; \delta, \psi) &= \hat{C}_m(\infty; \hat{\alpha}, \hat{\beta}) \cos \psi - \hat{C}_n(\infty; \hat{\alpha}, \hat{\beta}) \sin \psi \\ C_{m\lambda}(\infty; \delta, \psi) &= \hat{C}_{m_pB}(\infty; \hat{\alpha}, \hat{\beta}) \cos \psi - \hat{C}_{n_pB}(\infty; \hat{\alpha}, \hat{\beta}) \sin \psi \\ C_{mq}(\infty; \delta, \psi) &= \hat{C}_{mq_B}(\infty; \hat{\alpha}, \hat{\beta}) \cos^2 \psi + \hat{C}_{nr_B}(\infty; \hat{\alpha}, \hat{\beta}) \sin^2 \psi - \left[ \hat{C}_{nq_B}(\infty; \hat{\alpha}, \hat{\beta}) + \hat{C}_{mr_B}(\infty; \hat{\alpha}, \hat{\beta}) \right] \cos \psi \sin \psi \end{aligned} \right\} \quad (46)^*$$

\*Eq. (46) continued on following page.

$$\begin{aligned}
 C_{m_r}(\omega; \delta, \psi) &= \hat{C}_{m_{r_B}}(\omega; \hat{\alpha}, \hat{\beta}) \cos^2 \psi - \hat{C}_{n_{q_B}}(\omega; \hat{\alpha}, \hat{\beta}) \sin^2 \psi + [\hat{C}_{m_{q_B}}(\omega; \hat{\alpha}, \hat{\beta}) - \hat{C}_{n_{r_B}}(\omega; \hat{\alpha}, \hat{\beta})] \cos \psi \sin \psi \\
 C_{m_\delta}(\delta, \psi) &= \hat{C}_{m_{\alpha}}(\hat{\alpha}, \hat{\beta}) \cos^2 \psi - \hat{C}_{n_{\beta}}(\hat{\alpha}, \hat{\beta}) \sin^2 \psi + [\hat{C}_{m_{\beta}}(\hat{\alpha}, \hat{\beta}) - \hat{C}_{n_{\alpha}}(\hat{\alpha}, \hat{\beta})] \cos \psi \sin \psi \\
 C_{m_\psi}(\delta, \psi) &= \hat{C}_{m_{p_B}}(\omega; \hat{\alpha}, \hat{\beta}) \cos \psi - \hat{C}_{n_{p_B}}(\omega; \hat{\alpha}, \hat{\beta}) \sin \psi + \delta \hat{C}_{m_{\beta}}(\hat{\alpha}, \hat{\beta}) \cos^2 \psi + \delta \hat{C}_{n_{\alpha}}(\hat{\alpha}, \hat{\beta}) \sin^2 \psi \\
 &\quad - \delta [\hat{C}_{m_{\alpha}}(\hat{\alpha}, \hat{\beta}) + \hat{C}_{n_{\beta}}(\hat{\alpha}, \hat{\beta})] \cos \psi \sin \psi
 \end{aligned} \tag{46}$$

The analogous matches for the coefficients in  $C_n(t)$  may be obtained from Eq. (46) by replacing  $\hat{C}_{m_i}$  with  $\hat{C}_{n_i}$  and  $\hat{C}_{n_i}$  with  $-\hat{C}_{m_i}$ . The matches for the planar damping-in-pitch coefficient  $C_{m_\phi}$  and the side-moment coefficients  $C_{n_\phi}$  and  $(C_{n_\phi} - \gamma C_{n_\psi})$  are of particular interest. Equations (39) and (46) yield

$$\begin{aligned}
 C_{m_\phi}(\delta, \psi) &= C_{m_q} + \gamma C_{m_\delta} \\
 &= (\hat{C}_{m_{q_B}} + \gamma \hat{C}_{m_{\alpha}}) \cos^2 \psi + (\hat{C}_{n_{r_B}} - \gamma \hat{C}_{n_{\beta}}) \sin^2 \psi \\
 &\quad - [(\hat{C}_{n_{q_B}} + \gamma \hat{C}_{n_{\alpha}}) + (\hat{C}_{m_{r_B}} - \gamma \hat{C}_{m_{\beta}})] \cos \psi \sin \psi
 \end{aligned} \tag{47}$$

$$\begin{aligned}
 C_{n_\phi}(\omega; \delta, \psi) &= \gamma C_{n_\lambda} + \delta C_{n_r} \\
 &= \gamma (\hat{C}_{n_{p_B}} \cos \psi + \hat{C}_{m_{p_B}} \sin \psi) \\
 &\quad + \delta [\hat{C}_{n_{r_B}} \cos^2 \psi + \hat{C}_{m_{q_B}} \sin^2 \psi + (\hat{C}_{n_{q_B}} + \hat{C}_{m_{r_B}}) \cos \psi \sin \psi]
 \end{aligned} \tag{48}$$

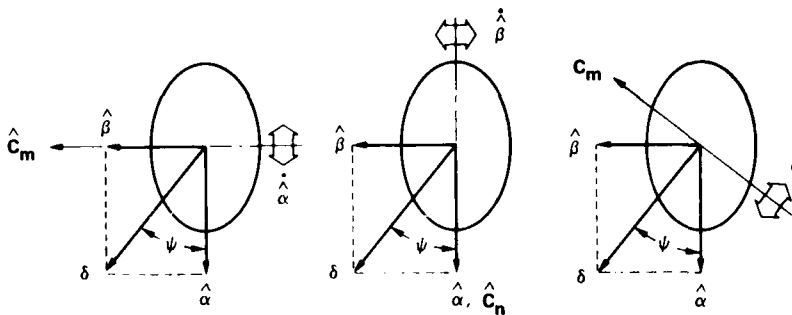
$$\begin{aligned}
 C_{n_\phi} - \gamma C_{n_\psi} &= \delta \left\{ (\hat{C}_{m_{q_B}} + \gamma \hat{C}_{m_{\alpha}}) \sin^2 \psi + (\hat{C}_{n_{r_B}} - \gamma \hat{C}_{n_{\beta}}) \cos^2 \psi \right. \\
 &\quad \left. + [(\hat{C}_{n_{q_B}} + \gamma \hat{C}_{n_{\alpha}}) + (\hat{C}_{m_{r_B}} - \gamma \hat{C}_{m_{\beta}})] \cos \psi \sin \psi \right\}
 \end{aligned} \tag{49}$$

Combining Eqs. (47) and (49) yields the following interesting relation between the responses to the oscillatory motions and to coning motion:

$$C_{n_\phi} - \gamma C_{n_\psi} + \delta C_{m_\phi} = \delta [(\hat{C}_{m_{q_B}} + \gamma \hat{C}_{m_{\alpha}}) + (\hat{C}_{n_{r_B}} - \gamma \hat{C}_{n_{\beta}})] \tag{50}$$

The term  $(\hat{C}_{m_{q_B}} + \gamma \hat{C}_{m_{\alpha}})$  has already been defined as the planar damping-in-pitch coefficient measured along  $y_B$  for small oscillations in  $\hat{\alpha}$  about  $\hat{\alpha} = \text{const}$  with  $\hat{\beta}$  held fixed at  $\hat{\beta} = \text{const}$ . Similarly,  $(\hat{C}_{n_{r_B}} - \gamma \hat{C}_{n_{\beta}})$  is the planar damping-in-yaw coefficient measured along  $z_B$  for small oscillations in  $\hat{\beta}$  about  $\hat{\beta} = \text{const}$ , with  $\hat{\alpha}$  held fixed at  $\hat{\alpha} = \text{const}$ . Thus, a measurement of  $(C_{n_\phi} - \gamma C_{n_\psi})$  would be equivalent to a measure of a combination of the three planar damping coefficients. The identity is shown schematically in Fig. 16. Equation (50) generalizes to the nonlinear case and to arbitrary bodies the relationship between  $(C_{n_\phi} - \gamma C_{n_\psi})$  and the planar damping coefficients that was pointed out and verified for bodies of revolution in the linear case in Ref. 26. It is noted that  $(C_{n_\phi} - \gamma C_{n_\psi}) = \delta (\hat{C}_{m_{q_B}} + \gamma \hat{C}_{m_{\alpha}})$  when  $\hat{\alpha} = 0$  and  $(C_{n_\phi} - \gamma C_{n_\psi}) = \delta (\hat{C}_{n_{r_B}} - \gamma \hat{C}_{n_{\beta}})$  when  $\hat{\beta} = 0$ . Under conditions where a linear formulation of the moment system can be assumed to hold (e.g., when  $\hat{\alpha} \rightarrow 0$ ,  $\hat{\beta} \rightarrow 0$ ) it is consistent to assume that the couplings between motions in  $\hat{\alpha}$  and  $\hat{\beta}$  will be negligibly small. Under these conditions, the measurement of  $(C_{n_\phi} - \gamma C_{n_\psi})$  at  $\hat{\alpha} = 0$  and again at  $\hat{\beta} = 0$  is all that is required to yield measures of the damping coefficients characteristic of the two uncoupled modes.

Note that the characteristic motions called for by the mathematical model formulated in terms of motion variables in the aerodynamic axis system (Fig. 14 and Eq. (40)) constitute a complete set for the case of small plunging. Similarly, the characteristic motions in the body axis system (Fig. 15 and Eq. (45)) also constitute a complete set. It is possible to build up the aerodynamic response of an aircraft to arbitrary motions from combinations of the responses to the characteristic motions in both formulations, through the use of the transformations (Eqs. (1)-(9) and Eqs. (46)-(50)). Care must be taken, however, to ensure that the resulting form also constitutes neither more nor less than a complete set. In other words, a form that combines responses to characteristic motions from both axis systems must be consistent with Eq. (40) and Eq. (45).



$$\frac{C_{n\phi} - \gamma C_{n\psi}}{\delta} = (\hat{C}_{m_{qB}} + \gamma \hat{C}_{m_{\alpha}}) + (\hat{C}_{m_{rB}} - \gamma \hat{C}_{m_{\beta}}) - C_{m_{\sigma}}$$

Figure 16. Schematic representation of the equality between  $(C_{n\phi} - \gamma C_{n\psi})/\delta$  and the three damping coefficients.

#### 4.6 Formulation for Body of Revolution

Several simplifications occur when the aerodynamic formulation is applied to model the aerodynamic response of a body of revolution. Recall that in the aerodynamic axis system the pitching-moment coefficient was specified as a functional of  $\delta, \psi, \dot{\alpha}, q, r$ . For an axisymmetric body the aerodynamic responses should be insensitive to the particular orientation  $\psi$  of the body relative to the cross-flow velocity vector, and can only be influenced by the time-rate-of-change of  $\psi$ . Thus for the body of revolution the pitching moment is assumed to be a functional of  $\delta, \psi, \dot{\alpha}, q, r$ . The resulting aerodynamic mathematical model, analogous to Eq. (40) for the case of a nearly rectilinear flight path, takes the form

$$C_k(t) = C_k(\infty; \delta(t)) + \frac{\dot{\psi} L}{V} C_{k\psi}(\infty; \delta(t)) + \frac{\dot{\alpha} L}{V} C_{k\alpha}(\delta(t)) + \frac{i L}{V} \frac{1}{\gamma} C_{k\phi}(\infty; \delta(t)); \quad k = \begin{matrix} X, Y, Z \\ \dot{\alpha}, m, n \end{matrix} \quad (51)$$

where the zeros in the notation belonging to  $i, q, r$ , and  $\dot{\psi}$  have been omitted. The characteristic motions from which the aerodynamic coefficients appearing in Eq. (51) are to be evaluated, are, with one exception, identical to those illustrated in Fig. 14 for the nonaxisymmetric body. For the body of revolution, however, the oscillations-in-roll motion for determining  $C_{k\psi}$  may be replaced by a steady motion in which the body spins about its  $x_B$  axis at constant rate  $\dot{\psi}$ , with  $\delta$  held fixed. This is, of course, the motion employed in determining the classical Magnus-moment coefficient. The term  $C_{n\psi}(\infty; \delta(t))$  is, then, the rate of change with  $\dot{\psi}L/V$ , evaluated at  $\dot{\psi} = 0$ , of the side-moment coefficient that would be evaluated in an experiment for the classical Magnus moment. No replacement of an unsteady characteristic motion in favor of a steady motion is obtained when the analogous aerodynamic formulation for the body of revolution is derived in the body-fixed axes. The resulting formulation and characteristic motions are identical to those applicable to the nonaxisymmetric body, Eq. (45) and Fig. 15, respectively. However, the symmetry of the body permits the choice of  $\psi$ , and thus the apportionment of  $\delta$  between  $\dot{\alpha}$  and  $\dot{\beta}$ , to be assigned at will.

The equivalence between the formulations in the aerodynamic and body axis systems allows us to demonstrate the nature of an error which several investigators have made in extending the linear aerodynamic mathematical model for a body of revolution encompassed by Eq. (51) into the nonlinear aerodynamic regime. In the linear model an equality exists between the damping-in-pitch coefficient and the side-moment coefficients due to steady coning and spinning motions. This is easily seen with the uses of Eqs. (47) and (50). Upon choosing  $\dot{\alpha} = 0$  ( $\psi = \pi/2$ ), Eq. (50) becomes

$$(C_{n\phi} - \gamma C_{n\psi})/\delta = \hat{C}_{m_{qB}}(\infty, 0, \dot{\beta}) + \gamma \hat{C}_{m_{\alpha}}(0, \dot{\beta}) \quad (52)$$

Similarly with  $\dot{\beta} = 0$  ( $\psi = 0$ ), Eq. (47) becomes

$$C_{m_{\sigma}}(\delta) = \hat{C}_{m_{qB}}(\infty; \dot{\alpha}, 0) + \gamma \hat{C}_{m_{\alpha}}(\dot{\alpha}, 0) \quad (53)$$

The planar motions implied by the right-hand sides of Eqs. (52) and (53) can be visualized from the motion indicated for  $(\hat{C}_{m_{qB}} + \gamma \hat{C}_{m_{\alpha}})$  in Fig. 16 by successively setting  $\dot{\alpha} = 0$  and  $\dot{\beta} = 0$ . When a linear formulation is valid, that is, as  $\dot{\beta} \rightarrow 0$  with  $\dot{\alpha} = 0$ , and  $\dot{\alpha} \rightarrow 0$  with  $\dot{\beta} = 0$ , the two planar motions are equivalent. Thus, for a body of revolution, within a linear formulation

$$\delta C_{m_{\sigma}} = (C_{n\phi} - \gamma C_{n\psi}) = \delta (\hat{C}_{m_{qB}} + \gamma \hat{C}_{m_{\alpha}}) \quad (54)$$

In the nonlinear aerodynamic regime the planar motions are no longer equivalent, and the equality between  $\delta C_{m_{\sigma}}$  and  $(C_{n\phi} - \gamma C_{n\psi})$  can no longer be expected to hold. It has been shown from a symmetry argument in which each of the terms of Eq. (54) is expressed as a power series in  $\delta$  (cf. Ref. 3) that the equality

Eq. (54) is valid only to terms of first order in  $\delta$ . At values of  $\delta$  where terms of  $O(\delta^2)$  become significant the equality breaks down. Further, the breakdown in the equality has been demonstrated by the results of experimental measurements for a slender cone in supersonic flow. Measurements of the coefficients  $C_{n\phi}$  and  $C_{m\phi}$  were obtained from experiments (Ref. 26) with an apparatus which simulated steady coning motion and steady spinning motion of a model in a wind tunnel. For the slender 10° half-angle cone that was investigated, the coefficient  $C_{n\phi}$  was found to be negligibly small; thus  $C_{n\phi}$  for this body is equivalent to  $(C_{n\phi} - \gamma C_{m\phi})$  for all values of  $\delta$ . The damping-in-pitch coefficient  $C_{m\phi}$  was obtained from the measured aerodynamic response to small-amplitude oscillations-in-pitch experiments (Ref. 27) that were conducted over a wide range of mean values of  $\delta$ . The variation of the measured values of  $C_{n\phi}$  and  $\delta C_{m\phi}$  with  $\delta$  are shown in Fig. 17. The theoretical value of  $\delta(C_{m\phi} + \gamma C_{n\phi})$ , obtained from an analytical solution of the linearized potential flow equations (Ref. 28), is also shown in Fig. 17. The equality between

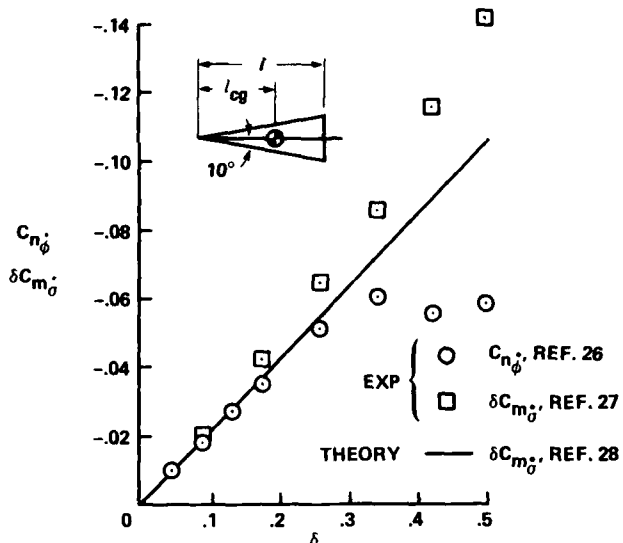


Figure 17. Variation of  $\delta C_{m\phi}$  and  $C_{n\phi}$  with  $\delta$ ; Mach number = 2.0,  $l_{cg}/l = 0.61$ .

the two experimental and the theoretical results at low values of  $\delta$  confirms the validity of Eq. (54) within a linear aerodynamic mathematical model. The results also demonstrate clearly that the equality does not hold at large values of  $\delta$  and that the differences between  $C_{n\phi}$  and  $\delta C_{m\phi}$  (reflecting the inequality between terms of second and higher order in  $\delta$ ) can be large. Consequently, attempts to extend the linear aerodynamic formulation into the nonlinear aerodynamic regime by simply allowing the constants which appear within the linear form to become functions of  $\delta$  while retaining the equality between  $(C_{n\phi} - \gamma C_{m\phi})$  and  $\delta C_{m\phi}$  are necessarily in error. A formulation incorporating this erroneous assumption can be shown to yield misleading results when used in a program for extracting nonlinear aerodynamic coefficients from free-flight data (Ref. 15). Retention of the equality may cause such a program to assign values to  $C_{n\phi}$ , the side-moment coefficient due to the Magnus motion, which are many times greater than those actually found to exist from wind-tunnel measurements.

#### 4.7 Aircraft Spin Motions

The emergence of coning motion as a characteristic motion in both the aerodynamic and body-axis systems emphasizes its importance in the nonlinear formulation. With  $P_B = 0$ , coning motion is equivalently the simultaneous periodic variation of two orthogonal planar motions; by enabling two planar motions to interact, coning motion can be said to characterize the coupling problem.

Further evidence of its importance is the obvious similarity between coning motion and the steady spin of an aircraft, suggesting that a moment formulation based on either Eq. (40) or Eq. (45) will properly describe the aerodynamic responses of spinning aircraft. This view is encouraged by the success achieved in several attempts to reproduce aircraft or model spin motions by calculations based on aerodynamic formulations bearing a similarity to those proposed here. In one attempt (Ref. 29), the actual spins of an F-100 aircraft were reproduced by calculations based on an aerodynamic formulation that called principally for wind-tunnel measurements of the conventional static forces and moments. In another (Ref. 30), the spins of a delta-wing model in a spin tunnel were reproduced by calculations based on an aerodynamic formulation that called principally for wind-tunnel measurements of the forces and moments on a model in coning motion. More recently (Ref. 31), predictions of flight motions based on the results of wind-tunnel measurements made on an aircraft model in coning motion were found to compare favorably to actual spin motion histories of the full-scale aircraft. The formulations based on Eqs. (40) and (45) in effect include these motions within the four characteristic motions whose force and moment contributions are required to build up the response to an arbitrary motion. It is known, however, that in the establishment of a spin the large asymmetric regions of separated flow on the wings of the aircraft may cause the aerodynamic responses to be

nonlinear functions of the spin rate, even at low spin rates. This contradicts the assumption underlying the development of Eqs. (40) and (45) that the aerodynamic responses be linear functions of the rates. The authors have shown (Ref. 17) how the formulations can be generalized to allow a nonlinear dependence on the coning rate, which should make them more fully applicable to the analysis of spin motions. The restriction imposed previously on the degree of cognizance of the past motion allowed the indicial response remains in force, however, so that aerodynamic hysteresis effects still cannot be acknowledged within the scope of the otherwise extended formulations. The main results are indicated below.

#### 4.7.1 Aerodynamic axis system

The generalized formulation paralleling that of Eq. (40) (again assuming a nearly rectilinear flight path) takes the form

$$\begin{aligned} C_k(t) = & C_k(\infty; \delta(t), \psi(t), \frac{\dot{\lambda}}{\gamma}(t)) + \frac{\dot{\lambda}}{\gamma} C_{k\alpha}(\delta(t), \psi(t), \frac{\dot{\lambda}}{\gamma}(t)) \\ & + \frac{\dot{\psi}}{\gamma} C_{k\psi}(\delta(t), \psi(t), \frac{\dot{\lambda}}{\gamma}(t)) ; \quad k = \begin{cases} X, Y, Z \\ Z, m, n \end{cases} \end{aligned} \quad (55)$$

That Eq. (55) reverts to Eq. (40) when the linearity condition on coning rate is reimposed can be seen by expanding the terms in Eq. (55) to first order about  $\dot{\lambda}/\gamma = 0$ . The first term in Eq. (55) is the coefficient that would be measured in a steady coning motion  $\delta = \text{const}$ ,  $\psi = \text{const}$ ,  $\dot{\phi} = \dot{\lambda}/\gamma = \text{const}$ . As before, the term  $C_{k\alpha}$  is the contribution to the moment coefficient due to pitch oscillations that would be evaluated from small-amplitude oscillations in  $\sigma$  about  $\sigma = \text{const}$  with  $\psi = \text{const}$  but now, in addition, in the presence of a steady coning motion  $\dot{\phi} = \dot{\lambda}/\gamma = \text{const}$ . Similarly,  $C_{k\psi}$  is the contribution to the moment coefficient due to roll oscillations that would be evaluated from small-amplitude oscillations in  $\psi$  about  $\psi = \text{const}$  with  $\delta = \text{const}$  and in the presence of a steady coning motion  $\dot{\phi} = \dot{\lambda}/\gamma = \text{const}$ . The indicated functional dependence on  $\delta$ ,  $\psi$ ,  $\dot{\lambda}/\gamma$  must be interpreted as follows: for flight with given values of  $\delta$ ,  $\psi$ ,  $\dot{\lambda}$ ,  $q$ ,  $r$  at a particular instant, the aerodynamic coefficients that are to be associated with that instant are those evaluated around a coning motion having constant values of  $\delta$  and  $\psi$  equal to the instantaneous flight values and a constant value of coning rate equal to the instantaneous value of  $\dot{\lambda}/\gamma$ .

Thus, the four contributions required in Eq. (40) to build up the response to an arbitrary motion reduce to three when a nonlinear dependence on coning rate is admitted. This is because the first term in Eq. (55)  $C_k(\infty; \delta, \psi, \dot{\lambda}/\gamma)$  is the general term which, it now appears, replaces two terms in Eq. (40) representing the expansion of  $C_k(\infty; \delta, \psi, \dot{\lambda}/\gamma)$  around  $\dot{\lambda}/\gamma = 0$  to first order in  $\dot{\lambda}/\gamma$ . The more important change, however, at least from the experimental standpoint, is that retaining a nonlinear dependence on coning rate requires for consistency that the oscillatory experiments be carried out in the presence of coning motion. The three motions are illustrated schematically in Fig. 18.

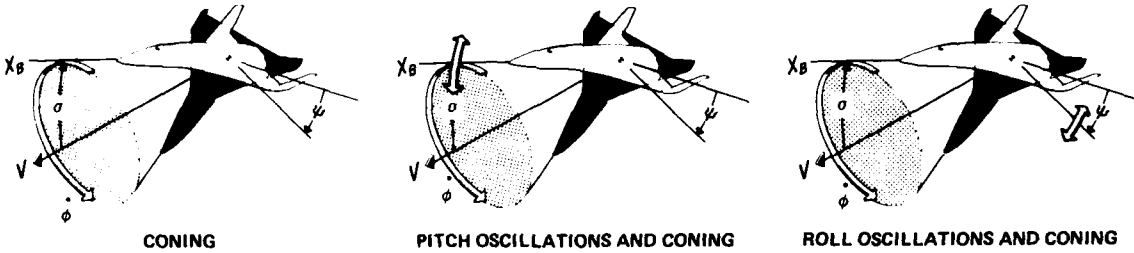


Figure 18. Characteristic motions in the aerodynamic axis system. Nonlinear dependence on coning rate.

#### 4.7.2 Body axis system

The generalized formulation paralleling that of Eq. (45) takes the form

$$\begin{aligned} \hat{C}_k(t) = & \hat{C}_k(\infty; \hat{\alpha}, \hat{\beta}, \frac{p_B}{\gamma}) + \frac{1}{\gamma} \frac{\dot{\lambda}}{V} \left[ \hat{C}_{kq_B}(\infty; \hat{\alpha}, \hat{\beta}, \frac{p_B}{\gamma}) + \gamma \hat{C}_{k\alpha}(\hat{\alpha}, \hat{\beta}, \frac{p_B}{\gamma}) \right] \\ & - \frac{1}{\gamma} \frac{\dot{\beta}}{V} \left[ \hat{C}_{kr_B}(\infty; \hat{\alpha}, \hat{\beta}, \frac{p_B}{\gamma}) - \gamma \hat{C}_{k\beta}(\hat{\alpha}, \hat{\beta}, \frac{p_B}{\gamma}) \right] ; \quad k = \begin{cases} X, Y, Z \\ Z, m, n \end{cases} \end{aligned} \quad (56)$$

Equation (56) reverts to Eq. (45) upon expanding the terms in Eq. (56) to first order about  $p_B/\gamma = 0$ . The first term in Eq. (56) is the coefficient that would be measured in a steady coning motion  $\dot{\phi} = p_B/\gamma = \text{const}$  with  $\hat{\alpha}$  and  $\hat{\beta}$  at the fixed inclinations  $\hat{\alpha} = \text{const}$ ,  $\hat{\beta} = \text{const}$ . The second term is the contribution to the moment coefficient due to pitch oscillations that would be evaluated from small-amplitude oscillations in  $\hat{\alpha}$  about  $\hat{\alpha} = \text{const}$  with  $\hat{\beta} = \text{const}$  and in the presence of a steady coning motion with  $\dot{\phi} = p_B/\gamma = \text{const}$ . The third term results from small-amplitude oscillations in  $\hat{\beta}$  about  $\hat{\beta} = \text{const}$  with  $\hat{\alpha}$  fixed at  $\hat{\alpha} = \text{const}$  and in the presence of a steady coning motion  $\dot{\phi} = p_B/\gamma$ . It should be noted that the coning rate  $\dot{\phi} = p_B/\gamma$  on which the terms depend in Eq. (56) is not equal in magnitude to the coning rate  $\dot{\phi} = \dot{\lambda}/\gamma$  in Eq. (55). The rates differ by  $\dot{\psi}/\gamma$ . Thus, in the body axis system, the appropriate constant value of the coning rate for the aerodynamic coefficients that are to be associated with an instantaneous flight condition is that formed from the instantaneous value of  $p_B/\gamma$ . The three motions required in the body axis system are illustrated schematically in Fig. 19.

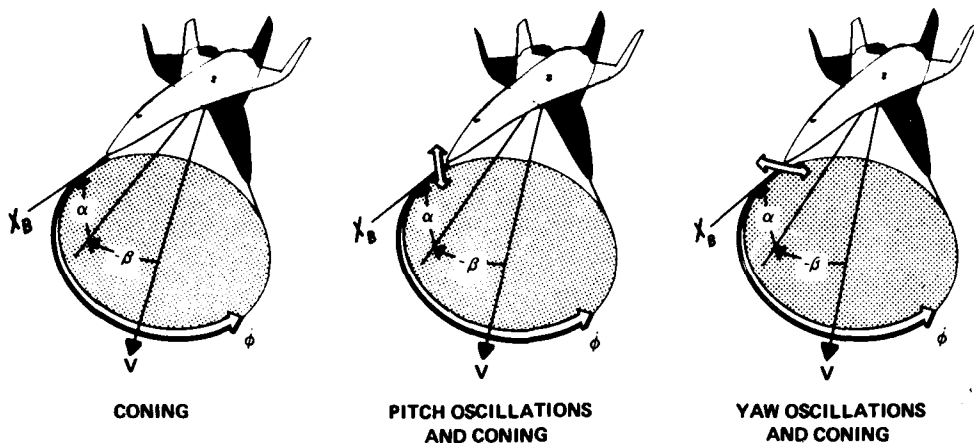


Figure 19. Characteristic motions in the body axis system. Nonlinear dependence on coning rate.

#### 4.7.3 Spin radius

Equations (55) and (56) were derived on the assumption of a nearly rectilinear flight path, which would apparently restrict their application to spin motions having essentially zero spin radius. It can be shown, however, that the results will apply as well to spin motions having constant spin radius. Motions having a constant spin radius can be characterized by the existence of a point other than the mass-center about which the body rotates. This point, which lies on the body  $x_B$  axis, is itself in essentially rectilinear motion. The existence of such a point usually will guarantee fulfillment of the conditions under which Eqs. (55) and (56) apply, namely,  $q - \dot{\delta} \approx 0$ ,  $r - \epsilon\lambda \approx 0$ . The principal restrictions are that  $|qx/V| \ll 1$  and  $|rx/V| \ll 1$ , where  $x$  is the distance along  $x_B$  between the mass center and the point in nearly rectilinear motion. Variations in spin radius  $x \sin \alpha$  also can be tolerated under the additional restriction  $|x/V| \ll 1$ .

#### 4.8 Evaluation of Stability Coefficients for Nonplanar Motions

The choice of the aerodynamic mathematical model specifies the characteristic motions, and the way in which the aerodynamic response of an aircraft to an arbitrary motion can be compounded from the known aerodynamic responses of the aircraft to the characteristic motions. The practicability of the models ultimately depends on the successful development of techniques for obtaining the requisite aerodynamic responses. As in the case of planar motions, this aerodynamic information can be obtained both from numerical flow-field computations and from experimental measurements.

##### 4.8.1 Computational methods

In spite of the recent advances in methods for the computation of flow fields and in computer technology (cf. Ref. 32 for a recent in-depth survey), such methods have not yet been widely applied to determine the stability coefficients of aircraft maneuvering at large angles of attack. Under such conditions the flow field, and thus the nonlinear aerodynamic responses, are generally dominated by separated viscous flow effects. At this date, the three-dimensional separated flow field surrounding an aircraft cannot be computed, even for the case of steady flow. Even if we discount the known inadequacies of currently available turbulence models to correctly simulate flows having large-scale separated regions, computer resources are now adequate only for computation of steady three-dimensional viscous flows over the simplest of body shapes (cf. Ref. 33 for an example of current computational capabilities). Numerical computation of the time-dependent flow-field responses to the oscillatory characteristic motions will require the availability of even greater computer speeds and storage capacity.

Although evaluation of the aerodynamic responses of aircraft at large angles of attack with computational techniques is not generally feasible at present, the aerodynamic responses in two angle-of-attack and Mach number regimes are currently amenable to investigation with numerical techniques. First, at low angles of attack the flows generally remain unseparated and the aerodynamic reactions vary linearly with the angle of attack. In this flow regime the inviscid linearized gasdynamic equations are applicable, which leads to greatly reduced requirements for computational resources. A variety of methods have been developed to compute the classical stability derivatives of simple wings and bodies (cf. Ref. 34 for an extensive bibliography) in this flow regime. A survey of these numerical and analytical methods is the subject of another lecture within this lecture series. The second flow regime where computational methods may be profitably employed is that of steady supersonic flow. In this regime the nonlinear gasdynamic equations are of hyperbolic nature with respect to the streamwise spatial coordinate, which permits the supersonic flows to be computed with efficient space-marching numerical methods. Consequently, steady supersonic flows around bodies at low and moderate angles of attack have been treated extensively with inviscid and viscous finite-difference methods. Results of computations for supersonic flows are compared to experimental measurements in recent survey articles concerned with three-dimensional flows (Refs. 35, 36). The results demonstrate the nonlinear variation of the aerodynamic reactions with increasing incidence.

The flow fields surrounding bodies in steady coning motion, and surrounding axisymmetric bodies in steady spinning (Magnus) motion, are time-invariant with respect to observers in the proper reference frames. For the former case, this permitted the computation of the nonlinear inviscid supersonic flow fields (Ref. 37) surrounding slender cones (of both circular and elliptical cross section) in coning motion. More recently, computations of the viscous supersonic flow surrounding circular cones in coning motion have

been carried out (Refs. 38, 39) using methods based on the parabolized Navier-Stokes equations. The steady viscous flow fields surrounding bodies of revolution in a steady spinning motion have been computed using methods based on a coupled inviscid flow-boundary layer method (Ref. 40), and more recently using the parabolized Navier-Stokes equations (Refs. 39, 41, 42).

In addition to their roles as characteristic motions, coning and spinning have a particular significance for bodies of revolution, since, as shown in Eq. (54), within a linear aerodynamic model the coefficients acting on a body in coning and spinning motion can be used to determine the planar damping-in-pitch coefficient. Thus the damping coefficient, which in general must be evaluated from time-dependent gasdynamic equations, can in this case be determined from time-invariant gasdynamic equations. This approach has been recently employed (Ref. 43) to determine the linear pitch-damping coefficients of a series of supersonic projectiles.

#### 4.8.2 Requirements for experiments

The significance of coning motion and the possible existence of aerodynamic cross-coupling effects for nonplanar motions within the nonlinear flight regime have led to additional requirements on the experimental evaluation of the stability coefficients. Within the assumptions of a linear dependence of the aerodynamic reactions on coning rate, the analysis suggests that the nonlinear aerodynamic response to arbitrary non-planar motions of an aircraft about a nearly rectilinear flight path can be synthesized from knowledge of the aerodynamic responses to four characteristic motions (Figs. 14 and 15). For wind-tunnel tests in terms of the characteristic motions in the aerodynamic axis system (Fig. 14) three types of experimental apparatus would be required:

1. A coning apparatus similar to the ones described in Refs. 26 and 44. Such an apparatus would permit measurement of the aerodynamic reactions due both to steady flow and to steady coning motion at fixed resultant angle of attack  $\sigma$  and roll angle  $\psi$ .
2. An oscillations-in-pitch apparatus for simulating small-amplitude oscillations in  $\sigma$  about a fixed  $\sigma$ , that is, oscillations about an axis oriented normal to the resultant-angle-of-attack plane.
3. An oscillations-in-roll apparatus for simulating small-amplitude oscillations in  $\psi$  about a fixed  $\psi$ , that is, oscillations about the  $x_B$  axis. (Alternatively, for axisymmetric bodies, an apparatus capable of providing a steady spin about the  $x_B$  axis could be employed to conduct the Magnus experiment.)

It is essential that the coning apparatus and both of the oscillatory devices incorporate the capability of measuring all components of the aerodynamic response to the motion even when considering bodies of revolution since the mathematical model requires evaluation of cross-coupling coefficients such as the side moment induced by pitch oscillations.

Wind-tunnel tests conducted in terms of the characteristic motions in the body axis system (Fig. 15) would require only the coning and oscillation-in-pitch devices. By suitable orientation of the oscillatory device it could be employed to simulate both the planar oscillations in  $\hat{\alpha}$  and those in  $\hat{\beta}$  as called for by the mathematical model. Development of advanced experimental devices capable of simulating small-amplitude pitch, roll, and yaw oscillations of a model in a wind tunnel at large mean angles of attack and yaw, and of measuring the aerodynamic responses including those due to cross-coupling have been reported recently (Refs. 45-48). These devices, among others, will be surveyed in depth in other lectures within this lecture series.

Results of tests conducted in terms of the characteristic motions in the aerodynamic axis system would be related to those of tests conducted in terms of the motions in the body-fixed axes through Eqs. (46)-(50). Carrying out both sets of wind-tunnel tests for one aircraft configuration and identical flow conditions would provide the information necessary for an experimental validation of Eq. (50), in particular. A positive validation would help to demonstrate the validity of the aerodynamic mathematical models, Eqs. (40) and (45).

Eliminating the assumption of a linear dependence of the moment on coning rate reduces the number of characteristic motions required from four to three. In either axis system, a coning motion and two oscillatory motions in the presence of coning (Figs. 18 and 19) are required. Experiments designed to reproduce the motions in the wind tunnel again require the coning apparatus and the types of oscillatory devices just described. The significant additional requirement that each of the oscillatory experiments be carried out, in the presence of coning means, of course, that now the oscillatory devices must be incorporated in the coning apparatus. These obviously difficult experiments, involving oscillatory and coning motions in combination, are required only where the moment contribution due to steady coning shows a significant nonlinear dependence on coning rate. Otherwise, the experiments may be conducted separately as described above.

#### 4.9 Selection and Verification of Mathematical Models

In previous sections we have discussed how the choice of a candidate mathematical model to describe the aerodynamic force and moment system defines a set of characteristic motions. We have also shown how the characteristic motions, in turn, define the types of computations or wind-tunnel tests needed to evaluate the aerodynamic information. Here we consider the remaining task (and the one we consider most critical) necessary to complete the process outlined in Fig. 2, namely that of selecting the simplest possible formulation, and of verifying that the formulation selected accurately describes the aerodynamics acting on the aircraft over the range of its possible maneuvers.

The simplest formulation that we believe is adequate to describe the aerodynamics of nonplanar maneuvers in the high-angle-of-attack flight regime is Eq. (40), or alternatively, Eq. (45). Thus, when defining the aerodynamics for a new aircraft configuration, we would advocate tests using either the set of characteristic motions shown in Fig. 14 or that shown in Fig. 15. We note again that all three aerodynamic force and moment

components must be measured simultaneously in each of the characteristic motions to provide the cross-coupling information required by the formulation. In the event that the aerodynamic reactions are found from testing to violate the assumptions of the basic formulation (for example, to vary nonlinearly with coning rate or with frequency of the oscillatory motions), then the formulation at the next level of complexity must be adopted, and the aerodynamics determined in terms of the characteristic motions called for by the new formulation. In the case of a nonlinear dependence of the aerodynamic reactions on the coning rate, the formulation would be given by Eq. (55) or, alternatively Eq. (56), and would call for the characteristic motions shown in Figs. 18 and 19. In this manner a mathematical model can be systematically selected at the lowest level of complexity needed to account for the aerodynamic phenomena (e.g., nonlinear coning rate dependence, hysteresis) that the vehicle is found to experience.

The process of verifying a candidate aerodynamic formulation would entail, after specifying an aircraft configuration: (a) determining, from wind-tunnel tests or computations, the aerodynamic information for the aircraft based on the characteristic motions called for by the formulation; (b) using the results from (a) together with the vehicle's equations of motion to predict a series of extreme flight maneuvers; and (c) for the same initial conditions, conducting flight tests to obtain actual flight responses. The predicted motion histories would be compared against the actual flight histories. Close agreement for all of the maneuvers would be a convincing demonstration of the validity of the candidate mathematical model.

##### 5. AERODYNAMIC HYSTERESIS

In Section 3 we used the case of an aircraft in a planar ( $\delta, q$ ) maneuver to illustrate the steps involved in the derivation of a general integral form for the aerodynamic pitching-moment response. We noted that, as developed, the integral form was valid on condition that the indicial responses within it were unique and continuous functions of their arguments. Further, as a result of simplifying the integral form to the second level of approximation, in which the indicial responses were said to depend only on the magnitudes of  $\delta$  and  $q$  at the origins of the steps, the indicial responses then had to be single-valued functions of their arguments. All of these conditions are violated together when hysteresis is present in the variation of the steady-state response with any of the motion variables. It is known (Refs. 18, 19) that hysteresis effects are present in the aircraft's steady-state pitching-moment response during certain kinds of stall. Hysteresis also has been noted, particularly in the variation of steady-state rolling-moment coefficient  $C_2$  with roll angle  $\psi$  or side-slip angle  $\beta$ , for slender wings (Ref. 49) and fighter-type aircraft (Refs. 20, 21) at high angles of attack. In Ref. 4, using a pitching maneuver as an example, we have shown how our formulation could be extended to accommodate the double-valued behavior of the aerodynamic response characteristic of hysteresis, albeit without explicit acknowledgment of the presence of discontinuities. In Ref. 7 we showed how the principal result of Ref. 4 could be adapted to the study of a problem of current interest, the wing-rock phenomenon. We shall take this opportunity to give a simplified version of our previous development, taking explicit account of the presence of discontinuities. In the present discussion, with application to the wing-rock problem in view, we shall use as our example a single-degree-of-freedom rolling maneuver. We formulate the problem in the aerodynamic axis system, in which the principal motion variable is roll angle  $\psi$ .

Let us postulate, as shown schematically in Fig. 20, the existence of a hysteresis loop in the variation of steady-state rolling-moment coefficient  $C_2(\infty; \psi, h, \sigma_0)$  with roll angle  $\psi$ .

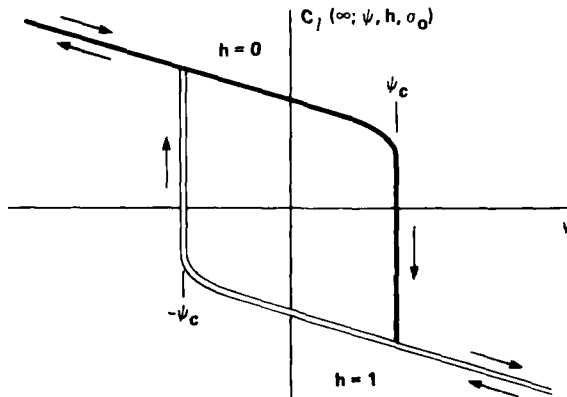


Figure 20. Schematic representation of aerodynamic hysteresis in steady-state rolling-moment coefficient.

As the notation is intended to indicate, the resultant angle of attack  $\sigma$  is considered a parameter, to be held fixed at  $\sigma = \sigma_0$  throughout the maneuver in  $\psi$ . The parameter  $h$  is used to distinguish between flow regimes representative of the two branches of the hysteresis loop; it is assigned the value  $h = 0$  on the upper branch and the value  $h = 1$  on the lower branch. More specifically,

$$\begin{aligned} h = 0 & \left\{ \begin{array}{l} \psi \leq -\psi_c \\ -\psi_c \leq \psi < \psi_c, \quad C_2 > 0 \end{array} \right. \\ h = 1 & \left\{ \begin{array}{l} \psi \geq \psi_c \\ -\psi_c < \psi \leq \psi_c, \quad C_2 < 0 \end{array} \right. \end{aligned} \quad (57)$$

We assign the jump in  $C_L$  at  $\psi = \psi_C$  to  $h = 0$  and the jump in  $C_L$  at  $\psi = -\psi_C$  to  $h = 1$ .

Let us now consider the development of an integral form for  $C_L(t)$  that will accommodate the double-valued variation of  $C_L(\xi; \psi, h, \sigma_0)$  shown in Fig. 20. For simplicity, we assume that the indicial response in  $C_L$  to a step change in  $\psi$  depends on values of  $\psi$  only in the recent past relative to its origin, and that, for a step originating at  $\xi = \tau$ , the recent-past motion  $\psi(\xi)$  is characterized sufficiently well by the first two coefficients of its Taylor series expansion at  $\xi = \tau$ , namely  $\psi(\tau), \dot{\psi}(\tau)$ . Additionally, since there is a region  $-\psi_C < \psi < \psi_C$  in which there are two possible steady-state values of  $C_L$ , at values of  $\psi$  within this region there must also be two possible indicial responses. Accordingly, just as with its steady-state value, we allow the indicial response to depend on  $h(\tau)$ , where  $h(\tau)$  is either 0 or 1 depending on the flow regime existent at the origin of the step. Then for a discrete step  $\Delta\psi$  at time  $\xi = \tau$ , the indicial response as measured at the time  $\xi = t$  has the functional form

$$\Delta C_L(t) = \Delta C_L(t - \tau; \psi(\tau), \dot{\psi}(\tau), h(\tau), \sigma_0) \quad (58)$$

We can now build up the response  $C_L(t)$  to an arbitrary motion  $\psi(t)$  as the summation of discrete responses  $\Delta C_L(t)$  to steps of finite size  $\Delta\psi$ . Figure 21 illustrates the quantities in question. We have

$$C_L(t) = C_L(0) + \sum_n \frac{\Delta C_L(t - \tau_n; \psi(\tau_n), \dot{\psi}(\tau_n), h(\tau_n), \sigma_0)}{\Delta\psi(\tau_n)} \Delta\psi(\tau_n) \quad (59)$$

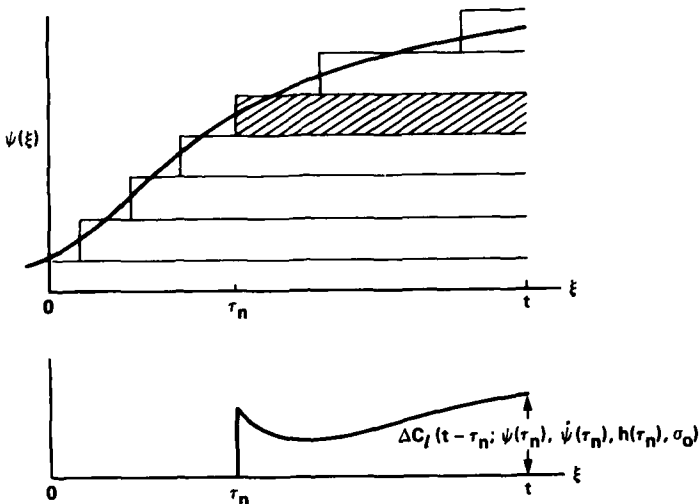


Figure 21. Summation of discrete responses to finite steps in roll angle.

Suppose that the limit

$$\lim_{\Delta\psi(\tau_n) \rightarrow 0} \frac{\Delta C_L(t - \tau_n; \psi(\tau_n), \dot{\psi}(\tau_n), h(\tau_n), \sigma_0)}{\Delta\psi(\tau_n)} = C_{L_\psi}(t - \tau_n; \psi(\tau_n), \dots) \quad (60)$$

exists everywhere except at certain points  $\xi = \tilde{\tau}_i$ ,  $i = 1, \dots, N$ , where  $h(\tau_n)$  changes from one of its two possible values to the other. Except for these special points, which can be extracted from the summation and dealt with separately, we can replace the summations representing the contributions from the intervals between these points by integrals. Thus,

$$\begin{aligned} C_L(t) &= C_L(0) + \int_0^{\tilde{\tau}_1 - \epsilon} C_{L_\psi}(t - \tau; \psi(\tau), \dot{\psi}(\tau), h(0), \sigma_0) \frac{d\psi}{d\tau} d\tau \\ &\quad + \int_{\tilde{\tau}_1 + \epsilon}^{\tilde{\tau}_2 - \epsilon} C_{L_\psi}(t - \tau; \psi(\tau), \dot{\psi}(\tau), h(\tilde{\tau}_1), \sigma_0) \frac{d\psi}{d\tau} d\tau \\ &\quad + \dots + \int_{\tilde{\tau}_N + \epsilon}^t C_{L_\psi}(t - \tau; \psi(\tau), \dot{\psi}(\tau), h(\tilde{\tau}_N), \sigma_0) \frac{d\psi}{d\tau} d\tau \\ &\quad + \sum_{i=1}^N \Delta C_L(t - \tilde{\tau}_i; \psi(\tilde{\tau}_i), \dot{\psi}(\tilde{\tau}_i), h(\tilde{\tau}_i), \sigma_0) \end{aligned} \quad (61)$$

Within each integral term, we can introduce the steady-state value of the indicial response and the deficiency function  $F$  through the equality

$$C_{L_\psi}(t - \tau; \psi(\tau), \dot{\psi}(\tau), h(\tau), \sigma_0) = C_{L_\psi}(\psi(\tau), h(\tau), \sigma_0) - F(t - \tau; \psi(\tau), \dot{\psi}(\tau), h(\tau), \sigma_0) \quad (62)$$

We note that, in accordance with observations, the steady-state value of the indicial response  $C_L(\infty; \psi(\tau), h(\tau), \sigma_0)$  does not depend on  $\dot{\psi}(\tau)$ . Further, since  $h(\tau)$  has only one value within an interval,  $C_L(\infty; \psi(\tau), h(\tau), \sigma_0)$  is now a single-valued function of  $\psi$  within each interval. Multiplied by  $(d\psi/d\tau)d\tau$ , it forms a perfect differential which can be integrated. Carrying out the integration over each interval results in

$$\begin{aligned} C_L(t) = & [C_L(\infty; \psi(\tilde{\tau}_1 - \epsilon), h(\tilde{\tau}_1 - \epsilon), \sigma_0) - C_L(\infty; \psi(\tilde{\tau}_1 + \epsilon), h(\tilde{\tau}_1 + \epsilon), \sigma_0)] \\ & + [C_L(\infty; \psi(\tilde{\tau}_2 - \epsilon), h(\tilde{\tau}_2 - \epsilon), \sigma_0) - C_L(\infty; \psi(\tilde{\tau}_2 + \epsilon), h(\tilde{\tau}_2 + \epsilon), \sigma_0)] \\ & + \dots + C_L(\infty; \psi(t), h(t), \sigma_0) \\ & - \int_0^{\tilde{\tau}_1 - \epsilon} + \int_{\tilde{\tau}_1 + \epsilon}^{\tilde{\tau}_2 - \epsilon} + \dots + \int_{\tilde{\tau}_N + \epsilon}^t F(t - \tau; \psi(\tau), \dot{\psi}(\tau), h(\tau), \sigma_0) \frac{d\psi}{d\tau} d\tau \\ & + \sum_{i=1}^N \Delta C_L(t - \tilde{\tau}_i; \psi(\tilde{\tau}_i), \dot{\psi}(\tilde{\tau}_i), h(\tilde{\tau}_i), \sigma_0) \end{aligned} \quad (63)$$

Just as we did with the integral terms, we can replace each  $\Delta C_L$  in the last term in Eq. (63) by the equality

$$\Delta C_L(t - \tilde{\tau}_i; \psi(\tilde{\tau}_i), \dot{\psi}(\tilde{\tau}_i), h(\tilde{\tau}_i), \sigma_0) = \Delta C_L(\infty; \psi(\tilde{\tau}_i), h(\tilde{\tau}_i), \sigma_0) - \Delta F(t - \tilde{\tau}_i; \psi(\tilde{\tau}_i), \dot{\psi}(\tilde{\tau}_i), h(\tilde{\tau}_i), \sigma_0) \quad (64)$$

When Eq. (64) is substituted in Eq. (63), we see that the jumps in  $C_L(\infty; \psi(\tilde{\tau}_i), h(\tilde{\tau}_i), \sigma_0)$  cancel identically, leaving as the net result

$$\begin{aligned} C_L(t) = & C_L(\infty; \psi(t), h(t), \sigma_0) \\ & - \left\{ \int_0^{\tilde{\tau}_1 - \epsilon} + \int_{\tilde{\tau}_1 + \epsilon}^{\tilde{\tau}_2 - \epsilon} + \dots + \int_{\tilde{\tau}_N + \epsilon}^t F(t - \tau; \psi(\tau), \dot{\psi}(\tau), h(\tau), \sigma_0) \frac{d\psi}{d\tau} d\tau \right\} \\ & - \sum_{i=1}^N \Delta F(t - \tilde{\tau}_i, \psi(\tilde{\tau}_i), \dot{\psi}(\tilde{\tau}_i), h(\tilde{\tau}_i), \sigma_0) \end{aligned} \quad (65)$$

Like the deficiency function  $F(t - \tau; \dots)$ , the transient terms  $\Delta F(t - \tilde{\tau}_i; \dots)$  all approach zero as  $(t - \tilde{\tau}_i) \rightarrow \infty$ . For a given value of  $t$ , only the last term of this sequence  $\Delta F(t - \tilde{\tau}_N; \dots)$  may be expected to make a significant contribution to Eq. (65), and this only when  $t$  is in the immediate vicinity of  $\tilde{\tau}_N$ .

Equation (65) is the desired integral form for the response in rolling-moment coefficient  $C_L(t)$  to an arbitrary rolling-moment maneuver  $\psi(t)$ . It can accommodate the double-valued, discontinuous behavior of the steady-state rolling-moment coefficient that was postulated in Fig. 20. Indeed, the first term in Eq. (65) represents just this variation. In the application of Eq. (65) to the study of arbitrary maneuvers, it remains to determine a logic for assigning the appropriate value of  $h$  to an indicial response. With the form of  $C_L(\infty; \psi(t), h(t), \sigma_0)$  presumed known from, for example, results of wind-tunnel experiments, the values of the critical points  $\psi = \pm \psi_c$  are also known, and this is all that is required to establish the necessary logic.

Assume that a step-by-step calculation is being made of a maneuver and that the calculation has advanced to the point  $\xi = \tau$  (Fig. 22). To continue the calculation one more step, it is necessary to assign the appropriate indicial response to the point  $\xi = \tau$ . The form of the indicial response, Eq. (58), indicates the parameters that have to be known:  $\psi(\tau), \dot{\psi}(\tau), h(\tau)$ . Since  $\psi(\xi)$  is known for  $\xi \leq \tau$ , the values of  $\psi(\tau), \dot{\psi}(\tau)$  can be specified. It remains to determine whether  $h = 0$  or 1 to complete the specification. The following three questions are asked: (1) Is there at least one  $\xi = \hat{\xi}$  where  $\psi(\xi) = +\psi_c$  and  $\dot{\psi}(\xi) > 0$ ? (2) Is there at least one  $\xi = \bar{\xi}$  where  $\psi(\xi) = -\psi_c$  and  $\dot{\psi}(\xi) < 0$ ? (3) If the answers to

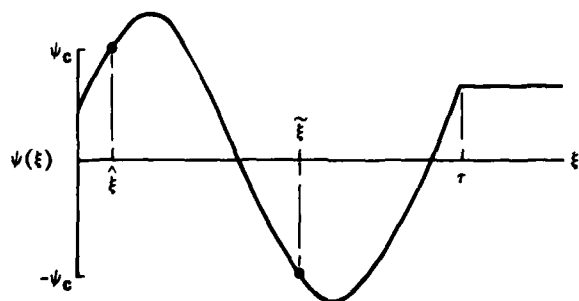


Figure 22. Step-by-step calculation of a roll maneuver.

(1) and (2) are yes, is  $\min(\tau - \xi) > \min(\tau - \hat{\xi})$ ? Yes or no answers to the three questions determine the value of  $h$ . Results are given in Table 1.

Table 1. Decision logic for  $h$ .

1	2	3	4
No	No	---	0 or 1
Yes	No	---	1
No	Yes	---	0
Yes	Yes	Yes	1
Yes	Yes	No	0

The one indeterminate case occurs when  $|\psi(\xi)|$  never exceeds  $\psi_c$ . Here, the value of  $h$  prescribed at  $\xi = 0$  remains the same for all  $\xi$ ,  $0 \leq \xi \leq \tau$ .

## 6. CONCLUDING REMARKS

A review of the basic concepts involved in the mathematical modeling of the aerodynamic response of an aircraft to arbitrary maneuvers has led from Bryan's original formulation, through the concepts of linear aerodynamic indicial functions and superposition integrals, to the extension of these concepts into the nonlinear regime. It has been shown that replacing the indicial functions within the superposition integrals by functionals, themselves dependent on the past motion, achieves the desired objective. A simple specification of the degree to which the reformulated indicial responses are cognizant of the past motion led to practicable nonlinear generalizations of the linear superposition and stability derivative formulations of the aerodynamic response to arbitrary motions. Applied to arbitrary nonplanar motions, the generalization yielded a form for the aerodynamic response built up of the contributions from a limited number of well-defined characteristic motions. The aerodynamic responses to the characteristic motions can, in principle, be evaluated either from flow-field computations or from experimental measurements. A further generalization led to a formulation accommodating the discontinuous double-valued behavior characteristic of hysteresis in the steady-state aerodynamic response.

## REFERENCES

1. Jones, B. Melville, Dynamics of the Aeroplane, Sec. N of Aerodynamic Theory (Vol. 5). W. F. Durand, ed., Dover Publications, New York, 1963.
2. Bryan, G. H., Stability in Aviation. MacMillan and Co., London, 1911.
3. Tobak, M. and Schiff, L. B., "On the Formulation of the Aerodynamic Characteristics in Aircraft Dynamics." NASA TR R-456, 1976.
4. Tobak, M. and Schiff, L. B., "The Role of Time-History Effects in the Formulation of the Aerodynamics of Aircraft Dynamics." AGARD CP-235, Dynamic Stability Parameters, Paper No. 26, May 1978.
5. Schiff, L. B. and Tobak, M., "Some Applications of Aerodynamic Formulations to Problems in Aircraft Dynamics." AGARD Lecture Series No. 114 on Dynamic Stability Parameters, Lecture No. 16, March 1981.
6. Chyu, W. J. and Schiff, L. B., "Nonlinear Aerodynamic Modeling of Flap Oscillations in Transonic Flow - A Numerical Validation." AIAA Paper 81-0073, St. Louis, Mo., Jan. 1981.
7. Schiff, L. B., Tobak, M., and Malcolm, G. N., "Mathematical Modeling of the Aerodynamics of High-Angle-of-Attack Maneuvers." AIAA Paper 80-1583-CP, Danvers, Mass., Aug. 1980.
8. Lanchester, F. W., Aerodonetics. A. Constable and Co., Ltd., London, 1908.
9. Etkin, B., Dynamics of Flight - Stability and Control. John Wiley and Sons, Inc., N.Y., 1959, pp. 164-166.
10. Garrick, I. E., "Nonsteady Wing Characteristics" (Sec. F of Aerodynamic Components of Aircraft at High Speeds), Vol. VII of High Speed Aerodynamics and Jet Propulsion. A. F. Donovan and H. R. Lawrence, eds., Princeton Univ. Press, Princeton, N.J., 1957.
11. Tobak, M., "On the Use of the Indicial Function Concept in the Analysis of Unsteady Motions of Wings and Wing-Tail Combinations." NACA Rep. 1188, 1954.
12. Tobak, M. and Pearson, W. E., "A Study of Nonlinear Longitudinal Dynamic Stability." NASA TR R-209, Sept. 1964.
13. Tobak, M., "On Nonlinear Longitudinal Dynamic Stability." AGARD-CP-17, Part 1, Stability and Control, 1966, pp. 161-175.
14. Tobak, M., Schiff, L. B., and Peterson, V. L., "Aerodynamics of Bodies of Revolution in Coning Motion." AIAA Journal, Vol. 7, No. 1, Jan. 1969, pp. 95-99.
15. Levy, L. L., Jr. and Tobak, M., "Nonlinear Aerodynamics of Bodies of Revolution in Free Flight." AIAA Journal, Vol. 8, No. 12, Dec. 1970, pp. 2168-2171.

16. Tobak, M. and Schiff, L. B., "Generalized Formulation of Nonlinear Pitch-Yaw-Roll Coupling. Part I: Nonaxisymmetric Bodies." AIAA Journal, Vol. 13, No. 3, March 1975, pp. 323-326.
17. Tobak, M. and Schiff, L. B., "Generalized Formulation of Nonlinear Pitch-Yaw-Roll Coupling. Part II: Nonlinear Coning-Rate Dependence." AIAA Journal, Vol. 13, No. 3, March 1975, pp. 327-332.
18. Volterra, V., Theory of Functionals and of Integral and Integro-Differential Equations. Dover Pub., Inc., New York, 1959.
19. Ericsson, L. E., "Unsteady Aerodynamics of Separating and Reattaching Flow on Bodies of Revolution," Recent Research on Unsteady Boundary Layers, Vol. 1. IUTAM Symposium, 1971, edited by E. A. Eichelbrenner, Les Presses de l'Université Laval, Quebec, Canada, 1972, pp. 481-512.
20. Ottensoser, J., "High Angle of Attack Aerodynamic Data for a 0.10 Scale A-7 Model Evaluated in the 7 by 10 Foot Transonic Wind Tunnel for Investigating the Stall Departure Phenomena, Phase 1." NSRDC TM-16-76-16, Oct. 1975.
21. Herman, J. F. and Washington, E. S., "Wind Tunnel Investigation of the Aerodynamic Hysteresis Phenomenon on the F-4 Aircraft and its Effects on Aircraft Motion." AEDC-TR-80-10, Sept. 1980.
22. Magnus, R. and Yoshihara, H., "Unsteady Flows over an Airfoil." AIAA Journal, Vol. 13, No. 12, Dec. 1975, pp. 1622-1628.
23. Steger, J. L., "Implicit Finite-Difference Simulation of Flow About Arbitrary Two-Dimensional Geometries." AIAA Journal, Vol. 16, No. 7, July 1978, pp. 679-686.
24. Chyu, W. J. and Davis, S. S., "Calculation of Unsteady Transonic Flow Over an Arbitrary Airfoil." AIAA Paper 79-1554, Williamsburg, Va., July, 1979 (also AIAA Journal, in print).
25. Miles, J. W., The Potential Theory of Unsteady Supersonic Flow. Cambridge Univ. Press, England, 1959.
26. Schiff, L. B. and Tobak, M., "Results from a New Wind-Tunnel Apparatus for Studying Coning and Spinning Motions of Bodies of Revolution." AIAA Journal, Vol. 8, No. 11, Nov. 1970, pp. 1953-1957.
27. Iyengar, S., "Experimental Damping-in-Pitch of Two Slender Cones at Mach 2 and Incidences up to 30°." LTR-UA-19, National Research Council, Ottawa, Canada, Jan. 1972.
28. Tobak, M. and Wehrend, W. R., "Stability Derivatives of Cones at Supersonic Speeds." NACA TN 3788, 1956.
29. Wykes, J. H. and Casteel, G. R., "Comparison of Computer and Flight Test Results for a Spinning Aircraft." AGARD-CP-17, Part 1, Stability and Control, 1966, pp. 103-125.
30. Scherer, M. and Aguesse, M., "Étude Analytique de la Vrille." AGARD-CP-17, Part 1, Stability and Control, 1966, pp. 127-138.
31. Langham, T. F., "Correlation of Experimental and Theoretical Steady-State Spinning Motion for a Current Fighter Aircraft Using Rotation-Balance Aerodynamic Data." AIAA Paper 78-1373, Palo Alto, Calif., Aug. 1978.
32. Chapman, D. R., Dryden Lecture: "Computational Aerodynamics Development and Outlook." AIAA Journal, Vol. 17, No. 12, Dec. 1979, pp. 1293-1313.
33. Pulliam, T. H. and Steger, J. L., "Implicit Finite-Difference Simulations of Three-Dimensional Compressible Flow." AIAA Journal, Vol. 18, No. 2, Feb. 1980, pp. 159-167.
34. Schneider, C. P., "Presentation of Stability Derivatives in Missile Aerodynamics and Theoretical Methods for their Prediction." AGARD CP-235, Dynamic Stability Parameters, Paper No. 20, May 1978.
35. Peake, D. J. and Tobak, M., "Three-Dimensional Interactions and Vortical Flows with Emphasis on High Speeds." AGARDograph No. 252, July 1980.
36. Szodruch, J. G. and Peake, D. J., "Leeward Flow over Delta Wings at Supersonic Speeds." NASA TM-81187, April 1980.
37. Schiff, L. B., "A Study of the Nonlinear Aerodynamics of Bodies in Nonplanar Motion." NASA TR R-421, Jan. 1974.
38. Lin, T. C., "A Numerical Study of the Aerodynamics of a Reentry Vehicle in Steady Coning Motion." AIAA Paper 78-1358, Palo Alto, Calif., Aug. 1978.
39. Agarwal, R. and Rakich, J. V., "Computations of Supersonic Laminar Viscous Flow Past a Pointed Cone at Angle of Attack in Spinning and Coning Motion." AIAA Paper 78-1211, Seattle, Wash., July 1978.
40. Sturek, W. B., Dwyer, H. A., Kayser, L. D., Nietubicz, C. J., Reklis, R. P., and Opalka, K. O., "Computations of Magnus Effects for a Yawed, Spinning Body of Revolution." AIAA Journal, Vol. 16, No. 7, July 1978, pp. 687-692.
41. Agarwal, R. and Rakich, J. V., "Computation of Hypersonic Laminar Viscous Flow Past Spinning Sharp and Blunt Cones at High Angle of Attack." AIAA Paper 78-65, Huntsville, Ala., Jan. 1978.

42. Sturek, W. B. and Schiff, L. B., "Computations of the Magnus Effect for Slender Bodies in Supersonic Flow" AIAA Paper 80-1586-CP, Danvers, Mass., Aug. 1980.
43. Sturek, W. B., Mylin, D. C., and Bush, C. C., "Computational Parametric Study of the Aerodynamics of Spinning Slender Bodies at Supersonic Speeds." AIAA Paper 80-1585-CP, Danvers, Mass., Aug. 1980.
44. Malcolm, G. N. and Davis, S. S., "New NASA-Ames Wind Tunnel Techniques for Studying Airplane Spin and Two-Dimensional Unsteady Aerodynamics." AGARD CP-235, Dynamic Stability Parameters, Paper No. 3, May 1978.
45. Hanff, E. S. and Orlik-Rückemann, K. J., "A Generalized Technique for Measuring Cross-Coupling Derivatives in Wind Tunnels." AGARD CP-235, Dynamic Stability Parameters, Paper No. 9, May 1978.
46. Orlik-Rückemann, K. J., "Techniques for Dynamic Stability Testing in Wind Tunnels." AGARD CP-235, Dynamic Stability Parameters, Paper No. 1, May 1978.
47. Hanff, E. S. and Kapoor, K. B., "Measurement of Dynamic Direct and Cross-Coupling Derivatives Due to Oscillatory Roll." ICIASF 1979 Record, Sept. 1979, pp. 186-193.
48. O'Leary, C. O., "Wind Tunnel Measurements of Lateral Aerodynamic Derivatives Using a New Oscillatory Rig, with Results and Comparisons for the Gnat Aircraft." RAE TR 77159, 1977.
49. Elle, B. J., "An Investigation at Low Speed of the Flow near the Apex of Thin Delta Wings with Sharp Leading Edges." R&M 3176, ARC 19 780, 1961.

## IMPACT OF HIGH-ALPHA AERODYNAMICS ON DYNAMIC STABILITY PARAMETERS OF AIRCRAFT AND MISSILES

Gerald N. Malcolm  
Ames Research Center, NASA  
Moffett Field, California 94035, U.S.A.

### SUMMARY

In this lecture, the aerodynamic phenomena associated with high angles of attack and their effects on the dynamic stability characteristics of airplane and missile configurations are examined. Information on dynamic effects is limited. Steady-flow phenomena and their effects on the forces and moments are reviewed. The effects of asymmetric vortices and of vortex bursting on the dynamic response of flight vehicles are reviewed with respect to their influence on (1) nonlinearity of aerodynamic coefficients with attitude, rates, and accelerations; (2) cross-coupling between longitudinal and lateral-directional modes of motion; (3) time-dependence and hysteresis effects; (4) configuration dependency; and (5) mathematical modeling of the aerodynamics.

### I. INTRODUCTION

Flight envelopes of modern aircraft and missiles have expanded considerably beyond those of the past because of increased demands for improved maneuverability. As a result, flight vehicles encounter higher angles of incidence and higher angular rates and accelerations. A number of aerodynamic phenomena relating to high angles of attack have been identified and investigated in detail. Nonlinearities in static aerodynamics of modern configurations and simplified research configurations have been well documented and continue to be of high interest. Less is currently known about dynamic effects at high angles of attack, but it is recognized that there are some important dynamic contributions to the forces and moments that govern the flight behavior of advanced aircraft and missiles. This lecture will review some of the static phenomena related to high-incidence flight and will discuss some examples of the effect of high incidences on dynamic stability parameters.

### 2. STATIC AERODYNAMIC PHENOMENA

There are numerous phenomena associated with high angles of attack that are nonexistent or negligible at low angles of attack. Among these are at least two phenomena that have received considerable attention and that also significantly affect the dynamic behavior of flight vehicles. One phenomenon that has been a focal point for basic research is the formation of forebody vortices and their development into an asymmetric distribution when the angle of attack reaches a critical value. This phenomenon is common to most modern aircraft that have long slender fuselage forebodies and to missiles. Another phenomenon that is often important at high angles of attack is the breakdown of the vortices formed at the leading edge of the wing and the effect of this breakdown on the forces exerted on the vehicle. The interaction of vortices from various vehicle components also has a significant influence on the aerodynamics and flight dynamics.

Analytical methods to compute the asymmetric forces on even simple configurations are not yet developed. Approximate methods utilizing empirical data from wind-tunnel experiments for determining flow separation location and vortex strength and position are being used to specify the character of the flow field and to estimate the aerodynamic forces and moments. Most research investigations have been experimental programs based on wind-tunnel tests. Experiments have consisted of force and moment measurements, surface pressure measurements, surface oil-flow studies, vapor-screen vortex flow visualization, laser velocimeter flow-field measurements, and water-tunnel flow visualization studies. Some of the results of these investigations will be reviewed. Phenomena observed in static tests have a large effect on dynamic characteristics; a review of these phenomena will provide an introduction to dynamic effects.

#### 2.1 Forebody Vortices

Extensive studies have been performed on the effects of angle of attack on the flow field about bodies of revolution and in particular on the formation of asymmetric vortices and the resulting side forces and yawing moments. Chapman and Keener (Ref. 1) and Ericsson and Reding (Ref. 2) provide extensive reviews of some of the investigations conducted to understand the effects of angle of attack on the basic flow field and the resulting forces and moments. Figure 1 (from Ref. 1) shows the four major flow types: vortex-free flow at low  $\alpha$ ; symmetric and asymmetric vortex flow fields at moderate to high  $\alpha$ ; and cylinder wake-like flow at extremely high  $\alpha$ . The effects on side and normal forces (Ref. 1) are illustrated in Fig. 2. In the vortex-free regime the normal force is nearly linear with angle of attack and the side force is zero. When the angle of attack increases sufficiently for the flow to separate as it flows around the body in the cross-flow plane and form symmetric vortices on the leeward side, the normal force increases nonlinearly in response to the added vortex lift. Further increases in angle of attack bring about an asymmetric vortex flow field and the introduction of a side force which can reach values comparable to the normal force. (For axisymmetric bodies with fins or wings, rolling moments can also develop.) Still further increases in angle of attack result in the phenomenon of the flow becoming very unsteady and assuming a wake-like behavior characteristic of the flow around a cylinder in cross-flow, with the mean side force decreasing toward zero. Figure 3 shows the different flow regimes (Ref. 1) and the onset boundaries as a function of angle of attack and fineness ratio (body length to diameter ratio,  $L/d$ ). A higher fineness ratio generally results, for example, in a side force appearing at a lower angle of attack. References 3-11 provide extensive documentation of the effects of high angles of attack on a variety of bodies of revolution, with emphasis on tangent-ogive forebodies and ogive-cylinders. Figure 4 shows a plot (Ref. 1) of the onset angle of attack, the angle where asymmetric vortex-induced side forces first appear, as a function of the semiaxial angle of the nose for various length-to-diameter ratios of the body. For a simple forebody without a cylindrical afterbody the

onset angle is approximately twice the semiapex angle. Figure 5 shows the effect of Mach number on the maximum side force (Ref. 1) for two different forebodies (fineness ratios of 2.5 and 5.0) and afterbody length-to-diameter ratios ranging from 0 to 11. The side forces occur primarily at subsonic Mach numbers and they rapidly decrease in magnitude as the Mach number is increased into the transonic range. The asymmetric vortex pattern persists, however, and for bodies with fins or tails the vortices can interact with these surfaces and produce large forces and moments.

Force and moment measurements have been supplemented in some of the cited references by surface oil-flow studies and by vapor-screen flow visualization to study the characteristics of the surface and vortex flow patterns. More recently, detailed pressure measurements have been made on extensively instrumented tangent ogive cylinder pressure models (Refs. 12-14). Effects of roll angle, Reynolds number, and angle of attack have been investigated, and the distribution of the forces and moments on the models, as well as the integrated total forces and moments, have been determined. Variation in the side force with roll angle (on a body of revolution) is one of the more interesting phenomena that have been observed; it significantly affects the dynamics of a spinning body. Figure 6 (from Ref. 14) shows the maximum side force as a function of roll angle for a tangent ogive-cylinder model with an  $\alpha/d = 2.0$  nose and an  $r/d = 5.5$  cylindrical afterbody. The model was at  $\alpha = 55^\circ$  at  $M = 0.25$ , and the forces were determined by integrating over 400 surface pressures on the body. The important behavior to note is that even though this is a body of revolution, the side force switches sign with a change in roll angle. The large side force, of course, is the result of an asymmetric flow field dominated by asymmetric vortices on the leeward side of the model. Intuitively, one would not expect the vortex pattern to change with roll angle since the body is axisymmetric. The direction or "hand" of the asymmetric vortices is apparently very sensitive to even the slightest imperfection on the body nose tip, and the asymmetric vortex pattern can be easily triggered to reverse. The effect of this switching on the dynamics of a vehicle in flight that is spinning or rolling about its own axis is an important question. An experiment was conducted on a spinning  $10^\circ$  half-angle cone (Ref. 15) fixed at  $\alpha = 60^\circ$ , and a real-time readout of the side force was recorded at several spin rates. Figure 7 shows the results of this experiment. The side-force variation with roll angle appears to repeat regardless of the spin rate, at least to moderate spin rates. Although there may be some smoothing of the peak value as the speed increases and although the magnitude of the force appears to decrease with increasing rate, there remains a fluctuating force (and moment) which a free-flight vehicle would experience. Further experiments were conducted on an ogive cylinder model (Ref. 16) to investigate the behavior of maximum side-force amplitude with spin rate. Also, the effects of artificially triggering the direction of the flow asymmetry with small trips on the model nose at various spacings around the circumference were investigated. Basically, the amplitude of the side force appears to decrease as the spin rate increases, but it was not consistently clear what the mean value of this fluctuating force would be in the limit of infinite spin rate. It was found, however, that one can artificially switch the vortex pattern with trips, the frequency of switching depending on the number of trips.

## 2.2 Vortex Breakdown

In addition to vortex asymmetry on missiles and aircraft forebodies, an important contribution to the total configuration aerodynamics is derived from the phenomenon of vortex bursting and breakdown. Vortices are found at the leading edge of the wing and, with increasing angle of attack, they eventually break down. Vortex breakdown, or vortex-burst, is characterized by a sudden decrease in the axial velocity component to near zero with a corresponding increase in the diameter of the vortex core and a decrease in the circumferential velocity. This vortex-burst phenomenon is a strong function of the leading-edge sweep angle. Figure 8 presents results (Refs. 17,18) from a water-tunnel test that shows, for sharp-edged delta wings of different sweep angles, that the variation in vortex-burst location is a function of angle of attack and sweep angle. Also, for a delta wing the angle of attack at which vortex-burst occurs at the wing trailing edge increases approximately linearly with the leading-edge sweep (Refs. 17,18), as shown in Fig. 9, where the different points represent values obtained both in air and in water. As the angle of attack increases further, the breakdown occurs gradually more and more forward of the trailing edge. For highly swept delta wings, the vortex flow field or the vortex-burst location may become asymmetric (Refs. 18,19) causing an onset of asymmetric aerodynamic reactions similar to the effects of forebody vortex asymmetry discussed previously (Fig. 10). It is interesting to note that in both cases the height of the vortex core above the surface of the wing (or of the body) also becomes quite different on the left and right sides of the configuration.

The flow phenomena about highly swept wings are similar to those occurring on the so-called wing leading-edge extensions (LEX) or wing-body strakes. Large interactions may occur on an aircraft configuration between the forebody vortices and the vortex systems emanating from the leading edges of the various wing surfaces. If the vortex breakdowns or the asymmetric vortices are located close to any stabilizing or control surfaces of the aircraft, significant effects on aerodynamic reactions may result.

Note also that although an aircraft flying at high angle of attack can develop asymmetric flow even at zero nominal sideslip (as discussed above), such an asymmetric flow will also occur, of course, at lower angles of attack when the aircraft is exposed to finite angles of sideslip. Since such a flight condition is encountered quite frequently, the remarks in this paper that deal with the effects of flow asymmetries have a rather general application. It has already been shown that the phenomenon of vortex-burst is quite sensitive to the sweep angle of the wing and therefore is also strongly dependent on the angle of sideslip (Ref. 20). Figure 11 illustrates, for example, that the effect of a wing/LEX (leading-edge extension) in sideslip can produce an asymmetric vortex-burst because of an effective increase in sweep on the leeward LEX and wing and a decrease on the windward LEX and wing. Also, even if an aircraft flies at an angle of attack below that at which vortex-burst occurs, an oscillatory variation in the instantaneous angle of sideslip may, under some circumstances, cause a corresponding periodic occurrence of the vortex-burst on the wings. A high angle of attack, therefore, is to some extent equivalent to a combination of a somewhat lower angle of attack and a finite angle of sideslip.

Of course, the phenomena mentioned so far are not necessarily associated with dynamic flight conditions; they occur in both steady and oscillatory flows. What makes the oscillatory flows particularly difficult is the introduction of the time element into this already rather complex picture. The forebody vortices change their lateral and vertical positions as functions of angle of attack, which itself is a function of time.

The same is true for the longitudinal location of "fully developed" leading-edge vortex bursts. The various components of the aircraft, such as the fin and the horizontal stabilizer, move in and out of local flow regions in which they are embedded. To make matters even more complex, these aerodynamic phenomena do not take place simultaneously with the motion of the aircraft, but experience a certain delay, due mainly to the convective time lag. The delay is a function of the distance of the station under consideration from the station at which a particular flow phenomenon, such as a vortex, leaves the surface of the aircraft. Thus, aerodynamic reactions that have components both in-phase and out-of-phase with the motion of the aircraft can be expected to materialize.

### 3. DYNAMIC STABILITY PARAMETERS

With the previous discussion of steady aerodynamic flow phenomena at high angles of attack as background, we can examine some of the effects these phenomena have on the dynamic behavior of vehicles and explore some of the other dynamic phenomena that are negligible or nonexistent at low attitudes. Orlitz-Ruckemann has reviewed some of the more important considerations in Refs. 21 and 22. The following discussion will draw heavily from his review but will also present some additional examples when they are available. The most important effects result from (1) large nonlinear variations of both static and dynamic stability parameters with angle of attack; (2) static and dynamic aerodynamic cross-coupling between longitudinal and lateral directional modes of motion; (3) time-dependent and hysteresis aerodynamics; (4) significant configuration dependency; and (5) mathematical modeling of the aerodynamic coefficient.

#### 3.1 Nonlinearities

##### 3.1.1 Oscillatory motion

Some examples of dynamic stability parameters that vary nonlinearly with angle of attack are shown in Figs. 12 and 13. In Fig. 12 pitch and yaw damping of a wing-body configuration (Fig. 14) tested at  $M = 0.7$  on a forced oscillation rig at NAE (Ref. 23) are shown. The curves show clearly the rapid changes in magnitude with angle of attack. It can be appreciated that if the angle of attack about which the oscillation takes place happens to be in the region where a sudden change in a derivative occurs, large effects of the amplitude of oscillation may be expected. In cases like this the linearized formulation concept for derivatives can only give an equivalent linearized description of the dependence of the aerodynamic reaction on the variable of motion, and a better mathematical formulation is definitely needed.

Similar nonlinearities in damping parameters were measured at Langley Research Center, NASA (Ref. 24) for a fighter aircraft at low subsonic speeds; the results are shown in Fig. 13. The yaw damping parameter exhibits a very sudden and very large unstable peak at angles of attack of about  $60^\circ$ . This is usually the result of the vortex pattern that is associated with long, pointed forebodies. The roll damping parameter shows marked irregularities and a large dependence on the amplitude of oscillation at angles of attack between  $25^\circ$  and  $45^\circ$ . The smaller the amplitude of oscillation, the more pronounced is the local instability in roll. It has also been observed (although not shown here) that a decreasing oscillation frequency has a similar destabilizing effect. The authors of Ref. 24 indicated that they found it necessary to incorporate this nonlinear behavior of the damping-in-roll coefficient within the equations of motion used in their simulator studies in order to achieve a satisfactory match with wing-rock motions observed in full-size flight experiments. It has been shown that one possible source of this observed nonlinearity in the damping-in-roll parameter may be a static hysteresis in the rolling-moment coefficient with roll angle. An analysis of this effect is presented in Lecture No. 16 by Schiff and Tobak.

Equally dramatic nonlinearities with angle of attack also occur in other dynamic parameters, such as those resulting from cross-coupling between the rolling and yawing degrees of freedom. Typical cross-coupling derivatives are shown in Fig. 15 (Ref. 25). It is interesting to note that the angle of attack at which these peaks occur is largely independent of both the wing-sweep angle and the presence of vertical tails. (The height of the peak, however, is decreased when the vertical tails are off and when the reduced frequency is increased.) This suggests that the primary mechanism for these effects may be associated with the existence and motion of the forebody vortices.

##### 3.1.2 Coning motion

Experiments have been performed in numerous facilities on rotary-balance rigs (see Lecture No. 6). For many configurations the variation in the aerodynamic parameters with both the angle of attack and the rotation rate is highly nonlinear.

A set of yawing and rolling moment parameters obtained from rotary-balance experiments for a current combat aircraft (Ref. 26) is shown in Fig. 16. The measured roll damping compares favorably with flight-test data up to  $\alpha = 20^\circ$ , but shows a nonlinear behavior at higher angles of attack that is different from estimates based on static wing pressure measurements. The measured yawing moment parameter, on the other hand, shows a much smoother variation with angle of attack than the predicted one, but exhibits a well-pronounced peak that is totally absent in the estimates. In both cases the nonlinearities are significant and, on the whole, not satisfactorily predicted.

Another example (Refs. 27,28) shows considerable nonlinearity with spin rate, but also shows large effects from angle of attack and Reynolds number. Experiments were conducted in the 12-Foot Pressure Tunnel at Ames Research Center at  $M = 0.25$  with the basic airplane-like model shown in Figs. 17 and 18. Multiple six-component force/moment balances were used in an exploratory test (Ref. 28) to evaluate separately the effects of nose, tail, and the complete configuration (including the wing) during a steady spin motion. Subsequent tests (Ref. 29), using specially designed force balances in the nose and tail sections and eliminating the wing section and the sting balance, concentrated principally on the nose effects. Some of the pro-spin flow mechanisms of interest are shown schematically in Fig. 17. These include asymmetric flow on square-type cross sections and vortex flow about a simple tail configuration. With rotation rates to 63 rad/sec (600 rpm), manual angle-of-attack settings at  $\alpha = 45^\circ$ ,  $60^\circ$ ,  $75^\circ$ , and  $90^\circ$ , and roll angles of up to  $10^\circ$  for

the nose, tail, and wing sections about the longitudinal axis of the model, it was possible to evaluate effects pertinent to "flat" spins ( $75^\circ < \sigma < 90^\circ$ ) and "steep" spins ( $45^\circ < \sigma < 75^\circ$ ).

An example of the aerodynamic characteristics in a flat spin motion at  $\sigma = 90^\circ$  (Ref. 28) is shown in Fig. 19. This example clearly illustrates the strong dependence of the nose side-force coefficient  $C_y$  on Reynolds number and rotation or spin rate ( $\Omega = wb/2V$ ). One interesting feature of this "flat spin case" is the hysteresis loop in  $C_y$  with rotation rate that occurs in the middle Reynolds number range. This phenomenon occurs as a result of the flow-separation characteristics on the nose section as the local angle of attack varies along the nose as the rotational speed is increased and then decreased. This interesting flow phenomenon is explained in detail in Ref. 28. No hysteresis effects were observed below  $\sigma = 90^\circ$ . Figures 20, 21, and 22 show the Reynolds number effects on the nose side-force coefficient at  $\sigma = 75^\circ$ ,  $60^\circ$ , and  $45^\circ$ , respectively. For the  $\sigma = 60^\circ$  and  $45^\circ$  cases, the flow behavior and resulting side force are quite different from those at  $\sigma = 90^\circ$  and  $75^\circ$ . The lowest Reynolds number conditions show anti-spin contributions rather than pro-spin, as for  $\sigma = 90^\circ$  and  $75^\circ$ . In fact, at  $\sigma = 45^\circ$  no condition produced a pro-spin contribution.

Another example (Ref. 30) of large nonlinearities in rotary balance data is shown in Fig. 23. Pitching, rolling, and yawing moments for a series of general aviation models are shown versus reduced spin parameter. The nonlinearity is pronounced, and the sense of the rolling and yawing moments can change from autorotative to damping with rotation rate. The pitching moment increases by as much as 50% over the static value, and the increase for this case was found to be due primarily to the horizontal tail effect.

An example (Ref. 31) of aerodynamic data for a simple body, a  $10^\circ$  half-angle cone, tested in coning motion on a small-scale rotary apparatus is shown in Fig. 24. The side moment (yaw moment) parameter, that is,  $\alpha C_{nq}/\alpha \phi$ , or rate of change of side moment with respect to  $\phi$ , the coning rate parameter, is shown versus resultant angle of attack for  $M = 1.4$  and  $2.0$ . At low values of angle of attack,  $C_{nq}$  is linear with  $\sigma$  and agrees with theory. At angles of attack beyond the cone half angle the measured values become highly nonlinear. The initial nonlinearity with increasing  $\sigma$  was shown from flow-field computations (Ref. 32) to be due to asymmetry within the inviscid surface-pressure distribution. At angles of attack beyond  $\sigma = 20^\circ$ , the nonlinearity in the side moment was shown to be due, in part, to asymmetric leeside vortices. It was further shown in Ref. 31 that up to the cone half-angle, the damping in pitch ( $C_{mq} + C_{ma}$ ) is equivalent to  $1/\sigma (C_{nq} - C_{nq})$ . ( $C_{nq}$  is the Magnus moment parameter. For these experiments the magnitude of the Magnus moment is near zero since the spin rate is quite low.) The conclusion from this aerodynamic math model derivation and experiment is that for the  $10^\circ$  cone it is possible to obtain the linear damping-in-pitch parameter,  $C_{mq} + C_{ma}$ , from steady measurements of the side-moment contributions from coning and spinning.

### 3.2 Aerodynamic Cross-Coupling

The second important effect of high angle of attack on dynamic stability considerations is the presence of aerodynamic cross-coupling caused by asymmetric flow conditions. As already mentioned, asymmetric flow occurs not only when an aircraft flies at nonzero sideslip but also when it flies at zero sideslip but at high angles of attack; this is a result of the asymmetric shedding of forebody vortices. In both cases we may expect the occurrence of secondary lateral aerodynamic forces and moments in response to a primary pitching maneuver, and, vice versa, the onset of secondary longitudinal reactions in response to a primary lateral maneuver. Because of various time lags, these secondary reactions will consist of components that are both in-phase and out-of-phase with the primary motion, and will give rise, therefore, to both static and dynamic cross-coupling effects. In the first approximation such effects can be described by introducing the concept of static and dynamic cross-coupling parameters. These quantities, which at the present time may be difficult to determine either theoretically or from flight tests, can now be obtained from special dynamic experiments in a wind tunnel, as discussed in other lectures. It should be mentioned also that in the presence of significant cross-coupling it becomes necessary to consider the lateral and the longitudinal equations of motion of an aircraft simultaneously and not in two separate groups, as has often been done in the past.

To gain some understanding of the fluid dynamics phenomena that may be responsible for aerodynamic cross-coupling, oil visualization of the surface flow is often very helpful. In Fig. 25 (from Ref. 23) such surface flow is shown for an aircraft-like configuration at several angles of attack, with the angle of sideslip held fixed at  $10^\circ$ , and Mach number held fixed at 0.7. One can see one of the primary separation lines moving from one side of the model to the other, as the angle of attack increases from  $12.5^\circ$  to  $14^\circ$  and then to  $17.5^\circ$ . This, of course, indicates a corresponding movement of one of the forebody vortices, which is located just above and a little to the side of the separation line. It can easily be appreciated that, if the same model was performing an oscillation in pitch around a mean angle of attack of  $15^\circ$  and with an amplitude of  $\pm 2.5^\circ$ , the vortex would be oscillating laterally back and forth across the vertical fin, thereby causing large lateral aerodynamic reactions as functions of the angle of attack. Because of the convective time lags involved, these lateral reactions are both in phase and out of phase with the model motion, giving rise to both static and dynamic yawing and rolling moments and to the side force, due to pitching. An additional contribution to these parameters, and one at least as important, is made by the highly dissimilar flow over the two wings (and highly dissimilar changes in this flow with angle of attack), also shown in Fig. 25. Cross coupling in the opposite sense is also possible, such as static and dynamic pitching moment coefficients due to yawing. All such parameters provide aerodynamic cross-coupling between the lateral and the longitudinal degrees of freedom of an aircraft and are called, therefore, cross-coupling parameters (reserving the name of cross parameters for the traditional parameters relating the two lateral degrees of freedom, such as the rolling moment due to yawing or vice versa).

In most cases, the determination of cross-coupling parameters requires access to special-purpose experimental equipment. Since the interest in these parameters is relatively recent, the necessary equipment is not yet generally available and, therefore, very little experimental data have so far been accumulated. One set of data, on the same aircraft-like configuration as that shown in the flow-visualization pictures, has been obtained at NAE (Ref. 33), and some examples are presented in Fig. 26. At the top, the dynamic yawing and rolling moment parameters due to pitching are shown, and at the bottom,

the pitching moment parameter due to yawing. In all cases the coefficients are relatively small for low angles of attack, but attain large values and display sudden variations at angles of attack of  $16^\circ$  to  $19^\circ$ , which coincides quite well with the angle of attack at which, according to the flow-visualization studies, one of the separated forebody vortices moves over the fin. Another series of rapid and large variations occurs for angles of attack of  $31^\circ$  to  $34^\circ$ . In all cases, both the level attained and the suddenness of variations is much larger for the lateral moments due to pitching than for the pitching moments due to yawing.

The inclusion of dynamic cross-coupling terms in the equations of motion may have large effects on the predicted motion time history, as shown in Fig. 27, where the angular rates following a sudden perturbation in  $\alpha$  of  $0.05$  rad are presented for a hypothetical military aircraft in a turning flight (Ref. 34). Had the dynamic cross-coupling terms not been included, the rates  $p$ ,  $r$ , and  $\dot{\beta}$  would have remained essentially constant. It was shown in the sensitivity study of Ref. 34 that among the dynamic cross-coefficients considered, lateral moments due to pitching were particularly significant and that in some cases they could have an effect on the predicted motion as large as that of some of the well-known damping and cross parameters. Similar results were independently obtained (Ref. 35).

### 3.3 Time-Dependent and Hysteresis Effects

In addition to quasi-steady effects, such as those represented by parameters of various aerodynamic reactions due to angular velocities, we have to consider the existence of purely unsteady effects, such as those due to the time rate of change of angular deflections,  $\dot{\alpha}$  or  $\dot{\beta}$ . The existence of these parameters has been realized for many years, since they constitute part of the dynamic results obtained with standard wind-tunnel techniques of oscillation around a fixed axis, which always give composite expressions such as  $(C_{m_q} + C_{m_\alpha})$ . Up to now, however, it was standard practice to ignore the  $\dot{\alpha}$  and  $\dot{\beta}$  effects (or to introduce a simple correction for them) and to use the composite expressions in place of the purely rotary ones, such as  $C_{m_q}$ . At low angles of attack, the error introduced by such a procedure was often small and the simplification significant enough to be justifiable.

At higher angles of attack, however, the  $\dot{\alpha}$  and  $\dot{\beta}$  effects unfortunately become quite substantial and can no longer be ignored or corrected for in a simple fashion. This is illustrated in Fig. 28, where the composite expressions obtained from oscillatory experiments around a fixed axis are compared (Refs. 17 and 36) with purely rotary parameters obtained from experiments in a curved or rotating flow for two fighter aircraft. The difference between each set of results represents the unsteady effects due to the time-rate-of-change of the angular deflection (in this case the angle of sideslip); it becomes quite significant for higher angles of attack.

Changes due to the time-rate-of-change of angular deflections are aerodynamically equivalent (in the first approximation) to changes due to translational acceleration in the same plane of motion. This fact renders them of high interest for aircraft designs in which direct-lift or direct-side-force controls are used and also makes it possible to determine them experimentally, using a translational oscillatory motion in the vertical or lateral direction (Ref. 37).

High angle of attack flow phenomena, such as asymmetric vortex shedding and vortex breakdown (vortex-burst), are frequently responsible for static aerodynamic hysteresis effects. Hysteresis is characterized by a double-valued behavior of the steady-state aerodynamic response to variations in one of the motion variables, such as angle of attack or angle of sideslip. An example of aerodynamically induced hysteresis is asymmetric vortices to the left or to the right with angle of attack changes. Figure 29 shows an  $\alpha$ -hysteresis in the variation of location of the vortex-burst on a delta wing (Ref. 38) and an example of  $\beta$ -hysteresis in the variation of lateral aerodynamic coefficients for an aircraft configuration (Ref. 17). These loops are traced in opposite directions and under dynamic conditions are manifested as strong damping effects. A much more comprehensive discussion on hysteresis is presented in Lecture No. 1. In the presence of such hysteresis effects the dynamic characteristics of an aircraft can be expected to be strongly dependent on both the amplitude and the frequency of oscillation. When conducting experiments in the critical range of, say,  $25^\circ < \alpha < 40^\circ$ , it is advisable to obtain data (both static and dynamic) in very small increments of angle of attack.

### 3.4 Configuration Dependence

The vortex pattern that exists around an aircraft configuration at high angles of attack is very sensitive to even small changes in aircraft geometry. A particularly critical part of the aircraft is the forebody, and especially the nose itself, which is the area where the body vortices are formed. An example is presented in Fig. 30, where the effect of a flat, broad nose (developed by Northrop and called the "Shark Nose"; Ref. 17) on the variation with angle of attack of the dynamic directional stability parameter,  $C_{n_B DYN}$ , is shown. The shark-nose geometry attenuates the unfavorable local reduction in that parameter and at the same time extends this favorable influence on stability to somewhat lower angles of attack. It has also been demonstrated in Ref. 17 (but not shown here) that the presence of the shark nose enhances greatly the directional stability at small nonzero angles of sideslip ( $|\beta| < 5^\circ$ ).

One of the most common methods of ensuring a symmetrical shedding of forebody vortices at zero sideslip is, of course, the use of forebody strakes. Although, when used alone, these strakes often prevent the formation of a unique vortex pattern at nonzero sideslip, thereby seriously reducing the directional stability of the configuration, they can be amazingly effective when used in combination with a suitable nose geometry. Figure 30 presents the effect of the shark nose used together with a particular leading-edge extension (LEX), which can be considered to be a form of strake. It can be seen that the negative peak in  $C_{n_B DYN}$  is almost totally eliminated and that the favorable influence on stability now extends to both lower and higher values of angle of attack.

The effects of strakes (or leading-edge extensions) on various dynamic stability parameters is shown in Fig. 31. In all cases the addition of strakes reduces the magnitude of the parameters, practically

eliminates nonlinearities with angle of attack in the range investigated (except for pitch damping), and makes the parameters independent of reduced frequency (Ref. 39). The dynamic yawing coefficient due to rolling becomes essentially zero. The negative damping in roll (for  $\alpha > 13^\circ$ ), in pitch (for  $12^\circ < \alpha < 23^\circ$ ), and in yaw (for  $\alpha > 11^\circ$ ) completely disappear.

As is well known, however, strakes do have certain disadvantages, and their successful development for a particular application may require much trial and error. For example, they often adversely affect the directional stability; if mounted near the tip of the nose radome, they may disturb the radar operations; and the strake vortices may adversely interact with aircraft components farther downstream, such as at air intakes or control surfaces. Therefore, alternative approaches continue to be of high interest.

### 3.5 Aerodynamic/Mathematical Modeling

In view of the complexity of the aerodynamic phenomena just reviewed and the effects on the forces and moments that govern the behavior of flight vehicles at high angles of attack, it is obvious that linear mathematical models used to represent the aerodynamic inputs in the equations of motion are no longer adequate. The first lecture in this series and Ref. 40 described a derivation of a nonlinear mathematical model designed to accommodate some nonlinear phenomena as well as cross-coupling. Included in these model representations are terms to handle spinning and coning as well as oscillatory motions. Time history and hysteresis effects (Ref. 41) were also discussed in Lecture No. 1. In terms of selecting a proper model to represent the aerodynamics on a configuration of interest, one should choose the simplest model possible that accommodates the expected motions. This is not a trivial task since one does not know a priori the response of a particular vehicle to a set of initial conditions. This inability to choose a mathematical model a priori becomes clear when one considers some of the highly nonlinear phenomena just discussed. The most difficult flight regime to model is that which occurs, for example, between stall and a steady spin on aircraft configurations. Post-stall gyrations or complicated motions beyond departure are difficult to model mathematically, but even more difficult is the task of designing and building apparatuses to perform, in the wind tunnel, the appropriate experiments defined by the mathematical model. The first lecture defined requirements for forced oscillation apparatuses with the capability for determining cross-coupling, as well as direct damping parameters. Required also is an apparatus to produce a coning motion in the wind tunnel, not only to model steady aircraft spin motions, but as one of the required characteristic motions for general motions. Subsequent lectures will discuss in detail some of the advanced apparatuses that have been and are being developed which relate to the aerodynamic/mathematical model requirements.

It is clear that considerable research is in progress in an effort to advance our understanding of aerodynamic phenomena resulting from flight at high attitudes, and there are ongoing efforts to establish proper and complete aerodynamic mathematical models to represent these complicated aerodynamic inputs. However, it is equally as important to provide a conclusive verification of the model and to establish confidence that the model actually works. One convincing way to validate a given mathematical model is to be able to compare a predicted flight motion with an actual flight motion and to show that they are the same. The predicted motion must derive from measured (or computed) aerodynamic coefficients in the form consistent with the derived aerodynamic/mathematical model. Motions would be calculated with six degrees of freedom and with specific initial conditions and compared with actual flight histories of the same configuration, using the same initial conditions to start the flight motion. This verification has yet to be done in a complete and consistent manner. Now that more sophisticated wind-tunnel apparatuses are being developed to handle the nonlinear dynamic coefficients, it may become possible in the near future to perform the long-needed flight verification experiments.

### 4. CONCLUDING REMARKS

The purpose of this lecture was to review the effect of high angles of attack on the dynamic stability parameters of airplane and missile configurations. Since there is very little quantitative information on dynamic effects, the approach taken was to point out some of the flow phenomena that have been observed and to discuss the resulting influence they have on the aerodynamic forces and moments. The effect of asymmetric forebody vortices, which occur both on airplane fuselage noses and on missiles, was reviewed. The phenomenon of vortex-burst, or vortex breakdown, was also examined. The effects of these highly complex, separated three-dimensional flows on the dynamic response of a flight vehicle were examined with respect to their influence on (1) nonlinearity of aerodynamic coefficients with attitude, rates, and accelerations, (2) cross-coupling between longitudinal and lateral-directional modes of motion, (3) time-dependence and hysteresis effects, (4) configuration dependency, and (5) mathematical modeling of the aerodynamics. Much remains to be learned about the effects of high angles on the dynamic stability characteristics. The overall aerodynamics of both aircraft and missiles is strongly driven by the nonlinearity of the steady inputs. The relative importance of dynamic contributions to the response of a flight vehicle is not as clear as it needs to be. Considerable effort is under way to assess the dynamic contributions through development of sophisticated experimental apparatuses for wind-tunnel tests. Simultaneous efforts must also be made to assess the importance of these contributions to the flight motions of the vehicles of interest. Contributions that are judged to be important to the accurate prediction of flight motion histories should be identified and the means to measure them pursued with vigor.

### 5. REFERENCES

- Chapman, G. T. and Keener, E. R., "The Aerodynamics of Bodies of Revolution at Angles of Attack to 90°." AIAA Paper 79-0023, Jan. 1979. (Written version unavailable.)
- Ericsson, L. E. and Reding, J. P., "Vortex-Induced Asymmetric Loads in 2-D and 3-D Flows." AIAA Paper 80-0181, Jan. 1980.
- Chapman, G. T., Keener, E. R., and Malcolm, G. N., "Asymmetric Aerodynamic Forces on Aircraft Forebodies at High Angles of Attack - Some Design Guides." Paper No. 12, AGARD CP-199, Stall/Spin Problems of Military Aircraft, 1975.

4. Keener, E. R. and Chapman, G. T., "Onset of Aerodynamic Side Forces at Zero Sideslip on Symmetric Forebodies at High Angles of Attack." AIAA Paper 74-770, 1974.
5. Keener, E. R. and Taleghani, J., "Wind Tunnel Investigation of the Aerodynamic Characteristics of Five Forebody Models at High Angles of Attack: Mach Numbers from 0.25 to 2.0." NASA TM X-62,502, 1975.
6. Keener, E. R., Chapman, G. T., and Kruse, R. L., "Effects of Mach Number and Afterbody Length on Onset of Asymmetric Forces on Bodies at Zero Sideslip and High Angles of Attack." AIAA Paper 76-66, Jan. 1976.
7. Keener, E. R., Cohen, G. T., and Teleghani, J., "Side Forces on a Tangent Ogive Forebody with a Fineness Ratio of 3.5 at High Angles of Attack and Mach Numbers from 0.1 to 0.7." NASA TM X-3437, 1977.
8. Keener, E. R., Cohen, G. T., and Teleghani, J., "Side Forces on Forebodies at High Angles of Attack and Mach Numbers from 0.1 to 0.7: Two Tangent Ogives, Paraboloid and Cone." NASA TM X-3438, 1977.
9. Keener, E. R. and Valdez, J., "Side Forces on a Tangent Ogive Forebody with a Fineness Ratio of 2.5 at High Angles of Attack and Low Speed." NASA TM X-73,176, 1976.
10. Jorgensen, L. H. and Nelson, E. R., "Experimental Aerodynamic Characteristics for a Cylindrical Body of Revolution with Various Noses at Angles of Attack from 0° to 55° and Mach Numbers from 0.6 to 2.0." NASA TM X-3128, 1974.
11. Jorgensen, L. H., "Reduction of Static Aerodynamic Characteristics for Slender Bodies Alone and with Lifting Surfaces to Very High Angles of Attack." NASA TR R-474, Sept. 1977.
12. Lamont, P. J. and Hunt, B. L., "Pressure and Force Distributions on a Sharp-Nosed Circular Cylinder at Large Angles of Inclination to a Uniform, Subsonic Stream." Journal of Fluid Mechanics, Vol. 76, Part 3, 1976, pp. 519-559.
13. Hunt, B. L. and Dexter, P. C., "Pressure on a Slender Body at High Angles of Attack in a Very Low Turbulence Level Air Stream." Paper No. 17, AGARD CP-247, High Angle of Attack Aerodynamics, 1978.
14. Lamont, P. J., "Pressure Measurements on an Ogive-Cylinder at High Angles of Attack with Laminar, Transitional, or Turbulent Separation." AIAA Paper 80-1556, Aug. 1980.
15. Kruse, R. L., "Influence of Spin Rate on Side Force of an Axisymmetric Body." Journal of Spacecraft and Rockets, Apr. 1978.
16. Fidler, J. E., "Active Control of Asymmetric Vortex Effects." AIAA Paper 80-0182, Jan. 1980.
17. Skow, A. M. and Titiriga, A., Jr., "A Survey of Analytical and Experimental Techniques to Predict Aircraft Dynamic Characteristics at High Angles of Attack." Paper No. 19, AGARD CP 235, Dynamic Stability Parameters, 1978.
18. Erickson, G. E., "Water Tunnel Flow Visualization: Insight Into Complex Three-Dimensional Flow Fields." AIAA Paper 79-1530, 1979.
19. Keener, E. R. and Chapman, G. T., "Similarity in Vortex Asymmetries Over Slender Bodies and Wings." AIAA Journal, Vol. 15, No. 9, 1977.
20. Moore, W. A., Erickson, G. E., Lorincz, D. J., and Skow, A. M., "Effects of Forebody, Wing and Wing-Body-LEX Flowfields on High Angle of Attack Aerodynamics." SAE TP 791082, Dec. 1979.
21. Orlik-Ruckemann, K. J., "Effect of High Angles of Attack on Dynamic Stability Parameters." Paper No. 1, AGARD CP-247, High Angle of Attack Aerodynamics, 1978.
22. Orlik-Ruckemann, K. J. and Hanff, E. S., "Dynamic Stability Parameters at High Angles of Attack." 12th Congress of the International Council on the Aeronautical Sciences, ICAS-80-7.1, Oct. 1980.
23. Orlik-Ruckemann, K. J., "Aerodynamic Coupling Between Lateral and Longitudinal Degrees of Freedom." AIAA Journal, Vol. 15, No. 12, 1977, pp. 1792-1799.
24. Chambers, J. R., Gilbert, W. P., and Nguyen, L. T., "Results of Piloted Simulator Studies of Fighter Aircraft at High Angles of Attack." Paper No. 33, AGARD CP 235, Dynamic Stability Parameters, 1978.
25. Grafton, S. B. and Anglin, E. L., "Dynamic Stability Derivatives at Angles of Attack from -5° to 90° for a Variable-Sweep Fighter Configuration with Twin Vertical Tails." NASA TN D-6909, 1972.
26. Matthews, A. W., "Experimental Determination of Dynamic Derivatives due to Roll at British Aerospace, Warton Division." Paper No. 4, AGARD CP 235, Dynamic Stability Parameters, 1978.
27. Clarkson, M. H., Malcolm, G. N., and Chapman, G. T., "Experimental Post-Stall Rotary Aerodynamic Coefficients for Airplane-Like Configurations." AIAA Journal, Vol. 13, No. 8, 1976, pp. 565-570.
28. Malcolm, G. N. and Clarkson, M. H., "Wind Tunnel Testing with a Rotary-Balance Apparatus to Simulate Aircraft Spin Motions." Proceedings of AIAA 9th Aerodynamic Testing Conference, Arlington, Texas, June 7-9, 1976, pp. 143-156.
29. Malcolm, G. N., "New Rotation-Balance Apparatus for Measuring Airplane Spin Aerodynamics in the Wind Tunnel." Journal of Aircraft, Vol. 16, No. 4, 1979, pp. 264-268.

30. Birhle, W., Jr. and Bowman, J. J., Jr., "The Influence of Wing, Fuselage and Tail Design on Rotational Flow Aerodynamics Data Obtained Beyond Maximum Lift with General Aviation Configurations." AIAA Paper 80-0455-CP, Mar. 1980.
31. Schiff, L. B. and Tobak, M., "Results from a New Wind-Tunnel Apparatus for Studying Coning and Spinning Motions of Bodies of Revolution." AIAA Journal, Vol. 8, No. 11, 1970, pp. 1953-1957.
32. Schiff, L. B., "Nonlinear Aerodynamics of Bodies in Coning Motion." AIAA Journal, Vol. 10, No. 11, 1972, pp. 1517-1522.
33. Orlík-Ruckemann, K. J. and Hanff, E. S., "Experiments on Cross-Coupling and Translational Acceleration Derivatives." Paper No. 8, AGARD CP 235, Dynamic Stability Parameters, 1978.
34. Curry, W. H. and Orlík-Ruckemann, K. J., "Sensitivity of Aircraft Motion to Aerodynamic Cross-Coupling at High Angles of Attack." Paper No. 34, AGARD CP 235, Dynamic Stability Parameters, 1978.
35. Butler, R. W. and Langham, T. F., "Aircraft Motion Sensitivity to Variations in Dynamic Stability Parameters." Paper No. 35, AGARD CP 235, Dynamic Stability Parameters, 1978.
36. Coe, P. L., Jr. and Newson, W. A., Jr., "Wind-Tunnel Investigation to Determine the Low-Speed Yawing Stability Derivatives of a Twin-Jet Fighter Model at High Angles of Attack." NASA TN D-7721, 1974.
37. Orlík-Ruckemann, K. J., "Techniques for Dynamic Stability Testing in Wind Tunnels." Paper No. 1, AGARD CP 235, Dynamic Stability Parameters, 1978.
38. Ericsson, L. E., "A Summary of AGARD FDP Meeting on Dynamic Stability Parameters." Paper No. 2, AGARD FMP Symposium on Stability and Control, Sept. 1978.
39. Staudacher, W., Laschka, B., Schulze, B., Poisson-Quinton, P., and Canu, M., "Some Factors Affecting the Dynamic Stability Derivatives of a Fighter-Type Model." Paper No. 11, AGARD CP 235, Dynamic Stability Parameters, 1978.
40. Tobak, M. and Schiff, L. B., "On the Formulation of the Aerodynamic Characteristics in Aircraft Dynamics." NASA TR R-456, 1976.
41. Tobak, M. and Schiff, L. B., "The Role of Time-History Effects in the Formulation of the Aerodynamics of Aircraft Dynamics." Paper No. 26, AGARD CP 235, Dynamic Stability Parameters, 1978.

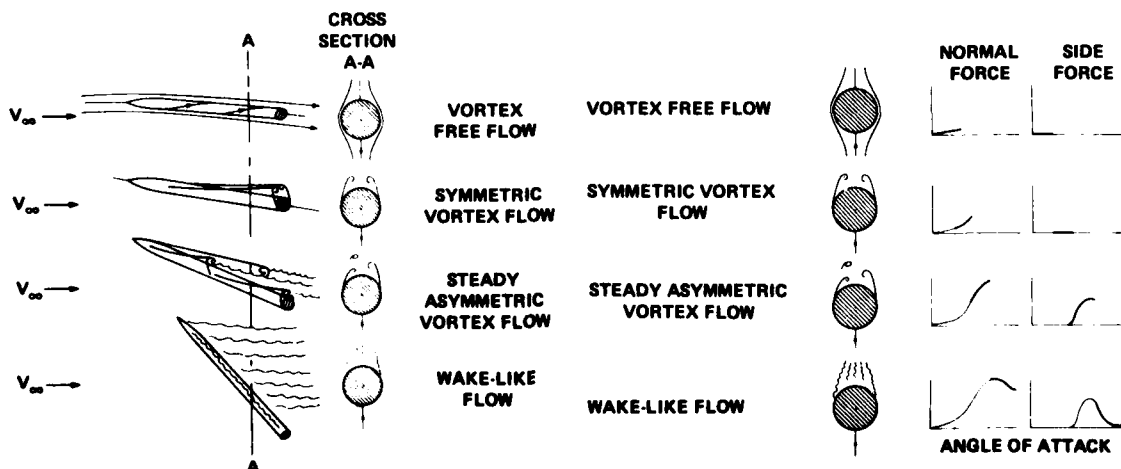


Figure 1. Flow types for increasing angle of attack on ogive-cylinder.

Figure 2. Force regimes for increasing angle of attack on ogive-cylinder.

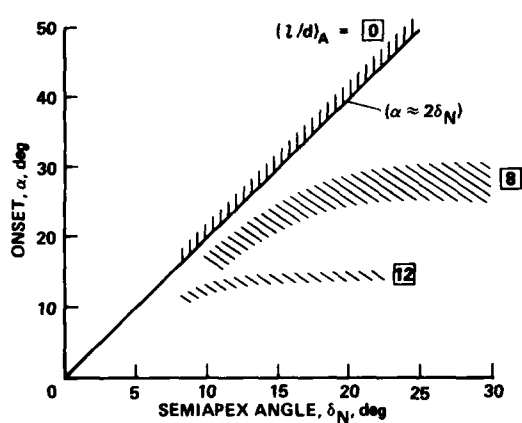
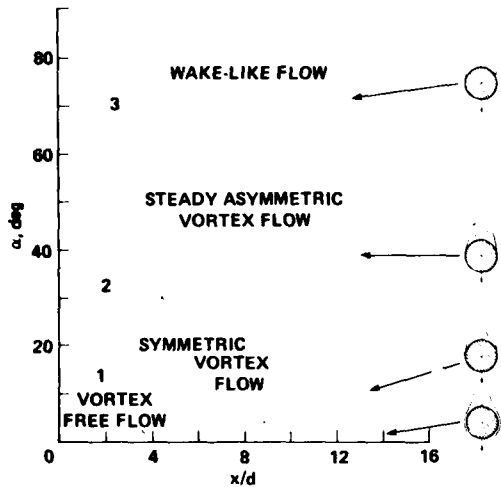


Figure 4. Boundaries for onset of aerodynamic asymmetry at  $\beta = 0$  for ogive-cylinders.

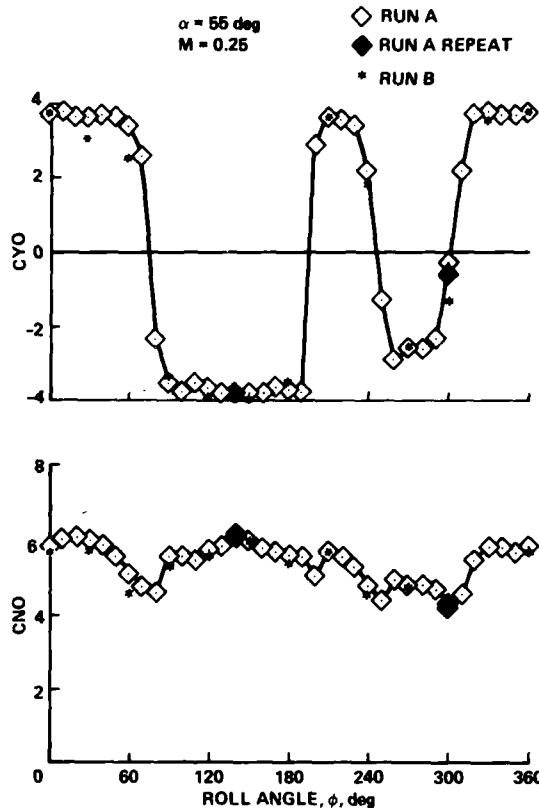
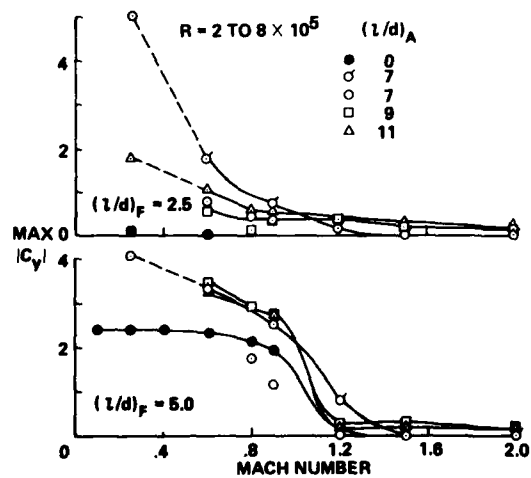
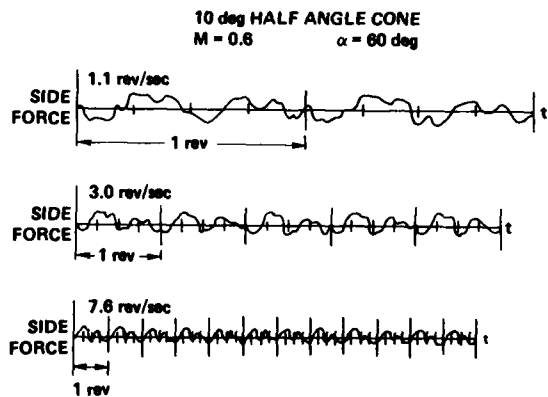


Figure 6. Variation of overall force coefficients with roll angle for ogive-cylinder at  $\alpha = 55^\circ$ .



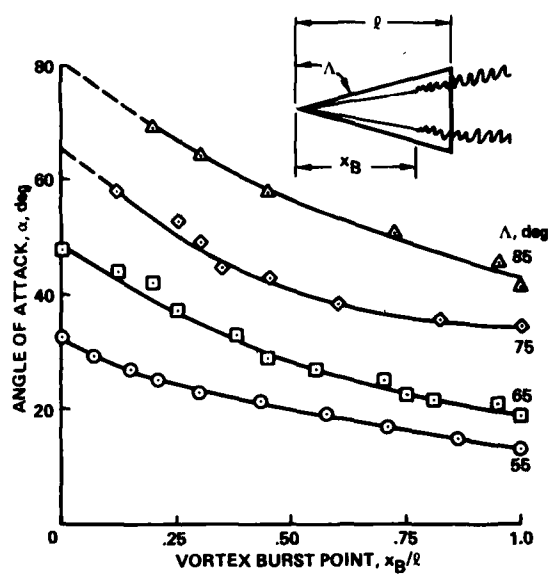


Figure 8. Vortex-burst point from water-tunnel tests for delta wing.

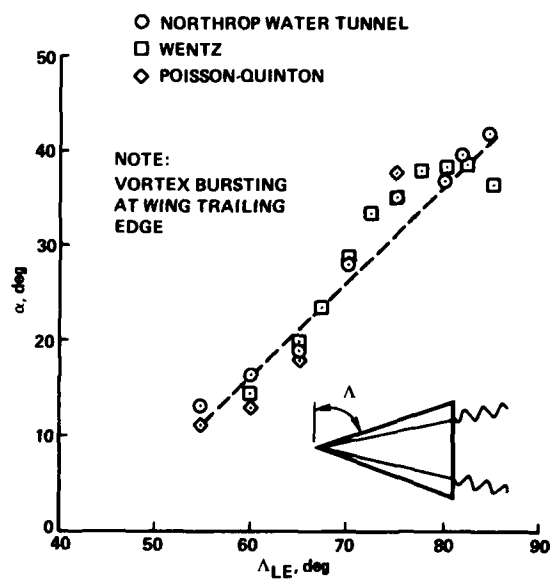


Figure 9. Angle of attack vs wing sweep angle for vortex burst at wing trailing edge.

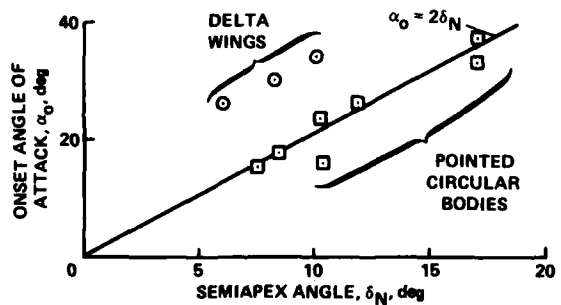


Figure 10. Onset of aerodynamic asymmetry for circular forebodies and delta wings.

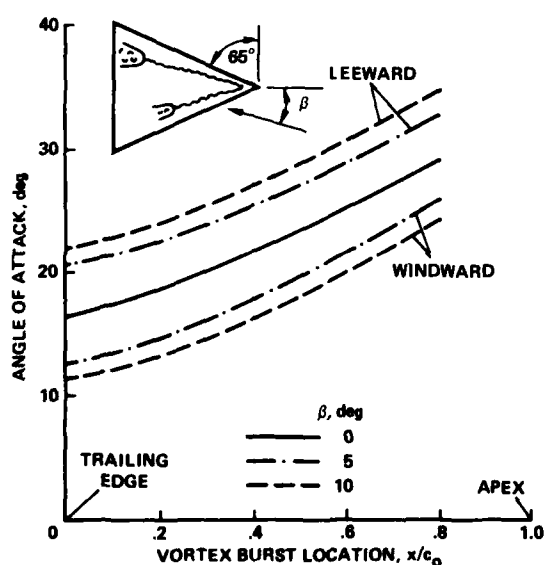
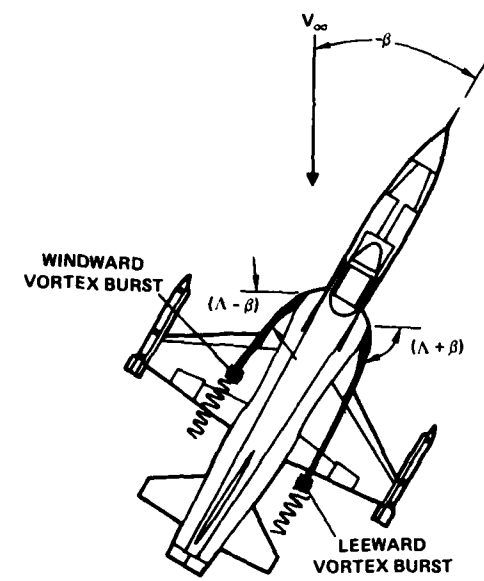


Figure 11. Asymmetric LEX vortex burst in sideslip.

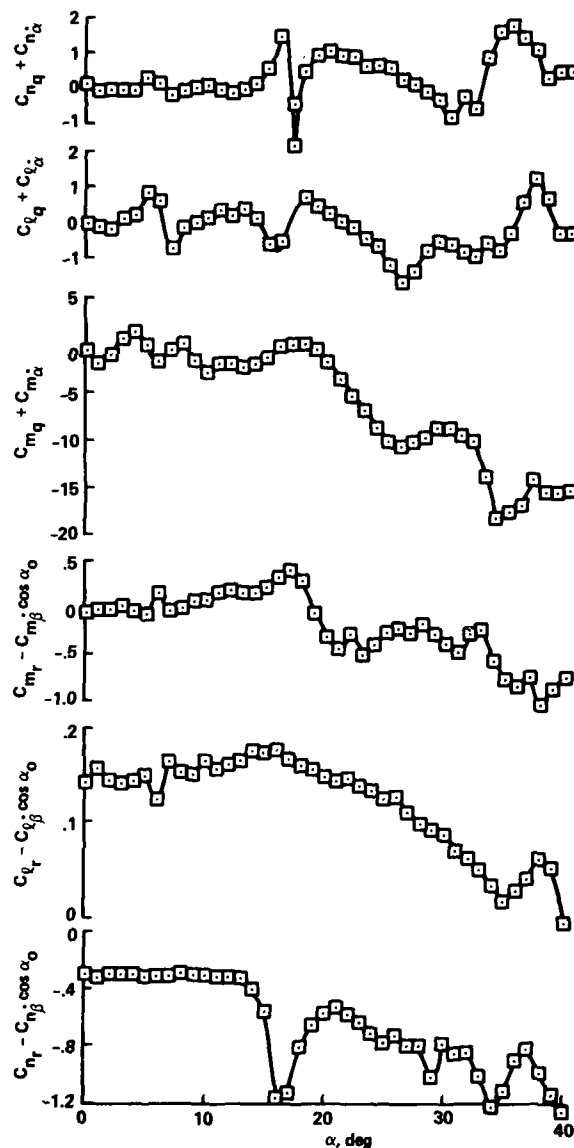
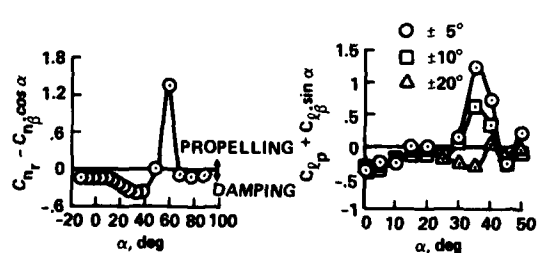
Figure 12. Subsonic damping derivatives for a wing-body configuration at  $M = 0.7$ ,  $\beta = 5^\circ$ .

Figure 13. Damping in yaw and roll for a fighter aircraft configuration.



Figure 14. Forced oscillation apparatus and model for direct and cross-coupling damping derivatives (NAE).

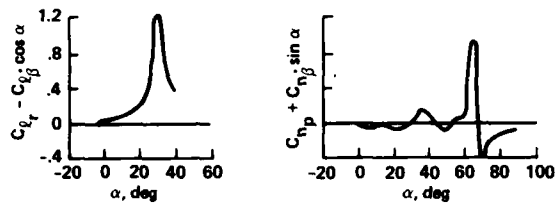


Figure 15. Low-subsonic cross derivatives for a swept-wing fighter configuration.

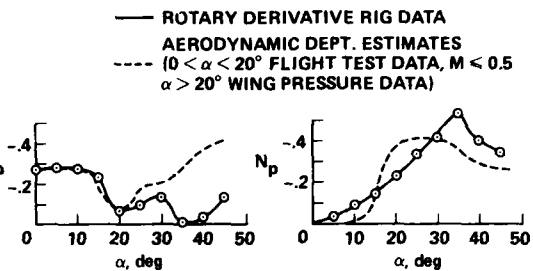


Figure 16. Rolling and yawing moment derivatives due to rolling for a current combat aircraft (wind axes).

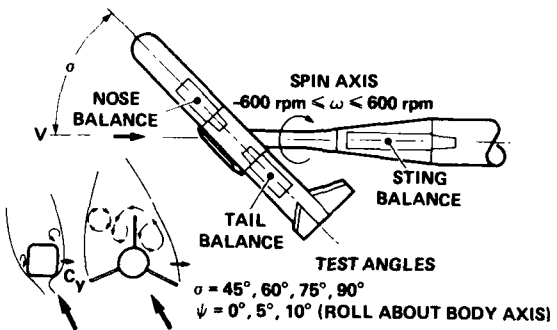


Figure 17. Rotary-balance and model arrangement; some pro-spin flow mechanisms.

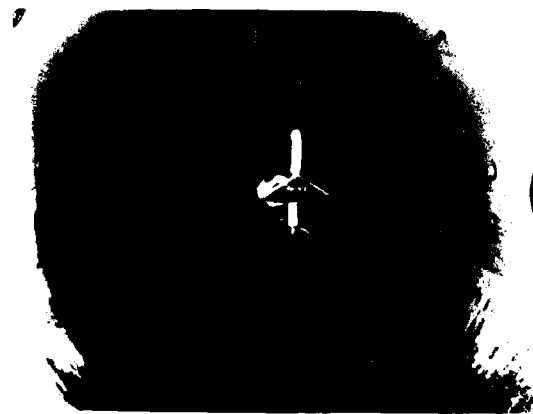


Figure 18. Photograph of model and rotary-balance apparatus in the 12-Foot Pressure Tunnel at Ames Research Center.

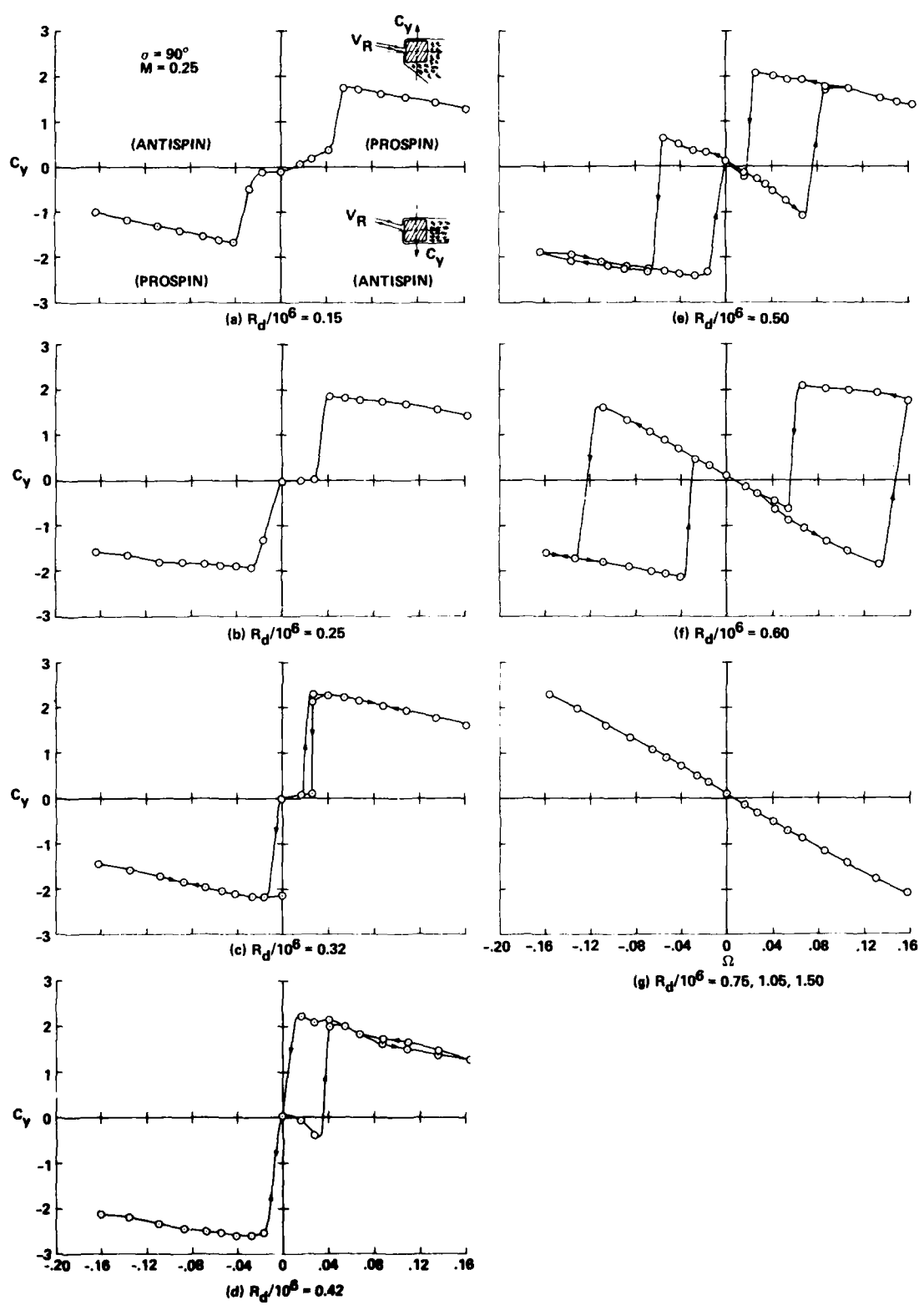


Figure 19. Nose side-force coefficient vs reduced spin rate for square cross section with rounded corners:  $\sigma = 90^\circ$ .

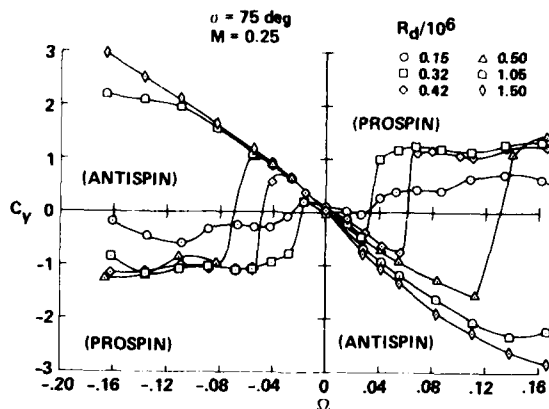


Figure 20. Nose side-force coefficient vs reduced spin rate for square cross section with rounded corners:  $\alpha = 75^\circ$ .

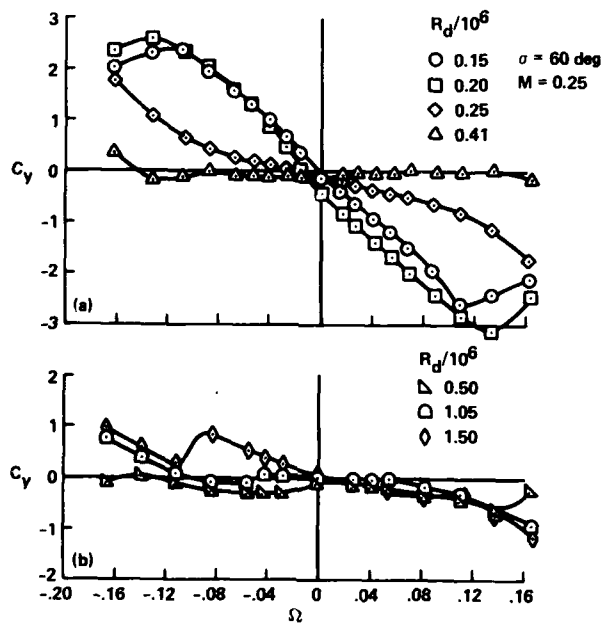


Figure 21. Nose side-force coefficient vs reduced spin rate for square cross section with rounded corners:  $\alpha = 60^\circ$ .

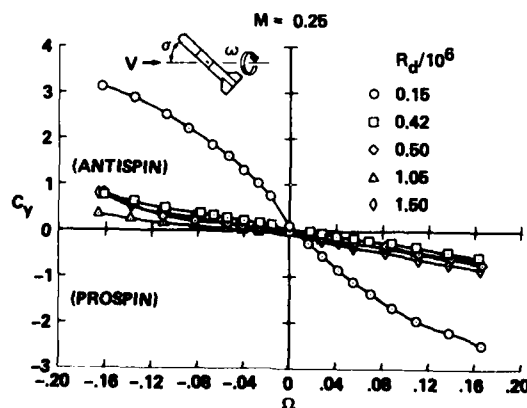


Figure 22. Nose side-force coefficient vs reduced spin rate for square cross section with rounded corners:  $\alpha = 45^\circ$ .

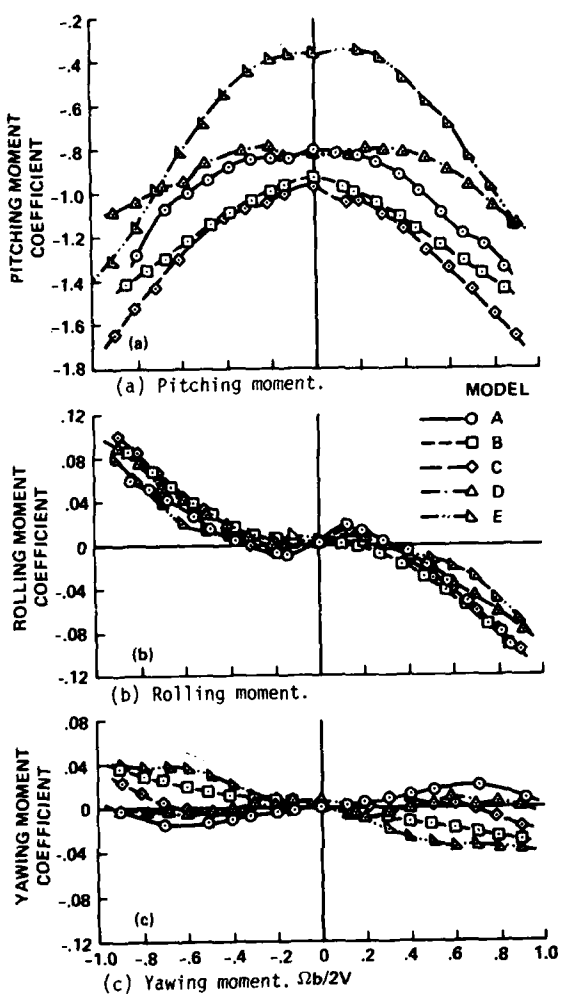


Figure 23. Effect of rotation rate on moment coefficients for general aviation configurations at  $\alpha = 60^\circ$ .

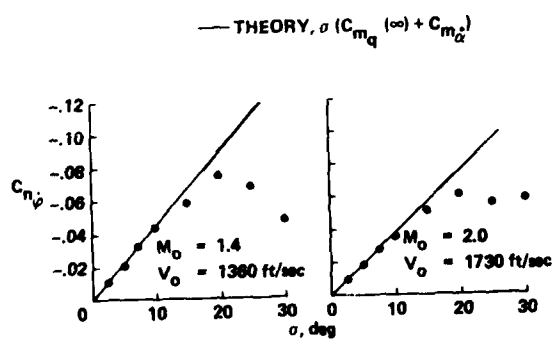


Figure 24. Side-moment derivative on 10° half-angle cone due to coning motion.

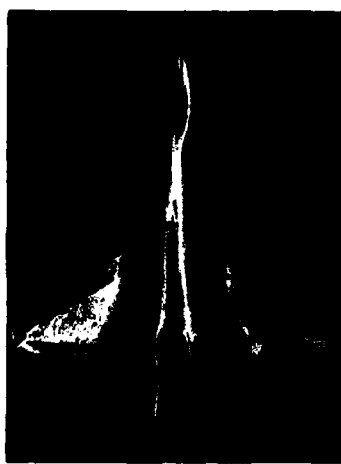
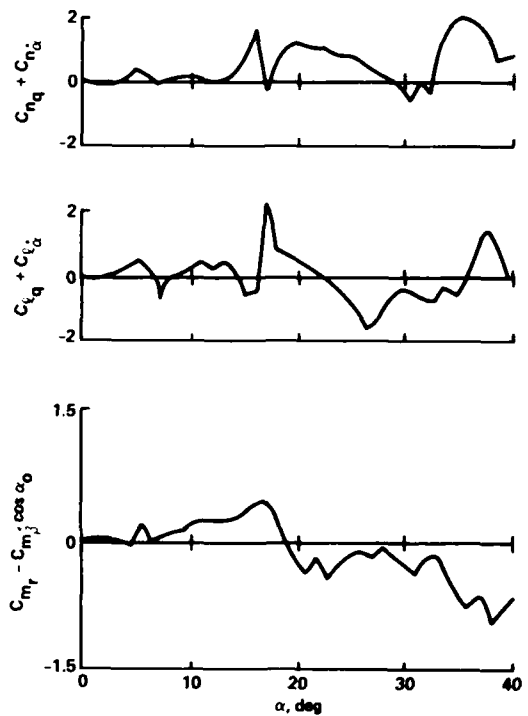
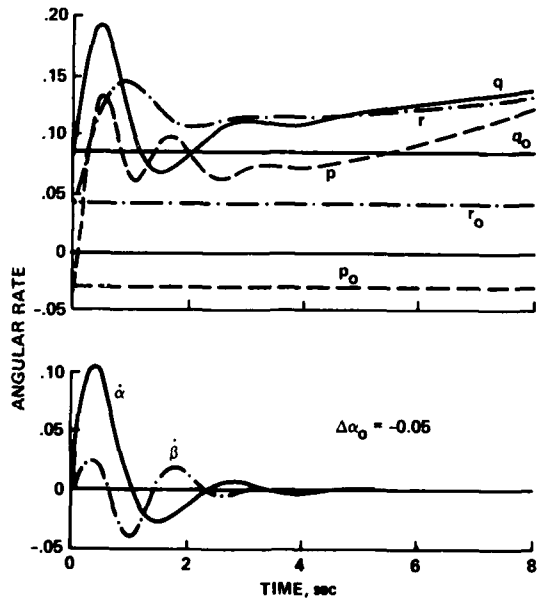
 $\alpha = 12.5 \text{ deg}, \beta = 10 \text{ deg}$  $\alpha = 14 \text{ deg}, \beta = 10 \text{ deg}$  $\alpha = 17.5 \text{ deg}, \beta = 10 \text{ deg}$ 

Figure 25. Aerodynamic cross-coupling visualized through surface oil flow.

Figure 26. Dynamic cross-coupling moment derivatives due to pitching and yawing, NAE airplane-like model:  $M = 0.7, \beta = 5^\circ$ .

NOTE 1: ANGULAR RATES FOR THE UNPERTURBED CASE  
REMAIN CONSTANT AND ARE DENOTED BY  
 $p_0, q_0, r_0$ .

NOTE 2: WITH ALL AERODYNAMIC CROSS-COUPLING  
DERIVATIVES EQUAL TO ZERO, THE RATES  $p, r$ ,  
AND  $\dot{\beta}$  REMAIN ESSENTIALLY CONSTANT WHEN  
PERTURBED BY  $\alpha$ .

Figure 27. Dynamic cross-coupling effects in 2-g turning flight for a fighter aircraft.

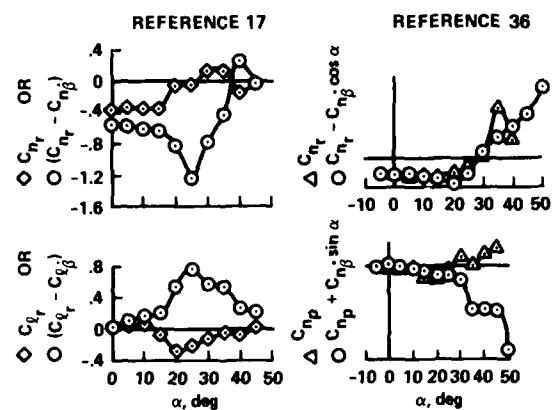
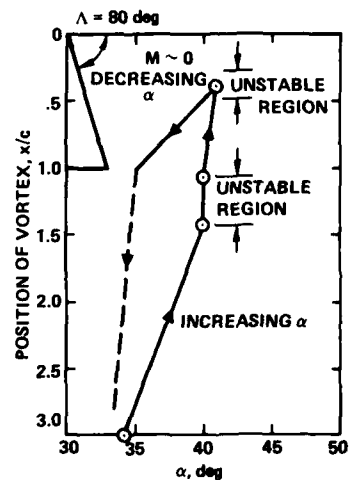
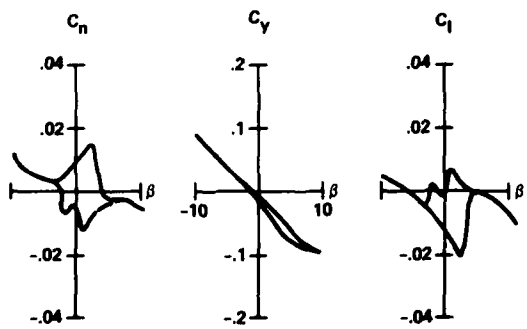


Figure 28. Dynamic derivatives with and without  $\beta$  contribution for two fighter aircraft.



(a) Vortex-burst location on delta wing.



(b) Lateral aerodynamic coefficients on a fighter configuration.

Figure 29. Aerodynamic hysteresis in a region of vortex breakdown.

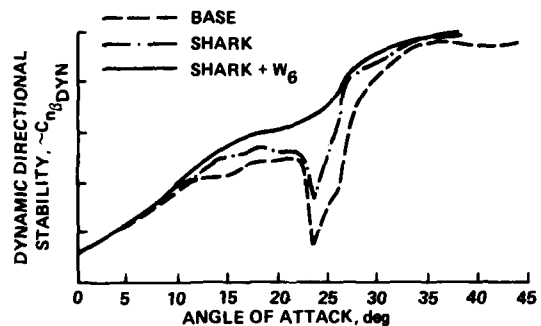
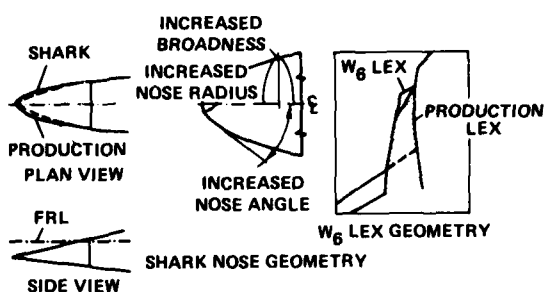


Figure 30. Configuration dependence, shark nose and leading-edge extension (LEX).

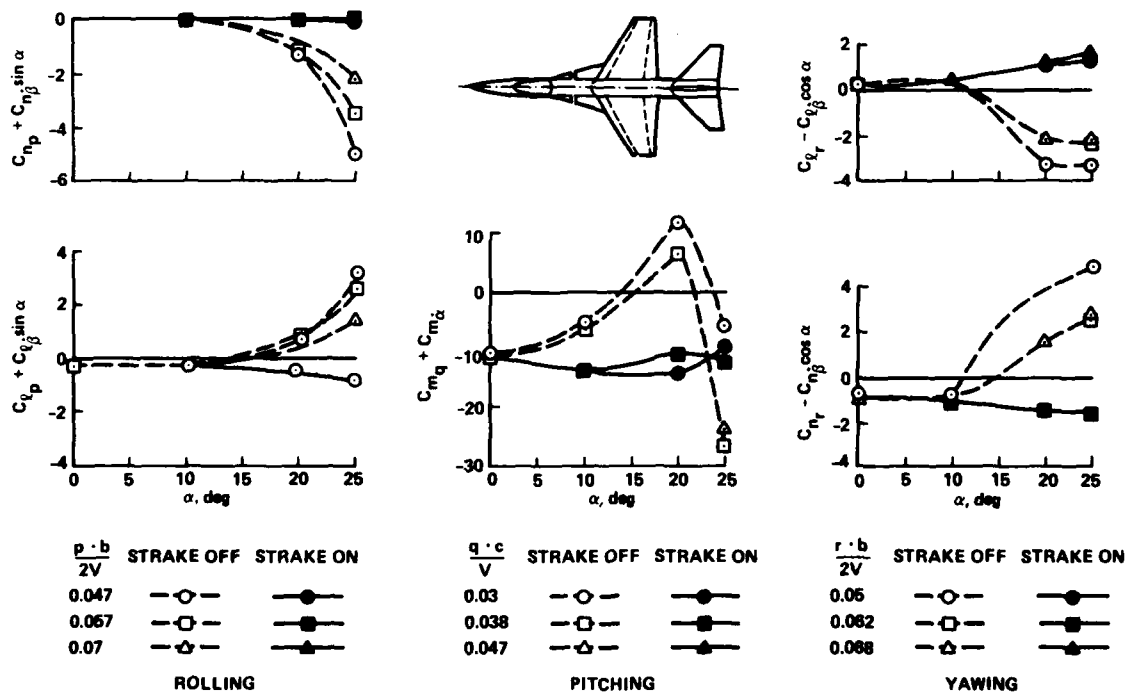


Figure 31. Configuration dependence, effect of strakes.

REVIEW OF TECHNIQUES FOR  
DETERMINATION OF DYNAMIC STABILITY  
PARAMETERS IN WIND TUNNELS

by

K. Orlik-Rückemann

Unsteady Aerodynamics Laboratory  
National Aeronautical Establishment  
National Research Council Canada  
Ottawa, Ontario, Canada

**1. INTRODUCTION**

The best way to obtain model-scale dynamic stability information at realistic Reynolds and Mach numbers is through dynamic experiments in a wind tunnel. In principle, of course, one can obtain this information also from model experiments in other types of facilities (Ref. 1). Here belong, for instance, tests in aeroballistic or hyper-velocity ranges, out-door free-flight tests using either rocket-propelled or radio-controlled gliding models, or spin-tunnel experiments. All these techniques, however, have one common disadvantage - they are not suitable for experiments at high Reynolds numbers. In addition, although some of them can be used for extraction of dynamic stability derivatives from the model motion history, this is rarely done. Thus the main use of these techniques is for visual studies of the stability characteristics and motions of the aircraft, all at low Reynolds numbers.

Dynamic stability derivatives can also be extracted from full-scale flight tests. Although the results of such tests are obtained too late to significantly affect the design of a new aircraft, it should be kept in mind that full-scale flight experiments are most essential for correlating the values of various dynamic stability parameters and the flight behaviour of already existing aircraft. Such correlations are badly needed for obtaining a better understanding of the relative importance of the various derivatives as well as for a realistic evaluation of the presently used methods of motion analysis, especially with regard to the high angle-of-attack, stall and spin conditions.

The simulation of the flight Reynolds number constitutes, of course, one of the standard requirements for all kinds of aerodynamic testing and may be particularly important at high angles of attack. Considerable efforts are presently being made to construct new facilities to satisfy this requirement as well as possible, despite various economical and technical constraints. It should be kept in mind, however, that after a certain amount of high-Reynolds-number dynamic stability information - for several configurations and at various flow conditions - has been accumulated, it may be possible to review the situation and perhaps to reduce the number of derivatives for which as complete as possible Reynolds number simulation is essential, thereby permitting some dynamic stability testing to be performed in smaller, less expensive, facilities.

**2. DYNAMIC STABILITY DERIVATIVES**

The concept of a stability derivative is of course related to the traditional form of equations of motion where the result of a small disturbance from the equilibrium flight condition is described by linear superposition of contributions caused by the change in various attitude variables and their time rates of change. The traditional stability derivatives are constants representing the rate of change of a given aerodynamic coefficient with the variable in question, at a point where the variable itself is zero. With present-day interest in flights at relatively high values of some of the displacement variables (such as  $\alpha$ ,  $\beta$  and the rate of spin) it is necessary to consider stability derivatives as functions of those variables and to apply the proper local values of the functions for each equilibrium condition. In cases where the variations described by these functions are relatively rapid or where the disturbances are no longer very small, it may also be necessary to replace a particular constant derivative with an analytical expression defining its variation in the vicinity of the equilibrium position.

Even if we have to recognize that a stability derivative is not always a constant but may sometimes be a function of one or more displacement variables, the basic experimental methods to obtain the required information remain the same as in the past. The number of required experiments, however, becomes much larger since, instead of determining a single value, we must now obtain enough points to define a function. It follows that it is even more important now than in the past to perform these experiments in an efficient manner.

The number of necessary experiments is also much larger because many more derivatives may now be needed. While in the past the dynamic derivatives of interest were often limited to the three damping derivatives with an occasional mention of the dynamic cross derivatives, up to three times that many derivatives may be needed for a modern fighter configuration. The various categories of dynamic derivatives are indicated in Table I, together with a set of definitions of dynamic moment derivatives that follows the North American usage. A similar table can be set up for the dynamic force derivatives which, however, are often of considerably lesser interest and will, therefore, not be dwelled on here in any detail. It should be remembered, however, that some dynamic force derivatives may be quite important in special cases, such as when considering direct-sideforce or direct-lift controls or when transferring dynamic moment derivatives from one axis to another.

TABLE 1  
DYNAMIC MOMENT DERIVATIVES

PURE ROTATION	TRANSLATIONAL ACCELERATION	OSCILLATION AROUND FIXED AXIS		
		DAMPING DERIVATIVES	CROSS DERIVATIVES	CROSS-COUPLING DERIVATIVES
$C_{lp} = \frac{\partial C_t}{\partial \dot{z}/2V}$	$C_{mp} = \frac{\partial C_m}{\partial \dot{z}/2V}$	$C_{ta} = \frac{\partial C_t}{\partial \dot{z}/2V}$	$C_{ma} = \frac{\partial C_m}{\partial \dot{z}/2V}$	$C_{na} = \frac{\partial C_n}{\partial \dot{z}/2V}$
$C_{lq} = \frac{\partial C_t}{\partial \dot{\beta}/2V}$	$C_{mq} = \frac{\partial C_m}{\partial \dot{\beta}/2V}$	$C_{lb} = \frac{\partial C_t}{\partial \dot{z}/2V}$	$C_{mb} = \frac{\partial C_m}{\partial \dot{z}/2V}$	$C_{nb} = \frac{\partial C_n}{\partial \dot{z}/2V}$
$C_{lr} = \frac{\partial C_t}{\partial \dot{r}/2V}$	$C_{mr} = \frac{\partial C_m}{\partial \dot{r}/2V}$			

In addition to the familiar damping derivatives ( $C_{mq}$ ,  $C_{nr}$  and  $C_{lp}$ ) and cross-derivatives ( $C_{np}$  and  $C_{qr}$ ), Table 1 contains also groups of derivatives labelled cross-coupling derivatives and acceleration derivatives. The first of those, cross-coupling derivatives ( $C_{nq}$ ,  $C_{lq}$ ,  $C_{mr}$  and  $C_{mp}$ ) are a direct result of the fact that the modern aircraft often flies in conditions causing significant flow asymmetry. These derivatives relate the longitudinal and the lateral degrees of freedom of an aircraft, providing aerodynamic coupling that did not exist in symmetrical flow conditions which were of main interest in the past. It follows that in cases where these derivatives are of a significant order of magnitude, the traditional (and very convenient) separation of equations of motion into longitudinal and lateral groups can no longer be considered acceptable and that in such cases all these equations have to be considered simultaneously.

The last group of derivatives is labelled acceleration derivatives and is represented by moment derivatives due to  $\dot{\alpha}$  and  $\dot{\beta}$ . The word acceleration refers to translational acceleration, which in the first approximation is proportional - from the aerodynamic point of view - to the time rate of change of the angular deflection in the same plane of motion. The aerodynamic reactions due to vertical acceleration, for example, are equivalent to those due to the time rate of change in the angle of attack ( $\alpha$ ). Similarly, the lateral acceleration is related to the time rate of change in the angle of sideslip ( $\beta$ ). The derivatives associated with these variables are of great interest in connection with the already mentioned applications of direct-sideforce or direct-lift controls. They may also be used to separate the purely-rotary derivatives (such as  $C_{mq}$ ) from their fixed-axis oscillatory counterparts (such as  $C_{mq} + C_{ma}$ ).

The reason why an oscillation around a fixed axis results in a sum of a purely-rotary derivative (such as  $C_{mq}$ ) and a translational acceleration derivative (such as  $C_{ma}$ ) sometimes creates confusion and so a few words of explanation may be in order here. Let us consider, as an example, the longitudinal case. For a free-flying aircraft the variations in the angle of pitch and in the angle of attack can occur independently of each other, and each gives rise to a different longitudinal distribution of the normal velocity. The distribution due to the angle-of-pitch variation (i.e. due to the pitching velocity  $q$ ) varies along the chord and intersects zero at the axis of rotation, while the distribution due to the angle-of-attack variation is constant along the chord. In the case of an oscillation around a fixed axis both variations occur at the same time and even if the two variables  $q$  and  $\dot{\alpha}$  are numerically equal, their effects are different and have to be superimposed. As already indicated, the contribution due to  $\dot{\alpha}$  is equivalent to one due to vertical acceleration, since  $\dot{\alpha} = \ddot{z}/V$ .

Similarly, in the lateral case, a rolling (p) or a yawing (r) motion around a fixed axis at an angle of attack causes a simultaneous variation in the rate of change of the angle of sideslip ( $\dot{\beta}$ ). If a system of body axes is used, the resulting composite expressions include a trigonometric function of  $\alpha$ , such as in  $C_{nr} - C_{n\dot{\beta}} \cos \alpha$  or  $C_{np} + C_{n\dot{\beta}} \sin \alpha$ .

### 3. EXISTING WIND-TUNNEL CAPABILITIES FOR DYNAMIC STABILITY EXPERIMENTS

In May of 1978 the Fluid Dynamics Panel of AGARD held a Symposium on Dynamic Stability Parameters in Athens, Greece. When studying the Proceedings of that Symposium (Ref. 2) and a few recent survey papers on the same subject (Refs. 3-4), it becomes apparent, that a large number of organizations in various countries has the necessary equipment to perform measurements of such parameters and that the activities in this

field, in several countries, are rapidly expanding. In Table 2 a list is presented of some thirty organizations in eleven countries that have the capabilities for dynamic stability experiments; the wind tunnels in which such experiments can be performed cover the entire speed range from low speeds to hypersonic (or hypervelocity). In most cases the capabilities are limited to simple damping experiments but an ever increasing number of facilities is now being equipped also with more sophisticated apparatuses, such as those required for rotary, translational or cross-coupling experiments. On the whole, however, although the progress is satisfactory, a lot remains to be done.

TABLE 2

## ORGANIZATIONS EQUIPPED FOR DYNAMIC STABILITY EXPERIMENTS IN WIND TUNNELS

Country	Organization	Location
Canada	National Aeronautical Establishment	Ottawa
France	Office National d'Etudes et de Recherches Aérospatiales	Chalais-Meudon
	Institut de Mécanique des Fluides	Modane
India	National Aeronautical Laboratory	Lille
Italy	Aeronautica Macchi, S.P.A.	Bangalore
	University of Naples	Varese
Japan	National Aerospace Laboratory	Napoli
South Africa	Council for Scientific and Industrial Research	Tokyo
Sweden	Flygtekniska Förskönsanstalten	Pretoria
	Kungl. Tekniska Högskolan	Stockholm
United Kingdom	Aircraft Research Association	Stockholm
	British Aircraft Corporation	Bedford
	Royal Aircraft Establishment	Bedford
	University of Southampton	Southampton
United States	AEDC PWT	Tullahoma
	AEDC VKF	Tullahoma
	Calspan Corporation	Buffalo
	GD Convair	San Diego
	Massachusetts Institute of Technology	Cambridge
	NASA Ames	Moffett Field
	NASA Langley	Hampton
	Naval Ship R & D Center	Washington
	Naval Surface Weapons Center	Silver Spring
	Sandia Corporation	Albuquerque
	Vought Aeronautics Company	Dallas
	Virginia Polytechnic Institute	Blacksburg
USSR	Kalinin Polytechnic Institute	Leningrad
W. Germany	DFVLR/Dornier/MBB/VFW	Göttingen
		Braunschweig
		Köln

## 4. METHODS OF MEASURING DYNAMIC DERIVATIVES

In a review made several years ago (Ref. 1) of the methods of measurement of aircraft dynamic stability derivatives, the present author introduced a systematic classification of the various methods, which included both the free flight conditions and situations where the model was constrained in one or more degrees of freedom, as is most often the case during wind tunnel experiments. Subsequent categories took into account the behaviour of the model in the test section (model moving versus model fixed) and the principal quantity to be measured (reactions versus motion). All in all, sixteen wind-tunnel methods were identified, many of them containing sub-categories and most of them represented by several apparatuses, which were in actual use in 1959 (the year of the review) or at any time prior to that.

In view of all the new developments that have taken place since 1959, it would be impractical to attempt to go over this 1959 review in any detail. Instead we will examine some of the more important methods and techniques that are in use today, with special emphasis on those that are adaptable to high-load (=high  $\alpha$  or high  $Re$ ) wind-tunnel testing. The old 1959 review (or its 1963 modified version, Ref. 5) still provides, however, a very useful reading for anybody thinking about developing and constructing a new apparatus in this field, since it contains a lot of information about various approaches and basic principles on which such an apparatus could be based or perhaps which, on the contrary, should not even be tried.

In Fig. 1 a list by category is presented of wind-tunnel methods which are in use today. All methods which cannot be used in a wind tunnel (such as range tests) and methods which only have historical (such as whirling arm) or conceptual (such as measurement of motion of the rolling flow around a stationary model) significance, have been omitted. Even so, the practical value of the remaining methods is somewhat uneven, with the methods employing an oscillating or rotating model being the most important, since they are best suited for measuring dynamic derivatives at realistic flight conditions (that is, with proper simulation of angles of attack and sideslip, Mach number and, if possible, also Reynolds number).

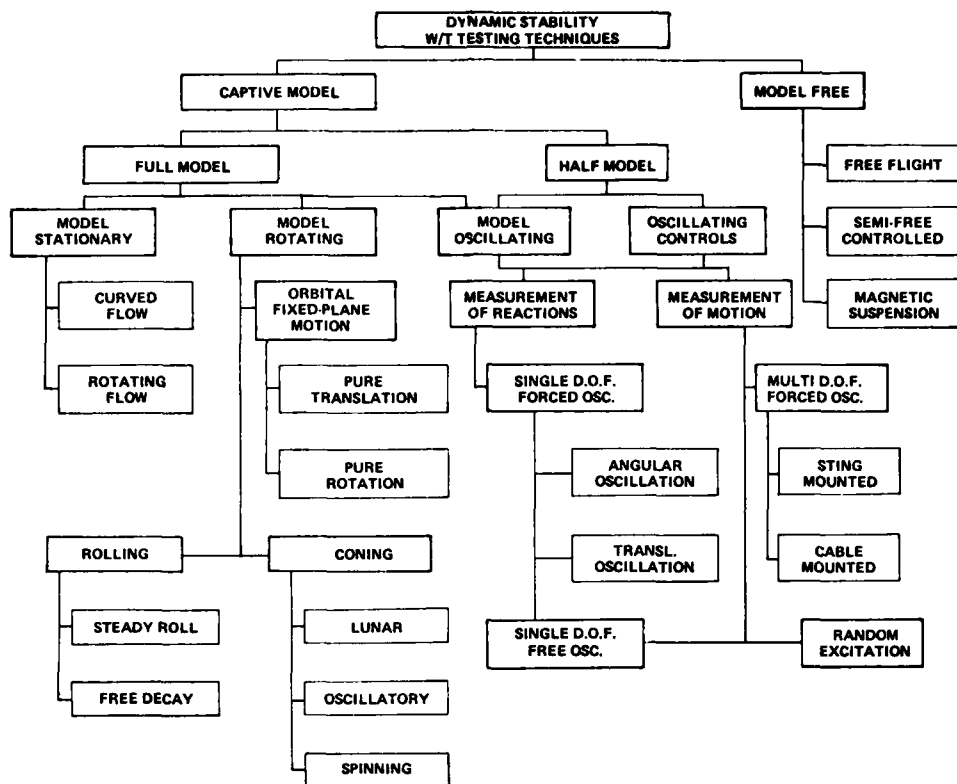


FIG. 1 DYNAMIC STABILITY W/T TESTING TECHNIQUES

It is, of course, difficult to include all the pertinent information on a figure such as Fig. 1. "Captive Model" refers to a model mechanically suspended, and magnetic suspension is therefore found under "Model Free". Similar methods can be employed for oscillating full and half models, but the latter can, of course, only be used when both the model and the flow around it are symmetrical. In the present context this restricts the use of half model techniques to studies of pitching and plunging oscillations at not too high angles of attack (say up to 20° or so), and to studies of the oscillating control surfaces and their effects. Although in the single-degree-of-freedom (single-DOF) forced oscillation experiments the motion is induced in one (the primary) DOF at a time, the reactions can be measured in only that DOF (to determine the direct derivatives such as damping and aerodynamic stiffness) or also in the secondary DOFs (to also measure various cross and cross-coupling derivatives). Such experiments can be performed using either constant oscillatory torque or constant oscillatory displacement (inexorable drive), the latter very important when testing untrimmed models at higher angles of attack, where a large static aerodynamic moment has to be overcome. The multi-DOF forced oscillation experiments are in reality often conducted in such a way that the motion takes place predominantly only in one or at most in two degrees of freedom. The cable-mounted models can also be used for free oscillation experiments, without providing any external mechanical excitation. The continuous rolling experiments can be performed using both forced and free rotation, whereas in coning and spinning the most usual measurement is that of aerodynamic reactions. Although in most cases each block in Figure 1 represents one particular technique or apparatus, there are cases where a single apparatus can perform, simultaneously or successively, functions indicated in two or more blocks, such as combining coning and spinning, pitching and plunging or using the same equipment for forced or free oscillation. A good example of such an "universal" apparatus will be given by describing a fixed orbital plane rotary apparatus that is currently being developed at NAE. Finally, the techniques employing free-flying (in a wind tunnel) or magnetically suspended models are not at present suitable for dynamic testing at realistic flight conditions, while experiments using a semi-free, remotely-controlled model usually lead to qualitative (pilot opinion) or cinematographic results, even if more recently attempts have been made to employ certain derivative-extraction procedures (originally developed for flight testing) for this type of semi-free flights in a wind tunnel. More about this later.

In the subsequent sections of this paper the methods indicated in Fig. 1 will be discussed in some detail, using examples of appropriate experimental equipment that is in use today in the U.S.A., Canada, and some European countries. In describing this equipment the present author will be drawing in some cases (indicated by quotation marks) on descriptions found in the original papers, on the assumption that no one is better qualified to describe an apparatus than the original researcher. Proper references will, of course, be indicated everywhere.

This review is based on the author's notes from a 1977 lecture series at the von Karman Institute for Fluid Dynamics (Ref. 4). However, the description of those methods and techniques that are separately discussed in the present Lecture Series has been replaced by a short paragraph and a suitable reference each. The same applies to material concerning instrumentation and data acquisition and reduction that will be covered by a separate detailed presentation.

##### 5. MEASUREMENT OF REACTIONS. SINGLE DEGREE-OF-FREEDOM FORCED OSCILLATION

As mentioned before, this group of techniques can be further subdivided according to the type of drive. If an *electromagnetic* drive is used, the amplitude of the applied torque (or force) is usually constant and the amplitude of the displacement depends on the total damping in the system. In addition, when the oscillation is around such an axis and such an angle that a considerable aerodynamic restoring moment exists, the equilibrium position with the wind on will be different from that with the wind off. If we assume that the mechanical restoring moment  $K(x - x_0)$  is zero for  $x = x_0$ , the wind-on restoring moment  $[K(x - x_0) + kx]$  will be zero for  $x = x'_0$ , such that  $x'_0 = x_0 K/(K + k)$ , where the aerodynamic stiffness  $k$  can be obtained from local conditions, e.g. for a pitching oscillation we have  $k = (C_m)_{\text{local}}/\alpha$ . In most cases where oscillation is around zero or small values of angles of attack or sideslip, the mechanical stiffness  $K$  is much larger than  $k$  and the difference between  $x'_0$  and  $x_0$  is small. For other cases, and especially for the important pitching oscillation around a high mean angle of attack,  $k$  may be appreciable and, unless cancelled out by some trimming device, may lead to situations where insufficient free space will be left for the model in which to oscillate (the model will be hitting a mechanical stop on one side).

The use of an inexorable drive, of the *mechanical* or *hydraulic* type, prevents all this from happening but usually results in a much more complicated and bulky apparatus. Most of the high-load apparatuses are of this type. The displacement amplitude is then kept constant and the amplitude of the applied torque or force is adjusted as needed. In this technique (also called rigidly forced oscillation) a preselected motion is imparted to the model and forces and moments between the model and the forcing part of the apparatus are measured. The model motion may be angular or translational and is usually sinusoidal, in which case the derivatives are obtained from the in-phase and quadrature components of the measured aerodynamic reactions. In principle both force and moment derivatives can be measured, and the measurement can be made in both the same degree of freedom as the imparted oscillation (resulting in direct derivatives) and in other degrees of freedom (resulting in cross and cross-coupling derivatives).

It is usually advantageous, especially for single-degree-of-freedom experiments, to operate at frequencies at or near the resonance, since this minimizes the torque or force required to sustain the oscillation and also increases the accuracy of the experiment.

In recent years, with more and more testing performed at high angles of attack, the method of reducing the large static pitching moment, which usually acts on a model at these angles of attack, by applying some trimming device (such as a control deflection) in the primary degree of freedom has become increasingly more popular. It is argued, that such a procedure, far from introducing a geometry change that may cause some erratic or undesirable results, in fact represents a very realistic configuration change, since the full-scale aircraft in order to fly (at least in equilibrium condition) must also be trimmed, probably in a similar way.

###### 5.1 NASA Langley, Full Scale Tunnel (M<0.1)

The NASA Langley forced-oscillation apparatus (Ref. 6) in the Full-Scale Tunnel can be used, with only minor changes in the experimental arrangement, for pitching, yawing or rolling experiments (Fig. 2). Force and moment derivatives due to pitching, rolling or yawing around a fixed axis can be measured at angles of attack up to  $110^\circ$ . The amplitude is adjustable and can be as high as  $\pm 30^\circ$ . A 6-component internal balance is used with on-line data reduction. The oscillatory motion is imparted to the model by means of a flywheel-driven system of pushrods and bellcranks, powered by a 3 h.p. electric motor. The frequency of oscillation (typically 0.5-1.5 Hz) is varied by changing the speed of the motor. Reference signals proportional to the sine and cosine of the flywheel rotation angle are generated by a precision sine-cosine potentiometer. By multiplying the balance signals by those reference signals and integrating, the aerodynamic derivatives that are in-phase and out-of-phase with the primary oscillation are obtained.

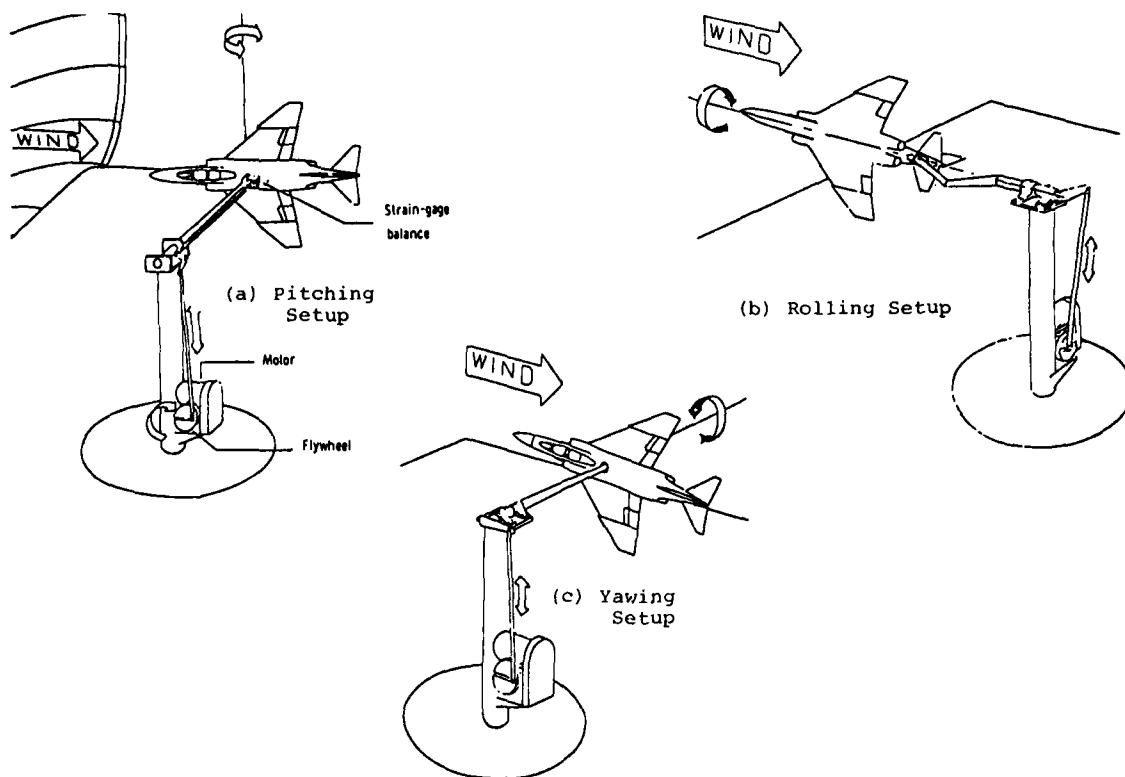


FIG. 2 FORCED OSCILLATION APPARATUS. NASA LANGLEY FULL SCALE TUNNEL (REF. 6)

## 5.2 ONERA, Chalais-Meudon

An apparatus similar to the one above is available in the large low-speed wind tunnels  $S_1$  and  $S_2$  at Chalais-Meudon, near Paris (Ref. 7). Moment derivatives due to pitching, yawing or rolling can be obtained with a 5-component moment balance at angles of attack up to  $30^\circ$  and angles of sideslip up to  $12^\circ$  in the frequency range of 1 to 2 Hz (Fig. 3).

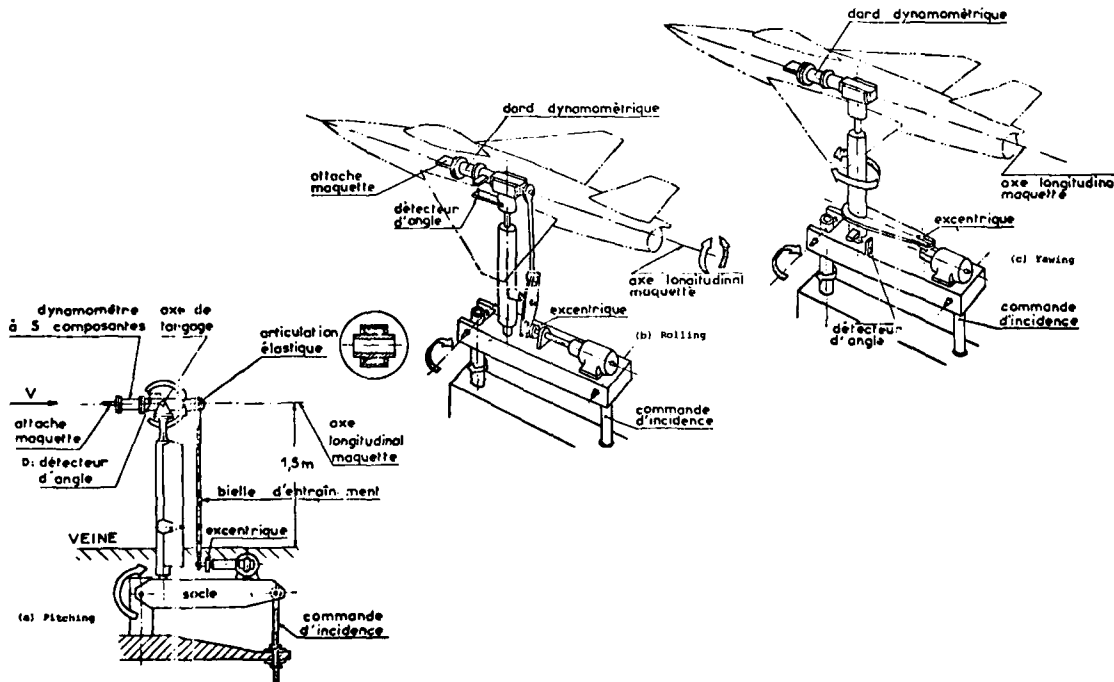


FIG. 3 FORCED OSCILLATION APPARATUS. ONERA CHALAIS-MEUDON (REF. 7)

### 5.3 NASA Langley, High-Speed Tunnels

In Ref. 8 a forced-oscillation roll apparatus is described that is compatible with both the 7 x 10 Foot High Speed Wind Tunnel ( $0.2 \leq M \leq 0.85$ ) and the 8-Foot Transonic Pressure Tunnel ( $0.2 < M < 1.2$ ). A 2 h.p. variable-speed motor is used to oscillate the sting and model by means of an offset crank. A torsion spring internal to the sting is connected to the front of the strain-gauge balance section and provides a restoring torque which, together with any existing aerodynamic spring, can balance out the model inertia, when the model is oscillated at velocity resonance. A system of resolvers, filters, and damped digital voltmeters is used to separate the torque signal into in-phase and out-of-phase components. The apparatus is designed for a maximum normal force of 1000 lbs and can be used at angles of attack (or angles of sideslip) of up to  $22^\circ$ .

A similar principle of operation is used for the forced-oscillation pitch/yaw apparatus depicted in Fig. 4. This apparatus is described in Ref. 9 and has been used in both the abovementioned wind tunnels. More recently, the hydraulic drive shown in Fig. 4 has been replaced by a mechanical actuator.

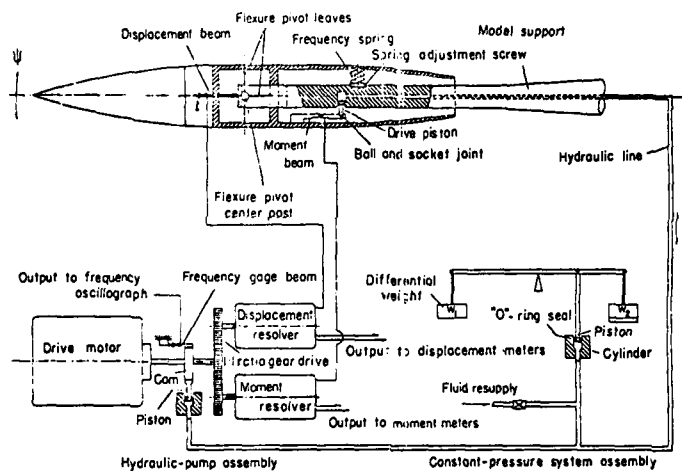


FIG. 4 FORCED-OSCILLATION PITCH/YAW APPARATUS. NASA LANGLEY HIGH SPEED TUNNELS (REF. 9)

### 5.4 ONERA Modane

Forced oscillation apparatuses are used in the high speed wind tunnel S<sub>2</sub> at Modane ( $0.2 < M < 3.2$ ) for oscillatory experiments in pitch or yaw (Fig. 5) and in roll (Fig. 6). An eccentric drive is used for the pitch (yaw) apparatus and a direct drive and a gearbox arrangement for the roll apparatus. A 5-component moment balance provides the pertinent static and damping information; in addition, the rolling apparatus is capable of measuring the cross derivative of the yawing moment due to rolling. Frequency range is of the order of 5 to 10 Hz (Ref. 7).

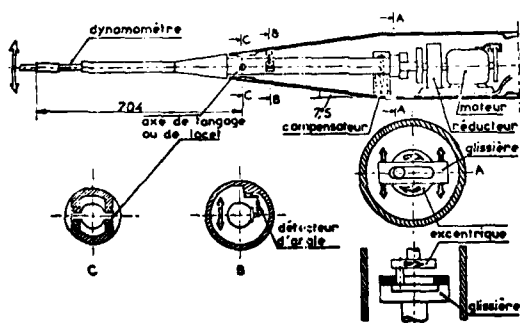


FIG. 5 FORCED OSCILLATION APPARATUS.  
ONERA MODANE (REF. 7).  
(PITCHING OR YAWING SETUP)

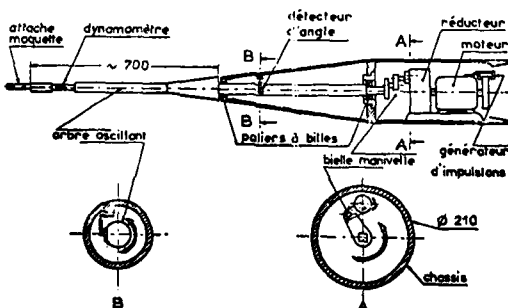


FIG. 6 FORCED OSCILLATION APPARATUS.  
ONERA MODANE (REF. 7).  
(ROLLING SETUP)

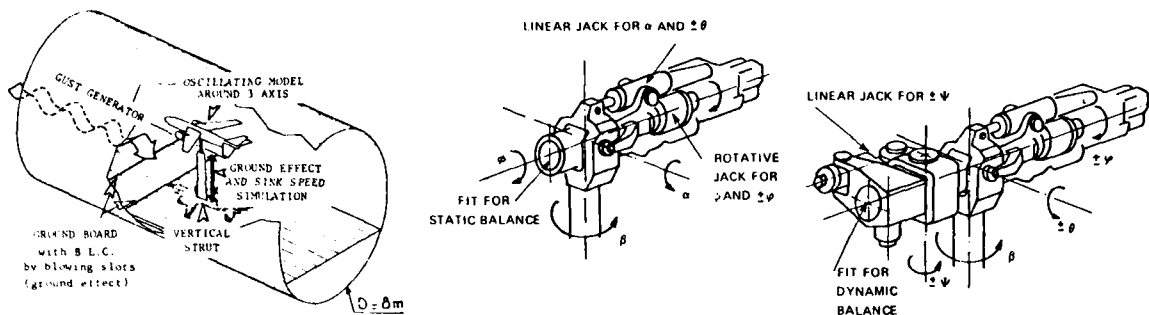


FIG. 7 FORCED OSCILLATION PITCH/YAW AND ROLL APPARATUS. ONERA MODANE TUNNEL S1 (REF.10)

Recently, a new "flight-mechanics rig" has been constructed for the 8 m diameter low speed wind tunnel S1 at Modane (Ref. 10). The direct and cross derivatives can be obtained from a dynamic balance attached to a "three-axis head" (Fig. 7), with which small amplitude oscillations in pitch, yaw or roll can be induced hydraulically. Frequency range is 0.5 to 2 Hz, maximum angle of attack is 30° and normal force capability is of the order of 8000 lb. The apparatus can also be used for static measurements, ground effect studies and simulation of vertical motion (by sliding vertical mast actuated by a hydraulic jack at vertical speeds up to 4 m/s).

##### 5.5 AEDC-VKF

One of the typical VKF forced-oscillation apparatuses for measuring pitch or yaw damping is shown in Fig. 8 (Ref. 11). The apparatus "utilizes a cross-flexure pivot, an electric shaker motor, and a one-component moment beam which is instrumented with strain gages to measure the forcing moment of the shaker motor. The motor is coupled to the moment beam by means of a connecting rod and flexural linkage, which converts the translation force to a pitching moment. The system operates at small amplitudes and at oscillation frequencies from 2 to 56 Hz. The cross flexures, which are instrumented with strain gages to provide a voltage proportional to the model pitch displacement, support the model loads and provide a restoring moment which cancels the inertia moment when the system is operating at the natural frequency of the model-flexure system. The motor is controlled by an electronic feedback loop which maintains constant oscillation amplitude of the model and thus provides a means of testing both dynamically stable and dynamically unstable models. The out-of-phase component of the AC voltage output of the moment beams and cross flexures provides a measure of the pitch-damping coefficient,  $C_{mq} + C_{ma}$ .

The in-phase component is used in conjunction with an accurate frequency measuring instrument to determine the slope of the pitching-moment curve,  $C_{ma}$ . The apparatus is equipped with a set of interchangeable cross flexures and moment beams, to be selected according to the test requirements. It can be used in several large transonic and supersonic wind tunnels at both VKF and PWT.

A VKF forced-oscillation roll apparatus is shown in Fig. 9 (Ref. 12). It "utilizes a water-jacketed, five-component balance, twin beam flexures, roller bearings to support the loads, and electric printed-circuit drive motors. The motors are directly coupled to the balance and supply up to 120 in.-lb roll moment to oscillate the system at amplitudes up to  $\pm 3^\circ$  and at frequencies from 2 to 20 Hz. The twin beam flexures mount from the stationary sting to the oscillating water jacket and provide a restoring moment which cancels the inertia moment when the system is operating at the natural frequency

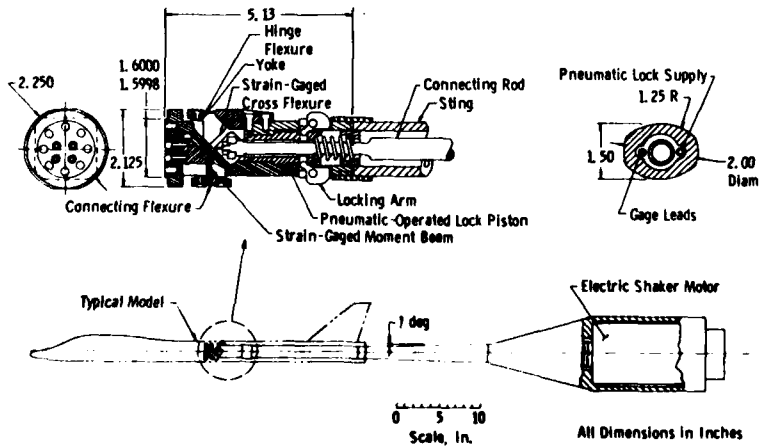


FIG. 8 FORCED OSCILLATION PITCH OR YAW APPARATUS. AEDC-VKF (REF. 11)

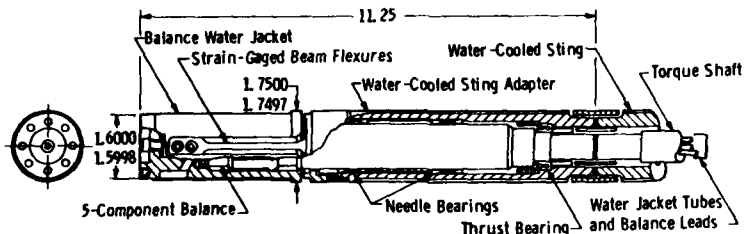


FIG. 9 FORCED OSCILLATION ROLL APPARATUS. AEDC-VKF. (REF. 12)

of the model-flexure system. The flexures are instrumented to measure the roll displacement. The entire mechanism is water-cooled to permit testing in the hypersonic tunnels. Maximum acceptable normal load is 1200 lb.". The apparatus can be used to obtain dynamic derivatives  $C_{\alpha p} + C_{\alpha \beta} \sin\alpha$ ,  $C_{\alpha p} + C_{\alpha \beta} \sin\alpha$  and  $C_{\gamma p} + C_{\gamma \beta} \sin\alpha$ . It can be calibrated by means of a specially developed two-arm magnetic damper with which known rolling moment, yawing moment and sideforce can be applied and compared to the output data obtained using the normal data-acquisition-and-reduction procedure.

#### 5.6 AEDC-PWT

Several forced-oscillation apparatuses are available at PWT for use in their 4-Foot and 16-Foot Transonic Tunnels and 16-Foot Supersonic Tunnel. They are designed for high loads (up to 8000 lb normal force) and are, therefore, hydraulically driven. One such apparatus is shown in Fig. 10 (Ref. 13). It was designed for testing finned bombs and missiles at high angles of attack. A cross-flexure pivot is used and the frequency can be adjusted by interchanging a cantilever spring. The damping torque and the amplitude are the quantities measured. This apparatus is at present limited to a normal force of 600 lb in the 4-Foot Transonic Tunnel but can be scaled up for use in the two 16-Foot Tunnels. A model sting cavity of 3.72 in. in diameter is required for an oscillation amplitude of  $\pm 3^\circ$ .

A high-load, pitch-yaw forced-oscillation apparatus has recently been put in operation at AEDC-PWT (Ref. 14). The apparatus is designed for 1:10 scale models and a normal force of 4000 lb, and is intended for use in the AEDC 16 foot transonic and supersonic wind tunnels. The basic apparatus is used to measure the direct derivatives in pitch and in yaw, and an additional "can" balance, which fits over the basic apparatus, can provide cross and cross-coupling derivatives. This apparatus, which has already been used for experiments at angles of attack up to  $50^\circ$ , is discussed in some more detail in Lecture no. 4. A similar pitch-yaw apparatus designed for a normal force of 1500 lb is also available. Companion apparatuses for roll oscillation experiments are being constructed.

#### 5.7 DFVLR

A mobile oscillatory derivative apparatus has been constructed for use in the 3m low-speed wind tunnels at DFVLR (Braunschweig), Dornier and TH Darmstadt (Ref. 15). The model is mounted on a moving head supported by a vertical strut and the oscillatory motion in pitch, yaw, roll or heave is inexorably induced by a mechanical drive system, employing three geared driving motors (to be used one at a time for different motions), eccentric discs and pushrods (Fig. 11). Maximum amplitude of all the angular motions is  $5^\circ$  and of the plunging motion 30 mm. Frequency range is 0.2 to 3 Hz. Direct and cross (and probably also cross-coupling) derivatives can be obtained with a five component internal strain-gauge balance. The maximum angle of attack is about  $15^\circ$ , but can be extended to  $50^\circ$  by installing the apparatus on a circular guide rail support, as illustrated. The measuring techniques and the derivative evaluation methods employed with this apparatus are described in some detail in Ref. 16.

#### 5.8 NAE

The first forced-oscillation apparatus capable of direct measurement of the full complement of damping, cross and cross-coupling moment derivatives due to pitching or yawing was constructed at NAE in 1973 (Fig. 12).

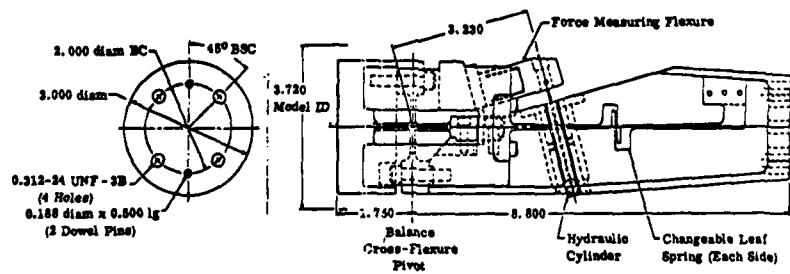


FIG. 10 FORCED OSCILLATION PITCH APPARATUS. VKF-PWT. (Ref. 13)

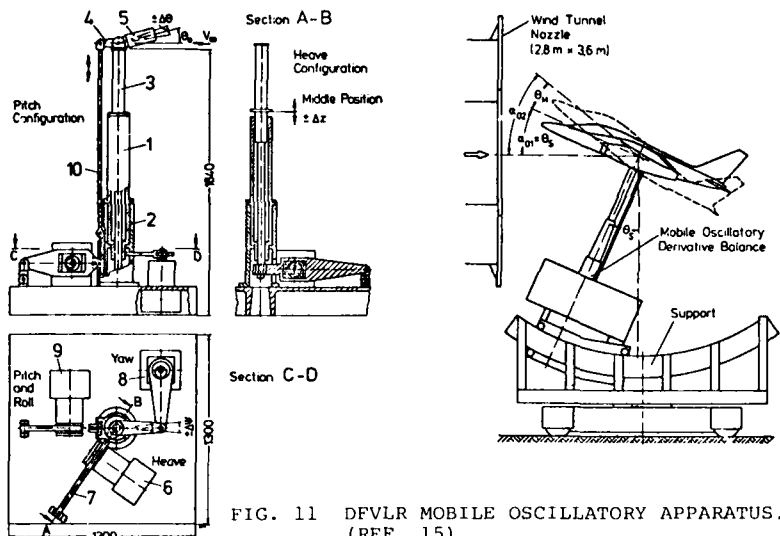


FIG. 11 DFVLR MOBILE OSCILLATORY APPARATUS.  
(REF. 15)

In the configuration shown this apparatus provides a primary oscillatory motion in pitch with resulting secondary motions in yaw and roll. By rotating the balance  $90^\circ$  around its longitudinal axis the primary motion may be imparted in yaw instead, with the induced secondary motions in pitch and roll. The model is driven electromagnetically by means of a single-turn drive coil that can move in a gap between two permanent magnets, and the balance consists of cruciform flexures in yaw and in roll and a crossed-flexure pivot in pitch. All moments are measured around the center of oscillation. Components of the secondary motions that are in-phase or out-of-phase with the primary motion are measured and converted into the corresponding components of the induced secondary moments. In addition, the torque, the amplitude, and the frequency of the primary motion are measured. All together, a set of two oscillatory experiments, one in pitch and one in yaw, is required to obtain a complete set of four static and four dynamic cross and cross-coupling moment derivatives as well as two static and two dynamic direct moment derivatives.

It should be noted that the technique described provides a direct measurement of all the derivatives, based only on an assumed relation between the secondary moment measured and the causative primary motion. Most often this relation is linear, but can be replaced by a non-linear or higher order formulation, if the need arises. Since the motion is essentially in one degree of freedom only, the measurement is totally independent of the remaining parts of the equations of motion and therefore the results may be expected to be valid for any formulation of these equations as long, of course, as the principle of superposition is still applicable, that is as long as the concept of stability derivatives can be used. In this context the stability derivatives need not be constants, but may be functions of some experimental parameters such as the nominal value of angle of attack or sideslip around which the oscillation takes place.

More recently, several new apparatuses have been developed at NAE that differ in several aspects from the pitch/yaw apparatus Mk 1 just described. Included are (a) the NAE roll apparatus, described in more detail in Lecture No. 4, the NAE pitch/yaw apparatus, Mk II (Fig. 13), and the NAE translational oscillation apparatus (Fig. 14). In all cases the model is mounted on a balance that in turn is attached to an elastic support system capable of deflecting in the appropriate degree of freedom. The primary motion is imparted by an electro-magnetic drive mechanism which oscillates the model with a constant amplitude at the resonance frequency in the primary degree of freedom. Each balance has a multi-component capability (but always without axial force) and is made in one piece - a most desirable feature for dynamic testing. Each drive mechanism utilizes a high-current coil (or coils) moving in a strong magnetic field that is generated by compact rare-earth permanent magnets. As a result, the apparatuses are



FIG. 12 FORCED-OSCILLATION PITCH/YAW APPARATUS, Mk 1, NAE (PITCHING SETUP). REF. 17.

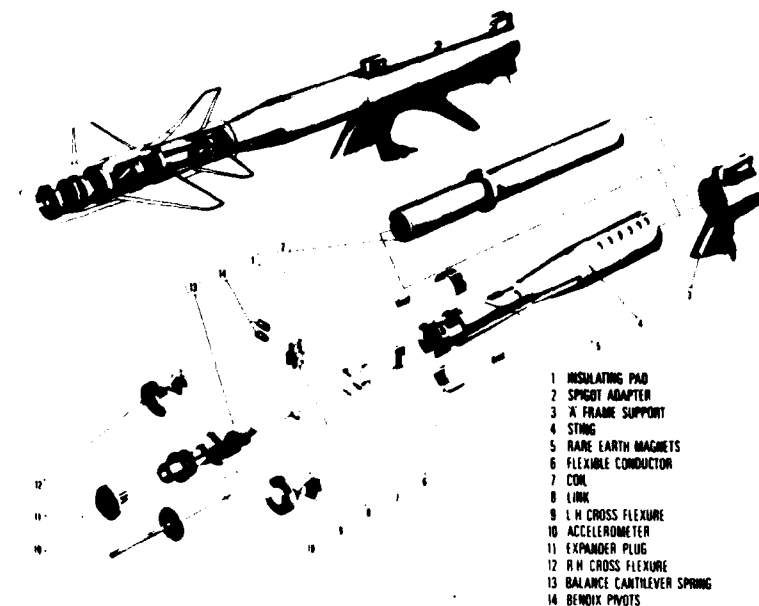


FIG. 13 FORCED OSCILLATION PITCH/YAW APPARATUS, MK II, NAE (PITCHING SETUP)

relatively slender and permit testing of realistic models of current aircraft configurations. In addition to measuring all the moment derivatives the new balances permit also obtaining some of the force derivatives of interest.

The pitch/yaw apparatus Mk II is equipped with two accelerometers, with which the absolute motion of the model can be determined. This additional feature may sometimes be very convenient to have, especially in cases where the model suspension point (front end of the sting), due to the inevitable flexibility of the sting and of the support, can no longer be considered fixed.

In the pitch/yaw apparatus Mk II the elastic support in the primary degree of freedom consists of cross flexures; to best utilize the very limited space available and to achieve the desired deflection and load-carrying capabilities both the width and the thickness of these flexures are suitably profiled. In the translational oscillation apparatus this elastic support consists of a multileaved cantilever flexure (Fig. 14).

The high complexity of the aforementioned techniques and the lack of any previous data on some of the recently identified dynamic derivatives made it necessary to develop a system that would independently verify the validity of the experimental technique and the data-reduction methods employed. The same system was also conceived as a diagnostic tool to identify, on a regular basis, equipment faults or software errors. A pictorial view of such a system developed at NAE and called a *dynamic calibrator*, is shown in Fig. 15. The aircraft model is replaced on the dynamic stability apparatus by a special calibrating frame, which is then oscillated in the primary degree of freedom by the drive mechanism of the apparatus. The three oscillatory aerodynamic moments, acting on the oscillating model during a wind tunnel test, are simulated by accurately known, electromagnetically induced, alternating loads, whose phase and amplitude can be adjusted at will. A comparison between the known applied loads and the outputs of the dynamic stability apparatus, obtained by processing the balance data and other relevant information by means of the same procedure as in the wind tunnel experiments, provides an overall calibration of the technique and all the mechanical and electronic systems involved.

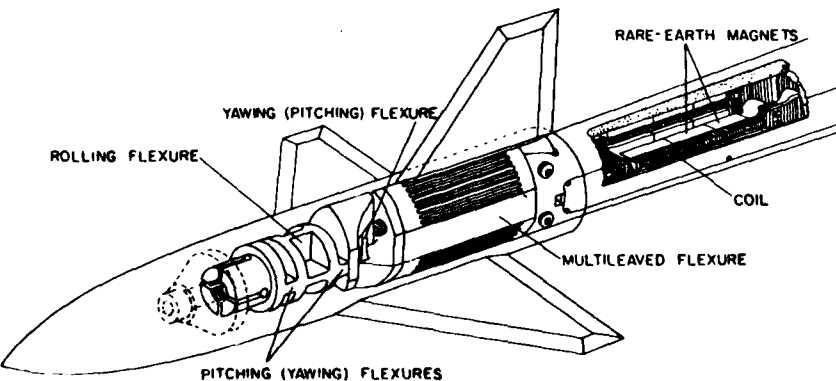


FIG. 14 FRONT PART OF THE FORCED OSCILLATION TRANSLATIONAL APPARATUS, NAE (LATERAL SETUP) (REF. 18)

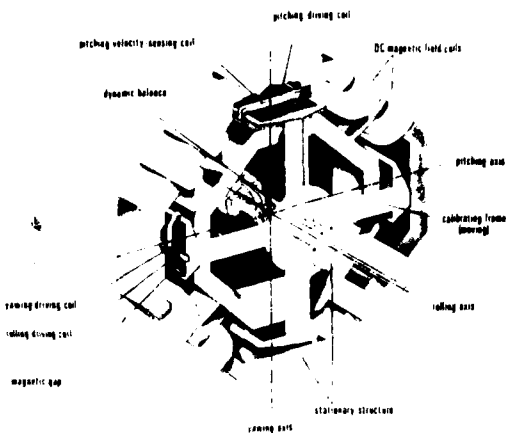


FIG. 15 NAE 3 DEGREE-OF-FREEDOM DYNAMIC CALIBRATOR, Mk I. (REF. 19)

A more advanced version of such a calibrator (Ref. 19) will be discussed in Lecture No. 4.

#### 6. MEASUREMENT OF MOTION. MULTI-DEGREE-OF-FREEDOM FORCED OSCILLATION.

Here belong techniques where the model is suspended elastically in such a way that it can oscillate in several degrees of freedom simultaneously, although one degree of freedom is usually predominant. As the excitation frequency varies, this predominant degree of freedom changes to another. The amplitude and phase of the various motions (rather than of the various reactions, as in the preceding section), together with the information about the forcing force (or torque) and frequency, are measured and fed into a system of equations of motion, which is then solved for the unknown stability derivatives. This is then quite different from the methods of the preceding section, where the cross and cross-coupling stability derivatives were obtained directly in each degree of freedom from the measured forced reactions and the known forcing motion.

In the limiting case of a single-degree-of-freedom oscillation, the techniques in this section reduce to the "constant-amplitude torque" subgroup of the preceding section, where the direct derivatives can be obtained from the amplitude and phase of the forced motion (and the information about the forcing torque and frequency in the same degree of freedom) by means of a direct calculation rather than indirectly by solving a system of equations.

Two different methods are presently employed to arrange for the multi-degree-of-freedom elastic suspension of the model. The first such method is to mount the model on a spring unit, which in turn is attached to the sting. Excitation of the model can then be arranged through the sting itself, as done at RAE, Bedford (Refs. 20-22), or through a separate vertical pushrod acting on the sting in the region of model base, as done by DFVLR-AVA (Ref. 23). In both cases, separate set-ups are needed for investigating a 2 DOF combination of pitching and plunging oscillation or a 3 DOF combination of yawing, rolling and lateral translation oscillation. Principle sketches of the RAE apparatus and the DFVLR apparatus are shown in Figs. 16 and 17, respectively, and a more detailed description of these techniques will be given in Lecture No. 5. It may be of interest to note, however, that the RAE apparatus exists in several different sizes, with the spring unit diameter of 50 mm, 75 mm and 100 mm, and the corresponding normal force capabilities of 4 kN, 9 kN and 18 kN, respectively.

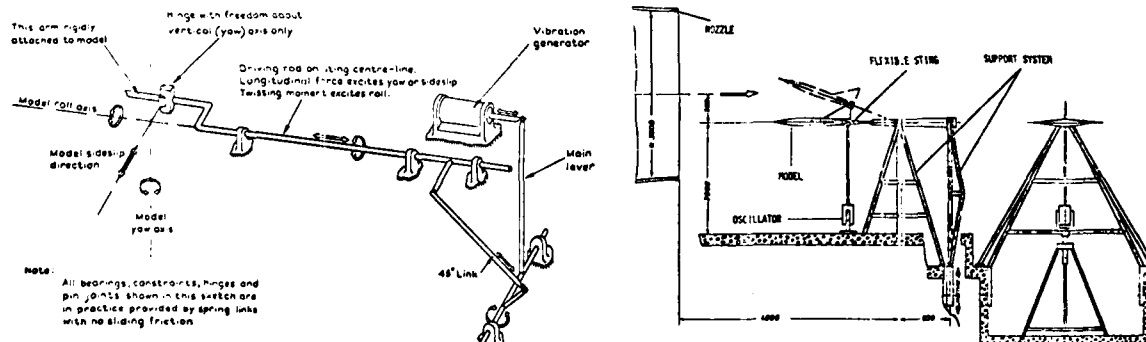


FIG. 16 FORCED-OSCILLATION 3 DOF APPARATUS. RAE-BEDFORD. DRIVE ARRANGEMENT. (REF. 20).

FIG. 17 FORCED-OSCILLATION 3 DOF APPARATUS. DFVLR-AVA. (REF. 23)

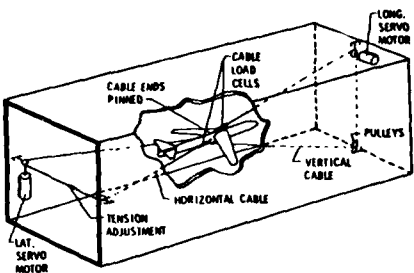


FIG. 18 FORCED OSCILLATION 5 DOF APPARATUS. NASA-LANGLEY.(REF. 24)

The second method of elastically suspending the model for multi-degree-of-freedom experiments is to use a suitable system of cables. Such a method, which permits a simultaneous oscillation in 5 degrees of freedom, is employed in the NASA Langley Transonic Dynamics Tunnel. The model is suspended in the wind tunnel by a two-cable mount system (Fig. 18) which allows lateral and vertical translation of the model as well as angular rotations about all three axes (Ref. 24). The procedure involves measuring the response of the model to known input disturbances such as control-surface deflections or external forces applied through the suspension cables. The stability derivatives are then extracted from equations of motion for the model suspension system using procedures developed initially for flight-test measurements. This method represents a modification (by providing excitation forces) of an old technique, used at NASA-Langley for many years, of "free-flying" the model in a wind tunnel for flutter and gust response investigations. The servo motors (one in each cable) used to provide the excitation can also be used to provide the necessary feedback for stability augmentation in situations where the static margin is negative.

#### 7. MEASUREMENT OF MOTION. SINGLE DEGREE-OF-FREEDOM FREE OSCILLATION.

The method of free oscillation is probably the oldest and is usually considered to be the simplest of the various oscillatory techniques. Usually no complicated drive or control system is required and the data reduction is relatively straightforward and lends itself well to automatic processing by computer. On the other hand, the method is usually limited to measurement of direct damping and stiffness derivatives and may not always be suitable for using under conditions of dynamic instability and in the presence of highly non-linear effects or large aerodynamic moments.

Basically, the method involves evaluation of a decaying oscillatory motion performed by an elastically suspended model following some initial disturbance. Elastic pivots (such as crossed flexures) or gas-bearing pivots (which contribute very little damping) are commonly used for mounting the model. The initial disturbance may take the form of (a) mechanical release from a displaced position, (b) application of a mechanical impulse, or (c) excitation at resonance and sudden interruption of the source of excitation. The first two of these methods are relatively simple to arrange but have the disadvantage of requiring large forces to obtain high initial amplitudes when the elastic stiffness of the flexure is large, and may introduce transient oscillatory effects at the beginning of the decaying oscillation. Method (c) overcomes this difficulty but requires more complicated equipment to impart to the model a constant-amplitude oscillation. This is usually done by means of electrical excitation; an alternative method involves use of pulsating air jets impinging on some suitable surface of the model.

It lies in the nature of the free-oscillation method that the results are representative of an amplitude range rather than of a discrete value of amplitude, but with modern instrumentation this amplitude range can be made very small so that the variation of results with amplitude (if any) can be obtained as conveniently as with constant-amplitude forced-oscillation methods.

##### 7.1 NAE

A simple application of the free-oscillation method is shown in Fig. 19 (Ref. 25). The model is sting mounted with the centre of oscillation defined by a flexural pivot and the main restoring moment provided by a cantilever spring. The combination of these two features was made possible by the use of a flexible link and two additional flexural pivots for attaching the rear of the cantilever spring to the sting. The deflection and release of the model prior to the start of oscillation is accomplished by a solenoid-actuated spring-loaded tripper that acts on a replaceable metal pad inside the model. The solenoid moves the tripper forward and keeps it inside until the model oscillation reaches its lower bound. At that time the power is turned off to retract the tripper, after which the solenoid can be activated again for the next deflection and release of the model. This cycle of operation can be repeated as many times as is necessary. Model-position information is obtained from strain gauges on the spring and on the sting.

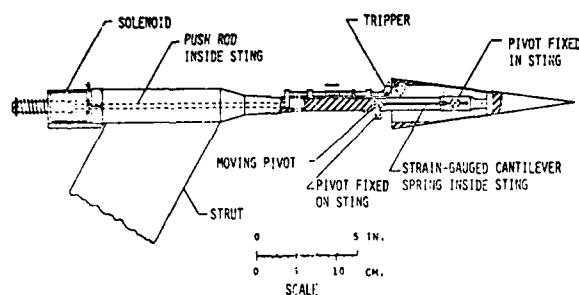


FIG. 19 FREE-OSCILLATION PITCH APPARATUS.  
NAE. (REF. 25)

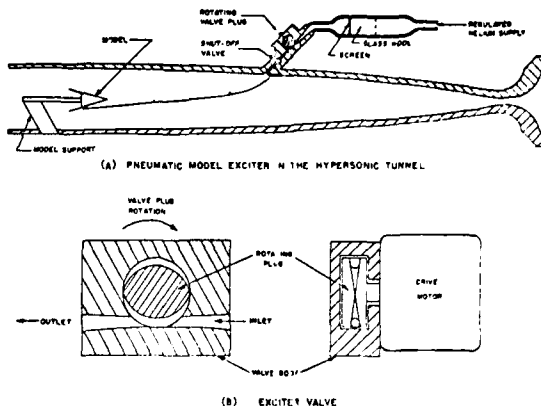


FIG. 20 EXTERNAL EXCITATION BY MEANS OF A  
PULSATING PNEUMATIC JET. NAE.  
(REF. 26)

In applications involving very small models in supersonic wind tunnels it may sometimes be very difficult to provide internal space for an excitation device. In such cases it may be possible to employ an external pulsating pneumatic jet, mounted at a certain distance upstream of the model, as shown in Fig. 20 (Ref. 26). The jet is pulsated by means of an exciter valve consisting of a short motor-driven cylindrical plug loosely fitted in a valve body with inlet and outlet ports tangential to the plug. The plug is contoured with circumferential slots to provide an approximately sinusoidal variation in open area through the valve for a constant rotational speed of the plug. The exciter is used to bring the model to the desired oscillation amplitude and is then turned off, and the resulting decaying oscillation is analyzed in the standard fashion, without any disturbing effects on the tunnel flow.

#### 7.2 AEDC-VKF

An example of the use of a gas-bearing pivot is shown in Fig. 21. Such pivots, of course, have an almost negligible internal damping, which may be important for testing at hypersonic Mach numbers, where the aerodynamic damping to be measured is itself very small. As an example, the relative contribution of the typical mechanical and still-air tare damping to the total damping measured for a blunted cone at various Mach numbers is shown in Fig. 22. It is obvious that as the Mach number increases extreme care must be taken to minimize the tare damping or, alternatively, to measure it with a high degree of accuracy. When using a gas-bearing pivot, such as in the apparatus shown in Fig. 21, there is no mechanical connection between the moving and the stationary parts of the mechanism; the models must therefore be statically and dynamically stable to be tested on such an apparatus. A special variable-reluctance, angular E-core transducer provides a continuous time history of the model displacement. This particular apparatus is designed for large-amplitude ( $+15^\circ$ ) oscillation, thereby making use of yet another advantage of gas-bearing pivots; a large oscillation amplitude would normally not be compatible with a cross-flexure pivot. The apparatus is water cooled to permit operation in hypersonic wind tunnels.

Another AEDC-VKF free-oscillation apparatus employs a system of alternative pulsating nitrogen jets (Fig. 23) to excite the model to the desired oscillation amplitude. The frequency of the pulsations can be set by an oscillating servo valve to the natural frequency of the flexure-model system.

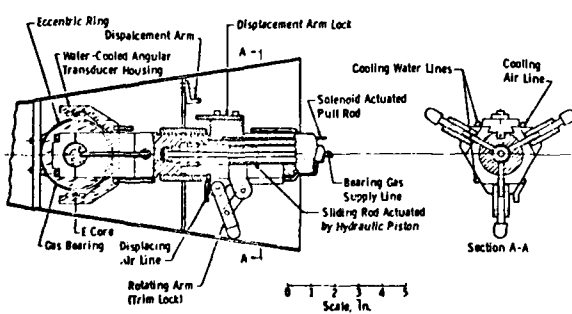


FIG. 21 LARGE AMPLITUDE FREE OSCILLATION  
PITCH APPARATUS USING GAS-BEARING  
PIVOT. AEDC-VKF. (REF. 13)

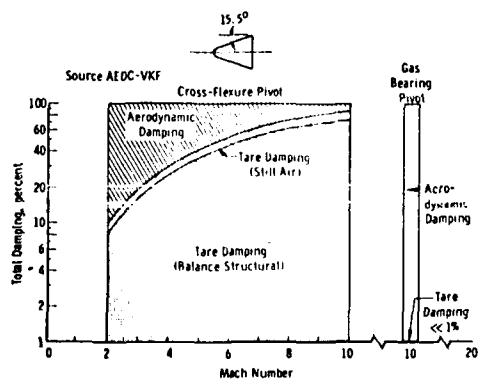


FIG. 22 CONTRIBUTION OF MECHANICAL  
AND STILL-AIR TARE DAMPING  
TO TOTAL DAMPING

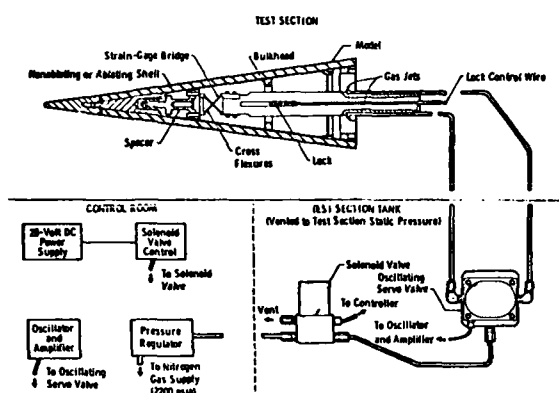


FIG. 23 FREE-OSCILLATION PITCH APPARATUS USING GAS-JET EXCITATION. AEDC-VKF. (REF. 13)

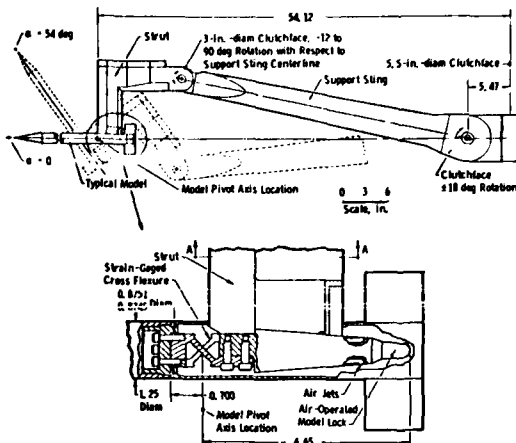


FIG. 24 HIGH ALPHA FREE-OSCILLATION PITCH APPARATUS. AEDC-VKF. (REF. 27)

Gas-jet excitation is also used in the VKF High-Alpha Pitch Damping Apparatus shown in Fig. 24 (Ref. 27). The apparatus utilizes a small-amplitude single-degree-of-freedom cross-flexure balance which is supported by a strut and sting that can be manually varied to provide angles of attack ranging from  $-15^\circ$  to  $90^\circ$ ; at the same time, the position of the strut-sting-model system can be adjusted for minimum aerodynamic interference. A pneumatic and spring-operated locking device holds the model during injection into the tunnel or retraction from it. Several interchangeable balances with different stiffnesses are available.

Free oscillation can also be used for more than one-degree-of-freedom experiments. Such applications, however, have nothing in common with the standard free-oscillation techniques. A three-degree-of-freedom apparatus consisting of a spherical gas bearing, a three-axis variable-reluctance angular transducer, a model-release mechanism and a model-locking system is available at VKF. This apparatus allows the model to freely pitch, yaw or roll on the gas bearing. The test procedure consists of releasing the model at the desired initial conditions and of monitoring its behaviour as function of time. The aerodynamic damping coefficients are obtained by fitting the proposed solution of the 3 equations of motion to the experimental data, as in free-flight-reduction procedures (but using only the moment equations of motion).

### 7.3 FFA, Stockholm

Some of the free oscillation mechanisms used at FFA are shown in Fig. 25. In addition to the standard cross flexure, a free flexure pivot (not shown) and a roller bearing were also tried (Ref. 28). The latter was found to introduce too high mechanical damping and its use was abandoned. In all cases the initial deflection and release is accomplished by a spring-loaded tripper, similar to the one described in Fig. 19, but manually operated by means of a rod and a flex-ball cable. Provisions also exist to remotely lock the model during the starting and the stopping of the wind tunnel at supersonic speeds.

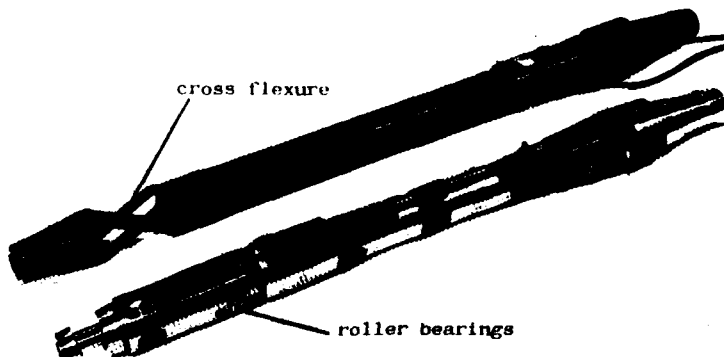


FIG. 25 FREE OSCILLATION PITCH APPARATUS. FFA

#### 8. MEASUREMENT OF MOTION. RANDOM EXCITATION.

Unsteadiness of the flow in a wind tunnel is usually considered as the inevitable evil that impairs the accuracy of aerodynamic experiments and has to be dealt with by proper application of various signal filtering and smoothing techniques. It is, therefore, tempting to turn things around and - instead of fighting it - utilize the flow unsteadiness for a useful purpose. The idea of using random disturbances for excitation purposes is not new, but has already been applied, quite successfully, in flutter testing, both in flight and in wind tunnel. The application to dynamic stability measurements is more recent (Refs. 29 and 30) but definitely looks promising even if in practice it may have to be limited to single-degree-of-freedom experiments.

Briefly, the technique requires the model to be elastically supported, and the model motion induced solely by flow unsteadiness is studied. The suspension of the model should be such that the model-spring combination constitutes a linear system, and the flow unsteadiness is assumed to have stationary "white noise" characteristics. System parameter identification techniques, such as the Fast Fourier Transform, are used to construct a mathematical model based on a sampled set of values of the model response. This mathematical model is then analyzed (by application of autoregressive processes) to obtain a digital spectrum of the response, from which the system damping and resonance frequency can be evaluated. The experimental apparatus is simple (since no external harmonic excitation is required), the time required for the experiments may be sufficiently short to permit application to intermittent wind tunnels, but the model-spring system must be statically and dynamically stable and the spectrum of the flow unsteadiness in the frequency range of interest for dynamic stability experiments should be reasonably flat. The technique appears most valuable for single DOF damping measurements in situations where the flow unsteadiness is high but its spectrum flat.

#### 9. ROTARY TECHNIQUES

There are a number of wind tunnel techniques where the model is performing a continuous *rotary* motion, rather than an *oscillatory* motion, as was discussed so far. Some confusion exists at the present time when attempting to identify and label the individual techniques. For the purpose of the present review the following terminology will be observed (often for historical rather than logical reasons):

**ROLLING** - a rotary motion of the model around the body axis or around the wind axis, at zero to moderate angles of attack, zero sideslip and low to moderate rotation rates. The main purpose of the rolling experiments is to determine stability derivatives due to rolling.

**SPINNING** (as applied to missiles and projectiles) - a rotary motion of the model around the body axis, at arbitrary angles of attack, zero sideslip and high rotation rates. The main purpose of the spinning experiments is to determine Magnus effects.

**CONING** - a rotary motion of the model around the wind axis, at arbitrary non-zero angles of attack, usually non-zero angles of sideslip and low to moderate rotation rates. The motion is sometimes referred to as the *lunar* motion and the apparatuses employed for such experiments are often called *rotary balances*. The main purpose of the coning experiments is to obtain the aerodynamic reactions as functions of the coning rate.

**SPINNING** (as applied to aircraft) - a coning motion where the center of gravity of the model is located off the axis of rotation and describes a circular motion with a radius called *spin radius*.

**OSCILLATORY CONING** - a coning motion around an axis that is slightly inclined to the wind axis, permitting (in principle) the determination of oscillatory stability derivatives.

**ORBITAL FIXED PLANE MOTION** - an orbital motion of the model such that the transverse axis of the model remains in a plane which maintains a fixed orientation in the inertial frame of reference. Can be used to obtain various rotary or acceleration derivatives individually or in combinations.

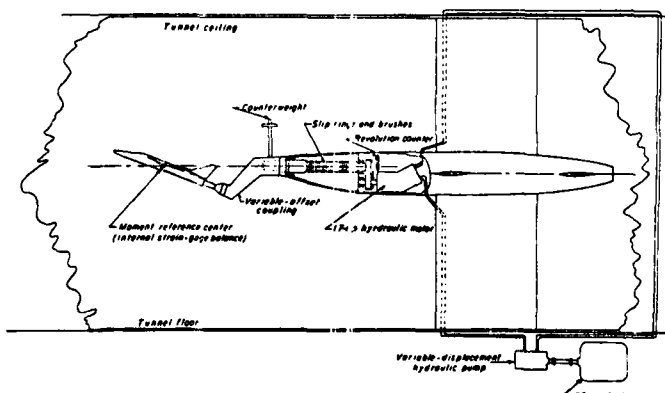


FIG. 26 STEADY-ROLL APPARATUS.  
NASA-LANGLEY. (REF.31)

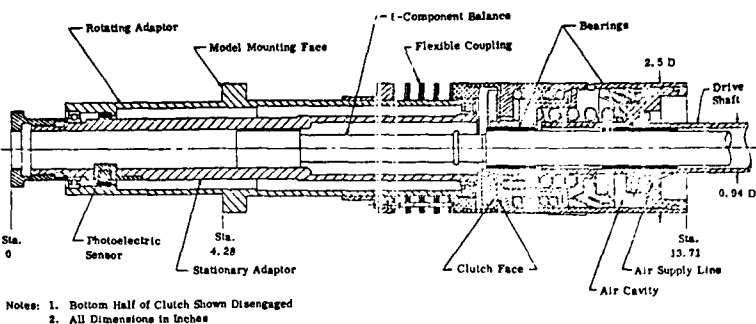


FIG. 27 FREE-DECAY ROLL APPARATUS.  
AEDC-PWT. (REF. 13)

### 9.1 Rolling Techniques

These techniques are in principle similar to the oscillatory techniques. They can be subdivided into techniques using steady roll (corresponding to forced oscillation) and free decay (corresponding to free oscillation). A few examples will be given below.

#### 9.1.1 NASA-Langley

The steady-state forced-roll apparatus which can be used in NASA-Langley 7 x 10 Foot High-Speed Wind Tunnel is shown in Fig. 26. The model is mounted on a six-component strain-gauge balance of the type normally used for static tests of sting-supported models. The angle of attack can be varied by means of interchangeable couplings between the balance and the rotating sting support. The model is driven by a constant-displacement, reversible hydraulic motor located inside the main sting body. The speed of rotation is varied by controlling the fluid displacement in a hydraulic pump, which actuates the hydraulic motor. Corrections have to be applied to the data for deflection of the balance and support under load and for the centrifugal forces introduced by these deflections and by any initial displacement of the model CG from the roll axis (Ref. 31).

#### 9.1.2 AEDC-PWT

A free-decay roll apparatus designed for experiments on short-finned missile or bomb models in the 4-Foot Transonic Wind Tunnel is shown in Fig. 27. The apparatus features a hydraulic-motor-driven sleeve mounted on ball bearings on a 6-component balance. The model is mounted on a sleeve and can be spun up to desired spin rate at which point a pneumatic-operated clutch is used to disengage the drive motor, permitting the model to rotate freely on the bearings. Spin rate and balance data are recorded during the free-spin cycle. The drive system can deliver 138 lb. in. of torque to the model at roll rates up to 5000 rpm.

#### 9.1.3 AEDC-VKF

The free-spin (or a free-decay) roll apparatus at AEDC-VKF (Fig. 28) is intended primarily for tests on missiles at high angles of attack. A six-component balance is supported by a strut that can be manually set in 6-deg. increments to provide various prebend angles. These manual settings along with the tunnel pitch mechanism provide an angle-of-attack range from -5 to 90 deg. The balance supports an adapter with three ball bearings and the model is mounted directly to the bearings. An air-operated brake is located on the front of the adapter and is used to stop model rotation. The brake as well as a mechanical lock can be used to obtain static force coefficients at zero spin rate. Roll-damping data are obtained as the model spins up (for models with canted fins) or as the model spins down after it is spun up by high pressure air jets impinging on the fins.

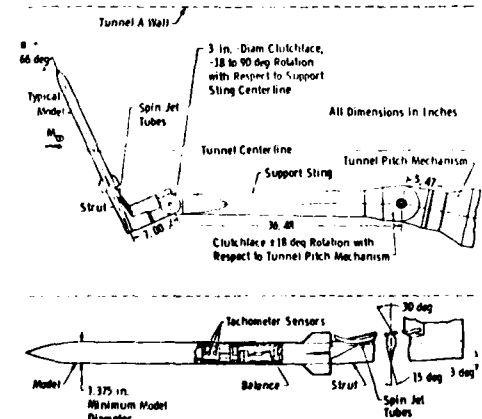


FIG. 28 FREE-SPIN HIGH ALPHA ROLL APPARATUS. AEDC-VKF. (REF. 27)



FIG. 29 STEADY-ROLL APPARATUS. FFA

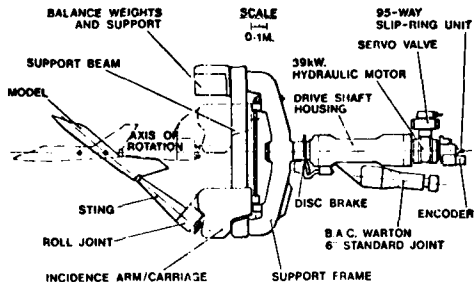


FIG. 30 MULTI-FACILITY ROTARY DERIVATIVE RIG, B.Ae. WARTON. (REF. 33)

The rotational speed, roll position, and roll direction are computed from the electrical pulses produced by a ring with alternating reflective and non-reflective surfaces passing three internally mounted infrared-emitting diodes and phototransistors. The mechanism is designed for spin rates up to 12,000 rpm and normal force loads of 300 lb." (Ref. 27). The apparatus requires a minimum model diameter of 1.375 inches.

A similar apparatus has recently been developed for testing large missile models in the PWT 16-foot transonic and supersonic wind tunnels (Ref. 32). The apparatus requires a minimum model diameter of 4.2 inches and is designed for spin rates up to 20,000 rpm and normal force loads up to 1200 lb. In addition to using canted fins on a model, the spinning-up can also be achieved by using a built-in turbine that can produce a developed torque of 140 lb. in. The apparatus can be used to measure 4-component static force and moment characteristics, Magnus effects and damping in roll at angles of attack up to 90° (up to 28° if used in the PWT 4-foot transonic wind tunnel).

#### 9.1.4 FFA

A continuous rolling apparatus (Fig. 29) is used in the 1 m supersonic wind tunnel at FFA. The apparatus is hydraulically driven, with rolling rates up to 600 rpm, and a conventional 6-component balance is used. Angle of attack can be changed by employing separate bent stings (up to 25°).

#### 9.1.5 B.Ae., Warton

A hydraulically driven, multi-facility "rotary derivative rig" is in operation at B.Ae., Warton Division (Fig. 30). Although mainly associated with the B.Ae. 1.2 m High Speed Wind Tunnel at Warton, the apparatus can also be used in three other UK wind tunnels (Ref. 33). The maximum angle of attack is 90° (although this can only be utilized in one of the wind tunnels), the maximum angle of sideslip is 10° (provided by rolling the model around its longitudinal axis) and the maximum roll rate is 600 rpm. The aerodynamic reactions and rotary derivatives due to rolling are obtained from a six-component internal strain-gauge balance via a slip-ring arrangement. A larger, air-motor driven, 60 rpm rotary derivative rig, primarily intended for the 5.5 m Low Speed Wind Tunnel is also available.

#### 9.1.6 DFVLR - Cologne

Another steady state forced-roll derivative balance is in operation at the 3 m low speed wind tunnel at DFVLR-Cologne (Ref. 15). The model is hydraulically rotated about the wind axis at rates up to 300 rpm. Angle of attack can be varied from 0° to 90° using three different bent stings. A six-component balance is used to obtain the aerodynamic reactions.

It should be noted that apparatuses used for steady rolling about a wind axis can in most cases be used interchangeably as rotary balances, that is, for the purpose of obtaining the various aerodynamic reactions as functions of the roll rate. The difference lies mainly in the instrumentation and in the data reduction. The rotary balances will be discussed next.

#### 9.2 Rotary Balances

In recent years there has been an increased emphasis on a better simulation of the aerodynamic phenomena that are associated with the spin motion of aircraft. Also, it was shown in Ref. 34 that to take into account the non-linear coupling effects that exist between pitch, yaw and roll, a generalized formulation of equations of motion was necessary, and that in this new formulation one of the important contributions to the total aerodynamic moment was related to the rotary or coning motion. To simulate such a motion in a wind tunnel the model, at some fixed combination of incidence and sideslip, is attached to a rotary balance, whose axis is parallel with the wind-tunnel centreline. Several such balances are now in existence, for both low-speed and high subsonic wind tunnels, including those at NASA-Langley, NASA-Ames, RAE-Bedford, B.Ae.-Warton, DFVLR-Cologne, Aeronautica Macchi and IMF.

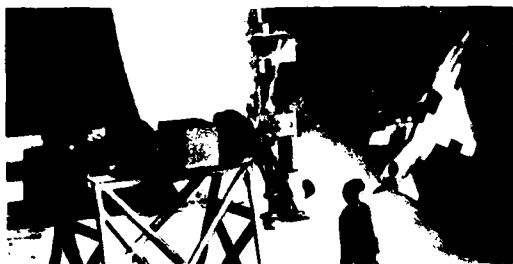


FIG. 31 ROTARY BALANCE. NASA-LANGLEY.  
FULL-SCALE TUNNEL. (REF. 35)

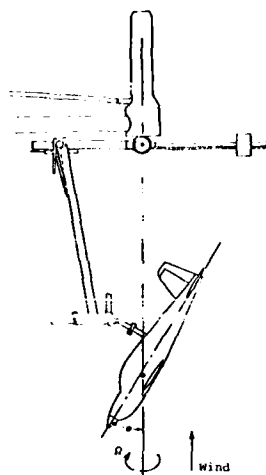


FIG. 32 ROTARY BALANCE. NASA-LANGLEY.  
SPIN TUNNEL. (REF. 36)

It should be noted that by slightly tilting the axis of a rotary balance it is possible, in principle, to superimpose an oscillatory motion in pitch or yaw on the main rotary motion. However, it is not yet known whether the accuracy involved in such an experiment would be sufficient to permit the determination of the derivatives due to pitching and yawing.

Rotary balances will be discussed in some detail in Lecture No. 6, but a few examples are included here for the sake of completeness.

#### 9.2.1 NASA Langley

The rotary balance at NASA-Langley Full Scale Tunnel (Ref. 35) is shown in Fig. 31. It is capable of providing six-component data over a range of angles of attack of  $45^\circ$  to  $90^\circ$  and in a range of nondimensional spin rate  $\Omega b/2V$  of  $\pm 0.3$ , at low speeds and at a Reynolds number up to 3.3 million/m. The apparatus is designed for tests employing relatively large-scale models which can also be used for flight tests involving drop model techniques. Thus the aerodynamic data can be measured with the rotary balance at the same value of Reynolds number as that obtained in flight tests, and the data can then be used, together with conventional static force data, as inputs to theoretical spin prediction programs for correlation with the results of flight tests.

An older, modernized, rotary balance is available at NASA Langley for experiments on 1:5 scale models in the Spin Tunnel (Fig. 32). This balance is capable of spin rates of up to 90 rpm in either direction, corresponding to the nondimensional spin rate of  $\pm 0.9$ . The range of angles of attack is from  $0^\circ$  to  $90^\circ$  (Ref. 36).

#### 9.2.2 NASA Ames

The new NASA-Ames rotary balance (Fig. 33) was designed specifically for use in the 12-Foot Pressure Tunnel and the 11-Foot Transonic Tunnel. The apparatus allows a remote change of angles of attack and sideslip, up to a combined value of  $30^\circ$ ; the use of bent stings and top-mounted models permits a further adjustment of the angle of attack to  $100^\circ$  and of the angle of sideslip to  $25^\circ$ . The apparatus has a spin-rate capability of 400 rpm (Ref. 37).

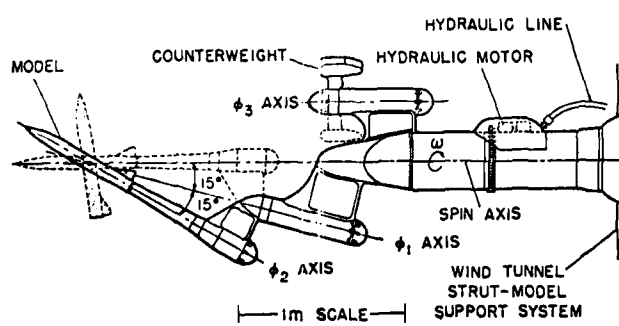


FIG. 33 ROTARY BALANCE. NASA-AMES.  
(REF. 37)

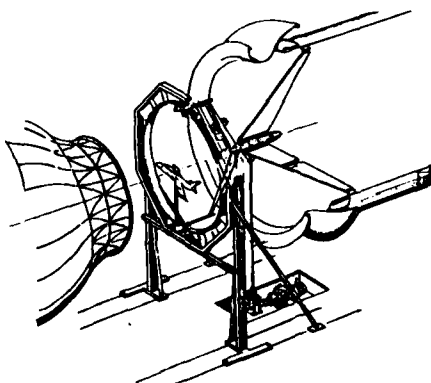


FIG. 34 ROTARY BALANCE. AERONAUTICA MACCHI. (REF. 38)

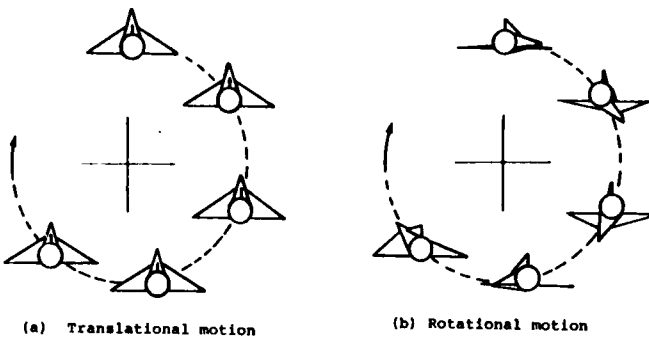


FIG. 35 ORBITAL FIXED-PLANE MOTION. NAE (REF. 39)

#### 9.2.3 Aeronautica Macchi

A new rotary balance has recently been constructed (Fig. 34) for low-speed experiments at angles of attack up to  $90^\circ$ . All six aerodynamic components can be measured and a finite radius of spin can be simulated. The experimental arrangement includes an unusual circular rail which serves to take up the centrifugal force acting on the model and to eliminate elastic distortion of the support arm (Ref. 38).

#### 9.3 Orbital Fixed-Plane Motion

An orbital motion where the model is rotated in such a way that its transverse axis remains at all times in a plane which maintains a fixed orientation in the inertial frame of reference is called here an orbital fixed-plane motion (Ref. 39). The two special cases of that motion, that are important for the determination of stability derivatives are illustrated in Fig. 35. These are:

(a) Pure Translation - the model performs a combination of a vertical oscillation and a lateral oscillation. The two motions are  $90^\circ$  out of phase. No rotation is involved. All the position angles are constant and all body angular velocities are zero. Only the aerodynamic angles are variable. With proper, rather complex, experimental procedures the dynamic derivatives due to  $\alpha$  and  $\beta$  can be determined.

(b) Pure Rotation - the model axis is tilted through the angle induced by the orbital motion; the model continuously follows the velocity vector during a circular translation. As a result, the model performs a combination of a pure pitching oscillation and a pure yawing oscillation. The two motions are again  $90^\circ$  out of phase. In the ideal case (not excessively large angles of attack), all the aerodynamic angles remain constant and the roll rate is zero. The dynamic derivatives due to pure pitching ( $q$ ) and due to pure yawing ( $r$ ) can be determined.

An apparatus based on these principles is now being designed at NAE. The beauty of this concept lies in the fact that a single apparatus may be capable of determining individual derivatives due to  $\alpha$ ,  $\beta$ ,  $q$  and  $r$ . In addition, by suitably locking the model to the sting the apparatus may also be used for steady rolling experiments. Thus, with a single apparatus and three experiments one may be able to perform the work for which previously three different apparatuses and five experiments were needed.

#### 10. HALF-MODEL TECHNIQUES

The use of half models for static testing of symmetric configurations at symmetric flow conditions has been a recognized experimental procedure for a long time (see, for example, Ref. 40). This technique eliminates all interference problems usually associated with the presence and with the oscillation of a sting, permits the use of models larger than otherwise possible and allows for a more convenient arrangement of the test equipment (outside of the wind-tunnel wall). On the other hand, the technique has some problems of its own, such as the possible effect of the gap between the model and the tunnel wall and the effect of an interaction between the shock and the wall boundary layer. And, of course, the applications are strictly limited to symmetrical flow conditions.

The application of the half-model technique to pitching and plunging oscillation experiments has been pursued by many organizations, notably FFA (Ref. 41) and NAE (Ref. 42). The technique is particularly recommended for cases where static or dynamic sting interaction may be expected to be significant or where the shape of the model afterbody is incompatible with a sting mounting. Other possible applications include the determination of the dynamic interference between two oscillating models and the determination of the effect of a jet exhaust plume on the damping in pitch of an aircraft model. The application of half-model techniques to dynamic stability testing will be discussed in detail in Lecture No. 9.

#### 11. DERIVATIVES DUE TO TRANSLATIONAL ACCELERATION AND PURE ROTATION.

As discussed in Section 2, the results of oscillation experiments around a fixed axis always appear as composite expressions containing derivatives due to pure rotation

(such as  $q$  or  $r$ ) and derivatives due to time-rate-of-change of the angular deflection in the plane of motion (such as  $\dot{\alpha}$  or  $\dot{\beta}$ ). To separate the two parts, additional experiments are required, in which either a pure angular motion (with the appropriate aerodynamic deflection angles remaining constant) or a pure translation (with the appropriate angular rates remaining zero) is simulated. As also discussed in Section 2, the latter is aerodynamically equivalent to the time-rate-of-change of an aerodynamic deflection angle.

There is a relatively wide range of techniques, with which the two pure motions can be simulated individually or in known combinations. Of course, the results pertaining to the individual motions can be obtained from an analysis of results of at least two widely-spaced known combinations. Some examples of such techniques and apparatuses will be given below.

### 11.1 NAE (Orbital Fixed-Plane Motion)

As discussed in Section 9.3, an apparatus (yet to be constructed) based on the concept of orbital fixed-plane motion would be capable of measuring derivatives due to both pure translation ( $\dot{\alpha}$ ,  $\dot{\beta}$ ) and pure rotation ( $q$ ,  $r$ ).

### 11.2 Calspan (Forced-Oscillation 2 DOF Apparatus)

A 2 degree-of-freedom apparatus with which known combinations of pitching (or yawing) and vertical (or lateral) oscillations could be obtained was developed at Calspan (Cornell) in the early 1960s (Ref. 43), for use in their 8-Foot Transonic Wind Tunnel. The system had the ability to force the model inexorably in any planar sinusoidal motion, including limiting cases of pure translation and pure rotation. The yawing or lateral oscillations were investigated by rotating the model 90° around the sting. The desired motion was imparted to the model by a mechanical drive system, consisting of linkages and connecting rods, eccentrically mounted on two high-inertia flywheels (Fig. 36). The available frequency range was from 3 to 12 Hz and amplitudes up to  $\pm 5^\circ$  and  $\pm 0.5$  ft and accelerations of up to 200 rad/sec<sup>2</sup> or 20 g:s could be achieved in the rotational and translational case, respectively. The normal force capability, at the model center of gravity, was 1200 lb. Models could be installed at non-zero angles of attack, using bent stings, subject to load limitations. This apparatus has not been used for some time now and it is not known whether it can still be considered operational. It seems certain that at least the electronics part of it, including the instrumentation used for data analysis, may need updating.

The simulation of a pure rotary motion such as pure pitching is achieved by generating a so-called "snaking motion" which is a particular planar combination of rotational and translational motions (in the pitch plane) such that the instantaneous angle of attack - which includes vector components generated by these two motions - remain at all times constant. If we write the instantaneous angle of attack as

$$\alpha = \alpha_0 + \theta_0 e^{i\omega t} + (z/V_0) e^{i\omega t}$$

the above condition is satisfied if  $\theta_0 = -(z/V_0)$ , i.e., if the contributions of the rotary oscillation and of the plunging oscillation are equal in amplitude but opposite in phase.

### 11.3 NASA Langley (Snaking Motion)

Long before the Calspan apparatus was constructed, a concept of a similar snaking motion, but generated by different mechanical means, was used at NASA Langley to simulate pure yawing motion (Ref. 44). The proper combination of the fixed-axis oscillation and the lateral oscillation was achieved by attaching the model (via a strain-gauge balance) to a transversal strut supported at the ends by counter-rotating flywheels, as shown in Fig. 37. This apparatus was used in the Langley stability tunnel for systematic investigations, yielding good-quality results on derivatives  $C_{nr}$ ,  $C_{lr}$  and  $C_{Yr}$ . It has

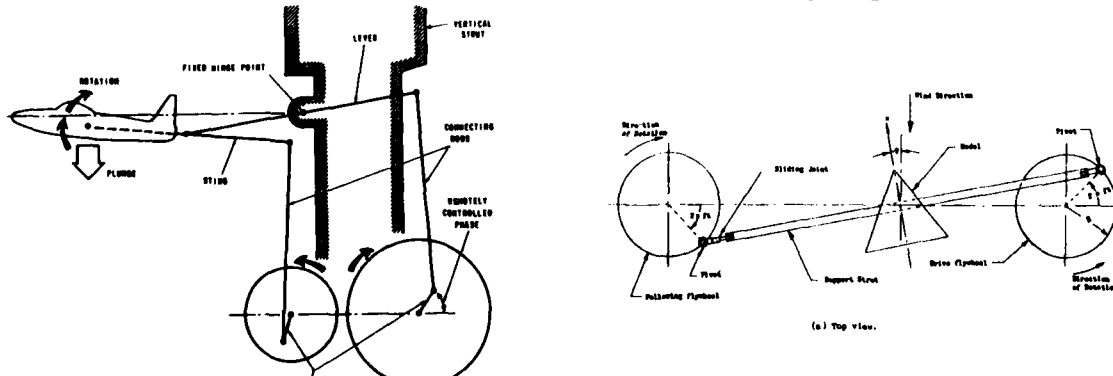


FIG. 36 FORCED-OSCILLATION 2 DOF PITCH OR YAW APPARATUS. CALSPAN. (REF. 43)

FIG. 37 SNAKING MOTION APPARATUS FOR SIMULATION OF PURE YAWING. NASA LANGLEY. (VPI) (REF. 44)

now been moved to the Virginia Polytechnic Institute (VPI) but, to the best of the present author's knowledge, it has not yet been used in its new location.

#### 11.4 VPI (Curved Flow)

A curved-flow 6 ft x 6 ft test section, originally developed at NASA Langley (Ref. 45) is now in use at the Virginia Polytechnic Institute, which in 1958 acquired the Langley stability tunnel. The curved-flow technique is based on the concept of simulating a steady curved-flight condition by using a fixed model and arranging wind-tunnel flow in such a way that it is curved in a circular path in the vicinity of the model and that it has a velocity variation normal to the streamlines in direct proportion to the local radius of curvature. This is achieved by using flexible side walls for curving the flow and by employing specially constructed vertical-wire drag screens upstream of the test section for producing the desired velocity gradient across the tunnel flow. These screens vary in mesh size across the wind tunnel, with the most dense portion of the screens located at the inner radius of the curved test section (Fig. 38). The technique allows measuring pure-yawing (due to  $r$  only) or pure-pitching (due to  $q$  only) derivatives with a fixed model mounted on a static balance. The simulation of the steady curved flight is not exact, however, and corrections have usually to be made for the buoyancy effect caused by the static-pressure gradient normal to the streamlines (which does not exist in curved flight). In addition, there are dissimilarities in the behaviour of the model boundary layer (which on the model in a curved flow tends to move toward the center of curvature, contrary to its normal tendency in curved flight), and possible problems due to a rather high degree of turbulence behind the wire screen. Hopefully, however, in many cases these phenomena may be considered to have only a minor effect on the measurement of purely-rotary derivatives. No other technique is at present available - and operational - for that purpose.

#### 11.5 VPI (Rolling Flow)

When a model at an angle of attack performs a rolling motion about a fixed body axis, the resulting aerodynamic reactions will be functions of both the roll rate and the simultaneously occurring time rate of change of the angle of sideslip. This is similar to previously discussed composite effects resulting from pitching or yawing oscillation around a fixed axis. To obtain aerodynamic derivatives due to "pure" rolling, one can use a stationary model immersed in a rolling flow. Such a technique is employed at the Virginia Polytechnic Institute (VPI), where a rolling-flow 6-foot diameter test section is available in conjunction with the old NASA-Langley stability tunnel (Ref. 46). To properly simulate a pure roll maneuver, the rotating flow must be generated in such a way that its velocity component normal to the tunnel axis increases proportionately to the radial distance. This is achieved by using a large rotor upstream of the test section with nine vanes that are specially shaped in order to impart a suitable solid core vortex motion to the flow (Fig. 39). For reasons similar to those mentioned in Section 11.4, the simulation of the pure roll maneuver is not exact, but for a symmetrical model which is symmetrically mounted the undesirable effects are negligible. In other cases a correction may be required.

#### 11.6 NAE (Translational Oscillation)

Derivatives due to  $\dot{\alpha}$  and  $\dot{\beta}$  can be measured directly using the NAE translational oscillation apparatus shown in Fig. 14 and discussed in Ref. 18. Derivatives due to  $\dot{\alpha}$  can also be obtained from experiments using the NAE half-model vertical oscillation apparatus, that will be discussed in some detail in Lecture No. 9.

#### 11.7 NASA Langley (Lateral Oscillation)

Derivatives due to  $\dot{\beta}$  were measured at NASA Langley in the 1950s, using a model mounted on a transversal strut which performed an oscillatory motion as indicated in Fig. 40. The motion was imparted to the strut by a system of pushrods eccentrically attached to a flywheel. The apparatus was used both in the free-oscillation (Ref. 47)

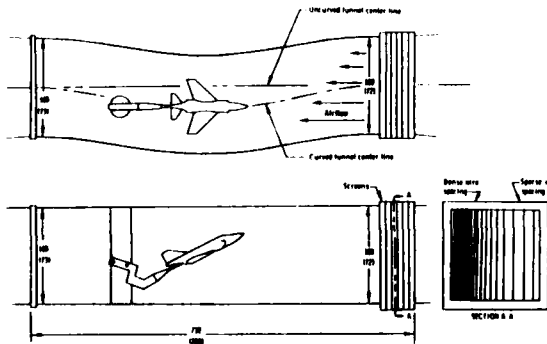


FIG. 38 CURVED-FLOW TECHNIQUE. VPI.  
FORMERLY AT NASA LANGLEY.(REF. 45)

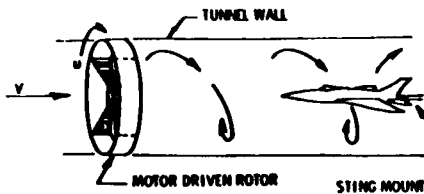


FIG. 39 ROLLING-FLOW TECHNIQUE. VPI.  
(REF. 46)

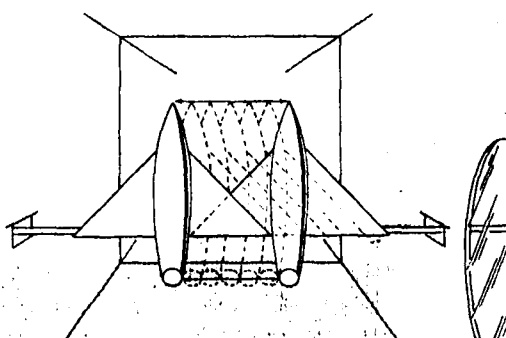


FIG. 40 LATERAL-OSCILLATION APPARATUS.  
NASA LANGLEY. (VPI) (REF. 47)

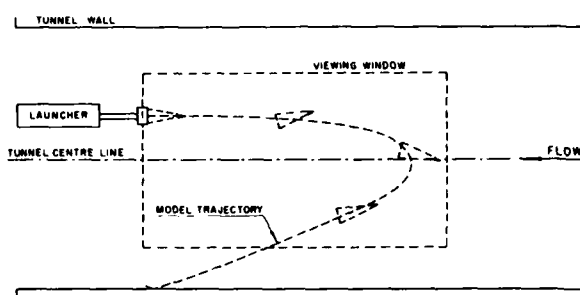


FIG. 41 FREE-FLIGHT TECHNIQUE USING  
LAUNCHED MODELS. NAE. (REF. 50)

and forced-oscillation (Ref. 48) modes of operation, in the 6 ft. x 6 ft. test section of the old NASA-Langley low-speed stability tunnel. The apparatus was employed for systematic investigations of the dynamic characteristics of wings and wing-body configurations, and good-quality, highly-consistent values of derivatives  $C_{L\beta}$  and  $C_{n\beta}$  were obtained. This apparatus has now been moved to the Virginia Polytechnic Institute.

A summary of the experience obtained by NACA and NASA concerning the low-speed lateral-directional dynamic derivatives due to lateral acceleration, pure yawing and the sum of these two effects is given in Ref. 49, which also includes an extensive bibliography. An analysis of the pertinent problem area and a detail discussion of some of the techniques mentioned in this section will be given in Lecture No. 7

## 12. MODEL FREE

Two of the major problems encountered in performing captive-model dynamic-stability experiments in wind tunnels is (a) the inevitable interference associated with a mechanical model support and its vibration, and (b) the inherent inability of any mechanical support to provide simulation of the unrestrained model motion. Thus it has been recognized that a definite need exists for a wind-tunnel technique with which experiments could be performed without having to employ a mechanical model support. Four such techniques will be considered in the present section, namely (a) techniques employing models launched into the wind-tunnel flow and performing free flight in the test section, (b) techniques employing remotely-controlled models flying in the test section with only a flexible control-and-safety cable attached to the model, (c) techniques employing cable-suspended models, which can perform motion in five degrees of freedom (all except longitudinal translation), and (d) techniques employing magnetically suspended and magnetically actuated models. At the present time techniques (a) and (d) have only been used with relatively small models and must therefore be considered as mostly useful for exploratory experiments rather than systematic or routine dynamic-stability testing.

### 12.1 NAE (Free Flight)

The free-flight technique has two main variants, depending on whether the model is initially suspended mechanically (e.g. by means of a wire that is then burnt off or cut off at the beginning of experiment) in the upstream part of the test section, or whether it is launched into the test section from an initial position downstream of it (as shown diagrammatically in Fig. 41). The first variant gives a better control of the initial model attitude, whereas the second gives a longer duration of experiment, since both the upstream and the downstream travel of the model can then be utilized. In each variant of the technique two methods of data acquisition can be applied; one in which the time history of the model flight in one or two planes of motion is obtained from film taken with a high-speed movie camera; and another where this information is deduced from accelerometer data transmitted by FM telemetry. Since other data such as pressure or temperature can also be transmitted by telemetry, a combination of these two methods of data acquisition is also possible. Once the motion of the model is known, the required aerodynamic coefficients and stability derivatives can be obtained by fitting, on a computer, the recorded flight history with the solution of pertinent equations of motion, and determining the coefficients and derivatives for the best fit.

The adaptation of the free-flight technique to the NAE helium hypersonic wind tunnel is described in Ref. 50. The system uses a pneumatic launcher and polystyrene injection-molded models. The data are obtained from a high-speed movie film at a typical speed of 3000-4000 frames per second. The optical system, permitting viewing the model in two orthogonal planes on the same frame, is shown in Fig. 42.

### 12.2 CSIR-NIAST (Free Flight)

Recent developments in the launching procedures used with the free-flight technique are described in Ref. 51. The pitch-jet launch system shown in Fig. 43 permits the model to be launched at a relatively small angle relative to the launch-gun axis and then to impart to it an angular velocity immediately after release; the maximum (large) angle of attack will then be attained only when the model reaches the observation area,

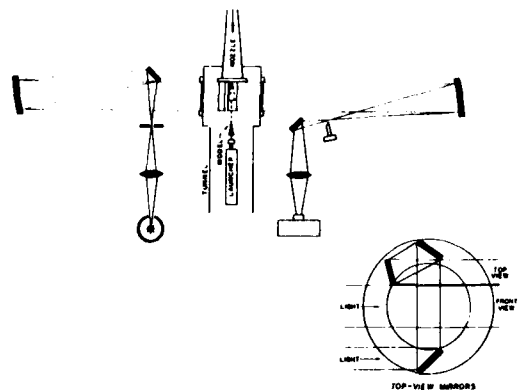


FIG. 42 FREE-FLIGHT TECHNIQUE. OPTICAL SYSTEM. NAE. (REF. 50)

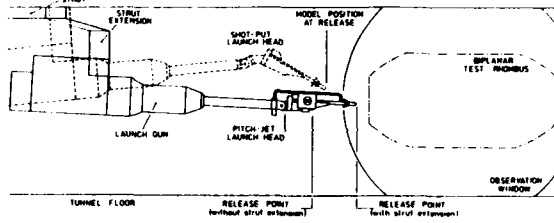


FIG. 43 FREE-FLIGHT TECHNIQUE. LAUNCHER. CSIR-ARU. (REF. 51)

without affecting the trajectory too much. The model can be spun-up on a spindle before the release and the angular velocity after launch is imparted by one or two air jets mounted on the launch head. An alternative shot-put launch is also shown in Fig. 43; it provides a rail-type support instead of the spindle, with one fin (of a missile) guided in a slot along the rail, which can be set at angles from 0 to 90°.

A comprehensive summary of procedural details concerning techniques which employ free flight in wind tunnels can be found in Refs. 51 - 53.

#### 12.3 NASA Langley (Remotely-Controlled Free Flight)

A unique free-flight testing capability exists in the NASA-Langley Full Scale Wind Tunnel. A relatively large (typically around 4 ft. span) powered model can be flown without restraint in the 30 ft. x 60 ft. open test section of that tunnel (Ref. 54). The model is controlled by three operators who can transmit pneumatic and electric power and control signals to the model via a flexible trailing cable (Fig. 44). This flexible cable also incorporates a thin steel safety cable which is passed through a pulley above the test section and which can be used to catch the model if an uncontrollable motion or mechanical failure occurs. The entire flight cable is kept slack during the flight and is controlled by a separate safety-cable operator. Typical results may include steady flights at high angles of attack, studies of pilot control techniques at high angles of attack and evaluation of artificial rate damping. The results are mainly qualitative and consist of pilot opinion of the behaviour of the model and of cinematographic records.

#### 12.4 NASA Langley (Cable-Mounted Semi-Free Models)

The NASA-Langley 5 DOF cable-mount system described in Section 6 in conjunction with forced-oscillation experiments can also be used (by removing the excitation forces) for studying the responses of a "free-flying" model to various flow disturbances. This can be used for flutter and gust response investigations and also, as described in Ref. 24, for the determination of stability derivatives, using procedures initially developed for flight-test measurements.

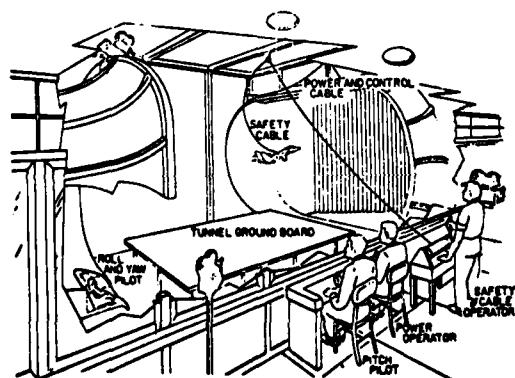


FIG. 44 REMOTELY-CONTROLLED FREE FLIGHT. NASA LANGLEY. (REF. 53)

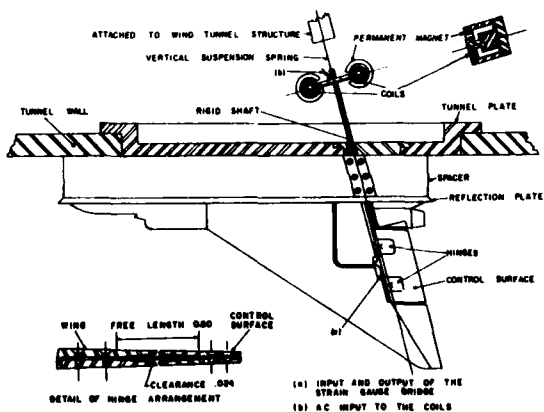


FIG. 45 CONTROL-SURFACE OSCILLATION. NAE. (REF. 57)

### 12.5 U. of Virginia, MIT, U. of Southampton (Magnetic Suspension)

Dynamic testing with magnetically suspended models has now been pursued for a number of years, mainly at MIT, at the University of Southampton and the University of Virginia. Dynamic derivatives such as  $C_{\ell p}$  and  $C_{mq} + C_{ma}$  have been successfully measured and some work has also been performed on studies of spinning and coning bodies. An experimental arrangement used at University of Virginia in a 11 cm x 11 cm vertical subsonic wind tunnel is described in Ref. 55. A large pair of Helmholtz coils produces a uniform field to magnetize the model and a second pair of opposed coils creates a vertical gradient which opposes the weight and drag of the model. The remaining coils create horizontal gradients, which introduce side forces on the model. The test section of the wind tunnel is located inside the coils. Model position is sensed optically and a feedback control system, which drives power amplifiers supplying current to the coils is used to keep the model centered. For the dynamic stability experiments, the model is forced periodically in a combined pitching and heaving motion. A theoretically predicted flight history is then fitted to the measured behaviour of the model by varying the stability derivatives in the analytical expressions for the best fit.

So far, no large-scale magnetic suspension systems have been constructed. However, work is continuing at MIT on some further developments which include model roll control and construction of superconducting coils, with the view of a possible application to large cryogenic wind tunnels.

A useful review of the techniques and procedures related to the use of magnetically suspended models can be found in Ref. 56.

### 13. CONTROL-SURFACE OSCILLATION TECHNIQUES

So far we have dealt with dynamic-stability testing of full or half models of complete configurations. Sometimes, however, the dynamics of a component of an aircraft is also of interest. Most often this applies to a control surface such as an aileron. In principle, knowledge of two different effects may be required: (a) the hinge-moment derivatives of an oscillating surface, and (b) the derivatives of aerodynamic reactions acting on the model due to the oscillation of a control surface. The necessary tests are most conveniently performed using a half model of the aircraft configuration; the hinge moment measurements can be performed with any of the free or forced-oscillation methods mentioned before, whereas the reactions of the model itself can be measured using methods similar to those employed for cross and cross-derivative measurement.

#### 13.1 NAE

An experimental arrangement for measuring the static and dynamic hinge-moment derivatives of a control surface on a half model of a delta-wing aircraft is shown in Fig. 45. Two small circular coils operating in ring-shaped gaps in two permanent-magnet units (mounted on the outside of the wind-tunnel wall) impart an oscillatory motion to the shaft of the control surface (Ref. 57). The method of free-oscillation with feedback excitation is used.

#### 13.2 RAE-Bedford

An apparatus which permits simultaneous measurement of hinge-moment derivatives and wing derivatives due to control oscillation is described in Ref. 58. The model is supported on a strain-gauge balance that measures the normal force, pitching moment and rolling moment due to control oscillation, while another strain-gauge unit measures the oscillatory hinge moment. The incidence, mean control angle, amplitude and frequency can be varied. The rig is used in RAE-Bedford 3 ft. x 3 ft. high-speed wind tunnel.

### 14. CONCLUDING REMARKS

In this review the emphasis was placed on the basic principles of various methods and on the practical aspects of various techniques, as illustrated by numerous examples, descriptions and sketches of actual existing apparatuses. These examples, collectively, are not necessarily intended to constitute a complete catalogue of all the existing equipment of this type; in fact, the author is certain that there are several apparatuses in various laboratories around the world, that have not been included. The author hopes, however, that all the important methods and techniques that are in use today have been covered. Techniques that are not applicable to aircraft testing (such as Magnus balances) have been omitted.

Topics such as detail design considerations, instrumentation, data acquisition and reduction, calibration methods, static and dynamic sting interference, wind-tunnel interference, small amplitude versus large amplitude testing, frequency effects, effects of wind-tunnel flow unsteadiness, model construction, sensitivity studies, typical results - are all highly pertinent to the subject matter of this review, but could not possibly be included due to unavoidable limitations which had to be imposed on this presentation. Some of these topics are described in some detail in Lectures No. 2, 4 - 9 and 13 - 15. Some other topics are discussed in the documents listed in the references, and, in particular, in papers of a slightly more general or summary nature, such as Refs. 1 - 5, 11, 13, 15, 34, 35, 49, 59 and 60. It is hoped that the present review may fulfil a useful role by serving as a guide to the astonishing variety of methods and techniques which are available for wind-tunnel investigations of the dynamic stability of aircraft.

## 15. REFERENCES

1. Orlik-Rückemann, K.J. Methods of Measurement of Aircraft Dynamic Stability Derivatives. NRC, Canada, LR-254, 1959.
2. Orlik-Rückemann, K.J. Dynamic Stability Parameters. AGARD CP 235, 1978.
3. Orlik-Rückemann, K.J. Dynamic Stability Testing of Aircraft - Needs Versus Capabilities. Prog. Aerospace Sci., Vol. 16, No. 4, pp 431-447, Pergamon Press. 1975.
4. Orlik-Rückemann, K.J. Dynamic Stability Testing in Wind tunnels. Von Kármán Institute for Fluid Dynamics. Lecture Series 99. "Aero-dynamic Inputs for Problems in Aircraft Dynamics" April 1977.
5. Orlik-Rückemann, K.J. Wind Tunnel Measurements of Dynamic Derivatives. Lecture Notes, University of California, Los Angeles. Second Edition, August 1963.
6. Grafton, S.B. Libbey, C.E. Dynamic Stability Derivatives of a Twin-Jet Fighter Model for Angles of Attack from  $-10^\circ$  to  $110^\circ$ . NASA TN D-6091, January 1971.
7. Scherer, M. Lopez, J. Progrès Réalisés dans les Techniques de Mesure des Dérivées Aerodynamiques en Soufflerie Méthode d'Oscillations Forcées. AGARD CP-17, pp 411-436, 1966.
8. Boyden, R.P. Effects of Leading-edge Vortex Flow on the Roll Damping of Slender Wings. Journal of Aircraft, Vol. 8, No. 7, 1971.
9. Braslow, A.L. Wiley, H.G. Lee, C.Q. A Rigidly Forced Oscillation System for Measuring Dynamic-Stability Parameters in Transonic and Supersonic Wind Tunnels. NASA TN D-1231, 1962.
10. Christophe, J. A New Rig for Flight Mechanics Studies in the ONERA Aerothermo-dynamic Test Center of Modane. AIAA 11th Aerodynamic Testing Conference, 80-0464, March 1980.
11. Testing Capabilities in the VKF Wind Tunnels A/B/C/F, 1978.
12. Burt, G.E. Forced-Oscillation Test Mechanism for Measuring Dynamic-Stability Derivatives in Roll. J. of Aircraft, Vol. 12, No. 1, 1975.
13. - Dynamic-Stability Measurement Capabilities in the AEDC Wind Tunnels. AEDC/B-2, 1976.
14. Coulter, S.M. Description of a New High-Alpha, High-Load, Pitch-Yaw Dynamic Stability Test Mechanism at AEDC. AIAA 11th Aerodynamic Testing Conference, 80-0451, March 1980.
15. Hafer, X. Wind Tunnel Testing of Dynamic Derivatives in W. Germany. AGARD FDP Symposium on Dynamic Stability Parameters, Paper 5, 1978.
16. v.d. Decken, J. Schmidt, E. Schulze, B. On the Test Procedures of the Derivative Balances Used in W. Germany. AGARD FDP Symposium on Dynamic Stability Parameters, Paper 6, 1978.
17. Orlik-Rückemann, K.J. Experiments on Cross-Coupling and Translational Acceleration Derivatives. AGARD FDP Symposium on Dynamic Stability Parameters, Paper 8, 1978.
18. Orlik-Rückemann, K.J. Haniff, E.S. Anstey, C.R. Wind Tunnel Apparatus for Translational Oscillation Experiments. AIAA 18th Aerospace Sciences Meeting, AIAA-80-0046, 1980.
19. Haniff, E.S. An Advanced Calibrator for Dynamic Wind-Tunnel Experiments. Proc. of the 25th ISA Intern. Instrumentation Symposium, pp 239-244, 1979.
20. Haniff, E.S. Oscillatory Derivative Measurements on Sting-Mounted Wind-Tunnel Models at RAE, Bedford. RAE TR66197, 1966 (also AGARD CP 17).
21. Haniff, E.S. Oscillatory-Derivative Measurements on Sting-Mounted Wind-Tunnel Models; Method of Test and Results for Pitch and Yaw on a Cambered Ogee Wing at Mach Numbers up to 2.6. ARI R&M 3355, July 1962.

22. O'Leary, C.O. Wind-Tunnel Measurement of Lateral Aerodynamic Derivatives using a New Oscillatory Rig, with Results and Comparisons for the Gnat Aircraft. RAE TR 77159, 1977.

23. Schmidt, E. Die AVA-Derivativawaage. DLR-Mitt, 74-32, 1974.

24. Bennett, R.M. Wind-Tunnel Technique for Determining Stability Derivatives from Cable-Mounted Models. J. of Aircraft, vol 15, no 5, pp 304-310, May 1978.

25. Mohr, R.L. Hall, W.E., Jr. Half- and Full-Model Experiments on Slender Cones at Angles of Attack. Journal of Spacecraft and Rockets, 11, no 9, pp 575-580, September 1973.

26. Orlik-Rückemann, K.J. Use of Pneumatic Model Exciter in a Hypersonic Wind Tunnel. DME/NAE Quarterly Bulletin. 1962(3).

27. Uselton, B.L. Jenke, L.M. Experimental Missile Pitch- and Roll-Damping Characteristics at Large Angles of Attack. J. Spacecraft, vol 14, no 4, pp 241-247, 1977.

28. Lundgren, S. Measurement of the Pitch Damping on Two AGARD B Models in the FFA S4 and S5 Wind Tunnels. FFA TN AU-556, 1977.

29. Lundgren, S. A Cross Flexure Sting and Measurement of Dynamic Stability Derivatives of Two Schematic Models at M=4 and M=7. FFA Report AU-637, 1972.

30. Murthy, H.S. Jategaonkar, R.V. Balakrishna, S. Dynamic Stability Measurements from Tunnel Unsteadiness Excited Random Response. J. Aircraft, vol 17, no 1, pp 7-12, 1980.

31. Henderson, W.P. Phillips, W.P. Gainer, T.G. Rolling Stability Derivatives of a Variable-Sweep Tactical Fighter Model at Subsonic and Transonic Speeds. NASA TND-3845, 1967.

32. Collins, J.A. Verification Tests of the AEDC High Alpha Roll Dynamics System, AEDC-TSR-78-P50, 1978.

33. Matthews, A.W. Experimental Determination of Dynamic Derivatives Due to Roll at British Aerospace Warton Division, AGARD-FDP Symposium on Dynamic Stability Parameters, AGARD CP-235, Paper 4, 1978.

34. Tobak, M. Schiff, L.B. Generalized Formulation of Nonlinear Pitch-Yaw-Roll Coupling. AIAA Journal, vol. 13, No. 3, pp 323-332, 1975.

35. Chambers, J.R. Bowman, J.S. Jr. Stall/Spin Test Techniques Used by NASA. AGARD CP-199, Paper 13, 1975.

36. Bahrle, W. Jr. Hultberg, R.S. Mulcay, W. Rotary Balance Data for a Typical Single-Engine Low-Wing General Aviation Design for an Angle-of-Attack Range of 30° to 90°. NASA CR-2972, 1978.

37. Malcolm, G.N. Davis, S.S. New NASA-Ames Wind Tunnel Techniques for Studying Airplane Spin and Two-Dimensional Unsteady Aerodynamics. AGARD FDP Symposium on Dynamic Stability Parameters, Paper 3, 1978.

38. Bazzocchi, E. Stall Behaviour and Spin Estimation Method by Use of Rotating Balance Measurements. AGARD CP-199, Paper 8, 1975.

39. Beyers, M.E. A New Concept for Dynamic Stability Testing, AIAA 19th Aerospace Sciences Meeting, AIAA 81-0158, 1981.

40. Van der Blieck, J.A. Notes on Half Model Testing in Wind Tunnels. NRC, Aero-nautical Report LR-235, 1959.

41. Orlik-Rückemann, K.J. A Method for the Determination of the Damping-in-Pitch of Semi-Span Models in High-Speed Wind-Tunnels and Some Results for a Triangular Wing, FFA Report 62, 1956.

42. Orlik-Rückemann, K.J. Possible Use of Half-Model Oscillatory Techniques for the Study of Shuttle Abort Separation Dynamics. Proceedings of Space Transportation Systems Technology Symposium, Cleveland 1970, NASA TM X-52876, Vol. 1, 99-118, July 1970.

43. Statler, I.C. Tufts, O.B. Hirtreiter, W.J. The Development and Evaluation of the CAL/AF Dynamic Wind-Tunnel Testing System. AFFDL-TR-66-153, 1967.

44. Queijo, M.J.  
Fletcher, H.S.  
Marple, C.G.  
Hughes, F.M.  
Preliminary Measurements of the Aerodynamic Yawing Derivatives of a Triangular, a Swept, and an Unswept Wing Performing Pure Yawing Oscillations, with a Description of the Instrumentation Employed. NACA RM L55L14, 1956.

45. Bird, J.D.  
Jaquet, B.M.  
Cowan, J.W.  
Effect of Fuselage and Tail Surfaces on Low-Speed Yawing Characteristics of a Swept-Wing Model as Determined in Curved-Flow Test Section of Langley Stability Tunnel. NACA TN 2483, 1951 (Supersedes NACA RM L8G13, 1948).

46. Lutze, F.H.  
Experimental Determination of Pure Rotary Stability Derivatives using a Curved and Rolling Flow Wind Tunnel. AIAA-80-0309, 1980.

47. Riley, D.R.  
Bird, J.D.  
Fisher, L.R.  
Experimental Determination of the Aerodynamic Derivatives Arising from Acceleration in Sideslip for a Triangular, a Swept and an Unswept Wing. NACA RM L55A07, 1955.

48. Lichtenstein, J.H.  
Williams, J.L.  
Effect of Frequency of Sideslipping Motion on the Lateral Stability Derivatives of a Typical Delta-Wing Airplane. NACA RM L57F07, 1957.

49. Coe, P.L., Jr.  
Graham, A.B.  
Chambers, J.R.  
Summary of Information on Low-Speed Lateral-Directional Derivatives Due to Rate of Change of Sideslip,  $\dot{\beta}$ . NASA TN D-7972, 1975.

50. Lucjanek, W.W.  
Adams, P.A.  
Development of Free-Flight Technique for NAE Helium Hypersonic Wind Tunnel. DME/NAE Quart. Bull. 1966(3).

51. Beyers, M.E.  
Analysis of High-Manoeuvrability Vehicles in Free Flight. Ph.D. Thesis, U. of the Witwatersrand, Johannesburg. December 1977.

52. Beyers, M.E.  
Investigation of High-Manoeuvrability Flight Vehicle Dynamics. 12th Congress of the International Council of the Aeronautical Sciences, ICAS Proceedings 1980, pp 278-292, 1980

53. Dayman, B., Jr.  
Free-Flight Testing in High-Speed Wind Tunnels. AGARDograph 113, 1966.

54. Grafton, S.B.  
Chambers, J.R.  
Coe, P.L. Jr.  
Wind-Tunnel Free-Flight Investigation of a Model of a Spin-Resistant Fighter Configuration. NASA TN D-7716, 1974.

55. Bharathan, D.  
Fisher, S.S.  
Stability Derivative Measurements with Magnetically Suspended Cone-Cylinder Models. J. of Spacecraft and Rockets, vol. 14, no. 12, pp 719-723, December 1977.

56. Covert, E.E.  
Finston, M.  
Vlajinac, M.  
Stephens, T.  
Magnetic Balance and Suspension System for Use with Wind Tunnels. Progress in Aerospace Sciences, vol. 14, pp. 27 - 107, Pergamon Press, 1974.

57. Orlik-Rückemann, K.J.  
Some Data on Elevator-Damping and Stiffness Derivatives on a Delta Wing Aircraft Model at Supersonic Speeds. NRC NAE Aero Report LR-250, 1959.

58. Wight, K.C.  
Lambourne, N.C.  
A Control-Surface Oscillatory Derivative Rig for Use with Half-Models in High-Speed Wind Tunnels. RAE TR 75026, 1975.

59. Schueler, C.J.  
Ward, L.K.  
Hodapp, A.E., Jr.  
Techniques for Measurement of Dynamic Stability Derivatives in Ground Test Facilities. AGARDograph 121, 1967.

60. Scherer, M.  
Determination dans les Installations au Sol des Paramètres Aérodynamiques de Stabilité d'Aéronefs, AGARDographie 242, 1979.

**DIRECT FORCED-OSCILLATION TECHNIQUES FOR THE DETERMINATION  
OF STABILITY DERIVATIVES IN WIND TUNNELS**

by

E.S. HANFF  
Unsteady Aerodynamics Laboratory,  
National Aeronautical Establishment,  
National Research Council of Canada,  
Ottawa, Ontario, Canada.

**ABSTRACT**

The current state-of-the-art in the field of stability parameters measurement in wind tunnels using the direct forced oscillation technique is discussed. The principles on which the technique is based, and some typical wind-tunnel apparatuses and instrumentation systems are briefly described. Furthermore a rather detailed description of the data reduction procedures used at NAE to obtain both direct as well as cross and cross-coupling derivatives is given. Finally an advanced dynamic calibrator with which the validity of the experimental and analytical procedures can be independently verified is described.

**1. INTRODUCTION**

The knowledge of certain hitherto neglected dynamic stability derivatives is becoming recognized by an increasing number of investigators as an important aspect for the design of high performance aircraft (Ref. 1), and as a consequence a number of experimental techniques to determine them have been developed over the last few years (Ref. 2).

This lecture addresses itself to one of these techniques, namely the so-called "wind-tunnel direct forced oscillation technique". In this technique an aircraft model is forced to oscillate at a constant amplitude in a single degree of freedom which implies that any aerodynamic reaction coherent with such a motion - henceforth denoted "primary motion" - can only be due to that motion; or in other words a direct causal relationship between the aerodynamic reactions and the primary motion is established. This straightforward relationship permits a rather simple determination of the desired derivatives which does not involve the solution of equations of motion. On the contrary, experiments in which the primary oscillation takes place in different DOF's yield the various derivatives that can then be used as "building blocks" to be placed in the appropriate equations of motion. Most of the work related to the direct forced oscillation technique has been carried out at NAE, a fact reflected in the contents of this lecture.

The currently available wind tunnel apparatuses are listed in Table I together with the various derivatives that can be measured with them. As mentioned before all experiments are based on the application of a small amplitude oscillatory motion to a model in the primary DOF and the measurement of the aerodynamic reactions that such a motion produces in that as well as other (secondary) degrees of freedom. These reactions in turn yield the pertinent direct as well as cross and cross-coupling derivatives due to the motion under consideration. \* See footnote next page.

TABLE I  
CURRENTLY AVAILABLE FULL MODEL STABILITY TESTING CAPABILITIES

APPARATUS	PRIMARY MOTION	STATIC DERIVATIVES	DYNAMIC DERIVATIVES
Pitch/Yaw	Pitching Oscillation	$C_{L\alpha}$ , $C_{m\alpha}$ , $C_{n\alpha}$ $C_{Y\alpha}$	$C_{Lq} + C_{L\dot{\alpha}}$ $C_{mq} + C_{m\dot{\alpha}}$ $C_{nq} + C_{n\dot{\alpha}}$ $C_{Yq} + C_{Y\dot{\alpha}}$
Pitch/Yaw	Yawing Oscillation	$C_{L\beta}$ , $C_{m\beta}$ , $C_{n\beta}$ $C_{N\beta}$	$C_{Lr} - C_{L\beta}\cos \alpha$ $C_{mr} - C_{m\beta}\cos \alpha$ $C_{nr} - C_{n\beta}\cos \alpha$ $C_{Nr} - C_{N\beta}\cos \alpha$
Roll	Rolling oscillation	$C_{L\beta}\sin \alpha$ $C_{m\beta}\sin \alpha$ $C_{n\beta}\sin \alpha$ $C_{Y\beta}\sin \alpha$ $C_{N\beta}\sin \alpha$	$C_{Lp} + C_{L\beta}\sin \alpha$ $C_{mp} + C_{m\beta}\sin \alpha$ $C_{np} + C_{n\beta}\sin \alpha$ $C_{Yp} + C_{Y\beta}\sin \alpha$ $C_{Np} + C_{N\beta}\sin \alpha$
$\dot{\alpha}/\dot{\beta}$	Plunging oscillation	$C_{L\alpha}$ , $C_{m\alpha}$ , $C_{n\alpha}$ , $C_{Na}$	$C_{L\dot{\alpha}} + C_{m\dot{\alpha}}$ , $C_{n\dot{\alpha}}, C_{N\dot{\alpha}}$
$\dot{\alpha}/\dot{\beta}$	Lateral oscillation	$C_{L\beta}$ , $C_{m\beta}$ , $C_{n\beta}$ , $C_{Y\beta}$	$C_{L\dot{\beta}}, C_{m\dot{\beta}}, C_{n\dot{\beta}}, C_{Y\dot{\beta}}$

## 2. DESCRIPTION OF APPARATUSES

### 2.1 General

In order to implement the principles enunciated in the previous section the various wind-tunnel apparatuses must incorporate the following elements.

(i) *Sting support.*

(ii) *Elastic suspension mechanism* characterized by its relatively high compliance in the primary DOF and its high stiffness in the others. The former is required to permit the primary motion of the model while the latter are necessary to withstand the aero-dynamic loading with negligible resulting deflections.

(iii) *Balance* to measure the secondary reactions caused by the primary motion. Such a balance should preferably be made of one piece to avoid the problems associated with the use of a multiple-piece balance in the presence of dynamic loads. The balance stiffness in all DOFs must be high to minimize the corresponding deflections.

(iv) *Driving mechanism* to impart the oscillatory primary motion to the model. Both electromechanical and hydraulic driving mechanisms are used depending on the scale of the apparatus and the loading requirements.

(v) *Suitable sensors* to detect the primary motion as well as driving torque or force.

(vi) *Servomechanism* to ensure a constant amplitude primary motion.

Fig. 1 shows a schematic diagram of a typical full-model apparatus. The model is mounted on the balance which is in turn attached to one end of the elastic suspension. The other end is anchored to the sting. The driving mechanism straddles the suspension in order to impart the primary motion to the model.

The main difference between the various apparatuses is in their suspension geometry, required to accommodate the various primary motions. Furthermore, it has been found at NAE that rather than using the same balance for all apparatuses, it is preferable - in view of their simplicity and relative ease of construction - to use balances "dedicated" to each of the apparatuses. This approach allows the balance to be optimized for each application including the possibility of "building it into" the apparatuses thereby reducing the required space and number of usually undesirable joints.

A brief description of most of the apparatuses currently in use are given in Ref. 2 which also includes a substantial bibliography that the reader interested in further details can refer to. For the sake of completeness and clarity two apparatuses are briefly described below.

### 2.2 Roll Apparatus (NAE)

Fig. 2 depicts an exploded view of the roll apparatus. The suspension system consists of two rings joined by 12 axially oriented beams equally spaced around the periphery of the rings. Such a configuration provides the necessary compliance in roll while having a substantial stiffness in the other degrees of freedom. A five component balance is mounted on the rear suspension ring and protrudes forward through the cavity surrounded by the suspension beams, while the forward suspension ring is firmly attached to the end of the sting. The two pairs of flexures that sense the deflection in pitch and yaw are symmetrically located on both sides of the balance center - which coincides with the longitudinal center of the suspension beams, where the model center of pressure is generally located - thus improving the measurement accuracy. The balance also incorporates a cruciform roll flexure whose stiffness is many times that of the suspension system and is therefore assumed to be infinitely high. Moreover as is shown in Section 3 the roll flexure output is not required in the dynamic rolling experiments as the direct derivatives are obtained on the basis of other information. As in the case of other NAE balances the balance is made of a single piece and only semi-conductor strain gauges are used in order to increase the sensitivities and therefore signal to noise ratios.

The oscillatory rolling motion is imparted by a DC-like "commutator-less" oscillatory motor, located at the rear end of the sting, via a torque tube whose forward end is attached to the rear suspension ring and the balance. The inertia of the rotor is minimized while retaining the necessary driving capabilities by using powerful rare-earth magnets mounted on the rotor to act as the field while the heavier armature is located in the stator. The use of rare-earth magnets also ensures the

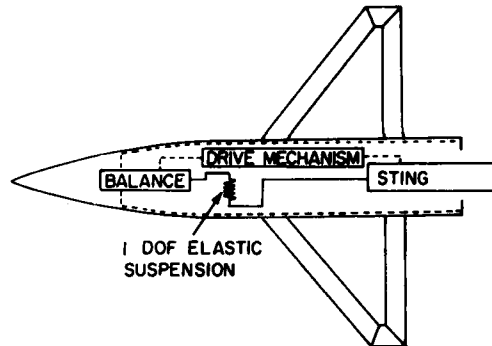
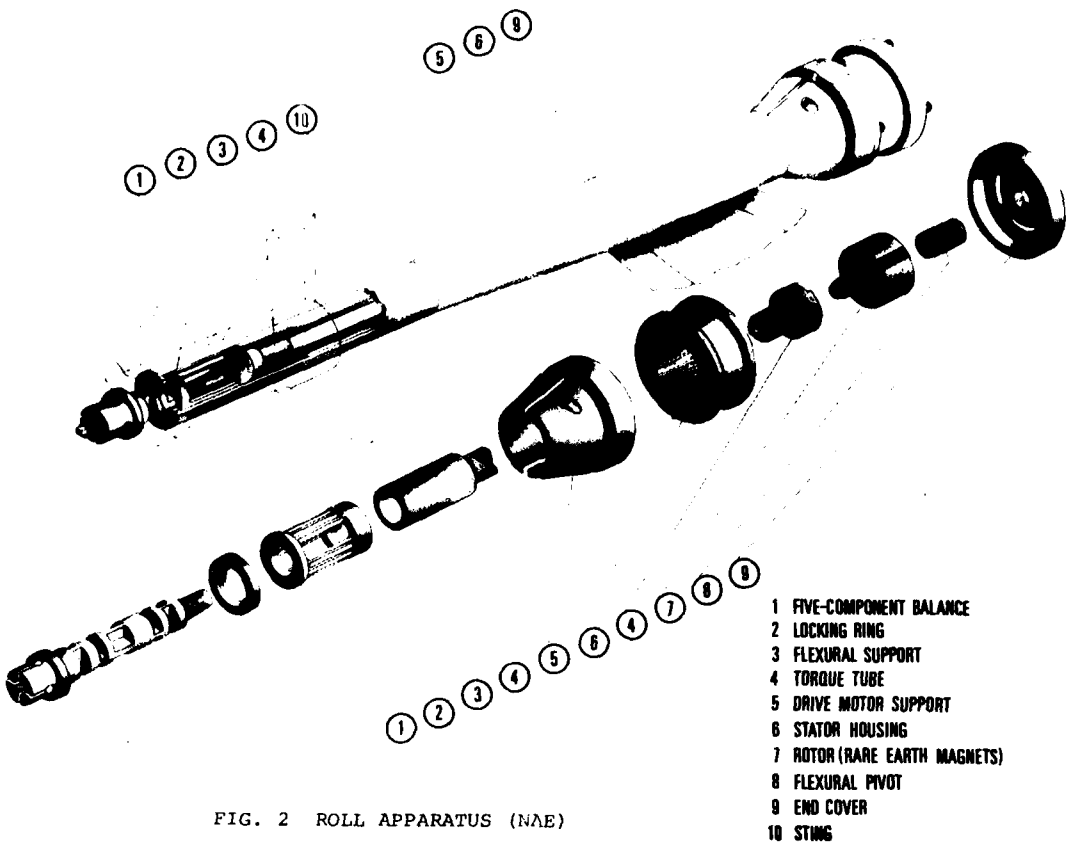


FIG. 1 FUNCTIONAL SCHEMATIC OF THE FULL MODEL APPARATUSES

\* The complete set of apparatuses is available at NAE.



necessary compactness of the drive mechanism. A gauged flexural pivot between the aft end of the rotor and the stationary sting is employed both to support the rotor in place and to measure the deflection in roll (primary motion). The driving torque is inferred from the oscillatory motor drive current. Additional details on the rolling apparatus may be found in Ref. 3.

### 2.3 Pitch/Yaw Apparatus (4000 lb) (AEDC)

In this case the suspension consists of a pair of cross flexures that provides the necessary compliance in pitch or yaw depending on the orientation of the model relative to the balance (Fig. 3). The primary motion is imparted by a hydraulic actuator in which the piston moves vertically exerting a driving force on a moment beam which links it to the moving end of the cross flexures. The beam is gauged and calibrated to measure the moment applied to the moving system. In order to obtain the desired primary oscillation the actuator is driven by a hydraulic servo-valve located at the sting base, which is in turn driven by a signal from the control system.

The cross flexure is instrumented to measure the primary angular deflection of the model and provides the restoring moment to balance the inertial moment when the system is oscillated at resonance. Provision is made to augment the suspension stiffness by adding suitable auxiliary leaf springs.

The secondary loads are measured by means of an external (can) 5-component balance that fits over the cross flexures. Fig. 4 depicts the assembled apparatus and the load capacity is given in Ref. 4.

### 3. DATA REDUCTION

#### 3.1 Direct derivatives. (Procedure I)

In this case the only information required is that associated with the primary motion. We are therefore dealing with a single DOF system excited by a suitable forcing function. As an example of the data reduction procedure let us consider a pitching experiment, in which case the equation of motion of the moving system comprising the model and the balance is

$$I_y \ddot{\theta} + c\dot{\theta} + K\theta = M(t) \quad * \quad (1)$$

\* Symbols are defined in the appendix.

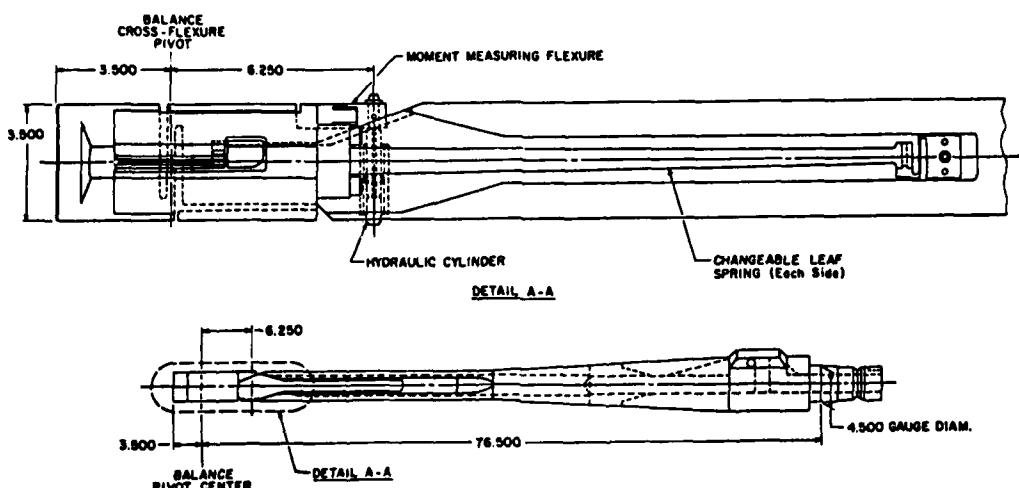


FIG. 3 SCHEMATIC OF AEDC PITCH/YAW SUSPENSION AND DRIVE MECHANISMS

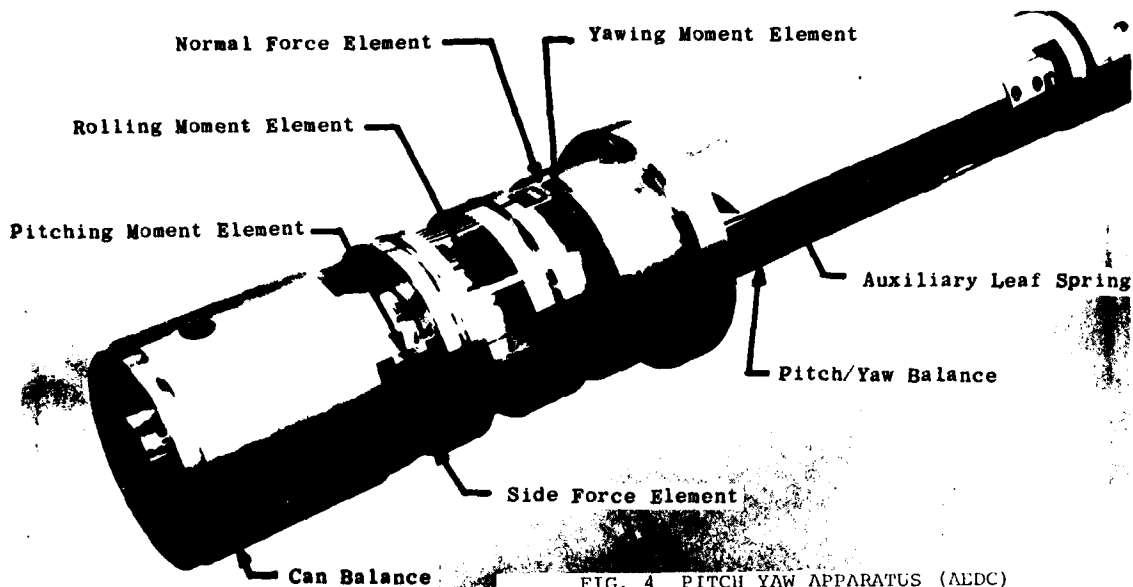


FIG. 4 PITCH YAW APPARATUS (AEDC)

Under steady state conditions

$$\theta = \bar{\theta} \sin \omega t$$

$$M(t) = \bar{M} \sin (\omega t + \mu) + n(t) *$$

The random component of the forcing moment ( $n(t)$ ) required to maintain a constant oscillation amplitude in the presence of flow unsteadiness is immaterial and can thus be disregarded. Therefore Eq. (1) becomes, in vectorial form

$$-I_{yy}\omega^2\bar{\theta}e^{i\omega t} + i\omega c\bar{\theta}e^{i\omega t} + K\bar{\theta}e^{i\omega t} = \bar{M}e^{i(\omega t+\mu)} \quad (2)$$

dividing through by  $e^{i\omega t}$  and recalling that under wind on conditions

$$c = \gamma - M_{\dot{\theta}}$$

$$K = k - M_{\dot{\theta}}$$

equation (2) becomes for tare and wind-on conditions, respectively, (referred to by subscripts T and W),

$$-I_{yy}\omega_T^2\bar{\theta}_T + i\omega_T\gamma\bar{\theta}_T + k\bar{\theta}_T = \bar{M}_T e^{i\mu_T} \quad (3)$$

\*  $\mu$  and all phase angles in the sequel are referred to the primary oscillation

$$-I_{yy}\omega_W^2\bar{\theta}_W + i\omega_W(\gamma - M_0)\bar{\theta}_W + (k - M_0)\bar{\theta}_W = \bar{M}_W e^{i\mu_W} \quad (4)$$

To obtain the aerodynamic stiffness  $M_0$  the real parts of (3) and (4) are taken

$$-I_{yy}\omega_T^2\bar{\theta}_T + k\bar{\theta}_T = \bar{M}_T \cos \mu_T \quad (5)$$

$$-I_{yy}\omega_W^2\bar{\theta}_W + (k - M_0)\bar{\theta}_W = M_W \cos \mu_W \quad (6)$$

Solving for  $k$  in (5) and substituting in (6)

$$M_0 = \frac{\bar{M}_T \cos \mu_T}{\bar{\theta}_T} - \frac{\bar{M}_W \cos \mu_W}{\bar{\theta}_W} + I_{yy} (\omega_T^2 - \omega_W^2) \quad (7)$$

Similarly to obtain the aerodynamic damping  $M_0$  the imaginary parts of (3) and (4) are used, namely,

$$\omega_T \gamma \bar{\theta}_T = \bar{M}_T \sin \mu_T \quad (8)$$

$$\omega_W(\gamma - M_0)\bar{\theta}_W = \bar{M}_W \sin \mu_W \quad (9)$$

Solving for  $\gamma$  in (8) and substituting in (9) yields

$$M_0 = \frac{\bar{M}_T \sin \mu_T}{\omega_T \bar{\theta}_T} - \frac{\bar{M}_W \sin \mu_W}{\omega_W \bar{\theta}_W} \quad (10)$$

Equations (7) and (10) therefore define the desired aerodynamic stiffness and damping in terms of the primary oscillation amplitude and frequency as well as the in-phase and quadrature components of the driving torque with respect to the primary motion. These quantities are readily measured during tare and wind-on conditions using suitable instrumentation systems as those described in Section 4.

If the model-balance system is driven at phase resonance ( $\mu = 90^\circ$ ) equations (7) and (10) can be duly simplified. Furthermore, if an inexorable drive is used the tare and wind-on oscillation frequencies can be made equal resulting in a simplification of Eq. (7).

In general it is advantageous to oscillate the model at resonance so that the inertial loads are resisted by the suspension rather than the drive mechanism, thereby increasing the accuracy of the measurements as well as decreasing the drive power requirements. The latter may be essential in cases where rather weak driving mechanisms are used.

Although the example shown above corresponds to a pitching oscillation case, the analysis is perfectly applicable to other single degree of freedom oscillation modes.

### 3.2 Cross and cross-coupling derivatives. (Procedure II)

Contrary to the case of the determination of direct derivatives, which can readily be obtained using the rather straight forward procedure outlined in the previous section, cross and cross-coupling derivatives must be obtained using a technique specifically developed to interpret the dynamic output signals originating from the balance. The difficulty in determining the loads that cause the measured balance deflections stems from the dynamic nature of the experiment, as in this case the dynamic behaviour of the balance-model subsystem may significantly affect the functional relationship between the balance deflections and their causative aerodynamic loads.

The data reduction procedure is based on the following assumptions:

i) The aerodynamic reactions are synchronous with the primary motion by virtue of the small primary oscillation amplitude which, in principle, ensures a linear system behaviour.\*

ii) Mechanical interactions between the primary motion and the secondary degrees of freedom are proportional to the primary oscillation amplitude only and can therefore be eliminated by means of tare measurements.\*\*

iii) Aerodynamic and mechanical interactions among the secondary degrees of freedom are negligible by virtue of the very small amplitude of the secondary motions. Effects of these on the primary output are neglected for the same reason.

\* Some "slightly" non-linear effects are discussed in Section 3.2.2.

\*\* The very small difference between tare and wind-on oscillation frequency generally permits neglecting the frequency effects on the mechanical interactions.

iv) The system can therefore be assumed to behave independently in each of the three planes (pitch, yaw and roll) in which the aerodynamic reactions are to be measured, its behaviour in each one of them being describable by suitable equations of motion.

The form of the equations of motion in each of these planes obviously depends on the number and type of degrees of freedom available to the system within the plane under consideration. Two different cases exist for the balances currently in use at NAE, namely:

i) One angular DOF is present in the roll plane of all full-model balances as well as in the yaw plane of the balance used in the plunge apparatus, since in both cases suitably oriented cruciform flexures are used to sense the pertinent moments.

ii) Two angular DOF's exist in the pitch and/or yaw planes as the corresponding loads are sensed by means of two beam-like flexures located at different stations in the balance.

The procedures required to obtain the aerodynamic loads in terms of the corresponding balance outputs (deflections) can now be determined. The reader is reminded that the following discussion applies to the *secondary* degrees of freedom and that the primary oscillation takes place in a *different* plane than the one under consideration.

### 3.2.1 One angular degree of freedom

In this case the equation of motion is

$$I\ddot{\delta} + c\dot{\delta} + k\delta = g(t) \quad (11)$$

Generally the moment  $g(t)$  consists of a static and an alternating component ( $G$  and  $\Delta G$  respectively) the latter being assumed to be synchronous with the primary motion, therefore

$$g(t) = G + \Delta G \sin(\omega t + \phi)$$

and consequently under the steady state conditions considered here

$$\delta = \delta_{ST} + \delta_0 \sin(\omega t + \beta)$$

where  $\delta_{ST}$  is the static component of deflection.

Since only the alternating component of  $g(t)$  is required, equation (11) can be rewritten in vectorial form

$$-\omega^2 I \bar{\delta} + i \omega c \bar{\delta} + k \bar{\delta} = \Delta G e^{i\phi} \quad (12)$$

where  $\bar{\delta} = \delta_0 e^{i\beta}$  and the  $e^{i\omega t}$  terms have cancelled out.

It should be noted that in this case the response of the system ( $\bar{\delta}$ ) is known and that the forcing function  $\Delta G e^{i\phi}$  is the unknown. It is therefore not necessary to solve the equation of motion in the traditional sense, but rather the forcing function - more specifically its aerodynamic component caused by the coupling between the primary motion and the degree of freedom under consideration - must be determined in terms of the measured deflections. To this end equation (12) must be rewritten for both tare and wind-on conditions. In the tare measurements the forcing function is only due to the inertial coupling between the primary motion and the degree of freedom under study, whereas in the wind-on measurements the forcing function includes the *unknown aerodynamic interactions* between the primary motion and the degree of freedom being considered, in addition to the mechanical coupling mentioned above. Furthermore, only mechanical stiffness and damping are present in the tare case while in the wind-on case there are additional *aerodynamic* components of these quantities. These components may be obtained from dynamic wind tunnel tests in which the model is oscillated in the relevant degree of freedom. Such tests are denoted "complementary" tests as the data they generate - specifically direct derivatives - complement the information obtained by other tests in order to determine the necessary cross and cross-coupling derivatives.

Letting  $A_T$  and  $A_W$  be the tare and wind-on primary oscillation amplitude, Equation (12) becomes

#### i) Tare conditions

$$-\omega^2 I \bar{\delta}_T + i \omega c_T \bar{\delta}_T + k_T \bar{\delta}_T = \Delta G_T e^{i\phi} \quad (13)$$

#### ii) Wind-on conditions

$$-\omega^2 I \bar{\delta}_W + i \omega c_W \bar{\delta}_W + k_W \bar{\delta}_W = \frac{A_W}{A_T} \Delta G_T e^{i\phi} + \Delta G_A e^{i\lambda} \quad (14)$$

We have that the desired aerodynamically induced moment is

$$\Delta G_A e^{i\lambda} = L.H.S. (14) - \frac{A_W}{A_T} L.H.S. (13) = a + ib$$

from which the amplitude and phase of the moment are respectively

$$\Delta G_A = \sqrt{a^2 + b^2}$$

$$\lambda = \arctan(\frac{b}{a})$$

### 3.2.2 Two angular degrees of freedom

A schematic diagram of the model-balance system as it concerns its behaviour in one plane (generally pitch or yaw) is shown in Fig. 5. The balance is rigidly anchored at one end and the model is attached to it at the other. The balance flexures - which are assumed to be the only parts of the system that can bend - are represented by circles with associated angular stiffnesses and damping constants, while the various masses are shown suitably lumped. In all cases the loading within the plane under consideration is assumed to consist of a force acting at the forward flexure as well as of a moment, which together produce an instantaneous balance deflection as shown.

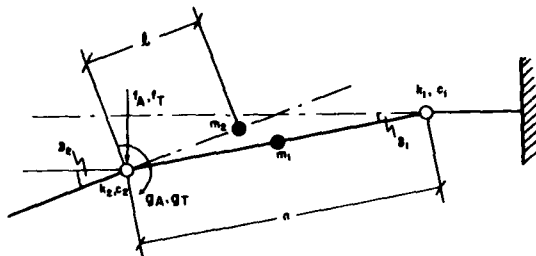


FIG. 5 SCHEMATIC OF BALANCE-MODEL SUBSYSTEM

where  $k_i, c_i$  = stiffness and damping constant of balance flexures

$m_1$  = mass of part of balance between flexures, lumped at its center of mass and assumed to be half way between the flexures

$m_2$  = total mass supported ahead of forward flexure (including the model) lumped at the pertinent center of mass

$\delta_i$  = angular deflections relative to the undeflected axial line

$f_T, g_T$  = inertial force and moment due to primary oscillation

$f_A, g_A$  = aerodynamic force and moment due to primary oscillation

$n$  = flexure spacing

$l$  = distance between forward flexure and center of mass of  $m_2$

The method used to determine the aerodynamic loads ( $f_A$  and  $g_A$ ) produced by the primary motion in terms of the measured balance deflections is analogous to that described in Section 3.2.1. The equations of motion are of course different, namely,

$$\ddot{\delta}_1 [m_2 n^2 + \frac{1}{4} m_1 n^2 + I_1] + \dot{\delta}_1 [c_1 + c_2] + \delta_1 [k_1 + k_2] - \ddot{\delta}_2 m_2 n l - \dot{\delta}_2 c_2 - \delta_2 k_2 = n[f_T + f_A] \quad (15)$$

$$-\ddot{\delta}_1 m_2 n l - \dot{\delta}_1 c_2 - \delta_1 k_2 + \ddot{\delta}_2 [m_2 l^2 + I_2] + \dot{\delta}_2 c_2 + \delta_2 k_2 = -(g_T + g_A) \quad (16)$$

Where  $I_1$  &  $I_2$  are the moments of inertia of  $m_1$  &  $m_2$  about their center of gravity.

As in the case of one degree of freedom discussed before, under tare conditions the stiffnesses and dampings are solely mechanical while the forcing functions are of inertial origin only, namely

$$f_T = \Delta F_T \sin(\omega t + \eta)$$

$$g_T = \Delta G_T \sin(\omega t + \chi)$$

Likewise under wind-on conditions the stiffnesses and damping constants have aerodynamic components (again obtainable from suitable complementary tests) in addition to the

mechanical ones. Furthermore, the forcing functions also incorporate aerodynamic reactions caused by the primary motion in addition to the aforementioned inertial terms.

In general we have that the aerodynamic force is

$$f_A = F_A + \Delta F_A \sin(\omega t + \xi)$$

and just as its magnitude varies as a function of the instantaneous primary deflection, its location can also be assumed to vary due to the changes in the flow field. The distance  $d$  between the force and the forward balance flexure can then be written as

$$d = D + \Delta D \sin(\omega t + \zeta)$$

Therefore by transferring  $f_A$  to the forward flexure we obtain

$$\begin{aligned} g_A &= f_A d = [F_A + \Delta F_A \sin(\omega t + \xi)][D + \Delta D \sin(\omega t + \zeta)] \\ &= G_{A_0} + \Delta G_{A_1} \sin(\omega t + \psi_1) + \Delta G_{A_2} \sin(2\omega t + \psi_2) \end{aligned}$$

where

$$G_{A_0} = F_A D + \frac{1}{2} \Delta F_A \Delta D \cos(\xi - \zeta)$$

$$\Delta G_{A_1} \sin(\omega t + \psi_1) = F_A \Delta D \sin(\omega t + \zeta) + D \Delta F_A \sin(\omega t + \xi)$$

$$\Delta G_{A_2} \sin(2\omega t + \psi_2) = -\frac{\Delta F_A \Delta D}{2} \cos(2\omega t + \xi + \zeta)$$

It is interesting to note that the above equations indicate that

- i) There is a static component of the moment as well as two alternating components, one of the same frequency as the primary oscillation and another of double that frequency.
- ii) The static component of the moment may be affected by the primary oscillation.

These effects, that may be present even under conditions of "small" primary oscillation amplitudes, can be considered as "slightly" non-linear since they are the result of the force and its location, each being linearly related to the primary motion. More severe non-linearities can of course prevail in the presence of larger primary oscillation amplitudes in which case the aerodynamic reactions cannot be expected to be so well behaved. The importance of the effects considered here clearly depends on the magnitude of  $\Delta D$ .

Rather limited preliminary wind-tunnel tests indicate that there may indeed be a double frequency moment component although its importance has not been assessed. No evidence of the influence of the primary oscillation on the value of the static component of the moment has been found yet. More extensive investigations are being planned to better establish the significance of these phenomena.

It is now possible to rewrite equations (15) and (16) for tare and wind-on conditions. Since the equations are valid at all times they must also be independently satisfied for the static and the two alternating components of the pertinent forcing functions and responses.

Let the deflections be

$$\delta_i = \delta_{i_0} + \delta_{i_1} \sin(\omega t + \phi_{i_1}) + \delta_{i_2} \sin(2\omega t + \phi_{i_2})$$

Therefore

$$\dot{\delta}_i = \omega \delta_{i_1} \cos(\omega t + \phi_{i_1}) + 2\omega \delta_{i_2} \cos(2\omega t + \phi_{i_2})$$

and

$$\ddot{\delta}_i = -\omega^2 \delta_{i_1} \sin(\omega t + \phi_{i_1}) - 4\omega^2 \delta_{i_2} \sin(2\omega t + \phi_{i_2})$$

where  $i=1, 2$  represent the aft and forward balance flexures respectively and the second subscript indicates the multiple of the primary oscillation frequency (0, 1, 2) of the component under consideration.

The tare and wind-on equations of motion for the static components are therefore

$$\delta_{10T}(k_{1T} + k_{2T}) - \delta_{20T}k_{2T} = 0 \quad (17)$$

$$-\delta_{10T}k_{2T} + \delta_{20T}k_{2T} = 0 \quad (18)$$

$$\delta_{10W}(k_{1W} + k_{2W}) - \delta_{20W}k_{2W} = nF_A \quad (19)$$

$$-\delta_{10W}k_{2W} + \delta_{20W}k_{2W} = -G_{A0} \quad (20)$$

From (17) and (18) it is obvious that  $\delta_{10T} = \delta_{20T} = 0$  indicating that any output signals are due to electrical DC offsets which must be eliminated. Therefore the static components of the forcing functions are:

$$F_A = \frac{(\delta_{10W} - \delta_{10T})(k_{1W} + k_{2W}) - (\delta_{20W} - \delta_{20T})k_{2W}}{n}$$

$$G_{A0} = [(\delta_{10W} - \delta_{10T}) - (\delta_{20W} - \delta_{20T})]k_{2W}$$

The tare and wind-on equations of motion for the single frequency components are in vectorial form

$$\bar{\delta}_{11T}[-\omega^2(m_2n^2 + \frac{1}{4}m_1n^2 + I_1) + k_{1T} + k_{2T} + i\omega(c_{1T} + c_{2T})] + \bar{\delta}_{21T}[\omega^2m_2n\ell - k_{2T} - i\omega c_{2T}] = n\Delta F_T e^{in} \quad (21)$$

$$\bar{\delta}_{11T}[\omega^2m_2n\ell - k_{2T} - i\omega c_{2T}] + \bar{\delta}_{21T}[-\omega^2(m_2\ell^2 + I_2) + k_{2T} + i\omega c_{2T}] = -\Delta G_T e^{ix} \quad (22)$$

$$\bar{\delta}_{11W}[-\omega^2(m_2n^2 + \frac{1}{4}m_1n^2 + I_1) + k_{1W} + k_{2W} + i\omega(c_{1W} + c_{2W})] + \bar{\delta}_{21W}[\omega^2m_2n\ell - k_{2W} - i\omega c_{2W}] = n[\frac{A_W}{A_T} \Delta F_T e^{in} + \Delta F_A e^{i\xi}] \quad (23)$$

$$\bar{\delta}_{11W}[\omega^2m_2n\ell - k_{2W} - i\omega c_{2W}] + \bar{\delta}_{21W}[-\omega^2(m_2\ell^2 + I_2) + k_{2W} + i\omega c_{2W}] = -\frac{A_W}{A_T} \Delta G_T e^{ix} - \Delta G_{A1} e^{i\psi_1} \quad (24)$$

Therefore

$$LHS(23) - \frac{A_W}{A_T} LHS(21) = a + ib = n\Delta F_A e^{i\xi}$$

$$\frac{A_W}{A_T} LHS(22) - LHS(24) = c + id = \Delta G_{A1} e^{i\psi_1}$$

from which  $\Delta F_A$ ,  $\xi$ ,  $\Delta G_{A1}$  and  $\psi_1$  can be readily obtained.

Finally for the case of the double frequency components it is clear that such components do not exist under tare conditions. Therefore

$$\bar{\delta}_{12T} = \bar{\delta}_{22T} = 0$$

Likewise under wind-on conditions the forcing function of (15) is zero and only (16) is required to obtain  $G_{A2}$  and  $\psi_2$ , namely,

$$\bar{\delta}_{12W}[4\omega^2m_2n\ell - k_{2W} - 2i\omega c_{2W}] + \bar{\delta}_{22W}[-4\omega^2(m_2\ell^2 + I_2) + k_{2W} + 2i\omega c_{2W}] = \Delta G_{A2} e^{i\psi_2}$$

thereby solving for the last of the unknown aerodynamic forcing functions.

As an illustration of the analysis of the 2 DOF case let us consider the equations for the single frequency components in the pitch plane for the case of an oscillatory rolling experiment. In this case we have that the flexures mechanical stiffnesses and damping constants are  $k_{\theta i}$  and  $\gamma_{\theta i}$  ( $i=1,2$ ) respectively, while their aerodynamic counterparts are  $M_{\theta i}$  and  $M_{\theta i}^*$ . The latter are obtained, as already indicated, from complementary tests where the direct pitching derivatives are determined. Therefore we have that in equations (21) to (24)

$$k_{iT} = k_{\theta i}$$

$$c_{iT} = \gamma_{\theta i}$$

$$k_{iW} = k_{\theta i} - M_{\theta i}$$

$$c_{iW} = \gamma_{\theta i} - M_{\dot{\theta} i}$$

Furthermore, the aerodynamic forcing functions are of course represented by the cross-coupling derivatives in the pitch plane due to the primary rolling motion. Assuming that the C.G. of the aircraft is at a distance  $\ell_1$  behind the forward balance flexure we have that

$$\Delta F_A e^{i\xi} = -\phi [N_B \sin\alpha + i\omega (N_p + N_B \sin\alpha)]$$

and therefore

$$\Delta G_A e^{i\psi_1} = \phi [M_B \sin \alpha - \ell_1 N_B \sin \alpha + i w \{ M_p + M_B \sin \alpha - \ell_1 (N_p + N_B \sin \alpha) \}]$$

where  $\phi$  is the amplitude of rolling oscillation and  $N_\beta$ ,  $M_p$ , etc. are dimensional derivatives of the normal force and pitching moment with respect to  $\beta$ ,  $p$ , etc.

From these equations the force and moment cross-coupling derivatives can be readily obtained.

An analogous approach is employed in the analysis of the 1 DOF case where equations (13) and (14) rather than (21) to (24) are used.

Fig. 6 shows how the complete set of moment derivatives can be obtained. Pitching, yawing and rolling oscillatory experiments are required. From each of these experiments the pertinent direct derivatives can be immediately obtained using "Procedure I" described in Section 3.1. Furthermore, each experiment generates information associated with its secondary degrees of freedom that must be combined with the pertinent aforementioned direct derivatives according to "Procedure II" described in Section 3.2 in order to obtain the desired cross and cross-coupling derivatives (Ref. 5). Needless to say the three "complementary" tests must be performed with the same model attitude and wind-tunnel conditions. In some cases some of the complementary runs may not be necessary as the effect of the pertinent aerodynamic stiffnesses and dampings in the equations of motion may be negligible. A careful assessment of whether this is indeed the case must be made before embarking in a reduced test program.

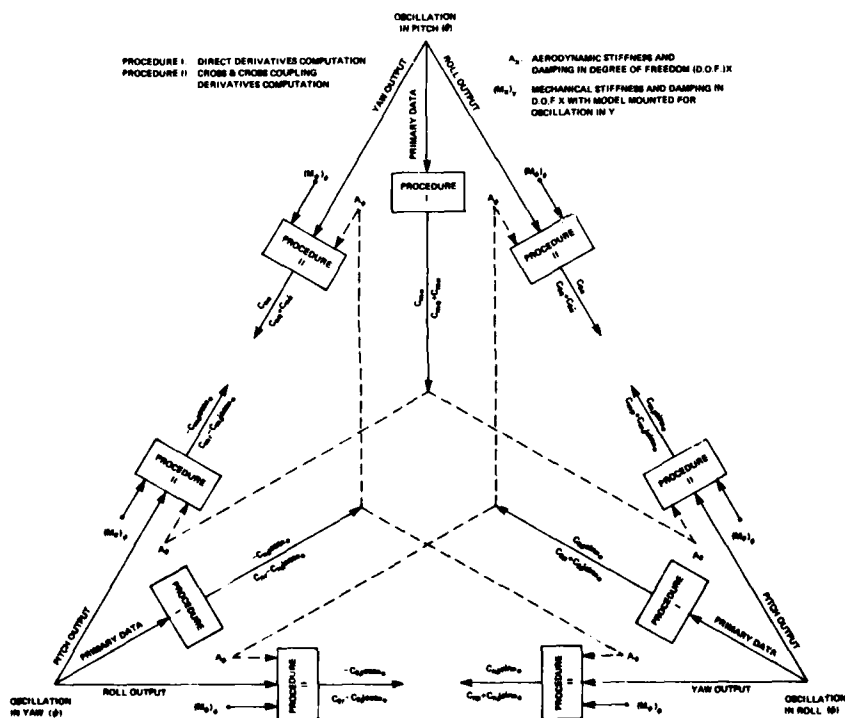


FIG. 6 INTERRELATION TRIANGLE FOR DIRECT OR CROSS AND CROSS-COUPLING DERIVATIVES

#### 4. INSTRUMENTATION

The procedures required to determine the various aerodynamic derivatives have been outlined in Section 3 where it was shown that *only* the secondary signals components *coherent* with the primary motion are of interest. Unfortunately however, in most cases such components are seriously contaminated by noise generated mainly by the flow unsteadiness. As the noise can be several times larger than the desired signals it is generally impossible to adequately extract them using conventional narrow band pass filters. Instead, the *a priori* knowledge that the signals are coherent with the primary motion permits the use of more sophisticated signal extraction techniques.

Two somewhat analogous approaches are in use namely,

- cross-correlation technique (NAE)
- coherent detection (AEDC), NASA Langley, etc.

both of which are especially suited to applications where a clean reference signal coherent with the one that needs to be extracted from the noise is available. In the applications under consideration the reference signal is provided by the primary motion which is generally a clean sinusoid by virtue of the primary drive mechanism characteristics, and of the fact that usually the primary oscillation is performed at the mechanical resonance frequency of the system, in which case full use is made of the high Q of such a system for the rejection of unwanted responses.

##### 4.1 Cross correlation technique

The cross correlation between two functions  $x(t)$  and  $y(t)$  is given by

$$R_{xy}(\tau) = \frac{1}{T} \int_0^T x(t)y(t+\tau) dt \quad (25)$$

In the cases under consideration the functions are

- i) Primary motion  $x(t) = P_0 \sin \omega t$
- ii) Secondary signal e.g.  $y(t) = S_0 \sin(\omega t + \eta) + n(t)$

and it is desired to separate the necessary coherent component of the secondary signal from the contaminating noise  $n(t)$  by identifying its amplitude ( $S_0$ ) and phase ( $\eta$ ) with respect to the known primary motion. This can be accomplished by substituting the above functions in equation (25) which - if the noise is assumed to be uncorrelated to the primary motion - becomes

$$R_{xy}(\tau) = \frac{P_0 S_0}{2} \cos(\omega \tau + \eta) \quad (26)$$

which is simply a sinusoid in terms of the time shift  $\tau$ .

Since in practice  $R_{xy}$  is known for a number of values of  $\tau$  it is clear that  $S_0$  and  $\eta$  can be readily obtained.

##### 4.2 NAE Instrumentation System

The cross correlation technique has been implemented at NAE by means of a mini-computer based digital system shown in Fig. 7.

The various analog signals originating from the balance and other transducers are amplified and filtered prior to being digitized by a sixteen channel A/D converter. To maximize the sampling rate the digital data is then fed to the computer by means of direct memory access. As is shown in the next section the timing of the sampling is critical and is thus controlled by a pacing circuit which is in turn programmed via the IEEE-488 bus. The primary oscillation frequency, which has to be accurately known, is measured with a counter whose output is fed to the computer through the same bus. A view of the complete system is shown in Fig. 8.

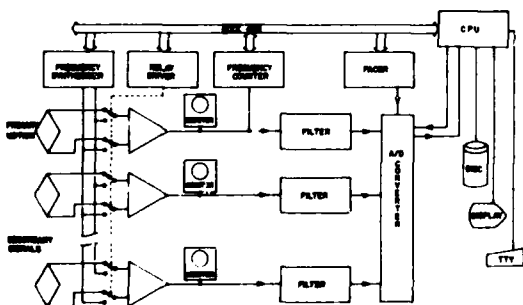


FIG. 7 INSTRUMENTATION SYSTEM (NAE)

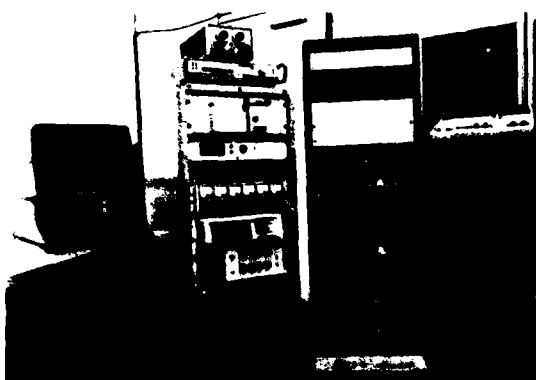


FIG. 8 VIEW OF INSTRUMENTATION SYSTEM (NAE)

As both the amplitude and phase information of the secondary signals are important in the data reduction procedure, it is imperative to know, at the frequencies of interest, the transfer functions of each channel in vectorial form. This is accomplished by feeding a sequence of sinusoids of known amplitude and phase to the front end of the system. This sequence of signals, at several frequencies around the operational one, are generated by a computer controlled synthesizer. The transfer functions at the calibrating frequencies are then determined by computing the cross-correlation between the "primary" and "secondary" calibration signals. Finally, analytical expressions for the frequency variation of the transfer functions are expressed by means of suitable polynomials fitted to the real and imaginary values of the transfer functions at the various calibration frequencies.

#### 4.2.1 Data Handling

During each run (~10 sec duration) of the NAE 30" intermittent wind tunnel, up to 50,000 samples may be taken. This number of data points is incompatible with the user available MOS memory of about 32 KB, particularly when the memory requirement of the various programs is taken into account. It is therefore necessary to rely heavily on disc storage which results in a somewhat cumbersome data handling procedure. Such a procedure is summarized in the flow chart shown in Fig. 9. During the tunnel run a "record" covering approximately 30 cycles of the primary oscillation, is stored in a buffer by sampling the various channels at a rate satisfying Nyquist's criterion. Once completed, the record comprising  $N$  samples per channel is dumped on to disc and the procedure repeated so that at the end of the run  $K$  such records have been stored.  $K$  depends on the record length, the sample rate and the disc transfer rate as well as on the duration of the wind tunnel run.

After the completion of the run the records are retrieved one at a time from the disc and - to avoid the presence of constant terms in the correlation functions - the mean values of the signals corresponding to each channel are subtracted from their respective data points. The cross correlation functions between the primary motion and the secondary signals for the record under consideration are then computed using the discrete expression for the unbiased cross correlation function (Ref. 6)

$$R_{xy}(rh) = \frac{1}{N-r} \sum_{n=1}^{N-r} x_n y_{n+r} \quad \text{for } r=0, 1, 2 \dots r_{\max}$$

where the sampling interval ( $h$ ), sample size ( $N$ ) and maximum lag number  $r_{\max}$  are chosen in terms of the frequency and signal-to-noise ratio of the secondary signals, desired accuracy, system bandwidth, etc. (Ref. 6).

The same process is repeated for subsequent records. A running average for the various cross correlation functions is continually maintained and as more records are correlated the average tends to approach the true cross correlation function

Since the correlation functions are known *a priori* to be sinusoidal and of the same frequency as that of the primary motion (when expressed as a function of  $\tau$  (equation 26)), suitable sinusoids can be fitted to the running average each time a preselected number of additional records has been processed. By observing the behaviour of these sinusoids an operator can decide when a sufficient number of records has been obtained.

The current assessment of the situation is that since this number depends on a variety of factors such as the signal to noise ratio of the secondary signals, spectrum of the contaminating noise, record length, etc., it is probably more efficient to rely on an observer than to attempt to set out a rigid set of rules that the computer could use to establish when sufficient records have been processed.

Once acceptable correlation functions are obtained they are corrected to compensate for the effects of transfer functions of their respective channels as well as for the skewing in the sampling process, thus yielding the final expressions from which the components of the secondary signals that are synchronous with the primary motion can be inferred. These quantities are then used to determine the required aerodynamic parameters using techniques such as the one described in Section 3.

#### 4.2.2 System Evaluation

A thorough evaluation of the system performance was carried out by feeding the apparatus signals that reasonably simulate those encountered in wind tunnel experiments. A sinusoid was used as the primary signal while a secondary signal was made up of the same sinusoid plus various amounts of noise. Two types of noise were used, namely white noise within the pass band of the anti-aliasing filters and a coloured noise obtained by passing the white one through a band pass filter. The white noise corresponds to cases where the resonance frequency of the mechanical system in the degree of freedom under consideration is sufficiently above the cut-off frequency of the anti-aliasing filters. The latter type of noise, on the other hand, is intended to simulate the dynamic behaviour in the pertinent degree of freedom, of the mechanical system used in the wind tunnel - assumed to be of the second order - whose resonance frequency is in this case assumed to be below the cut-off frequency of the anti-aliasing filters.

Typical examples of the results obtained during the system evaluation stage are shown below. They were obtained by using records with  $N = 140$  samples/channel and a lag number  $r_{\max} = 20$ . The sampling interval ( $h$ ) was 4 ms corresponding to a frequency that safely satisfied Nyquist's criterion.

Figures 10 and 11 show the running averages of the correlation functions in the presence of white noise as a function of  $(rh)$ . The various plots correspond to the running averages after regular numbers of records. Solid-sinusoids are fitted to the experimental points while the true correlation functions - obtained by cross correlating the same signal in the absence of noise - are shown by the dotted line.

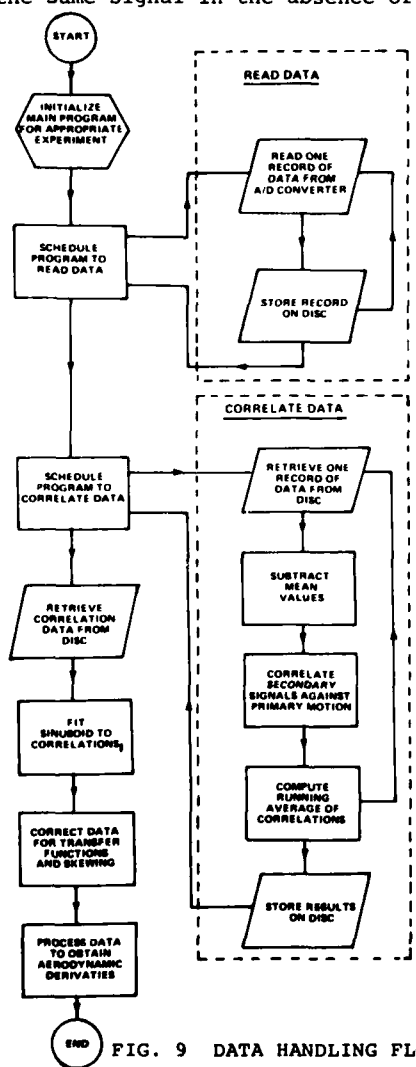


FIG. 9 DATA HANDLING FLOW CHART

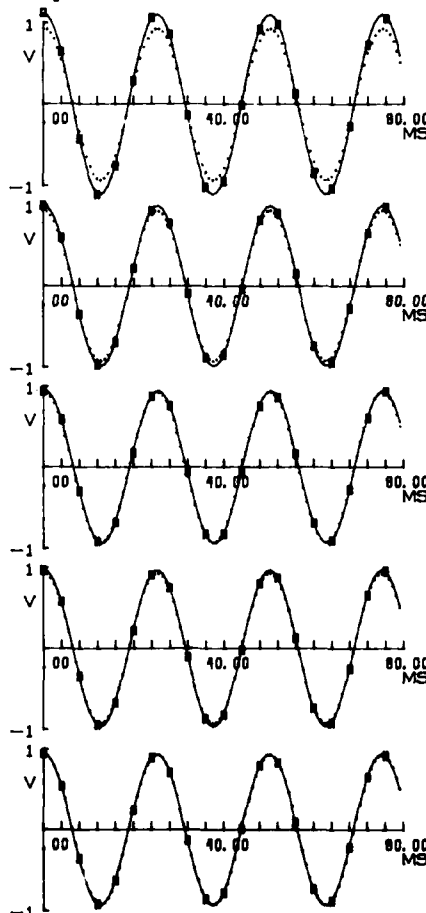


FIG. 10 COMPARISON OF TRUE AND COMPUTED  
CORRELATION FUNCTIONS  
S/N 0 db

RUNNING AVERAGE SHOWN FOR 2 RECORDS PER PLOT. TRUE CORRELATION FUNCTION SHOWN AS DOTTED LINE.

In Fig. 10 the S/N is 0 dB\* corresponding to a rather clean wind tunnel secondary output. The running average is computed every second record indicating that very few records are required in order to adequately approach the true correlation function. In Fig.11 however, the S/N is -20 dB, a figure worse than most of those encountered in the wind tunnel experiments. The running average in this case is shown at increments of 20 records indicating that many more records are necessary to reach an accuracy in the correlation function comparable to that of the previous case. Fig.12 shows the variation in the amplitude and phase of the running averages of the correlation functions in terms of the number of records averaged. The top pair was obtained with a 30 Hz signal in the presence of coloured noise peaked at 50 Hz (corner frequency of the anti-aliasing filter used was 55 Hz), which represents a rather unfavorable situation as in the wind tunnel apparatuses the secondary resonance frequencies are at least double the value of the primary frequency. The bottom pair corresponds to the same signal in the presence of white noise. In both cases the S/N is -20 dB and the amplitude and phase of the true correlation functions are 1 and 0° respectively. It should be noted that rather unnecessarily high accuracies are implied in these figures as under most experimental conditions the amplitudes of the correlation functions need to be known within 10-15% and the phases within 5°.

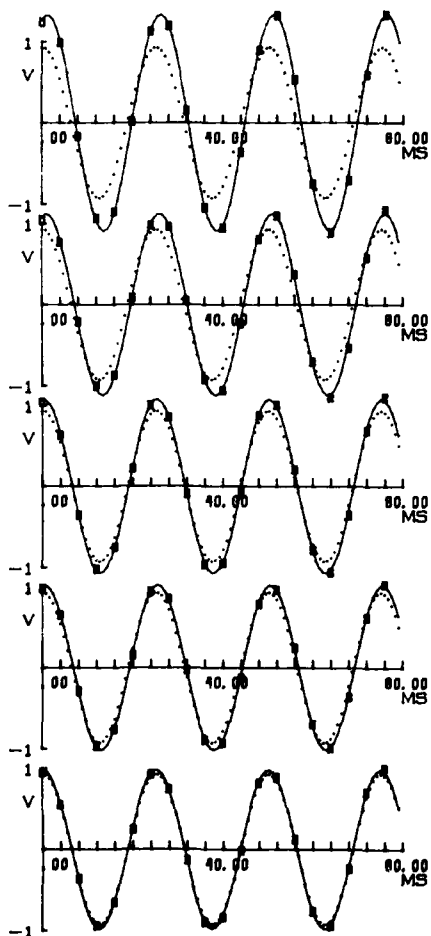


FIG. 11 COMPARISON OF TRUE AND COMPUTED CORRELATION FUNCTIONS  
S/N -20 db  
RUNNING AVERAGE SHOWN FOR 20 RECORDS PER PLOT. TRUE CORRELATION FUNCTION SHOWN AS DOTTED LINE.

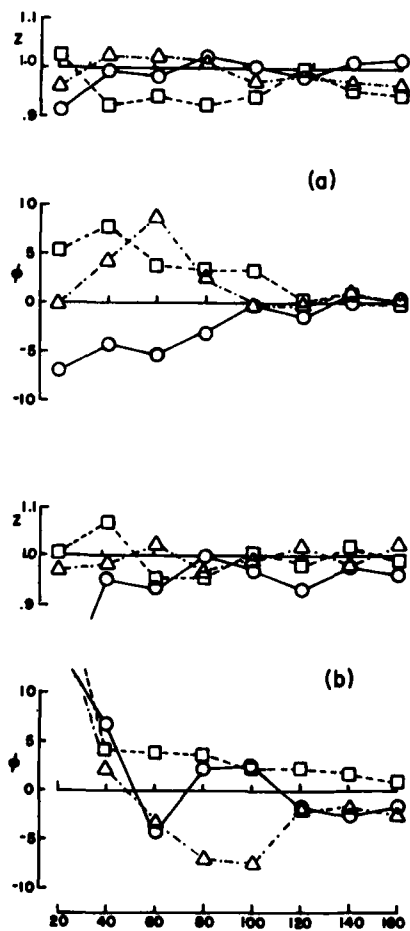


FIG. 12 CONVERGENCE OF CORRELATION FUNCTIONS TO TRUE VALUE  
SIGNAL 30 Hz S/N -20 db  
(a) COLOURED NOISE PEAKED AT 50 Hz  
(b) WHITE NOISE TRUE VALUES  
 $Z = 1.0$   
 $\phi = 0$  deg

\* all S/N are measured after the anti-aliasing filters

The data acquisition and processing system described above is in the process of upgrading at the time of this writing. The current four minute processing time required for the reduction of the data for a given model attitude is expected to be reduced by a factor of 50 with the use of a new, faster CPU that incorporates advanced firmware to substantially accelerate matrix operations. Furthermore a new operating system will be used that permits the handling of sufficient MOS memory to obviate the need for the frequent disc swapping of programs and data. Therefore a very simplified but basically similar data reduction procedure with significant time gains will be possible, an important feature when carrying out quasi on-line operation in conjunction with energy-hungry continuous wind-tunnels.

#### 4.3 Coherent Detection Method

In this method two versions of the reference signal-one shifted by  $90^\circ$  with respect to the original one - are multiplied by the noise contaminated signal as shown by the block diagram in Fig. 13.

As in the case discussed in Section 4.1 let

$$x(t) = P_0 \sin \omega t$$

$$y(t) = S_0 \sin(\omega t + \eta) + n(t)$$

The "in phase" and "quadrature" products  $\text{Prod}_0$  and  $\text{Prod}_{90}$  are

$$\text{Prod}_0 = P_0 \sin \omega t [S_0 \sin(\omega t + \eta) + n(t)]$$

$$\text{Prod}_{90} = P_0 \cos \omega t [S_0 \sin(\omega t + \eta) + n(t)]$$

The noise is generally wide band and can for the purpose of this argument be expressed in terms of a summation of discrete components

$$n(t) = \sum_{i=0}^{\infty} A_i \sin \omega_i t + \sum_{i=0}^{\infty} B_i \cos \omega_i t$$

Therefore we obtain

$$\begin{aligned} \text{Prod}_0 &= \frac{P_0 S_0}{2} [(1 - \cos 2\omega t) \cos \eta + \cos \omega t \sin \eta] + \sum_{i=0}^{\infty} \frac{P_0 A_i}{2} [\cos(\omega - \omega_i)t - \cos(\omega + \omega_i)t] + \\ &\quad \sum_{i=0}^{\infty} \frac{P_0 B_i}{2} [\sin(\omega + \omega_i)t + \sin(\omega - \omega_i)t] \end{aligned}$$

This signal is then filtered by a very low cut-off frequency low pass filter that eliminates all components above any desired frequency value. It can be seen that the noise can only affect the output through its components at  $\omega_i \approx \omega$ . In general however such components are negligible and their effect can be in any case minimized by lowering the filter cut-off frequency.

Therefore the filtered signal becomes

$$\text{Prod}'_0 = \frac{P_0 S_0}{2} \cos \eta \quad (27)$$

and similarly the "quadrature" product becomes after filtering

$$\text{Prod}'_{90} = \frac{P_0 S_0}{2} \sin \eta \quad (28)$$

Equations (27) and (28) yield the in phase and quadrature components of the secondary signal with respect to the known primary motion. It should be noted that they correspond to the correlation values for  $\tau = 0$  and  $\pi/2\omega$  respectively (equation (26)).

This approach has been used in a variety of facilities such as NASA Langley (Ref. 7), NAE (Ref. 8), etc. An equivalent approach using a digital Fourier harmonic analysis is used in West Germany (Ref. 9).

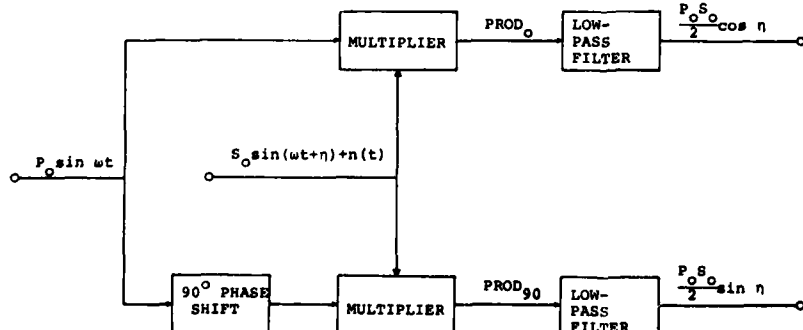


FIG. 13 BLOCK DIAGRAM OF COHERENT DETECTION

#### 4.4 AEDC Instrumentation System

A system based on the "coherent detection" approach is in use at AEDC and is shown in Fig. 14 (Ref. 4).

Each load measuring element in the balance is instrumented with three sets of strain gauges. One is fed with a D-C excitation voltage for static measurements while the other two are excited by alternating signals 90° apart generated by a two phase oscillator that also imparts the primary motion to the model via a suitable hydraulic system, thus ensuring that the strain gauge excitation signals are synchronous with the primary motion.

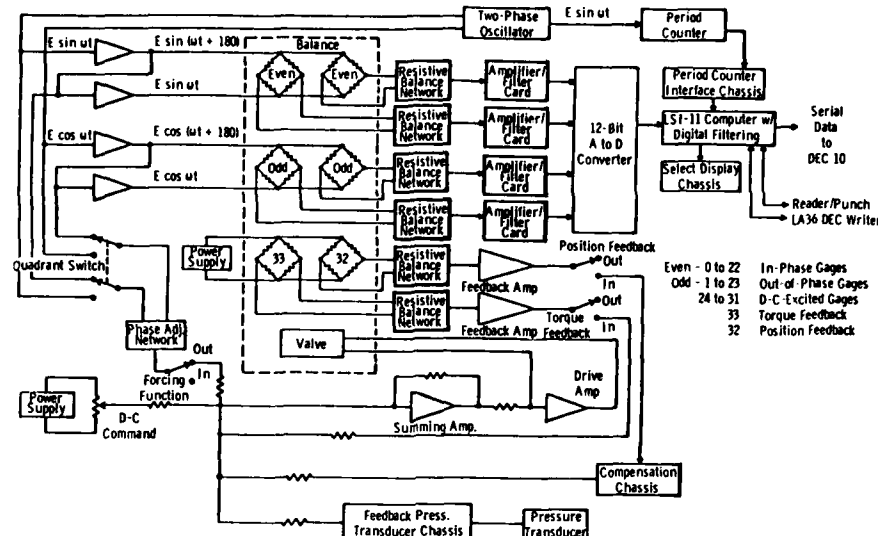


FIG. 14 AEDC INSTRUMENTATION BLOCK DIAGRAM

A phase shifting network is used to adjust the motion of the model so that it is in phase with the "in phase" oscillator output. The secondary loads are therefore obtained as explained below.

Let the sensitivity of one of the "dynamic" balance bridges be  $Z_0$ , obtained by exciting the bridge with a d-c voltage  $E_0$ . If the bridge is then excited with an alternating voltage  $E_0 \sin \omega t$  in phase with the primary motion its sensitivity becomes

$$Z = Z_0 \sin \omega t$$

and if a sinusoidal load  $S_0 \sin(\omega t + \eta)$  is applied to the balance element under consideration, the bridge output voltage becomes

$$V_0 = Z_0 \sin \omega t \cdot S_0 \sin(\omega t + \eta)$$

corresponding to the product of the primary motion with the secondary load as required by the coherent detection approach. This signal is then low-pass filtered resulting in

$$V_0 = \frac{S_0 Z_0}{2} \cos \eta$$

and similarly the "quadrature" bridge output is

$$V_{90} = \frac{S_0 Z_90}{2} \sin \eta$$

$V_0$  and  $V_{90}$  are digitized and fed to the computer where after correcting for balance interaction, sting vibration etc. the amplitude and phase of the secondary load is obtained from

$$S_0 = \sqrt{\left(\frac{2V_0}{Z_0}\right)^2 + \left(\frac{2V_{90}}{Z_{90}}\right)^2}$$

$$\eta = \arctan \frac{V_0 Z_{90}}{V_{90} Z_0}$$

## 5. VERIFICATION OF THE EXPERIMENTAL TECHNIQUE

The wind-tunnel apparatuses, instrumentation systems and analytical techniques described in this paper are used to obtain cross and cross coupling derivatives on which little or nothing is known, thus making it very difficult to establish the reliability of the results obtained. It was therefore deemed necessary to develop a technique that would *independently* verify the validity of the experimental and mathematical approach used to determine the derivatives. To this end the concept of an electromechanical calibrator emerged with which the various wind tunnel apparatuses, instrumentation system and analytical procedures could be routinely checked.

Similarly to a static calibration, where the outputs of a static balance are defined in terms of accurately known static calibrating loads, in a dynamic calibration the outputs of a dynamic stability apparatus are compared to a set of accurately known oscillatory loads applied synchronously with the primary oscillation. Thus while the dynamic stability apparatus is performing a known oscillatory primary motion, alternating loads, coherent with that motion and of known amplitude and phase are applied to the apparatus in one or more degrees of freedom simultaneously.

A comparison between the known applied loads and the dynamic stability apparatus outputs, obtained by processing the balance and other relevant information by means of the same procedure as in the wind tunnel experiments, provides an indication of the overall accuracy of the technique as well as of the existence of any possible hardware fault or software error. A rather simple three degrees of freedom electromechanical dynamic calibrator originally developed at NAE to be used in conjunction with both half and full model apparatuses has been successfully used for several years during which it became apparent that in addition to simulating the dynamic loads encountered in wind tunnel tests, it was also desirable to duplicate, at least approximately, the inertia characteristics of the model in order to obtain an adequate simulation of the system dynamic response to the calibration excitation.

This was indeed the case in the half model applications, but not so in the full model ones. Therefore the old calibrator is now being relegated to half model applications only and is therefore discussed in Ref.10. A new calibrator, currently in the process of assembly and specially designed for full model applications is described in the following sections.

### 5.1 Full Model Calibrator

The purpose of the calibrator is to apply accurately known alternating loads to the dynamic stability apparatus while it performs an oscillatory motion. These loads need to satisfy the following requirements.

- a) They must be coherent with the primary motion.
- b) They must be applied in up to 3 angular degrees of freedom simultaneously.
- c) They must be independent of each other, i.e. it should be possible to arbitrarily select their amplitudes and phases relative to the primary motion.
- d) Their amplitude should be of the same order of magnitude as those encountered in wind-tunnel experiments.
- e) There should be no interaction between the loads.

Since it is impractical to apply such loads directly to the model, the calibration is performed with a special calibrating frame (or "rotor") with which the model is replaced on the dynamic stability apparatus and to which the primary motion is imparted by the drive system of the dynamic stability apparatus in the same fashion as to the model in the wind tunnel tests.

The geometry of the rotor is effectively dictated by the need to simulate the inertia characteristics of the model. This simulation however, does not necessarily include the reproduction of products of inertia because the effects of the products of inertia between the primary and secondary degrees of freedom on the latter are accounted for by means of the tare measurements, while the effect on the former is negligible by virtue of the very small secondary deflections, particularly when only the components coherent with the primary motion are considered. Similarly the effect of the product of inertia between the secondary degrees of freedom can be neglected for the same reason.

In general the simulation of the moments of inertia of the model can be facilitated by making the basic rotor as light as possible and by providing for the addition of suitably located masses to adjust the moments of inertia to match those of the model. It turns out however that given the minimum realistic mass of the rotor required for the application of adequate loads its geometry must conform to criteria spelled out in the next section. Furthermore, in some cases the exact simulation of all moments of inertia is simply impossible and some judgement has to be exercised in the selection of the "optimum" simulation.

### 5.1.1 Moment-of-Inertia Considerations

The desirability of simulating accurately the moments of inertia of the models to be tested has already been mentioned. This section discusses the conditions that need to be satisfied, and the means required to accomplish such simulation.

Although in theory models with any inertia characteristics can be tested using the method described in the previous sections, considerable improvements in the accuracy of the results can be achieved by balancing the model such that

- the centre of gravity is on the primary axis of oscillation or, for plunging experiments, on the axis of the pitching (yawing) moment flexure;
- the principal axes of inertia coincide with the model axes\*.

The reasons for these requirements are as follows:

Kinematic and aerodynamic corrections due to sting vibrations are possible as long as the sting vibrations coherent with the primary motion are small. The fulfillment of requirement (a) eliminates the most important source of coherent sting vibration as this avoids the linear acceleration of the centre of gravity caused by inertia reactions.

In general, because of the lack of symmetry about the  $xy$  plane, the  $x$  and  $z$  axes of the model are not principal axes of inertia. Consequently, a finite product of inertia  $I_{xz}$  exists, leading to a possibly significant inertial coupling between yawing and rolling. Although in theory such a coupling is largely eliminated by means of tare measurements, in practice it can result in a degradation of the experimental accuracy.

Specifically, the inertial coupling in experiments involving yawing primary oscillation and rolling measurements or vice versa, may generate inertially induced secondary coherent outputs that are considerably larger than the aerodynamically induced outputs that are being investigated. The inertial output would then represent a form of noise that occupies a large portion of the equipment dynamic range, leading to a decrease in the accuracy of the aerodynamic measurements. Since the  $y$  axis of the model is almost always a principal axis of inertia, the above argument does not apply to pitching experiments or measurements.

In view of the relative ease of satisfying, to a reasonable extent, conditions (a) and (b), and of the considerable benefits accruing from the fulfillment of these conditions, the following arguments will be based on the assumption that (a) and (b) are indeed true. A substantial departure from these conditions would require a somewhat more complex albeit analogous approach.

Even if an aircraft has only one plane of symmetry, the calibrator rotor can easily be constructed to have two or three and to fulfill conditions (a) and (b). Assume that the unweighted rotor inertias are  $I_{xx_0}$ ,  $I_{yy_0}$  and  $I_{zz_0}$ . In order to simulate a given set of moments of inertia of a model, say  $I_{xx}$ ,  $I_{yy}$ , and  $I_{zz}$ , masses must be added to the rotor. The most straightforward way is simply to add them in pairs on each of the axes as shown in Fig. 15. It should be noted that the position of the masses on the axes is unimportant provided that the moments of inertia are properly reproduced and that the total mass of the rotor need not simulate the mass of the model. These conditions are indeed valid except for the plunging case, where it is the mass of the model that determines the resonance frequency of the primary (translational) oscillation and in which case an effort must be made to simulate both the mass and the moments of inertia of the model.

Assume therefore that pairs of masses  $m_x$ ,  $m_y$ ,  $m_z$  are added symmetrically about the origin at distances  $x$ ,  $y$  and  $z$ . The total inertias of the rotor then become

$$I_{xx} = I_{xx_0} + 2(m_y^2 + m_z^2)$$

$$I_{yy} = I_{yy_0} + 2(m_x^2 + m_z^2)$$

$$I_{zz} = I_{zz_0} + 2(m_x^2 + m_y^2)$$

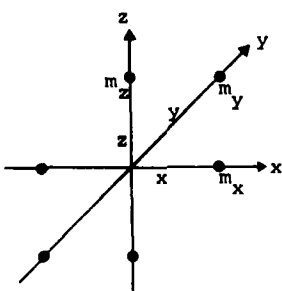


FIG. 15 SCHEMATIC OF CALIBRATOR INERTIA CHARACTERISTICS

\* Although the centre of gravity of the model should be at the same axial location as in the actual aircraft, practical considerations may prevent the  $x$  axis of the model to be oriented exactly as in the aircraft.

The masses required to obtain the necessary inertias are therefore as follows

$$m_x = \frac{(I_{xx} - I_{xx_0}) - (I_{yy} - I_{yy_0}) - (I_{zz} - I_{zz_0})}{-4x^2}$$

$$m_y = \frac{(I_{yy} - I_{yy_0}) - (I_{zz} - I_{zz_0}) - (I_{xx} - I_{xx_0})}{-4y^2}$$

$$m_z = \frac{(I_{zz} - I_{zz_0}) - (I_{xx} - I_{xx_0}) - (I_{yy} - I_{yy_0})}{-4z^2}$$

Since the moments of inertia are positive, the three numerators must be negative in order to obtain positive masses.

Therefore the conditions for simulation are

$$I_{xx} - I_{xx_0} \leq (I_{yy} - I_{yy_0}) + (I_{zz} - I_{zz_0}) \quad (29)$$

$$I_{yy} - I_{yy_0} \leq (I_{zz} - I_{zz_0}) + (I_{xx} - I_{xx_0}) \quad (30)$$

$$I_{zz} - I_{zz_0} \leq (I_{xx} - I_{xx_0}) + (I_{yy} - I_{yy_0}) \quad (31)$$

or, in general,

$$\Delta I_{kk} \leq \frac{1}{2} \Delta I_T \quad (32)$$

where

$$\Delta I_{kk} = I_{kk} - I_{kk_0} \text{ and } k = x, y, z$$

$$\Delta I_T = \Delta I_{xx} + \Delta I_{yy} + \Delta I_{zz}$$

If  $I_{kk} \gg I_{kk_0}$ ,  $\Delta I_{kk} \rightarrow I_{kk}$

which always satisfies inequality (32). It is therefore clear that for a given model geometry (or given inertia ratios) the ease to simulate its inertias improves with an increase in the weight of the model and a decrease in the weight of the rotor. This leads to the concept of a "simulation factor", , by which the mass and therefore the various inertias of the rotor ( $I_{xx_0}$ ,  $I_{yy_0}$  and  $I_{zz_0}$ ) are multiplied. By introducing

this factor in inequalities (29 - 31) and solving each of them for  $\gamma$  in the worst case, i.e. when the equal signs apply, three distinct values of  $\gamma$  are obtained, viz:

$$\gamma_1 = \frac{I_{yy} + I_{zz} - I_{xx}}{I_{yy_0} + I_{zz_0} + I_{xx_0}} \quad (33)$$

$$\gamma_2 = \frac{I_{zz} + I_{xx} - I_{yy}}{I_{zz_0} + I_{xx_0} + I_{yy_0}} \quad (34)$$

$$\gamma_3 = \frac{I_{xx} + I_{yy} - I_{zz}}{I_{xx_0} + I_{yy_0} + I_{zz_0}} \quad (35)$$

In order to be able to simulate the model inertias by adding masses to the rotor, all three values of  $\gamma$  must be larger than unity. The lowest value of  $\gamma$  denotes the most critical combination of inertias. If this lowest value is smaller than unity, all model moments of inertia cannot be simulated, which means that the three model frequencies cannot be duplicated. However, by dividing all model moments of inertia by this lowest value of  $\gamma$  and simulating these instead, all the ratios between the resonance frequencies in the various degrees of freedom can be duplicated, which is important for the checking out of the system.

Equations (33) to (35) indicate that the simulation factors are inversely proportional to the sum of the rotor inertias, confirming the notion that lighter rotors facilitate the simulation of the model inertias.

### 5.1.2 Description of Calibrator

A full model calibrator designed on the basis of the criteria advanced in the previous sections is shown in schematic form in Fig. 16. It consists of the aforementioned rotor and a stationary structure denoted "stator". The rotor is comprised of a very thin tubularly shaped "boom" with an internal diameter that permits its motion in pitch and yaw without interfering with the sting. A pair of disc shaped frames and a pair of cruciform shaped frames are attached to the mid-section and ends of the boom respectively. These frames in turn support sets of aluminum "loading" conductors through which rather substantial alternating currents coherent with the primary motion are passed. By imbedding the conductors in suitable DC magnetic fields the desired alternating loads are applied through the rotor to the dynamic stability apparatus. These DC magnetic fields are established by means of 5 electromagnets which collectively make up the stator.

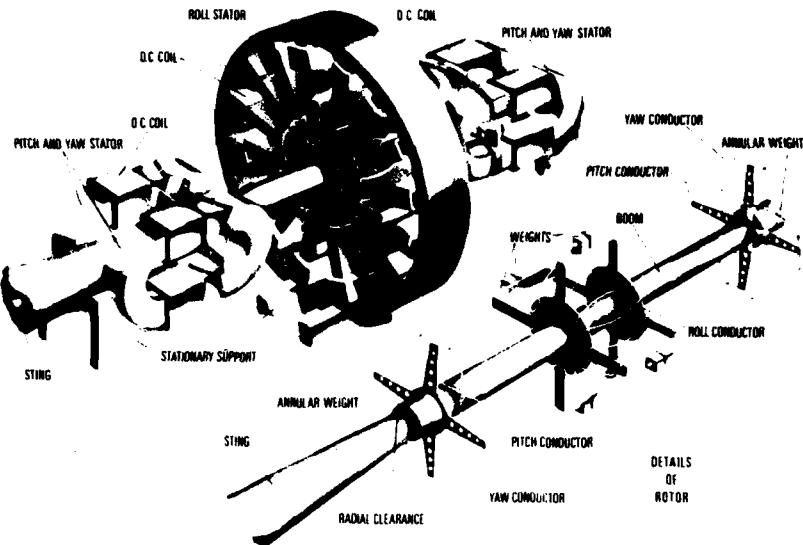


FIG. 16 PICTORIAL VIEW OF FULL MODEL CALIBRATOR

As the rotor must be able to move in three rotational degrees of freedom ( $\theta$ ,  $\psi$  &  $\phi$ ), the calibrator must have a certain spherical symmetry about the point where the three axes intersect. This requires the magnetic fields across the gaps to be radially oriented which is accomplished by spherically shaping the pole pieces. Likewise the loading conductors are curved to preserve the necessary angular relationship between the currents and magnetic fields.

Recalling that the force acting on a conductor carrying a current  $i$  within a magnetic field  $B$  is

$$\vec{F} = (\vec{i} \times \vec{B}) dl$$

where  $dl$  is the conductor length element. The three alternating aerodynamic moments acting on the model are therefore simulated electromagnetically as follows (recalling that all DC magnetic fields are radially oriented with respect to the centre of the apparatus):

#### a) Pitching Moment

The pitch loading conductors are supported by the forward and aft cruciform-shaped frames and located on two circles that also contain the model  $y$  axis. The pitching moment is obtained by suitably phasing the currents in the forward and aft conductors. Figure 17 shows an approximate spatial relationship of the field and currents in the pitch conductor at one of the boom ends. The opposite situation is required at the other end in order to obtain the required pitching moment.

#### b) Yawing Moment

The yaw loading conductors are also mounted at both ends of the boom, however, they are located on circles containing the model  $z$  axis in order to produce the desired moment. The other orientation and phasing requirements are analogous to those in the case of pitching.

c) Rolling Moment

The roll loading conductor is arranged in a "distributed winding" pattern along the periphery of the rotor disc frames, "weaving through" 16 magnetic gaps in the central portion of the stator with radial fields in alternating directions. The active segments of the conductor are located on circles containing the x axis as they pass through the various gaps.

Figure 18 shows the spatial distribution of the roll loading conductor and stator. This "distributed" configuration minimizes the required moment arm and thus rolling inertia, while being capable of producing the necessary rolling moments. Furthermore, the need to minimize the inertias also led to the use of the "single pass through the magnetic gaps" geometry for the various loading conductors. It is clear that such a geometry necessitates a larger current to generate a given moment than would a multi-pass geometry, which leads in turn to the requirement for larger conductors. This however results in stronger conductors that are virtually self supporting, thereby minimizing the need for additional mechanical reinforcements, and consequently a larger percentage of the total weight is effectively used in carrying current. By using a careful design and construction techniques, the rotor can be made significantly lighter than the models to be tested as stipulated in Section . It is therefore possible to adjust the inertia of the rotor by adding suitable weights which for simplicity are located in symmetrical pairs on the x, y and z axis. The first pair of weights are attached to the ends of the boom while the other two pairs are mounted on the four "arches" spanning the gap between the two disc frames that are attached to the mid-section of the boom.

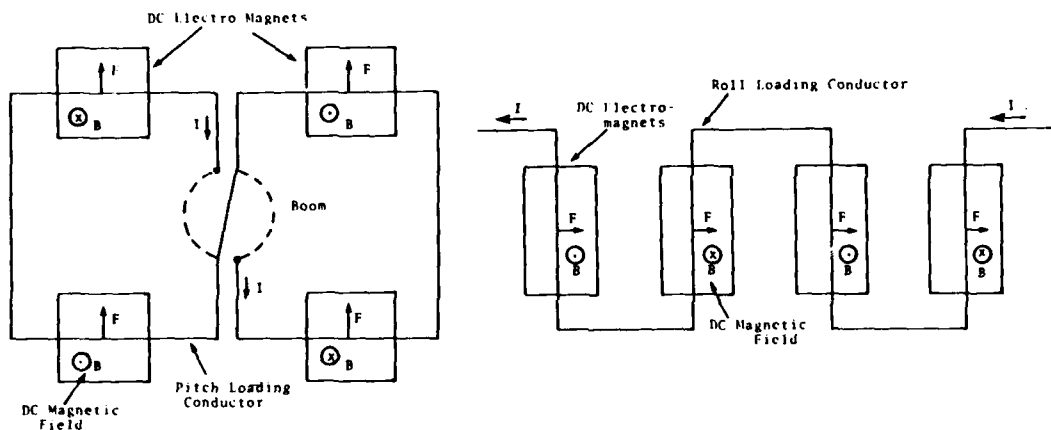


FIG. 17 PITCH CONDUCTOR GEOMETRY

FIG. 18 ROLL CONDUCTOR GEOMETRY

A block diagram of the circuitry required to operate the calibrator is shown in Figure 19. The signal representing the primary motion is applied to three similar branches that independently control the amplitude and phase of the current being fed to the various load conductors. The extremely low impedance presented by the conductors to the amplifiers make it imperative to use impedance matching transformers.

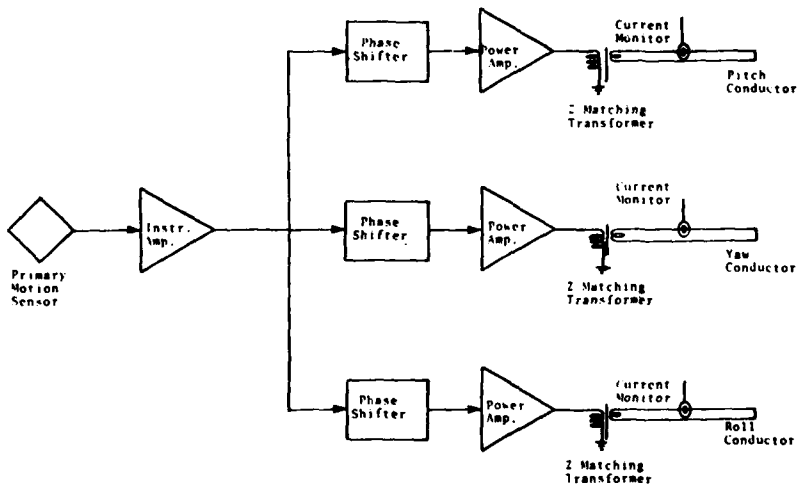


FIG. 19 CALIBRATOR DRIVING CIRCUITRY

The applied loads are inferred from the known loading currents and which are in turn measured using current transformers or shunts. Although Equation (1) should in general suffice to convert currents to loads, the difficulty in accurately accounting for fringing effects may necessitate a static calibration of the apparatus if such extreme accuracies are desired.

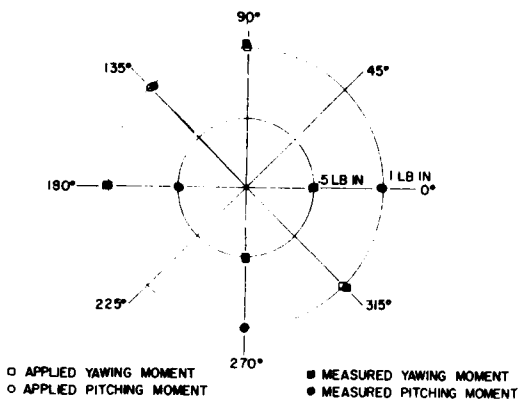


FIG. 20 TYPICAL CALIBRATION RESULTS

At the time of this writing the calibrator described above is in the process of final assembly and no experimental results are thus available. For the sake of completeness however, results obtained using the old and currently designated half-model calibrator are shown in Fig. 20, where a comparison between the applied and measured cross and cross-coupling (yaw and pitch) moments using the rolling apparatus are shown in vectorial form.

#### 6. CONCLUDING REMARKS

After a number of years of development, the direct forced oscillation technique for the measurement of aerodynamic stability derivatives has reached a stage of maturity that assures its future as a useful tool to the aerodynamicist involved in the design of high performance aircraft.

A variety of apparatuses have been developed with which most moment and force derivatives can be reliably obtained. Furthermore several approaches for the handling of the wind-tunnel data in order to extract the useful information from the noise that usually accompanies them have been developed and successfully used.

Mathematical procedures have been established with which the above information can be used to determine the desired static and dynamic direct, cross and cross-coupling derivatives and finally, the concept of *dynamic* calibration has been introduced, implemented, and very successfully used to verify the experimental and analytical procedures mentioned above.

This paper has dealt with the principles underlying the direct forced oscillation technique and has, for the purpose of elucidating them, provided examples of the work done at NAE and AEDC. Although these facilities have carried out much of the current work in this field, it should be borne in mind that substantial additional efforts are underway in other facilities, which are summarized in Ref. 2, where a comprehensive list of references is included that should prove useful to the reader interested in additional details.

#### 7. REFERENCES

1. K. J. Orlik-Rückemann, Dynamic Stability Testing of Aircraft - Needs versus Capabilities. *Prog. Aerospace Sci.*, vol. 16, 4, pp 431-447, Pergramon Press, 1975.
2. K. J. Orlik-Rückemann, Determination of Dynamic Stability Parameters in Wind Tunnels. AGARD Lecture Series No. 114, NASA Ames, VKI, March 1981.
3. E. S. Hanff, K. B. Kapoor, Measurement of Dynamic Direct and Cross-Coupling Derivatives due to Oscillation in Roll. *Proc. 8th Int. Cong. on Instrumentation in Aerospace Simulation Facilities*, Monterey, California, Sept. 1979.
4. S. M. Coulter, T. D. Buchanan, Description of a New High-Alpha, High-Load, Pitch-Yaw Dynamic Stability Test Mechanism at AEDC. *Proc. AIAA 11th Aerodynamic Testing Conf.*, Colorado Springs, March 1981.

5. E.S. Hanff, K.J. Orlik-Rückemann, A Generalized Technique for Measuring Cross-Coupling Derivatives in Wind Tunnels. Proc. AGARD Conf. on Dynamic Stability Parameters, CP 235, Paper 9, Athens, Greece, May 1978.
6. J.S. Bendat, A.G. Piersol, Random Data Analysis and Measurement Procedures. John Wiley Publications, 1971.
7. J.R. Chambers, S.B. Grafton. Static and Dynamic Longitudinal Stability Derivatives of a Powered 1/9 Scale Model of a Tilt Wing V/STOL Transport. NASA TN D-3591, September 1966.
8. E.S. Hanff, K.J. Orlik-Rückemann, Wind-Tunnel Measurement of Dynamic Cross-Coupling Derivatives. J. of Aircraft, Vol. 15, 1, January 1978.
9. J. van der Decken, E. Schmidt, B. Schulze, On the Test Procedures of the Derivative Balances Used in West Germany. Proc. AGARD Conf. on Dynamic Stability Parameters, CP 235, Paper 6, Athens, Greece, May 1978.
10. E.S. Hanff, Half Model Techniques. AGARD Lecture Series No. 114, NASA Ames, VKI, Brussels, March 198 .

## APPENDIX - LIST OF SYMBOLS

C	damping constant
g	secondary moment
G	static component of g
$\Delta G$	peak value of g component
$g_A$	aerodynamic component of secondary moment synchronous with primary motion
$G_A$	static component of $g_A$
$\Delta g_A$	peak value of $g_A$ component synchronous with the primary motion
K	stiffness
k	mechanical stiffness
i	$\sqrt{-1}$
I	moment of inertia <sup>1</sup>
$I_{xx}, I_{yy}, I_{zz}$	moment of inertia about x,y,z axes <sup>1,2</sup>
M	primary driving moment
$M_\theta$	aerodynamic stiffnesses in pitch
$M_{\dot{\theta}}$	aerodynamic damping constant in pitch
n(t)	noise component of signal
 Subscripts	
T	tare conditions
W	wind on conditions
 Y	mechanical damping constant
$\delta$	balance element angular deflection
$\delta_{ST}$	static component of $\delta$
$\theta$	pitching deflection
$\mu$	phase angle between driving moment and primary deflection
$\omega$	primary oscillation frequency

Other symbols are defined in the text.

<sup>1</sup> Moment of inertia of the moving system, i.e. the model, balance and part of the suspension mechanism.

<sup>2</sup> In the case of the calibrator the model is replaced by the rotor.

**WIND-TUNNEL MEASUREMENT OF AERODYNAMIC DERIVATIVES  
USING FLEXIBLE-STING RIGS**

by

C. O. O'Leary  
Aerodynamics Department,  
Royal Aircraft Establishment,  
Bedford, Bedfordshire, England

**SUMMARY**

Forced oscillation, flexible-sting rigs are used by several establishments for wind-tunnel measurement of aerodynamic derivatives. This paper describes the two multi-degree-of-freedom rigs at RAE Bedford and DFVLR.

Aircraft models are mounted on stings with built-in flexures and oscillations are excited in 2 or 3 degrees-of-freedom. The response is measured using strain gauges on the sting flexures. Measurements of lateral or longitudinal derivatives can be made. Details are given of the apparatus, technique and method of analysis. Current modifications to the RAE rig actuating system are described and differences in the RAE and DFVLR rigs are discussed.

Results are presented, from low-speed, high angle-of-attack tests on a combat aircraft model which were made with a new semi-circular sting support facility which allows testing up to  $\alpha = 90^\circ$ . A comparison is made of the derivative data from wind-tunnel tests, the corresponding data from flight tests and some theoretical estimates for two configurations: a jet trainer and a transport aircraft.

**1 INTRODUCTION**

Wind-tunnel rigs for the measurement of aerodynamic derivatives can be classified into two groups: those where the model is rigidly forced at constant amplitude or rate (inexorable rigs) and those where the model is spring mounted and executes free or forced oscillations at predetermined frequencies. The latter category is the subject of this paper but a brief comparison of the two classes of rig is given in Table 1.

At RAE Bedford in the UK a rig of the flexible-sting type has been developed because of the special constraints imposed at the inception of the project. At that time (about 1958) there was considerable uncertainty about the lateral derivatives of slender wing supersonic transport aircraft and a technique was required for measuring these parameters in wind-tunnels using sting mounted models. The diameter of the sting had to be small enough to fit into the fuselage of a slender model to be tested in the 8ft x 8ft supersonic tunnel at RAE. It was considered that a rigidly forced rig was not practicable for such an application so effort was concentrated on designing a rig which could be used in a number of wind tunnels without major modification of the existing sting support structures. Initially it was thought that relatively simple single degree-of-freedom spring units could be designed to measure pitch, yaw and roll derivatives but it soon became evident that the design and manufacture of such units was not straightforward. The difficulty arose in limiting the units to one degree-of-freedom only. Thus a spring unit intended for yawing was also, to some extent, flexible in sideslip and similarly a pitching unit was also flexible in heave. Some roll flexibility was also present. Rather than try to eliminate or attempt to correct for these unwanted flexibilities it was decided to design two multi degree-of-freedom units: one for lateral tests with flexibilities in yaw, sideslip and roll and one for longitudinal tests with flexibilities in pitch and heave.

A similar multi degree-of-freedom flexible-sting rig for low speed wind tunnels is also in use at DFVLR, West Germany. This rig was originally modelled on the RAE rig but there are now some differences which will be discussed later.

In addition to the direct derivatives, both the RAE and DFVLR rigs are designed to measure cross derivatives such as rolling moment due to rate-of-roll and rolling moment due to rate-of-yaw. However cross-coupling derivatives such as yawing-moment due to rate-of-pitch are not measured with the present equipment.

**2 THE RAE OSCILLATORY DERIVATIVE RIG**

The rig is used to measure lateral and longitudinal derivatives throughout the speed range of current aircraft. There are three major components: the spring unit, which is essentially a sting with built-in flexures, the drive system to excite the model oscillation and the measuring equipment. Two types of test are made: lateral, where the model oscillates in three modes approximating to yaw, sideslip and roll, and longitudinal, where there are two modes approximating to pitch and heave. The test procedure is to oscillate the model at or near the natural frequency of the rig in each mode in turn: this is the only way of obtaining reasonable amplitudes with the small excitation force available. By solving the equations of motion, using measured values of the amplitudes, frequencies

and excitation forces, together with previously determined values of the model inertias, the required aerodynamic derivatives are obtained as the differences between wind-off and wind-on values at the same amplitude. In solving the equations of motion it is necessary to assume that the derivatives are independent of frequency parameter within the small range between the various modes of vibration. This limitation is not considered serious however, because generally each derivative is determined primarily from measurements in one particular mode. Realistic values of the frequency parameter with respect to typical aircraft dynamic motions have been achieved without recourse to especially lightweight models, but both mass and inertia of the models used need to be monitored during design and construction.

The equipment is shown set up in the laboratory in Fig 1. A calibrating frame is seen mounted in place of the model on a lateral spring unit which is itself mounted on a surface table via a standard joint and rear sting. For wind-tunnel tests the rear sting is fitted into the incidence quadrant of the 8ft x 8ft high speed tunnel. The vibration generator and part of the drive mechanism are seen forward of the mounting block and racks containing the control equipment and signal conditioning units can be seen in the background.

### 2.1 Details of construction of spring units

The various spring units at present available are specified in Table 2. Brief descriptions of a lateral and a longitudinal spring unit from this range are as follows.

#### 2.1.1 Lateral spring unit

A sketch of the lateral spring unit for high speed tests (No.4 in Table 2), is shown in Fig 2a. The forward flexure has concave vertical surfaces to give maximum strength when loaded by normal force while ensuring that roll and yaw frequencies are within the desired limits. The rear flexure, in combination with the forward flexure, gives flexibility in sideslip. This flexure is made as long as practicable to reduce the sideslip frequency to less than the roll frequency while retaining adequate strength with respect to normal force. A constant stress level is maintained by varying the cross-section along its length. If the sideslip mode frequency is above that of the roll mode, model instability is likely to occur<sup>1</sup>. The male section of a standard conical sting joint is machined onto the rear of the spring unit to allow attachment to the rear sting which is fitted into the wind-tunnel angle-of-attack quadrant. The vibration generator and drive system are installed aft of the rear flexure and connected to the model attachment section by a rod which passes down a borehole in the sting. The front and rear flexures are strain-gauged for displacement measurement during dynamic tests and also to enable static measurements to be made of the usual forces and moments (except drag). With a typical model, mode frequencies for yaw, sideslip and roll are approximately 4 Hz, 6 Hz and 10 Hz respectively. Maximum allowable normal force is 18 kN.

#### 2.1.2 Longitudinal spring unit

A sketch of the longitudinal unit is given in Fig 2b. The rear flexure is similar to the rear flexure on the lateral unit rotated through 90°, but the forward flexure is not a horizontal flat spring since this could not sustain any appreciable normal force. Two types of pitch pivot have been used: the first is a crossed spring arrangement with a vertical flat strip reacting normal force and the appropriate stiffness provided by horizontal bars on each side of the vertical strip. This unit is limited to a maximum normal force of 1.3 kN. In a later unit (Fig 2b) the vertical strip was replaced by a needle roller bearing which increased the normal force limit to 5 kN. The contribution to damping of the roller bearing was found to be very little more than the previous crossed-spring arrangement. These longitudinal units have only been seldom used over recent years because of the greater interest in lateral behaviour of combat aircraft at high angle-of-attack.

### 2.2 Drive systems

For all wind tunnel tests made so far, a combined roll/yaw drive system has been used. With this system there are limits in the accuracy of certain measurements which will be discussed later. A separate roll/yaw drive has recently been built and tested and is expected to increase the accuracy of measurement of certain derivatives in future tests. Both these drive systems are described below.

#### 2.2.1 Combined roll/yaw drive

The system is shown diagrammatically in Fig 3. The electromagnetic vibration generator applies both a longitudinal force and a rolling torque to the offset arm which is rigidly attached to the model. The longitudinal force produces an internal couple between the model and the end of the sting which is equivalent to a combined external yawing moment and sideforce. The system thus provides yawing, rolling and sideforce excitation at the same time. Crossed spring pivots are used throughout and the ends of links are provided with flat spring flexures in the appropriate planes. There is a PTFE sliding bush situated towards the front of the driving rod but this serves only as a steady and carries very small side loads. To excite each mode of oscillation the oscillator is set to the appropriate frequency and the current adjusted to give the required amplitude.

The driving rod is inevitably rather flexible in torsion and this flexibility combined with the internal damping of the vibration generator introduces a troublesome phase difference between the current in the vibration generator and the forces applied to the model. The flexible drive system itself is therefore used as a dynamometer to measure the excitation force. The method is illustrated diagrammatically for a single degree-of-freedom system in Fig 4. Equation (1) is the equation of motion of the mass in terms of the driving force  $F$ . Equation (2) is simply the relation between the force  $F$  and the deflection of the driving system. Combining equations (1) and (2) gives equation (3) which is of exactly the same form as equation (1) but defines a slightly different system in which the drive system stiffness is added to the main stiffness and the driving force is proportional to the vibration generator displacement. The latter is measured in the actual drive system by means of strain gauges on the crossed spring pivots on the main lever shown in Fig 3. With this arrangement the measured damping does not include the internal damping of the vibration generator; this is important if it is required to measure small values of aerodynamic damping.

In designing the drive system two conditions have to be satisfied. If the maximum permitted force and displacement of the vibration generator are  $F$  and  $d$  respectively, then the first condition is that a force  $F$  should be required to hold the end of the drive lever in the neutral position when the model is deflected through  $1.5^\circ$ . The second condition is that with the model undeflected a force  $F$  should be applied at the lever to achieve a lever deflection  $d$ . These conditions ensure that the full capability of the vibration generator is used to oscillate the model at the required amplitude wind-off and in the presence of high damping, wind-on.

With most models tested so far the rolling mode is usually heavily damped and near maximum excitation power has been found to be needed to obtain the required amplitude of oscillation. This means that besides a large in-quadrature roll excitation force, large in quadrature yaw and sideslip components are also being fed in by the excitation system at the roll frequency because of the combined roll/yaw drive. These components cause most of the additional subsidiary yawing and sideslipping responses measured and as a result the responses due to aerodynamic excitation are somewhat masked. Thus the side-force and yawing moment due to rate of roll are measured mainly as the difference of two large quantities, the mechanical excitation and the response, which results in poor accuracy. By the introduction of two nominally independent drive systems, one to excite roll and the other to excite yaw and sideslip it is hoped to increase the accuracy of measurement of the derivatives due to rate of roll. This development is described below.

### 2.2.2 Separate roll/yaw drive

This new system, which is now ready for use, is shown diagrammatically in Fig 5. Both the yaw and roll drive systems utilise a common vibration generator and excite the model through the same driving rod as in the combined system. During the roll mode the yaw/sideslip excitation system is clamped to earth at the connection to the vibration generator, and similarly the roll system is clamped during the yaw or sideslip modes. The clamping operations are done by remote control so no access to the wind tunnel is required. Both systems have to satisfy the deflection and load requirements specified for the combined system, described in the last section.

As can be seen by a study of Fig 5, the roll mode is excited through torsion of the driving rod as in the combined system but the yaw and sideslip modes are excited using a special fore and aft 'spring' which is shown in Fig 5. Essentially, this consists of multiple flat steel plates which are jointly connected at one end to the drive lever and at the other end to the driving rod. Deflection of the drive lever produces an appropriate fore and aft force on the driving rod to excite the model in yaw or sideslip.

A deficiency of this separate drive system using a single actuator is that artificial damping cannot be applied to roll while forcing a yaw or sideslip oscillation and vice versa. It is therefore proposed to design a further system with two actuators, one for each drive, so that artificial damping can be applied to one or more channels during any of the modes of oscillation. The main problem anticipated is an engineering one; that of accommodating two actuators in a compact enough space for wind tunnel use.

### 2.3 Signal processing and control equipment

A block diagram of the equipment is shown in Fig 6. Displacement signals from the strain gauges on the spring unit flexures and excitation linkage are amplified and a signal mixing unit is used to eliminate interactions. Provision is made for five components (all except axial force). These signals are then fed in parallel to the display and control unit and to an analogue-to-digital converter. The signal display is used to monitor the amplitude and quality of the four signals whilst the tuning display is a plot of the primary signal of the selected mode against excitation; the operator uses this to adjust the frequency of the oscillator signal until a vertical ellipse is obtained. The oscillator signal is amplified and is used to excite the model through the actuator and drive system. Damping can be applied to any or all of the three modes by feeding back displacement signals through an artificial damping unit and thence to the same power amplifier and actuator used for excitation. This unit is provided with phase and gain controls on each of the three channels and if, for example, artificial damping in roll is required, the phase and gain of the roll signal are adjusted and fed back to limit roll oscillation whilst exciting any of the three modes.

#### 2.4 Measuring equipment

The purpose of these components is to measure the in-phase and in-quadrature components of the four displacements signals and this is achieved using the Fourier transform method on a PDP 11/20 computer as indicated in Fig 6. The analogue to digital converter provides four input channels and converts signals at a maximum level of  $\pm 10$  V to 14 bit (plus sign) outputs. The conversion time is 15  $\mu s$  per channel. The computer programme takes about 300  $\mu s$  for the necessary operations on each set of samples. At the frequencies used for the tests the system can operate on-line at an adequate sampling rate.

#### 2.5 Method of analysis

The derivatives are obtained by solving the equations of motion which, for lateral tests are:

$$(\omega^2 I_{zz} + j\omega N_\psi + N_\psi) \dot{\psi} + (\omega^2 m\bar{x} + j\omega N_y + N_y) \dot{y} + (-\omega^2 I_{zx} + j\omega N_\phi + N_\phi) \dot{\phi} + N_e = 0$$

$$(\omega^2 m\bar{x} + j\omega Y_\psi + Y_\psi) \dot{\psi} + (\omega^2 m + j\omega Y_y + Y_y) \dot{y} + (-\omega^2 m\bar{z} + j\omega Y_\phi + Y_\phi) \dot{\phi} + Y_e = 0$$

$$(-\omega^2 I_{zx} + j\omega L_\psi + L_\psi) \dot{\psi} + (-\omega^2 m\bar{z} + j\omega L_y + L_y) \dot{y} + (\omega^2 I_{xx} + j\omega L_\phi + L_\phi) \dot{\phi} + L_e = 0 .$$

The symbols are defined as follows:

##### Axes:

All forces, moments and displacements are referred to a system of earth axes fixed in the mean position of the oscillating model.

##### Displacements and velocities:

$\dot{\psi}$	yawing
$\dot{y}$	sideslipping
$\dot{\phi}$	rolling .

##### Inertias:

$m$	mass
$\bar{x}$	coordinates of CG
$I_{xx}$	roll inertia
$I_{zz}$	yaw inertia
$I_{zx}$	cross inertia (roll/yaw) .

##### Forces and moments:

$N$	yawing moment
$Y$	sideforce
$L$	rolling moment .

Derivatives are denoted by suffices, eg

$$N_\psi = \partial N / \partial \psi$$

$\omega$  is the circular frequency and the suffix e denotes an excitation force or moment.

These equations contain a total of 18 unknown derivatives. Eighteen equations are obtained from the above three by splitting them into real and imaginary parts and inserting data measured in three different modes of oscillation. Inertias are determined from previous calibrations, frequencies are measured directly and the strain gauge and excitation signals, together with the necessary transducer factors, give the signal ratios used in the final equations. It is assumed that the aerodynamic derivatives are given by the differences between the values measured wind-on and wind-off.

#### 2.6 Calibrations

Although in principle the strain gauges could be calibrated by applying known static displacements to the model, this is not a convenient operation and the following method has therefore been developed. First the strain gauges are calibrated statically as a five-component force measuring balance using ordinary loading techniques and interactions are cancelled by means of the signal mixing unit. Since the spring system is symmetrical, the roll signal can equally well be used to measure roll displacement. However, because of the yaw-sideslip cross-stiffnesses in the system, simple interactions are needed between the yawing moment and sideforce signals to convert them to yaw and sideslip displacement measurements. Special potentiometers are provided in the signal mixing unit for this purpose.

After this initial setting up procedure, the calibrations are made dynamically. The procedure is designed not only to give the required calibration factors and inertias but also to verify that the behaviour of the rig agrees with the equations of motion. Inconsistencies, which sometimes occur, have usually been found to be due to additional modes of vibration associated with the wind-tunnel support system. It is therefore important to make thorough checks when using any support system for the first time.

For the calibrations a special frame of the kind shown in Fig 1 is fixed to the model attachment section of the spring unit. This is designed so that accurately known changes in the inertias can conveniently be made. The tests consist of measurements, in all three modes of oscillation, for a systematic series of inertia changes. The measurements, together with assumed values for the strain gauge factors and the system stiffnesses are used to solve the equations of motion and obtain the system inertias. The changes in the inertias thus calculated are then compared with the actual changes known to have been made. Using these comparisons as the criterion, the best set of strain gauge factors and stiffnesses is obtained by an iterative trial and error process using an interactive program on the PDP 11/20 computer. The model then replaces the calibrating frame on the spring unit and a single set of measurements is used to calculate the model inertias.

In the calibrations described so far the frequency is always adjusted so that the component of the excitation in phase with the primary displacement is zero. The in-quadrature components are ignored and the resulting errors in the inertia calculations are negligible.

The excitation measuring system is calibrated by changing the frequency (in each mode) so that relatively large components of the excitation signal in phase with the primary displacement are introduced. Values for the excitation factors are assumed and the measurements, together with values already established for the inertias are used to calculate the stiffnesses. The excitation factors are obtained using the criterion that there should be no change in any stiffness with frequency.

### 2.7 Wind-tunnel sting supports

For oscillatory testing it is important that the support system is rigid enough to eliminate all risk of unwanted modes of oscillation and has negligible play in the joints. It has been found that many conventional sting supports designed for static testing do not satisfy these requirements. Two support structures designed for oscillatory testing in the 13ft x 9ft low speed wind tunnel are shown in Fig 7a&b. With the arrangement shown in Fig 7a models can be tested up to 26° angles-of-attack but changes are made manually by unbolting the rear support. More recently, when tests were required at angles-of-attack up to 90° the support system shown in Figs 7b and 8 was introduced. The two semi-circular sting carrier supports are each made of 75mm thick steel and are bolted to the upper and lower turntables. The sting carrier, located between the supports, is fitted with rollers which run in tracks cut out of the supports and travels through an angle-of-attack range of -30° to 90° at a rate of 1°/s. A steppermotor drive is used. The sting carrier can be firmly clamped to the supports by powerful spring loaded steel blocks which also bear on the tracks. For angle-of-attack changes the clamps are withdrawn by hydraulic actuators. A spring unit is mounted on the sting carrier using a conventional wind-tunnel joint so the support system can also be used for static testing by replacing the spring unit with a conventional strain gauge balance and sting.

For high speed testing, usually in the 8ft x 8ft wind tunnel at RAE, the arrangement shown in Fig 7c is used. The spring unit and rear sting are located in the standard quadrant housing used for static testing. This arrangement is satisfactory because of the high mass and great rigidity of the quadrant. It is planned to introduce a special cranked sting arrangement which will increase the angle-of-attack limit from the present 22° to 40°.

### 3 THE DFVLR MULTI-DEGREE-OF-FREEDOM RIG

This equipment is based on the same principle as the RAE rig but has developed along different lines to suit particular applications at DFVLR. Essentially the aim is to test models of aircraft and missiles in low speed wind tunnels where external mechanisms can be more freely used than in a high speed wind tunnel. To avoid the complication of an internal drive system, the components are external to the sting and the actuator drives the model through one or more rigid links.

The spring unit used for both longitudinal and lateral tests is shown in Fig 9. It is very similar to the RAE longitudinal spring unit. For pitch/heave tests the unit is used in the usual way with the twin bars on the forward flexure aligned in the horizontal plane giving pitch stiffness. For lateral tests the unit is simply rotated through 90° with the model maintained in the usual upright position. This technique is satisfactory for a small range of normal force, ie for tests at low wind speed and/or low angle-of-attack. The natural frequencies used in the tests are similar to those of the RAE rig and are all below 10 Hz. Fig 10 shows the rig arranged for longitudinal tests in an open section wind tunnel. The actuator is floor mounted and rigidly connected to the model by an external rod as shown. For lateral tests the actuator position and connections are changed to excite the mode required. In a later rig for a closed section wind tunnel (Fig 11) the actuator is fixed to the rear sting and externally connected to the model

by a linkage. This arrangement enables angle-of-attack to be varied without moving the actuator.

A block diagram of the control and measurement system is shown in Fig 12. Model excitation frequency is set on an oscillator. The signal is then amplified and fed to the actuator (similar to RAE vibration generator). A velocity transducer on the actuator shaft provides a feedback signal which is summed with the oscillator signal before amplification and is used to smooth spurious model motion due to wind tunnel unsteadiness. Excitation frequency is measured by a counter. The strain gauge signals are amplified and together with the excitation and feedback signals are resolved into in-phase and in-quadrature components by Resolved-Component Voltmeters. The RCVs generate voltages which are converted to digital form using integrating digital voltmeters. The information is then put on paper tape and line printer using a digital multiplexer. The strain gauge analogue signals and feedback signal are displayed on an oscilloscope for continuous monitoring.

The derivative evaluation method used by DFVLR differs from the RAE method. Instead of the analytical technique of solving the equations of motion, a 'global energy' method is used. Advantages claimed for this method are that less calibration effort is required and increased accuracy is obtained. The method is described in Ref 2.

From the foregoing description it is apparent that the RAE and DFVLR techniques differ in three main areas: mechanical excitation system, processing of strain gauge signals and analysis technique.

The excitation system used by DFVLR is simpler than the RAE system and also offers some advantages. The components are rigidly linked to the model and, since they are re-configured for each mode, tend to excite one degree of freedom only. Thus, for example, in a roll mode there is very little excitation in yaw and the problem of cross-excitation, as in the RAE rig with combined excitation system discussed in section 2.2.1, would be less evident. However, the RAE rig was required to be compatible with the sting support system of the 8ft x 8ft high speed wind tunnel so a compact system virtually contained within the sting was necessary.

The DFVLR method of measuring in-phase and in-quadrature components of strain gauge signals using resolved component voltmeters was also used by RAE until a few years ago when they became unreliable due to deterioration of components and were replaced by the computer based measuring system described in section 2. The advantages of a computer based system are speed, flexibility and accuracy. Readings can be averaged over any number of cycles, depending on unsteadiness, transferred direct onto a disk file and can then be readily accessed for on-line computation and graph plotting.

The analysis technique used by DFVLR is widely used in structural dynamics but the author is not familiar with the technique and is unable to comment on whether it is preferable to the analytical method used by RAE. This latter method has the attraction of allowing an insight into the response of the model from an examination of the terms in the equations at each stage of the solution. Questionable initial results can thus be easily investigated.

#### 4 EXAMPLES OF RESULTS

Results are presented for three models (Fig 13) tested over the past few years. Model A represents a combat aircraft with a 25° swept wing and Model B a trainer/interceptor with 40° swept wing. Model C is a typical transport configuration with a 20° swept wing.

Fig 14 shows some of the results obtained for Model A in the low speed wind tunnel using the 'A' frame support and the high angle-of-attack support. The derivatives are measured in earth axes fixed in the mean position of the oscillating model and in this system the model displacements are denoted by  $\psi$ ,  $y$  and  $\phi$ , ie yaw, sideways displacement and roll. These derivatives can be related to those in conventional body axes notation by the following:

$$\begin{aligned}
 m_{\dot{\theta}} &= m_q + m_w \cos \alpha = \frac{M_{\dot{\theta}}}{\frac{1}{2} \rho V^2 S c} \\
 l_{\dot{\phi}} &= l_p + l_v \sin \alpha = \frac{L_{\dot{\phi}}}{\frac{1}{2} \rho V^2 S b} \\
 n_{\dot{\psi}} &= -n_v \cos \alpha = \frac{N_{\dot{\psi}}}{\frac{1}{2} \rho V^2 S b} \\
 n_{\dot{y}} &= n_r - n_v \cos \alpha = \frac{N_{\dot{y}}}{\frac{1}{2} \rho V^2 S b} \\
 n_{\dot{\phi}} &= n_p + n_v \sin \alpha = \frac{N_{\dot{\phi}}}{\frac{1}{2} \rho V^2 S b}
 \end{aligned}$$

The pitch damping derivative  $m_z$  was measured during tests on the 'A' frame support only, where angle-of-attack was limited to  $24^\circ$ . For most configurations it is justifiably assumed that the acceleration component  $m_w$  is small compared with  $m_g$  so the separation of the two is not considered necessary. It is possible that the two components can be separated by testing over a wide range of frequency parameter  $v = \omega c/V$ . The measured aerodynamic stiffnesses include virtual inertia effects since the method of analysis does not distinguish them and the apparent stiffness  $m_z$  will represent  $m_z - v^2 m_{zv}$ . By comparing tests at different values of  $v$  it is possible to separate the stiffness  $m_z$  and the virtual inertia  $m_{zv}$ , making the assumption that both these derivatives are independent of  $v$ . (The apparent stiffness is plotted against  $v^2$  and the slope is the required derivative.) Thus  $m_z (= m_w)$  may be subtracted from  $m_g$  to obtain  $m_g$ . It should however be stated that this test remains to be attempted in the variable density (8ft x 8ft) wind-tunnel.

The damping in roll derivative,  $\dot{\psi}$ , and the yawing moment derivatives,  $n_y$  and  $-n_y$ , were measured during lateral tests on both the 'A' frame and high angle-of-attack sting supports and agreement between the two sets of results is good.  $\dot{\psi}$  is seen to reduce to a low value at about  $\alpha = 12^\circ$ , which is close to the stalling angle-of-attack for this model, but recovers at  $\alpha \approx 20^\circ$  to near the pre-stall value where it somewhat surprisingly remains up to  $\alpha = 90^\circ$ . The yaw damping,  $n_y$ , is substantial up to about  $\alpha = 35^\circ$  when it starts to diminish and reaches zero at about  $\alpha = 50^\circ$ . Between  $\alpha = 50^\circ$  and  $\alpha = 65^\circ$  the model is negatively damped and this unstable region coincides with a stable peak in  $-n_y$ , the yawing stiffness. It is likely that asymmetric flow effects on the model nose cause a restoring moment due to displacement in yaw but also cause a de-stabilising effect due to rate of yaw as illustrated in Fig 14 and also investigated in previous NASA tests<sup>3</sup>. It has only recently become possible to test models in these unstable angle-of-attack regions by the use of artificial damping described in section 2.

Results for Model B, tested at  $M = 0.7$ , are shown in Fig 15. The dynamic test results are compared with estimates of derivatives, using 'DATCOM' methods, and with results from flight tests on the full scale aircraft. Dynamic tests<sup>4</sup> were made on two separate occasions and the results give some indication of the accuracy of measurement. The greatest discrepancy occurs in  $n_y$ , where the two sets of results differ by about 20%. Estimates are generally in good agreement with dynamic results; the largest discrepancies occurring in  $n_y$  at the higher angles-of-attack and in  $n_y$  at  $\alpha \sim 0^\circ$ . As stated earlier,  $n_y$  is a combined derivative  $n_r - n_y \cos \alpha$ , but has been compared with an estimate of  $n_r$ . It is probable that for this configuration at low angle-of-attack  $n_y$  is insignificant and the comparison is justifiable. As in the case of  $m_z$ ,  $n_y$  can possibly be determined by testing over a range of frequency parameter, but results are likely to be inaccurate<sup>1</sup>. The wind tunnel results for  $\dot{\psi}$  are also in good agreement with the flight measurements, showing the trend towards zero roll damping at  $\alpha \approx 10^\circ$  measured in the flight tests.  $-n_y$  is somewhat less than measured in flight at high angle-of-attack.  $n_y$  is within the scatter of the flight measurements.

Results from low speed tests on Model C, the transport configuration, are shown in Fig 16. Comparisons are again made with estimates using DATCOM and with static test results for  $-n_y$ , fin and tailplane on and off. Some discrepancies are apparent in the results for fin and tailplane on but agreement is good between estimated and dynamic test results for fuselage and wing only. From results for  $-y_y$  not presented here, it was found that differences in fin centre of pressure position, estimated and measured statically and dynamically, would account for these discrepancies. The decrease in yaw damping,  $n_y$  (fin and tailplane on) with angle-of-attack indicated by dynamic tests is not obtained in the estimation and may possibly be due to dynamic effects from wake interference on the fin which caused a larger reduction in damping than allowed for in the estimation method. The estimate of yawing moment due to rate of roll is also considerably at variance with the dynamic test result but here there is some doubt about the accuracy of both results. The measured  $n_y$  is possibly inaccurate due to the effect of large excitation in yaw during the roll mode as discussed in section 2.2.1. The estimate of roll damping  $\dot{\psi}$  agrees well with test results but does not show the reduction due to the effects of separated flow at higher angles-of-attack.

## 5 CONCLUDING REMARKS

The RAE and DFVLR flexible-sting rigs for small amplitude, wind-tunnel tests have been described. The rigs have been developed to meet the changing requirements over the past 15 or 20 years. The RAE rig was conceived when there was a requirement to investigate the lateral stability of slender aircraft at speeds up to  $M = 2$  and at relatively modest angles-of-attack, but over the years the emphasis has shifted towards high angle-of-attack testing at speeds below  $M = 1$ . At DFVLR the emphasis has been on low-speed testing. Some development of the rigs at RAE is being pursued. New spring units and excitation systems have been introduced to improve the test capability and increase the accuracy of measurement. A new sting support for the low speed wind tunnel at RAE enables tests to be made up to  $90^\circ$  angle-of-attack and the introduction of artificial damping means that tests can be made through unstable angle-of-attack regions with safety.

Results from tests on three configurations have been presented and compared with estimates, static wind-tunnel test data and flight test results. In general there is fair agreement but discrepancies remain, notably in the case of  $n_y$  for Model C. A separate roll/yaw excitation system will be used in future tests and should improve the accuracy of measurement of this derivative.

Table 1  
FEATURES OF RIGIDLY FORCED AND FLEXIBLE STING DYNAMIC RIGS

	Rigidly forced	Flexible sting
Model motion	Various, usually oscillatory at constant amplitude displacement or constant roll rate (rolling rig)	Oscillatory, model is usually mounted on a multi-degree-of-freedom sting
Drive system	Inexorable (electromechanical or hydraulic)	Electromagnetic exciter at constant amplitude force
Primary measurements	Forces and moments on model	Usually response of model
Degrees-of-freedom	One or more	Up to three without sting changes
Advantages	<ul style="list-style-type: none"> <li>1. Frequency, amplitude and type of motion can be changed.</li> <li>2. Negative damping has no effect on test capability.</li> <li>3. Tests in short duration wind-tunnels are practicable.</li> </ul>	<ul style="list-style-type: none"> <li>1. Can use existing tunnel sting support system or modify to suit.</li> <li>2. Conventional model construction; specially lightweight not required.</li> <li>3. Low power required for excitation since models are tested near resonance.</li> </ul>
Disadvantages	<ul style="list-style-type: none"> <li>1. Strong, rigid support system required with probable modification of working section structure.</li> <li>2. May need special lightweight models.</li> <li>3. Large forces required to force model.</li> </ul>	<ul style="list-style-type: none"> <li>1. Change of frequency is difficult.</li> <li>2. Artificial damping required to test negatively damped models.</li> </ul>

Table 2  
RAE SPRING UNITS

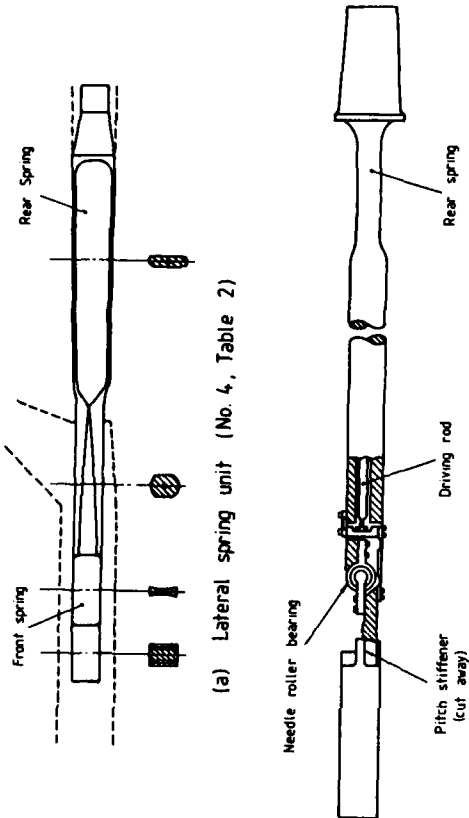
No.	Degrees-of-freedom	Maximum normal force (kN)	Model attachment	Remarks
1a	Pitch and heave	1.3	Circular 58.4mm dia	Crossed spring pitch pivot
1b	Pitch and heave	5	Circular 58.4mm dia	Roller bearing pitch pivot
2a	Yaw, roll and sideslip	4	Circular 58.4mm dia	}
2b	Yaw, roll and sideslip	2.7	Circular 58.4mm dia	
2c	Yaw, roll and sideslip	2.7	Circular 58.4mm dia	
3	Yaw, roll and sideslip	10	Circular 76.2mm dia	Different roll stiffnesses
4	Yaw, roll and sideslip	18	Rectangular 101.6 mm x 76.2 mm	

## REFERENCES

1. J.S. Thompson, R.A. Fail and J.V. Inglesby. Low speed wind-tunnel measurements of the oscillatory lateral stability derivatives for a model of a slender aircraft (HP 115) including effects of frequency parameter. RAE Technical Report 69018 (1969)
2. Dr. -Ing Jan von der Decken, Dr. -Ing Eberhard Schmidt and Dipl. -Ing Bernd Schulze. On the test procedures of the derivative balances used in West Germany. AGARD-CP-235.
3. Sue B. Grafton, Joseph R. Chambers and Paul L. Coe, Jr. Wind-tunnel free-flight investigation of a model of a spin-resistant fighter configuration. NASA TN D-7716.
4. C.O. O'Leary. Wind-tunnel measurement of lateral aerodynamic derivatives using a new oscillatory rig, with results and comparisons for the Gnat aircraft. RAE Technical Report 77159 (1977)



Fig 1 RAE oscillatory derivative rig



(a) Lateral spring unit (No. 4, Table 2)

(b) Longitudinal spring unit (elevation) (No. 1b, Table 2)

Fig 2 Examples of spring units used at RAE

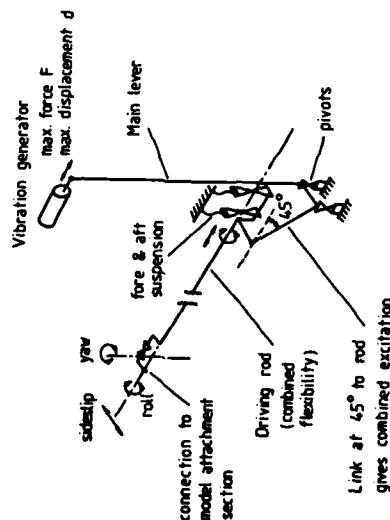


Fig 3 Combined excitation system

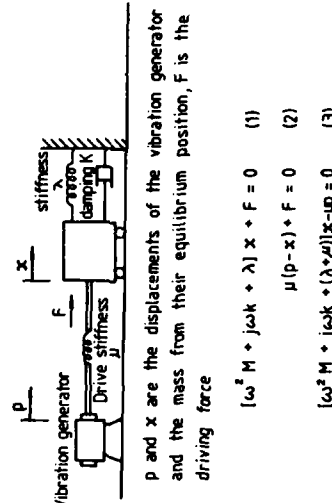


Fig 4 Excitation measurement

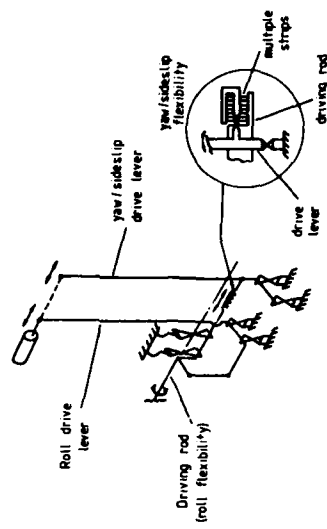


Fig 5 Separate roll and yaw/sideslip excitation system

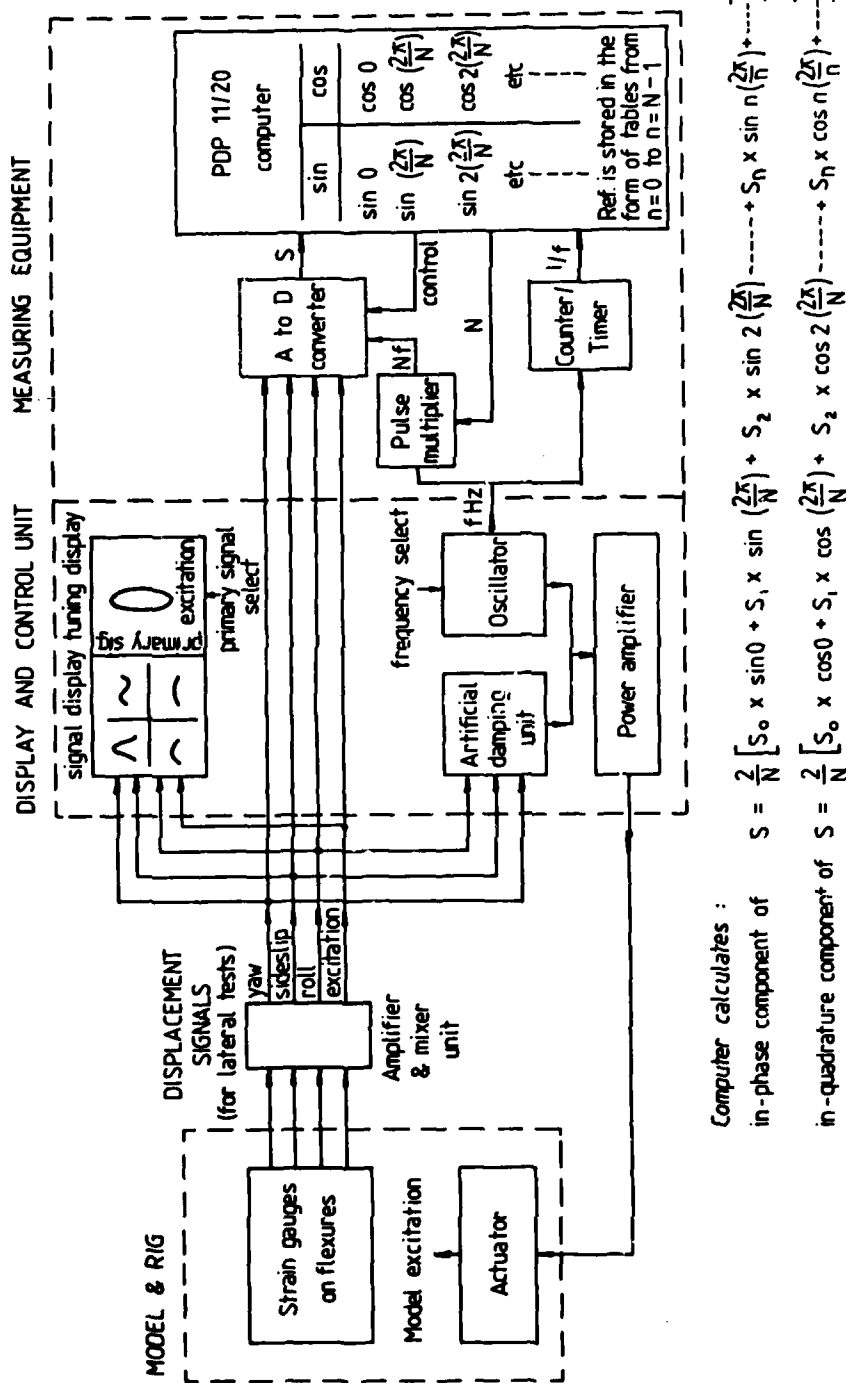
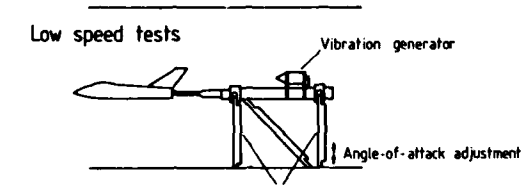
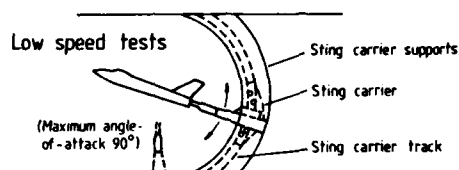


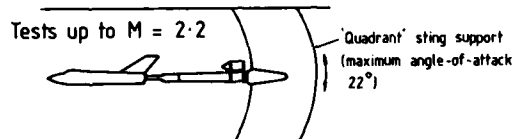
Fig 6 RAE wind-tunnel oscillatory derivative measurement



(a) 13ft x 9ft wind-tunnel 'A' frame support



(b) 13ft x 9ft high angle-of-attack support



(c) 8ft x 8ft wind-tunnel support

Fig 7 Wind-tunnel sting supports



Fig 8 Model A on high angle-of-attack sting support in 13ft x 9ft low speed wind tunnel

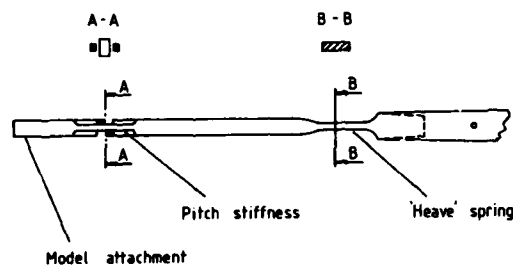


Fig 9 DFVLR sting

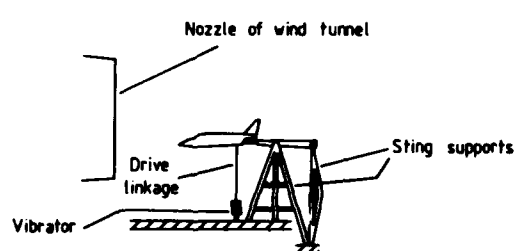
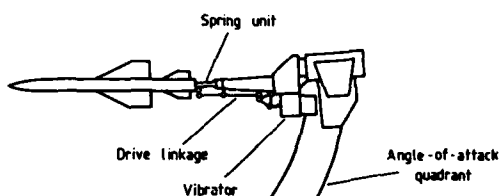


Fig 10 DFVLR support system for open section wind tunnel

Fig 11 DFVLR support system for closed section wind tunnel

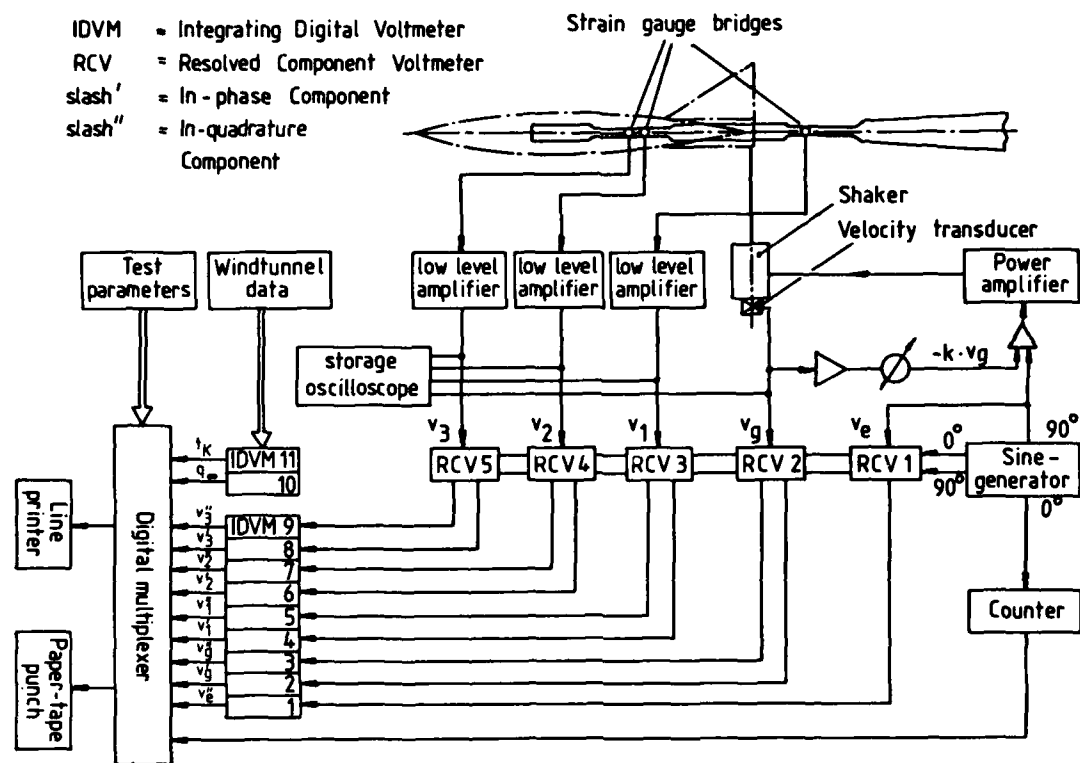


Fig 12 Block diagram of DFVLR measuring equipment

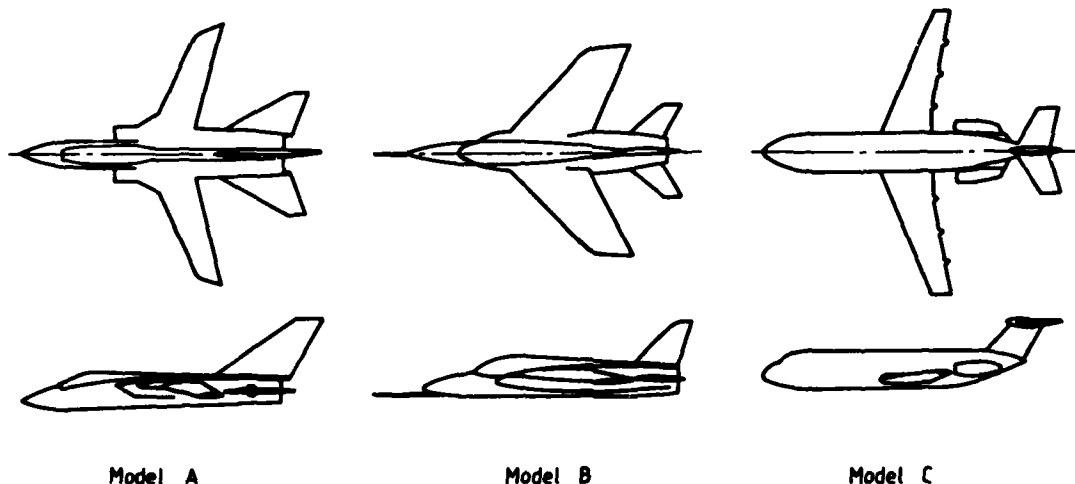


Fig 13 Sketches of models tested

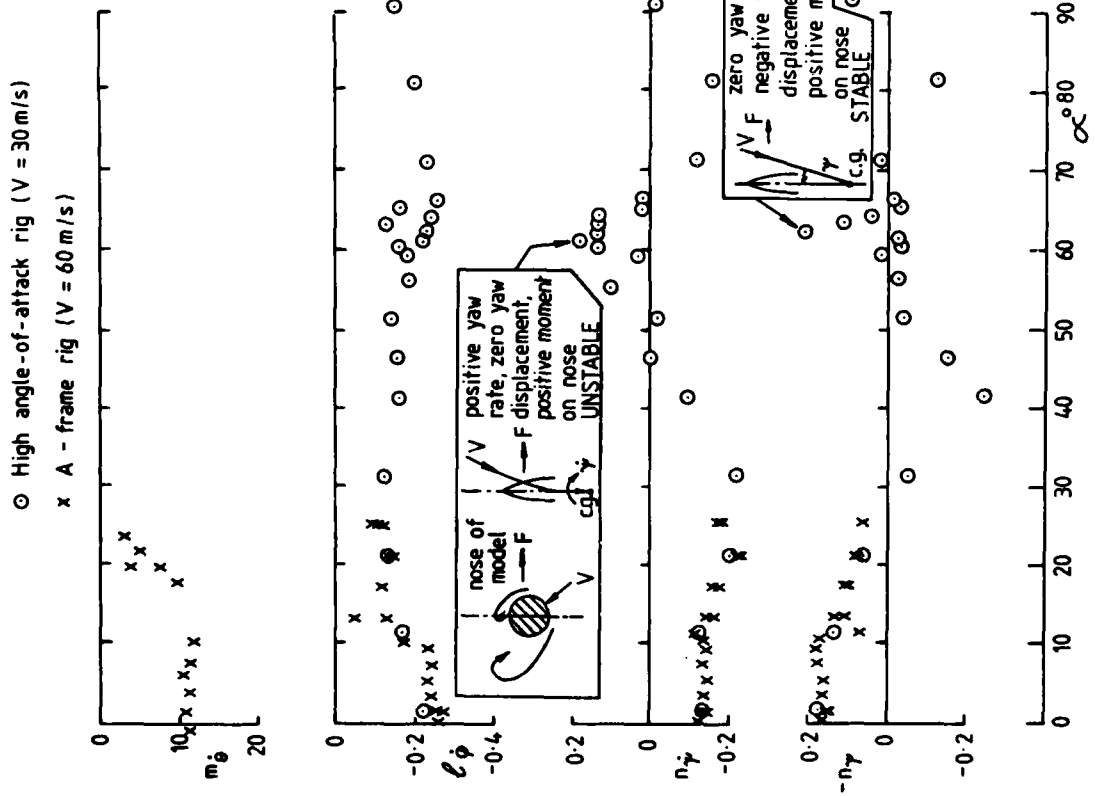
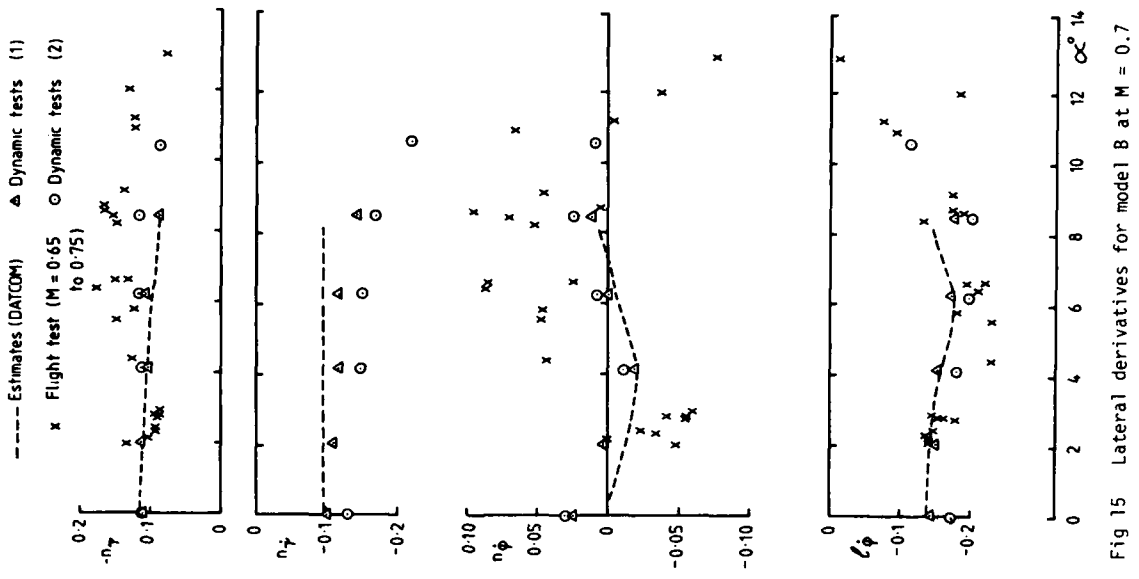


Fig 14 Derivatives for model A at low speed

Fig 15 Lateral derivatives for model B at  $M = 0.7$

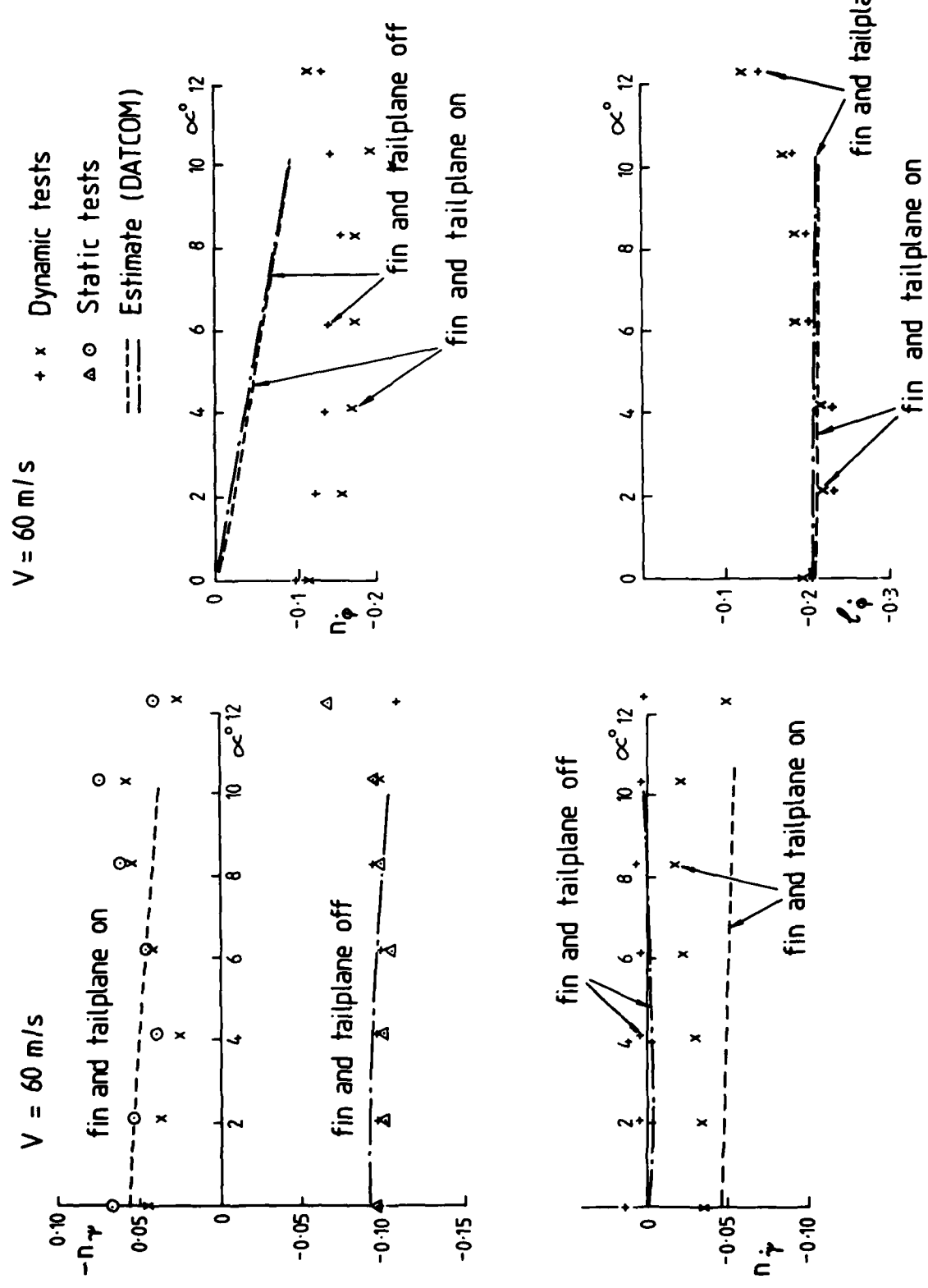


Fig 16 Lateral derivatives for model C at low speed

## ROTARY AND MAGNUS BALANCES

Gerald N. Malcolm  
Ames Research Center, NASA  
Moffett Field, California 94035, U.S.A.

## SUMMARY

This lecture presents a description of two wind tunnel techniques for determining part of the aerodynamic information required to describe the dynamic behavior of various types of vehicles in flight. Force and moment measurements are determined with a rotary-balance apparatus in a coning motion and with a Magnus balance in a high-speed spinning motion. Coning motion is pertinent to both aircraft and missiles, and spinning is important for spin stabilized missiles. Basic principles of both techniques are described, and specific examples of each type of apparatus are presented. Typical experimental results are also discussed.

## 1. INTRODUCTION

In previous lectures in this series, various characteristic motions that must be produced in the wind tunnel to determine experimentally the aerodynamic coefficients that properly represent the governing forces and moments of a vehicle in various modes of flight have been discussed. One of these motions, illustrated in Fig. 1, is described as a "coning" motion, or continuous rolling of the vehicle's longitudinal axis about the free-stream velocity vector. Another, shown in Fig. 2, is a continuous rolling

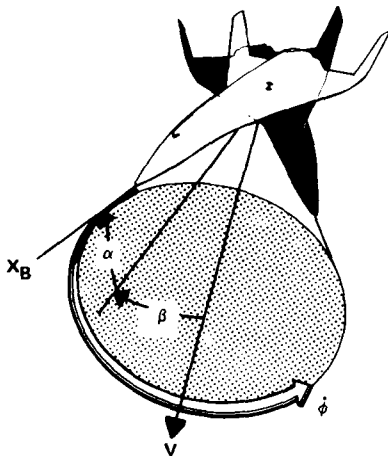


Figure 1. Coning motion.

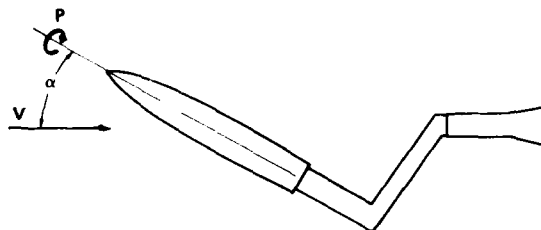


Figure 2. Spinning motion.

motion of the body about its own longitudinal axis or "spinning" as usually associated with spin-stabilized bodies of revolution or axisymmetric bodies. The purposes of this lecture are (1) to describe in some detail the reason for producing each of these motions in the wind tunnel; (2) to present some examples of devices that are currently in use or are under development to accomplish these experiments; and (3) to show some typical experimental results. The lecture, then, will be divided into two sections, as the title indicates. The first will be devoted to devices sometimes referred to as rotary-balance apparatuses, that produce the "coning" motion; the second part will deal with devices, referred to as Magnus balances, that provide high-speed spinning motions.

## 2. ROTARY-BALANCE TECHNIQUE

The need for rotary-balance apparatuses has been recognized by aerodynamicists for a long time. A brief historical background of that recognition, presented recently in Ref. 1, is summarized here.

## 2.1 Background

Before modern efforts to derive a mathematical model of the aerodynamics of an airplane maneuvering at high angles of incidence, it was generally recognized by early aviation researchers that to analyze spin motions, one needed some method for determining the steady-state rotational flow aerodynamics. For example, Glauert (Ref. 2) attempted to obtain these data theoretically in 1919, using strip theory, by calculating the local velocity and angle of attack of each strip of the aircraft as a function of rotation rate and its distance from the center of rotation. By the early 1920s, techniques with rolling balances were being developed to some degree to obtain these data experimentally. By 1926, Gates and Bryant (Ref. 3) concluded that the simple rolling balance should be replaced with one that reproduces an actual spin motion in the wind tunnel. This type of apparatus is known today as a rotary-balance apparatus. In 1928 Irving and Batson (Ref. 4) stated that using only static nonrotational force and moment data leads to erroneous conclusions about spin motion, and that rotary-balance data should be used. By 1933, Allwork (Ref. 5) reported

on a rotary balance in use in the British NPL 7-Foot Wind Tunnel. Bamber and Zimmerman (Ref. 6) reported in the same year that a rotary balance had been installed in the NACA 5-Foot Vertical Tunnel. This particular apparatus was capable of measuring three force components and three moment components as functions of angle of attack, angle of sideslip, and rotation rate. Several years afterward, Bamber and Zimmerman (Ref. 7) and Bamber and House (Ref. 8) reported a method for solving the three moment equations for steady-state equilibrium conditions, using rotary-balance data, and thereby predicted steady spin conditions. This particular analytical technique was developed out of absolute necessity. Attempts to solve simultaneously the six equations of motion (three rotational and three translational motions) and other associated mathematical expressions before the availability of analog and high-speed digital computers was a monumental task that required laborious manual integration procedures.

The effectiveness of the first NACA rotary balance (Ref. 6) was limited by the model and tunnel size. Also, the six-component balance, which was mounted externally to the model, was relatively large compared with the model and of dubious accuracy. By 1945 a new rotary balance (Ref. 9) was installed in Langley Research Center's 20-Foot Spin Tunnel. Because of limited instrumentation capability, an inordinate amount of time was required to obtain even a small amount of data, which in many cases was not particularly repeatable. For many reasons, the rotary balance was all but abandoned in the late 1940s. By the mid-1950s, fighter configurations were being developed with their mass much more heavily concentrated in the fuselage than in previous aircraft; one of the concerns was vertical tail loads during rolling pullout maneuvers due to inertial coupling effects. Analog computers became available about the same time, and a large number of engineers were introduced to large-angle, six-degree-of-freedom calculations. Eventually, the "inertial coupling" studies were extended beyond stall by simply extending conventional aerodynamic models to higher angles of attack. The need for rotary-balance data on aircraft configurations was virtually overlooked from the mid-1950s to the late 1960s. An experiment was conducted by Clarkson (Ref. 10), however, which showed that the autorotational effects of an airplane nose could dominate the total moment on a configuration, including pro-spin contributions from the wings, thus leading to spin. In some instances, extension of conventional aerodynamic models to high angles of attack may be attributed to the lack of rotary-balance data to use in predicting flight motions, and it was expedient to use static data alone. Unfortunately, some investigators claimed success in matching spin flight records with static data alone. Despite the fact that others found the computational methods lacking when applied to their configurations, it became the conventional technique for calculating spin motions. Wykes and Casteel (Ref. 11) compared, with reasonable success, flight-test results and computed results for an airplane in a spinning motion. They used static aerodynamic coefficients obtained from wind-tunnel tests and rotary derivatives calculated from strip theory, or "strip hypothesis." Briefly, strip hypothesis assumes that the airplane component of interest can be divided into numerous narrow strips and that the force acting on each strip is the same as it would be if the whole component were moving without rotation but with linear velocity and with an angle of attack equal to that of a point lying on the strip. It also assumed that there are no induced effects between adjacent strips. Scherer and Aguesse (Ref. 12) demonstrated, in experiments with a rotary-balance apparatus, that the variation of yawing moment with rotation rate can be very nonlinear and that an estimate from strip theory assuming linearity may be in error for some configurations.

To resolve the noted discrepancies, NASA supported studies to determine the ability of the accepted analytical technique to compute the flight motions from unstalled flight through the incipient, developed, and recovery spin phases. Two of these studies (Refs. 13, 14) showed that spin motions computed in the conventional manner, with static aerodynamics data, did not match the time histories from a free-flight drop-model, whereas the spin computed from rotary-balance data did match. It was, therefore, indicated very clearly that aerodynamics determined from a rotary balance were indeed significant for the study of steady spin motions and warranted a continuing effort to measure them.

It is also important to note that in addition to the demonstrated need for rotary-balance data to support studies of steady-state spin and spin recovery, the coning motion of the rotary-balance is also one of the fundamental characteristic motions derived in the mathematical models of Tobak and Schiff (Refs. 15, 16) and is required even for prediction of conventional, nonspinning maneuvers. Prior to the formulation of the mathematical models derived by Tobak and Schiff for airplane configurations, some work had been done at Ames Research Center on bodies of revolution undergoing combined "coning" and "spinning" motions (Refs. 17-19).

## 2.2 Rotational Flow Field

A simple explanation of the flow field (in terms of local velocity induced from rotation and free-stream velocity contributions) in a rotational regime will be helpful in understanding the importance of acquiring aerodynamic data in this mode. Referring to Fig. 3, a simple case is one corresponding to an airplane in a flat spin. In this case the free-stream velocity vector is perpendicular to the  $x-y$  plane of the aircraft, and the aircraft is spinning about its  $z$  axis (which is colinear with the velocity vector). The local flow angle at any point on the airplane is dependent on both the velocity due to rotation and the free-stream velocity (or sink rate in the case of a vertical spin axis). In fact, it is proportional to the ratio of the velocity due to rotation at a particular point on the airplane to the free-stream velocity. It is common practice to use a reference nondimensional rotation rate expressed in terms of the angular velocity  $\omega$ , linear, or free-stream velocity  $V$ , and a model geometric reference, that is, half the wing span,  $b/2$ . In this case, the ratio of the velocity at the wing tip to the free-stream velocity is then  $(\omega b/2)/V$  or  $\omega b/2V$ . This is also equal to the arc tangent of the helix angle at the wing tip when an airplane is in an equilibrium steady spin. (Note,  $\omega$  and  $\Omega$  are used interchangeably throughout the text.)

Since airplanes do not necessarily spin about an axis coincident with the center of mass, there may be a spin radius, as defined in Fig. 4. Efforts have been made in the development of some rotary-balance rigs to provide a capability for spin radius. It can be shown, however, that spin radius can be simulated through properly selected values of angles of attack and sideslip (additional sideslip angle is nearly equivalent to providing a spin radius).

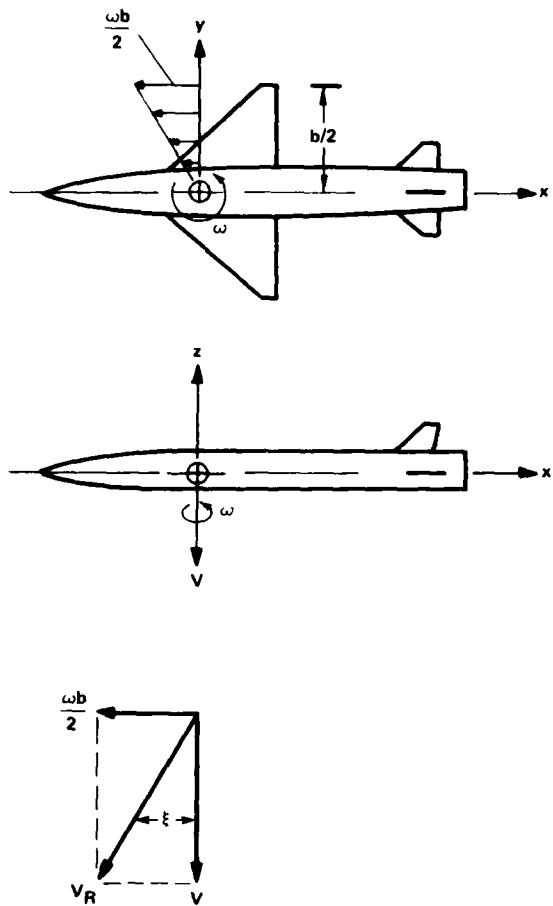


Figure 3. Rotational flow field, helix angle (flat spin case).

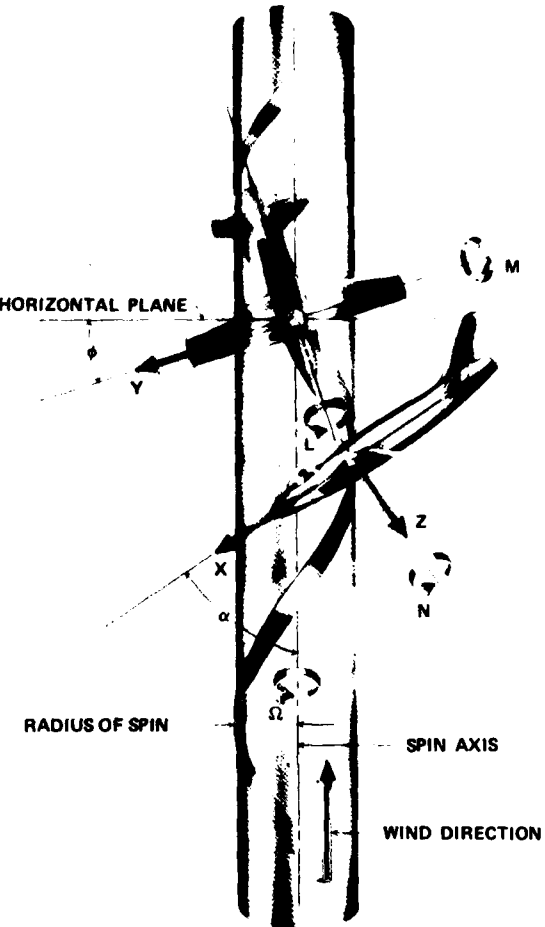


Figure 4. Illustration of steady spin with spin radius.

### 2.3 Coning Motion in the Wind Tunnel

To generate a coning motion in the wind tunnel, a model is fixed to some type of support system that can be rotated at constant rotation speed about an axis that is usually parallel to the free-stream velocity vector of the wind tunnel. In so doing, the model sees a constant attitude with respect to the airstream throughout a rotational cycle. The primary purpose of the experiment is to determine the forces and moments on the model as a function of the coning rate. These forces and moments are typically determined from a six-component strain-gage balance mounted internally in the model and fastened to a sting, either through the rear or tail of the model or, for high angles of attack, through the top of the model fuselage. A typical example of model-mounting procedure is shown in Fig. 5.

#### 2.3.1 Rotary tare loads

It must be recognized that when the model is rotated in the wind tunnel, there are contributions to the forces and moments measured by the balance from three sources. The first is from the inertial forces and moments of the model itself, which vary with model attitude and rotation speed; the second is from the gravitational (model weight) cyclical variation, which can either be compensated for or filtered out with low-pass filters; and the third is from the aerodynamic loads. In order to separate the aerodynamic contribution, it is necessary to measure the inertial contributions in a wind-off condition and to subtract these tare loads from the combined loading with the wind on.

The magnitude of the inertial loads can be calculated if the moments of inertia about the principal axes of the model are known and if the location of the model center of mass with respect to the rotation axis is known. The moments due to inertia effects are derived in the Appendix; it is assumed in the derivation that the model center of mass is on the spin axis. These moments are derived in terms of the model moments of inertia, angles of attack and sideslip, and rotation rate. The equations are the following:

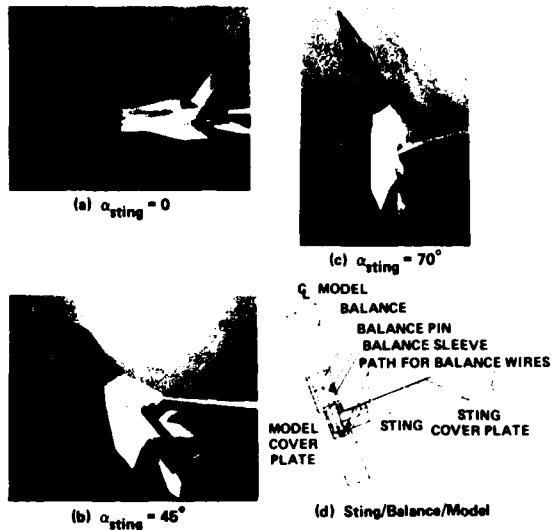


Figure 5. Typical sting/model/balance mounting arrangements.

Roll moment:

$$L = \omega^2 [\sin \beta \sin \alpha \cos \beta (I_y - I_z)]$$

Pitch moment:

$$M = \omega^2 [\sin \alpha \cos \beta \cos[\sin^{-1}(\sin^2 \beta + \sin^2 \alpha \cos^2 \beta)^{1/2}]] [I_z - I_x]$$

Yaw moment:

$$N = \omega^2 [\sin \beta \cos[\sin^{-1}(\sin^2 \beta + \sin^2 \alpha \cos^2 \beta)^{1/2}]] [I_x - I_y]$$

where

- $\alpha$  = angle of attack
- $\beta$  = angle of sideslip
- $\omega$  = rotation rate
- $I_x, I_y, I_z$  = moments of inertia about body  $x, y, z$  axes

The resulting equations for the three moments illustrate several interesting points. First, the magnitude of the inertial moments is a function of  $\omega^2$  and depends on differences in body moments of inertia. Second, if the moments of inertia of the model about the point in the model intersected by the coning axis are known, then the rotary moment tare can be calculated analytically. To minimize the magnitude of the inertial tare loads, one must minimize the moments of inertia or at least minimize the moment of inertia differences. Minimizing the moments of inertia can be achieved by constructing models of low-density material and concentrating the mass near the center of rotation. However, requirements for adequate material strength to withstand the aerodynamic loads tends to lead to model designs of higher density material; so model design criteria are conflicting, and a compromise must usually be arrived at.

Despite the relatively straightforward equations for calculating the inertial tares, there are numerous problems in relying on computed values to subtract from the wind-on measured loads. An important consideration is that the model/sting combination will experience some deflection during rotation, and the mass center of the model will not be at exactly the same location relative to the rotary axis at all rotation speeds (even if the center of mass of the model is on the rotary axis to begin with at low speeds, as was assumed in the above derivation of the moment tare formulas). Any changes during the rotational motions that affect either the moments of inertia about the rotation center of the model or the model attitude will cause the tare load to vary from the analytically determined value. Therefore, it has been found necessary to measure wind-off tare loads at the model attitude and rotation rate conditions planned for wind-on tests. These measurements are stored in the data acquisition system and later subtracted from the wind-on measurements.

To be absolutely correct, tare loads should be measured with the model either in a vacuum or surrounded by an enclosure that rotates with the model to prevent any interaction of the surrounding still air with the model as it rotates. In some cases, depending on such factors as model size, rotation rates, and expected wind-on aerodynamic loads, the small contribution from this effect can be ignored. Where it cannot be ignored, enclosures such as thin-shelled rigid spheres (a hollow sphere with its center on the spin axis has no tare loads and therefore no influence on sting deflection, etc., because all moments of inertia are

equal) fastened to the sting and surrounding the model have been used; or, in some cases, if the tunnel cannot be pumped to a near vacuum, tare measurements at several tunnel pressure levels can be determined and the results extrapolated to the absolute vacuum condition. In most cases, the tare measurements can be made while the tunnel is occupied for the actual wind-on tests, but in cases in which tunnel occupancy time is at a premium, these tares must be determined in a separate test area outside the tunnel prior to tunnel entry. Tare tables can be produced, with values determined at conditions (i.e., model attitude and rotation rate combinations) identical with those to be run in the tunnel or, alternatively, a sufficient number of measurements can be made over a wide enough range of variable combinations to allow accurate interpolation of table values for any combination chosen later to run in the tunnel.

#### 2.4 Rotary-Balance Apparatuses

A number of rotary-balance apparatuses have been developed or are being developed for use in a variety of wind tunnels, both in the United States and in Europe. The next section will briefly describe some of these and show examples of results obtained from them. The first examples are drawn from apparatuses developed in England, France, Italy, and West Germany; the U.S. apparatuses, at NASA's Langley Research Center and Ames Research Center are then described. These examples do not necessarily cover all such apparatuses in existence; they are simply the ones the author is most familiar with because of published reports or personal contact with the researchers involved with them.

##### 2.4.1 British Aerospace/RAE apparatuses

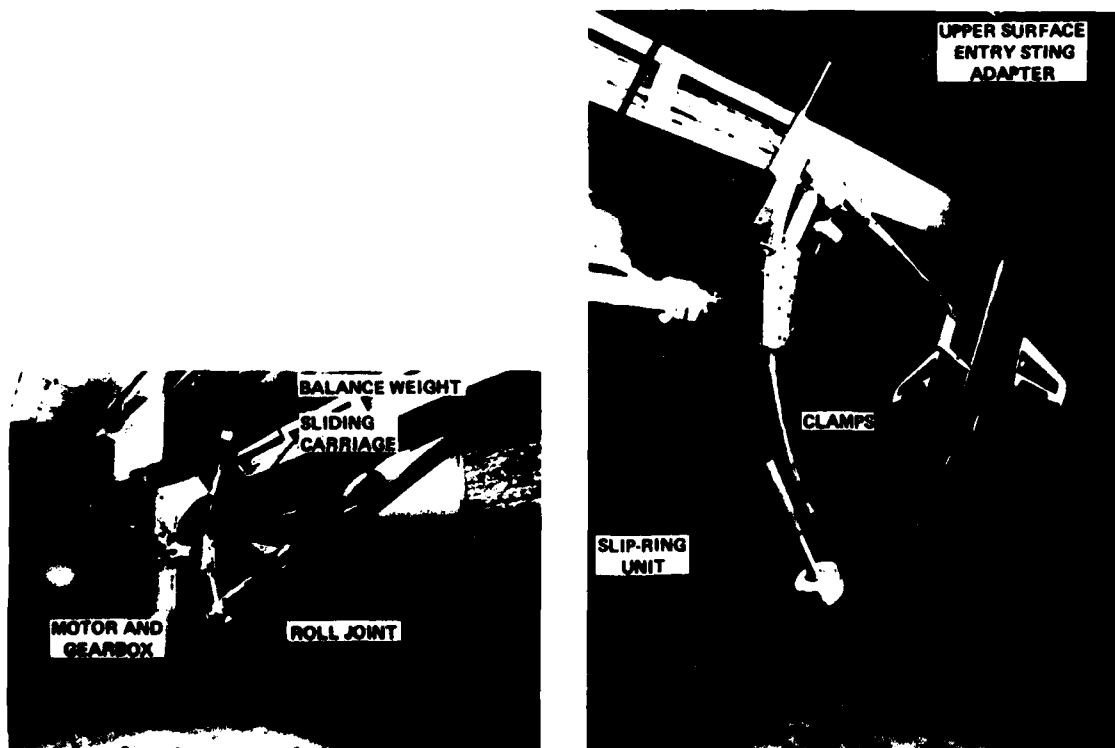
In Ref. 20, Matthews of British Aerospace discusses two apparatuses. One is for use at low Mach and Reynolds numbers in the British Aerospace (B.Ae.) 5.5-m LSWT (Low Speed Wind Tunnel) and the other, sponsored by the R.A.E., is primarily for testing in the B.Ae. 1.2-m HSWT (High Speed Wind Tunnel) at Warton; the latter apparatus can also be accommodated in a number of other U.K. facilities. The low-speed rig is operational; Ref. 20 provides a detailed description of the apparatus and gives some examples of results obtained with it. The high-speed rig was still under development at the time Ref. 20 was published, but initial results from the checkout phase were presented.

The low-speed rig is shown in Figs. 6 and 7. The basic capabilities of the rig are:

$$-45^\circ \leq \alpha \leq 90^\circ$$

$$-45^\circ \leq \beta \leq +45^\circ \text{ (at } \alpha = 0^\circ\text{)}$$

$$\frac{w_b}{2V} \leq 0.2$$



(a)  $0 < \alpha < 45^\circ$ .

(b)  $45^\circ < \alpha < 90^\circ$ .

Figure 6. British Aerospace LSWT rotary rig.

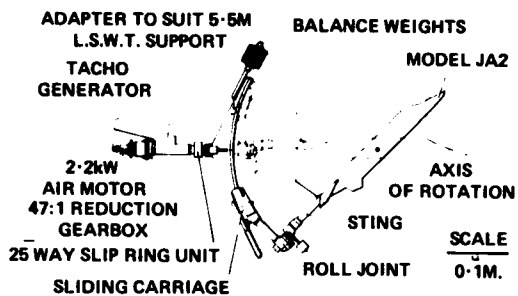


Figure 7. British Aerospace LSWT rotary rig.

The angle-of-attack range is achieved by mounting the model either through the base or the top and moving the sting around an arc centered at the model reference center. Sideslip is achieved by rotating the model about its body longitudinal axis. The rig is driven by an electric motor and can achieve rotational speeds to 60 rpm. The rig is balanced statically about the spin axis to reduce the cyclic gravitational variations on the required torque to drive the rig. Dynamic balancing was not attempted since the speeds are fairly low and because it is difficult to achieve in a simple design.

Model attitude changes are made manually (not a severe handicap in a 1-atm tunnel); this greatly simplifies the apparatus design. Balance signals are taken out through a 25-channel slip-ring unit. Output data from the balances are averaged over at least a cycle of rotation to eliminate the need for gravitational tares and to smooth unsteady data to acquire a mean value.

The high-speed rig, shown in Fig. 8, was designed primarily for operation in the 1.2-m HSWT at B.Ae., Warton Division (a blowdown tunnel), but it was also required to function in three other U.K. tunnels: the

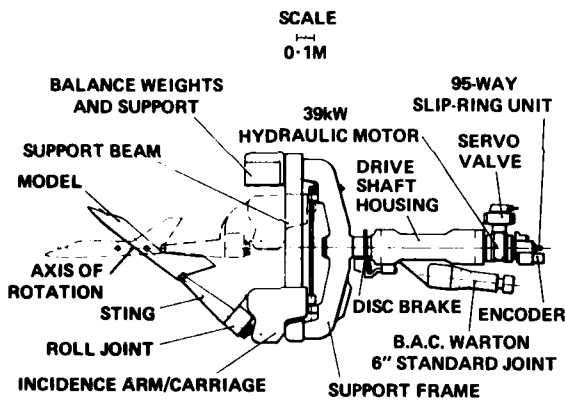


Figure 8. British Aerospace multifacility rotary rig.

2.7- by 2.1-m LSWT at B.Ae., Warton Division; the 9- by 8-Foot Transonic Tunnel at A.R.A., Bedford; and the 8- by 8-ft HSWT at R.A.E., Bedford. The design specifications included a maximum Mach number of 0.95, maximum Reynolds number of  $46 \times 10^6/m$ , angle of attack to  $40^\circ$  ( $0^\circ$ - $90^\circ$  in the 2.7- by 2.1-m LSWT), sideslip angles to  $10^\circ$  (up to  $\alpha = 20^\circ$ ), and roll rate of 600 rpm. This produced a reduced spin rate,  $w_b/2V$ , of 0.14 for  $M = 0.4$ , using a 1/20-scale model of a typical combat fighter. An additional requirement for this rig, because of the desired operation in a blowdown tunnel (with run time ranging from 25 sec at  $M = 0.4$  to 9 sec at  $M = 0.95$ ) is the capability of rapidly changing from one rotational speed to another and acquiring data at each stabilized incremental rotation rate. Unlike the 5.5-m LSWT rig, dynamic balancing was considered for the high-speed rig because of the high centrifugal-force imbalances caused by high rotation rates. The rig has provisions for choosing one of two different longitudinal positions of the counterweight, as well as being able to change the mass and radial position. One of the tasks in the checkout phase of this apparatus is to investigate the problems of dynamic balancing. Data acquisition and analysis are very similar to those described for the low-speed rig but with some special provisions to handle the data at much higher data rates because of the short run time.

An example of results obtained on the low-speed rig is shown in Fig. 9, where the roll derivative  $L_p$  is shown at different angles of attack as obtained from the rotary balance along with flight-test data below  $\alpha = 20^\circ$  and theoretical estimates at  $\alpha > 20^\circ$ . Experimental results agree well with flight-test data to  $\alpha = 20^\circ$  but are significantly different from the theoretical estimates above  $\alpha = 20^\circ$ .

#### 2.4.2 I.M.F. Lille apparatus

A rotary balance apparatus has recently been developed for operation in the spin tunnel at I.M.F. Lille in France (Ref. 21). A sketch of the apparatus installed in the spin tunnel is shown in Fig. 10. The maximum rotation rate  $\Omega$ , with a typical model of 1.5-m span, is 100 rpm, and the airstream is capable of 40 m/sec. Forces and moments are measured by an internal strain gage balance. Detailed sketches of the rotary-balance apparatus and the angular orientation capabilities of the various components are shown in Fig. 11. By rotating the model through angles  $\theta$ ,  $\phi$ , and  $\psi$  the model can be oriented with respect to the

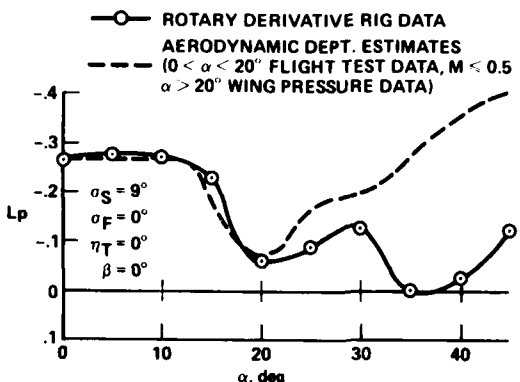


Figure 9. Rolling moment derivative vs angle of attack from British Aerospace LSWT rotary rig.

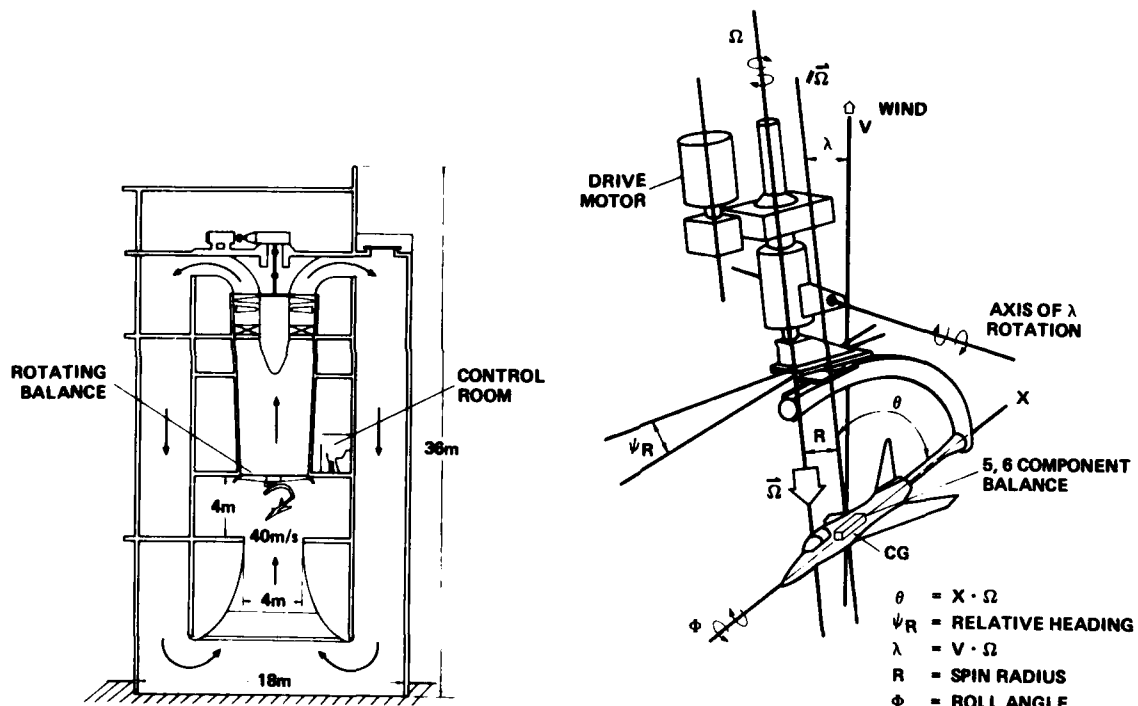


Figure 10. I.M.F. Lille rotary apparatus mounted in SV4 tunnel.

Figure 11. Degrees of freedom of I.M.F. Lille rotary apparatus.

airstream at desired angles of attack and sideslip. The range for these angles is  $\theta = 0^\circ$  to  $90^\circ$ ,  $\phi = 0^\circ$  to  $\pm 180^\circ$ , and  $\psi = 0^\circ$  to  $\pm 180^\circ$ . It is also possible to orient the rotational axis  $\Omega$  at an angle  $\lambda$  up to  $30^\circ$  to the airstream. By doing so, the model does not see constant angles of attack and sideslip through one revolution. Instead,  $\alpha$  and  $\beta$  vary sinusoidally with an amplitude,  $\lambda$ , about their mean values. Spin radii up to 0.2 m are also possible. Either a 5- or 6-component balance can be used as well as accelerometers and pressure transducers. Data from this apparatus were not available at the time the lecture was prepared.

#### 2.4.3 Aeronautica Macchi apparatus

Aeronautica Macchi in Italy has been building and using various rotary-balance apparatuses since 1950. Bazzocchi reported on several apparatuses in Ref. 22. Figure 12 is a sketch of an early rig, which used a "windmill" as a driver. The apparatus in Fig. 13 shows a rig, first used in 1956, for measuring moments around the spin axis and a yaw axis normal to it. The model angular orientation could be varied in pitch and wing tilt (or roll about longitudinal axis). Spin radius could also be varied. A new balance was built later (Fig. 14), and has been used for most experiments up to 1975. This particular apparatus, which can accommodate models with span up to 1.3 m, rotates at speeds to 150 rpm, with wind speeds to 50 m/sec yielding a reduced spin parameter,  $wb/2V$  up to 0.28. Measurements consist of pitching, rolling, and yawing moments and side force. Lift and drag were assumed to be obtainable, with sufficient accuracy, from fixed-model tests. Spin radius was set to zero for all tests conducted on this rig. More recently, a new apparatus capable of measuring all six components of forces and moments has been developed (Fig. 15).

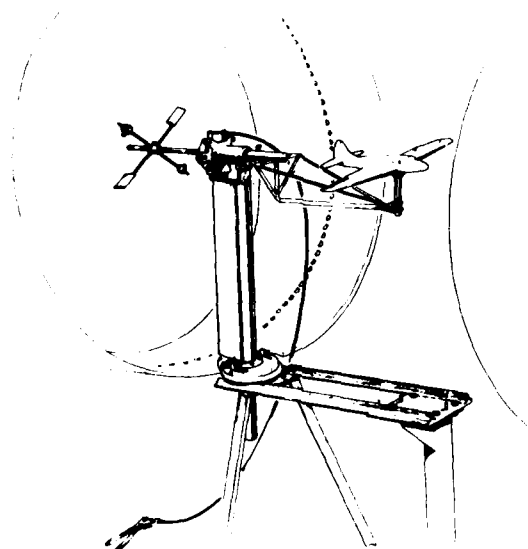


Figure 12. Early "windmill" rotary apparatus:  
Aeronautica Macchi.

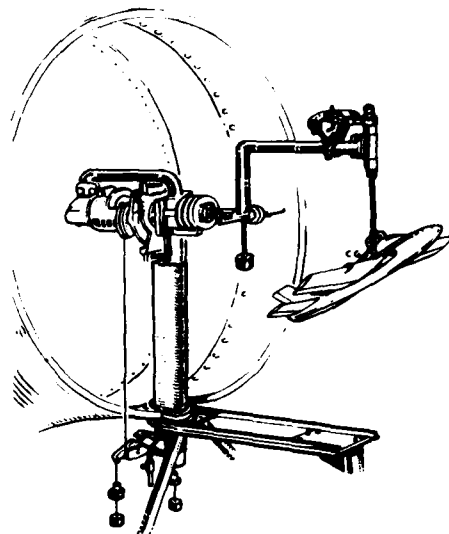


Figure 13. Three-component rotating balance:  
Aeronautica Macchi.

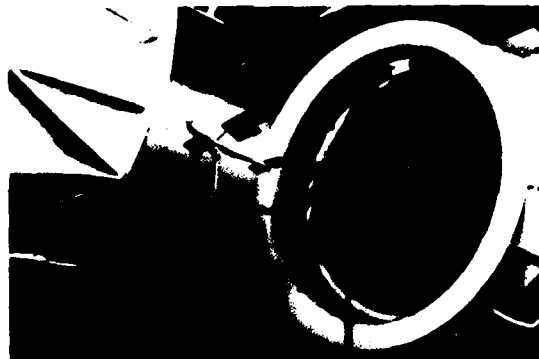


Figure 14. Four-component rotary balance: Aeronautica Macchi.

This apparatus provides for large spin radii and pitch attitudes to 90° (to simulate flat spin). A circular rail is provided to react to the large centrifugal force on the model and eliminate deflection of the supporting sting. Gravity forces and rotating loads due to model inertia are handled as they are in most other data acquisition systems.

An example of the type of data achievable from such an apparatus is illustrated in Fig. 16. The roll moment (measured in stability axes) is shown as a function of  $pb/2V$ , where  $p$  is the roll rate (equivalent to  $\omega$ , coning rate) about the apparatus spin axis (parallel to the tunnel wind axis). At small angles of attack, the moment is damped. For  $\alpha = 12^\circ$  and  $pb/2V = 0.12$  a discontinuity is experienced due to a local stall on the downgoing wing. As  $\alpha$  increases, the discontinuity occurs at lower roll rates and eventually at  $pb/2V \sim 0.8$  and  $\alpha = 14^\circ$  the roll moment becomes positive, and conditions for autorotation are present. Figure 17 shows the effects of hysteresis on the recover from autorotation. Although undoubtedly affected by Reynolds number, the presence of this phenomenon indicates a possibility for more than one equilibrium spin condition.

#### 2.4.4 DFVLR-Cologne apparatus

A new rotary-balance apparatus (Ref. 23) has been constructed for operation primarily in the 3-m low-speed tunnel of DFVLR-Cologne in West Germany. The general arrangement of the apparatus is shown in Fig. 18. The rotary balance was constructed as an attachment to an appropriate existing model support (1, Fig. 18). The angle between the rotary vector and the speed vector  $y_\Omega$  can be varied by changing the attachment with the model support. However, flight mechanical investigations of the free-flight rolling motion of fighter-type aircraft, which follows constant aileron inputs, showed that the angle  $y_\Omega$  fluctuates around a relatively small mean value. As a result, it was decided to select  $y_\Omega = 0$  for the rotary tests.

The main mechanical components of the rotary balance are the large bearing box with spindle (2, Fig. 18), the hydraulic drive system including a tooth belt transmission with a gear ratio of 1:4.5 (3), a device for remote setting of the angle of pitch (4), interchangeable stings (5), and a six-component strain-gage balance joined to the model (6).

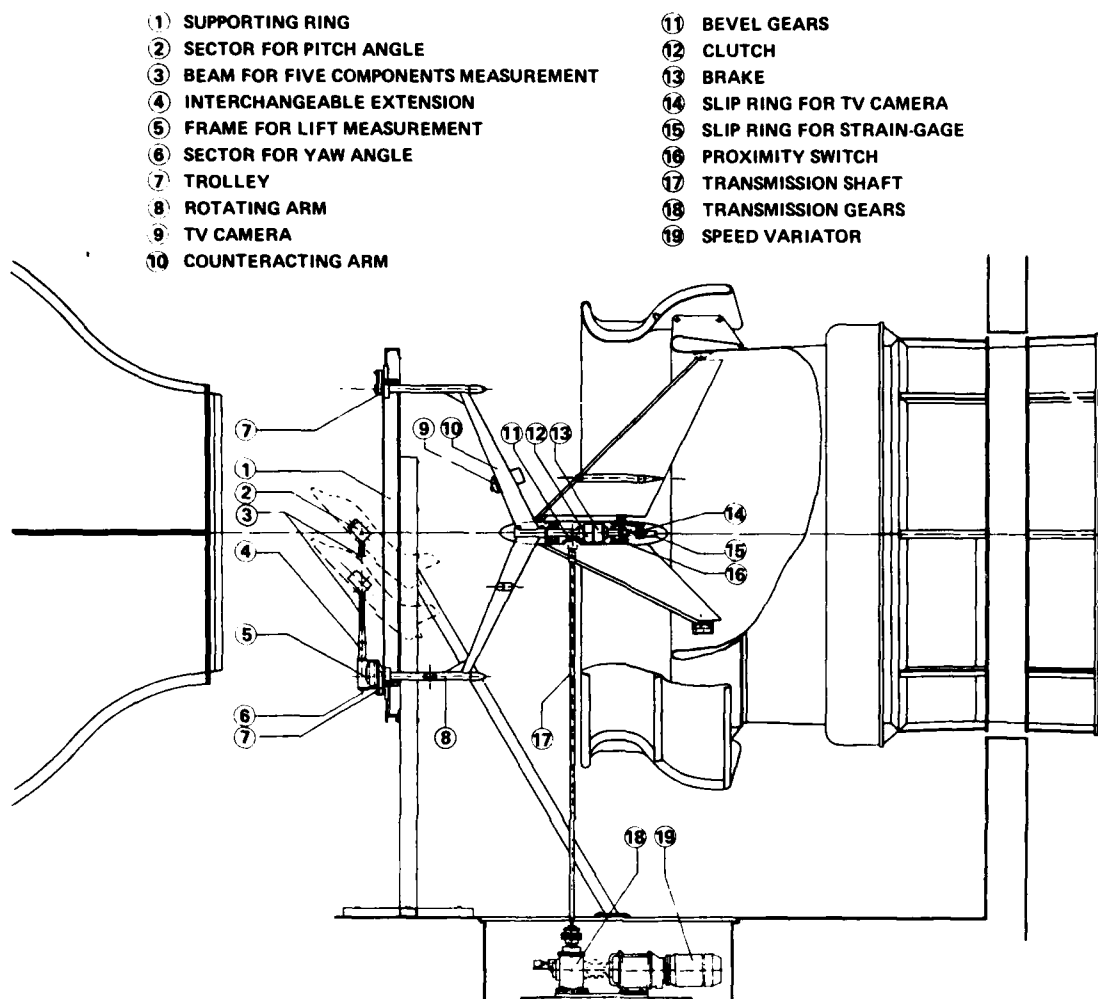


Figure 15. Six-component balance: Aeronautica Macchi.

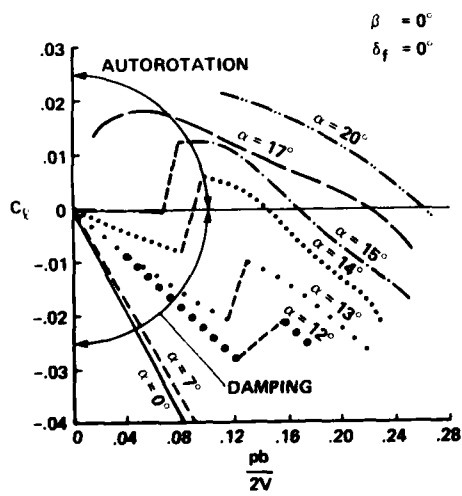


Figure 16. Roll damping of airplane model from Aeronautica Macchi six-component rotary balance.

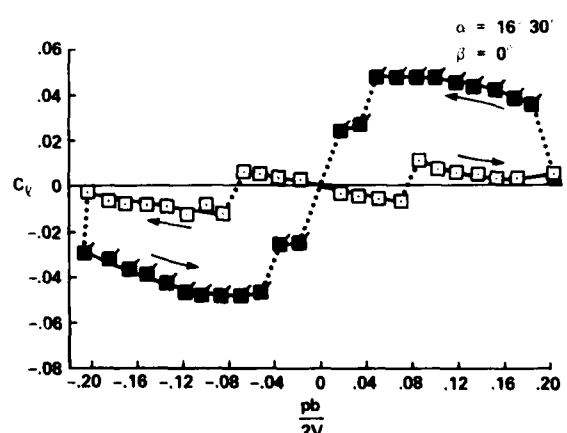


Figure 17. Roll damping (with hysteresis) for airplane model from Aeronautica Macchi six-component rotary balance.

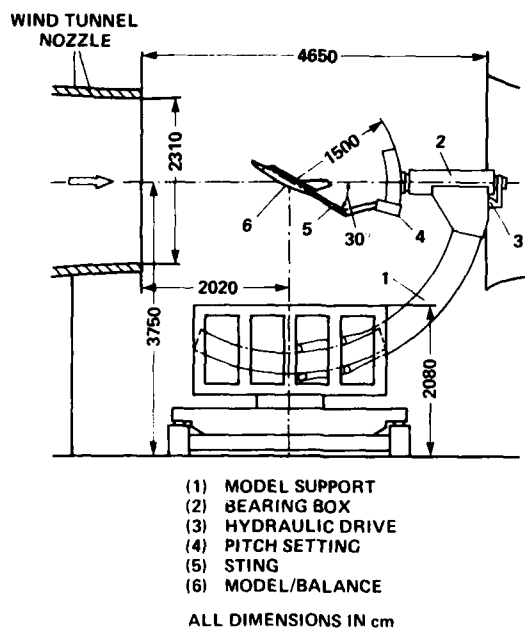


Figure 18. General arrangement of the DFVLR rotary derivative balance.

The rotary balance is driven by a constant displacement reversible hydraulic motor with a power of 4 kW. The speed — up to 300 rpm — and the direction of rotation are varied by controlling the fluid flow by means of an electrically controlled servo valve. An incremental angle encoder mounted at the downstream end of the bearing box is used to control the speed. This unit can also be used to position the model at any desired roll angle in the tunnel. Simulation of a finite spin radius can be achieved by rigid adapters fixed between the bent part and the forward part of the stings. Model wing spans of up to 1 m can be accommodated; the Reynolds number is limited by the maximum tunnel velocity of 80 m/sec.

#### 2.4.5 Langley Research Center apparatuses

There are two rotary-balance apparatuses in use at Langley Research Center (LRC). One was developed several years ago for operation in the Langley 9.1- by 18.2-m (30- by 60-ft) Full-Scale Tunnel; it is described very briefly by Chambers et al. (Ref. 24) and by Grafton and Anglin (Ref. 25). This apparatus is shown in Fig. 19. The rig was designed to accept relatively large models (typically about 1.5 m in span).

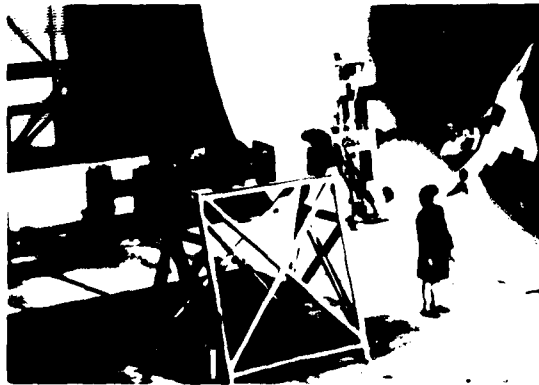


Figure 19. Large-scale rotary-balance apparatus: Langley Research Center.

for fighter models). In some cases, drop models, which are used for free-flight tests, can be tested on this rig; thus the aerodynamic data measured on the drop model in the tunnel will be at the same Reynolds number as that determined in flight. The angle of attack can be varied from 30° to 90° through a jackscrew located in the pitch motor housing. The moment center of the six-component internal strain-gage balance remains on the axis of rotation at all pitch attitudes. The reduced spin parameter  $wb/2V$  can be varied up to 0.28 at Reynolds numbers to  $3.3 \times 10^6/m$  ( $1 \times 10^6/ft$ ). Wind-off tare runs are conducted with the model enclosed within a thin, hollow sphere to eliminate still-air damping.

Typical results from the LRC large-scale rig are shown in the next few figures. Figure 20 shows the normal force and pitching moment coefficients as a function of the reduced spin rate,  $wb/2V$ , for  $\alpha = 45^\circ$  and  $90^\circ$ , for a fighter-type configuration. Both coefficients vary nonlinearly with rotation rate and are nearly symmetrical about  $wb/2V = 0$ . Figure 21 shows the lateral-directional coefficients of side force, yawing moment, and rolling moment with  $wb/2V$ . There is significant nonlinearity with rotation rate at

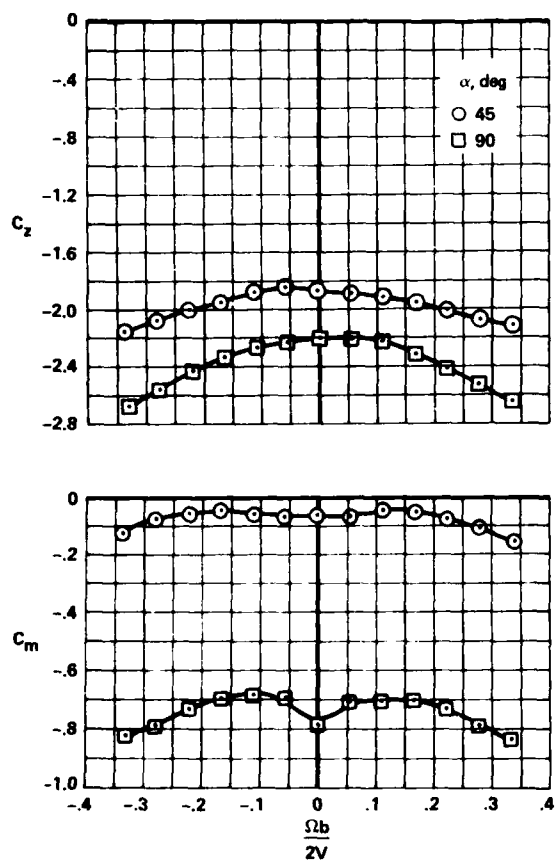


Figure 20. Longitudinal data from Langley Research Center's large-scale rotary-balance apparatus.

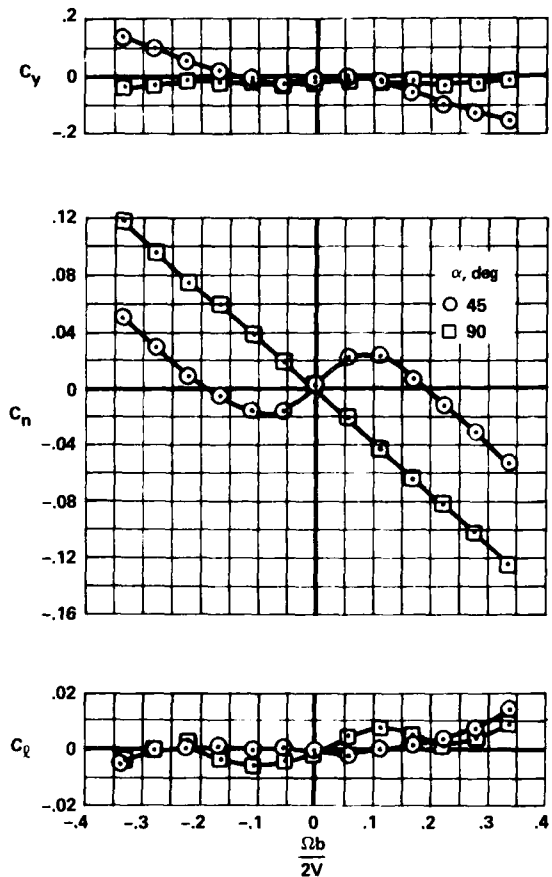


Figure 21. Lateral-directional data from Langley Research Center's rotary-balance apparatus.

$\alpha = 45^\circ$ , particularly in the yawing moment, which exhibits prospin moments between  $\Omega_b / 2V = 0$  and 0.2. At  $\alpha = 90^\circ$ , however, the coefficients are not nearly as nonlinear, particularly side force and yawing moment.

A second rotary-balance apparatus has recently been modernized for operation in the LRC spin tunnel; it is reported in some detail by Birlie and Bowman (Ref. 26). Figure 22 shows the apparatus in the tunnel with a general aviation model. Figure 23 is a sketch of the apparatus with some of the important components identified. The balance system's rotating portion, mounted on a horizontal supporting boom hinged at the wall, is mounted via cables from the wall to the tunnel center. The system's rotary arm, which rotates about a vertical axis, is attached to the horizontal supporting boom's outer end and is driven by a drive shaft through couplings and gears.

The test model is mounted on a strain-gage balance, which is affixed to the bottom of the rotary balance apparatus. Controls located outside the tunnel are used to activate motors on the rig that position the model to the desired attitude. The angle-of-attack range of the rig is  $0^\circ$  to  $90^\circ$ , and the sideslip angle range is  $\pm 15^\circ$ . Spin radius and lateral displacement motors allow the operator to position the moment center of the balance on the spin axis or at a specific distance from the spin axis. This is done for each combination of angle of attack and sideslip angle. It is customary to mount the balance's moment center at the cg location about which the aerodynamic moments are desired. Electrical current is conducted from the balance, and to the motors on the rig, through slip-rings located at the rig head.

The model can be rotated up to 90 rpm in either direction. A steady spinning airplane's motions can be simulated, using different rotational speeds and a specific airflow in the tunnel. Aerodynamic forces and moments can then be measured for values of  $\Omega_b / 2V$ , including the case of  $\Omega_b / 2V = 0$ , where static aerodynamic forces and moments can be obtained.

A NASA six-component strain-gage balance, mounted inside the model, is used to measure the normal, lateral, and longitudinal forces and the yawing, rolling, and pitching moments acting about the model body axis. Interactions between the six components, available from balance calibration tests, are accounted for after balance voltages are converted to forces and moments.

The data acquisition, reduction, and presentation system for the rotary balance setup is composed of a 12-channel scanner/voltmeter, a minicomputer, and a plotter. This equipment permits data to be presented via on-line digital print-outs or on graphical plots.

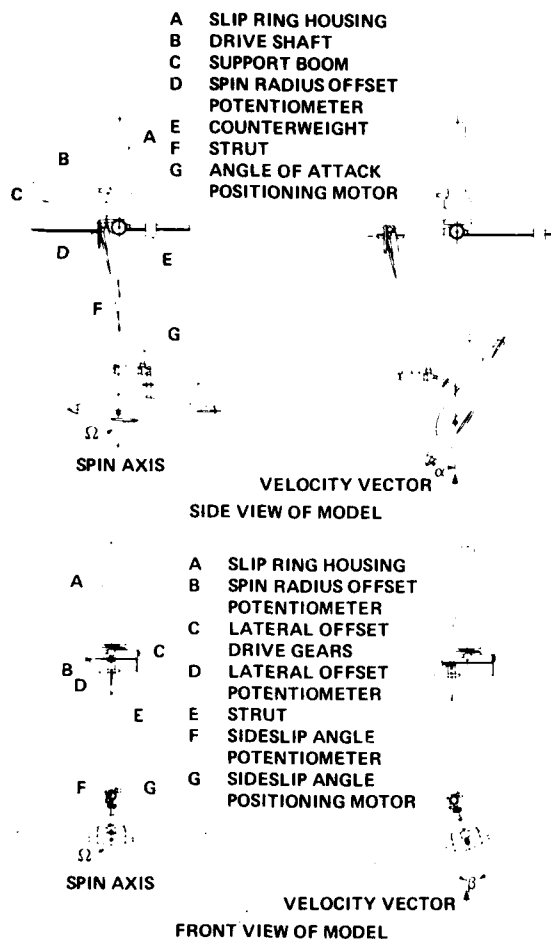


Figure 22. Langley Research Center's spin-tunnel rotary-balance rig.

Examples of the types of data acquired with this apparatus are shown in Figs. 24 and 25. It should be noted, first of all, that  $wb/V$  varies to high values (nearly 1.0) compared with previous data examples for typical fighter aircraft. This is characteristic of general aviation configurations, which have high spin rates and very low rates of descent consistent with low wing loadings. Figure 24 shows the pitching moment for five different models. The nonlinearities and wide variation in magnitude are clear. The yawing-moment coefficient for three of these configurations is shown in Fig. 25. The three different curves for each configuration illustrate the effects of different wing positions and of removing the wing completely.

#### 2.4.6 Ames Research Center apparatuses

The first rotary-balance apparatus (Ref. 18) developed at Ames Research Center (ARC) was run in the ARC 6- by 6-Foot Supersonic Tunnel. It was simply an ogive cylinder fixed rigidly, at an angle of attack, to a rotating sting with strain gages to measure pitching and yawing moments. The sting was rotated up to 600 rpm. Shortly after these exploratory experiments, Schiff developed an apparatus for the same tunnel to test a 10° semi-angle cone model undergoing simultaneous coning about the wind vector and spinning about its own axis of symmetry. The model attitude could be varied through a set of manually changed bent stings up to 30°. The coning and spinning rates were varied to 600 rpm. A photograph of the rig is shown in Fig. 26 and a sketch in Fig. 27. An example of the data showing the side-moment coefficient due to coning at varying angles of attack is shown in Fig. 28. The nonlinearity of the side moment and its comparison with the theoretically determined damping-in-pitch parameter,  $C_{m_q} + C_{m_\alpha}$ , are discussed in Ref. 19 and in Lecture No. 2 of this lecture series.

With an increased emphasis on research in airplane aerodynamics at Ames Research Center, one area being stall/spin problems, the rig was modified (in 1974) to accommodate a small airplane-like configuration for testing in the ARC 12-Foot Pressurized Wind Tunnel. The first experiments are reported in Ref. 27; subsequent, more refined experiments are reported in Refs. 28 and 29. A photograph of the model mounted in the wind tunnel is shown in Fig. 29. These were exploratory experiments undertaken to evaluate separately the effects of the nose, the tail, and of the complete configuration, including the wing, during a steady spin motion over a wide variation in Reynolds number. Some of the flow mechanisms that can contribute to prospin moments are shown in Fig. 30; they include asymmetric vortices on an ogive nose, asymmetric flow on a square-type cross section, and vortex flow on a simple tail configuration. An example of the aerodynamics on the nose with the square cross section in a flat spin motion ( $\sigma = 90^\circ$ ) is shown in Fig. 31.

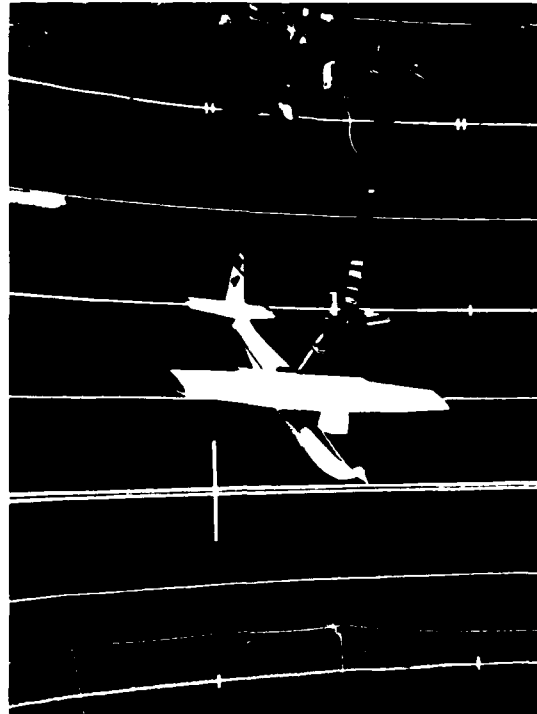


Figure 23. Langley Research Center's spin-tunnel rotary-balance apparatus.

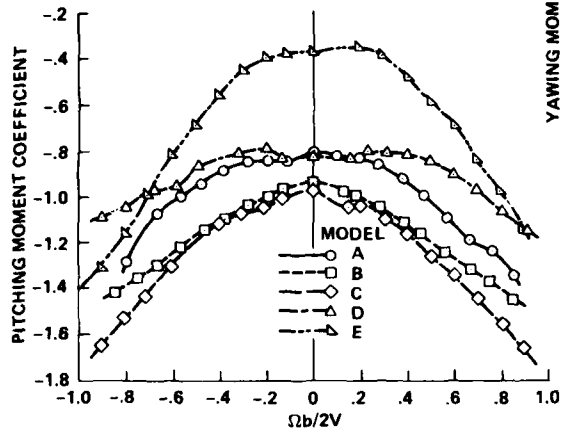


Figure 24. Effect of rotation rate on pitching moment at  $\alpha = 60^\circ$  for several models tested on Langley Research Center's spin-tunnel rotary-balance rig.

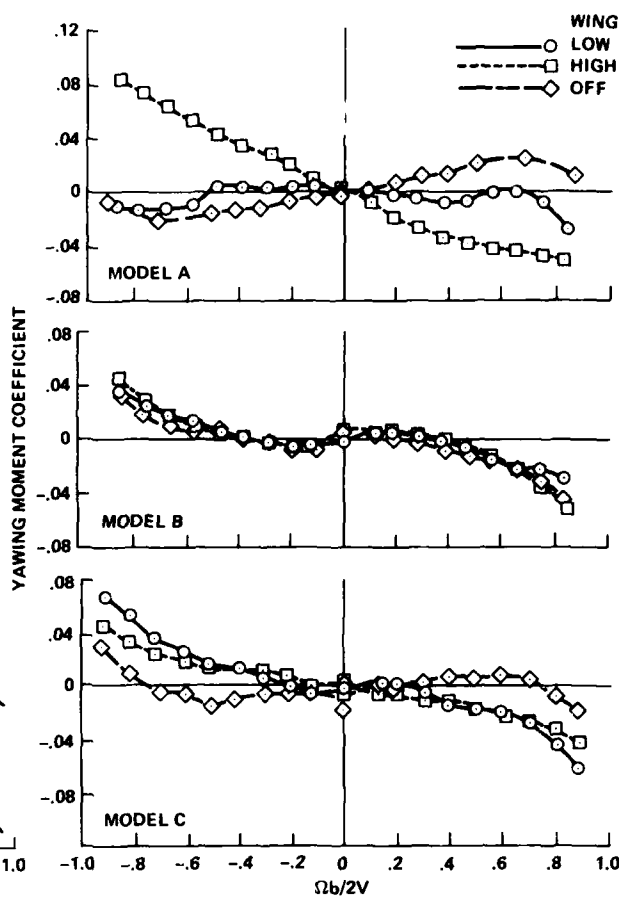


Figure 25. Yawing moment coefficient for three models at  $\alpha = 60^\circ$  measured with Langley Research Center's spin-tunnel rotary-balance rig.

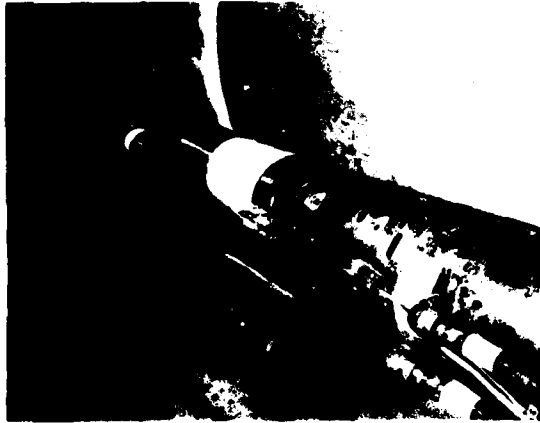


Figure 26. Early Ames Research Center rotary-balance rig with cone model.

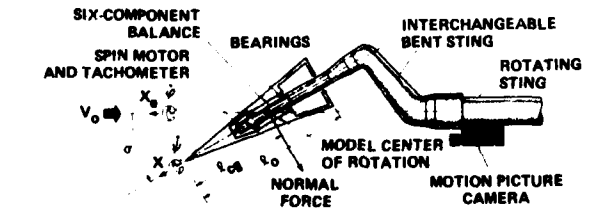


Figure 27. Early Ames Research Center rotary-balance rig.

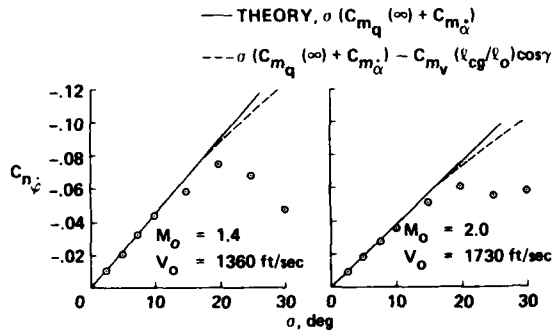


Figure 28. Side-moment coefficient on 10° half-angle cone caused by coning motion for various angles of attack.



Figure 29. Early Ames Research Center rotary-balance rig modified for airplane model.

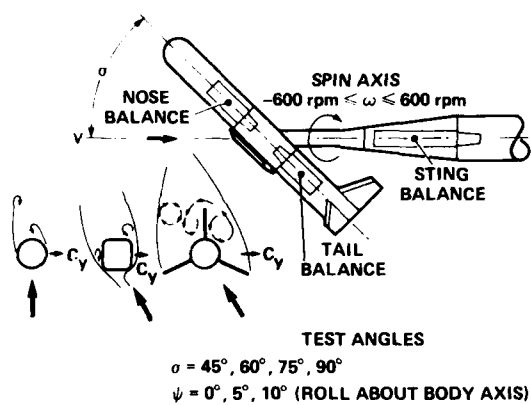


Figure 30. Prospin flow mechanisms investigated with Ames Research Center's rotary-balance rig.

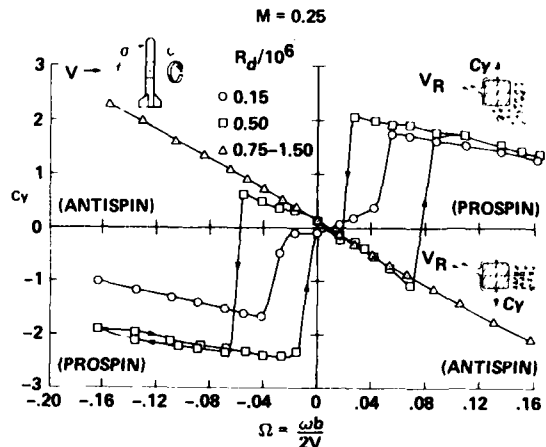


Figure 31. Effect of Reynolds number and rotation rate on nose side-force coefficient, Ames Research Center's rotary-balance rig with model at  $\sigma = 90^\circ$ .

This clearly demonstrates the strong dependence of the side-force coefficient on Reynolds number and rotation rate. One interesting feature of this case is the hysteresis loop with rotation rate that occurs in the middle Reynolds number range. This phenomenon occurs as a result of the flow separation characteristics, as the rotational speed (and consequently the local angle of the flow on the nose) is increased and decreased. A detailed explanation is included in Ref. 28. Another example is the case in which the angle of incidence is 45°; it is shown in Fig. 32. The results are much different in behavior than for the flat spin case; that is, the side force is antispin for all Reynolds numbers and rotation rates.

Although the modified rotary-balance apparatus has been very useful in exploratory investigations of simple airplane-like configurations, the need has long been recognized for an improved apparatus for efficient test operation and for providing the load capability required for large models at high Reynolds numbers. An effort has been under way at ARC for some time to construct and test a large-scale rotary apparatus for use in the ARC 12-Foot Pressure Wind Tunnel. This apparatus is described in some detail in Refs. 29 and 30. The rotary apparatus was designed to simulate full-scale, steady-spin motions by use of the proper combination of rotation speed and model size. Figure 33, a plot of reduced spin rate versus free-stream velocity, indicates the region for most full-scale airplane spins of the military fighter class. A rotary apparatus with a rotational speed capability of 42 rad/sec (400 rpm), along with the load capability for a model with a wing span of 61 cm (2 ft), provides a test envelope that encompasses most full-scale spin cases.

Avoiding unnecessary startups and shutdowns for model attitude changes is essential for efficient operation of a pressure tunnel. To accomplish this, the angles of attack and sideslip are capable of being changed remotely from outside the tunnel. The rotary apparatus was also designed to accommodate models of a practical size chosen to maximize the model Reynolds number but to minimize blockage effects or interference with the model. Figures 34 and 35 show the new apparatus. The angle of incidence of the model on a straight base-mounted sting with respect to the flow can be varied up to 30°. With the use of bent stings

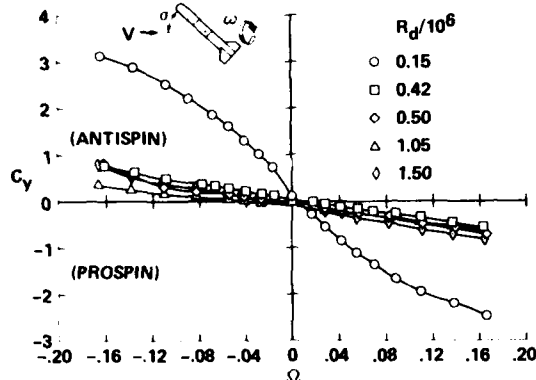


Figure 32. Effect of Reynolds number and rotation rate on nose side-force coefficient; Ames Research Center's rotary-balance rig with model at  $\sigma = 45^\circ$ .

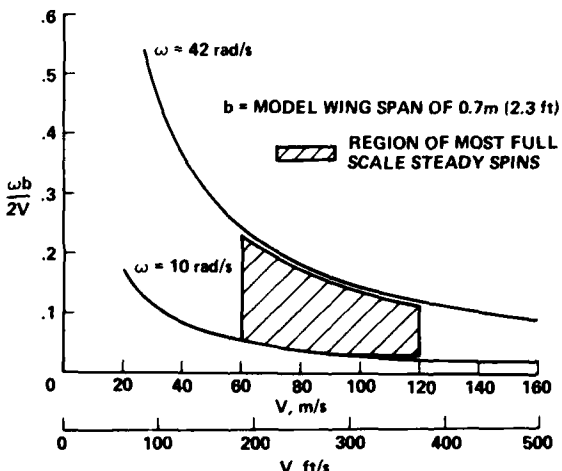


Figure 33. Reduced spin rate vs free-stream velocity for most full-scale spins of fighter-type aircraft.

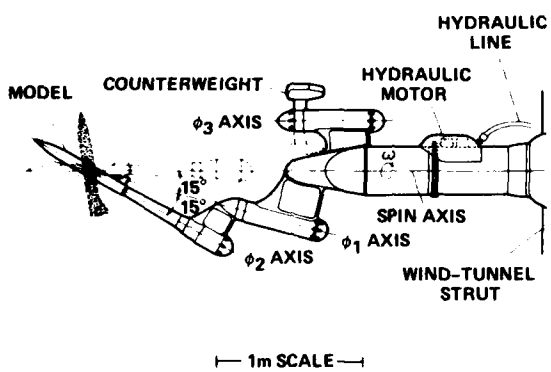


Figure 34. Ames Research Center's large-scale rotary-balance rig.



Figure 35. Ames Research Center's large-scale rotary-balance rig.

and top-mounted models, the angles of attack and sideslip can be varied to meet the required envelope of  $\gamma$  from  $-30^\circ$  to  $+100^\circ$  with  $\beta$  ranging between  $\pm 30^\circ$ .

Variations in the angles of attack and sideslip are accomplished through rotation about two axes ( $\phi_1$  and  $\phi_2$ , Fig. 34), which intersect the spin axis at the designated longitudinal location on the model representing the center of gravity of a full-scale, free-spinning vehicle. Changes in model orientation, made remotely with small electric motors mounted in the apparatus, are done before spinning the whole assembly in the tunnel. The counterweight assembly is driven to a predetermined position that statically balances the mass distribution of the system about the spin axis. No attempt is made to balance the system dynamically. The entire apparatus is then rotated in the wind-tunnel airstream, using a servo-controlled hydraulic drive system that can be varied in speed between 0 and 42 rad/sec (400 rpm) in either a clockwise or counterclockwise direction.

Figure 36 shows the attitude envelope obtainable with the stings selected for the first series of tests, including a base-mounted straight sting ( $\alpha_s = 0^\circ$ ) and two top-mounted bent stings ( $\alpha_s = 45^\circ$  and  $70^\circ$ ).

Electrical power leads to the positioning drive systems and the power and signal paths from the balance are provided by a slip-ring assembly mounted in the circular housing near the strut mount. This is a low-level signal slip-ring unit that contains 84 channels; it provides adequate signal paths to run two six-component, strain-gage balances simultaneously, in addition to providing for remote changes in model control deflections. An angle encoder to determine accurately position information about the spin axis, if needed, is mounted on the rear of the slip-ring unit. A tachometer to determine spin rate is mounted on the hydraulic drive motor shaft. Most experiments will be conducted with the spin axis parallel to the wind stream, which will result in a steady force output from the balance at any given rotation speed. The possibility exists, however, that by inclining the rotational axis to the wind stream, say  $3^\circ$  or  $4^\circ$ , one can produce oscillatory force variations that, if measured and interpreted properly, might provide information

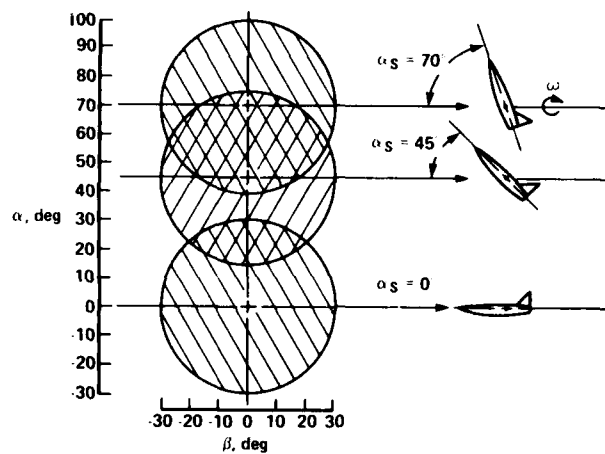


Figure 36. Attitude envelope for Ames Research Center's rotary-balance rig.

on damping derivatives. This method of obtaining damping data in lieu of a forced oscillation apparatus will be investigated in the future.

Efforts are progressing to check out the operation of the entire system on a special test stand. To minimize wind-tunnel occupancy time, most of the measurements of rotating inertial tares will be conducted outside the tunnel on the test stand, and only isolated checks will be made on the tares once the model and apparatus are installed in the tunnel.

### 3. MAGNUS BALANCE TECHNIQUE

Flight vehicles that are spin-stabilized at very high spin rates, such as projectiles and missiles, experience aerodynamic forces and moments at non-zero angle of attack that are different from those that would be experienced by the same but nonspinning body. The differences between these forces and moments are caused by Magnus effects, which result from a change in the boundary layer of the flow over the body produced by the high rotation rate. Magnus forces and moments acting in the yaw plane perpendicular to the normal force are generally an order of magnitude less than the pitch coefficients and require high sensitivity balances to be measured accurately in the wind tunnel. It has also been found that tunnel turbulence and airflow curvature in the test section can cause significant errors in the measurements (Ref. 31); consequently, it is very important that Magnus measurements be made in low-turbulence tunnels that have good flow qualities.

Magnus balances will be described here by (1) reviewing many of the important design considerations for Magnus balances, (2) by discussing some examples of Magnus balances that are known to the author, and (3) by showing a few examples of Magnus data. Two sources of information constitute most of the following discussion: the U.S. Army Ballistic Research Laboratory (BRL) and the U.S. Air Force Arnold Engineering Development Center (AEDC). Both have long histories of performing Magnus testing and have considerable expertise in the design, construction, and testing of Magnus balances. (There is also a good summary of both theoretical and experimental investigations of Magnus effects on arbitrary bodies of revolution with and without fins in Ref. 32.) The first section below will discuss typical design philosophy, derived mainly from BRL experience summarized in Ref. 33, and the second section will discuss some of the apparatuses used at AEDC.

#### 3.1 U.S. Army BRL Design Guidelines for Typical Balance System

The general BRL design for a model and balance for Magnus tests consists of several integrated parts (Fig. 37). The five-component strain-gage balance (two components in the pitch plane and three in the yaw

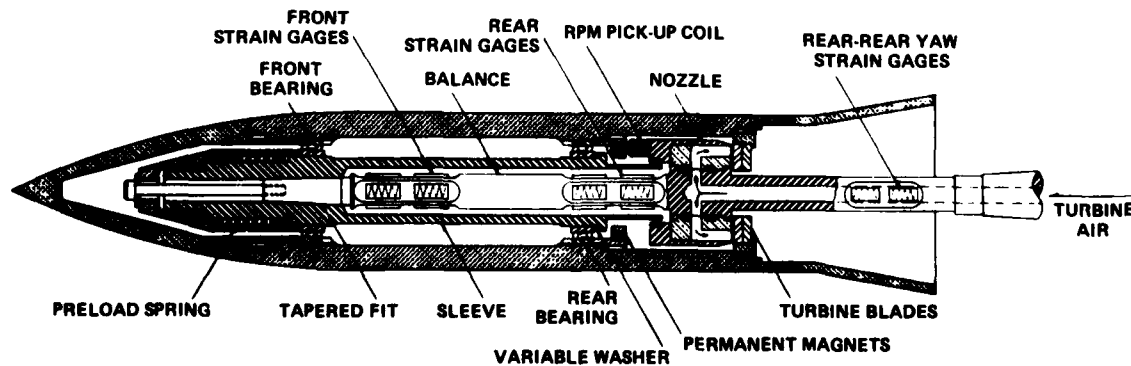


Figure 37. General design scheme for U.S. Army BRL spinning models/Magnus balance.

plane) is a cantilevered beam with a model supported at the free end. The model, which for BRL tunnels can vary in diameter from 1 to 3 in. and up to 15 in. in length, covers at least the forward half of the balance and is supported at the front of the balance through bearings and a nonrotating sleeve. The sleeve serves as the mount for the bearing inner race and also supports the spring assembly, which provides a preload for the bearings. Attached to the balance sting, just downstream of the sleeve, is the air turbine nozzle; it creates four sonic or supersonic jets that impinge on the turbine blades and spin the model up to rates as high as 50,000 rpm. (Finned models can be driven by jetting air externally onto the fins.) The model shell is mounted on the bearing outer races. The model is usually made in three sections (nose, body, and tail) with the body mounting on the bearings and holding the turbine blades and magnets for the spin rate monitoring system. The model, usually steel or aluminum or some combination thereof, should be simple, with as few parts as possible. The entire assembly must be dynamically balanced, and the fewer chances for roll disorientation of the various parts the better. It is also important to minimize discontinuities in the outer shell at joints between various pieces so as not to artificially alter the boundary layer from which all Magnus effects originate. In order to reduce bearing loads, the bearings should be placed as far apart as possible and should be approximately equally spaced about the normal force center of pressure. Bearing alignment and concentricity are critical; no misalignment can be tolerated at high speeds.

The strain-gage balance-sting is located on the model centerline with its forward end well inside the model (as shown in Fig. 37). Its purpose is not only to measure the pitch and yaw plane forces and moments, but also to support the model, conduct high-pressure air to the air nozzles, and to lead instrumentation wiring to the rear of the sting. The taper at the free end of the balance-sting is to provide a solid fit to the stationary model sleeve. The main gage sections (two pitch plane and three yaw plane) are located between the taper and the nozzle hub. Data from the two pitch gages determine the normal force and pitching moment, and the yaw gages determine the Magnus force and moment. Since the Magnus force is small and difficult to measure, a third yawing-moment gage has been added on the rear portion of the sting. The accuracy with which the force is measured is directly proportional to the distance between the gages, so greater accuracy is obtained using the gages that are farthest apart. It should be noted that some modern balances also include gages to measure roll moment and axial force, but they are considerably more costly. The size of the gage sections is arrived at through consideration of model natural frequency (which is excited by tunnel turbulence and forced oscillations from dynamic turbulences) and aerodynamic loads and available space inside the model. Gage sections should be larger to be stiffer, and therefore to have higher resonance frequencies, but they should be smaller to produce higher stresses and therefore higher sensitivity. To enable the use of stiffer gage sections, one must be able to increase the sensitivity of the gage itself. Although most gages in the past have been standard wire-wound foil gages, more use is being made in modern balances of solid-state or semiconductor gages, which have 30 to 100 times the sensitivity of foil gages; however, there have been some difficulties with signal drift due to temperature gradients along the gaged section. Reference 34 describes in detail the use of semiconductor gages and provides guidelines for their use in Magnus balances.

A key to a successful Magnus balance is the bearings. Unless considerable care is taken in their design, specification, and installation, the bearings simply will not survive at the high operational speeds to which they are subjected and they will seize. There are at least three adverse conditions for the bearings: (1) speeds are usually beyond those set by the bearing manufacturers, (2) outer race rotation is mandatory, which considerably increases the DN (diameter  $\times$  rpm) factor, and (3) normal lubrication techniques are impossible. With respect to (3), some lubrication can be attained by centrifuging oil into the bearings at the factory or specifying that the bearings be "grease plated." Bearing break-in periods are essential to wear a track in each bearing race before running at high speeds. Specific break-in procedures using temperature monitoring are outlined in Ref. 35. The air turbine, illustrated in Fig. 38, is a single-stage impulse turbine; it consists of a nozzle that creates high-speed air jets that impinge on the blades. The nozzle mounts on the balance just aft of the rear gage section. The blades attach to the rotating body just aft of the nozzle. High-pressure air (up to 180 lb/in.<sup>2</sup> at BRL) is supplied to the nozzle through an axial hole through the sting. The nozzles are crude de Laval nozzles and are run at supersonic speeds to achieve maximum exit velocity and thus maximum torque to the blades. The turbine blade diameter should also be as large as possible to provide maximum power at a given model spin rate.

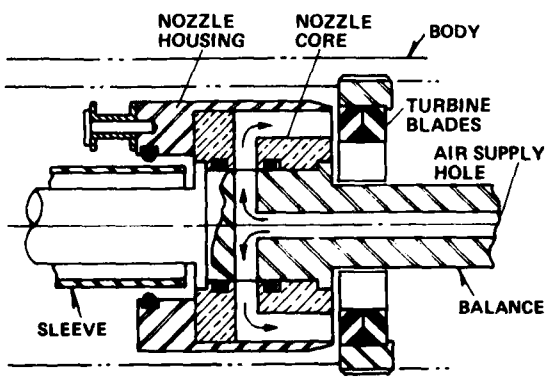


Figure 38. Turbine arrangement in U.S. Army BRL Magnus balance.

Dynamic balancing of the entire rotating assembly is essential. Any imbalance creates forced oscillations at resonance on the balance and affects the data acquisition as well as causing the more catastrophic problems of excessive loads and possible structural failures. Balancing is accomplished through a custom-made balancing rig, which uses the dynamic balancing principles found in most mechanics texts. Basically,

two planes perpendicular to the model axis are selected, one forward and one rearward where the mass can be adjusted. The model is suspended in a lightly damped mechanical system with a low natural frequency so that any mass unbalance of the rotating model will force a large amplitude response. The system can be adjusted so that forward and rear portions can be measured separately. By adding small amounts of mass (wax, for example) to the model surface at each of the balancing planes (until optimum mass and roll orientation are found) one can achieve a combination of mass adjustments that result in a balanced system. The amount of mass to be removed from the model (at a location 180° from where the mass was added) is determined and an appropriate amount of metal is cut away.

The data acquisition system must be capable of receiving and amplifying signals from the balance that range from a few microvolts to a few hundred microvolts, at least an order of magnitude less than the signals from the pitch gages. One must also account for interactions between the pitch and yaw gages in the balance gage calibrations. Interactions occur due to even minute misplacements of the various gages, non-homogeneity in the metal gage sections, small machining imperfections, etc. Signals are typically passed through a low-pass filter to eliminate tunnel aerodynamic noise. The data are obtained while the model is coasting from the highest spin rate to zero at a constant angle of attack. This eliminates the influence of forces generated on the turbine blades by the nozzle air jets. For most configurations, the Magnus characteristics are linear with spin rate if the Reynolds number is sufficiently high to assure completely turbulent flow on the model or low enough to assure laminar flow. If the Reynolds number is in a transitional regime, it is quite possible to observe a Magnus moment that varies nonlinearly with rotation rate. It is highly desirable to establish and verify that boundary-layer conditions are the same as expected on the flight vehicle of interest.

An example of data acquired with a Magnus balance (Ref. 36) is shown in Fig. 39 where the side-force coefficient on a secant-ogive-cylinder is shown as a function of reduced spin rate for various angles of attack. The variation is almost perfectly linear with speed, and the side force increases with angle of attack. Note the reversal in the side force for negative angles of attack.

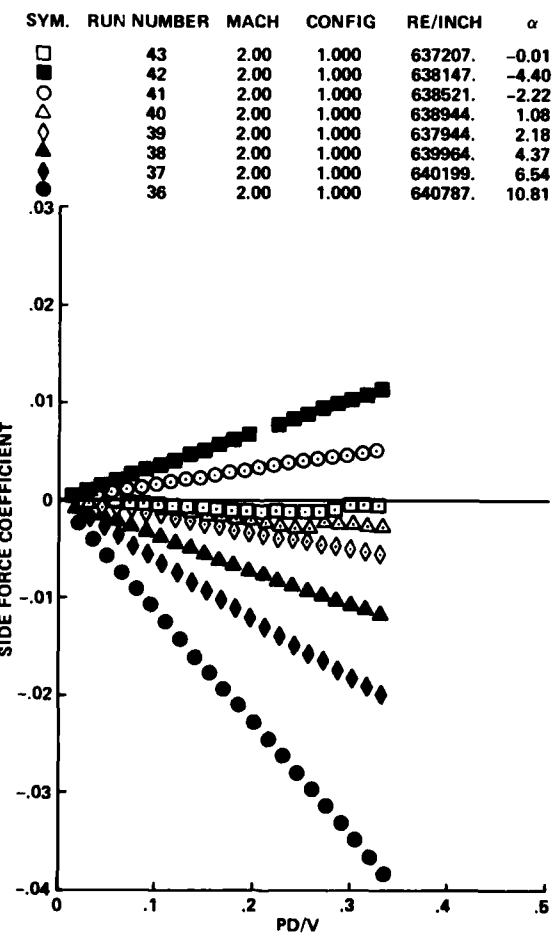


Figure 39. Side-force coefficient vs spin rate for secant-ogive-cylinder on U.S. Army BRL Magnus balance.

### 3.2 Magnus Test Capabilities at U.S. Air Force AEDC

Mechanisms have been developed at AEDC (Refs. 37-43) for measuring Magnus forces and moments on missile and other axisymmetric shapes for angles of attack ranging from 0° to 90°. A table of these mechanisms and their load restrictions is given below.

Mechanism	Angle-of-attack range, deg	Maximum normal force, lb	Minimum fuselage diameter, in
VKF Magnus	0 to 25	500	3.2
VKF 2.H	0 to 90	300	1.375
PWT high alpha	0 to 90	1200	4.25
PWT 4T Magnus	0 to 25	80	2.75

Each mechanism comprises a balance, ball bearings, tachometer, brake, and some type of spin-up device.

### 3.2.1 VKF Magnus-force test mechanism

The VKF Magnus-force mechanism (Ref. 37-39; Fig. 40) is obtained by replacing the gas bearing in the VKF-2.E roll damping mechanism with a four-component static force balance. The Magnus-force test mechanism has a sting-mounted, water-jacketed, four-component balance with a shell mounted on ball bearings over the water jacket. A two-stage air-driven turbine is mounted inside the model mounting shell at a fixed axial position near the forward end of the sting. The turbine is used to spin the model to some desired rotational speed and is then disengaged with an air-operated sliding clutch so that the model spins freely on the ball bearings. The balance data and spin rate are recorded as the spin rate decreases. The turbine produces a starting torque of about 50 in.-lb and a developed torque of 100 in.-lb. Spin rates up to about 25,000 rpm are normally obtainable on most projectiles.

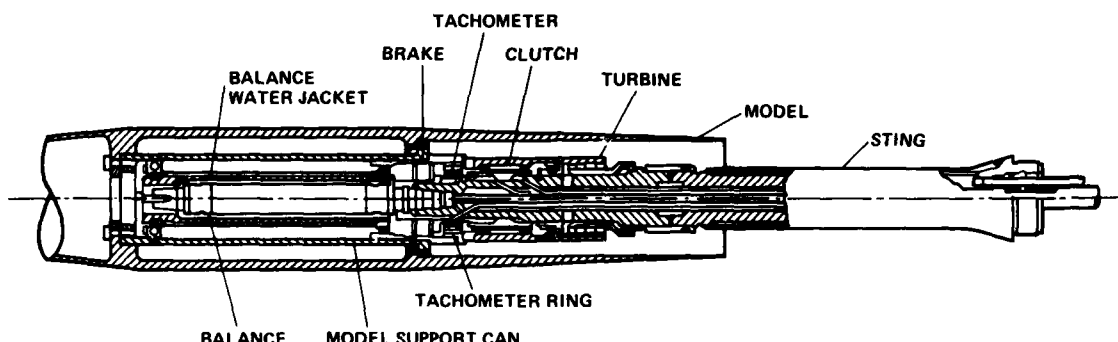


Figure 40. AEDC VKF Magnus balance mechanism.

The Magnus-force mechanism is designed to operate under normal-force loads up to 500 lb and axial-force loads of 125 lb. A wide range of models may be tested with the mechanism. For cone-cylinder-type models, there is a minimum cylinder diameter of about 3.2 in. and a maximum length of about 42 in. The maximum model diameters and frontal areas are limited by tunnel blockage considerations and not necessarily by the mechanism.

The VKF Magnus-force balance uses small outrigger side beams with solid-state strain gages to obtain the sensitivity required to accurately measure small side loads while maintaining adequate balance stiffness for large pitch loads. When a yawing moment is imposed on the balance, secondary bending moments are induced in the side beams. Thus, the outrigger beams act as mechanical amplifiers, and a normal-force to side-force capacity ratio of 20 is achieved.

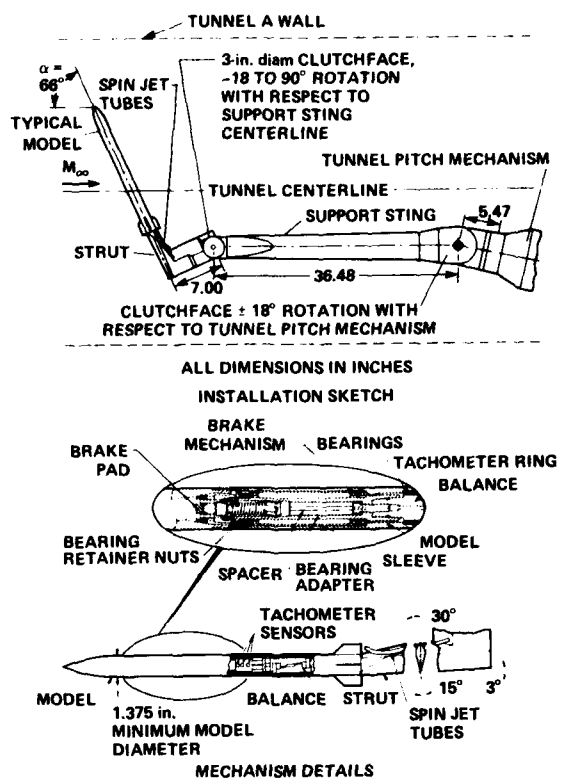
Static loads in each plane and combined static loads have been applied to the balance, simulating the range of typical model loads. The following uncertainties represent the differences between the applied loads and the corresponding values calculated from the final data reduction equations.

Balance component	Design load	Range of static loads	Measurement uncertainty
Normal force, lb	$\pm 500$	150	0.25
Pitching moment, in.-lb	$\pm 2500$	$\pm 1000$	0.30
Side force, lb	$\pm 25$	15	0.04
Yawing moment, in.-lb	$\pm 125$	60	0.15

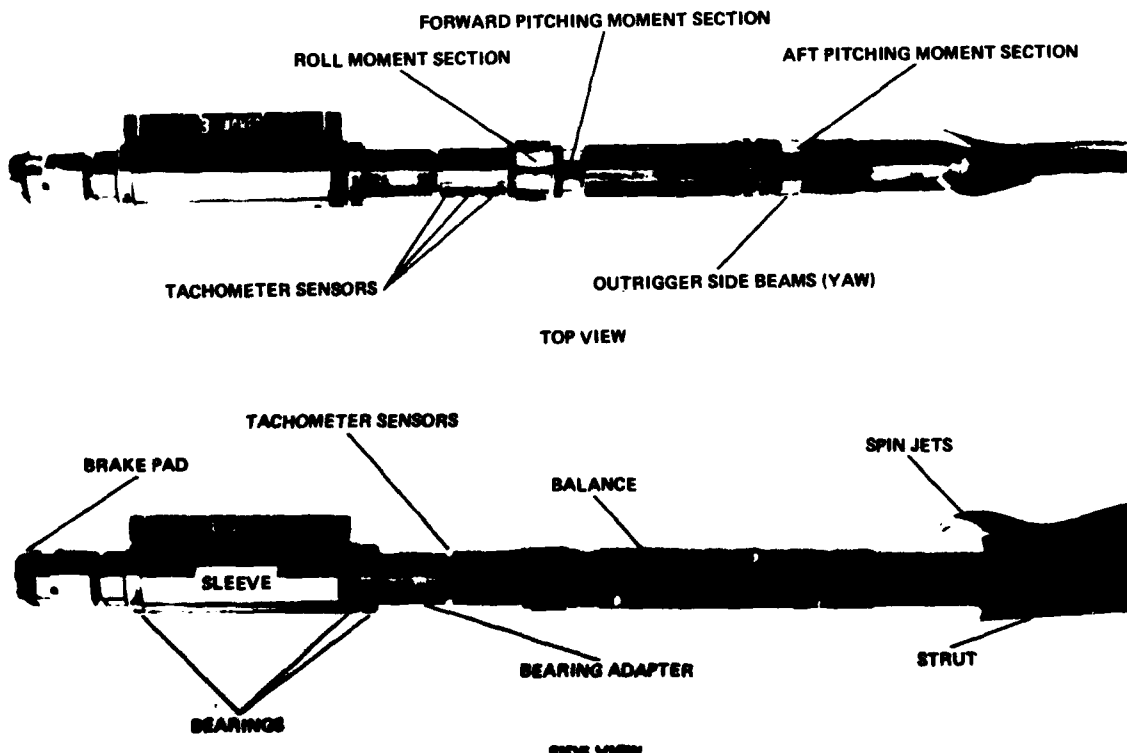
For the typical model, the Magnus-force and moment coefficients can be measured within 2% or less at the higher angles of attack.

### 3.2.2 VKF high-alpha Magnus test mechanism VKF-2.H

The VKF high-alpha missile roll-damping test mechanism (Refs. 37, 40, 41; Fig. 41) is a free-spin system. A six-component balance is supported by a strut that can be manually set in 6° increments to provide various prebend angles. These manual settings, along with the tunnel pitch mechanism, provide an angle-of-attack range from -5° to 90°. The balance supports an adapter with three ball bearings, and the model is mounted directly to the bearings. An air-operated brake is located on the front of the adapter and is used to stop model rotation. The brake, as well as a mechanical lock, can be used to obtain static force coefficients at zero spin rate. Roll-damping data are obtained as the model spins up (for models with canted fins) or as the model spins down after it is spun up by high-pressure air jets impinging on the fins.



(a) Installation and mechanism details.



(b) Photograph of assembly.

Figure 41. AEDC/VKF high-alpha missile roll-damping/Magnus test mechanism.

The VKF-2.H free-decay, roll-damping test mechanism can also be used to obtain Magnus-force and Magnus-moment measurements. The balance uses outrigger beams, but a normal force to side force ratio of only 6 was used because of possible large static side forces that might be experienced at high angles of attack as a result of asymmetric vortices. The balance is gaged with conventional wire strain gages but has sufficient sensitivity to measure the Magnus forces and moments on most models.

The rotational speed, roll position, and roll direction are computed from the electrical pulses produced by a ring with alternating reflective and nonreflective surfaces passing three internally mounted infrared-emitting diodes and phototransistors. The mechanism is designed for spin rates up to 12,000 rpm.

The pertinent capabilities of the mechanism are as follows:

- (1) Applicable tunnels: A, 4T
- (2) Maximum loads
  - Normal force: 300 lb
  - Pitching moment: 820 in.-lb
  - Side force: 50 lb
  - Yawing moment: 135 in.-lb
  - Axial force: 50 lb
- (3) Minimum model i.d.: 1.375 in.
- (4) Normal expected precision:  $C_{zP}$ ,  $\pm 5\%$  (finned vehicle)

An example of Magnus forces and moments from this balance on a basic finner model (consisting of a cone-cylinder with four rectangular fins) is shown in Fig. 42 (Ref. 41). These particular data show the Magnus force and moment at two Mach numbers, 0.22 and 2.5, over an angle of attack range from 0° to 90°. Maximum values for both Mach numbers occurred at  $\alpha \approx 50^\circ$ . However, for the subsonic data,  $M = 0.22$ , the variation in the side force and yawing moment with angle of attack was somewhat erratic above  $\alpha = 30^\circ$ . This probably results from the unsteady asymmetric vortex system that exists on slender bodies at high attitudes in subsonic flow. It is also interesting to note that the signs of both coefficients reversed between  $M = 0.22$  and  $M = 2.5$ .

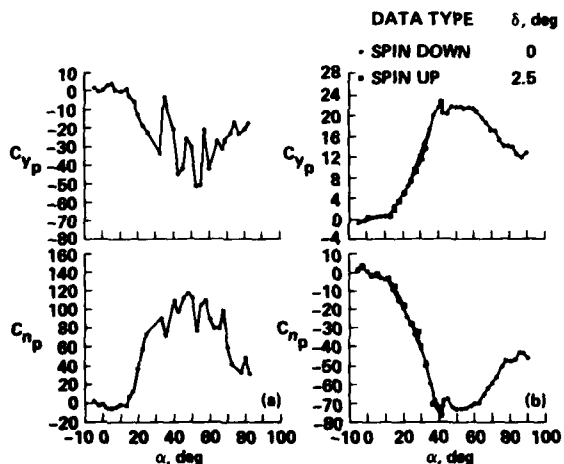


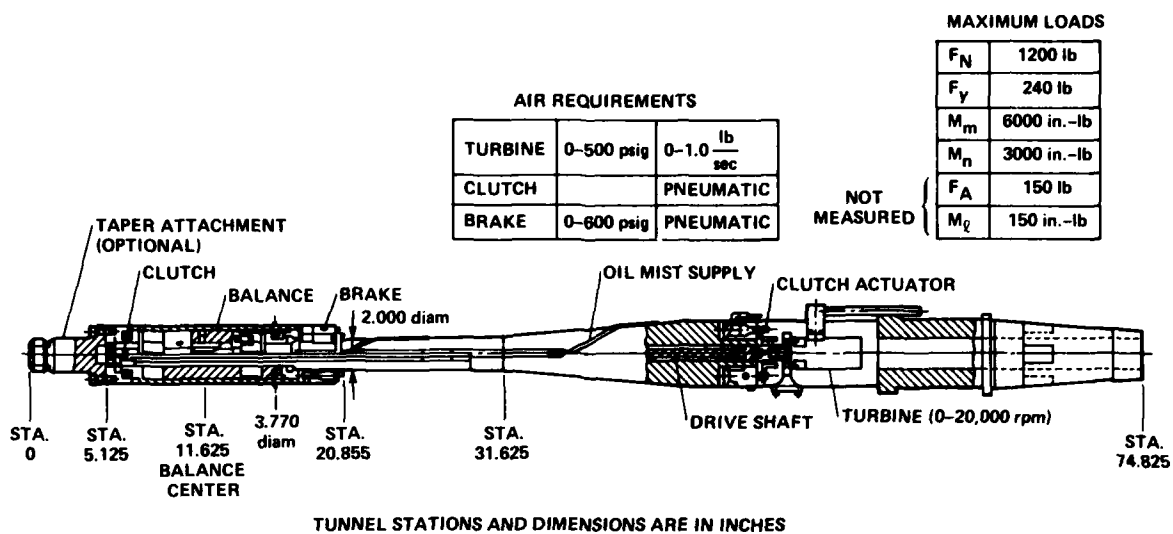
Figure 42. Magnus forces and moments measured on a basic finner model with AEDC/VKF high-alpha Magnus test mechanism VKF-2.H.

### 3.2.3 Large, high-alpha missile roll-damping test mechanism

The large, high-alpha missile roll-damping test mechanism (Ref. 42) is used to test models with diameters (typically) of 5.0 in. (4.25 in. minimum) and length-to-diameter ratios of 10. This mechanism (Fig. 43) can measure four-component static forces and moments and Magnus characteristic, and can determine roll damping characteristics. The design loads of the sting-mounted static balance are 1200 lb normal force, 6000 in.-lb pitching moment, 240 lb side force, and 1200 in.-lb yawing moment. The balance supports ball bearings and a balance housing to which the model is mounted directly.

The rotational speed, roll position, and roll direction are computed from the electrical pulses produced by a ring with alternating reflective and nonreflective surfaces passing three internally mounted light reflection transducers.

Spin rates up to 20,000 rpm can be obtained, using canted fins or the mechanism's turbine that produces 140 in.-lb of developed torque. A braking mechanism is available to stop the spinning model.



TUNNEL STATIONS AND DIMENSIONS ARE IN INCHES

Figure 43. AEDC large high-alpha missile roll-damping/Magnus test mechanism.

The pertinent capabilities of the system are as follows:

- (1) Maximum loads  
Normal force: 1200 lb  
Pitching moment: 6000 in.-lb  
Side force: 240 lb  
Yawing moment: 3000 in.-lb  
Axial force: 150 lb
- (2) Minimum model i.d.: 4.25 in.

#### 3.2.4 PWT Magnus-force test mechanism

The PWT-4T free-decay roll mechanism was designed for short-finned missile or bomb models with large roll-damping moments (Fig. 44). The system features a hydraulic-motor-driven sleeve mounted on ball bearings on a six-component balance. The model is mounted on a sleeve and can be spun up to the desired spin rate, at which point a pneumatically operated clutch is used to disengage the drive motor, permitting the model to rotate freely on the bearings. Spin rate and balance data are recorded during the free-spin cycle.

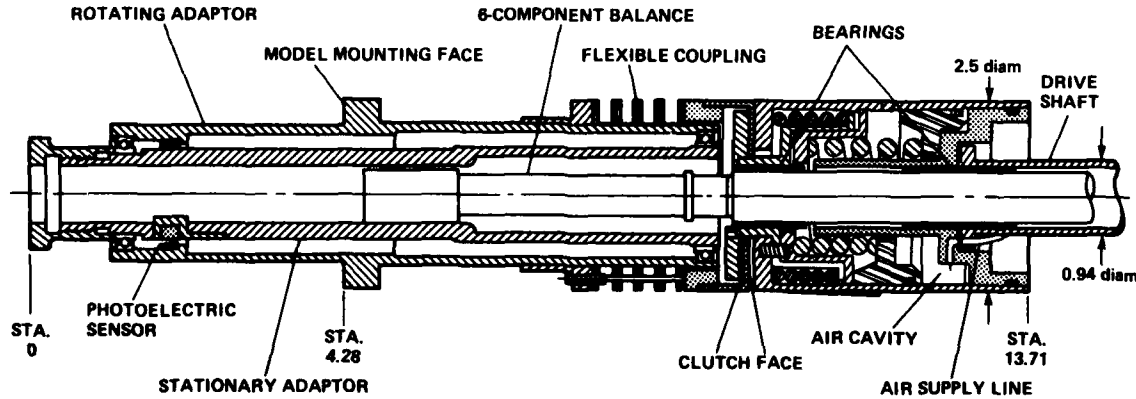


Figure 44. AEDC/PWT-4T free decay/Magnus balance test mechanism.

The PWT-4T free-decay roll-damping mechanism can also be used to measure Magnus-force and Magnus-moment data. The balance is gaged with conventional wire strain gages.

The drive system can deliver 138 in.-lb of torque to the model at roll rates from 0 to 5000 rpm. The pertinent capabilities of the mechanism are as follows:

Balance component	Design load	Uncertainty
Normal force, lb	$\pm 80$	0.3
Pitching moment, in.-lb	$\pm 160$	0.3
Side force, lb	$\pm 40$	0.2
Yawing moment, in.-lb	$\pm 120$	0.2
Axial force, lb	50	0.3
Rolling moment, in.-lb	$\pm 30$	0.2

#### 4. CONCLUDING REMARKS

The purpose of this lecture was to present the concepts of two techniques for determining part of the aerodynamic information necessary to describe the dynamical behavior of various types of flight vehicles. The coning motion produced by the rotary-balance technique has been shown to be tied closely to the problems of aircraft spin, but it also has been shown in previous lectures to be one of the important characteristic motions in the mathematical model for determining the aerodynamic response to a general motion. The principles of the experimental technique are quite straightforward, but putting them to use with practical wind tunnel apparatuses is a challenge. A significant increase in both the quantity and quality of rotary-balance experiments has taken place in the past 10 years. The recent availability of good-quality rotary-balance data has been a major contribution to an improved ability to predict spin motions and to the study of aerodynamic phenomena associated with spin motions.

Magnus balances have been used for many years and will continue to be used as long as flight vehicles are spin stabilized. The lecture has concentrated on describing at least one technique that has proved to be successful and has reviewed a number of high-quality balances available to the experimenter. Although other Magnus balances undoubtedly exist, both in the United States and in other NATO countries, it is believed that those reviewed here are representative of the characteristics of other such devices.

#### APPENDIX: ROTARY TARE MOMENTS

The moments experienced by the body-fixed force/moment balance due to the rotary motion of the rig will be calculated as a function of the model moments of inertia,  $I_x$ ,  $I_y$ , and  $I_z$ , rotary velocity  $\dot{\omega}$ , and the model angle of attack  $\alpha$  and sideslip angle  $\beta$ . It is assumed that the center of mass of the model is on the spin axis.

The general equations of motion of an airplane relative to a set of principal axes fixed in the airplane can be written as

$$\begin{aligned} -L &= \dot{p}I_x + qr(I_z - I_y) - (\dot{r} + pq)I_{xz} + (rp - \dot{q})I_{xy} + (r^2 - q^2)I_{yz} \\ -M &= \dot{q}I_y + rp(I_x - I_z) - (p^2 - r^2)I_{xz} - (\dot{p} + qr)I_{xy} + (pq - \dot{r})I_{yz} \\ -N &= \dot{r}I_z + pq(I_y - I_x) + (qr - \dot{p})I_{xz} + (q^2 - p^2)I_{xy} - (\dot{q} + pr)I_{yz} \end{aligned}$$

where

L is the rolling moment about  $X_B$  axis

M is the pitching moment about  $Y_B$  axis

N is the yawing moment about  $Z_B$  axis

For the specific case here the model is rotated at constant rotational velocity so all acceleration terms  $\ddot{p}$ ,  $\ddot{q}$ ,  $\ddot{r}$  are zero, and for models that are symmetric in the x-z plane,

$$I_{yz} = I_{xy} = 0$$

The equations reduce to:

$$\begin{aligned} L &= -qr(I_z - I_y) + pqI_{xz} \\ M &= -rp(I_x - I_z) + (p^2 - r^2)I_{xz} \\ N &= -pq(I_y - I_x) - qrI_{xz} \end{aligned}$$

Note that  $\dot{\omega}$  can be broken into components about the body axes  $X_B$ ,  $Y_B$ ,  $Z_B$  and called  $w_x$ ,  $w_y$ ,  $w_z$ :

$$\omega = |\dot{\omega}| = (\omega_x^2 + \omega_y^2 + \omega_z^2)^{1/2}$$

$$\begin{array}{ll} \omega_x = p & \omega_x/\omega = u_B/V \\ \omega_y = q & \text{also} \quad \omega_y/\omega = v_B/V \\ \omega_z = r & \omega_z/\omega = w_B/V \end{array}$$

$$\frac{L}{\omega^2} = \frac{-\omega_x \omega_z}{\omega^2} (I_z - I_y) + \frac{\omega_x \omega_y}{\omega^2} I_{xz}$$

$$\frac{M}{\omega^2} = \frac{-\omega_z \omega_x}{\omega^2} (I_x - I_z) + \left( \frac{\omega_x^2}{\omega^2} - \frac{\omega_z^2}{\omega^2} \right) I_{xz}$$

$$\frac{N}{\omega^2} = \frac{-\omega_x \omega_y}{\omega^2} (I_y - I_x) - \frac{\omega_y \omega_z}{\omega^2} I_{xz}$$

Rewriting:

$$\frac{L}{\omega^2} = -\frac{v_B}{V} \cdot \frac{w_B}{B} (I_z - I_y) + \frac{u_B}{V} \cdot \frac{v_B}{V} I_{xz}$$

$$\frac{M}{\omega^2} = \frac{-w_B}{V} \cdot \frac{u_B}{V} (I_x - I_z) + \left( \frac{u_B^2}{V^2} - \frac{w_B^2}{V^2} \right) I_{xz}$$

$$\frac{N}{\omega^2} = \frac{-u_B}{V} \cdot \frac{v_B}{V} (I_y - I_x) - \frac{v_B}{V} \cdot \frac{w_B}{V} I_{xz}$$

Note: See the sketch below.

$$\tan \alpha = \frac{w_B}{u_B} = \frac{w_B}{V} \cdot \frac{V}{u_B}$$

$$\sin \beta = \frac{v_B}{V}$$

$$\frac{w_B}{V} = \sin \alpha \cos \beta$$

$$\gamma = \cos \alpha = \frac{u_B}{V}$$

$$\alpha = \sin^{-1} \left[ \left( \frac{v_B}{V} \right)^2 + \left( \frac{w_B}{V} \right)^2 \right]^{1/2}$$

$$\frac{u_B}{V} = \cos \left[ \sin^{-1} (\sin^2 \beta + \sin^2 \alpha \cos^2 \beta)^{1/2} \right]$$

Now substitute these velocity ratios in moment equations

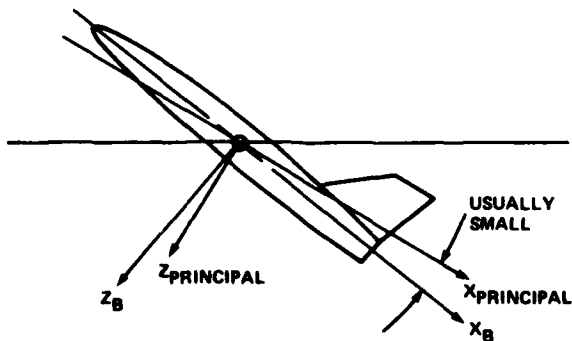
$$\frac{L}{\omega^2} = \sin \beta \sin \alpha \cos \beta (I_y - I_z) + \left\{ \cos \left[ \sin^{-1} (\sin^2 \beta + \sin^2 \alpha \cos^2 \beta)^{1/2} \right] \cdot \sin \beta \right\} I_{xz}$$

$$\frac{M}{\omega^2} = \sin \alpha \cos \beta \cos \left[ \sin^{-1} (\sin^2 \beta + \sin^2 \alpha \cos^2 \beta)^{1/2} \right] (I_z - I_x)$$

$$+ \left\{ \cos^2 \left[ \sin^{-1} (\sin^2 \beta + \sin^2 \alpha \cos^2 \beta)^{1/2} \right] - \sin^2 \alpha \cos^2 \beta \right\} I_{xz}$$

$$\frac{N}{\omega^2} = \cos \left[ \sin^{-1} (\sin^2 \beta + \sin^2 \alpha \cos^2 \beta)^{1/2} \right] \sin \beta (I_x - I_y) - \sin \beta \sin \alpha \cos \beta I_{xz}$$

We can assume that for most models  $I_{xz}$  is small since the principal x-z axis will be nearly the same as the body-fixed  $x_B$  axis (as long as the vertical tail is not fairly massive).



If  $I_{xz} \approx 0$ :

$$\text{Roll moment, } L = \sin \beta \sin \alpha \cos \beta (I_y - I_z) \omega^2$$

$$\text{Pitch moment, } M = \sin \alpha \cos \beta \cos [\sin^{-1}(\sin^2 \beta + \sin^2 \alpha \cos^2 \beta)^{1/2}] (I_z - I_x) \omega^2$$

$$\text{Yaw moment, } N = \sin \beta \cos [\sin^{-1}(\sin^2 \beta + \sin^2 \alpha \cos^2 \beta)^{1/2}] (I_x - I_y) \omega^2$$

#### REFERENCES

1. Birhle, W., Jr. and Barnhart, B., "Spin Prediction Techniques." AIAA-80-1564-CP, AIAA CP806, Danvers, Mass., Aug. 1980.
2. Glauert, H., "The Investigation of the Spin of an Airplane." R&M No. 618, British A.R.C., 1919.
3. Gates, S. B. and Bryant, L. W., "The Spinning of Aeroplanes." R&M No. 1001, British A.R.C., 1926.
4. Irving, H. B. and Batson, A. S., "Experiments on a Model of a Single Seater Fighter Airplane in Connection with Spinning." R&M No. 1184, British A.R.C., 1928.
5. Allwork, P. H., "A Continuous Rotation Balance for the Measurement of Yawing and Rolling Moments in a Completely Represented Spin." R&M No. 1579, British A.R.C., 1933.
6. Bamber, M. J. and Zimmerman, C. H., "The Aerodynamic Forces and Moments Exerted on a Spinning Model of the 'NY-1' Airplane as Measured by the Spinning Balance." NACA TR 456, 1933.
7. Bamber, M. J. and Zimmerman, C. H., "Spinning Characteristics of Wings. I.-Rectangular Clark Y Mono-plane Wing." NACA TR 519, 1935.
8. Bamber, M. J. and House, R. O., "Spinning Characteristics of the XNZY-1 Airplane." NACA TR 607, 1937.
9. Stone, R. W., Jr., Burk, S. M., Jr., and Birhle, W., Jr., "The Aerodynamic Forces and Moments on a 1/10-Scale Model of a Fighter Airplane in Spinning Attitudes as Measured on a Rotary Balance in the Langley 20-Foot Free Spinning Tunnel." NACA TN 2181, 1950.
10. Clarkson, M. H., "Autorotation of Fuselages." I.A.S. Aero. Rev., Feb. 1958, pp. 33-35.
11. Wykes, J. H. and Casteel, G. R., "Comparison of Computer and Flight Test Results for a Spinning Airplane." AGARD CP-17, Stability and Control, 1966, pp. 103-125.
12. Scherer, M. and Aguesse, M.-O., "Etude Analytique De La Vrille." AGARD CP-17, Stability and Control, 1966, pp. 127-158.
13. Birhle, W., Jr. and Barnhart, B., "Effects of Several Factors on Theoretical Predictions of Airplane Spin Characteristics." NACA CR 132521, 1974.
14. Birhle, W., Jr., "Correlation Study of Theoretical and Experimental Results for Spin Tests of a 1/10-Scale Radio Control Model." NASA CR-144995, 1976.
15. Tobak, M. and Schiff, L. B., "Generalized Formulation of Nonlinear Pitch-Yaw-Roll Coupling." AIAA Journal, Vol. 13, No. 3, Mar. 1975, pp. 323-332.
16. Tobak, M. and Schiff, L. B., "On the Formulation of the Aerodynamic Characteristics in Aircraft Dynamics." NASA TR R-456, Jan. 1976.
17. Levy, L. L. and Tobak, M., "Nonlinear Aerodynamics of Bodies of Revolution in Free Flight." AIAA Journal, Vol. 8, No. 12, Dec. 1970, pp. 2168-2171.
18. Tobak, M., Schiff, L. B., and Peterson, V. L., "Aerodynamics of Bodies of Revolution in Coning Motion." AIAA Journal, Vol. 7, No. 1, Jan. 1969, pp. 95-99.
19. Schiff, L. B. and Tobak, M., "Results from a New Wind Tunnel Apparatus for Studying Coning and Spinning Motions of Bodies of Revolution." AIAA Journal, Vol. 8, No. 11, Nov. 1970, pp. 1953-1957.
20. Matthews, A. W., "Experimental Determination of Dynamic Derivatives Due to Roll at British Aerospace, Warton Division." Paper No. 4, AGARD CP 235, Dynamic Stability Parameters, 1978.
21. Verbrugge, R., Balance Rotative de L'I.M.F. Lille et Techniques Experimentales Associees. 16eme Colloque d'Aerodynamique Appliquee. Lille - 13, 14, 15 Novembre 1979.
22. Bazzocchi, I. E., "Stall Behaviour and Spin Estimation Method by Use of Rotating Balance Measurements." Paper No. 8, AGARD CP-199, Stall/Spin Problems of Military Aircraft, 1975.
23. Hafer, X., "Wind Tunnel Testing of Dynamic Derivatives in W. Germany." Paper No. 5, AGARD CP-235, Dynamic Stability Parameters, 1978.
24. Chambers, J. R., Bowman, J. S., Jr., and Malcolm, G. N., "Stall/Spin Test Techniques Used by NASA." Paper No. 13, AGARD CP-199, Stall/Spin Problems of Military Aircraft, 1975.

25. Grafton, S. B. and Anglin, E. L., "Static and Dynamic Aerodynamic Characteristics of a 0.15 Scale Model of the YF-17 Airplane at Spin Angles of Attack." NASA TM SX-3217, Nov. 1975.
26. Birhle, W., Jr. and Bowman, J. S., Jr., "The Influence of Wing, Fuselage, and Tail Design on Rotational Flow Aerodynamics Data Obtained Beyond Maximum Lift with General Aviation Configurations." AIAA Paper No. 80-0455, March 1980.
27. Clarkson, M. H., Malcolm, G. N., and Chapman, G. T., "Experimental Poststall Rotary Aerodynamic Coefficients for Airplane-Like Configurations." AIAA Journal, Vol. 13, No. 8, Aug. 1976, pp. 565-570.
28. Malcolm, G. N. and Clarkson, M. H., "Wind Tunnel Testing with a Rotary-Balance Apparatus to Simulate Aircraft Spin Motions." Proceedings of AIAA 9th Aerodynamic Testing Conference, June 1976, pp. 143-146.
29. Malcolm, G. N., "New Rotation-Balance Apparatus for Measuring Airplane Spin Aerodynamics in the Wind Tunnel." J. of Aircraft, Vol. 16, No. 4, Apr. 1979, pp. 264-268.
30. Malcolm, G. N. and Davis, S. S., "New NASA-Ames Wind Tunnel Techniques for Studying Airplane Spin and Two-Dimensional Unsteady Aerodynamics." Paper No. 3, AGARD CP 235, Dynamic Stability Parameters, 1978.
31. Platou, A. S., "The Influence of Wind Tunnel Flow Distribution and Turbulence on the Measurement of Magnus Forces." U.S. Army BRL Memorandum Report No. 1969, Apr. 1969.
32. Jacobson, I.D., "Magnus Characteristics of Arbitrary Rotating Bodies." AGARDograph No. 171, Nov. 1973.
33. Platou, A. S., Coburn, R., and Pedgonyay, J. S., "The Design and Dynamic Balancing of Spinning Models and a Testing Technique for Obtaining Magnus Data in Wind Tunnels." U.S. Army BRL Memorandum Report No. 2019, Oct. 1969.
34. Platou, A. S. and Ricci, H. A., "Wind Tunnel Tests of Solid State Strain Gages." U.S. Army BRL Memorandum Report No. 1928, July 1968.
35. Platou, A. S. and Sternberg, J., "The Magnus Characteristics of a 30 mm Aircraft Bullet." U.S. Army BRL Report No. 994, Sept. 1959.
36. Nietubicz, C. J. and Opalka, K. O., "Supersonic Wind Tunnel Measurements of Static and Magnus Aerodynamic Coefficients for Projectile Shapes with Tangent and Secant Ogive Noses." U.S. Army BRL Memorandum Report ARBRL-MR-02991, Feb. 1980.
37. Uselton, J. C. and Burt, G. E., "Dynamic-Stability Measurement Capabilities in the AEDC Wind Tunnels." AEDC/B-2 Brochure, Aug. 1976.
38. Uselton, J. C., "Aerodynamic Testing of Spin-Stabilized Projectiles at AEDC." AEDC Brochure.
39. Jenke, L. M. and Shadow, T. O., "Experimental Magnus and Static Stability Characteristics of Ballistic Projectiles with Various Boattail Angles and Lengths at Mach Numbers from 0.5 through 2.5." AEDC-TR-75-40, Aug. 1975.
40. Jenke, L. M., "Experimental Roll Damping, Magnus and Static Stability Characteristics of Two Slender Missile Configurations at High Angles of Attack (0 to 90°) and Mach Numbers 0.2 through 2.5." AEDC-TR-76-58, July 1976.
41. Uselton, B. L. and Jenke, L. M., "Experimental Missile Pitch- and Roll-Damping Characteristics at Large Angles of Attack." J. of Spacecraft & Rockets, Vol. 14, No. 4, Apr. 1977, pp. 241-247.
42. Burt, G. E. and Collins, J. A., "A New AEDC Test Mechanism for Obtaining Roll-Damping, Magnus, and Static Stability Characteristics of Slender Missile Configurations at High Angles of Attack (0 to 90°)." Presented at NASA/Military/Industry Missile Aerodynamics Workshop, NASA-Langley Research Center, Virginia, 1979.
43. Shadow, T. O., "Transonic Static Stability and Roll-Damping Characteristics of a Directional Control Anti-Tank Missile." AEDC-TR-73-131, Aug. 1973.

**CURVED-FLOW, ROLLING-FLOW, AND OSCILLATORY  
PURE-YAWING WIND-TUNNEL TEST  
METHODS FOR DETERMINATION OF  
DYNAMIC STABILITY DERIVATIVES**

by

Joseph R. Chambers and Sue B. Grafton  
NASA Langley Research Center  
Hampton, Virginia 23665  
U.S.A.

and

Frederick H. Lutze  
Department of Aerospace and Ocean Engineering  
Virginia Polytechnic Institute and State University  
Blacksburg, Virginia 24061  
U.S.A.

#### SUMMARY

Conventional wind-tunnel test techniques such as forced- or free-oscillation methods are constrained by the kinematic relationships imposed by the fixed direction of the airstream. In particular, the dynamic stability parameters measured by such techniques normally consist of combinations of individual stability derivatives. In recognition of this inherent test limitation, additional methods have been devised to obtain "pure" derivatives due to pitching, rolling, and yawing motions. The paper discusses the unique test capabilities of the Stability Wind Tunnel of the Virginia Polytechnic Institute and State University to measure pure derivatives. The discussion includes (1) a description of the tunnel hardware, (2) tunnel calibrations for curved- and rolling-flow tests, (3) considerations of oscillatory "snaking" tests to determine pure yawing derivatives, (4) representative aerodynamic data recently obtained for a current fighter configuration using the curved- and rolling-flow techniques, and (5) the application of dynamic derivatives obtained in such tests to the analysis of airplane motions in general, and to high angle-of-attack flight conditions in particular.

Curved-flow tests are conducted in a square test section by creating a uniform curvature to the flexible walls of the tunnel and by using variable-spaced steel wires upstream of the model to produce the velocity distribution of curved flight. The rolling-flow tests utilize a special circular test section and a nine-bladed rotor to impart the desired rolling velocity distribution to the airflow over a fixed model. The apparatus used for the oscillatory "snaking" tests consisted of a combination of flywheels, gears, and struts driven by a motor in such a manner that lateral velocity was maintained at zero during the yawing motions. Operational experience gained with these test methods has shown that individual stability derivatives can be measured; and that variations in the derivatives at high angles of attack for some wing configurations are not predicted by the combined parameters measured by conventional forced-oscillation methods.

Results recently obtained for a current fighter configuration over a large range of angle of attack and for several values of sideslip angle show that the effects of yawing velocity, rolling velocity, and sideslip were linear and independent at low angles of attack. However, at high angles of attack, the aerodynamic forces and moments became highly nonlinear, such that the magnitude and sense of the damping in roll and yaw, as well as the static derivatives were dependent on the angle of sideslip, roll rate, and yaw rate.

Although results obtained from these test methods indicate large differences from those obtained in oscillation tests, the significance of the differences is not clearly understood; particularly for current airplane configurations at high angles of attack.

#### SYMBOLS

$b$	wing span	$p$	roll rate
$C_L$	lift coefficient	$r$	yaw rate
$C_\ell$	rolling-moment coefficient	$y$	lateral displacement
$C_n$	yawing-moment coefficient	$R$	radius of curvature
$\alpha$	angle of attack		
$\beta$	angle of sideslip		
$\dot{\beta}$	rate of change of sideslip		
$\delta$	local flow angle due to rolling		
$\psi$	yaw angle		
$q$	dynamic pressure		
$V$	velocity		
$P_{st}$	static pressure		
$\frac{pb}{2V}$	non-dimensional roll rate		
$\frac{rb}{2V}$	non-dimensional yaw rate		

$\frac{\omega_b}{2V}$	reduced frequency parameter
$C_{n_r}, C_{l_r}$	yawing derivatives obtained from steady yawing tests
$C_{n_r}, C_{l_r}, \omega$	yawing derivatives obtained from oscillatory pure yawing tests
$C_{n_r} - C_{n_\beta}$	yawing parameter obtained from forced-oscillation tests
$C_{l_p}, C_{n_p}$	rolling derivatives obtained from rolling-flow tests

## INTRODUCTION

At some point in the airplane development cycle, the designer is faced with the requirement for a definition of the variations of aerodynamic forces and moments with the angular velocities in pitch, roll, and yaw. If these variations are reasonably linear and well-behaved, the classical stability derivatives of small disturbance theory are derived and used for analysis. If the conditions under consideration result in nonlinear aerodynamic variations, the analyst usually is required to retain the complete aerodynamic representation and linearized derivatives are of little use. Throughout the history of aeronautical engineering, many theoretical and experimental methods have been devised to provide information on the basic nature of aerodynamic data resulting from dynamic motions of the aircraft. The purpose of the present paper is to review the test capabilities of an existing wind tunnel which was specifically designed for several unique types of dynamic stability tests. This wind tunnel, known as the Stability Wind Tunnel, is located at the Virginia Polytechnic Institute and State University (VPI) where it is operated by the Department of Aerospace and Ocean Engineering for research and commercial applications. The test techniques to be discussed include curved-flow tests, rolling-flow tests, and oscillatory or "snaking" tests. The hardware and special equipment used in the tests are described, the tunnel flow calibrations are discussed, and representative data obtained in past studies of simple wing-fuselage combinations are presented. In addition, results of recent curved- and rolling-flow tests of a current fighter configuration are presented, including the effects of high angles of attack and angle of sideslip. Finally, a discussion of the applications and potential use of the test methods is given.

## DESCRIPTION OF FACILITY

The concept of a wind tunnel devoted exclusively to the static and dynamic stability testing of aircraft designs was originally proposed by Mr. M. J. Bamber of the National Advisory Committee for Aeronautics (NACA) at the Langley Research Center in the early 1940's. An overall view of the tunnel which resulted from that proposal is shown in figure 1. The tunnel was operated at Langley for about 15 years, during which time much basic information was provided regarding static and dynamic stability derivatives (particularly lateral-directional derivatives) at high angles of attack where estimation procedures became invalid. By the mid 1950's, however, interest in such tests began to diminish due to two reasons. First, it was generally accepted that the classical derivatives at low to moderate angles of attack could be estimated to a reasonable degree using theoretical methods. The second reason for lack of engineering interest was a de-emphasis of requirements for flight at high angles of attack. More specifically, military planners did not envision a need for highly-maneuverable fighters at that time. Subsequently, the tunnel was acquired by VPI in 1958 for educational and research purposes, and it is currently in operation at that institution. The facility may be classified as a continuous, closed-jet, single-return subsonic wind tunnel with interchangeable circular and square test sections. The tunnel is powered by a  $4.47 \times 10^5$  watt (600 HP) d.c. motor driving a 4.27 m (14 ft.), 8-bladed propeller. The maximum dynamic pressure in the test section is about  $1915 \text{ N/m}^2$  ( $40 \text{ lb/ft}^2$ ) and the tunnel turbulence factor is about 1.08. A photograph of a typical model test installation for conventional static tests is shown in figure 2.

During its operational status at the Langley Research Center, the facility was equipped to measure dynamic stability derivatives and parameters by almost every method in existence at the time, including free-oscillation tests, forced-oscillation tests, plunging tests, forced-rolling tests, curved-flow tests, rolling-flow tests, and oscillatory "snaking" tests. Today, the Stability Tunnel is used for conventional static force tests, curved-flow tests, and rolling-flow tests. The following sections of the paper discuss the current curved- and rolling-flow test concepts, as well as the snaking test concept previously used in the tunnel.

## ROLLING-FLOW TESTS

The circular test section shown in figure 3 was designed to enable the aerodynamic simulation of an aircraft in rolling flight by imparting the appropriate rolling velocity distribution to the flow. The test section is 7.32 m (24 ft) long and 1.83 m (6 ft) in diameter. Starting from the upstream end, the tunnel section transitions from a square to a round cross section in the first 2.2 m (4 ft). At that station, a rotor is installed to provide the desired rolling flow velocity distribution. The rotor which is 0.46 m (1.5 ft) wide is followed by 3.0 m (10 ft) of an essentially constant diameter section for testing. The remaining length of 2.6 m (8.5 ft) includes a section that increases in diameter and then transitions back to the square cross-sectional shape.

The section has provisions for both strut and sting mounting of the model. The strut mount can be oriented in any sideslip orientation while the sting mount employs the vertical blade support shown in figure 2. The blade is aligned with the tunnel centerline, and sideslip is obtained by rotation of the sting-model combination.

The unique portion of the rolling flow test section is the rotor located just upstream of the test area. The rotor rim is made of a heavy laminated wood which rests on a set of rubber wheels located about the circumference of the tunnel. The rotor is belt driven by a  $0.3 \times 10^5$  watt (40 HP) d.c. motor and is

capable of rotational speeds up to approximately 100 rpm. Attached to the rotor rim are 9 steel rotor vanes as shown in figure 3. A sketch of a typical rotor vane is shown in figure 4, and a close-up photograph of the rotor is shown in figure 5. The cross-sectional shape of the rotor vanes is a NACA 0012 airfoil. A photograph of a typical model installation for rolling-flow tests is shown in figure 6.

The rolling-flow test section is calibrated in terms of the value of non-dimensional roll rate  $\frac{pb}{2V}$  (for a reference wing span) associated with a given rotor speed. Two procedures can be used to accomplish the desired calibration. One method is to measure the rolling moment experienced by a rigidly mounted wing in the test section for various rotor speeds. The same wing is then used in forced-rolling tests to measure the rolling moment experienced by the wing as it rolls at various angular rates in the test section with the rotor stationary. By matching values of rolling moments for the two test methods, the required calibration curve of non-dimensional roll rate vs. rotor speed is obtained. The second calibration method consists of measuring the flow angularity distribution across the test section for various rotor speeds. From this distribution an associated non-dimensional roll rate can be determined. The latter method is used for current calibrations. The means for obtaining the required information is by a pitot-yaw head tube with which the necessary surveys of the test section are made.

The pitot-yaw head tube consists of a standard pitot tube with four additional pressure openings located symmetrically about the total pressure opening in the vertical and horizontal planes. The tube is calibrated by recording the differential pressures across the openings for selected angles of pitch or yaw. The tube is mounted on a calibration rig which allows the tube to change its pitch (yaw) angle while maintaining the tip of the tube at the same point in the flow.

Flow angularity measurements taken at 17 stations located about 10.16 cm (4 in) apart across the test section with station number 1 located on the left looking upstream are shown in figure 7. The rotor speeds were set using the rotor motor tachometer at values of  $\pm 1250$ , 1000, 750, 500 and 250 RPM. Note that a positive rotation creates air flow relative to a model such that it simulates a positive roll rate (the rotor turns counter-clockwise looking upstream). From the survey curves in figure 7, it can be seen that the flow angularity is approximately a linear function of the distance from the centerline. The equivalent non-dimensional roll rate can be determined from the slope using the following physical relationships. The local velocity due to roll rate and the flow angularity are related by:

$$V_y = py \approx V\theta \quad (1)$$

$$p = \frac{dV_y}{dy} = V \frac{d\theta}{dy} \quad (2)$$

Thus, the non-dimensional roll rate is given by:

$$\frac{pb}{2V} = \frac{bd\theta}{2dy} \quad (3)$$

The results of a current calibration are shown in figure 8 where the non-dimensional roll rate is plotted vs. the rotor motor tachometer reading for positive and negative rotor directions of rotation at a value of dynamic pressure of  $766 \text{ N/m}^2$  ( $16 \text{ lb/ft}^2$ ) for a model with a wing span of 1.2 m (4 ft).

Previous NACA investigations of the rolling-flow test method concentrated on rolling characteristics of simple wing-fuselage combinations. An example of the past data (reference 1) is presented in figure 9, which shows the incremental rolling-moment coefficient produced by roll rate for a rectangular wing tested with the rolling flow technique and the forced-rolling technique with the rotor stopped. The data are presented in terms of incremental values from zero rotation rate because it was found that substantial rolling of the flow occurred at zero rotor speed due to the rotor vane angles, thereby inducing considerable rolling moment on the model. The data which are presented for angles of attack of  $0^\circ$  and  $8^\circ$ , varied linearly with  $\frac{pb}{2V}$ , and the agreement between the rolling-flow and rolling-model test methods was exceptionally good.

Using this test method, the dynamic derivatives  $C_l$ ,  $C_n$ , and  $C_y$  may be obtained over an extensive range of angle of attack for zero and nonzero values of sidelip. It should be noted that since the rolling-flow environment is simulated about the relative wind, or velocity vector, the derivatives obtained will be due to rolling about the velocity vector, and the stability axis system (rather than the body axis system) will be a natural reference system for the data.

#### CURVED-FLOW TESTS

The square test section shown in figure 10 can be used for conventional testing or to simulate flight in a curved path (steady yawing or pitching). In the conventional mode of operation with straight walls, the test section is nominally 1.83 m (6 ft) square and 7.32 m (24 ft) long. The vertical walls are designed to have enough flexibility so that they can be deflected into a curve creating curved air flow past the model. In order to provide this flexibility, each of the vertical walls is made of 0.32 m (0.125 in) thick steel divided into three sections with approximately 0.30 m (1 ft) overlap between the sections to allow for the increase in length when the walls are made to follow a curved line. The tunnel walls are curved by a series of jack-screws positioned at regular intervals along the test section which pull the outer wall and push the inner wall into the desired location.

In order to complete the simulations of curved flight, it is necessary to redistribute the velocity profile so the velocity variations normal to the circular arc streamlines are in direct proportion to the local radius of curvature. This distribution is obtained by installing wire screens similar to that shown

in the sketch of figure 11 in the flow upstream of the test section. Each of the screens is basically a wooden frame with vertical wires having a varying spacing across the jet. Each wire is held taut by a spring under tension, with the widest spacing toward the outer wall. Six screens having different wire size and spacing are incrementally used to obtain the desired total-head and velocity distributions required for each increase in curvature. A photograph of a model installed in the tunnel for yawing tests is shown in figure 12 (reference 2). It will be noted in figures 10 and 12 that the tunnel curvature is such that negative values of  $r_b$  are normally produced by the tests.

$$\frac{rb}{2V}$$

Although curved-flow tests can be utilized for pitching and yawing derivatives, the present paper stresses the use of the technique to determine derivatives due to yawing. The velocity distribution at the moment center of the model for yawing flow is given by:

$$V = Rr \quad (4)$$

The non-dimensional yaw rate is then given by:

$$\frac{rb}{2V} = \frac{b}{2R} \quad (5)$$

Consequently the non-dimensional yaw rate is independent of speed and in theory one tunnel curvature setting can be used for a given value of non-dimensional yaw rate at all speeds. In practice, however, with the walls held at constant curvature, viscous effects cause the value of  $r$  to change with speed. Consequently, the flow has to be calibrated at all speeds to determine the exact value of  $r$  for each curvature selected.

A curved flow in the tunnel for simulation of a curved-flight condition of a given curvature has specific variations in the free stream of the dynamic, static, and total pressures normal to the streamlines. The variation of these pressures in the free stream along a streamline ahead of and behind the test region is zero. The velocity variation normal to the streamline (and thus the dynamic pressure) is determined by the particular flight path being simulated. The static- and total-pressure variations may be obtained by equating the pressure forces in the air to the centrifugal forces. These factors, specifically the dynamic and total pressures together with the angularity of the air stream, are used during calibration of the test section to indicate how well the test section reproduces ideal conditions.

Representative surveys made at the center and a rear survey station for various flow curvatures are given in figure 13 (reference 2). This figure, which presents the variation of dynamic pressure and air stream angularity with distance across the tunnel, indicates reasonably good agreement between the theoretical and actual results for the model test region in the center of the tunnel. Large angles of yaw would place the tail surfaces of the model in a region where the flow representation is not so accurate as in the center region.

Curved flow is not an exact simulation of curved flight because of the static-pressure gradient which exists normal to the streamlines in curved flow. A typical variation of static pressure across the curved-flow test section is shown in figure 14. This gradient produces a buoyancy which does not exist in curved flight and, in addition, a tendency for the low-energy boundary-layer air of the model to flow toward the center of rotation. The normal curved-flight tendency is for the boundary layer to move outward. A correction has been devised to account for the effect of the buoyant force. The boundary-layer effect is as yet considered to be second order.

In addition to the static-pressure gradient, there exists behind the drag screens a rather high degree of turbulence which is graded according to the spacing of the wires. The influence of the gradient in the turbulence on the aerodynamic characteristics of the model is believed to be small because the mixing of the turbulent wakes is believed to be sufficient to cause a relatively uniform turbulence downstream at the test section.

The curved flow testing technique was used by the NACA primarily to determine yawing derivatives of simple wing-fuselage shapes. Since the yawing velocity representation was about an axis perpendicular to the relative wind in the tunnel, the stability derivatives obtained included  $C_l$ ,  $C_{n_r}$ , and  $C_y$  in

stability axes. As the NACA began to explore the characteristics of dynamic derivatives of swept wings at high angles of attack, some extremely important differences were noted in the values of derivatives measured using different testing techniques. For example, shown in figure 15 (reference 3) are variations of the aerodynamic damping in yaw with angle of attack as obtained for a 60° delta wing-fuselage model in curved-flow tests and in free-oscillation tests. The values of  $C_{n_r}$  obtained in curved-flow tests show a

modest decrease in  $C_{n_r}$  at high angles of attack; however, the dynamic parameter  $C_{n_r} - C_{n_B}$  obtained from

the free-oscillation tests shows a marked increase in damping at high  $\alpha$ . Analysis of these and similar data obtained from further studies subsequently identified the potential existence of extremely large values of the derivative  $C_{n_B}$  at high- $\alpha$  for certain highly-swept wing designs. This work was later

followed by extensive research which combined yawing tests and linear-oscillation tests in an effort to isolate the individual derivatives at high- $\alpha$ . However, it is accurate to say that many questions remain as to the basic nature of oscillatory and curved-flow derivatives, particularly for high- $\alpha$  conditions with the presence of strong vortex flows.

### SNAKING TESTS

The interest in isolating individual stability derivatives in a form unattainable with conventional forced-oscillation tests led to the development of additional test rigs and methods, including linear-oscillation tests and combined-motion oscillation tests. One such combined-motion test developed by the staff of the NACA at Langley was the oscillatory test method known as snaking, which combined yawing and lateral motions of a model in such a manner as to produce pure yawing flow in a conventional straight-wall wind tunnel. The oscillation equipment (reference 4) was designed to generate an oscillatory motion in the XY-plane so that the airplane would always be heading into the relative wind or, more specifically, so that there would be no resultant lateral velocity component at the airplane center of gravity. The sketch of figure 16 illustrates the path and attitude of an airplane performing a pure sinusoidal yawing oscillation. The condition of no lateral resultant velocity at the model center of gravity is fulfilled when  $V \sin \psi = y'$ . For small angular motion of the model this condition can be written as  $V\psi = \dot{y}'$  and was approximated by use of the apparatus shown schematically in figure 17.

The streamline tube was supported on the ends by opposite rotating flywheels, which were driven by means of various shafts, gears, and a variable-frequency motor-generator set. The yaw angle of the model at any instant, if small angular motions of the model are assumed, is given by

$$\psi = \left( \frac{2R}{l} - \frac{e'}{e} \right) \sin 2\pi ft \quad (6)$$

The distance between the model mounting point and the center of the drive flywheel is  $y' = \frac{l}{2} \cos \psi + R \cos 2\pi ft$ . For small angular displacements of the model,  $y' = \frac{l}{2} + R \cos 2\pi ft$ ; hence, the velocity of the model toward the drive flywheel is  $\dot{y}' = -2\pi f R \sin 2\pi ft$  which for small angular motions can be taken to be the sideslip velocity  $\dot{y}'$ . For a pure yawing oscillation the relation between  $V$  and  $f$  is then

$$V = \frac{-2\pi f R \sin 2\pi ft}{\left( \frac{2R}{l} - \frac{e'}{e} \right) \sin 2\pi ft} \quad (7)$$

$$= - \frac{2\pi f R}{\frac{2R}{l} - \frac{e'}{e}}$$

or

$$f = - \frac{V}{2\pi R} \left( \frac{2R}{l} - \frac{e'}{e} \right) \quad (8)$$

Therefore, for a given velocity and a given distance between flywheels, proper conditions for the required motion could be obtained at different frequencies by adjusting  $R$ ,  $e'$ , and  $e$ .

The yawing and rolling moments acting on the models during the tests were measured by means of a strain-gage balance. The signals from the strain gage were passed into the instrumentation which permitted direct measurements of quantities proportional to the moments due to yawing velocity and acceleration. A description of the design and function of the instrumentation is given in reference 4.

One of the first applications of the snaking test method was to correlate values of yawing and rolling derivatives obtained in this oscillatory technique with values from steady yawing tests in the curved-flow test section. Such studies indicated that large differences existed in data obtained by the two methods. For example, shown in figure 18 (reference 4) are comparisons of  $C_{n_y}$  and  $C_l$  for a  $60^\circ$  delta

wing model in snaking and steady-yawing tests. As indicated, the trends and magnitudes of the data are not in agreement, indicating that substantial differences probably occur in basic aerodynamic flow phenomena acting on the model under oscillatory conditions.

As previously stated, this apparatus was also used in several studies to isolate individual lateral-directional stability derivatives by combining results obtained from several oscillatory tests at similar conditions. One example of the application of the testing technique is shown in figure 19, which presents results (reference 4) of tests of delta, swept, and unswept wings conducted to determine the correlation of results from various dynamic test techniques. Shown in figure 19 are rolling and yawing dynamic stability parameters obtained from the snaking tests, linear lateral acceleration tests, and forced-oscillation tests. For each wing, the oscillatory pure-yawing results (such as  $C_{l_{r,\omega}}$ ) are combined with

results from the lateral-acceleration tests (such as  $C_{l_B}$ ) and the resulting stability parameter (in this case  $C_{l_{r,\omega}} - C_{l_B}$ ) is compared with the result obtained from forced-oscillation tests ( $C_{l_r} - C_{l_B}$ ).

The data of figure 19 indicate that the algebraic summation of the derivatives showed trends with angle of attack which were in good agreement with the variation shown by the measured combined derivatives. The agreement in magnitude of the derivatives was considered fair. The encouraging correlation of results indicates that the analyst might make use of similar oscillatory-type tests for extraction of  $\beta$  derivatives. It should also be kept in mind that the use of steady yawing-flow results in combination with oscillatory results for this purpose may not be appropriate in view of the differences previously discussed for results obtained in snaking and steady yawing tests.

## RECENT RESULTS

Following the transfer of the Stability Tunnel to VPI, the general lack of interest in dynamic stability in the scientific community resulted in a 20-year period in which the foregoing test methods were not applied. In the 1970's, however, a dramatic increase in emphasis on maneuvering fighters led to a renewed interest in flight at high angles of attack. Subsequently, extensive static and dynamic wind-tunnel studies have been conducted for numerous configurations, but many of the questions regarding the measurement and application of dynamic derivatives remain as unanswered as they were 20 years ago. In an attempt to provide some fundamental information regarding derivatives for current configurations, the NASA Langley Research Center has recently sponsored research at VPI to renovate and apply the dynamic test capability of the Stability Tunnel. To date, the curved- and rolling-flow test methods have been put back into operation, and work is under way to update the oscillatory test capabilities as well. Tests have been conducted for three current fighter configurations, including the effects of sideslip and component build-up tests for a large range of angle of attack. Several interesting aspects of dynamic derivatives obtained at high angles of attack have been noted in these studies, and some representative data are now discussed for one of the fighter configurations.

Presented in figure 20 is a three-view drawing of a twin-engine, single seat fighter design recently tested by NASA in order to determine aerodynamic and design features which promote a high degree of spin resistance for the particular design (reference 5). A 1/10-scale model was tested by VPI in the curved-and rolling-flow test sections of the Stability Tunnel in order to provide data to aid in the interpretation of forced-oscillation data previously measured at Langley. The tests at VPI were limited to a determination of the yawing derivatives  $C_{Y_r}$ ,  $C_{n_r}$ , and  $C_{l_r}$ ; and the rolling derivatives  $C_{Y_p}$ ,  $C_{n_p}$ , and  $C_{l_p}$ . The tests included model component build-up tests, the effects of sideslip, and an extended range of angle of attack from  $0^\circ$  to  $45^\circ$ .

The specific fighter configuration is of particular interest to the aerodynamicist because its aerodynamic characteristics at high angles of attack become dominated by the effects of the relatively long pointed fuselage forebody, as discussed in reference 5. Shown in figure 21 are the static lift characteristics of the model components as determined in the Stability Tunnel. The data of figure 21 and associated flow visualization studies indicate wing stall to occur near  $\alpha = 15^\circ$ , but the relatively broad fuselage continues to produce lift, such that  $C_L$ <sub>max</sub> for the complete configuration is obtained near  $\alpha = 350^\circ$ .

Some of the more significant results of yawing- and rolling-flow tests to determine dynamic lateral-directional derivatives are now discussed. Examples of data are provided for angles of attack associated with conventional flight ( $\alpha = 50^\circ$ ); post-wing stall but at a lower than  $\alpha$  for  $C_L$ <sub>max</sub> ( $\alpha = 250^\circ$ ); and an angle of attack beyond  $C_L$ <sub>max</sub> ( $\alpha = 450^\circ$ ).

The data of figures 22 to 24 show the results of conventional static slideslip tests to determine the derivatives  $C_{n_\beta}$ ,  $C_{l_\beta}$ ; to evaluate the overall linearity of the data; and to determine the model component most dominant relative to aerodynamic behavior at high angles of attack. The data indicate the expected stabilizing effect of the tail surfaces at  $\alpha = 50^\circ$ , particularly on  $C_{n_\beta}$ . At  $\alpha = 250^\circ$ , however, the vertical tail has become less effective due to impingement of the low-energy stalled wing wake on the tail. At  $\alpha = 450^\circ$ , the vertical tail has lost all effectiveness; however, the complete configuration is directionally stable due to a pronounced increase in directional stability of the fuselage forebody at high  $\alpha$ . As discussed in reference 5, this characteristic is a result of a favorable pressure distribution on the forebody which results from the particular forebody cross-sectional shape employed by the design. Also worthy of note in figure 24 is the large asymmetric yawing moment coefficient obtained at  $\beta = 0^\circ$ . This result is produced by asymmetric vortex flows shed by the forebody, and is discussed in detail in the literature.

The results of the rolling-flow tests are presented in figures 25 to 27. At  $\alpha = 50^\circ$ , the data of figure 25 show well behaved, expected trends. The variations of  $C_l$  and  $C_n$  with  $p_b$  and  $\beta$  are linear, indicating negative values of  $C_{l_p}$  and  $C_{n_p}$ ; and  $p_b$  is seen to have no noticeable effect on  $C_{l_\beta}$  and  $C_{n_\beta}$ . Thus, the mathematical description of the aerodynamic data at  $\alpha = 50^\circ$  is linear and straightforward, and the concept of stability derivatives is valid. Figure 26 shows similar trends at  $\alpha = 250^\circ$ , although the effect of  $\beta$  on  $C_{n_p}$  exhibits some nonlinearity. For  $\alpha = 450^\circ$ , the data of figure 27 show extremely unconventional trends, with a high degree of nonlinearity and asymmetry. The large asymmetric values of  $C_n$  and  $C_l$  noted in the static tests previously discussed reappear; the variations of  $C_n$  and  $C_l$  with  $p_b$  are now unstable and nonlinear; and the values of  $C_{n_p}$ ,  $C_{l_p}$ ,  $C_{n_\beta}$ , and  $C_{l_\beta}$  are all dependent on  $p_b$  and  $\beta$ . At  $\alpha = 450^\circ$ , therefore, the mathematical modelling of the aerodynamic trends become extremely complicated and the concept of stability derivatives is very limited in application.

The results of the yawing-flow tests for the model are shown in figures 28 to 30. At  $\alpha = 50^\circ$  (figure 28), the data are again well-behaved and conventional. The data are reasonably linear, and the effects of  $r_b$  and  $\beta$  are independent. The values of  $C_{n_r}$  and  $C_{l_r}$  are negative and positive, respectively, as would be expected. When  $\alpha$  was increased to  $250^\circ$  (figure 29), the expected effect of wing stall on reducing  $C_{l_r}$  was

apparent, and  $C_{n_r}$  was also reduced. For  $\alpha = 45^\circ$  (figure 30), the large asymmetries in  $C_n$  were again noted at  $r_b = 0$ ; however, the direction of asymmetry had reversed from the static and rolling-flow tests. The data indicated unstable values of  $C_{n_r}$  and large positive values of  $C_{l_r}$ , although the latter trend occurs because of body-axis yawing moments transferred to the stability axis system. The unstable  $C_{n_r}$  results from the statically stabilizing forebody, and the phenomena is discussed in detail in reference 5.

In summary, the results of rolling- and curved-flow tests on a current fighter configuration have indicated extremely unconventional aerodynamic behavior at high angles of attack. The data were dominated by the effects of the fuselage forebody, including large asymmetries in  $C_n$ , unstable values of  $C_{n_r}$  and  $C_{l_r}$  and dependence of the dynamic and static derivatives on both angular rate and sideslip.

#### CONCLUDING REMARKS

The present paper has attempted to summarize and discuss the hardware and conduct of curved-, rolling-, and oscillatory pure-yawing wind-tunnel test techniques to determine dynamic stability parameters. In reviewing our current knowledge and appreciation of the data obtained from such tests, one is impressed by the fact that little application or progress has been made with the techniques over the past 20 years in the aeronautical world. It is extremely interesting to note, however, that same test techniques (such as snaking) which were originally developed for wind-tunnel tests of airplane designs are now used extensively in world-wide applications to the dynamics of submarines and surface ships (reference 6). No doubt, the revived interest in high- $\alpha$  aerodynamics and the associated problems of mathematically modeling airplane spin entry motions will require new emphasis on such fundamental studies, and it is encouraging to note recent analysis (reference 7) of such data.

With regard to research priorities of each of the three techniques discussed, it is the authors' opinions that the rolling-flow and snaking test techniques have more important applications than the curved-flow technique. The snaking technique, when coupled with linear- and forced-oscillation methods, promises to be a powerful tool with which to begin to understand the important  $\beta$  derivatives for current configurations at high angles of attack. The rolling-flow technique at first glance offers little advantage over the more popular rotary-balance techniques in widespread use today. However, one potential application to studies of spinning is worthy of note. Specifically, since the model is fixed in rolling-flow tests, the possibility exists to impart forced oscillations to the model and thereby permit the measurement of damping and cross-derivatives which could then be combined with the basic rolling-flow or rotary-balance data for a more accurate mathematical model for studies of the incipient spin and spin entry, particularly for oscillatory spins.

#### REFERENCES

1. MacLachlan, Robert; and Letko, William: Correlation of Two Experimental Methods of Determining The Rolling Characteristics of Unswept Wings. NACA TN 1309, May 1947.
2. Bird, John D.; Jaquet, Byron M.; and Cowan, John W.: Effect of Fuselage and Tail Surfaces on Low-Speed Yawing Characteristics of a Swept-Wing Model as Determined in Curved-Flow Test Section of Langley Stability Tunnel. NACA TN 2483, October 1951.
3. Johnson, Joseph L., Jr.: Low-Speed Measurements of Rolling and Yawing Stability Derivatives of a 60° Delta-Wing Model. NACA RM L54G27, December 1954.
4. Letko, William; and Fletcher, Herman S.: Effects of Frequency and Amplitude on the Yawing Derivatives of Triangular, Swept, and Unswept Wings and of a Triangular-Wing-Fuselage Combination With and Without a Triangular Tail Performing Sinusoidal Yawing Oscillations. NACA TN 4390, September 1958.
5. Grafton, Sue B.; Chambers, Joseph R.; and Coe, Paul L., Jr.: Wind-Tunnel Free-Flight Investigation of a Model of a Spin-Resistant Fighter Configuration. NASA TN D-7716, June 1974.
6. Goodman, Alex; Gertler, Morton; and Kohl, Robert: Experimental Techniques and Methods of Analysis Used at Hydronautics for Surface-Ship Maneuvering Predictions. Technical Report 7600-1. Paper Presented at 11th ONR Symposium on Naval Hydrodynamics, London, United Kingdom, 1976.
7. Hreha, Mark A.; and Lutze, Frederick H.: Linear Analysis of Poststall Gyration. Article No. 80-4103, Journal of Aircraft, Vol. 17, No. 10., October 1980.

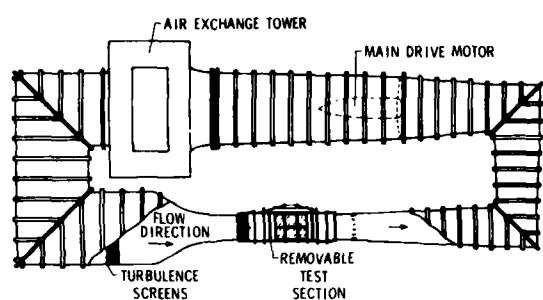


Figure 1.- Sketch of the Stability Wind Tunnel of the Virginia Polytechnic Institute and State University.

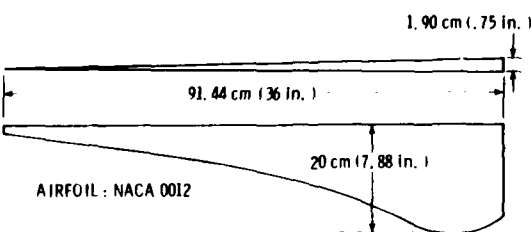


Figure 4.- Details of rotor vane.

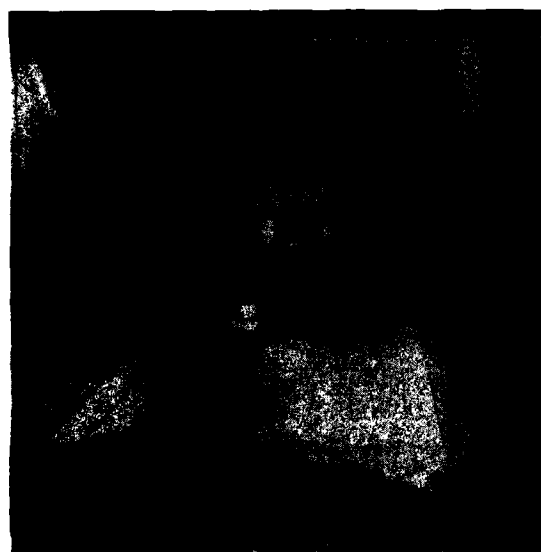


Figure 2.- Model mounted for conventional static tests in the Stability Tunnel.



Figure 5.- Close-up view of rotor.

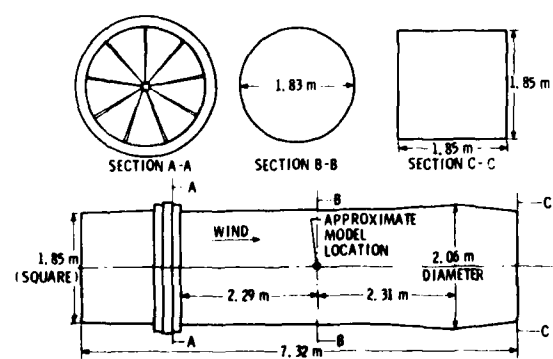


Figure 3.- The rolling-flow test section of the Stability Tunnel.



Figure 6.- Model mounted in the rolling-flow test section.

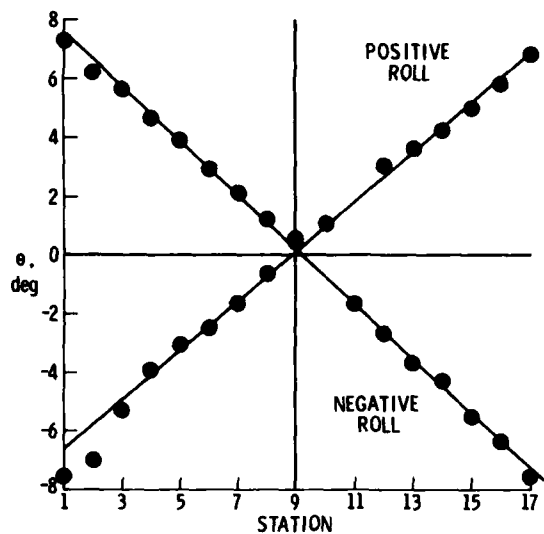


Figure 7.- Flow angularity measurements across the test section for positive and negative rotor rotation.  $\bar{q} = 766 \text{ N/m}^2$  ( $16 \text{ lb/ft}^2$ )

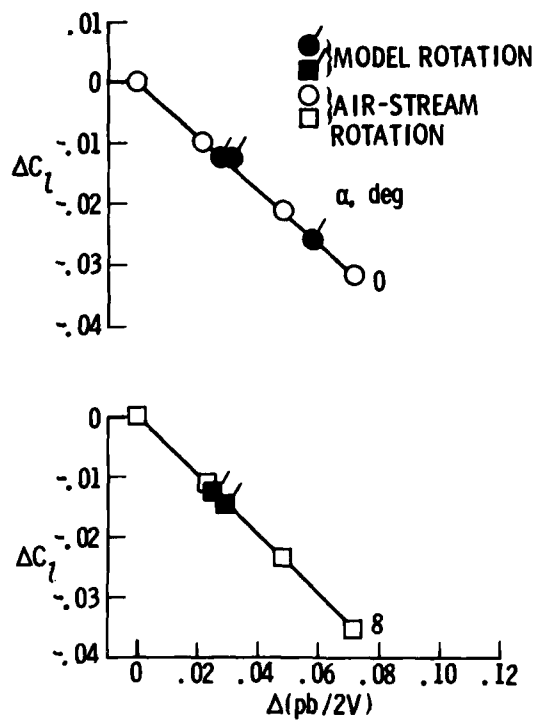


Figure 9.- Comparison of rolling-flow and forced-rolling results for a rectangular-wing model.

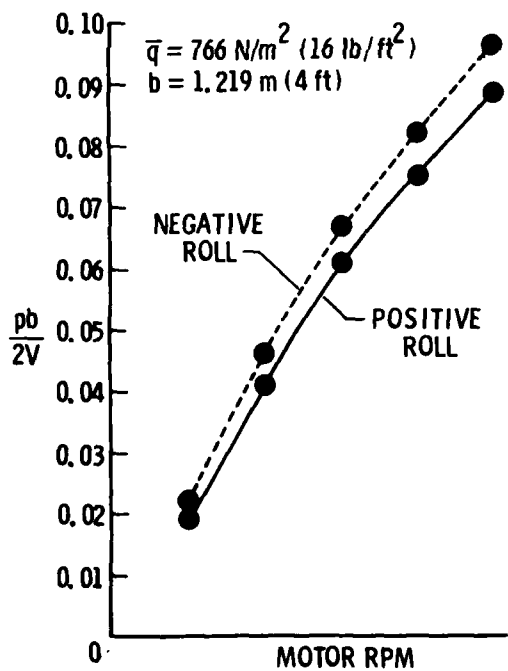


Figure 8.- Results of rolling-flow calibration.  
 $\bar{q} = 766 \text{ N/m}^2$  ( $16 \text{ lb/ft}^2$ );  $b = 1.22 \text{ m}$  (4 ft).

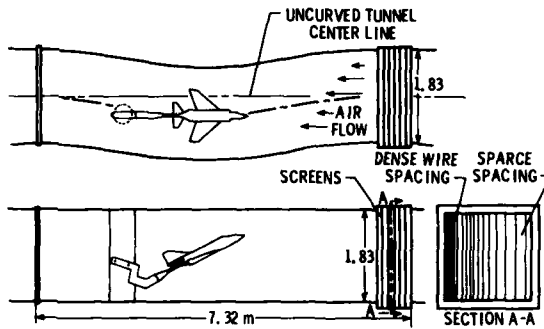


Figure 10.- Sketch of the curved-flow test section of the Stability Tunnel.

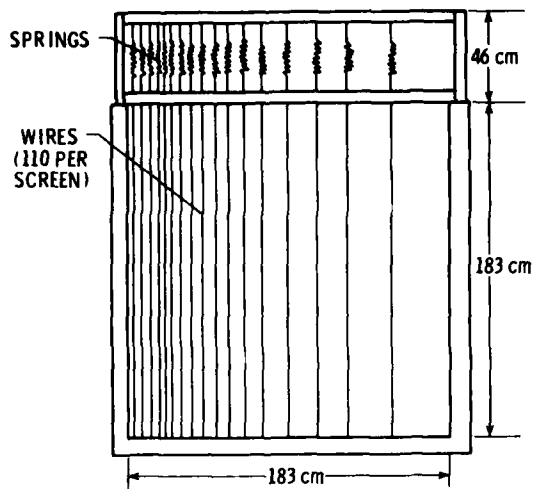


Figure 11.- Typical wire screen used for curved-flow tests.

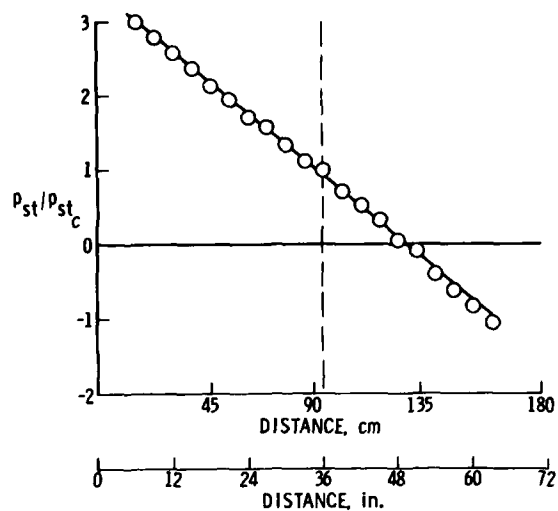


Figure 14.- Typical variation of static pressure across test section.  $\bar{q} = 766 \text{ N/m}^2$  ( $16 \text{ lb/ft}^2$ ).

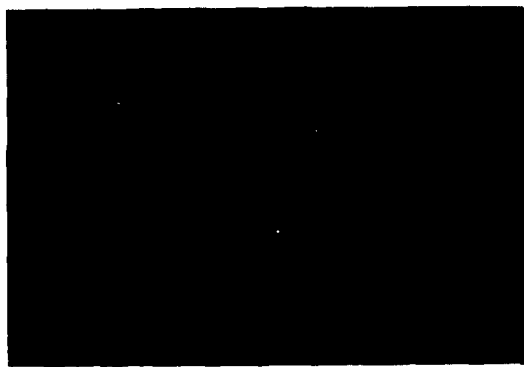


Figure 12.- Model mounted in the curved-flow test section.

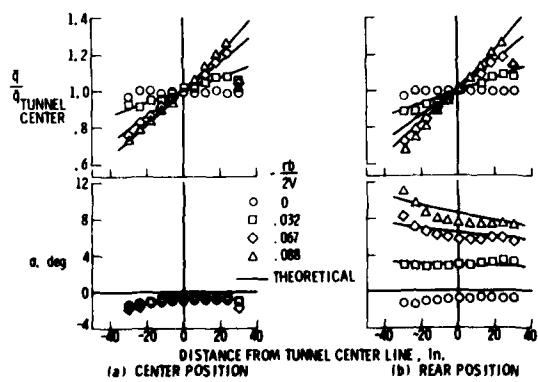


Figure 13.- Calibration of yawing-flow for four flow curvatures. Rear position at  $l = 0.79 \text{ m}$  (2.61 ft);  $b = 0.94 \text{ m}$  (3.07 ft).

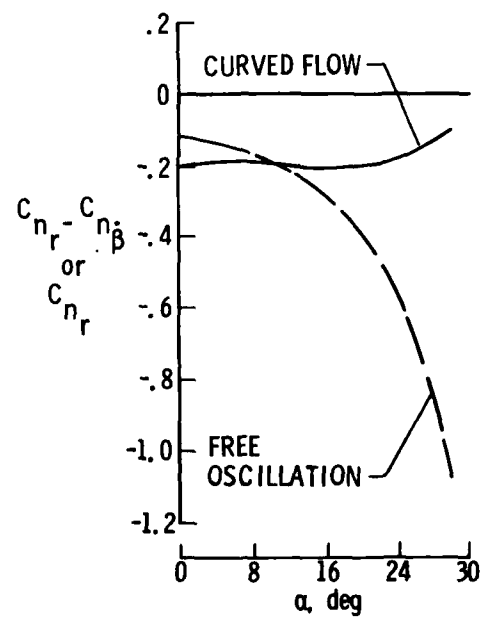


Figure 15.- Comparison of damping in yaw measured in curved-flow and free-oscillation tests for model with a  $60^\circ$  delta wing.

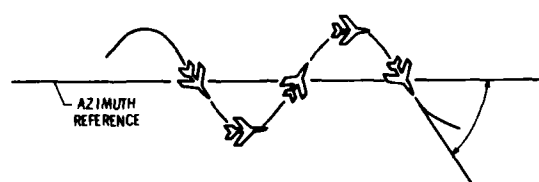


Figure 16.- Sketch of airplane performing sinusoidal yawing motion with  $\beta = 0^\circ$ .

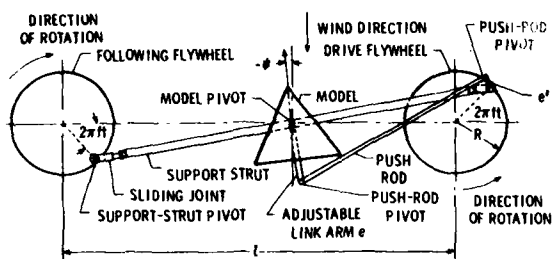


Figure 17. Schematic diagram of sinusoidal yawing apparatus.

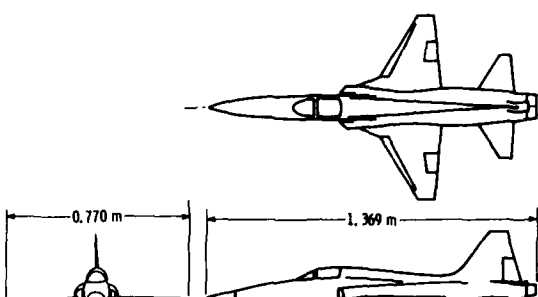


Figure 20.- Three-view drawing of the 1/10-scale model.

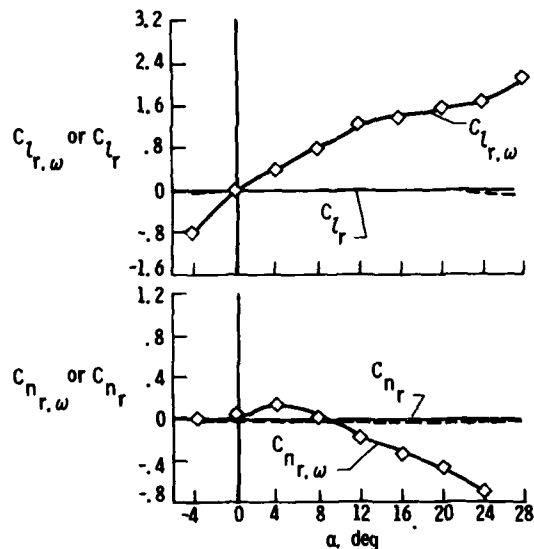


Figure 18. Comparison of yawing derivatives for a 60° delta wing obtained in steady yawing and sinusoidal yawing tests.

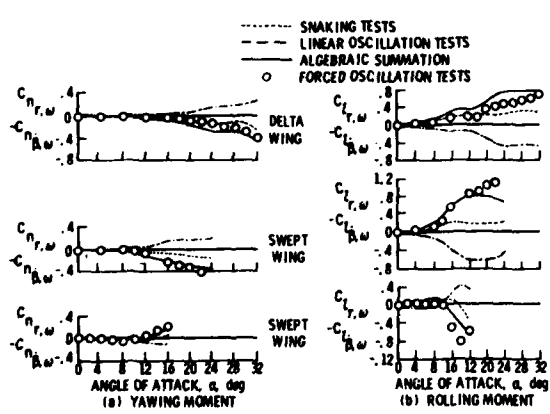


Figure 19.- Comparison of combined snaking and linear  $\beta$  test results with forced-oscillation results.

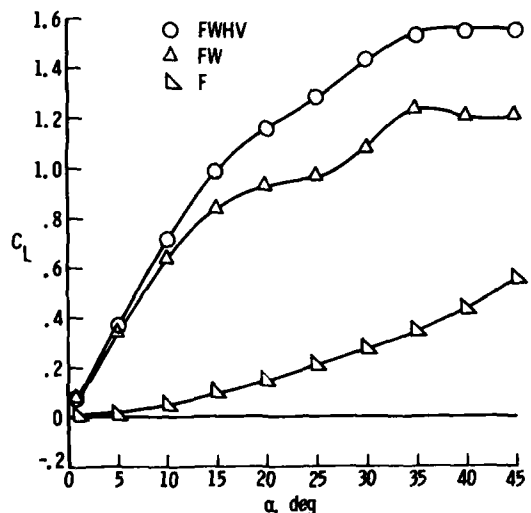


Figure 21.- Lift characteristics of model components.

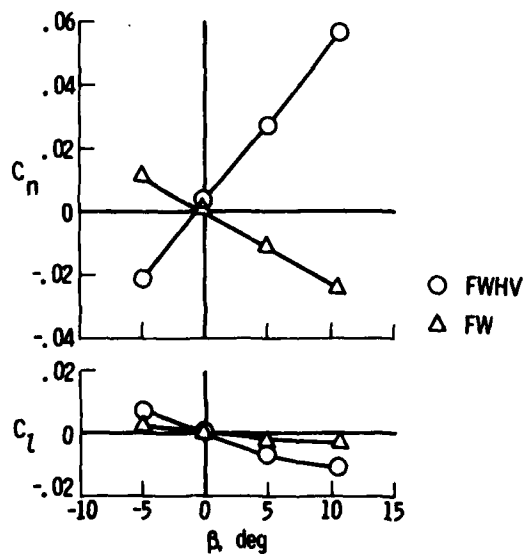


Figure 22.- Static lateral-directional characteristics for  $\alpha = 50^\circ$ .

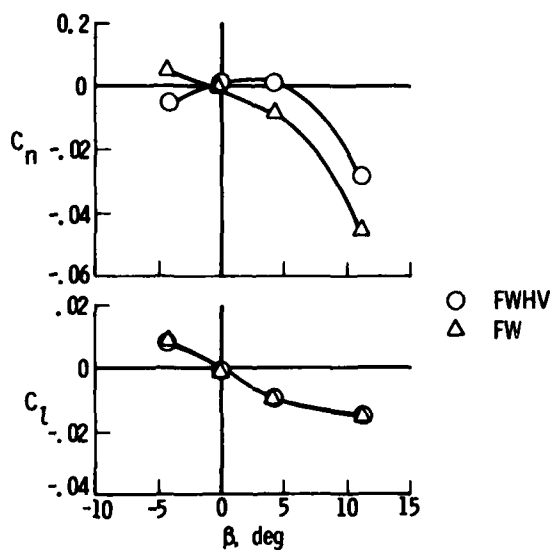


Figure 23.- Static lateral-directional characteristics for  $\alpha = 25^\circ$ .

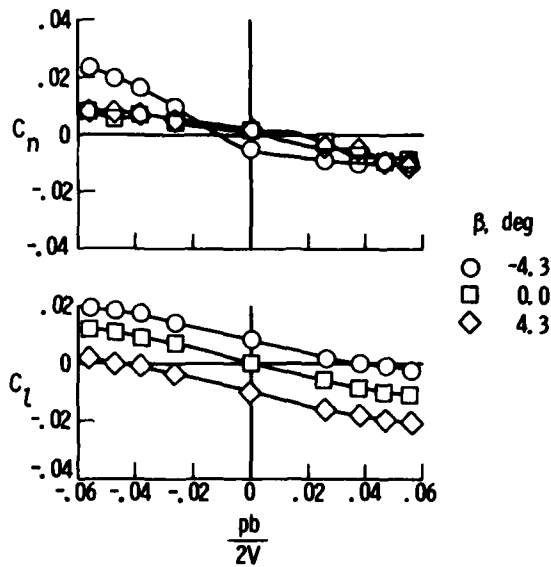


Figure 26.- Rolling-flow results for basic configuration.  $\alpha = 25^\circ$ .

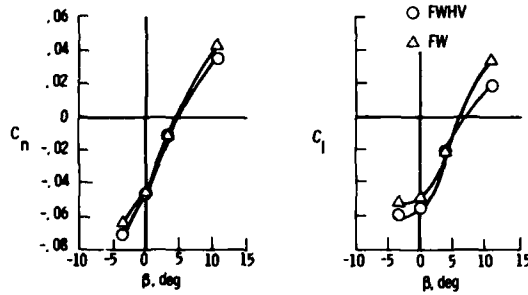


Figure 24.- Static lateral-directional characteristics for  $\alpha = 45^\circ$ .

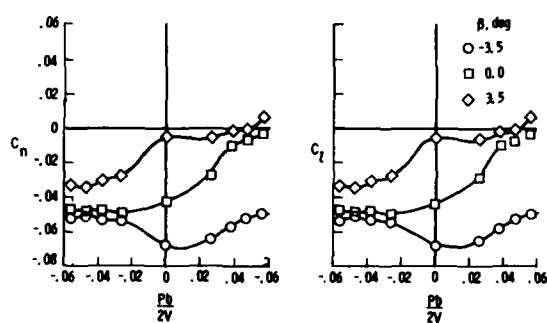


Figure 27.- Rolling-flow results for basic configuration.  $\alpha = 45^\circ$ .

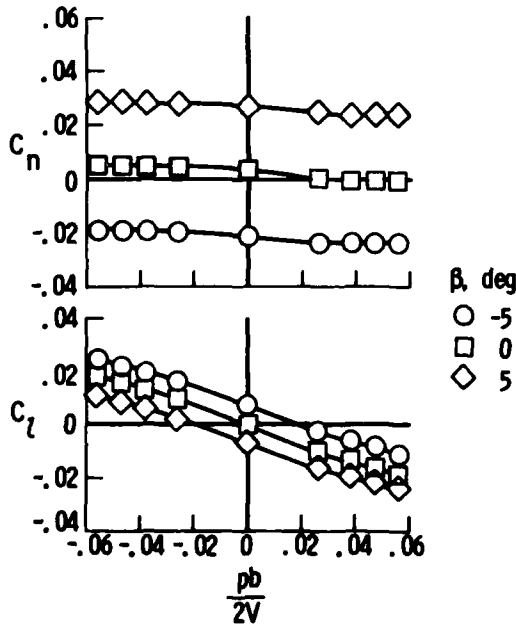


Figure 25.- Rolling-flow results for basic configuration.  $\alpha = 5^\circ$ .

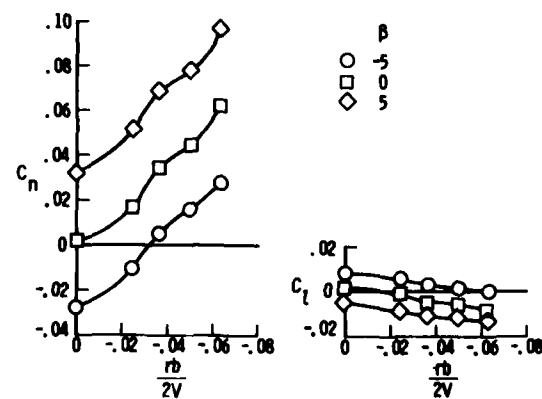


Figure 28.- Yawing-flow results for basic configuration.  $\alpha = 5^\circ$ .

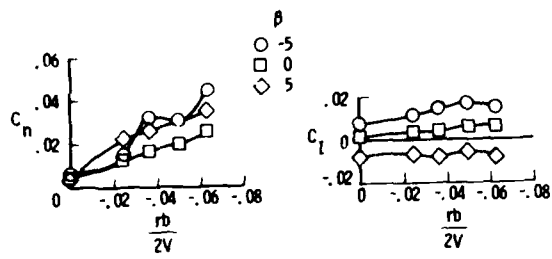


Figure 29.- Yawing-flow results for basic configuration.  $\alpha = 25^\circ$ .

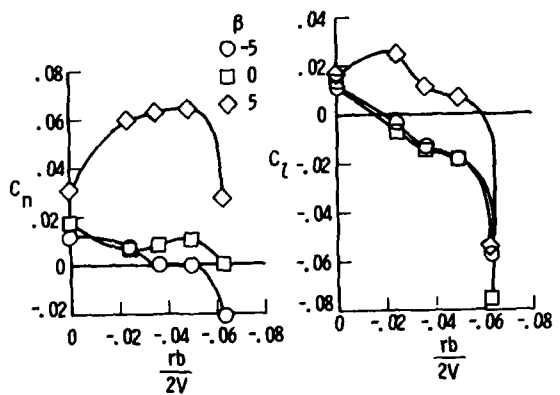


Figure 30.- Yawing-flow results for basic configuration.  $\alpha = 45^\circ$ .

## SUPPORT INTERFERENCE

L. E. Ericsson  
 Lockheed Missiles & Space Company, Inc.  
 Sunnyvale, California, USA

## SUMMARY

The existing information about support interference has been reviewed, with particular emphasis on dynamic interference effects and the special problems encountered at high angles of attack. It is found that the support interference effects are much more severe in dynamic than in static tests. Furthermore the support interference is aggravated greatly by a boat-tail or dome shaped base, even by modest base shoulder roundness, from what it is for a flat-based model. The general conclusion is that asymmetric stings or sting-strut combinations should be avoided. For slender bodies at low angles of attack a transverse rod comes close to permitting the true dynamically destabilizing effect of a bulbous base to be measured whereas even a very slender sting will distort the near wake effect and produce an unconservatively high measure of the dynamic stability. At intermediate and high angles of attack the sting support is superior to the other support methods, the transverse rod or the strut mounting. In many cases half-model testing provides the means to avoid most of the support interference effects. In some cases, as for a short blunt body such as the Viking configuration, the best approach appears to be to allow sting plunging, using a very slender sting.

## 1. INTRODUCTION

The problem of support interference has, of course, existed as long as the wind tunnel. However, it did not become of real concern until tests started to be performed at transonic and supersonic speeds. Some of the early work on static support interference will be reviewed before going into the more complex problems of present concern, i.e., dynamic support interference and the special problems associated with static and dynamic tests at very high angles of attack.

## 2. MODEL SUPPORT

In most wind tunnel tests<sup>#</sup> the model has to be held in place by a support. Figure 1 shows examples of the different types used. The wire-suspension method (Fig. 1a) is for all practical purposes restricted to low speed testing, whereas the strut and sting supports alone (Fig. 1b and 1c) or in combination (Fig. 1d) are used at all speeds. Although all of the support methods will be discussed, the main emphasis will be placed on the sting support system, as it is by far the most common.

The discussion will first focus on testing at moderate angles of attack, starting with static support interference before going into the more difficult problem of dynamic support interference. The special difficulties encountered in static and dynamic tests at very high angles of attack will be dealt with last.

## 2.1 Static Support Interference

According to Whitfield<sup>1</sup>, the supersonic sting support problem was first pointed out by Perkins<sup>2</sup> for continuum flow and by Kavanau<sup>3</sup> for rarefied flow conditions. Whitfield's review will be used as the starting point before discussing more recent results.

## 2.1.1 Sting Support

The sting interference problem for static tests at supersonic speeds was envisioned by Whitfield as shown in Fig. 2. For a small diameter cylindrical support the interference comes from the downstream conic fairing (the sting flare). As shown in Fig. 2, the interference starts to occur when the sting flare has been moved forward to the body wake "throat". Thus, the critical sting length is determined by the extent of the base recirculation region. As this separated flow extent is strongly dependent upon where boundary layer transition occurs<sup>4</sup>, the critical sting length is very sensitive to the transition location (Fig. 3).

When the flow is completely laminar, with transition well downstream of the wake "throat", the critical sting length increases with increasing Reynolds number<sup>3</sup> (Fig. 4), in complete agreement with the Re-trends for the extent of laminar flow separation<sup>4,5</sup>. When transition occurs in the near wake, the trends with Reynolds number are reversed<sup>3</sup> (Fig. 5), exactly as for transitional boundary layer separation<sup>4,5</sup>. When transition occurs well up on the body, the critical sting length is very small, but does increase with increasing Reynolds number (Fig. 5), in agreement with the Ke trends for turbulent flow separation<sup>4,5</sup>.

In addition to Reynolds number, Mach number also has a strong effect on the critical sting length. The M-trends for the separated flow extent for backward facing steps<sup>6</sup> and near wakes<sup>7</sup> makes one expect the critical sting length minimum at  $M \approx 4$ . This Mach number trend is displayed by Kavanau's flow (Fig. 4). The apparent reversal of this M-effect at transitional wake conditions (Fig. 5) simply reflects the fact that the transition Reynolds number increases with increasing Mach number. One can visualize how the true Mach number trend will be recovered for turbulent flow (See results for  $M = 3.00$  and  $M = 3.98$  in Fig. 5). When increasing the Mach number above  $M = 4$ , one expects the critical sting length to increase and finally level out at some hypersonic Mach number. When the Mach number is decreased from  $M = 4$  one finds, as expected, that the critical sting length peaks out at sonic speed<sup>8</sup>.

<sup>#</sup> The exceptions are tests in the free flight tunnels and in facilities that use a magnetic support system.

The concern so far has been with the large effect of the sting flare. What is the effect of the slender cylindrical sting? Strivers and Levy<sup>9</sup> used a thin, wide plate to split the sting in two halves, one of which they varied in size down to zero. They found their results to indicate that there is no sting diameter, no matter how small, for which the sting support interference on the base pressure disappears, at least not for the transonic Mach number range,  $0.60 \leq M \leq 1.40$ , that they investigated. In static tests this effect of the cylindrical sting portion is usually negligible. However, this is not the case for dynamic support interference, as will be shown later.

All the results discussed so far are for a slender body with a flat base. When the aft body has a boat-tail or bulbous base, the support interference problem becomes much more serious<sup>10</sup>. Perkins<sup>2</sup> found that the support interference influenced the separated flow region on the boat tail. Thus, not only the base pressure and associated drag is affected but also the normal force and moment characteristics<sup>10</sup>, (Fig. 6). The difference between rod-mounted and sting mounted models is mainly an indication of the static support interference from a cylindrical sting. Thus, in presence of a bulbous base even a slender cylindrical sting produces significant support interference in the transonic speed region.

Comparing the results for flat and bulbous base in Fig. 6 one finds that the base supports a positive normal force component that generates a stabilizing moment contribution. The results show further that the base force and associated stabilizing moment contribution are reinforced by the interference from the cylindrical sting. The schematic flow pictures in Fig. 7 illustrate what happens. The sting induces a positive normal force on the bulbous base by affecting the location of the flow separation. When the sting is pitched, there is an increase in the strength of the windward side recompression pressure. This increases the return mass flow rate and causes a forward movement of the windward side separation boundary on the bulbous base. Opposite effects occur on the leeward side, and a positive load is induced on the base as a result (Fig. 7a).

Similar reasoning can be used to explain the positive load induced by a free wake (Fig. 7b). The flow developed on the forebody, generating a positive lift, directs the wake downward. Because the wake is gradually turned back into the free stream direction, a transverse pressure gradient exists in the wake. The higher windward side recompression pressure at the wake throat is communicated forward to the base, generating a positive normal force on the bulbous base (Fig. 7b), in the same manner as for the sting mounted body (Fig. 6). The shadowgraphs and flow sketch in Fig. 8 not only substantiate that the windward side wake-recompression shock is strongest, but also shows that it is closer to the base, thus further facilitating the upstream communication of the windward side recompression pressure.

The base flow and associated aerodynamic loads are also affected by viscous forebody cross flow (Fig. 9b). Forebody crossflow causes the leeward side boundary layer to become thick and attain a separation prone velocity profile. This occurs through collection of low energy fluid, swept from the windward side. The same flow process serves to make the windward side boundary layer stronger, less separation prone. The resulting promotion of flow separation on the leeward side and delay on the windward side generate a negative normal force component on the base,  $\Delta^i C_N < 0$  (Fig. 9b). These two opposing effects vary in relative magnitude such that the wake effects dominate in one Mach number region and forebody crossflow effects in another (Fig. 10).

The drastic variation of the aerodynamic effects of a bulbous base between  $M = 0.8$  and  $M = 1.2$  in Fig. 10 can be explained as follows: Figure 11 shows how the base pressure and minimum body surface pressure vary with Mach number on slender cones and cone-cylinder bodies<sup>11-13</sup>. It is clear that at subsonic speeds a sizeable compression is needed to get from the body shoulder pressure to the base pressure. Such an adverse pressure gradient will cause the flow to separate ahead of the base<sup>14-16</sup>, as is illustrated in the top left insert in Fig. 11. The strength of the shock is affected by the wake via base pressure changes. The base pressure change due to angle of attack is small compared to the pressure rise through the shock. Thus, the upstream communication effect from the wake recompression region will be small, and the main contribution to the force on the bulbous base will be generated by forebody crossflow effects. Hence one can expect the large rounded base shoulder to have a statically destabilizing effect, in agreement with the results in Fig. 10.

Returning to Fig. 11, it appears that minimum compression is needed between shoulder and base pressure when the Mach number is slightly supersonic ( $M \approx 1.05$  for  $\theta_s = 10^\circ$ ). This situation is depicted in the top right inset of Fig. 11. In this case, with no terminal shocks on the body, a more direct communication with the wake exists. Hence, the upstream wake effect will dominate, and one can expect the large bulbous base to have a statically stabilizing effect, in agreement with the supersonic data trend in Fig. 10.

How the sting can distort this balance between downstream and upstream viscous flow effects is illustrated by the experimental results<sup>10</sup> in Fig. 12. At  $M = 0.8$  the dominance of the forebody crossflow effects are truthfully represented by the rod mounted test results. The sting, however, reinforces the wake recompression effects so much that they dominate at low angles of attack. Also at  $M = 1.1$ , where the upstream wake communication effects dominate for the free and rod mounted body, the sting shows this strong reinforcement of the wake recompression effect. As the Mach number is increased, the sting support interference gradually decreases and has practically disappeared at  $M = 4.4$ .

### 2.1.2 Other Support Systems

Another common way to support the model is by the use of a strut support. It has been used successfully, especially in regard to the testing of aircraft models. However, it can have a strong effect on the pressure distribution on an aircraft fuselage or a slender body, as is demonstrated by the results obtained by Ruben<sup>17</sup> for his strut design (Fig. 13). Perkins<sup>2</sup> showed the strut interference to be large for a boat-tailed slender body. In that case the support interference is enhanced by the interaction between the strut wake and the separated flow over the bulbous base. This is similar to the interference from the rod wake for a rod-mounted model<sup>10</sup> (Fig. 14).

<sup>#</sup>With flat-based models

A wire support system reported by Whitfield also was found to have a large interference effect on the base flow of a boat-tailed, blunted cone (Fig. 15). Apparently, the wires attached to the boat-tail energize the base flow (compared with the effects of upstream roughness), thereby causing a decrease of the base pressure. Adding an upstream tow line further decreases the base pressure. It has been found that the tow line acts as a flow separation spike on trailing blunt, conical decelerators<sup>18</sup>, causing a large decrease in the forebody drag. This decrease of nose drag for the body in Fig. 15 makes it act as a pointed rather than a blunted cone. This flowfield change results in a decrease of the base pressure. One strongly suspects that also in this case, as in the case of the cylindrical sting support discussed earlier<sup>9</sup>, there is no wire size small enough to eliminate the interference effect.

## 2.2 Dynamic Support Interference

The support interference is more of a problem in dynamic than in static tests. To start with the support system is often much bulkier than in static tests. This is because of the increased demands on rigidity. In the static test the effects of sting vibrations are usually time-averaged out to have negligible effect on the experimental results. In dynamic tests, however, the sting oscillation presents an additional, unwanted degree of freedom of the model motion. In the case of forced oscillations the support system has to house the driving mechanism, further increasing the size requirements.

Even if the support dimensions were the same in static and dynamic tests, the support interference will affect the data accuracy much more in the dynamic than in the static case. The reason for this is twofold. The relative motion between model and support increases the effect of the support interference on the moment derivative,  $C_{mq}$ . In addition, the measured phase relationship, which converts the static derivative  $C_{mq}$  to the dynamic derivative  $C_{mq} + C_{m\dot{a}}$ , is severely distorted by the support interference. As a result, it is not unusual to find the support interference effect to be one order of magnitude larger for  $C_{mq} + C_{m\dot{a}}$  than for  $C_{mq}$ .

### 2.21 Symmetric Slender Sting

The cylindrical sting presents the simplest example of this support category. It was discussed earlier how the cylindrical sting reinforced the upstream wake recompression effect in static tests. In the dynamic case the support interference is quite different<sup>9</sup> as is illustrated in Fig. 16. As the model pitches relative to the sting, the interference from the dynamic support will be negative, statically destabilizing, i.e. opposite to what it is in a static test (compare Figs. 16a and 16b). When the rotation center is well forward of the base, which usually is the case, base plunging relative to the sting amplifies the dynamic support interference effect.

For the oscillating model the interference load lags the vehicle motion due to the time required for convection downstream to the wake neck and back to the base through the recirculation region. Thus, a residual interference load occurs, as the body pitches downward through  $\alpha = 0$ , which opposes the motion (compare Figs. 16c and 16d). Consequently, the dynamic sting interference effect is damping, but statically destabilizing. That is, the cylindrical sting interference produces an erroneous, often very conservative measure of the damping of bulbous-based bodies, as is demonstrated by the results in Fig. 17. They also illustrate the fact alluded to earlier, i.e. the sting-induced effects on  $C_{mq} + C_{m\dot{a}}$  are one order of magnitude larger than those on  $C_{mq}$ .

The data in Fig. 17 illustrate further that at high subsonic speeds even a modest amount of shoulder roundness is enough to allow the wake recompression effects to propagate forward of the base. At supersonic speeds the very slender sting causes no interference, and would not do it at any speed for a flat-base model. Thus, the figure illustrates amply how base roundness aggravates the problem of support interference. One is tempted to conclude that, as in the case of the interference effect on base pressure<sup>9</sup> discussed earlier, there is probably no sting diameter small enough to eliminate subsonic dynamic support interference for a model with rounded base shoulder. Wehrend's results<sup>20</sup> seem to support this, as there is no "plateauing" tendency with decreasing sting diameter (Fig. 18).

Wehrend<sup>20</sup> showed that a symmetric, slender flare could reinforce the damping interference effect of a cylindrical sting (Fig. 19). Similar results have been obtained for a flat-based cone at supersonic speeds<sup>21</sup> (Fig. 20). Adding a splitter plate to the sting support has also a damping interference effect for the bulbous base (Fig. 19), but has no effect in the case of a flat-based model<sup>20,21</sup>. Apparently, the splitter plate deforms the wake, making it unsuitable to use when testing bulbous-based bodies.

When the model consists mainly of the bulbous base itself, as in the case of the Viking reentry configuration, one can, of course, expect the support interference to become especially large. The problem is well illustrated by the test results<sup>22,23</sup>, both in regard to the effect of sting diameter (Fig. 21) and distance to a slender, symmetric sting flare (Fig. 22). Use of a sting support can completely mask the wake-induced negative aerodynamic damping, if great care is not exercised. It is obvious that the true level of negative damping for the Viking configuration can not be ascertained from the dynamic tests performed<sup>22,23</sup>.

It is clear from the discussion so far that, when the model has a boat-tail or rounded base shoulder, it is practically impossible to avoid dynamic sting interference. For a model with a flat base, sting support interference is usually not a problem. There are, however, two exceptions. One is tests at hypersonic, low density flow conditions, which will be discussed more in the following section. Another is tests at a Reynolds number such that boundary layer transition occurs on the aft body near the base<sup>24</sup>. Wehrend's results for a sharp cone<sup>20</sup> illustrate the problem (Fig. 23). The nonlinear variation with  $\alpha$  of the pitch damping must be caused by viscous flow effects, more specifically by boundary layer transition response to the sting movement (see inset in Fig. 23). The large effect of rotation center location on the nonlinear hump at  $\alpha = 0$  is explained by this.

It is shown in Ref. 24 that transition indeed occurs on the body near the base, and that the transition-augmented support-interference effect can be computed from Wehrend's data<sup>20</sup>. Figure 24 shows that when the damping data are corrected for the sting interference they agree well with other experimental results<sup>25</sup> and with theory<sup>26</sup>. Similar transition-augmented sting interference has been documented by

Orlik-Rückemann et al<sup>27</sup> at  $M = 2$  for a  $7.5^{\circ}$  cone (Fig. 25).

### 2.2.2 Asymmetric Support

Figure 26 shows the asymmetric slender sting used by Adcock<sup>28</sup> to obtain the results in Fig. 27. The opposite data trends for  $C_{mg} + C_{m\dot{a}}$  and  $C_{ma}$  are apparent, indicating the dominating base recirculation effects on the bulbous-based models. The strong correlation between  $C_{mg}$  and  $C_{m\dot{a}}$  indicates that much of the wake-induced loads on the bulbous bases is generated by support interference. The interference derivative  $C_{m\dot{a}}$  was obtained in static tests by deflecting the sting angle  $\delta_S$  relative to the model (Fig. 26) and pitching the model-sting combination. The results were then carpet-plotted<sup>29</sup> (Fig. 28) to yield the interference derivative  $C_{m\dot{a}}$ . The sign of the interference derivative,  $C_{m\dot{a}} > 0$ , indicates that the interference effect of the slender asymmetric sting (Fig. 28) is opposite to that of a slender symmetric sting, i.e., it is undamping.

Figure 28 shows that the effect of sting deflection  $\delta_S$ , is highly nonlinear, with a more or less discontinuous  $C_m$ -change between  $\delta_S = 0$  and  $\delta_S = -10^{\circ}$ . The pressure distribution tells the story (Fig. 29). As the sting is pitched to the windward side,  $\delta_S = 0$ , its leeward side becomes deeper submerged in low energy wake-flow. The windward side reattachment pressure increases relative to the leeward side until it through the upstream communication flips the wake to the leeward side (as described in Refs. 19 and 20). Therefore, a negative base load (Fig. 29) and a discontinuous, statically destabilizing increase of the pitching moment results (Fig. 28).

At low subsonic Mach numbers the negative force is the result not only of the differential separation and associated pressure differential over the base, which is the mechanism at transonic speeds (Fig. 29a), but differential pressures propagated forward of the base also contribute (Fig. 29b). It can be seen that the same type of base load can be generated by having the sting at  $\delta_S = 0$  and deflecting the model to negative angles of attack. The asymmetric sting flare directs the wake downward at  $\alpha = \delta_S = 0$ , causing a positive base load (Fig. 30), and an associated strongly stabilizing pitching moment (Fig. 28). It is obvious from the discussion earlier of Fig. 16 that the statically stabilizing support interference effect in Figs. 28-30 will be undamping, accounting for much of the measured large undamping in Fig. 27. It is described in Refs. 10 and 31 how experimental results, such as those in Figs. 27-30, can be used to correct the experimental data for the asymmetric sting interference, giving the corrected data shown in Fig. 31.

In hypersonic low density flow even flat based models experience sting support interference, as a thick boundary layer opens up the communication between aft body and wake. The presence of the support affects the lip shock strength via the wake recompression pressure, propagated upstream through the near wake recompression region. The resulting shoulder pressure change is felt upstream of the base to an extent roughly proportional to the boundary layer thickness<sup>31</sup>. At high Mach numbers and very low Reynolds numbers the lip and wake recompression shocks appear to merge<sup>31</sup>, allowing the sting to affect the lip shock almost directly. This explains why the nonlinear damping results of Hobbs for a flat-based cone<sup>32,33</sup> bear such similarity with the subsonic results for the bulbous-based cone<sup>28</sup> (Fig. 32). The asymmetric flared sting has very similar effects in the two cases, causing a large decrease of the damping at  $\alpha = 0$ , where the wake flipping has its largest effect (Fig. 28).

Another rather common asymmetric sting-strut arrangement, used in hypersonic dynamic tests, is the one investigated by Walchner et al<sup>34,35</sup> (Fig. 33). The asymmetric sting-strut juncture causes divergent oscillations when it is too close to the model base. The base pressure variation for the short sting (Fig. 34) shows that at  $\alpha_c = 6.20^{\circ}$ , where the oscillations started (Fig. 33),  $p_B > p_\infty$  rather than the expected  $p_B < p_\infty$ . This indicates that the sting-strut juncture acts as the sabot<sup>36</sup> in Fig. 35, opening up the wake, (see flow sketch in Fig. 34) to produce a base pressure reading  $p_B/p_\infty > 4$ . The flow sketch illustrates how this pressure rise will be propagated over the windward side base shoulder to produce a positive statically stabilizing aft body load. Due to the time lag effect, it will be dynamically destabilizing, thus accounting for the initial divergence of the oscillations in Fig. 33. When the amplitude has increased to produce  $\alpha_c + \Delta\theta \geq 6.25^{\circ}$ , the wake is "flipped", as illustrated in the flow sketch<sup>#</sup> (Fig. 34), producing a loss of shoulder pressure on the top side and resulting in a discontinuous increase of the aft body load. To the discontinuous increase of static stability corresponds a discontinuous decrease of damping, explaining the sudden amplitude increase in Fig. 33.

The pressure data for the long sting,  $l_S/d = 4.2$ , show also large, discontinuous changes of base pressure (Fig. 36), rather similar to those for the short sting. Why, then, are not the oscillation traces also similar (Fig. 33)? The answer lies in the fact that the initial release angle,  $\alpha_c + \Delta\theta = 6.10^{\circ}$ , was in the case of the long sting enough to flip the wake, and a close to normal (support free) near wake is established (see sketch in Fig. 36). The oscillations never dipped below  $\alpha_c - \Delta\theta = 1.90^{\circ}$ , and could, therefore, not catch the base pressure discontinuity in the return loop at  $\alpha_c = 1.50^{\circ}$  (Fig. 36).

When the sting-strut juncture was faired over with a splitter plate - extension of the strut, the base pressure variation for the long sting was close to the one expected for a free wake<sup>35</sup> (Fig. 37). Thus, one would expect essentially interference-free dynamic data for this sting arrangement. Test data with a faired, shorter sting-strut arrangement confirms this<sup>37</sup> (Fig. 38). This is at least true for  $x_{CG}/l = 0.60$ , (Fig. 38b) whereas there is some indication of interference for  $x_{CG}/l = 0.55$ , i.e. when  $l_S/d$  was decreased from  $l_S/d = 2.38$  to  $l_S/d = 2.24$  (Fig. 38a).

A compilation of experimental results contains several examples of dynamic support interference at hypersonic speeds<sup>38</sup> (Fig. 39). The data points at  $M = 18$  were obtained with the asymmetric sting-strut support<sup>39</sup> shown in Fig. 40, which obviously exerted the same undamping interference as the asymmetric arrangement just discussed<sup>34,35</sup> (Fig. 33). The data points at  $M = 20$  were obtained<sup>40,41</sup> by a support very similar to the one shown in Fig. 40. The data trends indicate the presence of discontinuous and hysteretic support interference of the type investigated by Walchner et al<sup>34,35</sup> (Fig. 41).

<sup>#</sup> The flow sketch illustrates how the deflection  $\theta = 2.250^{\circ}$  relative to the sting makes the wake flip already at  $\alpha_c + \theta = 6.250^{\circ}$ , instead of at  $\alpha_c = 80^{\circ}$ , as in the case of  $\theta = 0$ .

The data obtained with a stiff flexure show increasing damping with decreasing Reynolds number, whereas the data obtained with a soft flexure show the opposite trend. For the low reduced frequency of the test,  $\bar{\omega}^2 \ll 1$ , there are no frequency effects according to inviscid theory (Fig. 41a). Figure 41b shows how the frequency effects decrease with increasing Reynolds number (and associated dynamic pressure) until they have disappeared at  $Re > 0.3 \times 10^6$ . This might suggest that the data trend is caused by mechanical support damping that was not adequately accounted for. However, the frequency trend goes the wrong way. It can be shown<sup>42,43</sup> that the total damping should increase with decreasing frequency, a trend opposite to that displayed by the low frequency data in Fig. 41.

Based upon the similarity shown in Fig. 32 the bulbous-base results (Fig. 28) will be used to explore the possible sting interference effect that can explain the data trend in Fig. 41. The wake flipping (Figs. 28-30) causes a highly nonlinear moment change that can be represented by a discontinuity,  $\Delta^i C_m$ , for finite amplitude oscillations. Judging by the results in Fig. 34 hysteresis effects are also likely to be present. The effect of these nonlinearities on the measured pitch damping interference can be expressed as follows<sup>38</sup>.

$$\Delta^i C_{\bar{m}\theta} = (\Delta^i C_{\bar{m}\theta})_d + (\Delta^i C_{\bar{m}\theta})_h \quad (1)$$

$$\Delta^i C_{\bar{m}\theta d} = -\frac{2}{\pi} \frac{\Delta^i C_m}{\Delta\theta} \cdot \frac{U_\infty \Delta t}{c} \quad (2)$$

$$\Delta^i C_{\bar{m}\theta h} = -\frac{2}{\pi} \frac{\Delta^i C_m}{\Delta\theta} \cdot \frac{1}{\omega} \frac{\Delta\alpha_h}{\Delta\theta} \quad (3)$$

where  $\Delta^+$  and  $\Delta\alpha_h$  are lumped representations of the time lag and hysteresis effects<sup>10</sup>. Figure 28 shows that the moment jump is statically stabilizing,  $\Delta^i C_m < 0$ . Thus, according to the expressions above, the sting interference is undamping,  $\Delta^i C_{\bar{m}\theta} > 0$ . The pure discontinuity causes an effect that is inversely proportional to the amplitude  $\Delta\theta$ , Eq. (2), whereas the hysteresis effect is inversely proportional to the amplitude squared,  $\Delta\theta^2$ , and the reduced frequency,  $\bar{\omega}$ , Eq. (3). Applying this formulation to the data in Fig. 41, trying to find a curve for zero hysteresis, from which the frequency effects given by Eq. (3) will fit the data, gives the results shown in Fig. 42. That is, the frequency trend could be explained by asymmetric sting interference with hysteresis of the type observed by Walchner et al.,<sup>34,35</sup> (Fig. 34 and Fig. 36).

The Reynolds number trend of the hypothetical curve for no hysteresis,  $\Delta\alpha_h = 0$ , could possibly be explained by the Re-effect on the wake. That is, at  $Re_{1\infty} = 0.3 \times 10^6$  the sting-strut juncture is located in the wake throat, giving maximum interference.

From the evidence presented it is clear that all asymmetric sting or sting-strut arrangements produce a strong source of support interference. The initial asymmetry forces a large nonlinear, even discontinuous flow change to take place near  $\alpha = 0$ , where most tests are performed.

Judging by the results obtained by Walchner et al.<sup>34,35,37</sup> (Figs. 37 and 38), extending the strut all the way, giving a symmetric sting-strut arrangement, as the one used in the NAE hypersonic wind tunnel<sup>44</sup> (Fig. 43), should alleviate and possibly eliminate the support interference from the sting-strut juncture. It should be possible to avoid dynamic support interference for flat-based models in this manner. However, based upon the experience with slender sting supports, discussed earlier, one doubts that this will eliminate support interference for a bulbous-based model. The use of splitter plates or symmetric strut arrangements will change the wake, preventing measurement of the free-wake effects on a bulbous-based model.

The openings in the base, needed to permit the relative sting movement will also hinder the measurement of true bulbous base effects<sup>45</sup> (Fig. 44). It has been shown by Wehrend<sup>46</sup> that the undamping effect of a bulbous base can be all but eliminated by providing the base contour with flow fences, that cut off the communication between aft body and near wake. A concave base or a base lip could perform the same task<sup>47</sup> (Fig. 45).

The concave base increases the base pressure, decreasing the drag<sup>47</sup>. One has reason to believe that the base pressure level on the inside of the lip is rather insensitive to angle of attack. The exception appears to be when boundary layer transition occurs in the near wake. As the transition is sensitive to forebody crossflow effects<sup>48</sup>, the transition location in the near base flow region is sensitive to  $\alpha$ . Thus, through the strong effect of transition location on base pressure<sup>4</sup>, differential lip pressures are established. The resulting force is statically destabilizing and damping, according to experimental evidence.

### 2.2.3 Other Dynamic Support Systems

One obvious solution to the problem of sting support interference is to use a transverse rod support. However, Dayman<sup>49</sup> has shown that at  $M = 4.64$  a wire support, located at the mid point of a 30 deg. cone, shortens the near wake recirculation region. This could, of course, be the type of wire interference discussed in conjunction with Fig. 15, but then one would not expect it to disappear when the Mach number is lowered to  $M = 2.02$ , as Dayman found to be the case. This leads one to speculate that the interaction from the wire or rod shock with the base flow may affect the wake geometry (Fig. 46). This would explain the Mach number sensitivity found by Dayman<sup>46</sup>. The rod-interference would be similar to the rod wake-base wake interaction (Fig. 14), causing a local dynamic pressure reduction over the base-shoulder region, thereby generating a positive, statically stabilizing normal force. Because of time lag effects the interference effect would be dynamically destabilizing.

A direct measurement of the transverse rod interference is hard to find. Usually one can only compare rod data with sting data. This, however, may not be as futile as it appears. For example, Fig. 47 reveals that the measured dynamic stability differs little for a flat-based model whether or not a rod or sting support is used (Fig. 47a), whereas the support system makes a difference in the case that the model has a rounded base shoulder (Fig. 47b). Experimental evidence indicates that the very slender sting support

used should not have any interference effect on the flat-based model. And if there were any it should be dynamically stabilizing, as has been illustrated earlier. At transonic speeds only the rod wake effect is present, which for small amplitude oscillations at  $\alpha = 0$  has little chance to spread from the lateral meridian to influence the normal force and pitching moment.

As the difference between rod-and sting-mounted data in Fig. 47a goes the wrong way, statically destabilizing and damping rather than the expected opposite rod interference trend, one can conclude that there is no rod interference for the flat-based model. Adding base shoulder roundness should not affect the rod interference appreciably, whereas it is known to have a very large effect on the slender sting interference. Thus, the results in Fig. 47b indicate that the true undamping wake recirculation effect was measured with the rod mounted model. Because of the large time lag for the base recirculation effect itself and its sting-induced perturbation, the dynamic data show clearly the sting-induced damping whereas no distinct data trend can be resolved from the static data.

At hypersonic speeds, the rod interference becomes significant, as has been shown by Hobbs<sup>32,33</sup>(Fig. 48). A significant dynamically destabilizing effect of the rod support was observed until turbulent base flow conditions were reached, when all support interference effects become small, as has been illustrated (Fig. 3). There are several reasons for the increasing rod interference at hypersonic speeds. In addition to the emergence of rod shock effects (Fig. 46), the rod wake effect is enhanced by large boundary layer crossflow, sweeping the rod wake up from the lateral meridian and facilitating it influencing the normal loads on the aft body. Whereas the inviscid stream lines may obtain twice the free stream flow inclination on the body, the viscous flow can produce four times the free stream angle of attack at hypersonic speeds<sup>50</sup>.

At higher angles of attack and/or amplitudes the rod interference will, of course, become important at all speeds, as the effects of the rod wake no longer is restricted to the lateral meridian. A flat-based sting-mounted model shows no effect of varying the oscillation amplitude from 2 to 10 degrees, whereas the rod mounted model shows a very large effect (Fig. 49). This is a clear-indication of rod interference. At transonic speeds one does not expect any nonlinear amplitude effects for a flat-based model. The measured rod effect is to increase static stability and decrease damping, all in agreement with the expected rod support interference effect.

In addition to this  $\alpha \neq 0$  case the rod support is also a poor choice for a short blunt body, such as the Viking configuration discussed earlier (Figs. 21 and 22). The wire support interference for a boat-tailed body (Fig. 15) amply illustrates the problem one would encounter in this case. It is unlikely that any support system can be found that will not have a significant interference effect on a short blunt body, such as the Viking configuration.

Half model testing is an alternative which avoids many of the support interference effects discussed here. It has been shown to eliminate the problem of transition-augmented slender sting interference<sup>27</sup> (Fig. 25), and similar beneficial effects could be expected in regard to the support interference on bulbous-based models. The problem is, of course, to account for the wall or mounting plate boundary layer and its effects on the near wake flow of the model. (The splitter plate problem discussed earlier, Fig. 19). Even if it may be possible through careful calibration steps to extrapolate to zero boundary layer thickness, this may not account for all of the splitter plate effect. The presence of a zero-boundary-layer-thickness side plate could still influence the non-axisymmetric wake flow generated at non-zero angle of attack. Thus, one could be faced with the same problem as in the case of zero diameter sting and wires discussed earlier.

We have seen that the sting support interference becomes a problem when communication is opened up between the aft body and the base recirculation region, e.g., by a bulbous base at subsonic and transonic speeds, via boundary layer transition at all speeds, and through the thickened body boundary layer in hypersonic low density flow. There is another more general case which causes dynamic sting interference at all speeds, and that is when the body itself is engulfed in separated flow, as in the case of a blunt-nose cylinder-flare body at transonic speeds<sup>51</sup> (Fig. 50). Sting interference results, when the leeside separated flow engulfs the flare and joins with the wake. This happens at  $\alpha > 20^\circ$ , where the slender sting causes unconservatively high damping derivatives to be measured.

Although there may be no sting size small enough to eliminate all interference, it is in many cases possible to minimize the interference to an acceptable value by using a very slender sting support, as in Fig. 47. In so doing, however, one usually changes the testing from a single-degree-of-freedom (pitch only) to a two-degrees-of-freedom system (pitch and plunge)<sup>52</sup>. For the usual subcritical sting stiffness, the result is that the measured damping is increased for a slender body (with  $C_{1\alpha} > 0$ )<sup>52</sup>. If one measures the sting plunging, it is relatively easy to correct for its effect on the measured stability derivatives. This is especially true for linear aerodynamic characteristics<sup>53,54</sup>. It can also be done in the case of highly nonlinear moment characteristics, provided that the lift characteristics can be approximated by a linear segment for the  $\alpha$ -range of interest for each data point<sup>52</sup>.

There is one case for which this two-degrees-of-freedom testing of a sting support model is the only means, short of free flight, that can provide a reasonable measurement of the dynamic stability derivative. The case in point is dynamic tests of short, blunt bodies such as the Viking configuration (Figs. 21 and 22). By varying the sting diameter down to very small sizes, an assessment of the interference from a finite size sting could be made. The problem of the interference for a zero size sting still remains. However, as  $C_{1\alpha} < 0$  for short, blunt bodies, the sting plunging will produce a dynamically destabilizing influence<sup>52</sup>. Thus, it is much less likely that measurements with a very slender sting will produce an unconservative, (too damped), measure of the blunt body dynamic stability.

### 2.3 High- $\alpha$ Testing

The complications arising in flight at high angles of attack were discussed extensively in a recent AGARD meeting<sup>55</sup>. One of the conclusions drawn from the meeting<sup>56,57</sup> was that the interference effects from the large, bulky support systems used in high- $\alpha$  testing needed to be investigated. According to an extensive survey of dynamic testing techniques<sup>58</sup> the support systems shown in Fig. 51 are typical. It is

obvious that these support systems will interfere with the separated flow vortices and wakes shed from the model, as is pointed out in Ref. 57. Only two papers in the AGARD conference<sup>55</sup> addressed this problem by comparing the wind tunnel data with free flight results for combat aircrafts<sup>59,60</sup> (Fig. 52). It can be seen that significant differences between wind tunnel and flight test results exist already at moderate angles of attack. The most likely cause for the deviations is support interference rather than wind tunnel wall interference or Reynolds number mismatch.

How powerful the support interference can be on shed vortices is illustrated by Hummel's results<sup>61</sup> (Fig. 53). An obstacle placed one (center) chord length downstream of the trailing edge, on one half of a 76° swept delta wing, causes the vortex breakdown to move from 80% to 40% chord, thereby changing the wing loading extensively. Hummel's experiment was recently repeated for a 70° arrow wing<sup>62</sup> (Fig. 54), giving the results shown in Fig. 55. Figure 56 shows the lateral stability characteristics measured by two different support systems<sup>62</sup>.

Although only the curved strut is likely to cause early vortex burst, the vertical strut support can have its own interference effect according to results for a swept wing-ogive cylinder configuration<sup>63</sup>. This could, of course, be the strut-body interference to be discussed shortly. However, the leeward side separated flow on highly swept delta wings can be very sensitive to disturbances on the windward side, as is demonstrated by Lambourne's results<sup>64</sup> (Fig. 57). In the thorough calibration of the test setup it was discovered that the pressure transducer housing, protruding slightly from the bottom surface, could cause a severe disturbance of the leeside vortex flow, if placed near the leading edge. If one examines the oil flow pattern closely, one finds evidence of a new reattachment line close to the leading edge, starting at  $\xi_1$ . This indicates that a new vortex has started at station  $\xi_1$ , at the same time as the "old one" starts to bend aft towards the freestream direction. The implication is rather clear. A wire attachment on the underside of a wing could have a similar effect. A strut could distort the windward side flow, especially at non-zero angles of side slip, thereby affecting the leeside vortex shedding.

The problem of strut interference on bodies at high angles of attack has been demonstrated very vividly<sup>65</sup> (Fig. 58). By testing with dummy sting and dummy strut the results in Fig. 59 were obtained showing the severe support interference caused by the leeward side strut support. The similarity between the leeside strut effect and the effect of a splitter plate on the vortex shedding from a cylinder in two-dimensional flow has been pointed out recently<sup>66</sup>. As the splitter plate interferes with the cross-wake communication necessary for Kármán vortex shedding, so the strut interferes with the steady counterpart, the vortex shedding from a slender body at high angles of attack<sup>67,68</sup>. Minuscule windward side blowing can have a very large effect on the asymmetric vortex shedding from an inclined slender body, as is evidenced by the measured side moment<sup>69</sup> (Fig. 60). In view of this it is not hard to visualize that a windward side strut support can interfere strongly with the body vortex shedding.

### 3. CONCLUSIONS AND RECOMMENDATIONS

A review of support interference effects on measured stability derivatives reveals the following:

- o All Support systems cause interference of one kind or another.
- o Support interference is much more of a problem in dynamic than in static tests.
- o Support interference is increased greatly by the presence of a boat-tail or dome-shaped base, and at transonic speeds even by modest base shoulder roundness.
- o The support interference is particularly a problem at transonic and hypersonic Mach numbers.
- o When boundary layer transition occurs near the base, on the aft body or in the wake, the problem of support interference is aggravated greatly.
- o Asymmetric sting or sting-strut supports should be avoided.
- o In tests at low angles of attack of slender bodies with bulbous bases the transverse rod mount looks promising.
- o In tests at moderate to high angles of attack the slender, symmetric sting causes little support interference.
- o In high- $\alpha$  tests all strut supports cause significant interference.
- o In many cases half model testing provides the means to avoid troublesome support interference.
- o When the model consists of a short, bulbous-based body, using a very slender sting and, if possible, measuring the sting plunging provides the best testing means short of free flight.
- o In many cases the true dynamic stability characteristics can not be ascertained from measurement with only one type of support system.
- o It appears that combining half-model testing with tests of rod or sting mounted models could often provide the information needed to "encircle" the true dynamic stability derivative.

## 5. REFERENCES

1. Whitfield, J. P., "Support Interference at Supersonic Speeds" AGARD Report 300, March 1959.
2. Perkins, E. W., "Experimental Investigations of the Effects of Support Interference on the Drag of Bodies of Revolution at a Mach Number of 1.5", NACA TN 2292, Feb. 1951.
3. Kavanau, L. L., "Base Pressure Studies in Rarefield Supersonic Flow", J. Aer. Sci., Vol. 23, March 1956, pp. 193-207.
4. Chapman, D. R., Kuehn, D. M., and Larson, H. K., "Investigation of Separated Flows in Supersonic and Subsonic Streams With Emphasis on the Effect of Transition", NACA TN 3869, 1957.
5. Needham, D. A. and Stollery, J. L., "Boundary Layer Separation in Hypersonic Flow", AIAA Paper No. 66-455 (1966).
6. Nash, J. F., "An Analysis of Two-Dimensional Turbulent Base Flow, Including the Effect of the Approaching Boundary Layer", NPL AERO REP. 1036, National Physics Lab., Great Britain, July 1962.
7. Love, E. S., "Base Pressure at Supersonic Speeds on Two-Dimensional Airfoils and on Bodies of Revolution With and Without Fins Having Turbulent Boundary Layers", NACA TN 3819, Jan. 1957.
8. Lee, G. and Summers, J. L., "Effects of Sting-Support Interference On the Drag of an Ogive-Cylinder Body at 0.6 to 1.4 Mach Number", NACA RM A 57I09, Dec. 1957.
9. Stivers, L. S. Jr. and Levy Lionel, L. Jr., "Effects of Sting-Support Diameter on the Base Pressures of an Elliptic Cone at Mach Numbers from 0.60 to 1.40", NASA TN D-354, Feb. 1961.
10. Ericsson, L. E. and Reding, J. P., "Aerodynamic Effects of Bulbous Bases", NASA CR 1339, Aug. 1969.
11. Foster, A. D., "A Compilation of Longitudinal Aerodynamic Characteristics Including Pressure Information for Sharp-and Blunt Nose Cones Having Flat and Modified Bases", SANDIA SC-R-64-1311, Jan 1965.
12. Iversen, J. D., "Base and Surface Pressure Variation with Mach Number on a Right Circular Cone" SANDIA SCTM 202-56-51, Sept. 1956.
13. Robertson, J. E. and Chevalier, H. L., "Characteristics of Steady-State Pressures on the Cylindrical Portion of Cone-Cylinder Bodies at Transonic Speeds", AEDC TDR 63-104, Aug. 1963.
14. Ericsson, L. E., "Steady and Unsteady Terminal-Shock Aerodynamics on Cone-Cylinder Bodies", NASA CR-61560, Oct. 1967.
15. Woods, P and Ericsson, L. E., "Aeroelastic Considerations in a Slender Blunt-Nose Multistage Rocket", Aerospace Eng., Vol. 21, 1962, pp. 42-51.
16. Ericsson, L. E., "Aeroelastic Instability Caused By Slender Payloads", J. Spacecraft and Rockets, Vol. 4, 1967, pp. 65-73.
17. Rubin, D. V., "Effect of Lateral Support Strut on Body Pressure Distributions at Transonic Speeds", AOMC RD-TR-72-6, Jan. 1972.
18. Reding, J. P. and Ericsson, L. E., "Loads on Bodies in Wakes", J. Spacecraft and Rockets, Vol. 4, 1967, pp. 511-518.
19. Reding, J. P. and Ericsson, L. E., "Dynamic Support Interference", J. Spacecraft and Rockets, Vol. 9, 1972, pp. 547-553.
20. Wehrend, W. R., Jr., "An Experimental Evaluation of Aerodynamic Damping Moments on Cones With Different Centers of Rotation", NASA TN-D-1768, March, 1963.
21. Uselton, B. L. and Cyran, F. B., "Critical Sting Length as Determined by the Measurement of Pitch-Damping Derivatives for Laminar, Transitional and Turbulent Boundary Layers at Mach Numbers 3 for Reduced Frequencies of 0.0033 and 0.0056", AEDC-TR-77-66, July 1977.
22. Uselton, B. L. and Wallace, A. R. "Damping-in-Pitch and Drag Characteristics of the Viking Configuration at Mach Numbers From 1.6 through 3", AEDC-TR-72-56, May, 1972.
23. Steinberg, S. Uselton, B. L., and Siemers III, P. M., "Viking Pitch Damping Derivatives as Influenced by Support Interference and Test Techniques", J. Spacecraft and Rockets, Vol. 10, July 1973, pp. 443-449.
24. Ericsson, L. E. and Reding, J. P., "Transonic Sting Interference", J. Spacecraft and Rockets, Vol. 17, 1980, pp. 140-144.
25. Yanagizawa, M., "Measurement of Dynamic Stability Derivative of Cones and Delta-Wings at High Speeds" NAL TR-172, National Aerospace Lab., Tokyo, Japan, 1969.
26. Liu, D. D., Platzer, M. F., and Ruo, S. Y., "On the Calculation of Static And Dynamic Stability Derivatives for Bodies of Revolution at Subsonic and Transonic Speeds", AIAA Paper No. 70-190, New York, Jan. 1970.

27. Orlík-Rückemann, K. J., Laberge, J. G., and Inyengar, S., "Half-and-Full-Model Experiment on Slender Cones at Angle of Attack", *J. Spacecraft and Rockets*, Vol. 10, 1973, pp. 575-580.
28. Adcock, J. B., "Some Experimental Relations Between the Static and Dynamic Stability Characteristics of Sting-Mounted Cones with Bulbous Bases", *Transactions of the 3rd Technical Workshop on Dynamic Stability Problems*, Paper 5, Vol. II, NASA Ames R.C., Moffet Field, Calif., Nov. 1968.
29. Jecmen, D. M., Reding, J. P. and Ericsson, L. E., "An Application of Automatic Carpet Plotting to Wind-Tunnel Data Reduction", *J. Spacecraft and Rockets*, Vol. 4, 1967, pp. 408-410.
30. Ericsson, L. E., Reding, J. P. and Guenther, R. A., "Analytic Difficulties in Predicting Dynamic Effects of Separated Flow", *J. Spacecraft and Rockets*, Vol. 8, 1971, pp. 872-878.
31. Hama, F. R., "Experimental Studies of the Lip Shock", *AIAA Journal*, Vol. 6, 1968, pp. 212-219.
32. Hobbs, R. B. Jr., "Hypersonic Dynamic Stability, Part II, Conical Body Experimental Programs", *FDL TDR-64-149, Pt. II*, Jan. 1967.
33. Hobbs, R. B. Jr., "Private Communication of Sting Geometry", 1968.
34. Walchner, O. and Clay, J. T., "Nose Bluntness Effects on the Stability Derivatives of Cones in Hypersonic Flow", *Transactions of the 3rd Technical Workshop on Dynamic Stability Problems*, Paper 5, Vol. II, NASA Ames RC, Moffet Field, Calif. Nov. 1968.
35. Walchner, O., "Private Communication of Unpublished Data on Hypersonic Dynamic Support Interference", June, 1968.
36. Slattery, R. E., Clay, W. C., and Stevens, R. R., "Interactions Between a Hypersonic Wake and a Following Hypersonic Projectile", *AIAA Journal*, Vol. 1, 1963, pp. 974-975.
37. Walchner, O., Sawyer, F., Quinn, B., and Friberg, E., "Hypersonic Stability Derivatives for a Standard 10 Degree Cone", *ARL 67-0099*, May, 1967.
38. Ericsson, L. E. and Reding, J. P., "Viscous Interaction or Support Interference-The Dynamicist's Dilemma", *AIAA Journal*, Vol. 16, 1978, pp. 363-368.
39. Morrison, A. M., Holmes, J. E., and Lawrence, W. R., "An Investigation of the Damping in Pitch Characteristics of a Ten Degree Cone", *NSWC/WOL/TR 75-84*, June 1975.
40. Urban, R. H., "A Dynamic Stability Balance for Hypervelocity (Hot-Shot) Tunnels", *AEDC-TR-65-222*, Oct. 1965.
41. Urban, R. H. and Shanahan, R. J., "Dynamic Stability Characteristics of a 10 Degree Cone at Mach Number 20", *AEDC-TR-65-80*, April 1965.
42. Welsh, C. J. and Ward, L. K., "Structural Damping in Dynamic Stability Testing", *AEDC-TR-59-5*, Feb., 1959.
43. Schueler, C. J., Ward, L. K., and Hodapp, A. E. Jr., "Techniques for Measurement of Dynamic Stability Derivatives in Ground Test Facilities", *AGARDograph 121*, Oct. 1967.
44. Orlík-Rückemann, K. J. and LaBerge, J. G., "Static and Dynamic Pitching Moment Measurements on a Family of Elliptic Cones at Mach Number 11 in Helium", *LTR-UA-14*, NRC National Aeronautical Establishment, Ottawa, Canada, July 1970.
45. Uselton, J. C. and Uselton, B. L., "Validity of Small-Amplitude Oscillation Dynamic-Stability Measurement Technique", *J. Spacecraft and Rockets*, Vol. 13, 1976, pp. 266-270.
46. Wehrend, W. R., "A Wind-Tunnel Investigation of the Effect of Changes in Base Contour on the Damping in Pitch of a Blunted Cone", *NASA TND-2067*, Nov. 1963.
47. Compton, W. B. III, "Effect on Base Drag of Recessing the Bases of Conical Afterbodies at Subsonic and Transonic Speeds", *NASA TND-4821*, Oct. 1968.
48. Ericsson, L. E., "Correlation of Attitude Effects on Slender Vehicle Transition", *AIAA Journal*, Vol. 12, 1974, pp. 523-529.
49. Dayman, B. Jr., "Optical Free-Flight Wake Studies", *JPL TR 32-364*, Nov. 1962.
50. Rakich, J. V. and Cleary, J. W., "Theoretical and Experimental Study of Supersonic Steady Flow Around Inclined Bodies of Revolution", *AIAA Journal*, Vol. 8, 1970, pp. 511-518.
51. Reese, D. E. Jr., and Wehrend, W. R. Jr., "An Investigation of the Static and Dynamic Characteristics of a Series of Blunt-nosed Cylinder Flare Models at Mach Numbers from 0.65 to 2.20", *NASA TM X-110*, Jan. 1960.
52. Ericsson, L. E., "Effect of Sting Plunging on Measured Nonlinear Pitch Damping", *AIAA Paper No. 78-832*, April 1978.
53. Burt, G. E. and Uselton, J. C., "Effect of Sting Oscillations on the Measurement of Dynamic Stability Derivatives", *J. Aircraft*, Vol. 13, 1976, pp. 210-216.

54. Canu, M., "Measure eu Soufflerie de l'Amortissement Aérodynamique en Tangage d'une Maquette d'Avion Oscillant Suivant Deux Degrés de Liberté", La Recherche Aérospatiale, No. 5, Sept. Oct., 1971, pp. 257-267.
55. Many authors, "Dynamic Stability Parameters", AGARD CP-235, Nov. 1978.
56. Ericsson, L. E., "Technical Evaluation Report on the Fluid Dynamics Panel Symposium on Dynamic Stability Parameters", AGARD-AR-137, April 1979.
57. Ericsson, L. E., "A Summary of AGARD FDP Meeting on Dynamic Stability Parameters", Paper 2, AGARD CP-260, Sept. 1978.
58. Orlík-Rückemann, K. J., "Dynamic Stability Testing in Wind Tunnels", Paper 1, AGARD CP-235, Nov. 1978.
59. Matthews, A. W., "Experimental Determination of Dynamic Derivatives due to Roll at BAC, Warton," Paper 4, AGARD CP-235, Nov. 1978.
60. Hafer, X., "Wind Tunnel Testing of Dynamic Derivatives in W. Germany", Paper 5, AGARD CP-235, Nov. 1978.
61. Hummel, D., "Untersuchungen über das Aufplatzen der Wirbel an schlanken Delta Flügeln", Z. Flugwiss., Vol. 13, 1965, pp. 158-168.
62. Johnson, J. L. Jr., Grafton, S. B., and Yip, L. P., "Exploratory Investigation of Vortex Bursting on the High-Angle-of-Attack Lateral-Directional Stability Characteristics of Highly-Swept Wings", AIAA Paper No. 80-0463, March 1980.
63. Brannstrom, B. and Lindan, O., "Investigations of Interference Effects in a Wind Tunnel From a Model Support Strut on a Reflection-Plane Mounted Half Model", FFA Technical Note AU-1335, The Aer. Res. Inst. of Sweden, 1978.
64. Lambourne, N. C., Bryer, D. W., and Maybrey, J. F. M., "Pressure Measurements on a Model Delta Wing Undergoing Oscillatory Deformation", NPL Aero Report 1314, Aer. Res. Council, Great Britain, March 1970.
65. Dietz, W. E. and Altstatt, M. C., "Experimental Investigation of Support Interference on an Ogive-Cylinder at High Incidence", AIAA Paper 78-165, Jan. 1978, Also J. Spacecraft and Rockets, Vol. 16, 1979, pp. 67-68.
66. Nelson, R. C. and Mouch, T. N., "Cylinder/Splitter-Plate Data Illustrating High- $\alpha$  Support Interference", J. Spacecraft and Rockets, Vol. 16, 1979, pp. 126-128.
67. Ericsson, L. E. and Reding, J. P., "Vortex-Induced Asymmetric Loads in 2-D and 3-D Flows", AIAA Paper No. 80-0181, Jan. 1980.
68. Ericsson, L. E. and Reding, J. P., "Vortex Induced Asymmetric Loads, Review and Further Analysis", submitted for publication to Z. Flugwiss.
69. Almosnino, D. and Rom, J., "Alleviation of the Lateral Forces and Moments Acting on a Slender Body at High Angles of Attack, Using Jet Injection at Subsonic and Transonic Speeds", AIAA Paper No. 80-1558-CP, Aug. 1980.

#### ACKNOWLEDGEMENTS

The author wants to acknowledge the contributions by J. Peter Reding, not only through all the referenced material but also through our continuing dialogue. The author is also indebted to Nancy Lipsanopoulos, without whose ability to transform a stack of handscribbled notes into readable material the present paper is not likely to have appeared in AGARD LS-114.

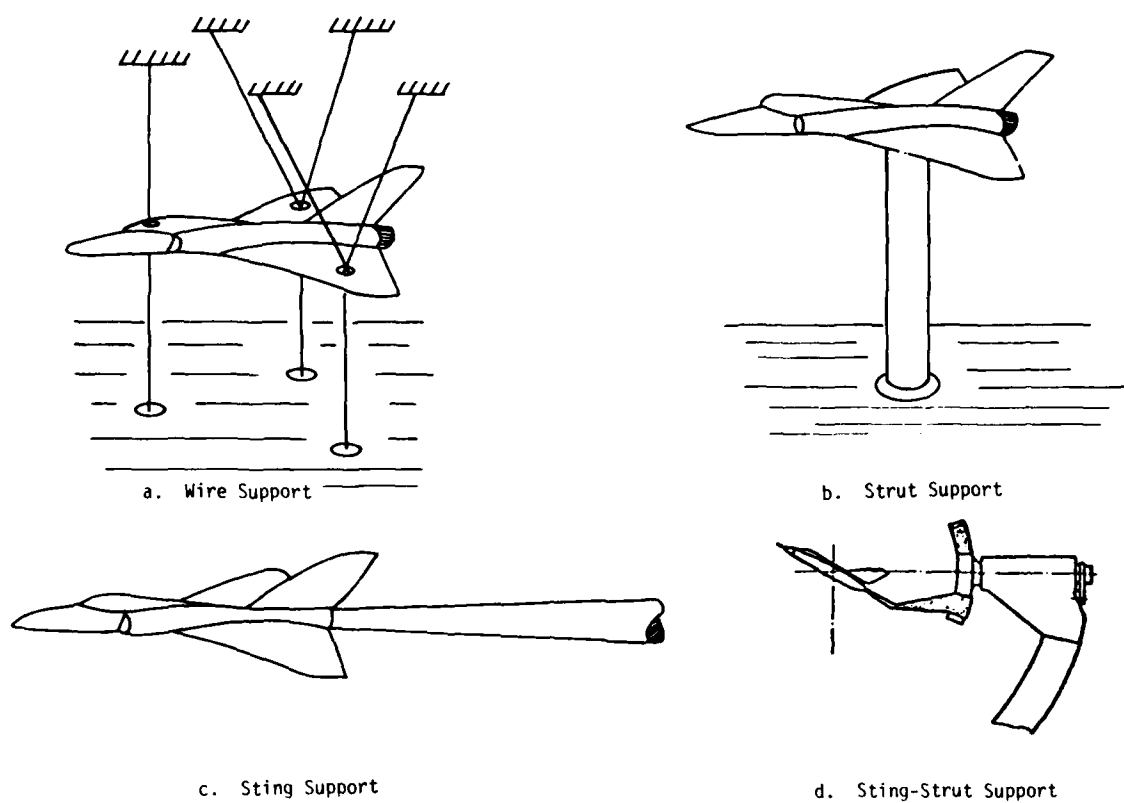


Figure 1. Support Systems

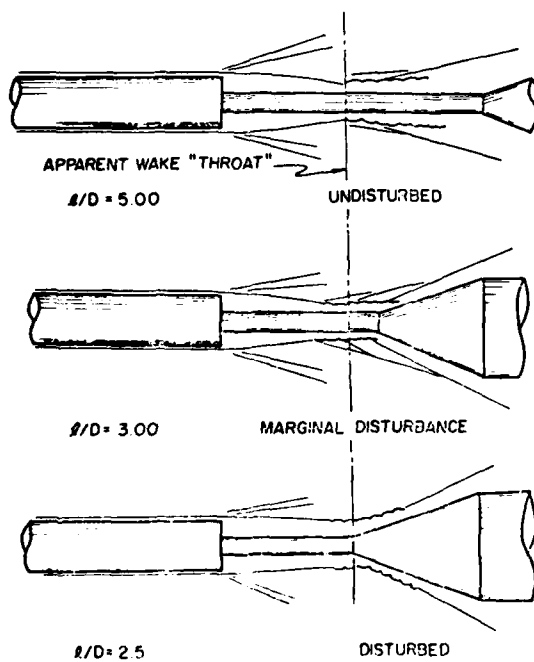


Figure 2. Schematics of Schlieren Photographs of Sting Support Flow Patterns (Ref. 1).

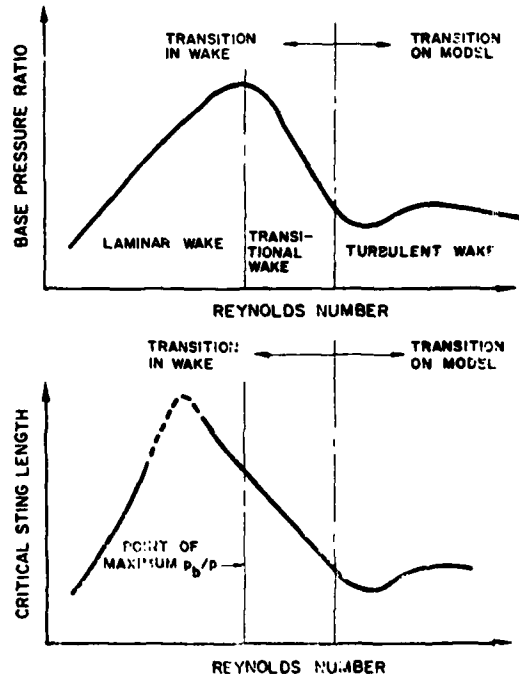


Figure 3. Typical Effect of Reynolds Number on Base Pressure and Critical Sting Length (Ref. 1).

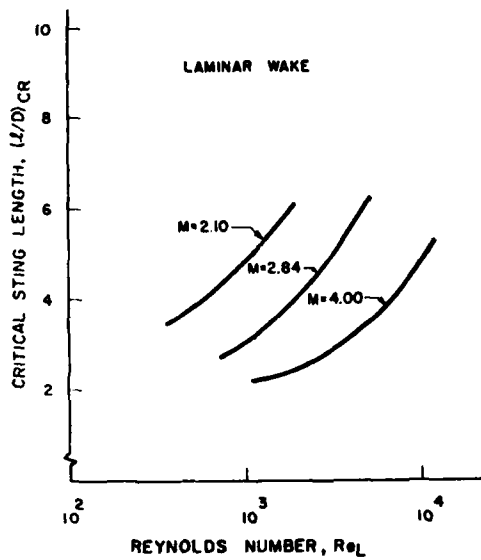


Figure 4. Critical Sting Lengths for Laminar Wakes (Ref. 3)

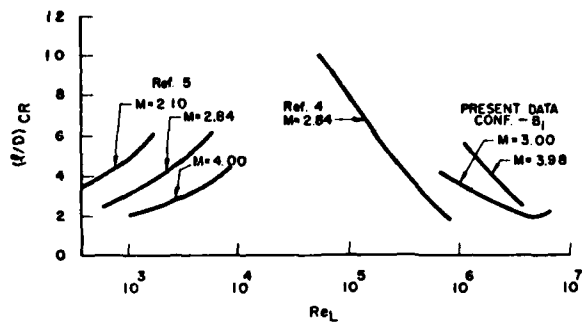


Figure 5. Critical Sting Length Comparison (Ref. 1).

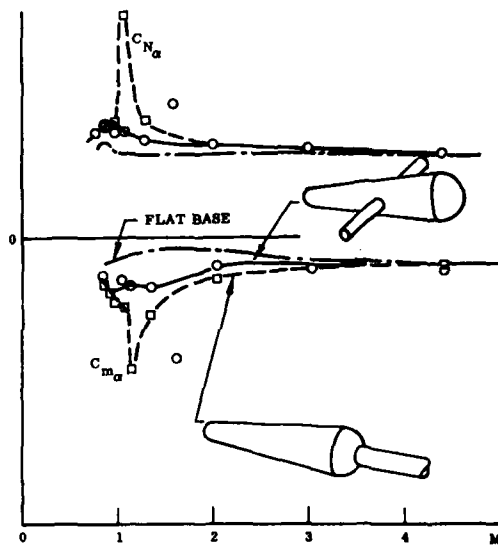


Figure 6. Static Derivatives at  $\alpha = 0$  of a Slender Cone With Hemispherical Base (Ref. 10).

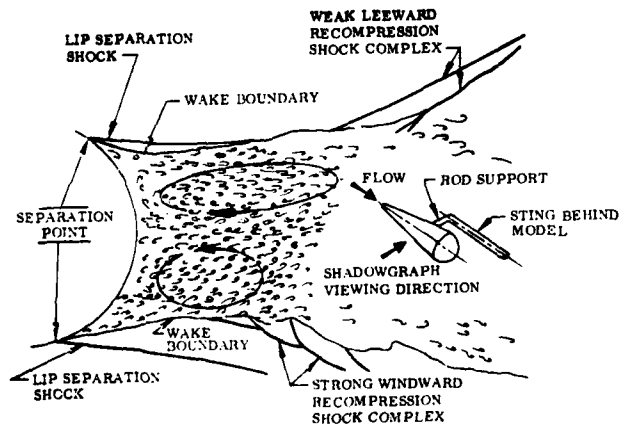


Figure 8. Near Wake Flow Pattern of a Slender Cone With Bulbous Base,  $M = 2$ ,  $\alpha = 12^\circ$  (Ref. 10).

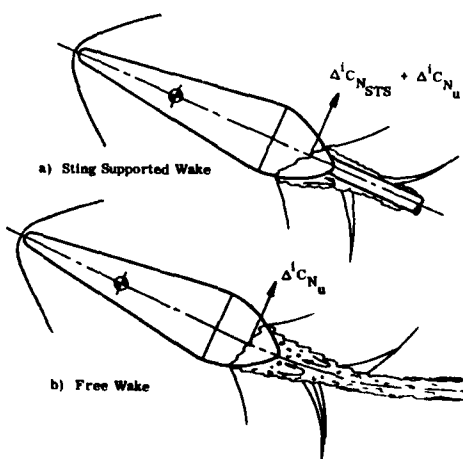


Figure 7. Wake-Induced Forces on a Large Bulbous Base (Ref. 10)

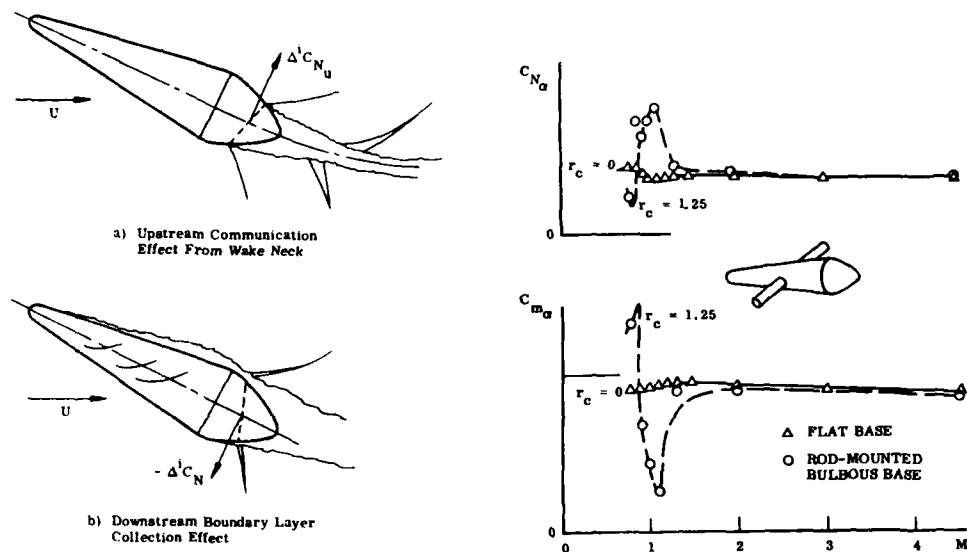
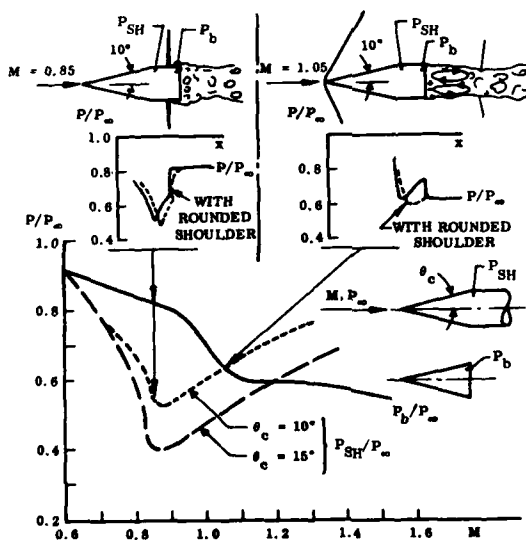


Figure 9. Forces Induced on a Large Bulbous Base (Ref. 10).

Figure 10. Effect of Large Bulbous Base on Static Derivatives of a Slender Cone at  $\alpha = 0$  (Ref. 10).



**Figure 11. Pressure Distributions and Flow Patterns Over Slender Cone-Cylinder Configurations at Transonic Mach Numbers (Ref. 10).**

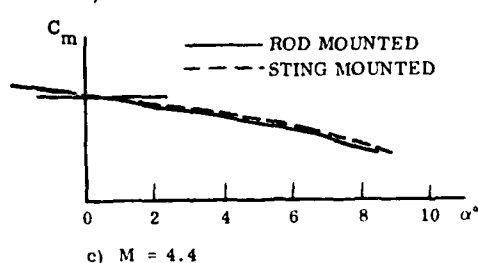
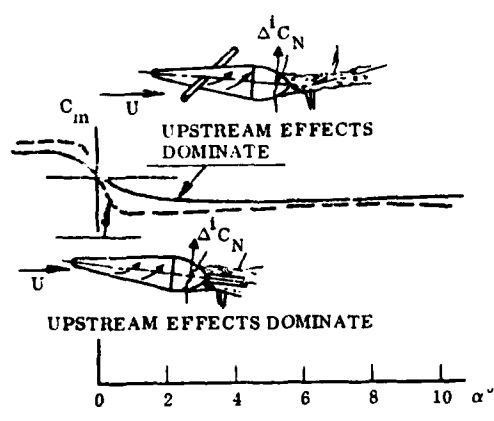
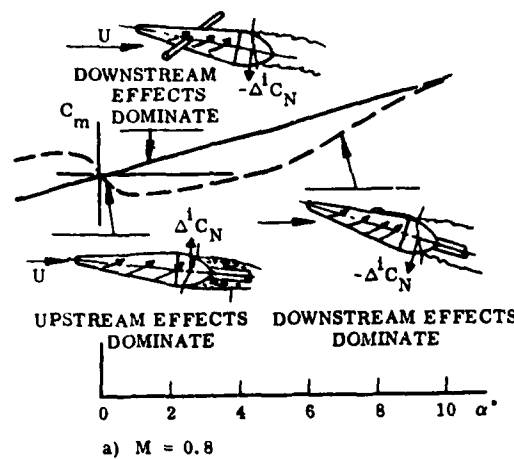


Figure 12. Sting Interference Effects on Static Stability Characteristics of a Slender Cone With a Large Bulbous Base (Ref. 10).

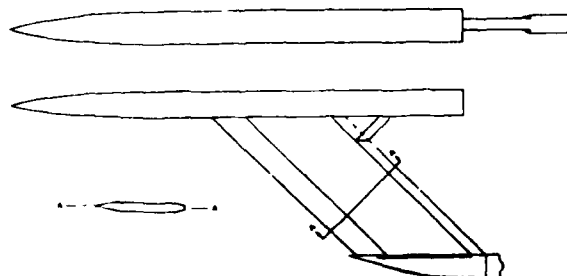


Figure 13. Strut-Mounted Slender Body (Ref. 18).

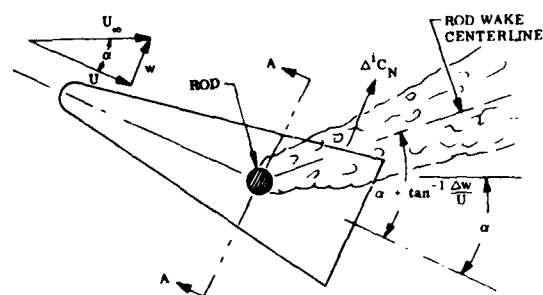


Figure 14. Rod Wake Interference at Large Angles of Attack (Ref. 10).

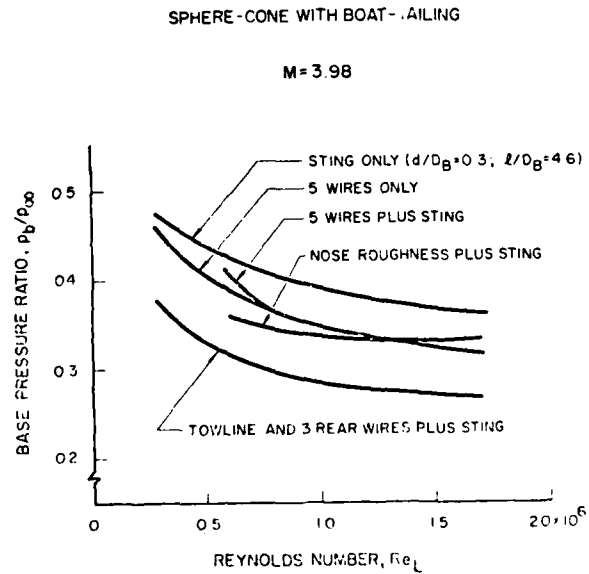
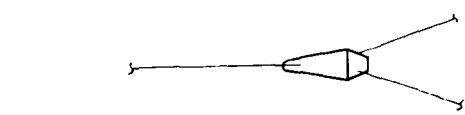
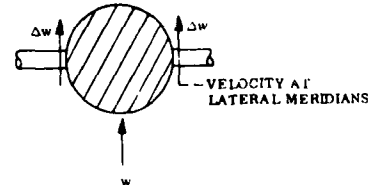


Figure 15. Effect of Wire Supports on Base Pressure (Ref. 1).

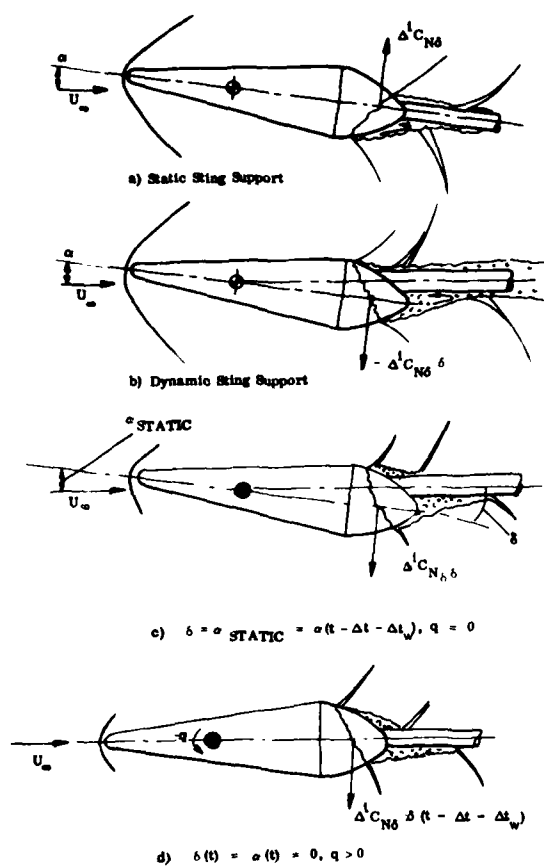


Figure 16. Sting-Induced Forces on a Bulbous Base (Ref. 19).

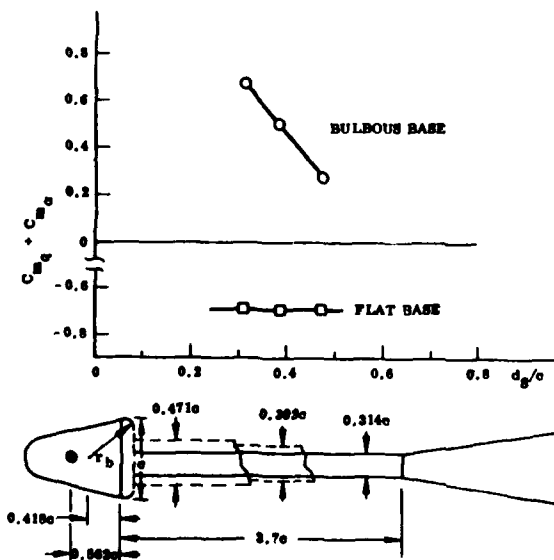


Figure 18. Effect of Sting Diameter on the Damping of a Bulbous-Based Cone at  $M = 0.65$  (Ref. 20).

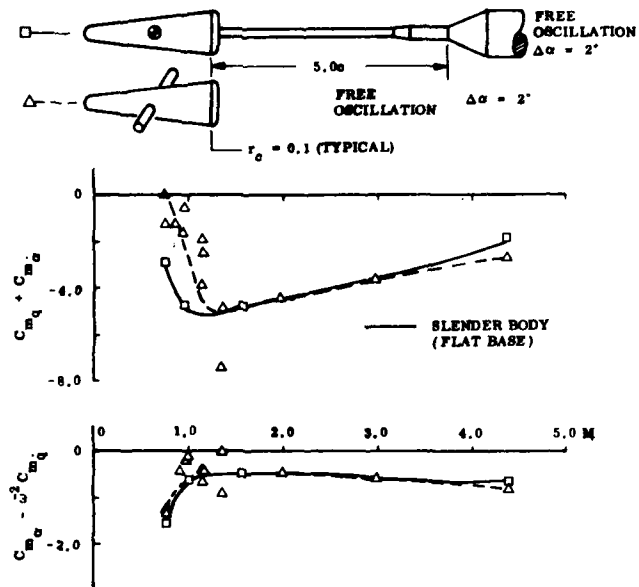


Figure 17. Effect of Mounting Method on Dynamic Stability of a Bulbous-Based Slender Cone (Ref. 10).

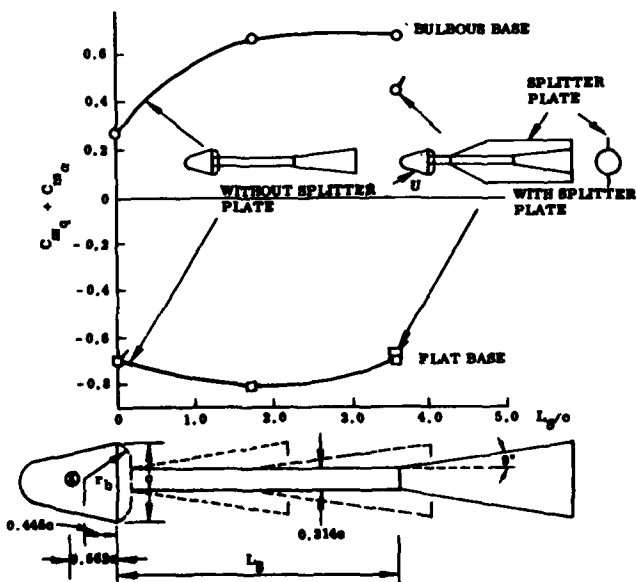


Figure 19. Effect of Sting Flare on the Damping of a Bulbous-Based Cone at  $M = 0.65$  (Ref. 20).

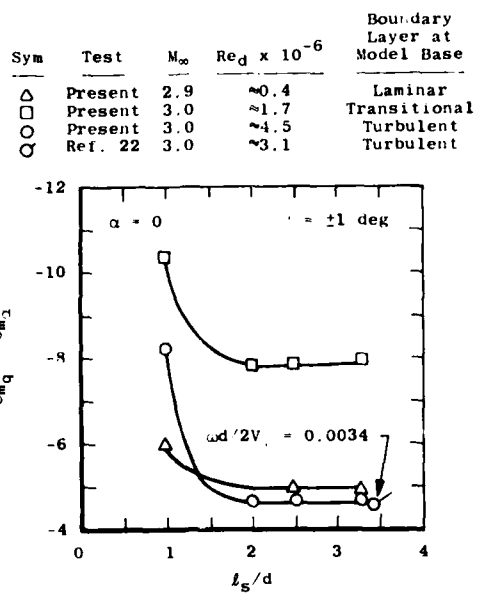


Figure 20. Effect of Sting Length on the Damping of a Flat-Based 7° Cone (Ref. 21).

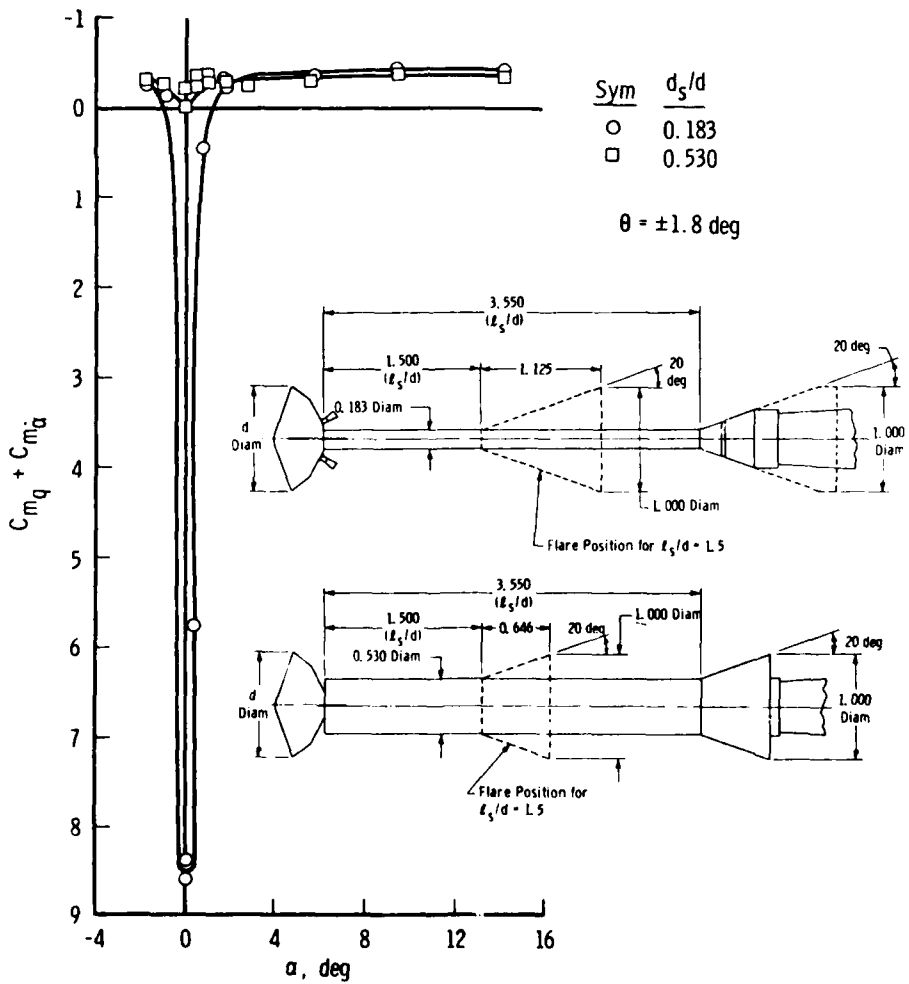


Figure 21. Effect of Sting Diameter on the Damping of the Viking Configuration (Ref. 22).

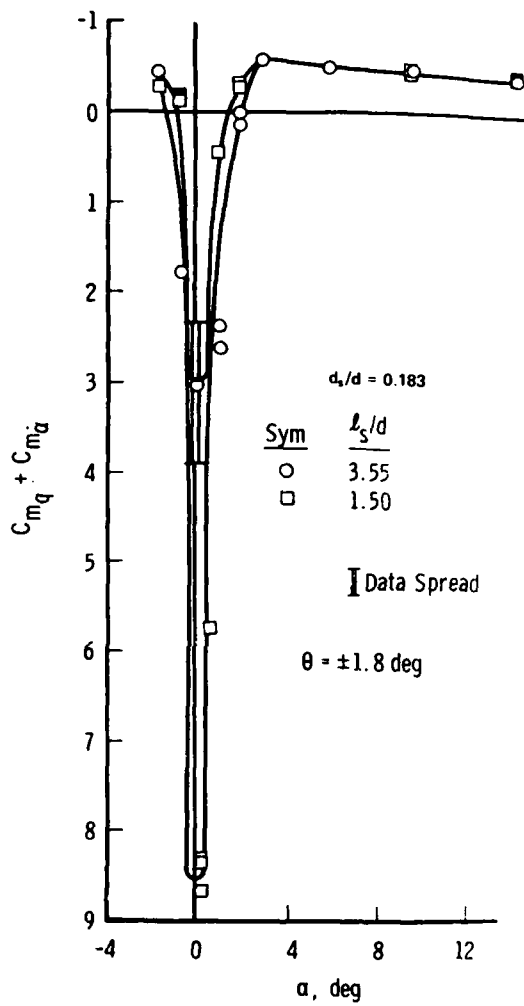
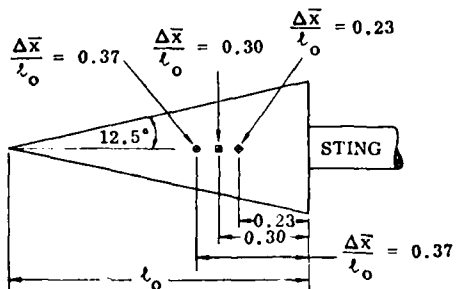
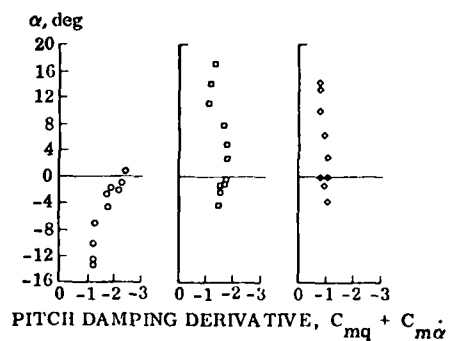
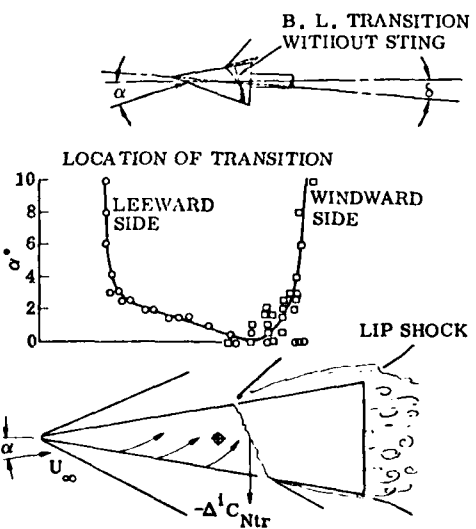


Figure 22. Effect of Sting Length on the Damping of the Viking Configuration (Ref. 22).



a. Effect on Damping (Ref. 20)



b. Effect on Boundary Layer Transition (Ref. 24)

Figure 23. Angle-of-Attack Effects on Slender Cone Aerodynamics.  
a. Effect on Damping (Ref. 20)  
b. Effect on Boundary Layer Transition (Ref. 24).

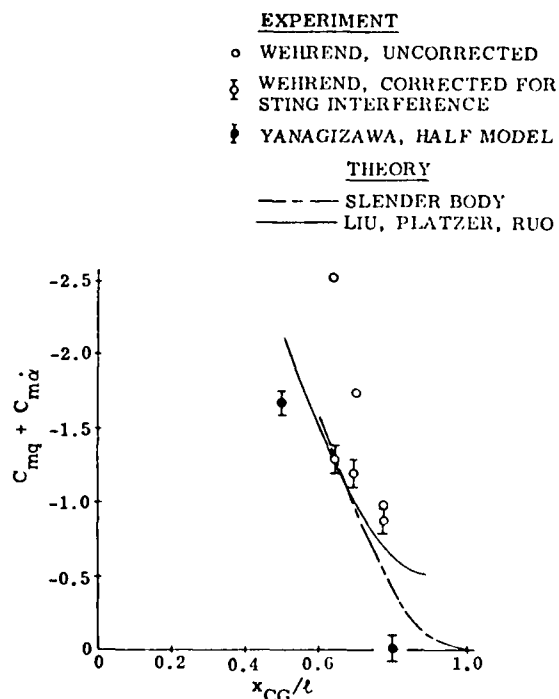


Figure 24. Damping of a 12.5° Sharp Cone at  $M_\infty = 1$  for Various Rotation Centers (Ref. 24).

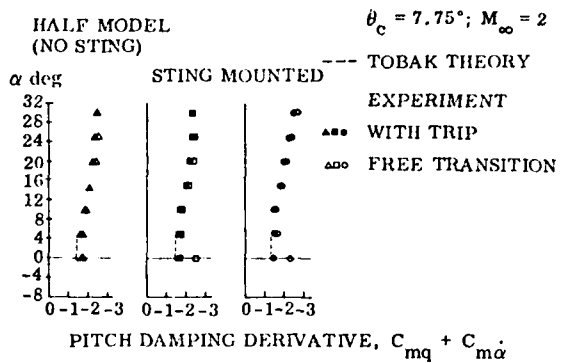


Figure 25. Documentation of Transition-Amplified Sting Interference for a 7.75° Sharp Cone (Ref. 27).

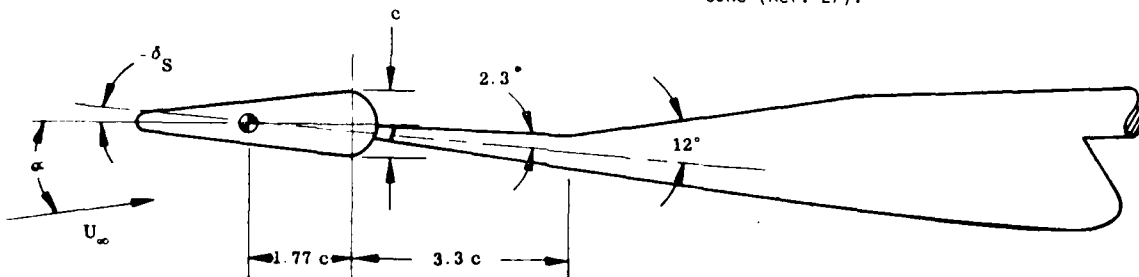


Figure 26. Asymmetric Sting and Bulbous-Based Model (Ref. 28).

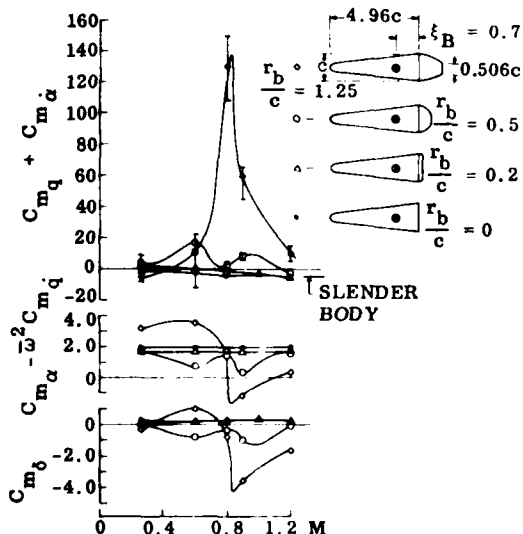


Figure 27. Correlation of Sting-Support-Induced Moment with Static and Dynamic Stability (Ref. 10).

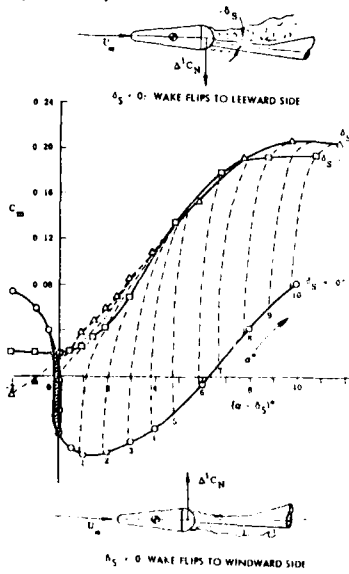


Figure 28. Pitching Moment Carpet Plot for  $M = 0.26$  (Ref. 10).

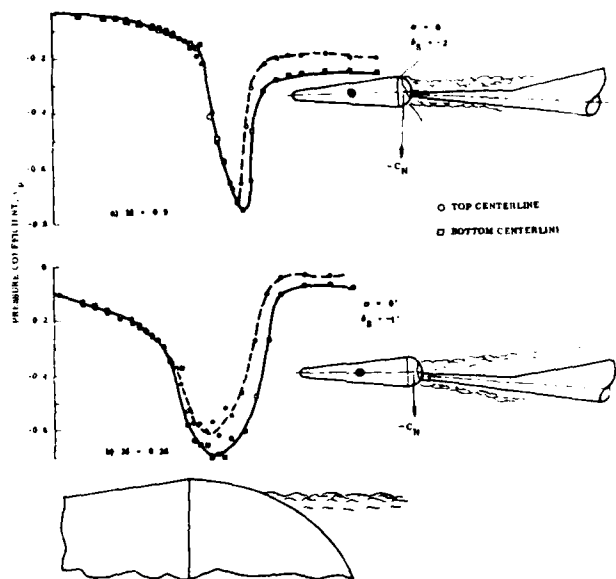


Figure 29. Pressure Distribution on Cone With Hemispherical Base at  $\alpha = 0$ ,  $\delta_S < 0$ .

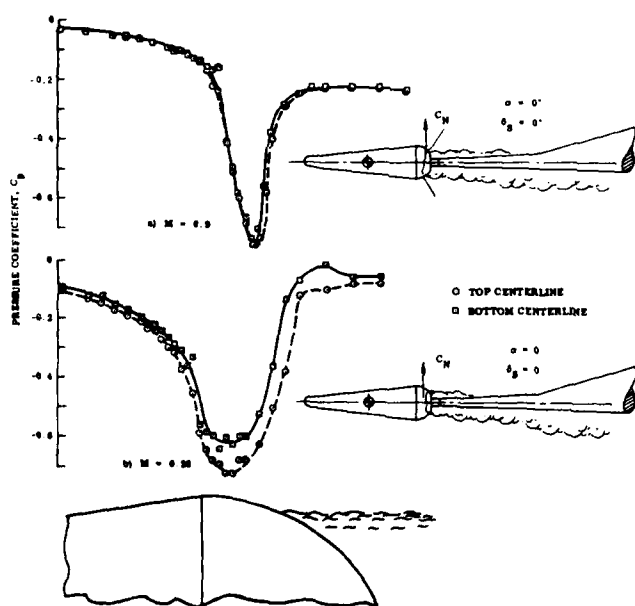


Figure 30. Pressure Distribution on Cone With Hemispherical Base at  $\alpha = 0$ ,  $\delta_S = 0$ .

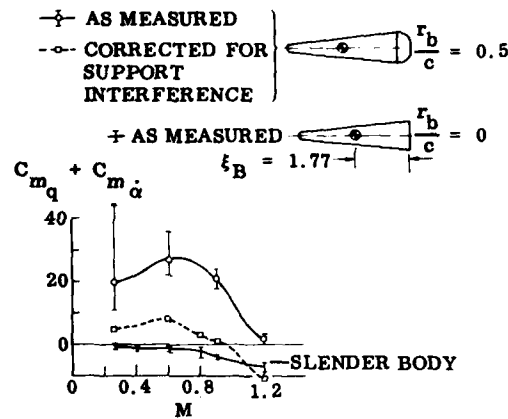


Figure 31. Damping of Hemispherical-Base Cone Corrected for Support Interference (Ref. 10).

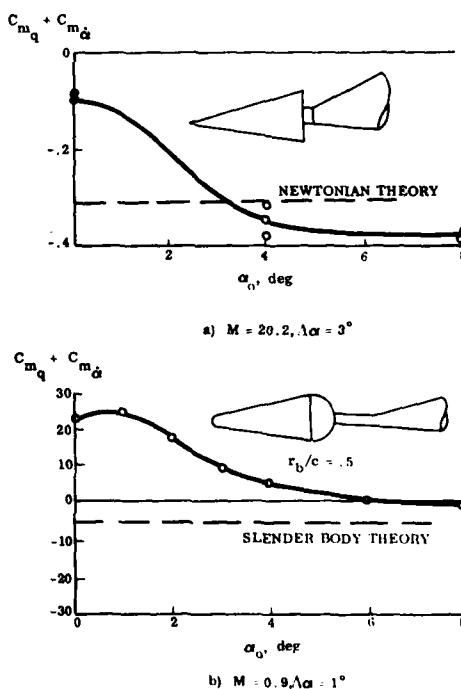


Figure 32. Comparison of Hypersonic and Transonic Asymmetric Sting Interference (Ref. 19).

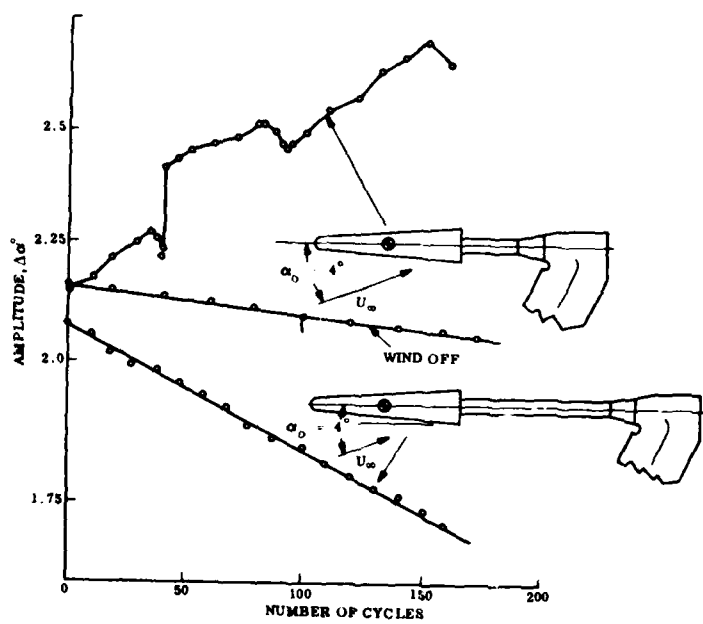


Figure 33. Hypersonic Dynamic Support Interference at  $M = 14$  (Ref. 34).



Figure 35. Effect of Sabot on Hypersonic Wake (Ref. 36).

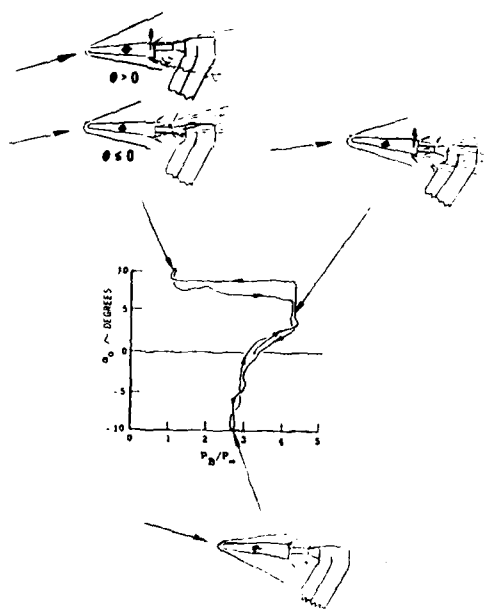


Figure 34. Asymmetric Support Interference on Slender Cone Base Pressure at  $M = 14$ , Short Sting

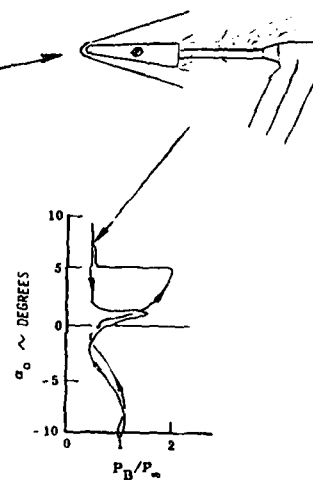


Figure 36. Asymmetric Support Interference on Slender Cone Base Pressure at  $M = 14$ , Long Sting.

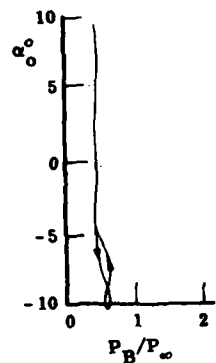
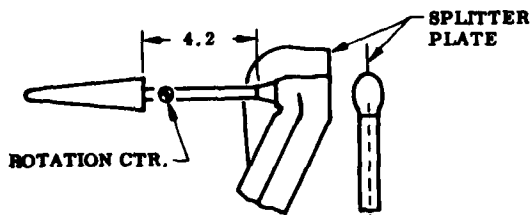


Figure 37. Alleviation of Asymmetric Support Interference on Slender Cone Base Pressure at  $M = 14$  Through the use of a Splitter Plate (Ref. 35).

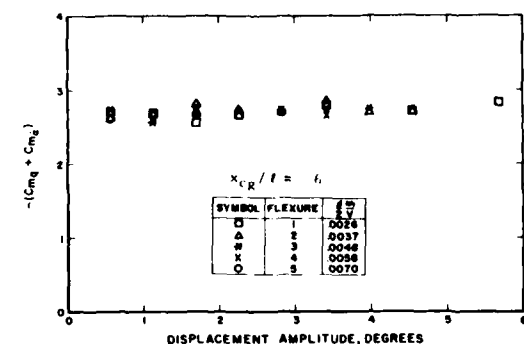
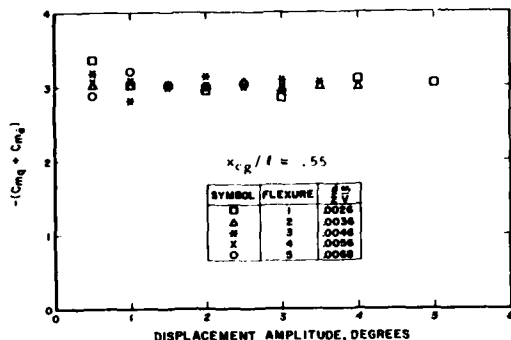


Figure 38. Damping of a  $10^\circ$  Sharp Cone at  $M = 12.55$  (Ref. 37).

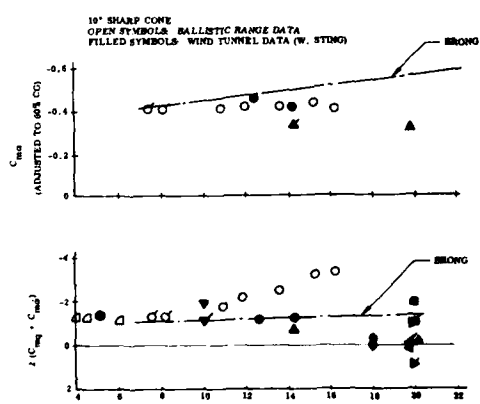


Figure 39. Unsteady Aerodynamic Characteristics of  $10^\circ$  Cones (Ref. 38).

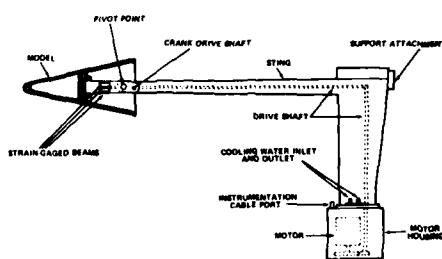
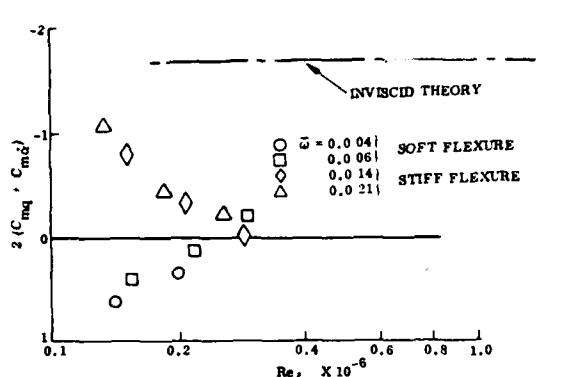
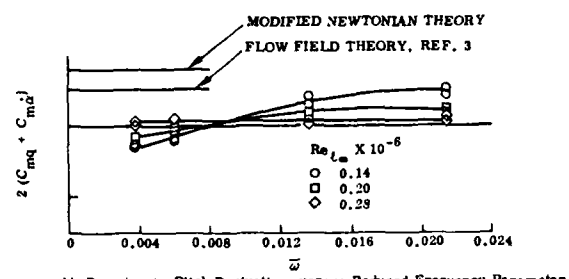


Figure 40. Asymmetric Support for Forced Oscillations (Ref. 39).



a) Damping-in-Pitch Derivatives versus Reynolds Number



b) Damping-in-Pitch Derivatives versus Reduced Frequency Parameter

Figure 41. Nonlinear Support Interference (Ref. 40)

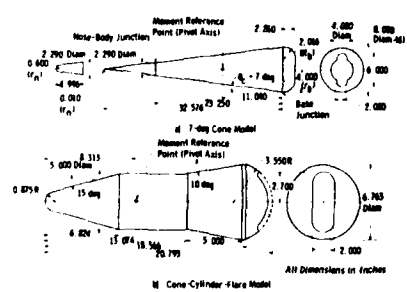


Figure 44. Base Cutouts for Test of Bulbous-Based Models (Ref. 45).

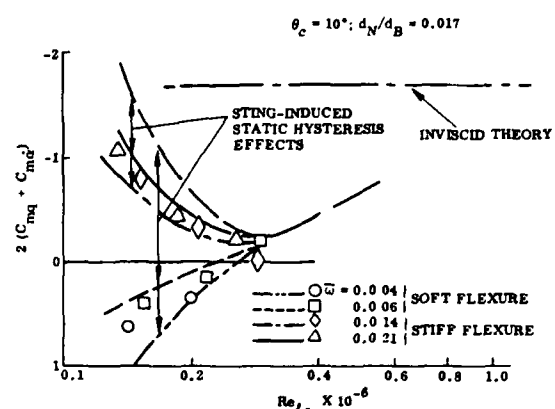


Figure 42. Combined Effects of Aerodynamic Discontinuity and Hysteresis on Dynamic Support Interference (Ref. 38).

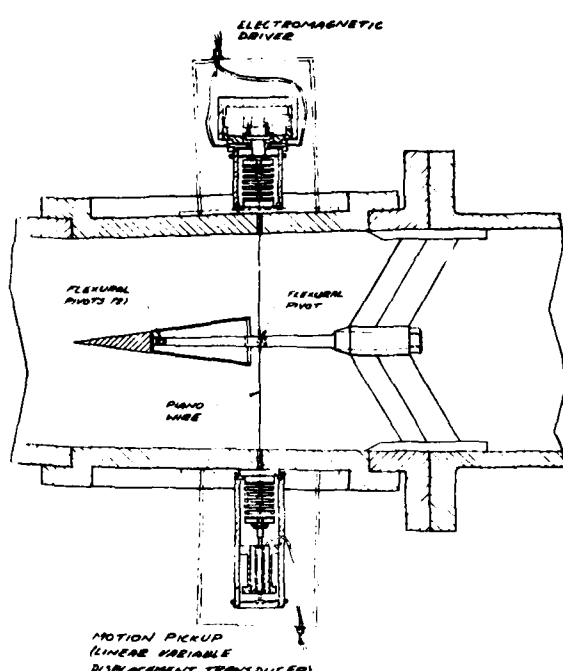


Figure 43. Symmetric Strut-Sting Support Used at NAE (Ref. 44).

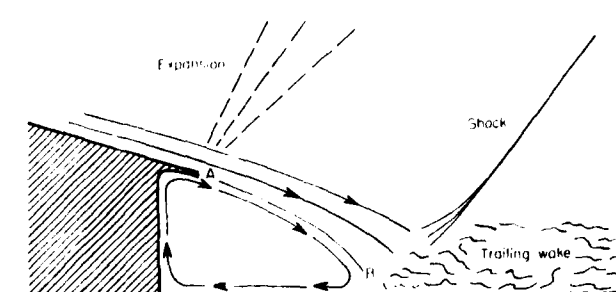


Figure 45. Concave Base Flow (Ref. 47).

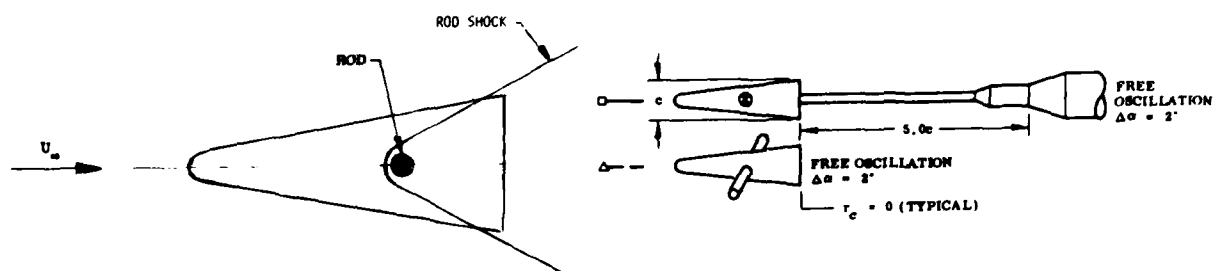


Figure 46. Rod Shock Interference.

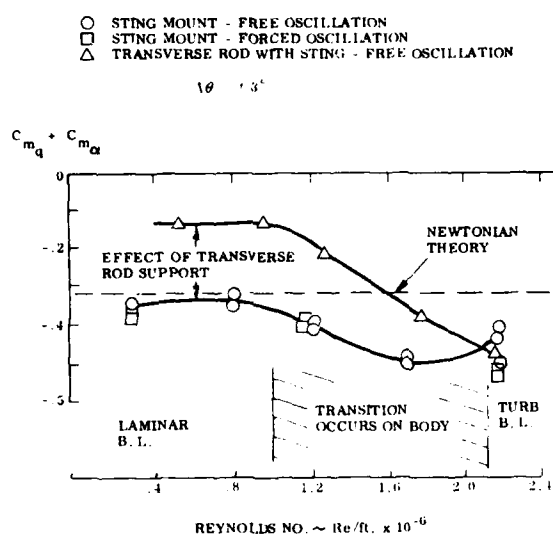
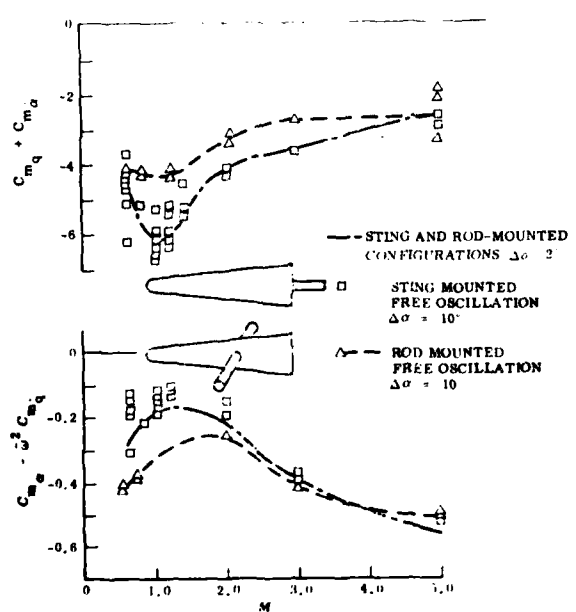
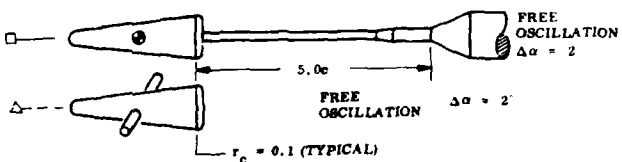
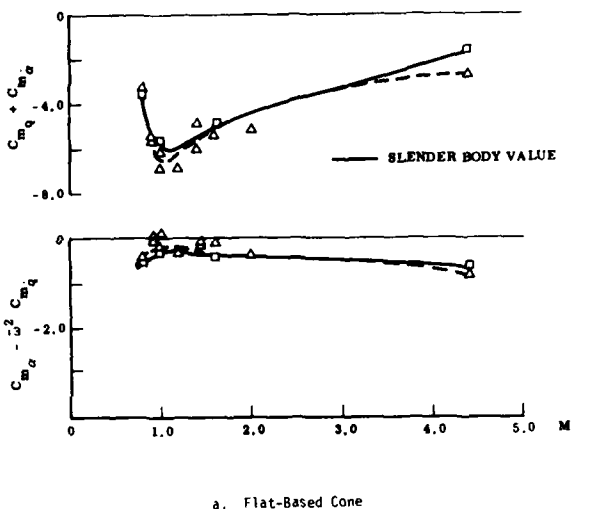
Figure 48. Transverse Rod Interference at  $M = 10$ . (Ref. 32).

Figure 49. Rod Interference at High Amplitudes (Ref. 10).

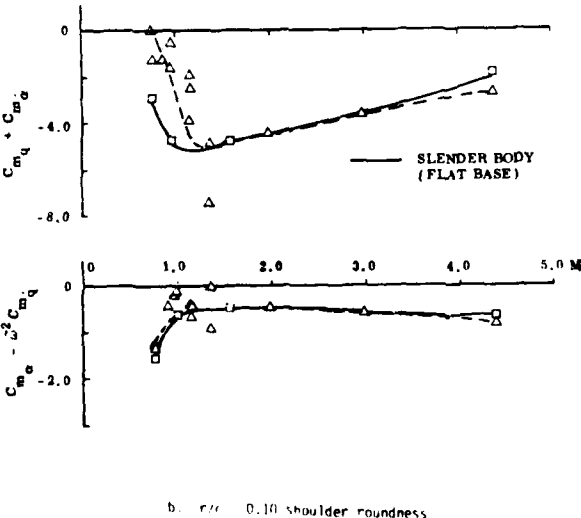
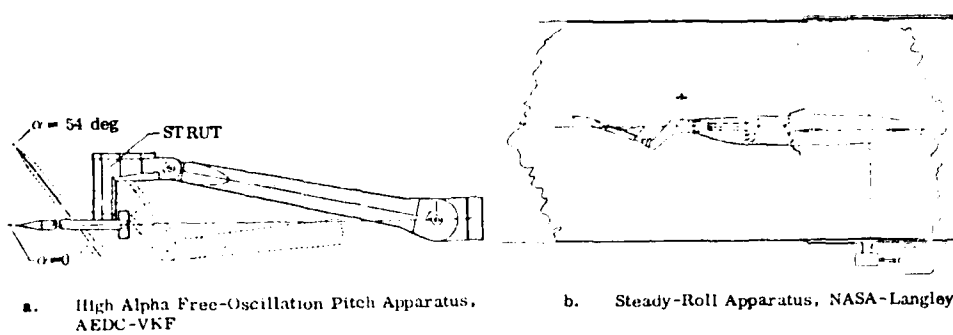
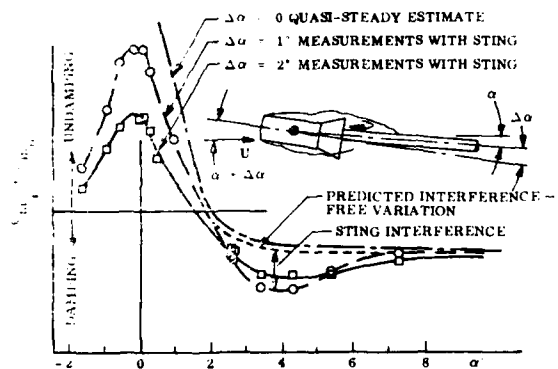
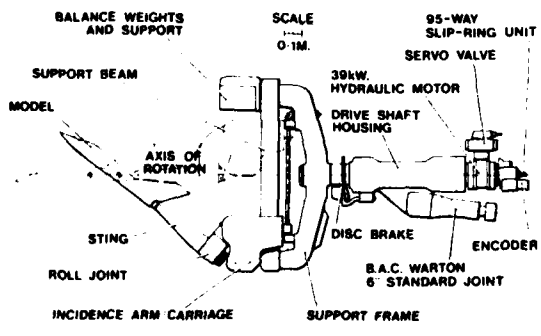
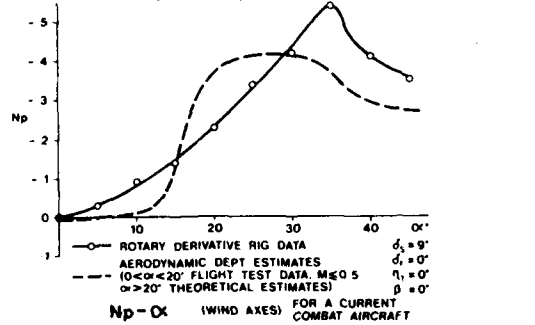
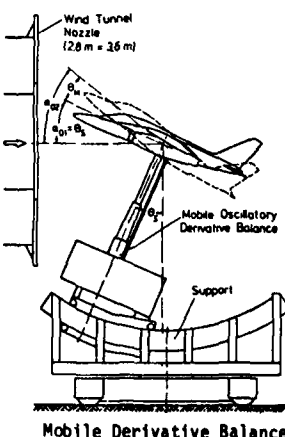
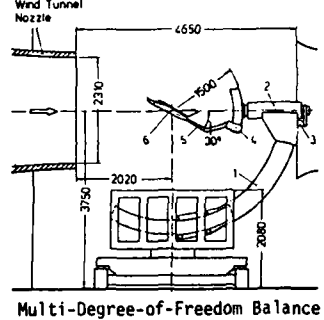
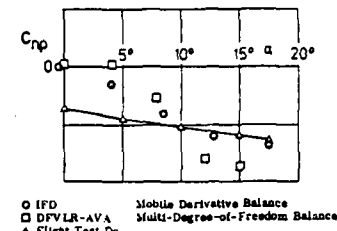


Figure 47. Effect of Model Mounting on Dynamic Stability.  
 a. Flat-Based Cone  
 b. 10 Percent Shoulder Roundness,  $r/c = 0.10$

Figure 51. High- $\alpha$  Model Support Systems (Ref. 58).Figure 50. Effect of Cylindrical Sting on the Damping of a Cylinder-Flare Body at  $M = 0.65$  (Ref. 51).

a. BAC, Warton, Div., UK (Ref. 59)



b. DFVLR, West Germany (Ref. 60)

Figure 52. Comparison of Side Moment Characteristics Measured in Wind Tunnel and Obtained in Free Flight.

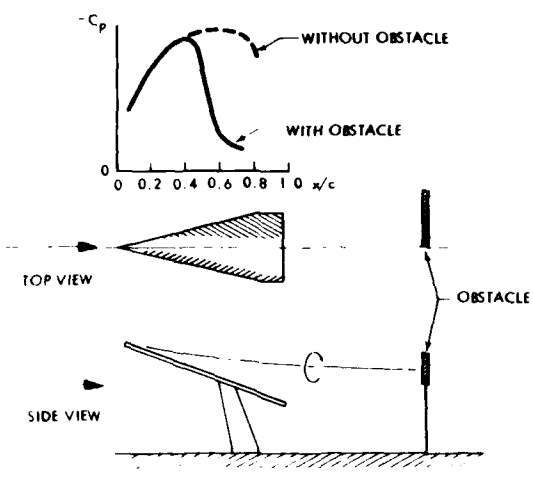


Figure 53. Vortex Burst Caused on 76-Deg.-Delta Wing By Downstream Obstacle, (Ref. 61).

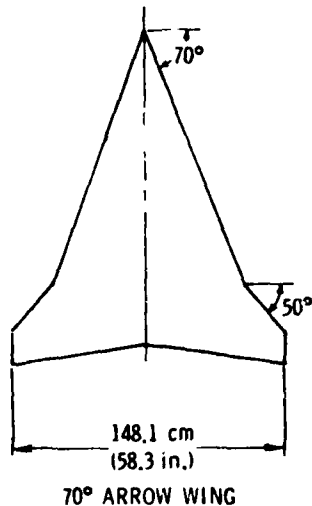


Figure 54. Arrow Wing Configuration (Ref. 62).

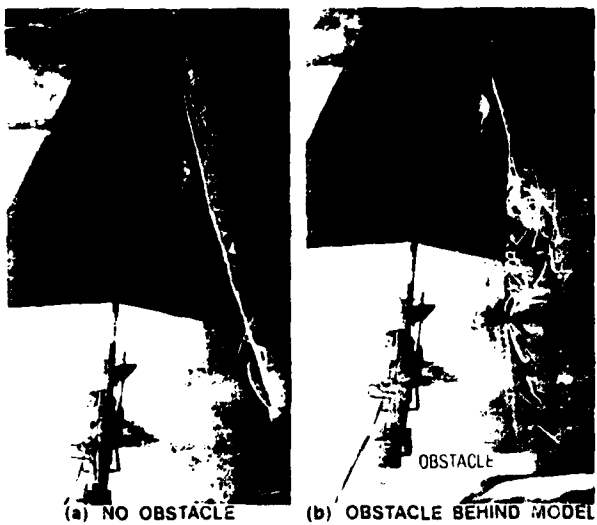


Figure 55. Vortex Burst Induced By Downstream Obstacle (Ref. 62).

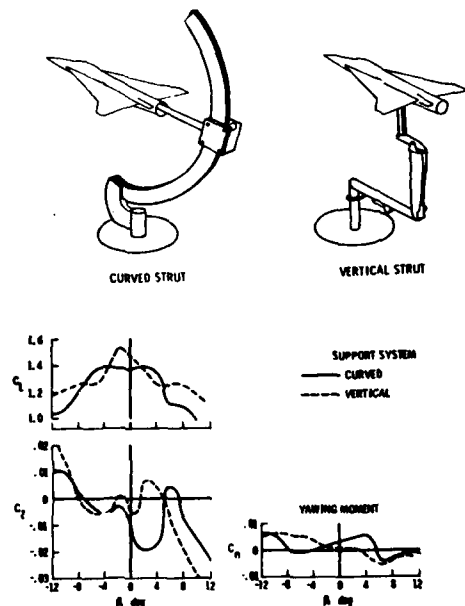


Figure 56. Effect of Model Support on Lateral Characteristics (Ref. 62).

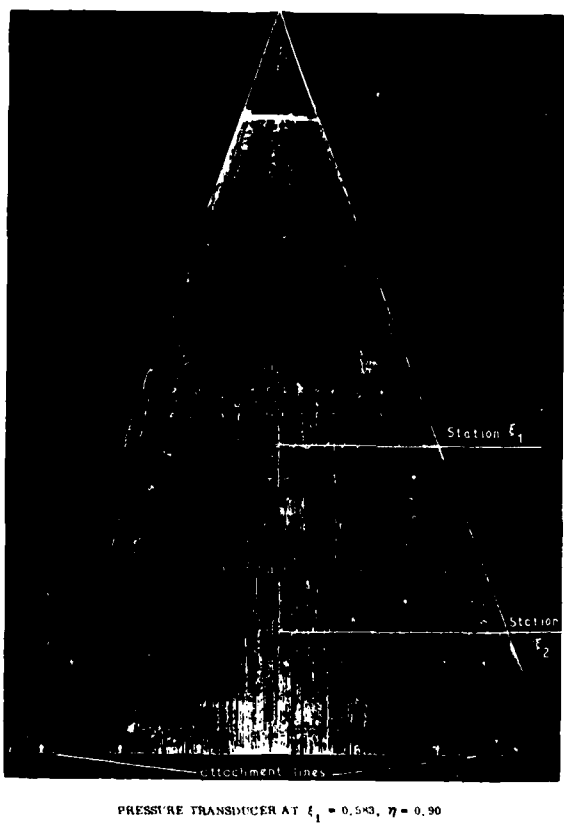


Figure 57. Effect of Windward Side Protuberance on Leeside Vortex Flow (Ref. 64).

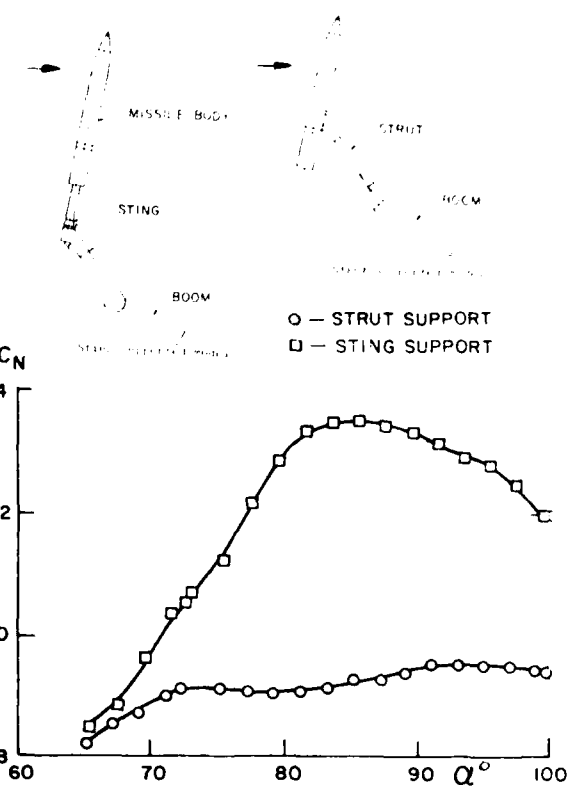
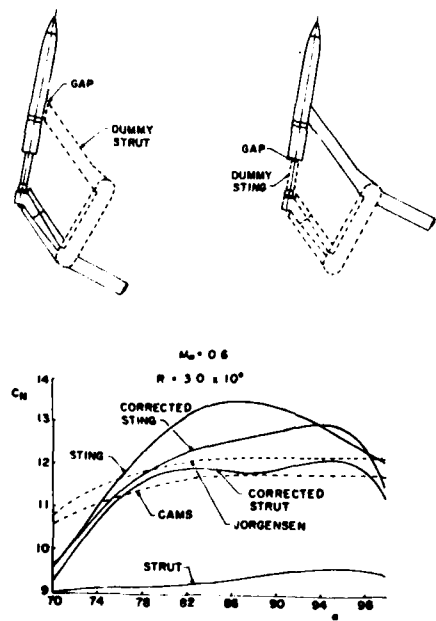


Figure 58. Effect of Model Mounting on Ogive Cylinder Normal Force Characteristics of High Angles of Attack (Ref. 65).

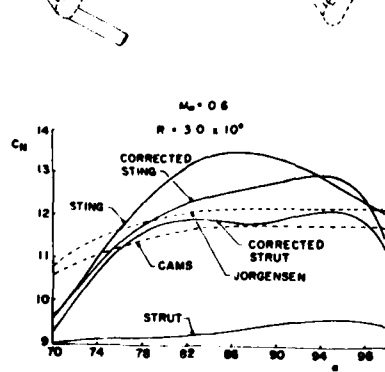


Figure 59. Corrected Normal Force Coefficient Data (Ref. 65).

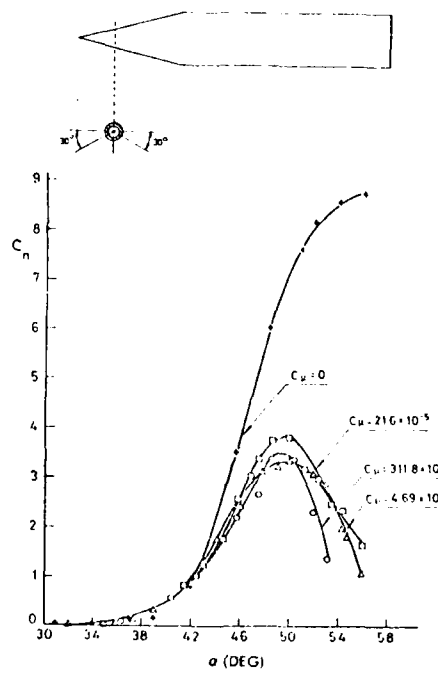


Figure 60. Effect of Windward Side Blowing on Vortex-Induced Side Moment (Ref. 69).

**APPLICATIONS OF HALF-MODEL TECHNIQUE IN  
DYNAMIC STABILITY TESTING**

by

E. S. Hanff

Unsteady Aerodynamics Laboratory  
National Aeronautical Establishment  
National Research Council of Canada  
Ottawa, Ontario, Canada

**ABSTRACT**

Rather than providing an in-depth theoretical background on the half-model technique in general, this lecture concentrates on the applications of that technique to oscillatory wind-tunnel experiments. The practical advantages and disadvantages of using the half-model technique for dynamic stability testing are briefly stated and compared with those of its full model counterpart.

Examples are given of various wind-tunnel dynamic experiments for which the half-model technique is particularly suitable. Descriptions of pitching, plunging and dynamic calibrating apparatuses are given as well as a brief review of the data analysis required for the determination of direct derivatives using the free and forced oscillation technique. Methods to obtain "cross derivatives" in the longitudinal plane are also indicated.

**SYMBOLS**

$c$	damping constant
$F(t)$	plunging driving force
$I$	pitching moment of inertia
$K$	stiffness
$k$	mechanical stiffness
$m$	mass of moving system
$M_\theta$	aerodynamic stiffness in pitch
$M_\theta$	aerodynamic damping constant in pitch
$z$	vertical deflection
$Z_z$	aerodynamic stiffness in plunge
$Z_z$	aerodynamic damping constant in plunge
$Z_z$	"aerodynamic mass" in plunge
$\gamma$	mechanical damping constant
$\theta$	pitching deflection
$\mu$	phase angle between driving force and plunging deflection
 <b>Subscripts</b>	
$T$	tare
$W$	wind-on

**1. INTRODUCTION**

The use of half models for static testing of symmetric configurations at symmetric flow conditions has been a recognized experimental procedure for a long time (see, for example, Ref. 1). This technique eliminates all interference problems usually associated with the presence and with the oscillation of a sting, permits the use of models larger than otherwise possible and allows for a more convenient arrangement of the test equipment (outside of the wind-tunnel wall). On the other hand, the technique has some problems of its own, such as the possible effect of the gap between the model and the tunnel wall and the effect of an interaction between the shock and the wall boundary layer. And, of course, the applications are strictly limited to symmetrical flow conditions. It is outside the scope of this lecture to delve into the details of these phenomena, instead, they are merely pointed out to remind the reader of the limitations of the technique. The emphasis is placed on the discussion of the practical applications where the half-model technique proves to be so invaluable.

Following its successful application to static experiments, the half-model technique has been used routinely for oscillatory experiments around zero or nearly-zero mean angles of attack (Refs. 2 and 3). In order to utilize it in connection with problems of flight at higher angles of attack, it became important to determine the range of angle of attack for which the condition of flow symmetry was satisfied. This was investigated partly by measuring the static side force on full models at zero yaw, to determine the highest angle of attack at which the flow over an unyawed full model was still symmetrical, and partly by conducting a flow visualization study to find the highest angle of attack at which the surface flow on full and half models still was in reasonably good agreement. On the basis of such investigations carried out on two cones and one ogive-cylinder configuration it was found (Ref. 4) that the highest angle of attack for which the above conditions were satisfied was of the order of 15° to 20° at *subsonic* and *supersonic* speeds. This was subsequently confirmed by a direct comparison of oscillatory results obtained with full and half models (*ibid*). It is expected that for wing-body configurations where the main aerodynamic contributions come from the wing this limiting angle of attack may be even higher, due to the shielding effect of the body. However, similar comparisons conducted at *transonic* speeds (Ref. 5) have yielded somewhat less satisfactory results.

Of course, in order to obtain satisfactory results with a half-model technique, certain precautions have to be taken to ensure that the possible sources of errors are minimized. Thus the effect of tunnel-wall boundary layer can be reduced significantly by the use of a properly designed reflection plate and by the resulting removal of the half model from the main portion of the boundary layer. The effect of the gap can be minimized by making the gap between the model and reflection plate as small as possible, at the same time ensuring that the gap is still located within the outer region of the tunnel-wall boundary layer. In some cases the use of a small fence at the root of the half model may be desirable.

The gap effect can also be eliminated by using a reflection plane attached to and therefore moving with the model (*ibid*). In this case, however, the aerodynamic characteristics of the reflection plane must be independently determined, a particularly difficult task as these characteristics are affected by the presence of the model. This effect is generally not considered, thus leading to a loss of accuracy in the results.

Historically the first dynamic stability experiments were carried out using the free oscillation technique, as the data it generates was more amenable to being analyzed using the instrumentation systems then available. Although the use of the free oscillation technique has decreased over the last several years it is still employed occasionally, particularly in half model tests in which only direct derivatives are required. Therefore a brief description of this technique will be presented in addition to the more commonly used forced oscillation technique in Section 3.

The differences between the full and half model techniques - summarized in Table I - indicate that there are a number of applications where the latter can be used to great advantage. Some of these applications are described in Section 5.

TABLE I  
COMPARISON OF FULL AND HALF MODEL TECHNIQUES

	Full Model	Half Model
Model geometry	Any <sup>(1)</sup>	Symmetrical
Space limitations for stability apparatus	Possibly serious	None <sup>(2)</sup>
Load capacity	Usually limited	Virtually unlimited
Permissible model size	Limited by load capacity	Limited by tunnel blockage i.e. larger than for full model technique
Permissible α	Unlimited	About 20° <sup>(3)</sup>
Primary motion	Any DOF	Within longitudinal plane, i.e. pitching or plunging
Measurable reactions	In any DOF	In longitudinal plane
Support vibrations	Yes	No
Sting interference	Yes	No
Wind tunnel wall boundary layer interactions	No	Yes <sup>(4)</sup>
Suitability for 2D applications	No	Yes
Multiple oscillatory models	Extremely difficult	Relatively easy
Applicability to jet exhaust plume simulation	No	Yes

- (1) Provided there is sufficient cavity space to accommodate dynamic stability apparatus as well as an adequate base geometry to permit the use of a sting. Problem areas are slender missiles, boat-tail and twin exhaust geometries, etc.
- (2) Stability apparatus is usually located outside wind tunnel.
- (3) Beyond which the flow around an unyawed full model may cease to be symmetrical.
- (4) Can be reduced by the use of reflection plate that extends little beyond model nose.

Bearing in mind that both the primary motions and measured reactions must be in the longitudinal plane it follows that only pitching and plunging apparatuses are possible. The derivatives that can be measured with them are shown in Table II.

TABLE II HALF MODEL APPARATUSSES

Apparatus	Direct Derivatives	Cross Derivatives
Pitching	$C_{ma}$ , $C_{mq} + C_{m\dot{a}}$	$C_{za}$ , $C_{zq} + C_{z\dot{a}}$ *
Plunging	$C_{zz}$ , $C_{z\ddot{z}}$	$C_{m\ddot{z}}$ , $C_{m\ddot{z}}$

## 2. DESCRIPTION OF TYPICAL HALF-MODEL APPARATUSSES

### 2.1 General

The main difference between the two types of half model apparatuses is in their suspension geometries required to accommodate the different primary motions with, of course, the corresponding modifications in the drive mechanism.

Contrary to the situation encountered in full-model testing however, the static model deflections induced by the aerodynamic loading do not in general cause a problem as sufficient clearances are available. It is therefore common to resort to electro-mechanical or other non-inexorable drive mechanisms. An example of both pitching and plunging apparatuses are given below for the sake of completeness.

### 2.2 Pitching Apparatus (AEDC)

The wall mounted apparatus is shown in Fig. 1. The half model is supported by a rigid shaft which is in turn suspended from an inner shell by 3 sets of cross flexures that allow it to rotate around its axis. The apparatus is intended for free oscillation tests only and the required transient excitation is provided by a pneumatic cock and release mechanism. Changes in angle of attack are implemented by rotating the inner shell relative to the outer one. To avoid vibration problems, any movement between the inner and outer shell is prevented during the cock and release cycle by means of a pneumatically activated clamping ring. Additional information regarding this apparatus may be found in Ref. 5.

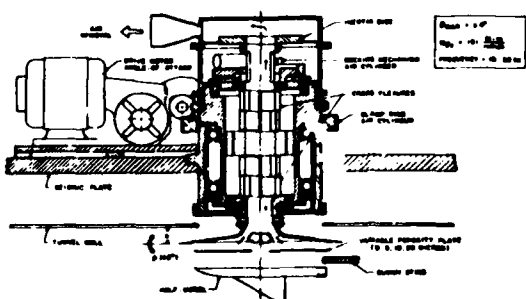


Fig. 1 Pitching Apparatus (AEDC)

\* The half model apparatus geometry permits the measurement of these derivatives much more accurately than with the full-model technique as in the latter case the large inertial loads, unavoidably sensed by the pertinent balance elements, considerably affect the accuracy of the measurements.

### 2.3 Plunging apparatus (NAE)

The plunging apparatus is shown in Fig. 2. It constitutes a modification of the previously developed half model pitching apparatus (Ref. 2). The model is mounted on a simple cruciform-shaped balance capable of sensing the pitching moments required to determine the cross derivatives. A pair of cantilever springs support the balance and allow it to translate in the desired DOF. The necessary driving force is provided by a pair of coils - carrying suitable alternating currents - imbedded in DC magnetic fields generated by electromagnets. The driving force, required for the determination of direct derivatives, is inferred from the driving coil current; furthermore, the primary deflection is obtained from strain gauges on the cantilever beams.

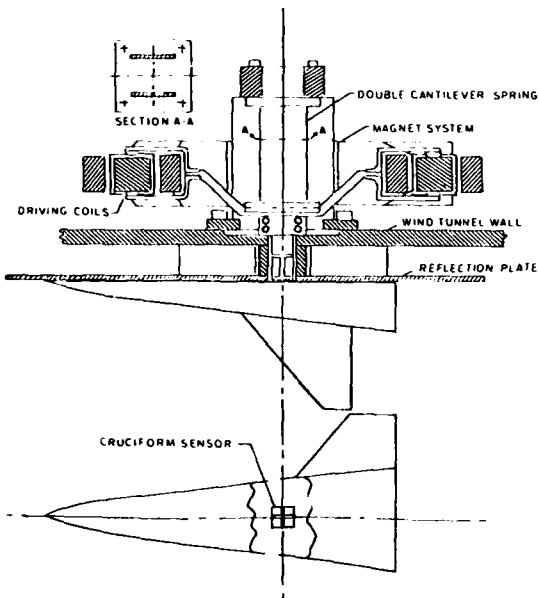


Fig. 2 Plunging Apparatus (NAE)

## 3. DATA ANALYSIS

### 3.1 Direct Derivatives

Both the free and forced oscillation techniques can be used to determine direct derivatives, therefore an example of the data analysis for each of these cases is shown in the following sections.

#### 3.1.1 Free Oscillation Method

Let us consider a pitching experiment in which the model is initially deflected from its equilibrium position and then released. The equation of motion is, after the time of release,

$$I\ddot{\theta} + c\dot{\theta} + k\theta = 0 \quad (1)$$

or

$$\ddot{\theta} + 2a\dot{\theta} + \omega_0^2\theta = 0$$

where

$$2a = \frac{c}{I}, \quad \omega_0^2 = \frac{k}{I}$$

The solution of the equation depends on whether the system is underdamped ( $a < \omega_0^2$ ), critically damped ( $a = \omega_0^2$ ), or overdamped ( $a > \omega_0^2$ ). Since in all practical cases the system is underdamped only the corresponding solution is considered, namely

$$\theta = \theta_0 e^{-at} \cos (\omega_d t + \eta)$$

where  $\omega_d^2 = \omega_0^2 - a^2$  and  $\theta_0, \eta$  are constants.

Under tame conditions Eq. (1) is

$$I\ddot{\theta}_T + r\dot{\theta}_T + k\theta_T = 0$$

Therefore

$$2a_T = \frac{r}{I}, \quad \omega_{0T}^2 = \frac{k}{I}$$

and

$$\omega_{dT}^2 = \frac{k}{I} - \frac{\gamma^2}{4I^2}$$

Under wind-on conditions Eq. (1) is

$$I\ddot{\theta}_W + (\gamma - M_\theta)\dot{\theta}_W + (k - M_\theta)\theta_W = 0$$

Therefore

$$2a_W = \frac{\gamma - M_\theta}{I}, \quad \omega_{DW}^2 = \frac{k - M_\theta}{I}$$

and

$$\omega_{dT}^2 = \frac{k}{I} - \frac{M_\theta}{I} - \frac{\gamma^2 - 2\gamma M_\theta + M_\theta^2}{4I^2}$$

Hence

$$M_\theta = 2I(a_T - a_W)$$

and

$$M_\theta = \left( \omega_{dT}^2 - \omega_{DW}^2 \right) I + \frac{2\gamma M_\theta - M_\theta^2}{4I}$$

$\gamma$  and  $I$  are given by

$$\gamma = 2a_T I$$

$$I = \frac{k}{\omega_{dT}^2}$$

and  $k$  is determined by means of a static calibration.

### 3.1.2 Forced Oscillation Method

The forced oscillation analysis is in general analogous to the one described for the full model technique in Ref. 6. However, some very interesting plunging tests - described in Section 5 - in which the model is subjected to ground-like effects due to the proximity of other bodies, require a somewhat different analysis, described below.

Bearing in mind that  $z_z$  may not be zero in the presence of ground effects, the equation of motion is

$$(m - z_z'')\ddot{z} + (\gamma - z_z')\dot{z} + (k - z_z)z = F(t) \quad (2)$$

For a sinusoidal excitation (2) becomes in vectorial form

i) Tare conditions

$$-\omega_T^2 m \bar{z}_T + i\omega_T \gamma \bar{z}_T + k \bar{z}_T = F_T e^{i\mu_T} \quad (3)$$

(ii) Wind-on conditions

$$-\omega_W^2 (m - z_z'') \bar{z}_W + i\omega_W (\gamma - z_z') \bar{z}_W + (k - z_z) \bar{z}_W = F_W e^{i\mu_W} \quad (4)$$

Taking the real part of (3) and (4)

$$-\omega_T^2 m \bar{z}_T + k \bar{z}_T \approx F_T \cos \mu_T \quad (5)$$

$$-\omega_W^2 (m - z_z'') \bar{z}_W + (k - z_z) \bar{z}_W = F_W \cos \mu_W \quad (6)$$

Solving for  $k$  in (5) and substituting in (6) and letting

$$z' = z_z - \omega^2 z_z''$$

we obtain

$$z' = \frac{F_T \cos \mu_T}{\bar{z}_T} - \frac{F_W \cos \mu_W}{\bar{z}_W} + m \left( \omega_T^2 - \omega_W^2 \right) \quad (7)$$

Likewise, by taking the imaginary parts of (3) and (4) and solving for  $\gamma$  as in Ref. 6 we obtain

$$z'_z = \frac{F_T \sin \mu_T}{\omega_T z_T} - \frac{F_W \sin \mu_W}{\omega_W z_W} \quad (8)$$

In order to separate the two components of  $z'$  it is necessary to perform static tests to determine  $z'_z$ . On the other hand, if  $z'_z$  is known not to vary significantly with frequency, it is possible to separate the two derivatives by performing the same oscillatory test at several frequencies.

### 3.2 Cross derivatives

Bearing in mind that in the case of half-model experiments both the primary motion and measured reactions are in the longitudinal plane, it follows that the concept of cross derivatives is somewhat different from the one used in the full model case, where, such derivatives correspond to aerodynamic reactions caused by a motion in the primary plane on other (secondary) planes. Instead, cross derivatives are here defined by the analytical procedure that is required for their determination, namely, Procedure II described in detail in Section 3.2 of Ref. 6. In principle the free oscillation technique could also be used to determine cross derivatives, but the data would be harder to reduce and the results would in any case be less accurate as the secondary reactions - assumed to be proportional to the primary motion - would be smaller.

In general the balances are of the single angular DOF type and therefore the corresponding version of Procedure II must be used (Section 3.2.1 ibid). Furthermore the instrumentation systems required to acquire and process the wind tunnel data are the same as those described in the reference.

### 4. DYNAMIC CALIBRATOR

The need for, and features of, a dynamic calibrator to be used in conjunction with dynamic stability testing of the type under consideration, is discussed in detail in Ref. 6 where NAE's new full model version of such a device is described. An earlier model, now largely devoted to half model applications is shown in Figs. 3 and 4.



Fig. 3 Front View of NAE Half Model Calibrator

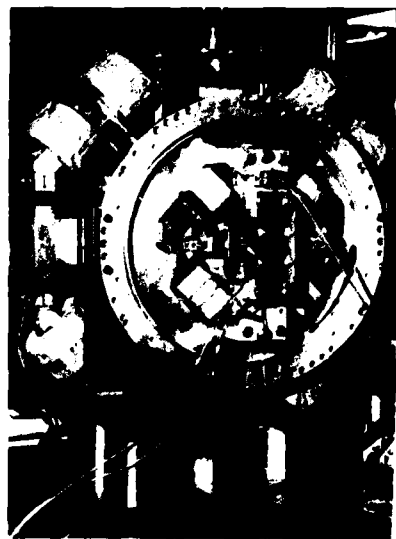


Fig. 4 Rear View of NAE Half Model Calibrator

It consists of a stator comprising two concentric octagonally shaped stationary structures that form a magnetic circuit necessary to establish a DC magnetic field across four air gaps located on the horizontal and vertical axes of symmetry of the octagons, the latter not being required in half model applications.

A calibrating frame (rotor) - mounted on the stability apparatus in lieu of the model - consists of a boom aligned with the model x axis that supports driving conductors at both ends (oriented parallel to the y axis) which are imbedded in the aforementioned magnetic fields. The desired loads, i.e. pitching or plunging reactions, can be applied to the rotor by driving suitable currents through the conductors. As the primary motion may be translational (plunging) or angular (pitching), slight geometrical modifications are required in order to accommodate such motion without mechanical interference between the stator and rotor. In the angular experiments the

pole pieces are spherical sections (see vertical gaps in Fig. 3) and the driving conductors curved accordingly, whereas in the translational cases both of the above are planar. (See horizontal gaps in Fig. 3.) The electronic system used to drive the calibrator is described in Ref. 7. A typical half model calibration of the pitching apparatus is shown in Fig. 5.

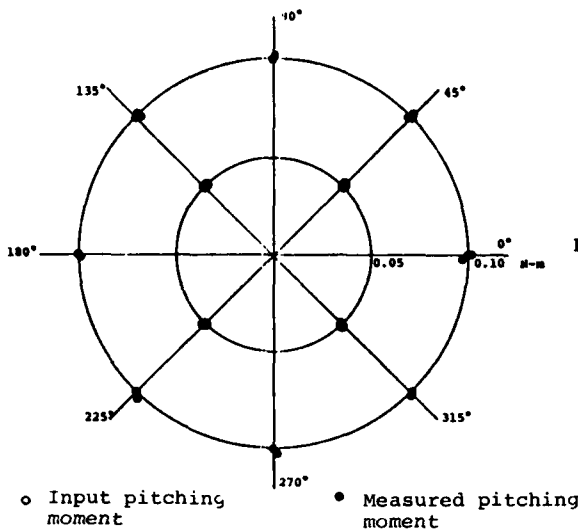


Fig. 5 Typical Calibration of Half Model Pitching Apparatus

##### 5. WIND-TUNNEL EXPERIMENTS

In order to illustrate the usefulness of the half-model technique, a sample of some of the various experiments that can be effectively performed are briefly described below.

###### 5.1 Damping-in-pitch experiments

This type of experiment can in general be readily performed, but is of particular value in cases where the model geometry does not lend itself to being sting mounted. One of the early such applications of the technique was by K. J. Orlik-Rückemann and C. O. Olsson (Ref. 8) in which the damping-in-pitch derivative  $C_{m\dot{\theta}}$  for a triangular wing was determined by means of the free oscillation method. Rather than using an oscillogram of the model-response time history in order to compute the damping, a new device, the dampometer - developed by the same investigators - was used to automatically determine the logarithmic decrement and frequency of the oscillation (Ref. 9). The desired derivatives could then be readily obtained (Ref. 10). Modern instrumentation systems and data reduction techniques however, can readily determine these derivatives in terms of the raw data, thus obviating the need for the dampometer.

###### 5.2 Interference effects

A very interesting application of half-model oscillatory techniques involves the determination of the dynamic interference between two (oscillating) aircraft flying in close proximity. If the entire maneuver occurs in the longitudinal plane of symmetry, with the two aircraft one above the other (as it fortunately happens to be the case in many practical situations), the half-model technique provides a relatively straightforward, practical approach. Fig. 6 shows an example of such an experimental arrangement, as applied for investigating the interference effect on the damping in pitch of the two component vehicles of the fully reusable, early version of the space shuttle immediately after a hypothetical abort separation (Ref. 11).

The model on which the derivatives are to be measured (orbiter in this case) is mounted on the pitch apparatus whereas the mounting of the other model (booster) depends on whether static or dynamic interference experiments are desired.

For the static interference experiments, the second model is attached to the reflection plate in such a way that its vertical and longitudinal separation distances and the incidence relative to the first model can be easily varied. The incidence of the whole configuration is varied by rotating the oscillatory rig (with the reflection plate). For the dynamic interference experiments, the second model is mounted on a pivot which defines its center of oscillation, while an oscillatory motion of a known amplitude is imparted by means of an eccentric drive connected to a synchronous motor; the two motions can be made synchronous, and the phase relationship between them varied as required by means of the circuitry shown in Fig. 7.

In the synchronous mode of operation, which is the one of principal interest here, the output signal  $V_1$  from the orbiter displacement transducer is applied to a clipping

amplifier whose output is a square wave of fixed amplitude over the complete range of input signal amplitude. The harmonic frequencies of the square wave are eliminated by means of a low-pass filter, and the fundamental component is fed into an adjustable phase shifter whose output is amplified before being applied to the synchronous motor that drives the booster through an eccentric mechanism. Thus, the signal supplied to the motor has a constant amplitude regardless of the amplitude of the oscillation of the orbiter; this is necessary for an optimum operation of the motor, which thus imparts a perfectly controlled motion to the booster.

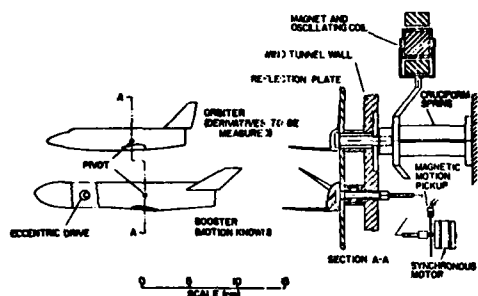


Fig. 6 Experimental Arrangement for Static and Dynamic Interference Study on Shuttle Abort Separation

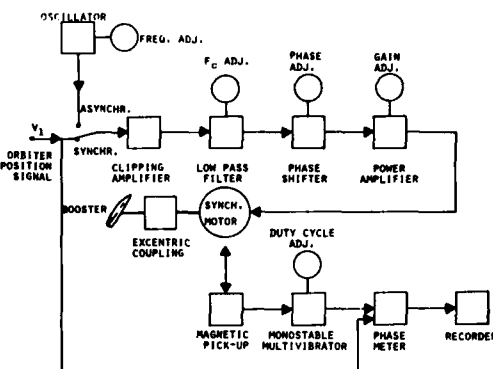


Fig. 7 Instrumentation for Booster Oscillation

The phase relationship between the motions of the two models can be adjusted by shifting the signal that drives the booster. The phase is determined by means of a phase meter connected between the displacement signal of the orbiter and a corresponding signal for the booster. The latter is generated with a magnetic pickup which produces a spike when the rotor of the motor is at a given position. For proper operation of the phasemeter, it is necessary to transform this signal into a more suitable waveform, which is accomplished by means of a monostable multivibrator with a 50% duty cycle.

Results obtained at a Mach number of 2, zero incidence for both models and a separation between their respective C.G.'s of  $\Delta x/l = -0.06$  and  $\Delta z/l = 0.19$  where  $l$  is the booster length are summarized in Fig. 8 for the damping in pitch derivative. The figure indicates a rather small static interference although it is clear that the dynamic interference effect i.e., the difference between the curves presented and the interference-free value, is up to two orders of magnitude larger than the static interference effect and may result in values of the damping derivative which are between +13 and -8 times the interference-free value. Such large variation in damping and, especially, the occurrence of large negative damping (positive  $C_m \theta$ ), could have a significant effect on the flight dynamics of the orbiter. Should the two vehicles perform synchronous oscillation while in close proximity, and should the phase angle between the two motions be one for which a high negative damping has been observed, the abort-separation maneuver could be critically affected.

Fig. 9 where the static pitching moment derivatives, obtained under the same condition are shown, also indicates that the dynamic interference effect is much larger than its static counterpart. An assessment of the effect of the above results on the abort separation maneuver is discussed in Ref. 12.

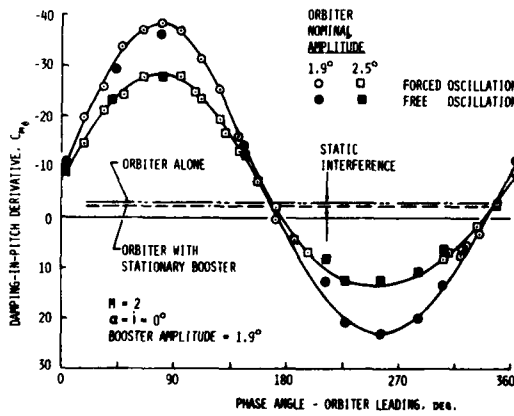


Fig. 8 Dynamic Interference Effect on the Damping-in-Pitch of Delta-Wing Shuttle Orbiter Oscillating Synchronously with the Booster

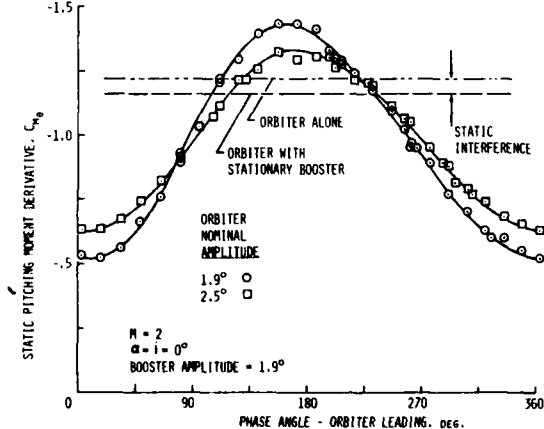


Fig. 9 Dynamic Interference Effect on the Static Pitching-Moment Derivative of the Delta-Wing Orbiter Oscillating Synchronously with the Booster

### 5.3 Flow visualization

A useful feature of the half-model technique is the ease with which the flow on the plane of symmetry around the model can be observed using simple surface oil flow visualization techniques on the reflection plate. The possibility of wall boundary layer effects must of course be kept in mind in this type of test.

A typical photograph of the flow visualization for the experiment described in Section 5.2 is shown in Fig. 10 where some of the flow features responsible for the interference effects can be observed.

### 5.4 Exhaust plume interference

Another application of the dynamic half-model technique involves the determination of the exhaust-plume interference on the damping-in-pitch derivative of an aerospace vehicle. The half-model technique is eminently suitable for such an investigation since it eliminates entirely the undesirable reaction that would otherwise occur between an oscillating plume and the stationary sting of a full-model conventional arrangement. Fig. 11 shows a flow-visualization photograph of a half model of the launch configuration of the early fully-reusable shuttle described in Section 5.2. A high-pressure nitrogen supply line was incorporated in the model suspension system, and a pressure chamber and an exhaust nozzle was inserted in the body of the booster. The shape and the size of the plume were simulated by duplicating the nozzle-exit wall angle, the initial plume-boundary angle and the ratio of the initial plume-boundary Mach number to the specific-heat ratio. Details on the experimental arrangement as well as typical results are given in Ref. 11.



Fig. 10 Oil-Flow Visualization of Straight-Wing Shuttle in Abort Separation at Mach 1.8



Fig. 11 Oil-Flow Visualization of the Launch Configuration of the Delta Wing Shuttle with Simulated Exhaust Plume.  $M=2$ ,  $\alpha=0$

### 5.5 2D testing

The half-model dynamic apparatuses lend themselves very well for stability testing of two-dimensional models, in which case of course, it becomes necessary to add a suitable fence at the model tip. An example of this type of work has been done at NAE in which the stability characteristics of some external trays-carrying control and fuel lines - mounted on the shuttle external fuel tank were investigated. Figs. 12 and 13 show the location of the trays and the substantial cross flows that may be present at some stations, conditions under which instability of the trays may arise if proper measures are not taken.

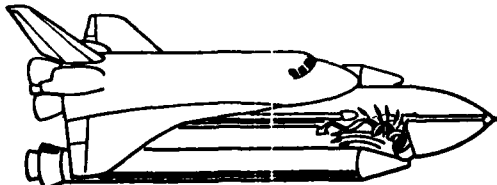


Fig. 12 Shuttle SRB-HO Interference Flow Field



Fig. 13 External Trays Location on Shuttle HO Tank

A typical experimental arrangement - where the external tank is simulated by a ground plane - is shown in Fig. 14. For the purpose of this flow visualization photograph the model was not oscillated during the run.



Fig. 14 Experimental Arrangement of Shuttle Tray Test

### 5.6 Control surface oscillation techniques

Sometimes it is of interest to determine the hinge moment derivative of an oscillating control surface such as an aileron and the effect such an oscillation has on the complete model. The half-model technique lends itself well to this type of testing by virtue of the geometry of the associated wind-tunnel apparatuses which readily permit the driving of the control surface and the measurement of the aerodynamic reactions on both the hinge as well as the complete model. Such an apparatus has been in use at RAE for a number of years and is shown in schematic form in Fig. 15 (Ref. 13). The elements that sense the various loads on the model and the force transducer required to measure the hinge moments are clearly shown. Details of the model mounting and control surface drive are shown in Fig. 16.

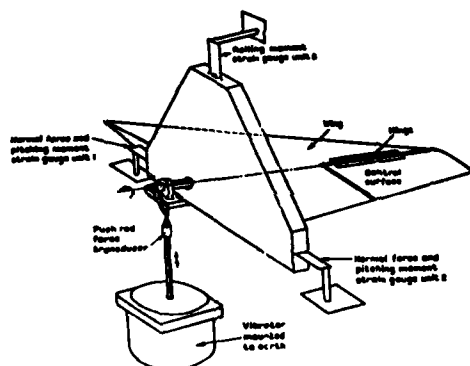


Fig.15 Control surfaces oscillatory apparatus (RAE).

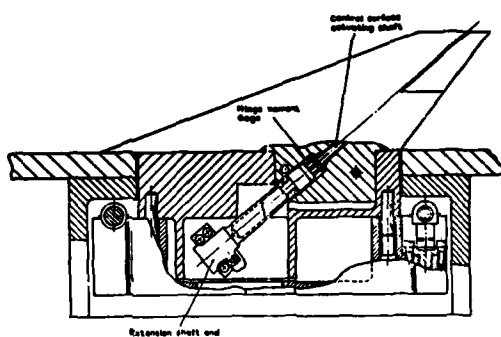


Fig.16 Details of wing mounting and control surface drive.

### 6. CONCLUDING REMARKS

The main features of the half-model technique for the determination of dynamic stability parameters are briefly outlined; as an illustration of the usefulness of the technique a number of wind-tunnel experiments for which the technique is specially indicated is described. The reader should however keep in mind the limitations of the technique, a subject that for lack of space could only be rather superficially broached. More information can be found in the references.

### 7. REFERENCES

1. Van der Blieck, J. A. Notes on Half-Model Testing in Wind Tunnels. NRC Aeronautical Report LR-235, 1959.
2. Orlik-Rückemann, K. J. Static and Dynamic Longitudinal Stability Characteristics of a Series of Delta and Sweptback Wings at Supersonic Speeds. NRC Aeronautical Report LR-396, 1966.

3. Orlik-Rückemann, K. J.  
Adams, P. A.  
LaBerge, J. G.  
Dynamic Stability Testing of Unconventional Configurations. *J. of Aircraft*, V 9, 12, 1972.
4. Orlik-Rückemann, K. J.  
Half and Full Model Experiments on Slender Cones at Angles of Attack. *J. of Spacecraft and Rockets*, V 11, 9, 1973.
5. Shadow, T.O.  
An Investigation of the Half-Model Reflection-Plane Technique for Dynamic Stability Testing at Transonic Mach Numbers. *AEDC-TR-76-165*, 1976.
6. Hanff, E. S.  
Direct Forced Oscillation Techniques for the Determination of Stability Derivatives in Wind Tunnels. Lecture #4 AGARD LS 114 Lecture Series, 1981.
7. Hanff, E. S.  
A Dynamic Calibrating Apparatus for Cross Derivative Experiments. *Proc. 7th Int. Cong. on Instrumentation in Aerospace Simulation Facilities*, 1977.
8. Orlik-Rückemann, K. J.  
Olsson, C.O.  
A Method for the Determination of the Damping in Pitch of Semi-Span Models in High Speed Wind-Tunnels, and Some Results for a Triangular Wing. *FFA Report No. 62*, 1956.
9. Olsson, C. O.  
Orlik-Rückemann, K. J.  
An Electronic Apparatus for Automatic Recording of the Logarithmic Decrement and Frequency of Oscillation in the Audio and Sub-Audio Frequency Range. *FFA Report No. 52*, 1954.
10. Orlik-Rückemann, K. J.  
Dynamic Stability Testing in Wind Tunnels. *NRC NAE LTR-UA-41*, 1977.
11. Orlik-Rückemann, K. J.  
LaBerge, J. G.  
Hanff, E. S.  
Supersonic Dynamic Stability Experiments on the Space Shuttle. *J. of Spacecraft and Rockets*, V 9, 9, 1972.
12. Orlik-Rückemann, K. J.  
Iyengar, S.  
Example of Dynamic Interference Effects between Two Oscillating Vehicles. *J. of Spacecraft and Rockets*, V 11, 9, 1973.
13. Wight, K.C.  
Lambourne, N. C.  
A Control-Surface Oscillatory Derivative Rig for Use with Half-Models in High-Speed Wind-Tunnels. *RAE Technical Report 75026*, 1975.

**DETERMINATION OF AIRCRAFT DYNAMIC STABILITY  
AND CONTROL PARAMETERS FROM FLIGHT TESTING**

by

P. G. Hamel

Institut für Flugmechanik

Deutsche Forschungs- und Versuchsanstalt  
für Luft- und Raumfahrt e.V. (DFVLR)  
D 3300 Braunschweig-Flughafen, West Germany

**SUMMARY**

Static and dynamic wind tunnel testing plays an important role in the preliminary aircraft design although aerodynamic scale effects, wind tunnel as well as model deficiencies may lead to limitations in the applicability of wind tunnel data. Therefore, flight tests are important and necessary to isolate limits and uncertainties from the prediction techniques of aircraft aerodynamics and flight mechanics. Perhaps more than any other technique parameter identification (PI) provides the basis for flight/ground testing correlation by extracting as much information as possible from subscale and fullscale wind tunnel and free flight tests.

The present state of the art of aircraft PI techniques from flight test data is reviewed together with a critical appraisal of current methods developed and applied to various aircraft configurations and flight conditions. Particular emphasis is placed on practical aspects and results of PI techniques in order to generate information useful not only to the flight mechanic engineer but also to the aerodynamicists in industry and applied research facilities. This is especially relevant for data correlation and for increasing confidence in static and dynamic wind tunnel prediction techniques.

Recent experience for fixed as well as rotary wing aircraft PI will be presented as well as identification results for extreme flight regimes. In addition, information on pilot-in-the-loop and closed loop aspects of aircraft PI will be given with special reference to the interrelationship between stability and controllability. Finally, the application potential and experience of PI methods for dynamic wind tunnel testing will be discussed including requirements necessary for gaining more insight and confidence in using static and dynamic wind tunnel data for flight/ground testing correlation.

**1. INTRODUCTION**

Modern flight vehicles like fixed-wing aircraft, rotorcraft and missiles often encompass large amplitude and high load factor maneuvers in extreme flight regimes due to new mission requirements. Such flight conditions induce flow phenomena like flow separation and interference as well as vortex shedding and bursting which are highly motion sensitive and configuration dependent. These unsteady and nonlinear aerodynamic effects may lead to strong coupling effects between the longitudinal and lateral modes of motion which, in turn, may cause severe flying qualities deficiencies.

Considerable advances are required in the ability to describe and model such phenomena [1]. Hence, one of the most important steps needed to gain a satisfactory phenomenological understanding of the flight mechanics of an aircraft exposed to complex flow fields is the establishment and the verification of an adequate mathematical model to describe its motions. The verification should be conducted by estimating a complete set of stability and control parameters for the aircraft configuration to be investigated by simulating a series of mission oriented maneuvers or selected control inputs, and then comparing them with actually flown time histories [2].

Although the lowest necessary level of sophistication of the mathematical model should be sought for, it is important to realize that conventional linearized constant coefficient equations of motions are describing properly only small perturbation aircraft motions under orderly and attached flow conditions. Generally, there will be non-linear dependencies of almost all stability and control parameters on angles of attack and sideslip.

Adequate modeling of aircraft flight mechanics in extreme maneuvering conditions like high angles of attack ( $\alpha$ ) or sideslip ( $\beta$ ) as well as large roll rates ( $p$ ) must include off-diagonal coupling terms in the stability and control matrices. These aerodynamic and inertial coupling examples in flight mechanics are shown in Figure 1 together with coupling situations generated by aircraft asymmetries like wing skewing ( $\Lambda$ ) and rotor coupling ( $\Omega$ ).

The introduction of modern digital flight control systems and its potential to cure flying quality deficiencies by implementing so-called Active Control Technology (ACT) is offering the promise of improved aircraft performance and operational capabilities. The use of ACT in this way may require departure from existing design practice in the direction of decreased static aerodynamic stability, increased control authority, increased bandwidth of control servos and reduced structural strength and stiffness. Additionally, the application of ACT to reduce dynamic structural loads and suppressing elastic modes will involve an improved interdisciplinary understanding of the anticipated external disturbance, aerodynamic and structural characteristics as well as control dynamics.

Figure 2 indicates the important influence of Active Control Technology on the overall aircraft flight mechanics by including the capabilities of a full-time, full-authority and high frequency bandwidth digital flight control system. It is imperative that the aerodynamic stability and control parameters of such ACT aircraft have to turn out as predicted, since the inherent rigid body and elastomechanical stability margins will be lower. Hence, independent from the pilot, significant inputs have to be transmitted to the aerodynamic control surfaces for the purpose of not only augmenting the vehicle performance but also the handling and ride qualities as well as the structural dynamics from a load and fatigue relief standpoint. Consequently, so-called high-order system (HOS) dynamics have to be modeled in order to describe ACT aircraft configurations incorporating multiple interacting and interfering aerodynamic force and moment producers (motivators). This is shown schematically in Figure 3.

From the above lines it is apparent that aircraft configurations and missions are becoming more and more complex and expensive resulting in significant development risks. These can only be reduced by improving the ability to predict and evaluate the flight characteristics of such systems with more confidence. Data correlation is the ultimate way of measuring the validity of any mathematical model, wind tunnel experiment and flight test technique.

The aim of this paper is to review and highlight flight test techniques which are specifically designed for data correlation. The primary goal of this kind of aircraft flight testing is to estimate flight-determined aircraft characteristics, such as stability and control parameters which can be compared with calculated and wind tunnel predictions. These methods for the determination of aircraft characteristic parameters from flight tests and the problems associated with them are more generally defined as Aircraft State and Parameter Identification.

During the past decade there has been an increasing effort to expand the practical experience and application spectrum of Parameter Identification procedures. Several factors are involved in this tendency. One of which is the fact that the evolution of flight test instrumentation as well as analytical and computational capabilities nowadays make aircraft parameter identification methods to routine procedures, which, in turn, have generated sufficient practical experience to gain more confidence in utilizing these techniques [3].

As a result of increased complexities and capabilities of new air vehicle systems there is a need for precise measurement techniques and an increased number of parameters recorded during flight tests (Figure 4, [4]). Together with the increased accuracy and amount of information provided by high quality sensors and additional data channels the extended frequency bandwidth due to the implementation of Active Control Systems has placed more severe demands on the flight test instrumentation. This development is mainly visible in the data rate necessary for flight tests. As an example, Figure 5 displays the projected increase of data rates for dynamic wind tunnel and flight testing at the DFVLR Institut für Flugmechanik for the next five years [5].

Therefore, critical considerations have to be given to limit the opportunities offered by modern instrumentation and computation capabilities in order to conserve flexible and efficient flight testing for the future. Otherwise, a further escalation in the number of parameters requested by specialists of different disciplines can be foreseen with respect to constraining flight testing costeffectiveness. Also, the feasibility of the art and science of aircraft parameter identification, to be surveyed in this paper, has then to be questioned. Similar conclusions on everincreasing technical sophistication and cost developments can be drawn for dynamic wind tunnel testing facilities. Therefore, the necessity exists not only to achieve an optimum balance between the efforts of dynamic wind tunnel testing and flight testing but also to improve the interdisciplinary communication and cooperation between wind tunnel aerodynamicists and flight test engineers. This paper is intended to fill up some of the communication gaps existing between the wind tunnel and the flight test people, of course, from a flight mechanics standpoint.

## 2. REVIEW OF RECENT AGARD ACTIVITIES

Before going into more technical details of Parameter Identification (PI) methods it is worthwhile mentioning the substantial role the AGARD Flight Mechanics Panel (FMP) has played to identify and support the importance of estimating aircraft stability and control parameters from flight tests. Table 1, for example, provides a multitude of documentations within the various AGARD publication series which have been published since 1955 [6]. This table includes also some related information about dynamic wind tunnel test techniques. Special reference should be made to an AGARD FMP Specialist's Meeting held at NASA Langley Research Center in November 1975 [7, 8]. As a direct outcome from this Specialist's Meeting a Lecture Series (LS 104) on Parameter Identification was organized by the AGARD Flight Mechanics Panel at the Delft University of Technology (DUT), The Netherlands, and at the Royal Aeronautical Society, London, UK, in fall 1979 [9]. In further consequence, the AGARD Flight Mechanics Panel has asked Dr. Kenneth W. Iliff, the most experienced NASA specialist in this field, to prepare an AGARDOgraph entitled Parameter Identification as a follow-on activity to the aforementioned Lecture Series LS 104. The AGARDOgraph is prepared within the wellknown AGARD Flight Test Manual Series and will address the parameter identification flight test analysis methodology in a more unified way.

### 3. GENERAL ASPECTS OF PARAMETER IDENTIFICATION

#### 3.1 DEFINITIONS FOR PARAMETER IDENTIFICATION

The aircraft dynamic response behaviour (output) due to disturbance (gusts) and control (pilot) inputs is described by the interaction of inertial and aerodynamic forces as well as elastomechanic and control forces.

It is evident that aircraft stability, controllability and sensitivity are in principle influenced by all four kinds of forces. The relative effects of these forces on the aircraft's dynamic response is varying between different aircraft configurations and operations.

Whereas static and dynamic structural and control force influence parameters can be properly modeled without airloads by ground test techniques, the identification of aerodynamic forces and loads require wind tunnel and flight testing. Static and dynamic wind tunnel testing methods play an important role in the preliminary aircraft design although aerodynamic scale effects and wind tunnel model deficiencies may lead to severe limitations in the applicability of wind tunnel data.

Therefore, flight tests are important and necessary to isolate limits and uncertainties from the prediction techniques of aircraft aerodynamics and flight mechanics. Perhaps more than any other technique parameter identification provides the basis for flight/ground testing correlation by extracting as much information as possible from subscale and full-scale wind tunnel and free flight tests.

Precisely defined, parameter identification is the determination on the basis of input and output of a system within a specified class of systems to which the system under test is equivalent. This means realistically expressed with respect to the present problem area that aircraft parameter identification is related to the flight test verification of qualitative (model) and quantitative (coefficients) aerodynamics from a flight mechanics standpoint. Hence, aircraft parameter identification may be subdivided into two distinct areas:

- System identification, primarily concerned with the mathematical structure of aircraft models and
- Parameter estimation, the quantifying of parameters or coefficients for a selected aircraft model.

#### 3.2 REQUIREMENTS FOR PARAMETER IDENTIFICATION

Although the essential flight vehicle aerodynamic characteristics can be predicted with rather satisfactory accuracy by means of theoretical calculations and wind tunnel measurements, the requirements for more precise, experimentally determined aircraft flight mechanics parameters have increased.

For example, the acceptance flight testing of the flying qualities of modern weapon systems with respect to the requirements of military specifications is costly and time consuming. A considerable portion of the flight test programme can be eliminated by implementing aircraft parameter identification techniques. This method would be employed to extract the aircraft stability and control derivatives from data obtained through a preselected limited number of flight test points. The specification of flight test points is a matter to insure that flight envelope parameters like Mach number, angle of attack and normal load factor are adequately covered. In turn, the derivatives would be used to verify the handling qualities of the aircraft with the military specification requirements [10, 11].

Also, requirements for increased maneuverability of modern combat aircraft make the task of assessing the overall handling qualities or precision controllability more difficult. The analysis of precision tracking tasks depends heavily on the integration of the pilot, flight control systems and the aircraft dynamics. From a flight mechanics standpoint, the adoption of tracking flight tests offer a closed-loop task that has the advantage of permitting a quantitative evaluation in addition to the qualitative pilot assessment [12, 13]. Such pilot-in-the-loop precision tracking flight test provides actual flight vehicle data not only for the extraction of stability and control derivatives of the aircraft within a matrix of angle of attack and normal load factor but also for the identification of pilot dynamics.

In addition, the identification of closed loop pilot-aircraft dynamics is especially important when pilot induced oscillations (PIO) are encountered. It is probably safe to say that PIO should be expected to occur with each new aircraft because the problem cannot be predicted authentically without accurate knowledge of the aircraft/flight control system dynamics. For advanced aerodynamic configurations and modern digital flight control systems it is therefore essential to require baseline tracking tests during initial stages of flight testing to enable a rapid detection and elimination of hidden PIO problems [14]. Here again, parameter identification techniques can contribute to more effective quantitative flight testing.

In contrary to fixed wing aircraft, rotorcraft identification is a still more complicated task due to strong coupling of all rigid-body modes plus additional flexible modes introduced by the rotor blade system. HOS rotorcraft of the future implementing fly-by-wire control and higher-harmonic active control systems will require unique and sophisticated flight test methods for the accurate identification of not only stability and control derivatives but also aerelastic (rotor) parameters. High vibration levels and inefficient instrumentation in extreme flight regimes are further aggravating factors.

Due to the fact that rotorcraft have to meet stringent flying qualities requirements arising from various well defined operational needs like NOE of TF flight missions under all weather and severe combat conditions, again it can be stated that the existing military flying qualities requirements for rotorcraft are inadequate for proper application. Also, there is a lack of mutuality with regard to military handling and ride quality requirements within a country among the military services, civil service and between countries within NATO [15].

Therefore, joint research in the field of mission oriented flying qualities for advanced rotorcraft systems is required. Practical and reliable parameter identification flight testing can provide a powerful and cost-effective tool to improve and unify rotorcraft handling and ride qualities acceptance testing in the future.

### 3.3 APPLICATION SPECTRUM FOR PARAMETER IDENTIFICATION

#### BASIC APPLICATIONS

Including the foregoing stated broad requirements for aircraft parameter identification in the field of handling qualities verification the basic application spectrum for exact and reliable stability and control parameters is the following:

- Acceptance testing of aircraft handling qualities including effects of mission and configuration changes as well as external store interference.
- Data correlation for increasing confidence in flight mechanic prediction techniques.
- Data utilization of industry for isolation and identification of nonanticipated aerodynamic effects and further aircraft development.
- Optimization of aircraft stability augmentation and active control systems by accurate description of airframe parameters.
- Data generation for basic computer simulations, fixed and moving base ground simulators and airborne simulators.
- Improvement of flight test and data evaluation methodologies in general.
- On-line identification of aircraft parameters for adaptive control.

#### SPECIFIC APPLICATIONS

Specific problem areas have accentuated the need for parameter identification. Some of these problem areas are concerned with the in-flight determination of:

- High angle of attack flight mechanics generating nonlinear (amplitude dependent) and unsteady (frequency dependent) aerodynamic characteristics [16].
- High angle of attack flight mechanics providing kinematic and aerodynamic cross-coupling between lateral and longitudinal degrees of freedom [16, 17, 18].
- Closed loop stability and control augmentation effects on handling qualities evaluations [10, 19].
- Critical aerodynamic characteristics of full-authority active control surfaces due to flow separation, interference and coupling [20, 21].
- Important structural mode parameters for optimizing aeroservoelastic coupling effects by means of active control technology [22].
- Engine-airframe coupling parameters due to inlet control deficiencies or extreme flight conditions [23].
- Critical airload parameters of fixed-wing and rotorcraft in extreme dynamic flight conditions for certification purposes [24, 25].
- Rotor-airframe control and coupling parameters for improved rotorcraft stability and control augmentation [26, 27].

- Aircraft proneness to pilot induced oscillations by gaining adequate information on airframe-flight control system parameters [14, 28].

## 4. PARAMETER IDENTIFICATION METHODOLOGY

### 4.1 IDENTIFICATION FRAMEWORK

Figure 6 illustrates the general procedure for determining the flight vehicle states and parameters from flight tests. The parameter identification (PI) framework can be divided into three major parts:

- *Instrumentation and Filters* which cover the entire flight data acquisition process including adequate instrumentation and airborne or ground based digital recording equipment. Effects of all kinds of data quality have to be accounted for.
- *Flight Test Techniques* which are related to selected aircraft maneuvering procedures in order to optimize control inputs. The input signals have to be optimized in their spectral composition in order to excite all aircraft response modes from which parameters are to be estimated.
- *Analysis of Flight Test Data* which includes the mathematical model of the aircraft and an estimation criterion which devises some iterative computational algorithm to adjust some kind of starting value or a priori estimate of the unknown parameters until a set of best parameter estimates is obtained which minimizes the response error.

Corresponding to these three strongly interdependent topics some important aspects will be discussed more detailed in the following. If not specially referred to, most of the background information used for the preparation of this section is following the lines of AGARD documentations [8, 9, 29], NASA publications [30] and partially unpublished DFVLR contributions [31].

### 4.2 INSTRUMENTATION AND FILTERS

#### RELEVANT DOCUMENTATION

Classic information on flight test instrumentation for parameter identification is given in Ref. [32]. To satisfy the need for specialized documentation in the field of sophisticated flight test instrumentation, and to promote a better understanding between the flight test engineer and the instrumentation and data processing specialists, the AGARD Flight Mechanics Panel started a renewed effort to establish a series of separately published monographs on selected subjects of flight test instrumentation. Within this AGARD Flight Test Instrumentation series several new Volumes have been produced which provide valuable information on instrumentation system design for parameter identification purposes [33, 34, 35]. Well designed instrumentation and filtering systems have increased the parameter identification accuracy dramatically [36]. More information on aspects of optimum flight test instrumentation design is given in Reference [37].

#### DATA QUALITY

A principal source of inaccuracy in identifying aircraft parameters is the error in the flight test instrumentation. Therefore, the PI accuracy is highly dependent on the quality of the flight measured data [30]. Two basic factors in data quality are the instrument signal resolution and the sampling rate.

Investigations have shown that non-control signal resolutions as low as 1/10 of the maximum signal amplitude can be tolerated without significantly reducing the quality of the parameter estimates and the fit of computed and flight data [3, 30]. But this is only true if

- measurement noise levels are low,
- many signals are used for time history matches and/or
- sampling rates are sufficiently high.

Similar conclusions can be drawn with respect to sampling rates. For a conventional aircraft sampling rates as low as 5 to 10 samples per second are often adequate for acceptable parameter estimates [3]. Problems of acceptance of these low sampling rates can arise as soon as there are

- fast responding aircraft motions,
- high bandwidth control surface dynamics
- structural mode effects and/or
- short flight record lengths.

#### DATA CHANNEL COMPATIBILITY

In order to avoid wasting of valuable flight test, research and computer time due to signal incompatibility between various signals, flight test data analysis should determine as early as possible whether the data channels are compatible. Adjustments can be made by application of special computing techniques for estimating aircraft states (positions, velocities and attitudes) from measurements recorded in-flight [38, 39, 40]. It is nowadays appropriate to use as a measuring unit a strap down inertial system providing angular rate and acceleration information. If, in addition, an airflow vane is available for measuring the airflow angle of attack and the inertial angle of attack (computed from the inertial velocities) it provides a measure of turbulence acting on the airframe [41].

One very important factor influencing the accuracy of parameter estimates is given by time or phase shifts between various measured data [3]. These can be produced for different reasons like

- non-simultaneously signal sampling in one time frame, especially if a control input signal is involved,
- signal phase or time shifting due to different instrumentation filters,
- signal response lag due to various types of sensor dynamics, particularly when air data instrumentation is involved and/or
- delayed interaction of turbulence, measured by a nose boom mounted vane, with the main aerodynamic surfaces of the airframe like wing and tail.

The effect of time shifting due to signal sampling at significantly different times can be compensated for by time shifting the appropriate signals before data analysis. Signal phase shifting due to filtering can be prevented by using the same filters for all signals to be investigated. Signal lag due to sensor dynamics can be corrected before AD signal conversion by tuning the signals with classical instrumentation filters like RC-networks to a reference time [42]. A more flexible means of signal, respectively data conditioning is achieved by computerized time shift corrections of the affected data channels before data analysis is initiated.

As an example, the effect of time shifts in the signal channels of roll rate  $p$ , sideslip  $\beta$  and aileron input on the estimated lateral stability parameter  $L$  is illustrated in Figure 7. The yaw rate and lateral acceleration were also used in the analysis, but they were not time shifted. The zero shift is assumed to be the correct estimation of  $L$ , and a positive shift indicates that all other signals lead the shifted signal [3]. A positive time shift of 0.1 sec for  $\delta_a$  results in a 50-percent error in  $L$ . A negative time shift of 0.1 sec in  $p$  also results in about a 50-percent error. This is, of course, physically meaningful due to the fact, that a roll rate response is more or less directly related to an aileron control input and a phase lag of roll rate is equivalent to a phase lead of an aileron input.

Referring to the aforementioned interaction of turbulence with airframe, Figure 8 shows another example of time shift effects on parameter estimates. Here, time shifting of the vane-measured turbulence signal by the amount of time required for the gusts to travel from the vane to the aircraft aerodynamic center ( $\Delta T$  = distance from vane to aircraft A.C./forward airspeed; NASA C-8A powered lift aircraft:  $\Delta T = 0.4$  sec) is required to estimate the parameters near their predicted values [41]. This provision is important for parameter estimates of slow flying and/or large aircraft encountering air turbulence.

Instrument positions and angular orientations are additional important factors in analyzing flight data. Precise locations with respect to the center of gravity and alignments related to the body axes are necessary to provide satisfactory fits of estimated and flight data. If, for example, corrections for accelerometer positions have not been made some discrepancies may arise. A wrong assumed vertical location of a lateral accelerometer yielded strong mismatches in the fit of the data for the lateral acceleration, particularly where significant roll acceleration signals are apparent. Correcting the vertical location of the sensor to the proper value a better fit results. As can be seen from Figure 9 this small inconsistency of vertical sensor location produced errors as large as 50-percent in the estimated value of the side-force parameter  $C_{y\beta}$  [3].

Finally, software techniques are available for redundancy management of modern digital flight control systems which implement observer techniques to the reconstruction of failed or erroneous sensor outputs. These techniques may offer the advantage to provide additional redundancy, compatibility and more confidence in signal conditioning methods. Kalman filter algorithms to estimate the state and observation vectors of the system to be identified [3] as well as extended and modified Kalman filtering and smoothing algorithms to generate smoothed estimates of the state vector and to reconstruct the flight path of the aircraft [43, 44] are the first successful steps in this direction.

#### 4.3 FLIGHT TEST TECHNIQUES

##### INPUT DESIGN

The importance of adequate design of flight test maneuvers for parameter identification

purposes is well recognized [45, 46, 47]. The reliability of aircraft parameter extraction from flight test maneuvers depends heavily on the amount of information available in the response. Therefore, the shapes of the control inputs should be chosen such that they excite each pertinent mode of the aircraft dynamics as much as possible. Generally, as there is neither an ideally located single control surface nor a single control input shape possible which could excite all modes of the aircraft response equally well, it is mandatory to design and apply specific optimum inputs for all available control surfaces of the aircraft under investigation within the flight envelope of interest.

The design of optimum input signals can be performed in the frequency or time domain considering system criteria and estimation error criteria. Evaluations, practical applications and performance comparisons of optimum inputs are discussed in Reference [47].

#### PILOT INPUT IMPLEMENTATION

The optimized inputs can be generated manually by the pilot or if available by some automatic input device like a fly-by-wire control system. With an automatic device any kind of optimum continuous input signals can be performed. In the other case of manual inputs, multistep type sequences like combination of some fundamental types (doublets, pulses and steps) can be implemented by the pilot in practice.

Figure 10 shows typical examples of the pilot's ability to realize prescribed control inputs. On the left side of Figure 10 the optimum DFVLR 3211 input signal was flown by a pilot in a small transport aircraft CASA 212 within a Spain-West Germany cooperative flight test programme [48]. The input signal was connected electrically to the left needle of a dual vertical scale instrument. The right needle was driven by the control surface deflection signal (elevator). With this simple visual cue the pilot needed only to try to cause by control column deflection the right needle to follow the left needle commands. The elevator has then to perform the programmed deflections. This system enabled the pilot, after spending a minimum amount of training, to fly the wanted signals quite well.

On the right side of Figure 10 a special designed Calspan rudder input signal was nicely implemented by the pilot in practice on a F-106 A during a flight experiment conducted by the USAF. Alternating with the rudder, additional aileron input signals were applied by the pilot to perform a pseudo-sideslip maneuver [49].

#### MULTI INPUT MANEUVER

As was discussed previously in this section, there are problems to accurately identifying flight vehicle parameters when only one control input is used to excite all modes of the vehicle. The inability to estimate some terms accurately is because the influence of these terms on the flight vehicle dynamics is small. An equivalent situation is given if there exists a strong dependency between two motion variables or between a motion variable and a control input (linear dependence problem [50]). A classical example in flight mechanics, which is also well-known to the experts of dynamic wind tunnel testing, is the difficulty to separate the translational acceleration derivatives independent of the angular rate derivatives due to the fact that translational acceleration and angular rate are nearly dependent. It has been shown ingeniously [50], that properly designed multi input maneuvers can circumvent these linear dependence problems. As an example, large roll or pitch attitude excursions introduce a rather independent rate of change of angle-of-attack component through the gravity term in the lift equation. This wanted response can be mechanized by a series of elevator pulses superimposed on an aileron roll. A sample maneuver and resulting parameter estimates for rate of change of angle of attack (i.e. vertical acceleration) and pitch rate derivatives will be given in section 5.5.

In general, it can be concluded that identification problems due to high correlation of measured signals can be overcome by multiple input maneuvers. Also, the interaction of turbulence with the airframe may, if properly modeled, aid in the identification of aircraft parameters. This is because turbulence acts as another input signal in addition to the usual control input [41]. More details will be presented in section 5.6.

Finally, multiple input design is also attractive for identification of the effectiveness of active control surfaces. In selecting the optimum input for control parameter identification, it is mandatory to excite also the eigenmotion of the airplane since the technique of identifying active control parameters involves also the identification of stability parameters. A poor identification of the latter parameters would affect the quality of the active control parameters [51]. Two examples are given in section 5.4.

#### MULTIPLE MANEUVERS

Further, the evaluation of aircraft parameters can also be improved by using selected multiple maneuvers with single or multiple inputs. The use of a large amount of information from multiple data runs is especially meaningful for identification of rotorcraft parameters in unstable flight regimes [52] as well as for augmented aircraft with various highly correlated measured signals [53]. Both aspects will also be discussed in more detail in the subsequent sections 5.3 and 5.7.

The procedure of combining several selected time segments of different maneuvers can also omit the those time pieces during which negligible aircraft response occurs between different inputs. In conclusion, the implementation of the multiple maneuver approach can enhance the data analysis by providing a more reliable set of estimates by using several maneuvers bearing more information contents. A prerequisite, of course, is that the maneuvers to be combined and analyzed are made at about the same reference flight conditions. Examples of multiple maneuvers are illustrated in Figure 18 (section 5) and Figure 33 (section 6).

#### 4.4 ANALYSIS OF FLIGHT TEST DATA

##### ESTIMATION TECHNIQUES

In recent years several groups of time domain estimation techniques for the identification of aircraft parameters from flight tests have evolved [29, 54]. They include the Equation Error method, Instrument Variable method, Output Error method, Basic and Generalized Maximum Likelihood methods and the Extended Kalman Filter [43, 54, 55] method. In addition, combined methods like the EBM System Identification technique have been developed in order to improve estimation techniques of nonlinear aerodynamics in extreme flight regimes [44].

Most practical experience, so far, has been gained with the Basic and Generalized Maximum Likelihood [ML] methods [56, 57]. These methods are now widely accepted as highly flexible and efficient. An especially impressive record of ML parameter identification results is held by the experts of the NASA Dryden Flight Research Center who have analyzed about 3500 maneuvers performed by more than 32 different aircraft [3].

Before the ML estimation method and practical identification examples will be discussed in more detail, it is worthwhile mentioning several attempts for developing and improving parameter estimation techniques in the frequency domain [54]. An important driver in this direction is the fact that time domain estimation methods are rather time consuming in analyzing flight test data with high sampling rates. It can be shown that the aforementioned time domain evaluation methods are equally well formulated in the frequency domain for linear models of the aircraft system under test. The measured data for these methods can be either the frequency response curves or the Fourier transformed input and output time histories. Frequency domain aircraft parameter estimation may be advantageous for the identification of aeroelastic and unsteady aerodynamic effects [58]. Also, this technique is attractive for estimating so-called equivalent time-delay effects of high order system (HOS) dynamics of future high bandwidth active control technology aircraft systems. Equivalent time-delay modeling aspects are also discussed for integration into future handling qualities criteria of highly augmented aircraft systems [59]. More background information on possible definitions of low order systems (LOS), high order systems (HOS), equivalent low order systems (ELOS) and equivalent high order systems (EHOS) and its application spectrum can be found in Reference [6].

##### MAXIMUM LIKELIHOOD ESTIMATION

Several digital computer programmes have been developed to mechanize the Maximum Likelihood (ML) method and its derivatives [57]. The ML method is now used routinely in several NATO countries for the estimation of stability and control derivatives of aircraft within research programmes and acceptance flight test procedures.

A brief discussion of the basic Maximum Likelihood algorithm will be given here along with the main features of a classic computer programme which was developed about ten years ago by NASA Dryden [60]. This example was selected here because the problem of understanding and information exchange between the wind tunnel and the flight mechanics people is becoming quite obvious.

The ML estimator uses a modification of the Newton-Raphson algorithm to identify the unknown coefficients in a set of linear differential equations. The technique computes time histories using an initial set of derivatives (a priori values, usually wind tunnel data), and compares these calculated time histories with flight measured data. From this comparison a mean squared error is obtained and put in the form of a cost functional  $C_F$  as listed in Figure 11, where  $T$  is the total observation time of the maneuver,  $y(t)$  the calculated response vector and  $z(t)$  the measured response vector, and  $R_1$  the measurement error covariance matrix. The objective of the ML estimator is to vary the vector  $c$  of unknown coefficients (stability and control derivatives) in the equations of motion in such a way as to minimize the cost functional.

In addition to permit any derivative to be fixed if it is not involved in the maneuver (preset values) the ML estimator programme contains two weighting features  $R_1$  and  $R_2$  which allow the analyst to have some control over the estimation process:

- The  $R_1$  matrix is a diagonal weighting matrix whose elements correspond to the flight state (response) parameters. The purpose of the  $R_1$  matrix is to account for the amount of measurement noise in any particular channel (measurement error covariance matrix).
- The  $R_2$  matrix is a diagonal weighting matrix whose elements correspond to each of the unknown coefficients of the parameter vector  $c$ . These weigh-

- tings account for the relative confidence placed in the starting (a priori) values of the parameters (a priori error covariance matrix).

Whereas a set of  $R_1$  weightings will be determined from two to four runs of the computer programme for a particular aircraft, the elements of the  $R_2$  weighting matrix have to rely on the individual data accuracy the wind tunnel people can provide to the flight test engineer. Hence, in order to improve the parameter estimates not only the mean values of the wind tunnel determined a priori parameters are important but also their variances. For example, the wind tunnel determined static stability parameter  $C_{Mq}$  has in general a reasonable accuracy, and will receive a high weighting in the  $R_2$  matrix, whereas the dynamic stability parameter  $C_{Mq}^D$  will be obtained with less confidence. Therefore, a lower weighting will be placed on this parameter due to its higher variance.

It is quite obvious that the  $R_2$  a priori weighting procedure is becoming more of an artist's tool as soon as the aircraft flight mechanics are approaching the high angle-of-attack regime. Here, flow separation and vortex shedding generate nonlinear and unsteady aerodynamic interference effects which may have to be accounted for by amplitude and frequency dependent aerodynamic derivatives as can be seen from the wind tunnel data in Figure 12 [61, 62]. Although certain interrelationships between static and dynamic derivatives exist because separation - induced aerodynamic forces are affecting static and dynamic stability in opposite ways [63], as illustrated in Figure 13, more physical understanding complemented by additional means of dynamic wind tunnel measurements is needed to improve the status of a priori information for successful parameter estimation applications in extreme flight regimes.

#### ESTIMATION CONFIDENCE

The Maximum Likelihood Estimator provides an estimate of the reliability of each extracted parameter based on the information content of the flight test maneuver. The estimate of the reliability analogous to the standard deviation or the square root of the variance is called the Cramer-Rao bound. This bound is sometimes multiplied by a scalar and is then referred to as the uncertainty level [3]. When carefully used, these confidence levels are useful tools for assessing the validity of estimated parameters. Examples are given in Figures 9 and 20 where the confidence levels are indicated by vertical bars around the estimated derivatives.

#### DIAGNOSTIC WIND TUNNEL EXPERIMENTS

One means for gaining more a priori knowledge about aerodynamic phenomena at high angles of attack and its impact on the dynamic response behaviour of aircraft is the planning and interpretation of appropriate "diagnostic" WT experiments [64]. The purpose is not only to investigate the qualitative characteristics and to find the appropriate model structure but also to identify characteristic parameters.

For example, one can expect the appearance of fluctuating forces or moments on a rigidly mounted wind tunnel model with increasing angles of attack. Whereas the classical static six-component strain gage WT balances will be measuring only *mean* aerodynamic forces and moments, signal time histories of the *fluctuating* components in the aerodynamic forces and moments due to flow separation yield additional important information which can be analyzed. By this method statistical properties of wide-band flow separation as well as narrow-band vortex shedding phenomena may be identified in order to indicate, as an example, the onset of wing-rocking of a full-scale aircraft.

In this context, a wind tunnel test programme was conducted at DFVLR, Braunschweig, in order to investigate wing flow separation and vortex shedding phenomena of a model, resembling a fighter-type close-coupled canard-wing configuration at high angles of attack. The aerodynamic forces and moments generated by the aircraft model were measured by means of an internally mounted six-component strain-gage balance. With increasing angle of attack, fluctuations of the rigidly sting-mounted model developed which were associated with the existence of separated flow. Calibrated strain-gage force and moment time histories were statistically analyzed in order to obtain power spectra of the model response forces and moments [31].

As an example, the power spectral densities  $\Phi_{LL}(w)$  of the rolling moment response of the model with and without canard are illustrated in Figure 14. Not considering the 50 Hz mains hum peak as well as the low frequency peaks of the balance mechanics below 30 Hz there are three significant unsteady aerodynamic flow conditions developing with increasing angle of attack from 0 to 39 degrees:

- wideband random fluctuations due to wing flow separation (stalled wing flow) mainly in the frequency band from 1 to 50 Hz,
- narrow band vortex shedding from the forebody in the 60 Hz frequency regime and
- narrow band vortex shedding from the canard around 70 Hz.

Without canard, the canard vortex energy peak around 70 Hz is diminishing.

In conclusion, the statistical analysis of fluctuating aerodynamic force and moment time histories observed on rigidly mounted wind tunnel models may provide additional information for investigating the qualitative and quantitative characteristics of aircraft dynamics at high angles of attack. Therefore, statistical wind tunnel data like power spectra and variances may contribute to an improved understanding and mathematical description of aircraft flight mechanics in extreme flight regimes. Wing rocking, for example, can be described physically more meaningful in this way and yield more practical a priori information for future parameter identification tests in extreme flight regimes.

## 5. PARAMETER IDENTIFICATION FLIGHT TEST EXPERIENCE

### 5.1 IDENTIFICATION EXAMPLES WITH A PRIORI WEIGHTING

In order to gain some insight into the influence of a priori weighting on the sensitivity of parameter estimates and the corresponding fits of computed and flight data, high quality DHC-2 Beaver flight test data of a cooperative flight test programme between The Netherlands (DUT and NLR) and Germany (DFVLR) [47] were analyzed by DFVLR. Each element of the normalized a priori parameter vector  $\hat{\epsilon}_0$  was given a value of 1.1, i.e. 10 percent higher relative to the ML estimated elements of the parameter vector  $\hat{\epsilon}$  suppressing a priori information ( $K = 0$ ).

The estimated elements of the normalized parameter vector  $\hat{\epsilon}$  are plotted in Figure 15 as a function of the a priori weighting factor  $K$ . It is evident that the important elements (derivatives)

$$\hat{X}_a, \hat{X}_{a2}, \hat{Z}_a, \hat{M}_a, \hat{M}_q \text{ and } \hat{M}_{\delta e}$$

$$\text{where } \hat{X}_a = X_a(K)/X_a(K=0), \text{ etc.}$$

are forced smoothly into the a priori values with increasing K-weighting. However, the estimates of the minor derivatives

$$\hat{Z}_q \text{ and } \hat{Z}_{\delta e}$$

are responding more sensitively before approaching the a priori values.

Corresponding time history fits are illustrated in Figure 16 for three a priori weightings ( $K = 0.1, 0.5$  and  $100$ ). Due to excellent flight mechanic conditions for parameter identification (attached flow conditions, small dynamic maneuvers, no lateral-longitudinal coupling, no air turbulence, low measurement noise and reliable wind tunnel data), yielding a classical 3 DOF mathematical model and corresponding reliable derivative estimates, the effect of a priori weightings on the curve fits remains quite small.

As another example, the effects of a priori weighting on the parameter estimates and curve fits of a highly coupled rotorcraft system (BO-105) flying in a hovering mode was investigated by the DFVLR. In contrary to the aforementioned fixed wing data, the Bo 105, flight test data were of inadequate quality. Also, the confidence about some of the a priori values provided by the manufacturer was not too high. In Figure 17 an assortment of estimates of longitudinal, lateral/directional and cross-coupling derivatives as a function of a priori weighting  $K$  is displayed. It becomes quite obvious that various parameter sensitivities lead to different neighbourhoods of estimated and a priori derivatives for large K-weightings. In several instances, i.e.

$$Z_u, Z_w, M_q; L_u, N_r, M_p, L_u \text{ and } L_q,$$

there is a strong drive for coalescence with the a priori value. Other estimates like

$$M_w, L_w \text{ and } N_v$$

exhibit tendencies to remain at the values estimated without a priori information ( $K = 0$ ). Resulting time history fits are shown in Figures 18 and 19 for different a priori weighting factors ( $K = 0, 100, 300$  and  $1000$ ). Certain changes in the quality of curve fits are apparent for varying  $K$ . They are indicated by circles.

These two identification examples demonstrate the mechanism through which the a priori weighting of aircraft parameters is involved in the parameter identification cycle. Because of the different dependencies and sensitivities of aircraft parameter estimates and computed aircraft time histories on selected a priori values, it is mandatory to improve the interdisciplinary dialogue between wind tunnel aerodynamicists and the flight mechanic engineers. This exchange of information is also necessary to use more efficient available engineering resources in order to gain more physical insight and confidence into the art and science of aircraft parameter identification.

## 5.2 NONLINEAR AERODYNAMIC DERIVATIVES

The application of parameter identification techniques to each flight test programme must be considered individually, depending on the objectives of that testing. Problems can develop when modeling errors of the aircraft under test are apparent because the best form of the mathematical model is not always obvious. For example, this is true for the flight mechanics with flow separation at high angles-of-attack. In this case, there is a need to get into details of aerodynamic phenomena for adequate modeling of aircraft dynamics. If the model is inappropriate or incomplete, "best fit" parameters that are physically illogical might be computed [65].

Nonlinear models become necessary for extreme flight regimes where consideration of non-attached critical flow or controlled vortex flow is essential. In this case, the model form is established using series expansions or high order terms to represent nondimensional forces and moments for selected ranges of angle of attack. Strict care has to be taken when generating such curve-fitting polynominal models for aerodynamic coefficients, that these additional high order terms have physical interpretation from a flight mechanics standpoint. It is also important to notify that the estimated high order coefficient will generally tend to be only close to the actual coefficient in the angle of attack regime for the record from which they were estimated. Outside this range the validity of the estimates are doubtful [49]. Therefore, the ability to perform dynamic maneuvers in the flow separation regime is of paramount importance for estimating nonlinear aerodynamic parameters from flight data [67]. Detailed information on aircraft parameter identification experience in extreme flight regimes is given in Reference [66].

In recent years NASA Flight Research Center has been exploring ways to flight test advanced configurations in order to improve the understanding of the proper design for high-angle-of-attack stability and controllability. Also, there is a need for investigations into the reasons for the less than satisfactory correlations between wind tunnel model and full-scale flight data. For this kind of problems a F-15-type 3/8-subscale remotely piloted research vehicle (RPRV) was developed and flight tested is an effort to correlate the estimated stability and control parameters of this research vehicle, wind tunnel models and the full-scale airplane [68, 69].

The primary stability, control and damping derivatives obtained from the 3/8-scale flight data are illustrated in Figure 20 (from Ref. [69]). Comparisons between wind tunnel (1/10 scale model) and some low angle-of-attack full-scale flight data are included. The vertical bars represent uncertainty levels as discussed in section 4.4 with the longer bars at higher angles-of-attack indicating less confidence in the data. In general, it can be stated that the 3/8-scale flight data at low angles-of-attack are in good agreement with the full-scale flight and wind tunnel data. It is evident that significant effects of nonlinearities and increasing uncertainties are apparent for angles-of-attack around 24 degrees due to flow separation and interference effects.

A number of combat-type aircraft are involved in lateral handling qualities deficiencies at high angles-of-attack and high subsonic speeds. An adverse phenomenon has been termed by the pilots as *wing rock*. At the RAE, these uncommanded roll oscillations were flight-investigated in more detail using a *Gnat* research aircraft [66]. Parameter identification techniques were applied in order to relate the dynamic responses to the aerodynamic forces and moments causing these oscillations. Relatively simple but physically meaningful mathematical models were chosen which produced an adequate fit to the flight data. Representative results of flight-estimated lateral directional stability parameters  $c_{l\theta}$  and  $c_{N\theta}$  as well as roll damping parameters  $c_{lp}$  are compared with wind tunnel estimates in Figures 21 and 22 (from Ref. [66]).

The effects of flow separation on the rolling moment due to sideslip is clearly indicated in the lower part of Figure 21 for increasing angles-of-attack. The four values at the highest angles-of-attack were obtained from flight responses of initial growth of wing rock, and follow the trend of estimates obtained by either Dutch Roll flight responses or static and dynamic wind tunnel measurements.

From Figure 22 it can be seen that the variation of the roll damping estimates with increasing angles-of-attack is the decisive factor in the occurrence of wing rock. Whereas positive values of roll damping autorotation were identified for the clean aircraft it is apparent that the presence of external stores (tanks on) carried close to the under-wing surface at midspan is maintaining adequate roll damping throughout the angle-of-attack regime investigated.

In conclusion, the above flight test results have shown that capabilities are available to conduct successful research at high angles-of-attack for reasonable accurate parameter identification. Also, the effect of configuration changes on the sensitivity of the dynamic response behaviour and its related parameter estimates were demonstrated.

## 5.3 CROSS-COUPING DERIVATIVES

Investigations of aerodynamic coupling are of current interest because aircraft flying at high angles of attack exhibit kinematic and aerodynamic coupling due to effects of separated flow [16]. Asymmetric flight conditions and corresponding aerodynamic coupling [70, 71, 72] can also arise from asymmetric aircraft components like the oblique wing [52], asymmetric stores and engine out/off conditions as well as from uncoordinated turns and active control disharmony [20].

In principle, the application of the Maximum Likelihood estimation method is straightforward to the identification of flight vehicles with kinematic, aerodynamic and aeroelastic coupling between the longitudinal and lateral-directional modes. However, a multitude of practical computational and numerical problems may arise from this approach due to a high number of states, observations and control inputs.

This is especially true for rotorcraft parameter estimations where complex mathematical models, mainly due to the periodic rotor aeromechanics, have not only to include the strongly coupled rigid body modes but also elastic modes due to the rotor blades, shaft and fuselage flexibility including tail rotor dynamics. Therefore, a large number of unknown rotorcraft parameters have to be identified. More detailed information about rotorcraft related identification problems and experience can be found in Reference [27].

Many problems resulting from the handling of a large number of unknown parameters can be alleviated if the longitudinal and lateral-directional motions are analyzed separately. The longitudinal and lateral models are generally complete in that all cross-coupling terms are included (Mode Separation Technique).

Therefore, these models are together capable of describing all degrees of freedom and large amplitude aircraft responses. This is done in the longitudinal analysis by using the measured lateral-directional responses as inputs to the longitudinal equations and, vice versa, the lateral-directional analyses uses the measured longitudinal responses [41, 52]. The assumption necessary for this approach can be seen in analogy to the prerequisite of the classical equation error method, that is, the measurements are relatively accurate and without noise contamination. Also, the cross-coupling terms must be small compared with the standard terms.

As an illustration, an example of aerodynamic cross-coupling will be discussed in more detail along the lines of Reference [30]. Aerodynamic and kinematic cross-coupling exist for asymmetric aircraft like the NASA *Oblique Wing RPRV* at all angles-of-attack. Figure 23 shows on the left hand side a comparison of flight-measured and computed lateral-directional data obtained with the wing skewed to 45 degrees. All cross-coupling terms were ignored in the mathematical model for this fit, whereas on the right hand side of Figure 23 the data are shown for the same maneuver when both cross-coupling effects have been included into the mathematical model by the above discussed Mode Separation Technique. Corresponding estimated cross-coupling derivatives are given in Figure 24 together with predictions. These derivatives are especially important during turning maneuvers of oblique wing aircraft.

#### 5.4 DIRECT FORCE CONTROL DERIVATIVES

DFVLR flight test investigations have shown that the activation of two direct force control devices like DLC flaps and spoilers can generate nonlinear interference effects which have to be accounted for (Figure 25). Using the DFVLR sweptforward wing Airborne Simulator *Hansa Jet* it was demonstrated that better fits between flight-measured and computed flight data were obtained by using combined flap/spoiler input signals [6, 51].

Figure 25 indicates the flight test estimated flap and spoiler control derivatives for different reference deflections (index 0). It is apparent that the flap control effectiveness derivatives

$$c_{M\delta_F} \quad \text{and} \quad c_{L\delta_F}$$

are only slightly influenced by superposed spoiler dynamics whereas the spoiler control moment effectiveness

$$c_{M\delta_{sp}}$$

reveals a strong nonlinear effect (amplitude sensitivity) with respect to flap dynamic interference.

Further specific aerodynamic interference effects of active control surfaces have been observed during flight testing of two other airborne simulators. For example, the original midwing located active side-force control surfaces of the airborne simulator Calspan *TIFS* generated substantial and unexpected flow separation on the wing which caused a large decrease in the aircraft lift and a large increase in induced drag. In addition, there were changes in the side force effectiveness experienced due to interactions with the active lift flap deflections [73]. A modified Maximum Likelihood estimation technique was used to determine the aerodynamic derivatives of the airborne simulator *NASA-Jet Star*. The aircraft was equipped with direct lift and side force control surfaces. The two side force control surfaces were mounted side by side beneath the center wing. Figure 26 indicates a significant interference effect of the side force generator on the lateral stiffness and damping parameter at low angles -of-attack, whereas the side force control effectiveness remains merely unchanged. Similar trends of strong interference could be discovered also for other stability and control parameters [74].

Finally, recent flight test experience involving the CCV/YF-16 testbed vehicle demonstrated impressively that active control surfaces used to decouple aircraft motions and

implement ACT concepts can be expected to exhibit aerodynamic nonlinearities and interference. These aerodynamic interactions can produce adverse effects and limits beyond which aircraft flight control system fixes of aerodynamic characteristics are no longer feasible [20].

Therefore, it can be concluded that aerodynamic force generators for active control implementation have to be modeled and accurately estimated from flight test data in order to identify and solve potential adverse aerodynamic interaction problems.

##### 5.5 ACCELERATION DERIVATIVES

With reference to section 4.3 it was stated that identification problems due to high signal correlation can be solved by multi input maneuvers. The need for identification and separation of vertical acceleration derivatives like  $M_d$  and angular rate derivatives like  $M_q$  of combined dynamic derivatives like  $M_d + M_q$  is fourfold:

- At high subsonic and transonic flight regimes both derivatives may yield time vectors of opposite sign in the time vector diagrams (mode shapes) of the corresponding moment equation causing reduced stability [75],
- At high angles-of-attack unsteady flow interference effects do no longer justify the use of combined derivatives [72],
- Acceleration derivatives may become important for aircraft configurations implementing high-bandwidth and -amplitude active direct force controls [76].
- Acceleration derivatives obtained in turbulence are resulting from different aerodynamic interactions (gust generation) than the ones estimated by aircraft maneuvering [29]. It is expected that both types of acceleration derivatives may play an important role in properly modeling the flight mechanics of ACT aircraft configuration with reduced natural static stability.

With reference to the last point, the difference of approximate modeling of vertical acceleration derivatives due to maneuvering and gust responses is demonstrated in Table 2 for a classical aircraft configuration. More details will be given in section 5.6 and 6.3.

A multi input sample maneuver for separately estimating vertical acceleration and pitch rate derivatives is shown in Figure 27. Smooth aileron rolling maneuvers lasting about 10 seconds induce sufficient large changes in the gravity terms of the lift equation generating  $\dot{\alpha}$ -components independent of  $\alpha$ ,  $q$  and  $\delta_e$ , thus avoiding the classical linear dependence problem between these variables. Superposed are impulsive elevator pitching inputs in order to excite the classical stability and control derivatives [50]. Figure 27 illustrates good fits between the flight-measured and computed time histories. From Figure 28 the independent estimates of pitch rate and vertical acceleration (angle-of-attack rate) derivatives are illustrated. These flight test results are unique and demonstrate a very successful symbiosis of the powerful and flexible tool of parameter identification together with highly qualified engineering thinking.

##### 5.6 TURBULENCE EFFECTS ON PARAMETER IDENTIFICATION

In general, most flight data analysis to date has been done with identification algorithms which do not take turbulence modeling into account. Consequently, fits of flight data obtained in atmospheric turbulence with computed data from a Maximum Likelihood estimator that does not account for turbulence (algorithm I, as described in section 4.4) are becoming unsatisfactory. The curve fits on the left hand side of Figure 29 are clearly indicating that the assumed mathematical model (algorithm I, no turbulence modeling) is inadequate [3, 77]. On the right hand side of Figure 29 the same comparison of flight and computed data yields very good agreement. In this case, the Maximum Likelihood estimation algorithm is including turbulence modeling (algorithm II). Corresponding derivatives estimated by ML algorithms I and II are presented in Figure 30 along with flight-determined estimates for smooth air and wind tunnel estimated (from Reference [3]). Comparing the standard deviations (uncertainty levels) of the estimated stability and control derivatives the superiority of the estimation algorithm II is definite.

Although the potential for estimating derivatives of aircraft flying in turbulent air has been demonstrated, certain differences between aerodynamic derivatives estimated from flights in smooth and turbulent air can be expected. For example, the separate importance of the derivatives  $M_d$  and  $M_q$  which were already discussed in this context in section 5.5 is apparent due to the fact that similar dynamic derivatives are modeling the aircraft's response to gust inputs. Only if the wave lengths of the turbulence are much greater than the tail length of the aircraft the differences between the "left hand side" vertical acceleration derivative  $M_d$  (modeling the eigenmotion) and the equivalent "right hand side" derivative  $M_{dG}$  (modeling the gust response) are expected to be negligible.

In conclusion, estimating stability and control derivatives from smooth air or turbulent air data are two different approaches which describe two different flight phenomena. Hence, care must be exercised in using derivatives obtained in turbulence for application in smooth air and vice versa. This is especially true if high frequency and interfering active control surfaces are involved.

### 5.7 CLOSED LOOP EFFECTS ON PARAMETER IDENTIFICATION

It was already discussed in section 4.3 (Multi Input and Multiple Maneuvers) that identifiability problems arise when strong dependencies between motion or control variables exist (linear dependence problems) due to inadequate control inputs.

Such problems emerge from aircraft configurations which are flown with engaged limit-authority stability augmentation systems (SAS). Still more estimation difficulties may become apparent when full-authority active control systems (ACS) are involved controlling aircraft in extreme flight regimes or destabilized flight modes. Without additional information, it is impossible to distinguish between the dynamics of the natural unaugmented airframe and the control system. To obtain derivatives of the airframe from SAS/ACS-on maneuvers, each actively controlled motivator must have an independent control input in addition to the SAS/ACS-feedback signal [10,30,53].

As long as stability augmentations or active control systems have a negligible dynamic behaviour, a constant feedback low order system (LOS) model can be applied to describe the dynamics of the closed-loop aircraft. Hence, the structure of the mathematical model is not changed in comparison to the open-loop model (equivalent low order system ELOS, [6,11]). Only, the flight-estimated parameters will change yielding a new set of derivatives often interpreted as equivalent derivatives. The flight test engineer must be cautious not to overlook significant SAS- or ACS-dynamics which, for example, are inherent in control input prefilters designed for attenuating structural mode excitation. Such control system dynamics change the model structure of the closed-loop aircraft system. Consequently, so-called higher order system (HOS) dynamics have to be modeled if deficiencies caused by inadequate model structures shall be prevented. In the following, an identification example describing the dynamic effects of an active lateral-directional stability augmentation system (SAS) on the dynamic response of a modern combat-type aircraft is discussed in more detail [53].

In Figures 31 and 32 (from Reference [53]) flight-measured and computed data of a lateral-directional stability augmentation system with two model structures are compared. In addition, the response of the SAS model provided by the manufacturer is illustrated. As previously discussed, independent control inputs have to be mechanized in order to prevent linear dependencies between different signals. In the case of the roll-channel two inputs are provided by roll rate and lateral stick deflection signals (Figure 31). Three inputs to the yaw-channel are implemented by yaw and roll rate and rudder pedal deflection signals (Figure 32). Furthermore, the identification procedure was improved by combining multiple maneuvers (Figure 31: four time segments, Figure 32: three time segments), as discussed in section 4.3.

From Figure 31 it can be seen, that the constant feedback model (first diagram) results in good fits in the first and fourth time segments, whereas this model is inaccurately representing the roll SAS in the two middle time segments. Hence, the dynamics of the roll SAS cannot be neglected in this case although two reasonable fits for pilot inputs (first and fourth time segment) were achieved. In the second diagram of Figure 31 the match between the flight-measured and computed data is improved using SAS model information of the manufacturer resulting in a high order model of the closed-loop aircraft system. From the third diagram (identified dynamic model) the curve fits are further improved by applying system identification procedures to high order model structures including the flight control system dynamics.

The same procedure was applied to the yaw SAS in Figure 32. Here again the best fit was achieved using the high order model structure including the yaw SAS dynamics.

## 6. PARAMETER DYNAMIC MODEL TESTING EXPERIENCE

### 6.1 GENERAL

To improve the identification quality of sensitive, low-influence or highly correlated parameters by careful selected flight test maneuvers it is important to gain sufficient physical insight into the phenomenon to be analyzed. This can be achieved in a more fundamental way by properly defined flight test maneuvers in dynamic windtunnel or free flight model testing facilities.

The introduction of parameter identification techniques into dynamic model testing, employing dynamically scaled controllable light-weight aircraft models, is attractive because more controlled experiments than flight tests are feasible. If, in addition, realistic and reproducible gust generating devices for discrete gust or continuous turbulence simulation are available the advantage of this type of dynamic windtunnel testing is the good observability of all state, control and disturbance variables acting on the aircraft model. All standard or optimized control or disturbance (turbulence) input signals for parameter identification such as single and multistep or continuous excitations, can be repeatedly performed [78,79,80]. More general information and practical experience

in free-flight and semi-free-flight dynamic model parameter identification is given in References [80-84].

## 6.2 FREE-FLIGHT CATAPULT MODEL IDENTIFICATION EXPERIENCE

An experimental method has been developed by IMFL since 1965 in order to investigate stability and control problems as well as ground and gust effects of dynamically scaled free-flight launched aircraft models [80]. Within a cooperation agreement between IMFL and DFVLR both research institutes applied parameter identification methods for the estimation of stability and control derivatives of an AIRBUS-type model from flight measured dynamic response data [81].

Using wing flap steps as input signals, seven short dynamic response time histories were combined in order to gain multiple maneuver information and evaluated by DFVLR. In Figure 33 resulting fits of flight-measured and computed time histories are illustrated together with the parameter estimates. The low influence of the present derivative  $c_{M\dot{A}}$  on the parameter estimates is clearly indicated. Due to unsteady interference between the flap-downwash and the tail the mathematical model structure could be improved by including a dynamic (time-delay) flap deflection term. In the validity range of first order power series approximations, i.e. at low frequencies ( $\omega \Delta T < 0.5$ ), the dynamic flap deflection term can be expressed as a flap rate derivative  $c_{M\ddot{A}}$  [81]. From Figure 33 the good consistency of this dynamic derivative is apparent. Equivalent thinking along these lines can be found in the section 6.3 where approximate quasistatic and dynamic derivatives are discussed in more detail (Table 2, see also References [82]).

## 6.3 SEMI-FREE-FLIGHT WIND TUNNEL MODEL IDENTIFICATION EXPERIENCE

Research studies were conducted at the DFVLR Dynamic Simulation in Wind Tunnels test facility [79]. Successful basic and project research has been accomplished using methods of parameter identification (PI). One specific PI research objective is to identify unsteady aerodynamics of lifting and active control surfaces in order to improve mathematical models for high frequency active control system optimization [79,82,83].

As an example, Figure 34 illustrates the dynamic wind tunnel model of the Dornier DO 28 TNT Experimental Light Transport Aircraft which was built and "flight-tested" by DFVLR within an active control gust alleviation research program [84].

For the investigations of unsteady aerodynamic effects due to high frequency control and turbulence inputs special dynamic wind tunnel tests were performed. Figure 35 shows the results of wind tunnel measurements of the model response in the case of quick acting flaps (DFVLR 3-2-1-1- input signals) in comparison with computed responses obtained by applying Maximum-Likelihood parameter estimation methods [82,83]. To analyse the aerodynamic effects two types of mathematical models were established. The first model takes into account the effects of relatively low frequency changes of lift on the downwash at the tail (elevator). This so-called quasistatic model displays discrepancies in the "flight"-measured and computed dynamic response (Figure 35, upper left). It is evident that the quasistatic model is not applicable in the case of high frequency or step inputs, which are required for ACT applications such as gust alleviation systems because of unsteady wing/flap-tail interference effects. In order to model these unsteady aerodynamic interference effects equivalent time-delay terms were introduced by modeling a dynamic tail angle-of-attack composed of dynamic angle-of-attack, flap deflection and gust angle-of-attack signals. The resulting dynamic model leads to an improved curve fit between the "flight"-measured and computed model response, as can be seen from the upper right diagram of Figure 35. The ML-estimated parameters for the quasistatic and dynamic model (C and D) are compared in Figure 35 with data obtained by static (A) and dynamic (B) wind tunnel measurements. More information about the aerodynamic terms and related approximate expressions which define the quasistatic and dynamic mathematical models are given in Table 2. It is important to realize that equivalent dynamic derivatives can be approximately estimated by static wind tunnel data (A) if certain components (tail pitching moment  $M_{oT}$  and wing-tail and flap-tail downwash factor  $c_{WT}$  and  $c_{FT}$ ) have been identified by static tail-on and tail-off measurements (low frequency model). In conclusion a modified ML parameter estimation method in combination with adequate model structures has been successfully applied to identify static and dynamic derivatives of a dynamically scaled wind tunnel model for ACT research.

## 7. CONCLUSIONS

It was the purpose of this paper to highlight some of the requirements, applications, advantages and problems as well as present and future potentials of aircraft parameter identification techniques.

Improved technologies in the field of instrumentation, data handling and data processing as well as improved methodologies for optimum control input design have contributed to broaden the application spectrum for parameter identification. For example, these methods are becoming standard procedures for aircraft handling qualities investigations and acceptance testing.

Future relevant research topics will deal with the identification of high order system aircraft dynamics including high angle-of-attack flight conditions incorporating nonlinear and unsteady flow separation dynamics. In addition, system identification demands for active control technology flight vehicles implementing aeroservoelastic coupling effects and control surface interactions within an extended frequency bandwidth will become subject of increased attention. Further, still existing limitations with systems have been eliminated. New activities in the fields of in-flight determined parameters of missile system flight mechanics and external store separation dynamics may evolve.

## 8. REFERENCES

1. Chalk, C.R., "Technical Evaluation Report on the Flight Mechanics Panel Symposium on Stability and Control", AGARD-AR-134, January 1979.
2. Anon., "Dynamic Stability Parameters", AGARD Conference Proceedings, AGARD-CP-235, November 1978.
3. Iliff, K.W. "Aircraft Identification Experience", AGARD-LS-104, Paper 6, November 1979
4. Statler, I.C., "Flight Mechanics - A Review of the Activities of the AGARD Flight Mechanics Panel", AGARD Highlights 78/1 (1978).
5. Karmann, R., "Programmable Multipurpose Flight Test Instrumentation System", AGARD Conference Proceedings, AGARD-CP-299, Paper 22, December 1980.
6. Hamel, P.G., "Aircraft Parameter Identification Methods and their Applications-Survey and Future Aspects", AGARD-LS-104, Paper 1, November 1979.
7. Hamel, P.G., "Status of Methods for Aircraft State and Parameter Identification", AGARD-CP-187.
8. Anon., "Methods for Aircraft State and Parameter Identification", AGARD Conference Proceedings, AGARD-CP-172, May 1975.
9. Anon., "Parameter Identification", AGARD Lecture Series, AGARD-LS-104, November 1979.
10. Koehler, R., Marchand, M. "Open/Closed Loop Identification of Stability and Control Characteristics of Combat Aircraft", AGARD-CP-260, Paper 16, May 1979.
11. Hodgkinson, J., La Manna, W.J., Heyde, J.L., "Handling Qualities of Aircraft with Stability and Control Augmentation Systems - a Fundamental Approach", Aeronautical Journal, Vol. 80, No. 782, February 1976.
12. Twisdale, T.R., Jones, G.L., Ashurst, T.A., "A Mission Oriented Flight Test Technique for Identifying Aircraft and Flight Control System Transfer Function", AGARD-CP-223, Paper 13, April 1977.
13. Sisk, T.R., "A Technique for the Assessment of Fighter Aircraft Precision Controllability", AIAA Paper 78-1364, 1978.
14. Smith, R.H., "A Theory for Longitudinal Short-Period Pilot Induced Oscillations", AFFDL-TR-77-47, June 1977.
15. Velkoff, H.R., "Technical Evaluation Report on the Flight Mechanics Panel Symposium on Rotorcraft Design", AGARD-AR-114, January 1978.
16. Anon., "High Angle of Attack Aerodynamics", AGARD Conference Proceedings, AGARD-CP-247, January 1979.
17. Ericsson, L.E., "Technical Evaluation Report on the Fluid Dynamics Panel Symposium on Dynamic Stability Parameters", AGARD-AR-137, April 1979.
18. Anon., "Stall/Spin Problems of Military Aircraft", AGARD Conference Proceedings, AGARD-CP-199, June 1976.
19. Gibson, J.C., "Flying Qualities and the Fly-By-Wire Aeroplane", AGARD-CP-260, Paper 22, May 1979.
20. Whitmoyer, R.A., "Aerodynamic Interactions on the Fighter CCV Test Aircraft", AGARD-CP-235, Paper 16, November 1978.
21. Ross, A.J., Thomas, H.H.B.M., "A Survey of Experimental Data on the Aerodynamics of Controls, in the Light of Future Needs", AGARD-CP-262, Paper 2, April 1979.
22. Kurzhals, P.R., ed., "Active Controls in Aircraft Design", AGARD-AG-234, November 1978.
23. Gilyard, G.B., "Determination of Propulsion-System-Induced Forces and Moments of a Mach 3 Cruise Aircraft", in NASA TN-D-7647, April 1974, pp. 369-374.
24. Park, G.D., "Parameter Identification Technology Used in Determining In-Flight Airload Parameters", J. Aircraft, Vol. 14, No. 3, March 1977.
25. Rauscher, E., "Structural Flight Load Testing, Calibration and Analysis", ICAS-Proceedings, Paper 80-17.3, 1980.
26. Rix, O., Huber, H. Kaletka, J., "Parameter Identification of a Hingeless Rotor Helicopter", Preprint No. 77.33-42, 33rd Annual National Forum of the American Helicopter Society, Washington, D.C., May 1977.

27. Kaletka, J., "Rotorcraft Identification Experience", AGARD-LS-104, Paper 7, November 1979.
28. Anon., "The Effects of Buffeting and other Transonic Phenomena on Maneuvering Combat Aircraft", AGARD Advisory Report, AGARD-AR-82, July 1975.
29. Iliff, K.W., "Estimation of Aerodynamic Characteristics from Dynamic Flight Test Data", AGARD-CP-235, Paper 15, November 1978.
30. Iliff, K.W., Maine, R.E., Montgomery, T.D., "Important Factors in the Maximum Likelihood Analysis of Flight Test Maneuvers", NASA Technical Paper 1459, April 1979.
31. Altenkirch, D., "Untersuchung dynamischer Kraftanteile stationärer 6-Komponenten Messungen am MBB-TKF-Modell", DFVLR-Institut für Flugmechanik, Interner Bericht IB 154-80/28, 1980.
32. Wolowicz, C.H., "Considerations in the Determination of Stability and Control Derivatives and Dynamic Characteristics from Flight Data", AGARD Rep. 549 - Part 1, 1966.
33. Bennett, G.E., "Magnetic Recording of Flight Test Data", AGARD Flight Test Instrumentation Series, AGARD-AG-160-Vol. 5, February 1974.
34. McLaren, I., "Open and Closed Loop Accelerometers", AGARD Flight Test Instrumentation Series, AGARD-AG-160-Vol. 6, July 1974.
35. Van Nunen, J.W.G., Piazzoli, G., "Aeroelastic Flight Test Techniques and Instrumentation", AGARD Flight Test Instrumentation Series, AGARD-AG-160-Vol. 9, February 1979.
36. Hosman, R.J.A.W., "Advanced Flight Test Instrumentation: Design and Calibration", AGARD-CP-172, Paper 6, May 1975.
37. Breeman, J.H., et al., "Aspects of Flight Test Instrumentation", AGARD-LS-104, Paper 4, November 1979.
38. Mulder, J.A., "Estimation of the Aircraft State in Non-Steady Flight", Delft University of Technology, Memorandum M-221, October 1974.
39. Winqrove, R.C., "Quasi Linearization Technique for Estimating Aircraft States from Flight Data", J. Aircraft, Vol. 10, No. 5, May 1973.
40. Klein, V., Schiess, J.R., "Compatibility Check of Measured Aircraft Responses Using Kinematic Equations and Extended Kalman Filter", NASA TN D-8514, August 1977.
41. Winqrove, R.C., "Parameter Estimation of Powered-Lift STOL Aircraft Characteristics Including Turbulence and Ground Effects", AGARD-CP-172, Paper 28, Mai 1975.
42. Wünnenberg, H., et al., "Determination of Stability Derivatives from Flight Test Results - Comparison of Five Analytical Techniques", AGARD Conference Proceedings, AGARD-CP 172, Paper 10, Mai 1975.
43. Mulder, J.A., et al., "Analysis of Aircraft Performance, Stability and Control Measurements", AGARD-LS-104, Paper 5, November 1979.
44. Stalford, H.L., "The EBM System Identification Technique and its Application to High Alpha/Beta Modeling of Aircraft", AIAA-80-1631-CP, August 1980.
45. Mehra, R.K., Gupta, N.K., "Status of Input Design for Aircraft Parameter Identification", AGARD-CP-172, Paper 12, May 1975.
46. Chen, R.T.N., "Input Design for Aircraft Parameter Identification: Using Time-Optimal Control Formulation", AGARD-CP-172, Paper 13, May 1975.
47. Plaetschke, E., Schulz, G., "Practical Input Signal Design", AGARD-LS-104, Paper 3, November 1979.
48. McCracken, J.R., Kaletka, J., Meyer, H., Rix, O., Gartung, B., "Spain-Federal Republic of Germany Cooperative Research Program CASA C-212 Flight Test and Parameter Identification", DFVLR-Interner Bericht IB 154-76/16, 1976
49. Eulrich, B.J., Govindaraj, K.S., Harrington, W.W., "Estimation of the Aerodynamic Stability and Control Parameters for the F-106 A Aircraft from Flight Data: Maneuver Design and Flight Data Analysis", AIAA Paper 78-1326, 1978.
50. Maine, R.E., Iliff, K.W., "Maximum Likelihood Estimation of Translational Acceleration Derivatives from Flight Data", J. Aircraft, Vol. 16, No. 10, October 1979.
51. Rix, O., Hanke, D., "In-Flight Measured Characteristics of Combined Flap-Spoiler Direct Lift Controls", AGARD-CP-262, Paper 16, April 1979.

52. Kloster, M., Kaletka, J., Schäufele, H., "Parameter Identification of a Hingeless Rotor Helicopter in Flight Conditions with Increased Stability", 6th European Rotorcraft and Powered Lift Forum, Bristol, England, Paper No. 58, 1980.
53. Koehler, R., Wilhelm, K., "Closed Loop Aspects of Aircraft Identification", AGARD-LS-104, Paper 10, November 1979.
54. Klein, V., "Identification Evaluation Methods", AGARD-LS-104, Paper 2, November 1979.
55. Chen, R.T.N., "A Recurrence Relationship for Parameter Estimation via Method of Quasi-Linearization and its Connections with Kalman-Filtering", Journal of AIAA, pp. 1696-1698, September 1980.
56. Wolowicz, C.H., et al., "Flight Test Experience in Aircraft Parameter Identification", AGARD Conference Proceedings, AGARD-CP-119, Paper 23, November 1972.
57. Iliff, K.W., Maine, R.E., "Practical Aspects of Using a Maximum Likelihood Estimator", AGARD Conference Proceedings, AGARD-CP-172, Paper 16, May 1975.
58. Klein, V., "Aircraft Parameter Estimation in Frequency Domain", AIAA Paper 78-1344, 1978.
59. A'Harrah, R.C., Lamanna, W.J., Hodgkinson, J., "Are Today's Specifications Appropriate for Tomorrow's Airplanes?", AGARD-CP-260, Paper 23, Mai 1979.
60. Iliff, K.W., Taylor, L.W., jr., "Determination of Stability Derivatives from Flight Data using a Newton-Raphson Minimization Technique", NASA TN D-6579, 1972.
61. Chambers, J.R., et al., "Results of Piloted Simulator Studies of Fighter Aircraft at High Angles of Attack", AGARD Conference Proceedings, AGARD-CP-235, Paper 33, November 1978.
62. Grafton, S.B., Auglin, E.L., "Dynamic Stability Derivatives at Angles of Attack from -5° to 90° for a Variable-Sweep Fighter Configuration with Twin Vertical Tails", NASA TN D-6909, October 1972.
63. Ericsson, L.E., Reding, J.P., "Effect of Flow Separation Vorties on Aircraft Unsteady Aerodynamics", AGARD Conference Proceedings, AGARD-CP-235, Paper 24, November 1978.
64. Jones, J.G., "Modelling of Systems with a High Level of Internal Fluctuations", AGARD Conference Proceedings, AGARD-CP-172, Paper 1, May 1975.
65. Hall, W.E., Gupta, N.K., Tyler, J.S., "Model Structure Determination and Parameter Identification for Nonlinear Aerodynamic Flight Regimes", AGARD Conference Proceedings, AGARD-CP 172, Paper 21, May 1975.
66. Ross, A.J., "Identification Experience in Extreme Flight Regimes", AGARD-LS-104, Paper 8, November 1979.
67. Stengel, R.F., Nixon, W.B., "Investigation of the Stalling Characteristics of a General Aviation Aircraft", ICAS-Proceedings, Paper 80-22.2, 1980.
68. Iliff, K.W., Maine, R.A., Shafer, M.F., "Subsonic Stability and Control Derivatives for an Unpowered Remotely Piloted 3/8 - Scale F-15 Airplane Model Obtained from Flight Test", NASA TN D-8136, January 1976.
69. Layton, G.P., "A New Experimental Flight Research Technique: The Remotely Piloted Airplane", AGARD Conference Proceedings, AGARD-CP-187, Paper 13, April 1976.
70. Hamel, P.G., "A System Analysis View of Aerodynamic Coupling", J. Aircraft, Vol. 7, No. 6, Nov.-Dec. 1970.
71. Johnston, D.E., "Identification of Key Maneuver-Limiting Factors in High-Angle-of-Attack Flight", AGARD-CP-235, Paper 36, November 1978.
72. Orlik-Rückemann, K.J., Hanff, E.S., "Dynamic Stability Parameters at High Angles of Attack", ICAS-Proceedings, Paper 80-7.1, 1980.
73. Anon., "Total In-Flight Simulator (TIFS)- Preliminary Design Report", Technical Report AFFDL-TR-71-119, August 1971, pp. 25-26.
74. Smith, H.J., "Flight-Determined Stability and Control Derivatives for an Executive Jet Transport", NASA TMX-56034, July 1975.
75. Statler, I.C. et al., "The Development and Evaluation of the CAL/AIR FORCE Dynamic Wind Tunnel Testing System", AFFDL-TR-66-153 Part I, February 1967.
76. Thomas, H.H.B.M., "Technical Evaluation Report on the Fluid Dynamics Panel Symposium on Aerodynamic Characteristics of Controls", AGARD-AR-157, March 1980.

77. Iliff, K.W., "Identification of Aircraft Stability and Control Derivatives in the Presence of Turbulence", in NASA TN D-7647, April 1974, pp. 77-113.
78. Bennett, R.M., Farmer, M.G., Mohr, R.L., Hall Jr., W.E., "Wind-Tunnel Technique for Determining Stability Derivatives from Cable-Mounted Models", J. Aircraft Vol. 15, No. 5, May 1978.
79. Hamel, P.G., Krag B., "Dynamic Windtunnel Simulation of Active Control Systems", AGARD-CP-260, Paper 16A, May 1979.
80. Verbrugge, R.A., Charon, W., Marchand, M., "Windtunnel and Free-Flight Model Identification Experience", AGARD-LS-104, Paper 9, November 1979.
81. Marchand, M., Charon, W., "Cooperation in Flight Mechanics-A.T.A. Parameter Identification", DFVLR-Institut für Flugmechanik, Interner Bericht IB 154-79/23 and Institut de Mécanique des Fluides de Lille, Report 7195, 1979.
82. Rohlf, D., "Steuerverhalten des Do 28 TNT-Modells bei der Dynamischen Simulation im Windkanal", DFVLR-Institut für Flugmechanik, Interner Bericht IB 154-80/25, 1980.
83. Wilhelm, K., Gmelin, B., "DFVLR-Dynamic Model Testing in Wind Tunnels for Active Control Research", ICAS-Proceedings, Paper 80-23.2, 1980.
84. Krag, B., Rohlf, D., Wünnenberg, H., "OLGA, A Gust Alleviation System for Improvement of Passenger Comfort of General Aviation Aircraft, ICAS-Proceedings, Paper 80-5.4, 1980.

YEAR	TITLE	AGARD REFERENCE *)
1955	Dynamic Measurements in Windtunnels	AG 11
1956	Some Correlations of Flight-Measured and Wind-Tunnel Measured Stability and Control Characteristics of High-Speed Airplanes	RP 62
1958	An Example of the Determination of Principal Aerodynamic Coefficients from Flight Tests	RP 189
1958	On the Extraction of Stability Derivatives from Full-Scale Flight Data	RP 190
1958	Application of Dynamic Testing Procedures to Stability and Control Flight Test Programs	RP 191
1958	Stability-Derivative Determination from Flight Data	RP 224
1959 (1963)	Stability-Derivative Determination from Flight Data	MN 1/2/10/2
1961	Current Progress in the Estimation of Stability Derivatives	RP 341
1961	Windtunnel and Flight Measurements of Aerodynamic Derivatives	RP 346
1966	Considerations in the Determination of Stability and Control Derivatives and Dynamic Characteristics from Flight Data	RP 549/1
1966	Un Nouveau Type de Fonctions Modulatrices pour la Méthode de Shinbrot	RP 549/2/1
1966	Experience with Shinbrot's Method of Transient Response	RP 549/2/2
1966	Stability and Control	CP 17/1/20,21
1969	Aeroelastic Effects from a Flight Mechanics Standpoint	CP 46/18
1972	Flight Test Techniques	CP 85/10,14,16
1972	Stability and Control	CP 119/13,14,23
1975	Methods for Aircraft State and Parameter Identification	CP 172/1 to 29
1976	Flight/Ground Testing Facilities Correlation	CP 187/6,8,13
1977	Flight Test Techniques	CP 223/5,11,12,13
1978	Rotorcraft Design	CP 233/20
1978	Dynamic Stability Parameters	CP 235/14,15,17,18
1978	Excitation and Analysis Technique for Flight Flutter Tests	RP 672
1979	Aeroelastic Flight Test Techniques and Instrumentation	AG 160/9
1979	High Angle of Attack Aerodynamics	CP 247/1,14
1979	Stability and Control	CP 260/16
1979	Aerodynamic Characteristics of Controls	CP 262/2,3,16
1979	Parameter Identification	LS 104
(1981)	Parameter Identification	AG to be announced

\*) see also AGARD Index of Publications 52/70 PtI,  
71/73, 74/76 and 77/79

AG = AGARDograph

RP = AGARD Report

MN = AGARD Flight Test Manual

CP = AGARD Conference Proceedings

LS = AGARD Lecture Series

Table 1 Review of AGARD Publications in the field of Aircraft Parameter Identification

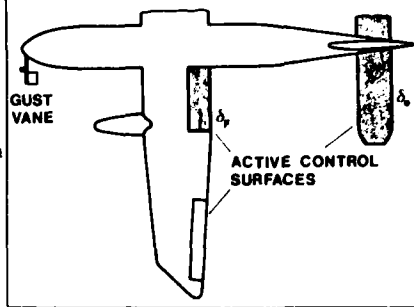
<b>I. PITCH ACCELERATION - HIGH FREQUENCY MODEL:</b> $\ddot{\alpha} = M_{\alpha}\dot{\alpha} + M_q\dot{q} + M_{\delta F}\dot{\delta}_F + M_{\delta E}\dot{\delta}_E + M_{\alpha G}\dot{\alpha}_G + M_{\alpha T}\dot{\alpha}_T \text{ DYN}$ <div style="display: flex; justify-content: space-around;"> <span>Quasistatic Term</span> <span>Dynamic Term</span> </div> <p>Tail Dynamic Angle-of-Attack:  <math>\dot{\alpha}_T \text{ DYN} = \epsilon_{WT}\alpha \text{ DYN} + \epsilon_{FT}\delta_F \text{ DYN} + (1+\epsilon_{WT})\alpha_G \text{ DYN}</math></p> <p>Dynamic Angle-of-Attack, Flap Deflection and Gust Angle-of-Attack (Wing Station):  <math>\dot{\alpha} \text{ DYN} = \alpha(t-\Delta T_{WT}) - \alpha(t); \quad \dot{\delta}_F \text{ DYN} = \delta_F(t-\Delta T_{FT}) - \delta_F(t); \quad \dot{\alpha}_G \text{ DYN} = \alpha_G(t-\Delta T_{WT}) - \alpha_G(t)</math></p> 																							
<b>II. PITCH ACCELERATION - LOW FREQUENCY MODEL (<math>\omega \Delta T &lt; 0.5</math>):</b> $\ddot{\alpha} = M_{\alpha}\dot{\alpha} + M_{\dot{\alpha}}\dot{\alpha} + M_q\dot{q} + M_{\delta F}\dot{\delta}_F + M_{\dot{\delta}_F}\dot{\delta}_F + M_{\delta E}\dot{\delta}_E + M_{\dot{\delta}_E}\dot{\delta}_E + M_{\alpha G}\dot{\alpha}_G + M_{\dot{\alpha}_G}\dot{\alpha}_G$ <p>Equivalent Rate of Angle-of-Attack, Flap Deflection and Gust Angle-of-Attack (Wing Station):  <math>\dot{\alpha} = -\alpha \text{ DYN}/\Delta T_{WT}; \quad \dot{\delta}_F = -\delta_F \text{ DYN}/\Delta T_{FT}; \quad \dot{\alpha}_G = -\alpha_G \text{ DYN}/\Delta T_{WT};</math></p>																							
<b>III. NOTATIONS:</b> <p><math>\epsilon_{WT}, \epsilon_{FT}</math> = Wing-Tail, Flap-Tail Downwash Factor</p> <p><math>\Delta T_{WT}, \Delta T_{FT}</math> = Wing-Tail, Flap-Tail Time Delay (sec)</p> <p><math>T_W, T_T</math> = Rotation Center-Wing Aerodynamic Center, - Tail Aerodynamic Center Equivalent Time Delay (sec)</p> <p><math>M_{\alpha T}</math> = Tail Angle-of-Attack Pitching Moment (<math>1/\text{sec}^2</math>)</p>																							
<b>IV. APPROXIMATE DERIVATIVES:</b> <table border="1" style="width: 100%; border-collapse: collapse;"> <thead> <tr> <th colspan="2" style="text-align: center;">Quasistatic Derivatives</th> </tr> </thead> <tbody> <tr> <td><math>M_{\alpha}</math></td> <td><math>= M_{\alpha W} + M_{\alpha T} (1 + \epsilon_{WT})</math></td> </tr> <tr> <td><math>M_q</math></td> <td><math>= M_{\alpha W} T_W + M_{\alpha T} T_T (1 + \epsilon_{WT} T_W/T_T)</math></td> </tr> <tr> <td><math>M_{\delta F}</math></td> <td><math>= M_{\delta F W} + M_{\alpha T} \epsilon_{FT}</math></td> </tr> <tr> <td><math>M_{\alpha G}</math></td> <td><math>= M_{\alpha W} + M_{\alpha T} (1 + \epsilon_{WT})</math></td> </tr> </tbody> </table> <table border="1" style="width: 100%; border-collapse: collapse;"> <thead> <tr> <th colspan="2" style="text-align: center;">Dynamic Derivatives</th> </tr> </thead> <tbody> <tr> <td><math>M_{\dot{\alpha}}</math></td> <td><math>= -M_{\alpha T} \epsilon_{WT} \Delta T_{WT}</math></td> </tr> <tr> <td><math>M_{\dot{\alpha}_G}</math></td> <td><math>= -M_{\alpha T} (1 + \epsilon_{WT}) \Delta T_{WT}</math></td> </tr> <tr> <td><math>M_{\dot{\delta}_F}</math></td> <td><math>= -M_{\alpha T} \epsilon_{FT} \Delta T_{FT}</math></td> </tr> <tr> <td colspan="2" style="text-align: center;">Low Frequency Model</td> </tr> <tr> <td colspan="2" style="text-align: center;">High Frequency Model</td> </tr> </tbody> </table>		Quasistatic Derivatives		$M_{\alpha}$	$= M_{\alpha W} + M_{\alpha T} (1 + \epsilon_{WT})$	$M_q$	$= M_{\alpha W} T_W + M_{\alpha T} T_T (1 + \epsilon_{WT} T_W/T_T)$	$M_{\delta F}$	$= M_{\delta F W} + M_{\alpha T} \epsilon_{FT}$	$M_{\alpha G}$	$= M_{\alpha W} + M_{\alpha T} (1 + \epsilon_{WT})$	Dynamic Derivatives		$M_{\dot{\alpha}}$	$= -M_{\alpha T} \epsilon_{WT} \Delta T_{WT}$	$M_{\dot{\alpha}_G}$	$= -M_{\alpha T} (1 + \epsilon_{WT}) \Delta T_{WT}$	$M_{\dot{\delta}_F}$	$= -M_{\alpha T} \epsilon_{FT} \Delta T_{FT}$	Low Frequency Model		High Frequency Model	
Quasistatic Derivatives																							
$M_{\alpha}$	$= M_{\alpha W} + M_{\alpha T} (1 + \epsilon_{WT})$																						
$M_q$	$= M_{\alpha W} T_W + M_{\alpha T} T_T (1 + \epsilon_{WT} T_W/T_T)$																						
$M_{\delta F}$	$= M_{\delta F W} + M_{\alpha T} \epsilon_{FT}$																						
$M_{\alpha G}$	$= M_{\alpha W} + M_{\alpha T} (1 + \epsilon_{WT})$																						
Dynamic Derivatives																							
$M_{\dot{\alpha}}$	$= -M_{\alpha T} \epsilon_{WT} \Delta T_{WT}$																						
$M_{\dot{\alpha}_G}$	$= -M_{\alpha T} (1 + \epsilon_{WT}) \Delta T_{WT}$																						
$M_{\dot{\delta}_F}$	$= -M_{\alpha T} \epsilon_{FT} \Delta T_{FT}$																						
Low Frequency Model																							
High Frequency Model																							

Table 2 Aircraft Pitch Acceleration Modeling for High Bandwidth ACT Application

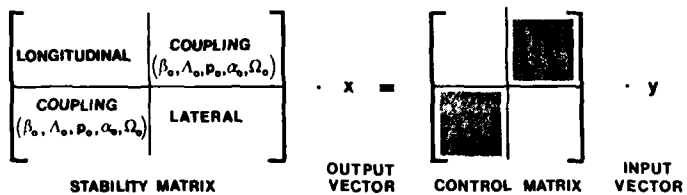
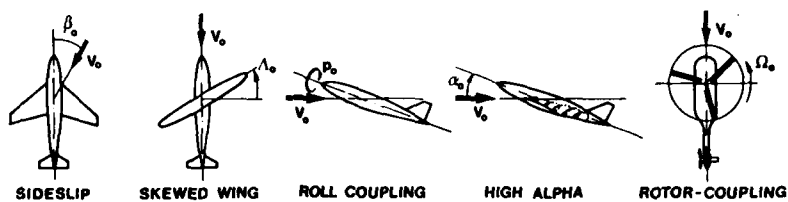


Fig. 1 Aircraft Coupling Examples

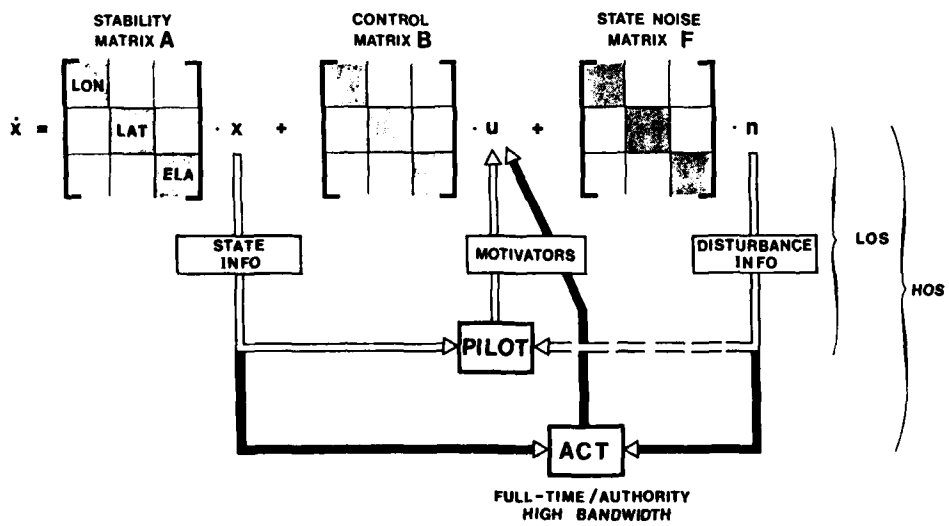


Fig. 2 Impact of Active Control Technology (ACT)  
on Aircraft Flight Mechanics  
(LON/LAT/ELA = Longitudinal/Lateral/Elastic Modes,  
LOS/HOS = Low Order/High Order System)

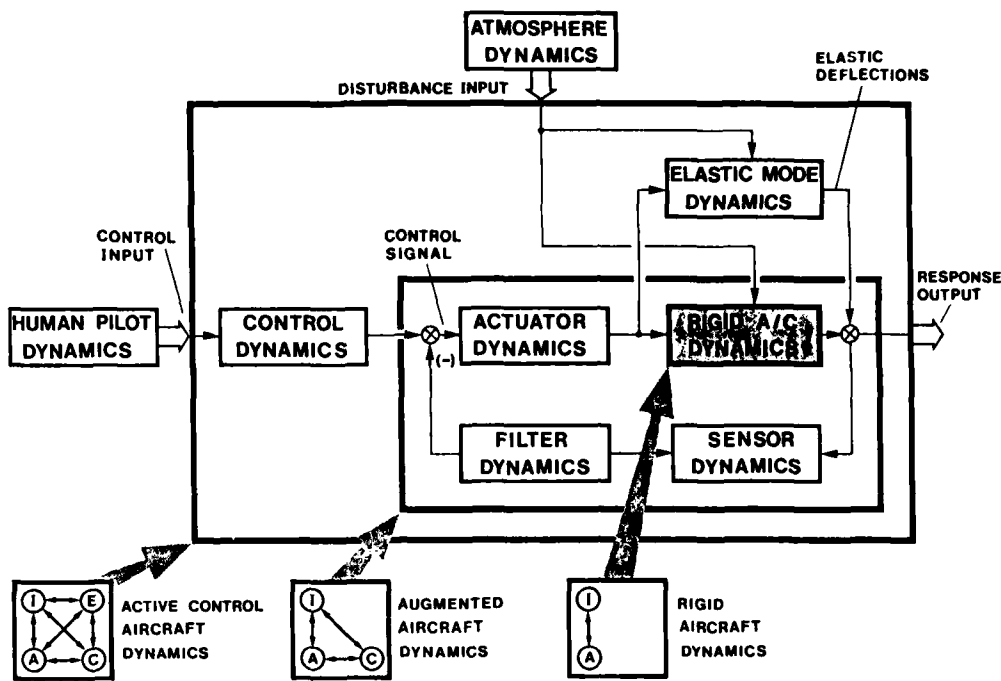


Fig. 3 Modeling Schematic of High Order System (HOS)  
Aircraft Dynamics  
(I, E, A, C = Inertial, Elastic, Aerodynamic and  
Control Forces)

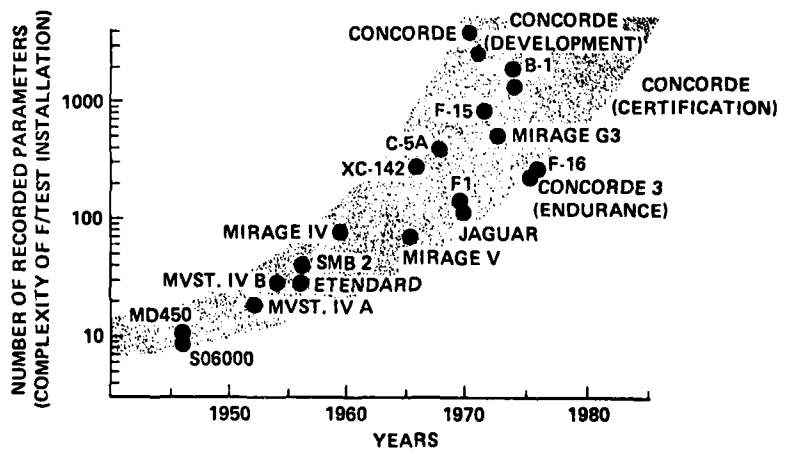


Fig. 4 Number of Flight Test Parameters Recorded

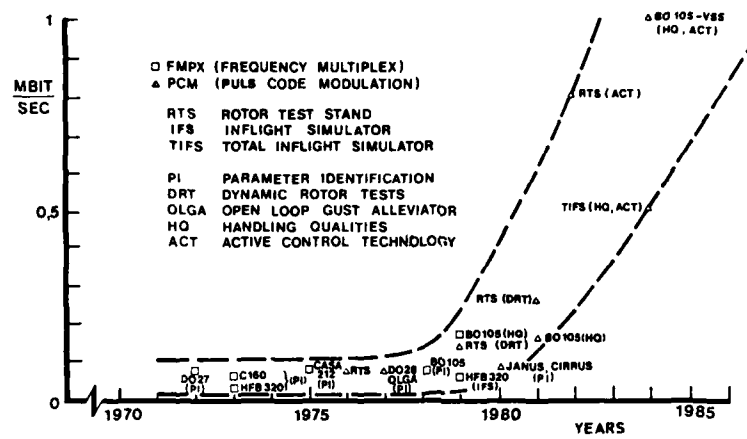


Fig. 5 Projected Data Rates for Dynamic Wind Tunnel and Flight Testing at the DFVLR Institut für Flugmechanik

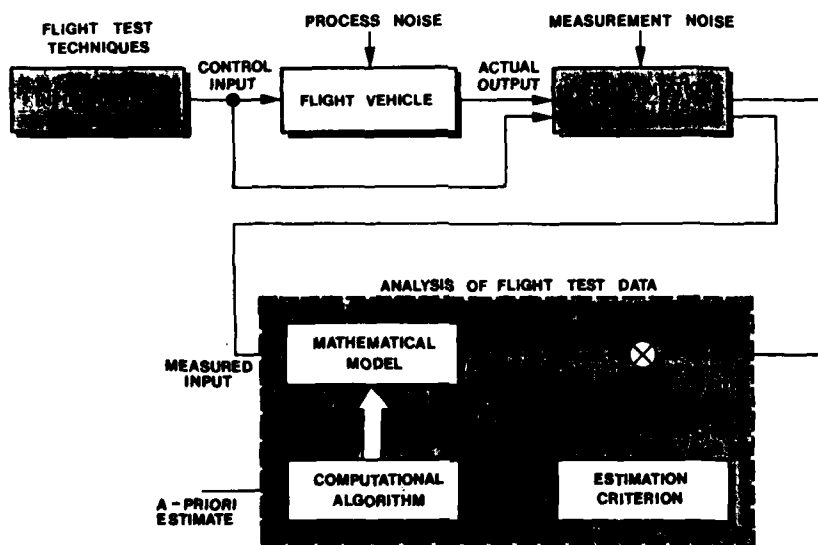


Fig. 6 Basic Parameter Identification Procedure

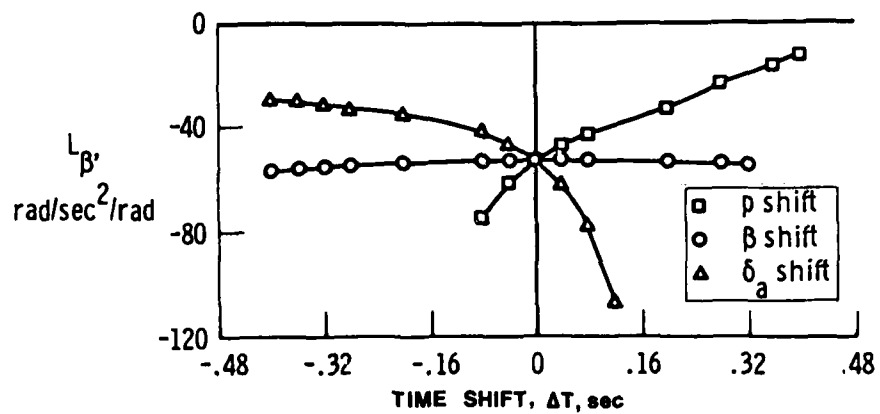


Fig. 7 Effect of Time Shifts in the Flight Data on Estimated Derivative  $L_\beta$

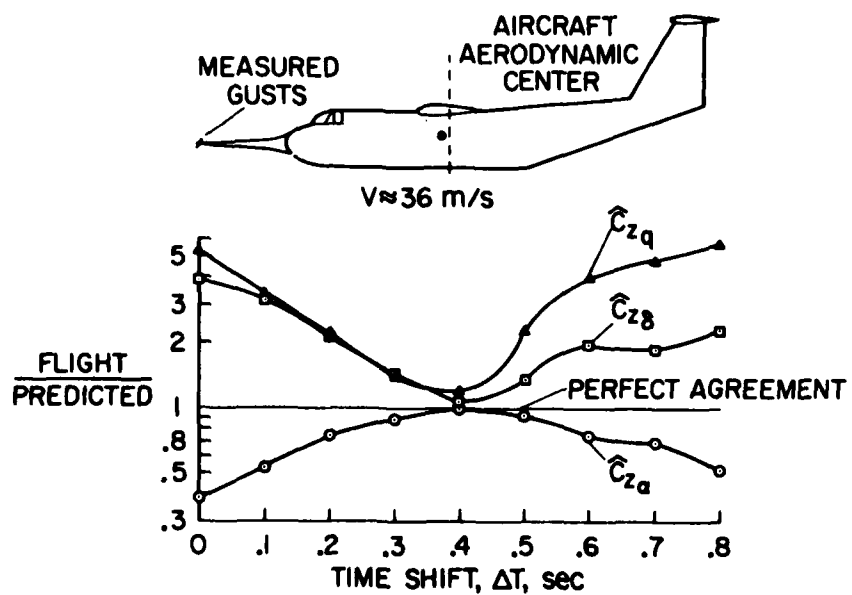
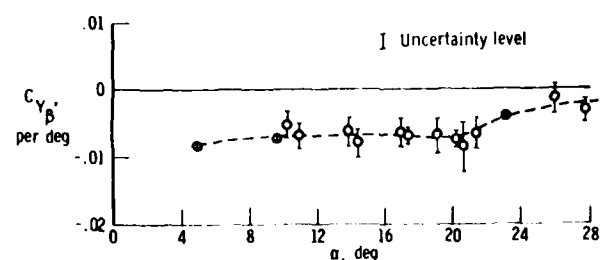
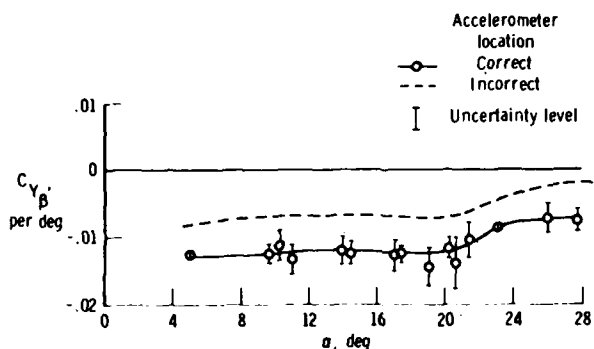


Fig. 8 Effect of Time Shifts in the Measured Turbulence Data on Estimated Derivatives (NASA Powered Lift Aircraft C-8A)

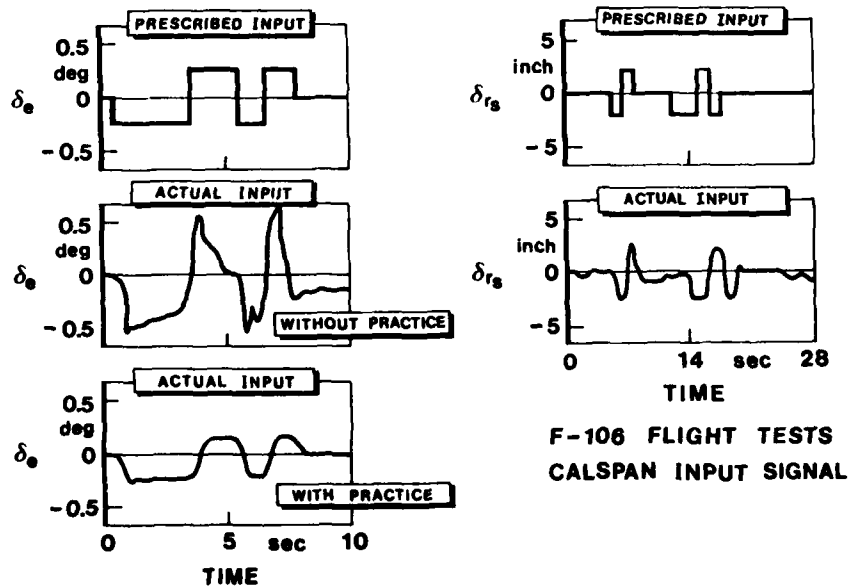


(a) Incorrect accelerometer location.



(b) Correct accelerometer location.

Fig. 9 Effect of Lateral Accelerometer Location on Estimated Derivative  $C_{Y\beta}$  (NASA F-15 RPRV Data)



CASA 212 FLIGHT TESTS  
DFVLR 3211 INPUT SIGNAL

Fig. 10 Manual Optimum Input Realization

**MAXIMUM LIKELIHOOD COST FUNCTIONAL (CF)**

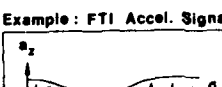
$$CF = \frac{1}{T} \int_0^T (z(t) - y(t))^T R_i^{-1} (z(t) - y(t)) dt + K (c - c_0)^T R_i^{-1} (c - c_0)$$


---

Measurement Error Covariance Matrix  
CONFIDENCE in FTI SIGNALS

Z (t) measured response vector  
y (t) calculated response vector  
T total maneuver time

Example : FTI Accel. Signal



A priori Error Covariance Matrix  
CONFIDENCE in WT DATA

C unknown parameter vector  
\$c\_0\$ a priori parameter vector  
K weighting factor

Example: WT Dynamic Derivative

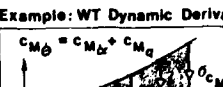


Fig. 11 Effect of Measurement and A Priori Error Covariance Matrices on Maximum Likelihood Cost Functional

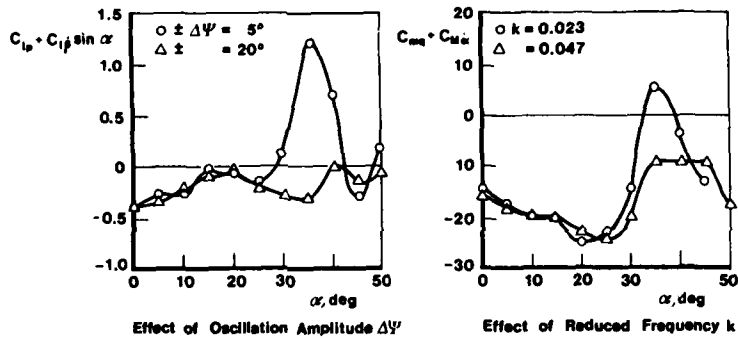


Fig. 12 Nonlinear and Unsteady Effects on Dynamic (Damping) Derivatives (NASA Wind Tunnel Model Data)

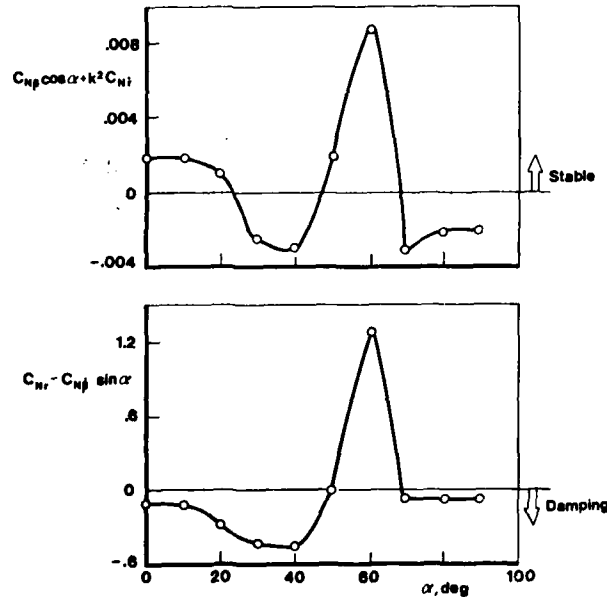


Fig. 13 Opposite Effects of Flow Separation on Lateral Static and Dynamic Stability (NASA Wind Tunnel Model Data)

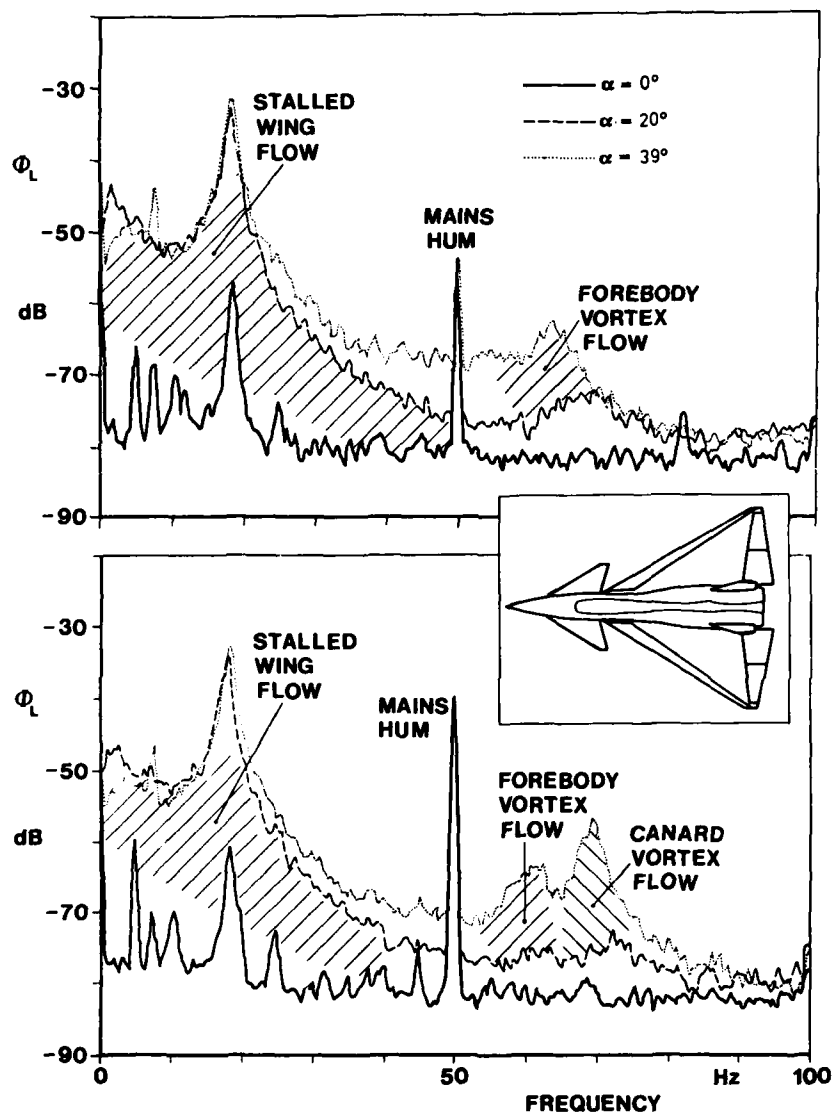


Fig. 14 Rolling Moment Power Spectral Density  $\phi_L$  of Fighter-Type Aircraft (DFVLR/MBB Wind Tunnel Model Data)

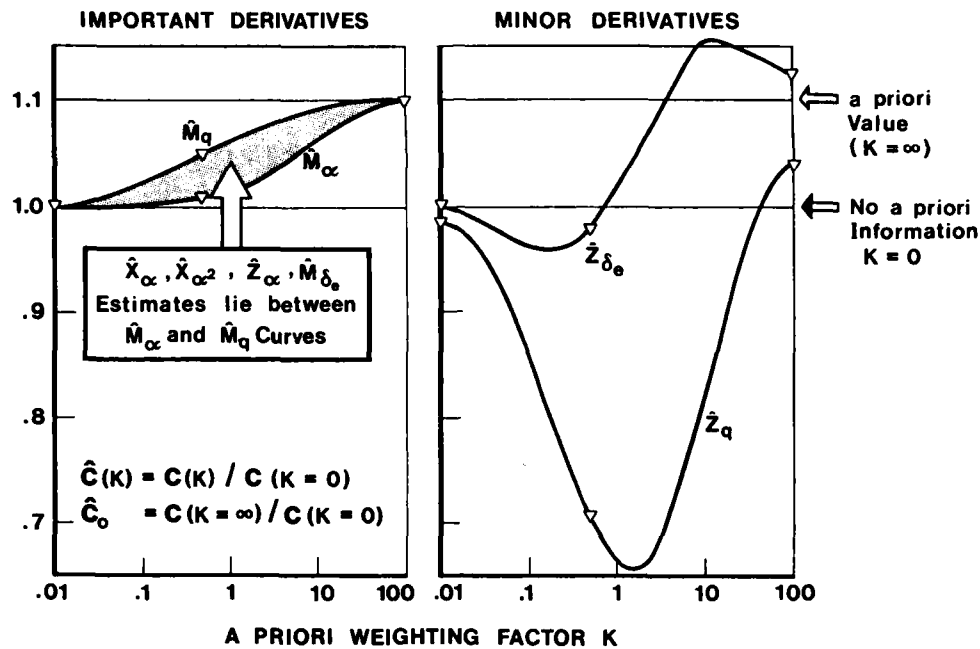


Fig. 15 Effect of A Priori Weighting K on Estimated Derivatives  
(Example 1 : DUT/NLR F-B-W-Aircraft DHC-2)

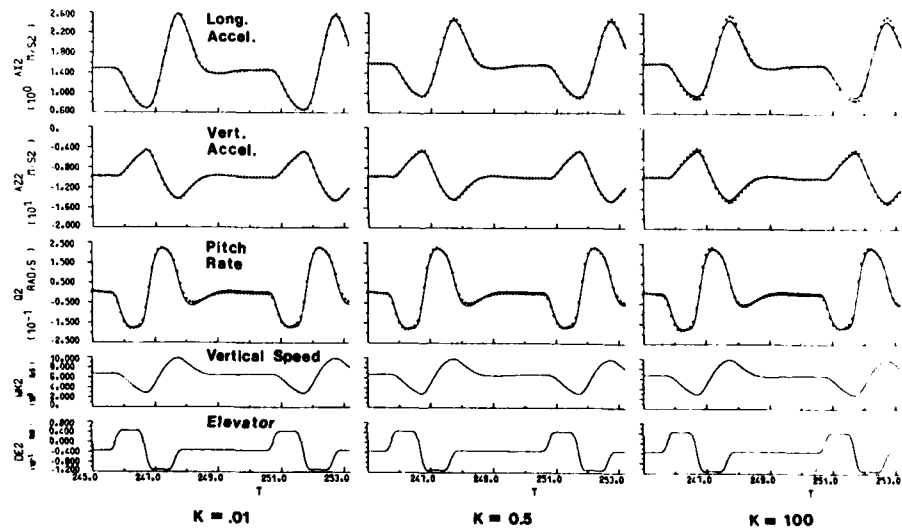


Fig. 16 Comparison of Flight-Measured and Computed Data for A Priori Weighting Factors K = 0.01, 0.5 and 100 (Example 1: DUT/NLR F-B-W-Aircraft DHC-2)

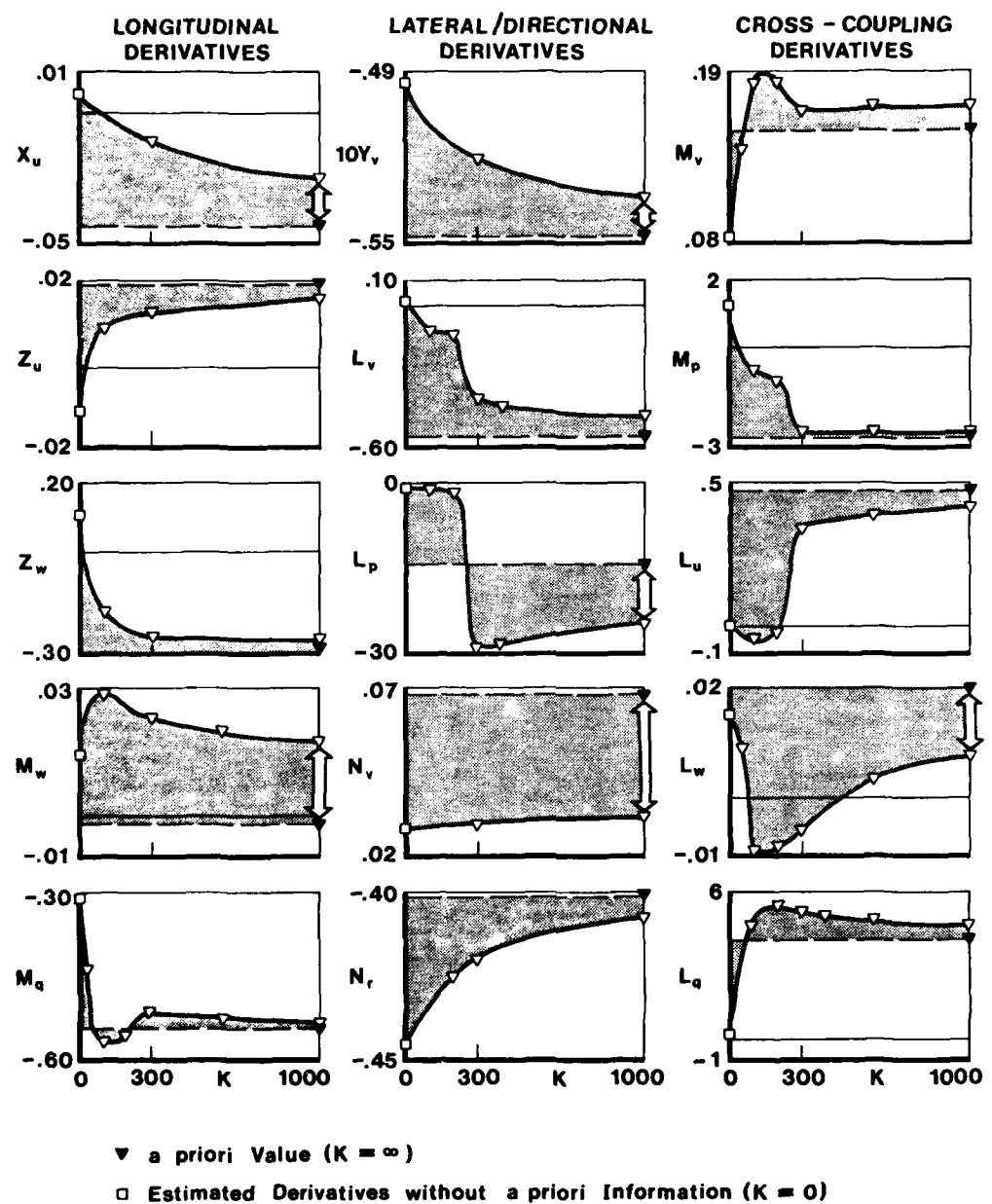


Fig. 17 Effect of A Priori Weighting  $K$  on Estimated Derivatives  
(Example 2: Hovering Rotorcraft BO-105)

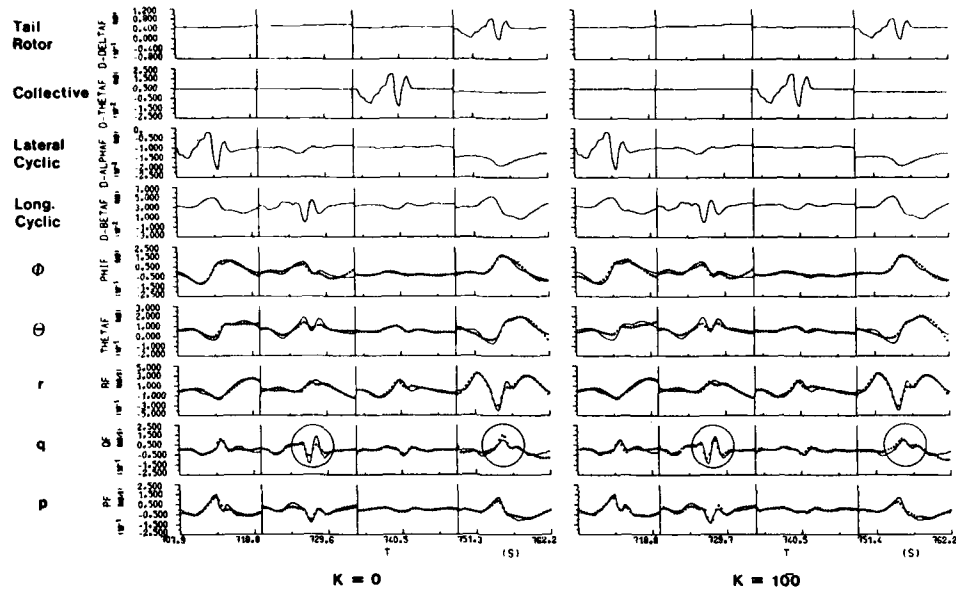


Fig. 18 Comparison of Flight-Measured and Computed Data for A Priori Weighting Factors  $K = 0$  and  $100$  (Example 2: Hovering Rotorcraft BO-105)

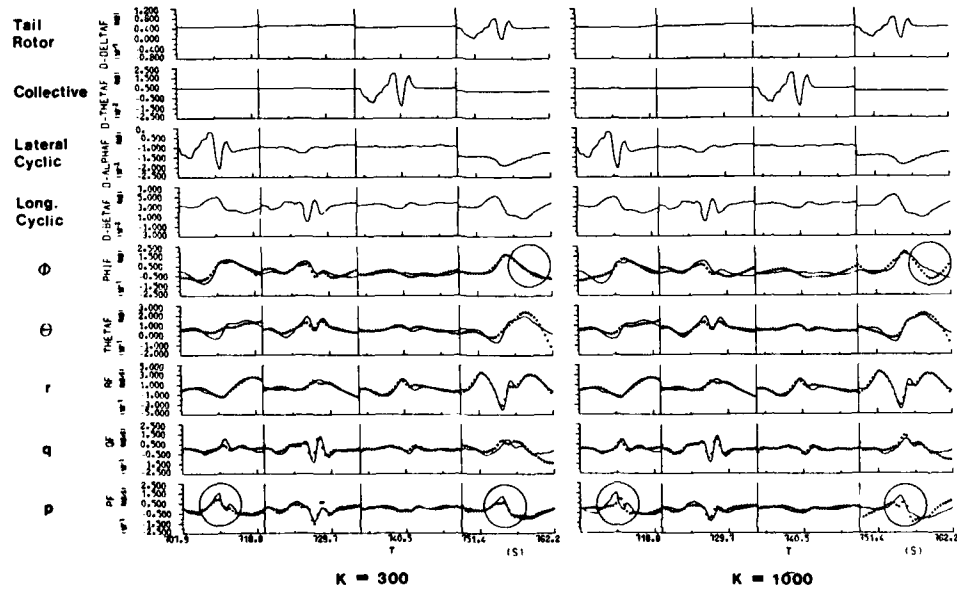


Fig. 19 Comparison of Flight-Measured and Computed Data for A Priori Weighting Factors  $K = 300$  and  $1000$  (Example 2: Hovering Rotorcraft BO-105).

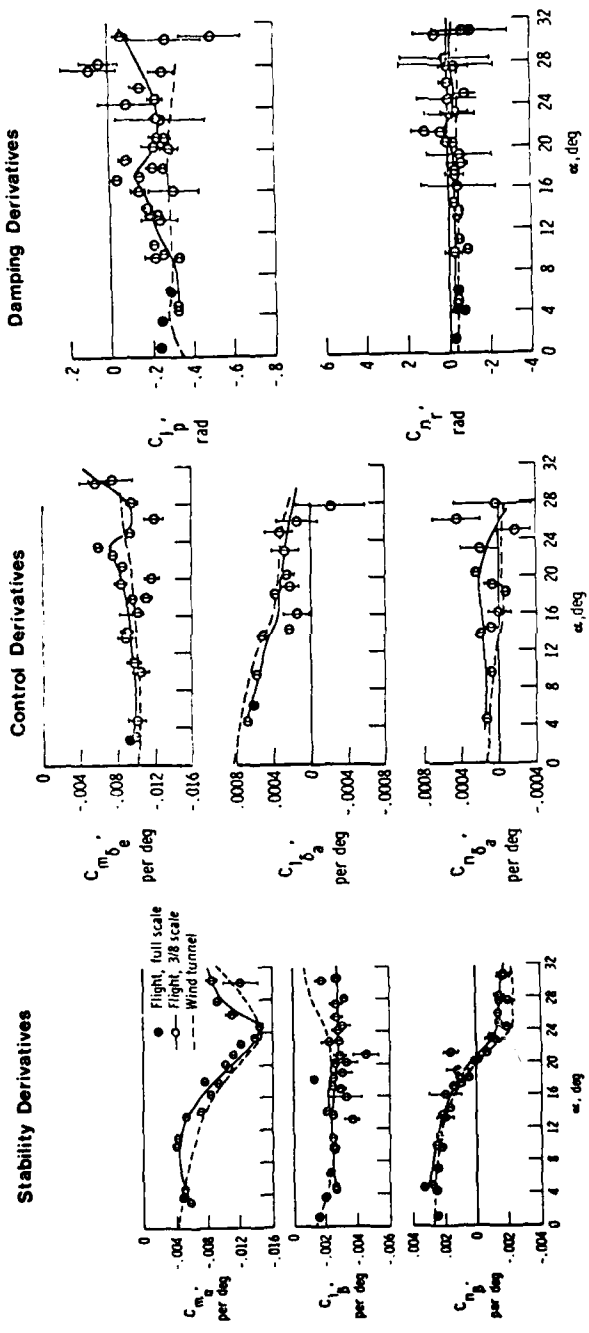


Fig. 20 Comparison of Flight and Wind Tunnel Derivative Estimates  
(NASA F-15 Aircraft)

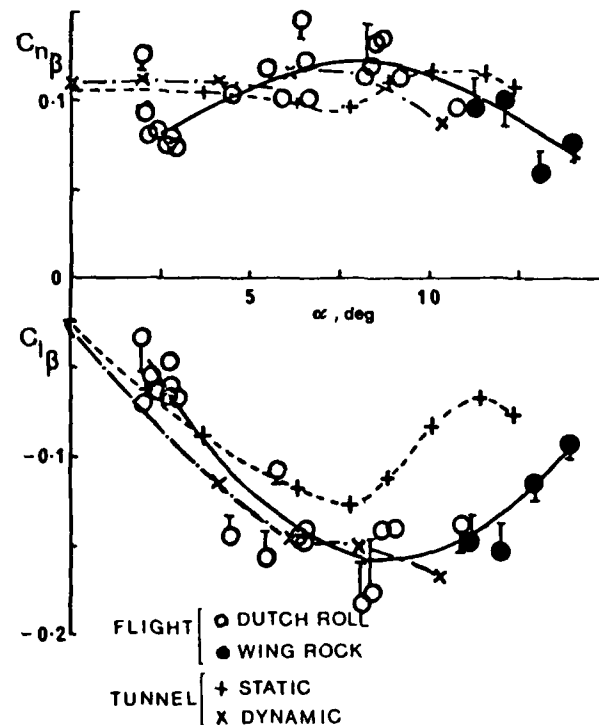


Fig. 21 Comparison of Flight and Wind Tunnel Derivative Estimates  
(RAE Gnat Aircraft)

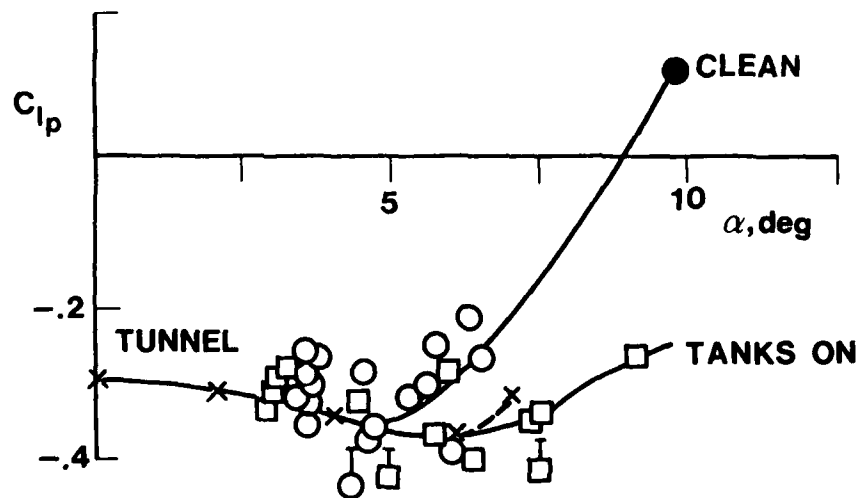


Fig. 22 Effect of External Stores on Estimated Roll Damping  
Derivative (RAE Gnat Aircraft)

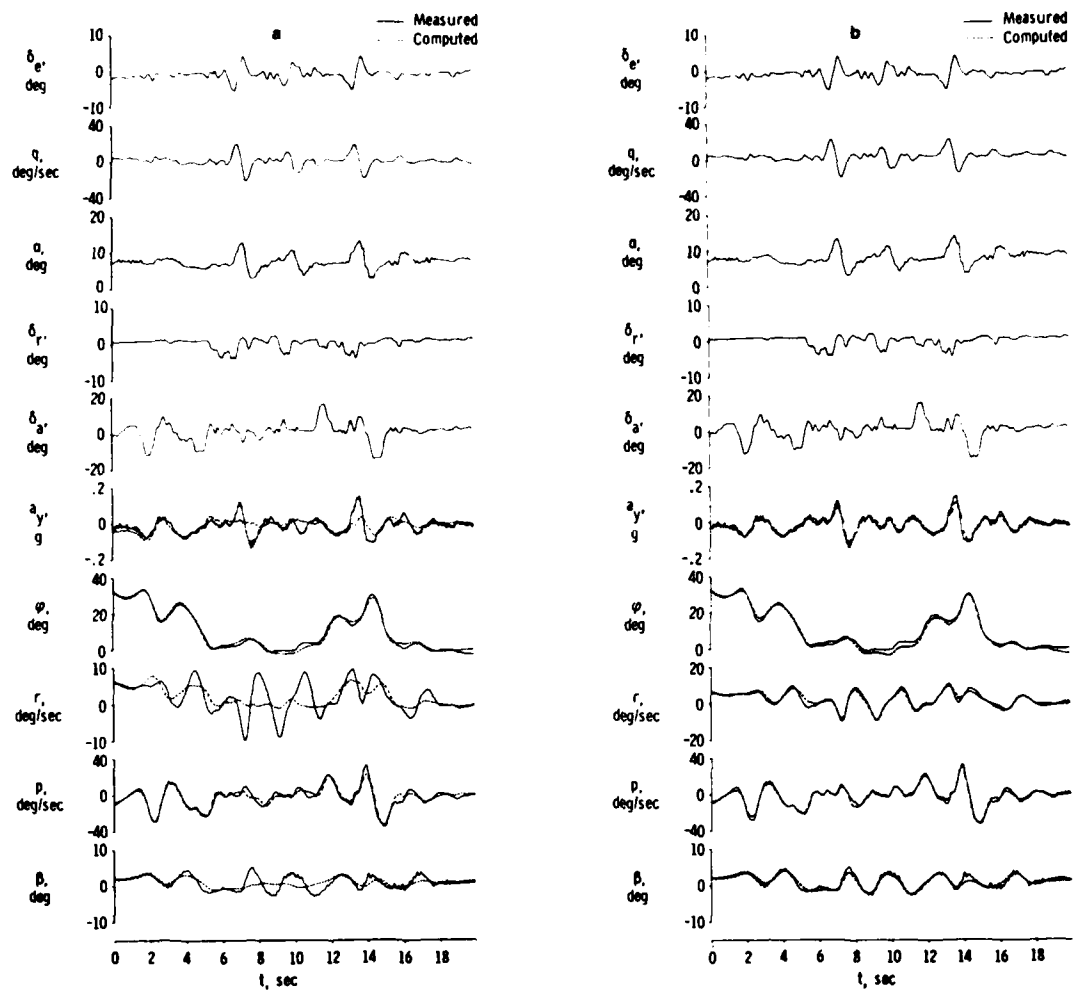


Fig. 23 Comparison of Flight-Measured and Computed Lateral-Directional Motions of Aircraft with 45° Wing Skew (NASA Oblique Wing RPRV)  
(a = Cross-Coupling Terms Omitted, b = Cross-Coupling Terms Included)

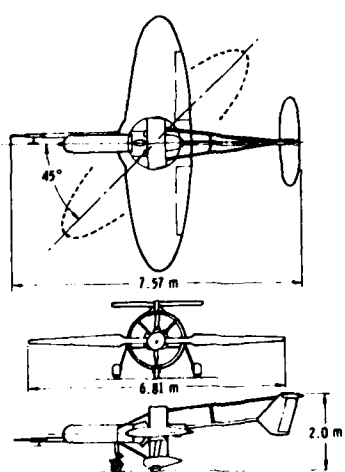


Fig. 24 Effect of Wing Skewing on Estimated Cross-Coupling Derivatives (NASA Oblique Wing RPRV)

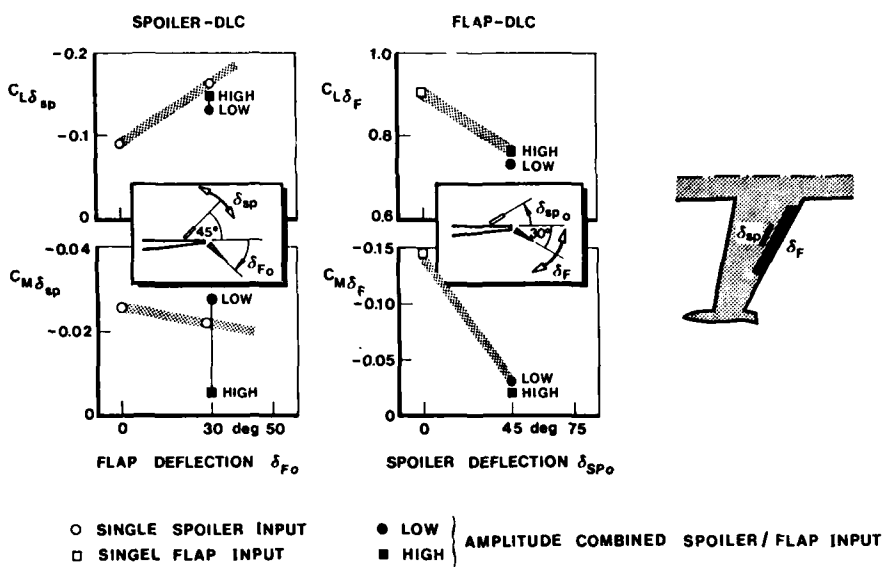


Fig. 25 Effect of Flap-Spoiler Interference on Estimated Direct Lift Control (DLC) Effectiveness  
 (DFVLR Airborne Simulator Hansa Jet)

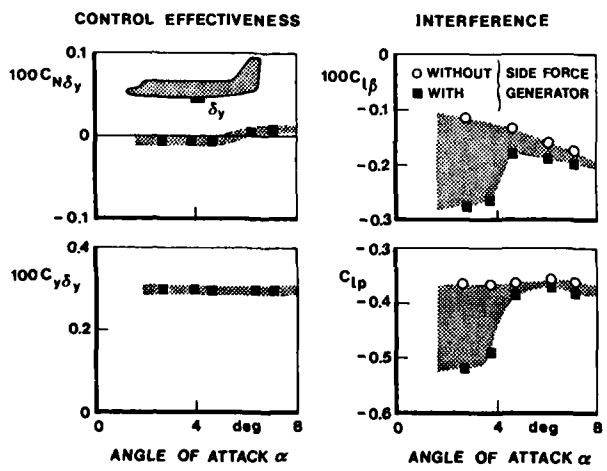


Fig. 26 Effect of Side Force Generator Interference on Estimated Control Effectiveness and Lateral Stability Derivatives  
 (NASA Test Aircraft Jet Star)

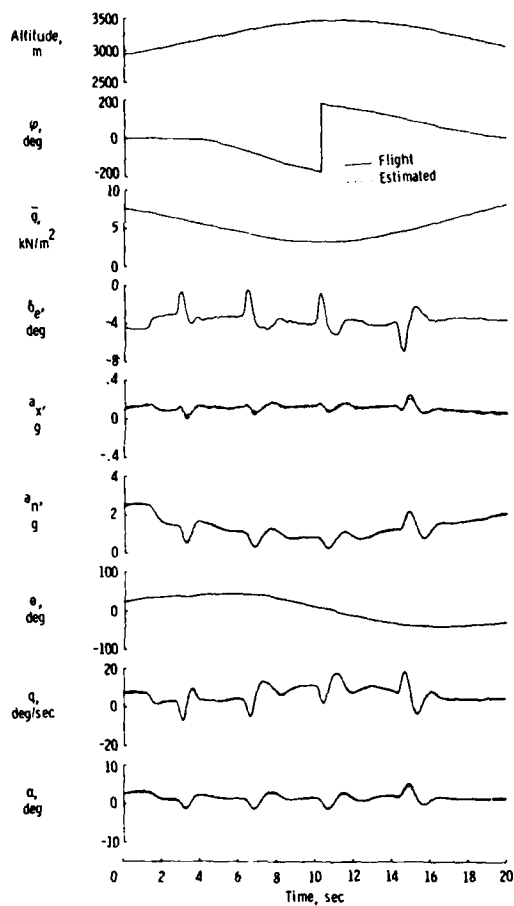


Fig. 27 Comparison of Flight-Measured and Computed Smooth Rolling/Impulsive Pitching Maneuvers Designed for Estimation of Vertical Acceleration Derivatives (NASA Test Aircraft T-37 B).

○	Two-point hesitation rolls
□	Smooth rolls
- - -	Calculations

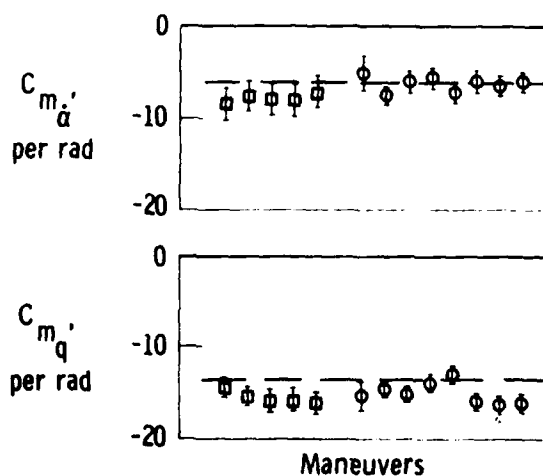
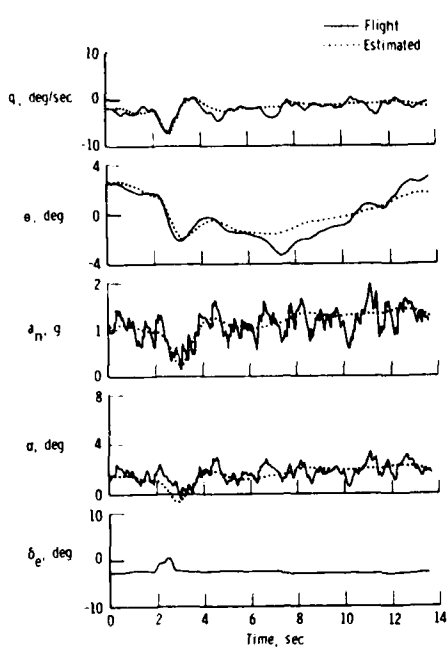
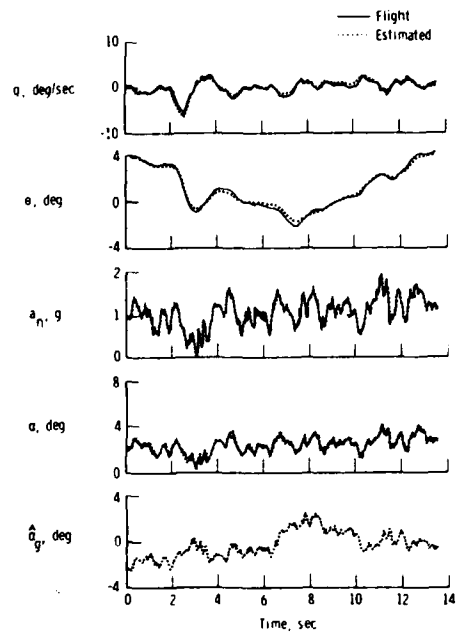


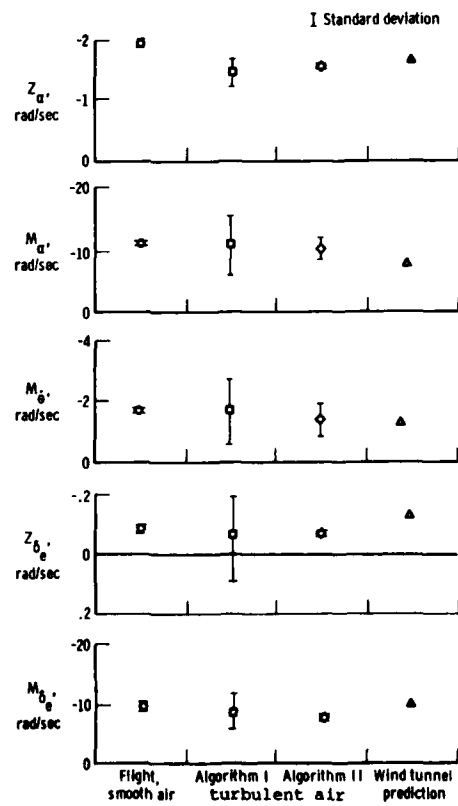
Fig. 28 Independent Flight Estimates of Pitch Rate and Vertical Acceleration (Angle-of-Attack Rate) Derivatives (NASA Test Aircraft T-37 B).



Algorithm I: No Turbulence Modeling



Algorithm II: Turbulence Modeling Included

Fig. 29 Comparison of Flight-Measured and Computed Dynamic Response  
(NASA Test Aircraft Jet Star)Fig. 30 Means and Standard Deviations using four Methods of Estimating Stability and Control Derivatives  
(NASA Test Aircraft Jet Star)

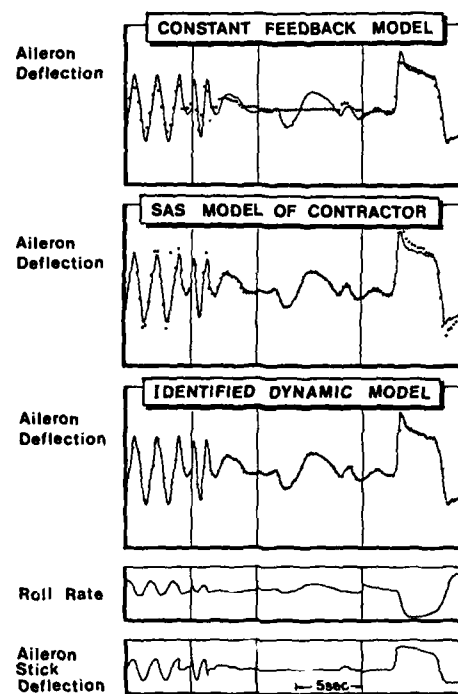


Fig. 31 Comparison of Flight-Measured and Computed Data (Model Output) of a Modern Combat Aircraft with an Active Roll Stability Augmentation System (SAS)

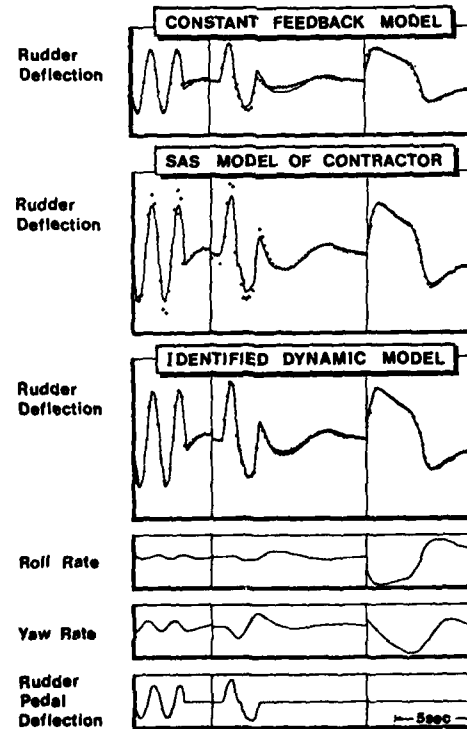


Fig. 32 Comparison of Flight-Measured and Computed Data (Model Output) of a Modern Combat Aircraft with an Active Yaw Stability Augmentation System (SAS)

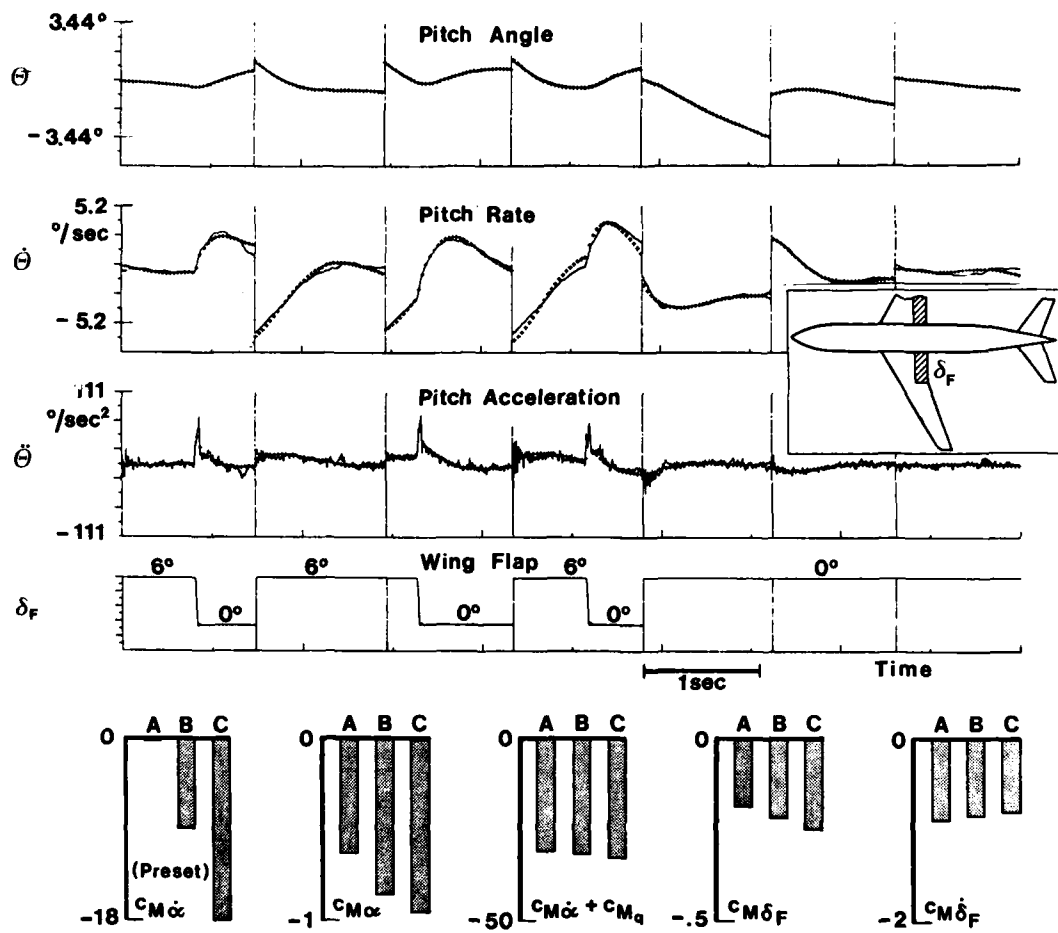


Fig. 33 Identification of Static and Dynamic Derivatives of an AIRBUS-type Free-Flight Model and Corresponding Fits of Flight-Measured (—) and Computed (++) Time Histories (IMFL-ATA-Model)

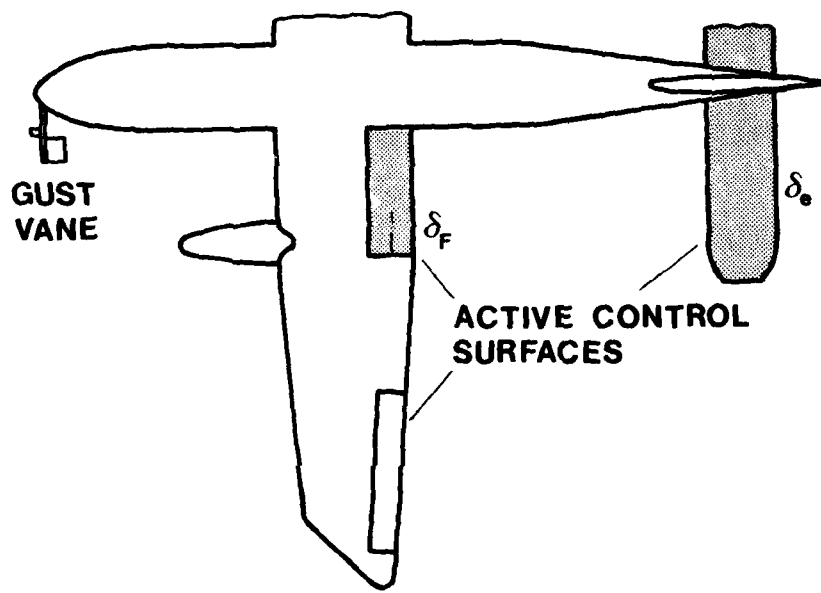
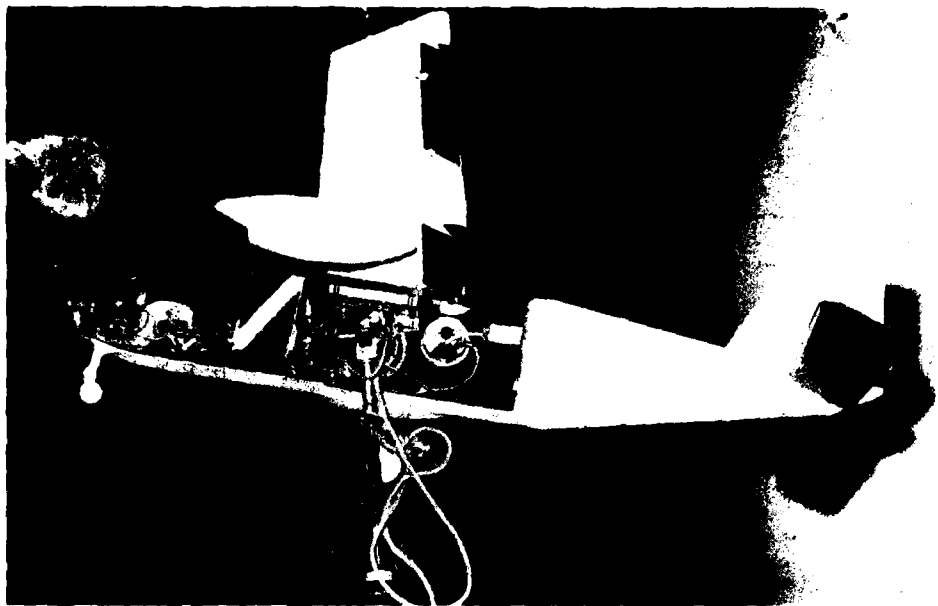


Fig. 34 Light Transport Aircraft Model with Active Control Gust Alleviation System in DFVLR Wind Tunnel Dynamic Simulation Facility (DFVLR/Dornier DO 28-TNT-Model)

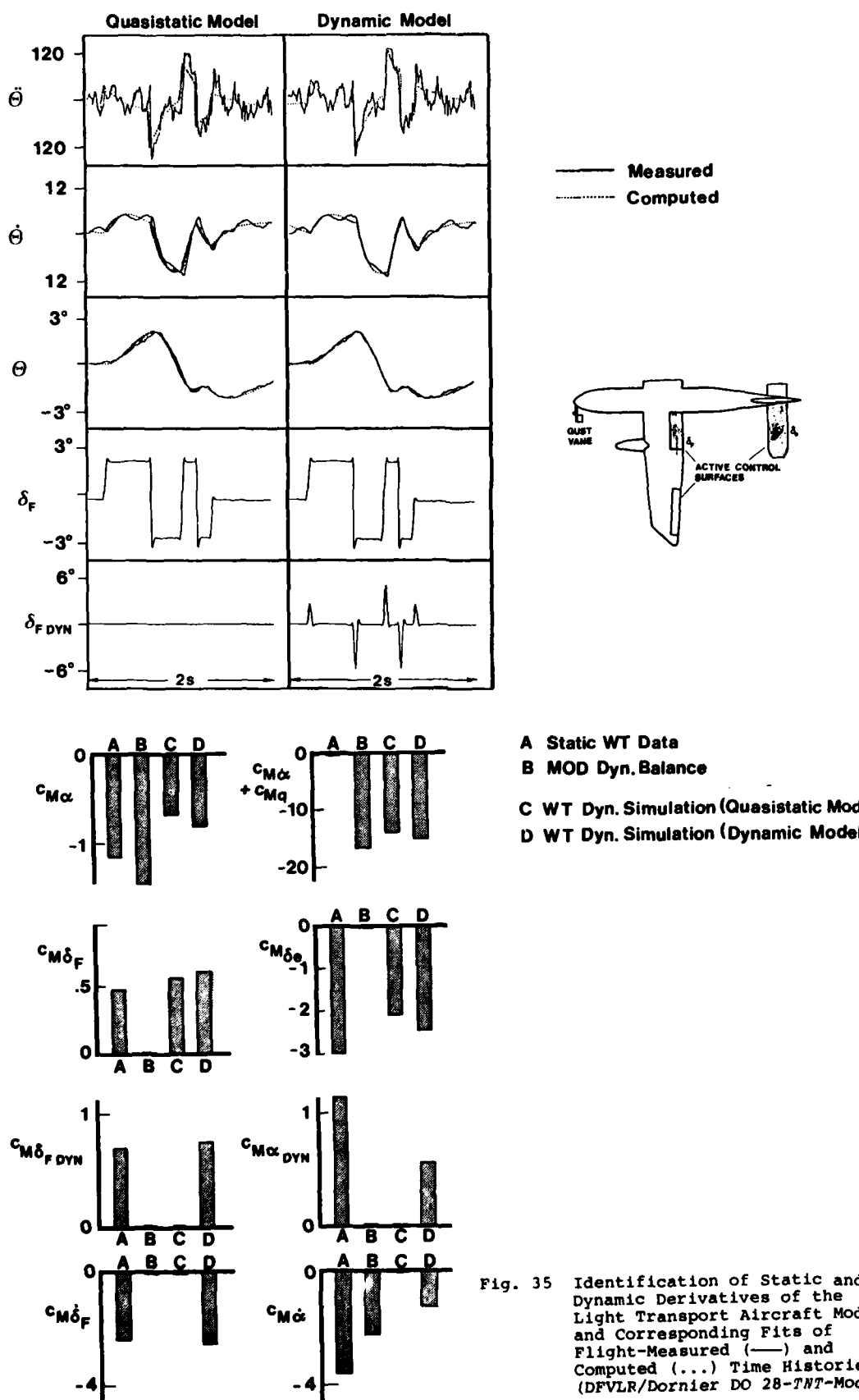


Fig. 35 Identification of Static and Dynamic Derivatives of the Light Transport Aircraft Model and Corresponding Fits of Flight-Measured (—) and Computed (...) Time Histories (DFVLR/Dornier DO 28-TNT-Model).

ESTIMATION OF DYNAMIC STABILITY PARAMETERS  
FROM DROP MODEL FLIGHT TESTS

By

Joseph R. Chambers  
NASA Langley Research Center  
Hampton, Virginia 23665  
U.S.A.

- and

Kenneth W. Iliff  
NASA Dryden Flight Research Center  
Edwards, California 93523  
U.S.A.

**SUMMARY**

A recent NASA application of a remotely-piloted drop model to studies of the high angle-of-attack and spinning characteristics of a fighter configuration has provided an opportunity to evaluate and develop parameter estimation methods for the complex aerodynamic environment associated with high angles of attack. The estimation methods employed were not unique to drop models. The paper discusses the overall drop model operation including descriptions of the model, instrumentation, launch and recovery operations, piloting concept, and parameter identification methods used. Static and dynamic stability derivatives were obtained for an angle-of-attack range from -20° to 53°.

The results of the study indicated that the variations of the estimates with angle of attack were consistent for most of the static derivatives, and the effects of configuration modifications to the model (such as nose strakes) were apparent in the static derivative estimates. The dynamic derivatives exhibited greater uncertainty levels than the static derivatives, possibly due to nonlinear aerodynamics, model response characteristics, or additional derivatives. As a result of extensive experience gained in this project and other applications of parameter identification methods, significant progress is being made toward the development of identification techniques for high angle-of-attack conditions.

**SYMBOLS**

$\alpha$	angle of attack of the body axis, deg
$a_n$	normal acceleration, g
$a_y$	lateral acceleration, g
$c_D$	drag coefficient
$c_L$	lift coefficient
$c_1$	rolling-moment coefficient
$c_m$	pitching-moment coefficient
$c_{m\dot{q}}$	pitching moment due to pitch rate, 1/rad
$c_N$	normal-force coefficient
$c_n$	yawing-moment coefficient
$c_{1\beta}$	roll due to sideslip derivative, 1/deg
$c_{n\beta}$	yaw due to sideslip derivative, 1/deg
$c_{1p}$	roll due to roll rate, 1/rad
$c_{1r}$	roll due to yaw rate, 1/rad
$c_{np}$	yaw due to roll rate, 1/rad
$c_{nr}$	yaw due to yaw rate, 1/rad
$l$	linear dimension, m
$m$	mass, kg
$p$	roll rate, deg/sec or rad/sec
$q$	pitch rate, deg/sec or rad/sec
$r$	yaw rate, deg/sec or rad/sec
$t$	time, sec
$\beta$	angle of sideslip, deg
$\delta_d$	differential tail deflection, deg
$\delta_e$	elevator deflection, deg
$\phi$	bank angle, deg

$\psi$  heading angle, deg  
 $\rho$  air density, kg/m<sup>3</sup>  
 $\theta$  pitch angle, deg

#### Subscripts:

$a$  airplane  
 $m$  model

#### INTRODUCTION

The National Aeronautics and Space Administration has conducted numerous investigations involving the application of drop model testing techniques (see references 1 and 2, for example). The objectives of the studies have varied greatly, ranging from studies of the opening-and gliding characteristics of para-wing vehicles to the maneuvering characteristics of extremely sophisticated, powered models. In recent years, interest in the stalling and spinning characteristics of military airplanes has led to the development and refinement of a remotely-piloted vehicle concept for such studies. As part of these investigations, it has been possible to evaluate parameter identification methods for a very large range of angle of attack not studied previously. Although the identification methods used are not unique to drop models, the results and experience gained regarding high angle-of-attack conditions has proven to be of great value in advancing the state of the art in parameter identification.

For completeness, the present paper first briefly describes the current applications of drop models within NASA; then a detailed description of the parameter identification study is presented, including a description of the overall drop model test operation and the identification methods used. Results are presented illustrating the trends and uncertainty levels of static and dynamic derivatives extracted from flight tests.

#### APPLICATIONS OF DROP MODELS

Drop model tests have, of course, been employed for many years in international studies of aerodynamics, structures, and controls. At the present time, NASA utilizes remotely-piloted drop models for studies at the NASA Langley Research Center and at the NASA Dryden Flight Research Center. The applications of drop models at the two Centers differ greatly in terms of test capability, objective, and cost.

##### Langley Research Center

The Langley Research Center utilizes helicopter-launched drop models for studies of stall/spin characteristics of highly-maneuverable military aircraft. The technique was developed about 20 years ago, and has been used to evaluate virtually every fighter design in the past decade. The technique consists of launching an unpowered radio-controlled model into gliding flight from a helicopter at an altitude of about 1525 m (5,000 ft), controlling the flight of the model from the ground, and recovering the model with a parachute.

A photograph of a drop model of the F-18 airplane mounted to the launch helicopter is shown in figure 1. The model is controlled by pilots seated in rapid-movement anti-aircraft-type trackers as shown in figure 2. The pilots control the model by visual cues and orientation of the model only. A ground-based digital computer is used for the simulation of advanced flight control systems, providing extensive flexibility for studies of automatic departure and spin prevention systems.

The drop tests are conducted at a site located about 8.1 km (5 mi) from the research center. An aerial view of the test site showing the helicopter landing pad and a pair of short runways used for tests of smaller subscale powered models is shown in figure 3. A close-up view of the site is presented in figure 4, showing the model preparation building; a trailer which houses the ground-based computer used for control law simulation and data acquisition; the pilot station; and a special wheeled vehicle used for retrieval of the model at the conclusion of the test.

During a typical study using this technique, the effects of various types of control inputs during post-stall motions will be determined. For example, the ability of a configuration to enter a developed spin following the application of only longitudinal control (with no lateral-directional inputs) will be compared with results obtained when full prospin controls are applied. Recovery from the incipient spin is evaluated by applying recovery controls at various stages of the post-stall motion; for example, controls may be neutralized at varying numbers (or fractions) of turns after the stall. The technique, therefore, determines (1) the spin susceptibility of a configuration, (2) control techniques that tend to produce developed spins, and (3) the effectiveness of various manual and automatic control techniques for recovery from out-of-control conditions.

To date, this drop model technique has not been used for parameter identification studies. The models used are of a size comparable with wind-tunnel test sections available at the research center, and the aerodynamic characteristics of the models are usually measured in wind tunnels, such as the 9.1 m-by-18.2 m (30 ft. by 60 ft.) Langley Full-Scale Tunnel.

##### Dryden Flight Research Center

The concept of using remotely-piloted research vehicles has been refined and advanced to a high level of sophistication at the Dryden Flight Research Center. Applications of remotely-piloted vehicles have ranged from full-scale, unmanned aircraft to subscale powered models. One of the recent applications of

remotely-piloted vehicle technology has been the use of the 3/8-scale model of the F-15 airplane shown in figure 5 to studies of stalling, spinning, and parameter identification at high angles of attack (reference 3). The model, referred to as the Spin Research Vehicle (SRV) is an unpowered vehicle launched from a B-52 aircraft and controlled from a ground-based pilot station. An in-flight photograph of the SRV mounted to the B-52 airplane is shown in figure 6. To date, 35 launches of the SRV have been made.

The remainder of this paper describes in detail the testing technique and the experience gained in the extraction of stability parameters from flight tests of the SRV (references 4 and 5).

#### DESCRIPTION OF TEST METHOD

##### Model

The model, shown in figure 7, is a 3/8-scale unpowered model of the F-15 airplane, which is a single-place, advanced air superiority fighter airplane with 45° swept leading-edge wing, two engines, and twin vertical tails. Pertinent model dimensions are given in table 1. The model was built primarily of fiber glass with metal load-carrying members in each section. It was designed to be as stiff as the full-scale airplane and to withstand normal loads five times 1-g flight. The inlets were drooped 11° to correspond to the low-speed configuration of the airplane and were blocked by a flat plate normal to the duct which was positioned just inside the inlet lip. There was no flow through the ducts, nor was there any thrust or simulation of thrust.

Control for the pilot was provided by conventional aerodynamic surfaces. Roll control was provided by aileron deflections and by differential horizontal stabilator deflections. A portion of each vertical stabilizer was deflected for rudder control. Rudder control was also commanded through an interconnect between the lateral stick position and the rudder.

The model was scaled geometrically to be as large as practical and was to be flown at flight levels similar to those of the full-scale airplane. The motivation was to provide a model large enough that it could be controlled "normally" by a pilot and to obtain data at higher values of Reynolds number than could be obtained in other tests, such as drop tests at Langley. The model was scaled dynamically according to the relationships shown in figure 8. Tests of a model designed and tested in accordance with these dynamic similarity relationships should give results that may be interpreted to predict full-scale results if Reynolds number and Mach number effects are insignificant. Also, model attitude angles should be the same as full-scale attitude angles, and angular velocities (time-dependent quantities) are predictable by the relationships shown.

The model was initially designed with no landing gear and was recovered by parachute using a midair retrieval (MARS) by helicopter. In the more recent test programs, the model was equipped with skis which permit a horizontal landing.

##### Remotely Piloted System

A functional block diagram of the remotely-piloted model system is shown in figure 9. The aircraft response variables are telemetered to a ground station where they are routed to a ground computer, the cockpit instrument panel, and analog strip chart recorders for real-time flight monitoring. The ground cockpit proportional control functions (longitudinal and lateral stick and rudder pedals) are processed by the analog-to-digital converter and are trunked to the ground computer together with the model panel signals. The ground computer calculates the command variables for the uplink encoder.

The remotely piloted system uses two uplink encoders. The computer encoder receives command variables from the computer, and the bypass encoder receives command variables directly from the ground cockpit. The pilot selects an encoder by means of a pushbutton on the mode control panel. The bypass encoder serves as a backup to the computer encoder if the computer malfunctions. The command signals are transmitted to the model where they are decoded and sent to the appropriate servochannel.

The pilot is given direct control of the model in the operation of the remotely piloted system, which permits experienced test pilots to extract the maximum research capability from the system. Accordingly, the ground cockpit is configured to give the remote test pilot information about the airplane model similar to that which would be provided in an airplane cockpit. Figure 10 shows the cockpit and displays, which are typical of a simulation-type cockpit although no particular aircraft cockpit is simulated. The displays include airspeed, altitude, rate of climb, angle of attack, angle of sideslip, yaw rate, pitch rate, normal acceleration, control positions, and commanded control position. Aircraft attitude and heading are presented on a three-axis attitude indicator. All the instruments display processed telemetered data from the model. The pilot controls the model with a conventional control stick and rudder pedals. The control feel is provided in each axis by a high-quality, computer-controlled, electric force-feel system which accurately simulates the full-scale airplane force-feel in pitch and roll.

Also shown in figure 10 is the mode control panel with which the pilot selects various control modes and gains. A pulse panel with which the pilot can apply control surface steps or doublets under computer control is located on the left console. The model control panel is used to select from four control modes in three axes (pitch, roll, and yaw) and provide programmable gain switches in each axis. The panel also allows the pilot to select the bypass mode or computer modes and inform him if any downlink variable fails a check which would result in telemetry lockout.

A black-and-white television monitor above the instrument panel shows the view from a forward-looking television camera in the model cockpit.

#### Telemetry Links

In addition to a requirement for high reliability, the telemetry link could not introduce unacceptable time delays if the links were to be used in the operation of closed-loop systems. The time delay of the data links was approximately 3.3 microseconds per kilometer, or about 0.5 millisecond for the uplink and downlink for an operational range of 75 kilometers. This delay is small compared to the update rate of 18.75 milliseconds and proved to be satisfactory for the computation times through the remotely piloted system.

The telemetry downlink provided aircraft response variables to the ground station at 200 samples per second. The characteristics of the PCM system were as follows:

- 144 000 bits per second
- 9 bits per data word
- 80 words per PCM frame
- 200 PCM frames per second
- No parity check
- L-band transmission
- 12-foot parabolic receiving antenna slaved to radar tracking antenna

The system had 40-hertz first-order-lag analog prefilters on all channels.

The telemetry uplink used for the system was developed by the U.S. Navy for the remote control of drone aircraft. The system was capable of several modes of operation, from the control of a single drone to the time-multiplexed control of a fleet of drones; therefore, the update rate of the system when controlling a single aircraft was comfortably high, and acceptable for the remotely piloted program. The characteristics of the system were:

- 16 bits per data frame (10-bit proportional command signal and 6 discrete signals)
- 4 data frames per cycle
- 53.33 cycles per second
- Two parity checks per data frame
- Synchronization and parity checks on each cycle
- UHF band transmission
- Frequency shift keying

As shown in figure 11, the telemetry uplink cycle consisted of four data words (frames) and a sync word transmitted at 53.33 samples per second (18.75 milliseconds cycle time). The transfer of each data word from encoder to receiver output on board the test airplane required 3.75 milliseconds. The four command signals were coded in the 10 most significant bits of the uplink words, and the remaining 6 bits were available for discrete signals to the test vehicle. Since parity checks were performed on each data word, intermittent dropout of the telemetry uplink signal was not expected to cause serious problems.

#### Ground Computer

The computer used in the remotely piloted system was a general-purpose minicomputer. As an indication of the capability of the computer to perform feedback control law computations, only approximately 0.7 millisecond was required to sum two feedback variables and a pilot command signal (each multiplied by a gain) and to operate on the resulting error signal with a first-order digital filter.

#### Instrumentation

The model instrumentation system consisted of regulated power supplies, sensors, signal conditioning, a pulse code modulation (PCM) system, and an L-band telemetering transmitter. The sensed quantities were transmitted to the ground station for display to the pilot, for inputs to the flight control system computer, and for recording. Quantities recorded included angles of pitch, roll, heading, sideslip, and attack; pitching, rolling, and yawing angular rates; longitudinal, lateral, and normal acceleration (center of gravity); airspeed; and altitude. The model control surface positions--each aileron position, each rudder position, and each horizontal stabilator position--were also recorded. The pilot's lateral and longitudinal stick position and force and rudder position and force as well as the commanded pitch, roll, and yaw trim were recorded. Twelve operational quantities, including battery voltages and hydraulic pressures, twelve discrete command signals, and twelve control system mode switch positions were recorded.

The resolution of the full-scale range of the recording indicates the accuracy of the model response variables. In each instance the measured quantity could be resolved to less than 1 percent of the full-scale recording range. Eight of the quantities (attitudes, rates, and accelerations) were recorded with full and expanded scales in the range of primary interest.

Each model quantity was transmitted at a rate of 200 samples per second. These quantities were prefiltered in the telemetry system by a 40-hertz first-order lag filter before they were sampled.

Postflight digital data processing routines applied a digital filter with a notch at 19 hertz and a third-order low-pass filter at 20 hertz to reduce the structural noise sensed primarily above 15° angle of attack in the acceleration and rate data. Additional digital data processing routines applied calibrations to the raw data, corrected angle of attack and angle of sideslip for local flow deflection, angular rates, and linear accelerations, and converted total and static pressure to the conventional air data functions. The angle of attack and sideslip vanes were 5.4 meters ahead of the center of gravity (figure 7).

Attitudes were measured by a four-gimbal, two-gyro platform system. The pitch, roll, and yaw angles were measured relative to the stable platform but were converted to and are presented as attitudes relative to an earth reference system as seen by the pilot.

#### FLIGHT TEST PROCEDURE

The model was air launched from the B-52 at an altitude of approximately 15,000 meters at a Mach number of 0.65. After the launch, the pilot flew the aircraft remotely through a planned flight profile. The stability and control maneuvers were performed either by pilot commands through conventional cockpit controls or through an input pulse panel. The input pulse panel switch initiated programmed control inputs once a desired flight condition was attained. The maneuvers were performed for small perturbation analysis about the desired steady state flight condition, where linearity of the airplane model could be assumed. The maneuvers were initiated with inputs in the longitudinal or lateral-directional mode and analyzed for that mode. Most of the data were obtained without a stability augmentation system engaged in the mode to be analyzed; however, stability augmentation was used in the other mode when the vehicle was difficult to stabilize. Stabilized flight conditions were difficult to maintain at extreme angles of attack.

Most of the maneuvers that did not result in satisfactory matches were made at high angles of attack. There was some aerodynamic flow separation above an angle of attack of 15°, and the separation was quite extensive above an angle of attack of 25°. The results presented for angles of attack greater than 30° are the best available but may be affected by nonlinearities.

#### Parameter Estimation Method

A maximum likelihood estimation method of analysis was used to determine the stability and control derivatives from the maneuvers made in flight. The method used (Newton-Raphson) is an iterative technique that minimizes the difference between the aircraft's measured and computed response by adjusting the stability and control derivative values used in calculating the computed response. The Newton-Raphson method is used to attain the minimizations. This method is called modified maximum likelihood estimation and is fully described in reference 6.

In addition to providing estimates of the derivatives, this method of analysis provides uncertainty levels associated with each derivative. Uncertainty levels are proportional to the approximation of the Cramer-Rao bounds described in reference 6 and 7 and are analogous to standard deviations of the estimated derivatives. The larger the uncertainty level, the greater the uncertainty in the estimated derivative. The most valid estimate of a derivative can be determined by comparing the uncertainty levels for the same derivative obtained from different maneuvers. The uncertainty levels in this way provide additional information about the validity of a derivative estimate.

#### RESULTS AND DISCUSSION

##### Lift and Drag

Measurements of normal and longitudinal acceleration and airplane attitudes were made during stabilized flight, and the data were reduced to lift and drag coefficients for comparison with results from low-speed wind-tunnel tests with a 1/10-scale model at a Reynolds number of approximately  $0.8 \times 10^6$  (figure 12). Reasonable agreement is indicated through the midlift range. The lift generated in flight near maximum lift appears to be less (no more than 5 percent) than that predicted by the wind-tunnel data.

The drag coefficient was calculated from stabilized flight data, and the results are compared with the low-speed wind-tunnel data in figure 13. Good agreement is indicated, although the flight data show slightly less drag throughout the angle of attack range covered. It should be noted that the SRV model tests were made with the model inlets blocked; thus neither engine thrust nor flow through the duct is accounted for.

##### Static Longitudinal Trim

The variation of elevator angle with angle of attack from trimmed flight was determined from stabilized flight data for a center-of-gravity location of 26-percent mean aerodynamic chord (figure 14). Two levels of longitudinal stability are shown in the data. Approximately 0.5° of longitudinal control produces approximately 1° of angle of attack change at low angle of attack, whereas in the higher angle of attack range approximately 1.4° of longitudinal control results in a 1° change in angle of attack. The airplane has more apparent longitudinal stability at the higher angles of attack, certainly a desirable design feature. Comparison of the flight data with the wind-tunnel data shows generally good agreement.

##### Dynamic Parameter Estimations

Computed and flight time histories for typical longitudinal and lateral-directional maneuvers are compared in figures 15 and 16. The results of the estimation of the stability and control derivatives from such maneuvers are given for the longitudinal mode in figures 17 and 18, and for the

lateral-directional mode in figures 19 to 21. Each symbol in the figures indicates an estimate made from one maneuver. The vertical line associated with each symbol indicates the uncertainty level associated with the estimate. The more valid estimates are readily identifiable by short vertical lines. A more complete explanation of the interpretation of uncertainty levels is given in reference 7.

The flight center of gravity position was constant for each flight. Data shown for angles of attack less than 38° were acquired with the center of gravity at 30.3-percent mean aerodynamic chord. For angles of attack greater than 38°, the data were acquired with the center of gravity at 38.5-percent mean aerodynamic chord. All the data were corrected to 26-percent mean aerodynamic chord.

Some of the scatter in the derivatives may be due to differences in trim stabilizer position, which were not corrected for. The trim deflection of the horizontal stabilizer for a given angle of attack was different for each center of gravity position, and the results of wind-tunnel tests indicate that  $\delta_e$  has a significant effect on lateral-directional derivatives.

Flight conditions at high angles of attack often varied significantly. This made matching the maneuvers more difficult and could have contributed to the apparent nonlinearities. Because of the uncertainties in the data for high angles of attack ( $\alpha > 30^\circ$ ), the fairings for these data are dashed in the figures. If discrepancies existed in data near the same flight condition, fairings were determined by referring to the quality of the match in addition to the uncertainty levels.

Some of the more pertinent static longitudinal derivatives are presented as a function of angle of attack in figure 17. Figure 17 summarizes the slope of the normal-force coefficient with angle of attack,  $C_{N_\alpha}$ , and the static stability derivative,  $C_{m_\alpha}$ , for the angle of attack range tested. Note that  $C_{N_\alpha}$  is well defined, in that a fairing passes within all of the uncertainty level bounds. The maximum value of the derivative occurs at an angle of attack of approximately 80°. The values decrease somewhat as angle of attack increases and the wing flow separation becomes more extensive. The estimates of the static stability derivative,  $C_{m_\alpha}$ , at all angles of attack are remarkably consistent. The configuration was stable at

large negative angles of attack and became almost neutrally stable near an angle of attack of -10°. Static stability then increased up to an angle of attack of approximately 25°. The level of static stability appeared to be nearly constant at the highest angles of attack.

The damping-in-pitch derivative,  $C_{m_q}$ , is shown in figure 18. The longitudinal damping derivative showed greater variability with angle of attack, from small positive values at the most negative angles of attack for which data were obtained to a value of approximately -7 per radian in the normal operating angle-of-attack range. The damping derivative appears to approach zero at an angle of attack of approximately 25°, but positive damping (negative  $C_{m_q}$ ) was indicated at greater angles of attack.

The lateral-directional stability and control derivatives are summarized in figures 19 to 21. The large uncertainty levels are probably due to the large number of unknown lateral-directional derivatives, nonlinear aerodynamics, and the difficulty of significantly exciting all the dynamic modes. Consistent trends with angle of attack are apparent for all major derivatives, and in most cases fairings that pass through most of the uncertainty levels are possible. An exception among the major derivatives is  $C_{n_B}$ .

The directional stability derivative,  $C_{n_B}$  (figure 19), shows a good level of stability at low positive angles of attack but decreases to zero at an angle of attack of approximately 20°. Recovery to a stable value is indicated at the highest test angle of attack. The dihedral effect derivative,  $C_{l_B}$ , has an unstable value at the most negative angles of attack and is generally stable for angles of attack greater than zero, with a maximum magnitude at an angle of attack of approximately 28°.

The roll and yaw damping derivatives are summarized in figures 20 and 21. Except for the damping-in-roll derivative,  $C_{p_B}$ , these derivatives had greater uncertainty levels than the static stability and control derivatives. However, generally satisfactory fairings are possible through most of the uncertainty levels. The estimates and uncertainty levels of the yaw rate derivatives for angles of attack from 20° to 30° suggest that the effects of wing-separated flow on the vertical tails was great. The values of the derivatives are small in this angle-of-attack region. The results are somewhat more consistent at the highest angles of attack.

There is a considerable amount of scatter in some of the derivatives, although all the derivatives presented herein were obtained from good fits between the measured and computed data. The data are based on the assumption that the airplane mathematical model is linear, and the scatter in the derivatives may be due to aircraft nonlinearities.

#### Effects of Nose Strakes

As part of an overall program to provide information on design procedures to improve spin resistance of military airplanes, the model was tested with nose strakes designed by wind-tunnel tests to improve  $C_{n_B}$  and eliminate asymmetric yawing moments at high angles of attack (reference 8). The nose stike configuration is shown in figure 22.

Figure 23 shows the values of  $C_{n_B}$ , obtained from flight with the nose stike off and on. In both stike

configurations, the nose boom was on. The data show a significantly higher level of  $C_{n_B}$  with the strake on at angles of attack above 15°, in agreement with the results of wind-tunnel tests.

#### CONCLUDING REMARKS

The remotely piloted technique for obtaining flight-test data on an unpowered 3/8-scale model of the F-15 airplane was found to provide adequate stability and control derivatives. The remotely piloted technique provided an opportunity to test the mathematical model in an angle-of-attack regime not previously examined in flight test. The derivatives were obtained for an angle-of-attack range from -20° to 53°. The variations of the estimates with angle of attack were consistent for most of the derivatives, particularly when the estimates were supplemented by uncertainty levels.

Some of the derivatives displayed evidence of nonlinearities and large uncertainties. These results were probably caused by nonlinear aerodynamic phenomena, inability to excite certain model motions, and effects of elevator setting.

Since the completion of the subject study, numerous additional attempts have been made to extract parameters from high angle-of-attack conditions (reference 9, for example), and notable progress has been made in parameter identification techniques (reference 10), particularly with regard to dynamic derivatives.

#### REFERENCES

1. Chambers, Joseph R.; and Bowman, James S., Jr.: Stall/Spin Test Techniques Used by NASA. AGARD-CP-199, Presented at the Flight Mechanics Panel Specialists' Meeting held at the Von Karman Institute, Rhode Saint Genese, Belgium, November 18-21, 1975.
2. Reed, R. Dale: Flight Research Techniques Utilizing Remotely Piloted Research Vehicles. AGARD Lecture Series No. 108 on Aircraft Assessment and Acceptance Testing. June 1980.
3. Holleman, Euclid C.: Summary of Flight Tests to Determine the Spin and Controllability Characteristics of a Remotely Piloted, Large-Scale (3/8) Fighter Airplane Model. NASA TN D-8052, 1976.
4. Iliff, Kenneth W.; Maine, Richard E.; and Shafer, Mary F.: Subsonic Stability and Control Derivatives for an Unpowered, Remotely Piloted 3/8-Scale F-15 Airplane Model Obtained From Flight Test. NASA TN D-8136, 1976.
5. Iliff, Kenneth W.: Stall/Spin Flight Results for the Remotely Piloted Spin Research Vehicle. AIAA Paper 80-1563-CP, August 1980.
6. Maine, Richard E.; and Iliff, Kenneth W.: User's Manual for MMLE-3, A General FORTRAN Program for Maximum Likelihood Parameter Estimation. NASA TP-1563, 1980.
7. Iliff, Kenneth W.; and Maine, Richard E.: Practical Aspects of Using a Maximum Likelihood Estimator. Methods for Aircraft State and Parameter Identification, AGARD-CP-172, May 1975, pp. 16-1--16-15.
8. Carr, Peter C.; and Gilbert, William P.: Effects of Selage Forebody Geometry on Low-Speed Lateral-Directional Characteristics of Twin-Tail Fighter Model at High Angles of Attack. NASA TP-1592, December 1979.
9. Nguyen, Luat T., Gilbert, William P.; Gera, Joseph; Iliff, Kenneth; and Enevoldson, Einar K.: Application of High Angle of Attack Control System Concepts to a Variable Sweep Fighter Airplane. AIAA Paper No. 80-1582-CP, August 1980.
10. Iliff, Kenneth W.: Estimation of Aerodynamic Characteristics From Dynamic Flight Test Data. AGARD-CP-235, May 1978.

TABLE 1.- GEOMETRIC CHARACTERISTICS OF THE SRV

<b>Model-</b>	
Length, m	7.15
Weight, N	-10,964
<b>Wing-</b>	
Area, m <sup>2</sup>	7.94
Span, m	4.89
Aspect ratio	3.0
Mean aerodynamic chord, m	1.82
Leading-edge sweep, deg	45.0
Taper ratio	0.25
Dihedral, deg	-1.0
Incidence, deg	0
Ailerons:	
Span, m	1.24
Deflection, deg	+20
<b>Horizontal tail-</b>	
Planform (exposed), m <sup>2</sup>	1.57
Span, m	3.24
Aspect ratio	2.05
Taper ratio	0.34
Leading-edge sweep, deg	50.0
Mean aerodynamic chord (exposed), m	0.94
Dihedral, deg	0
Tail length, m	2.30
Deflection, deg:	
Symmetrical	-15,-26
Differential	+11
<b>Vertical tails-</b>	
Area (both sides), m <sup>2</sup>	1.64
Span, m	1.18
Leading-edge sweep, deg	36.6
Mean aerodynamic chord, m	0.77
Tail length, m	2.02
<b>Rudders-</b>	
Area (total), m <sup>2</sup>	0.26
Span, m	0.54
Mean aerodynamic chord, m	0.24
Maximum deflection, deg	+30



Figure 1.- Photograph of F-18 drop model mounted for tests at Langley Research Center.

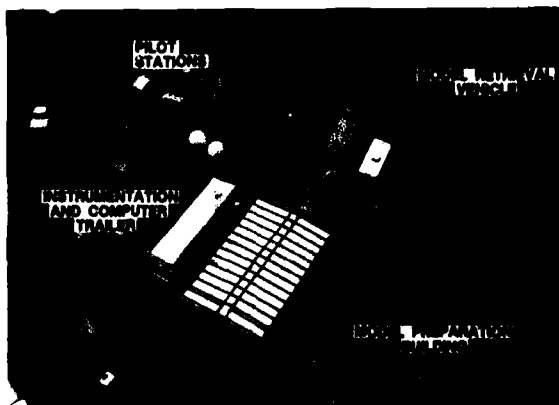


Figure 4.- Close-up view of test site.



Figure 2.- Pilots and trackers.

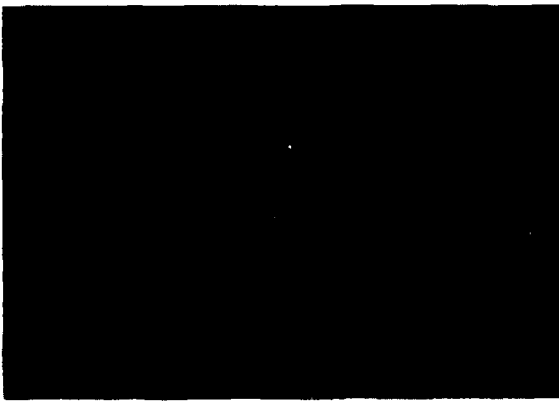


Figure 5.- Photograph of Spin Research Vehicle at Dryden Flight Research Center.

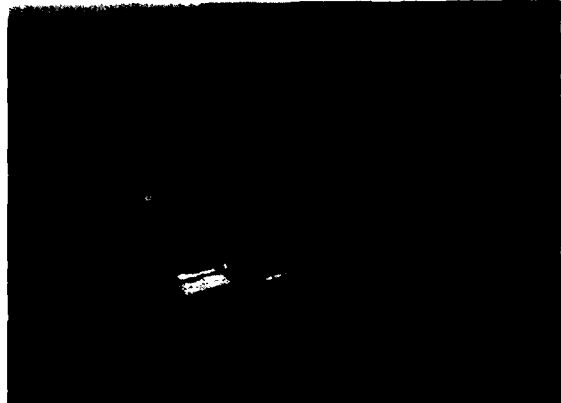


Figure 3.- Aerial view of test site.



Figure 6.- In-flight photograph of B-52 and Spin Research Vehicle.

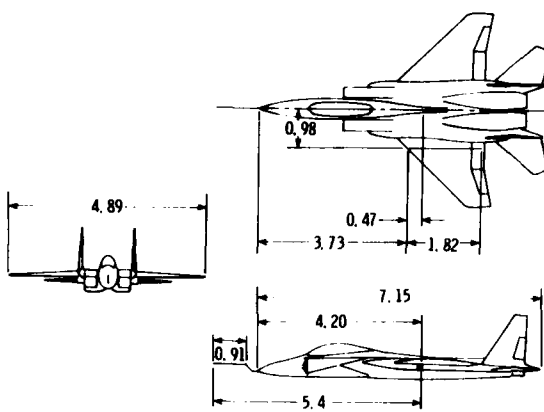


Figure 7.- Three-view drawing of Spin Research Vehicle. Dimensions in meters.

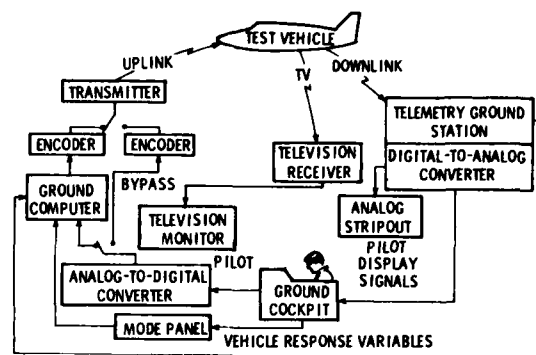


Figure 9.- Remotely-piloted model control concept.

MASS	$\frac{m_m}{m_a} = \frac{\rho_m}{\rho_a} \left( \frac{l_m}{l_a} \right)^3$
MOMENTS OF INERTIA	$\frac{l_m}{l_a} = \frac{\rho_m}{\rho_a} \left( \frac{l_m}{l_a} \right)^5$
TIME	$\frac{t_m}{t_a} = \left( \frac{l_m}{l_a} \right)^{1/2}$
LINEAR VELOCITIES	$\frac{v_m}{v_a} = \left( \frac{l_m}{l_a} \right)^{1/2}$

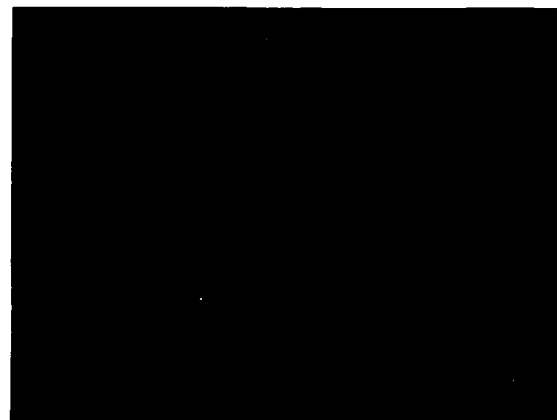


Figure 10.- Pilot station.

LINEAR ACCELERATIONS	$\frac{\ddot{v}_m}{\ddot{v}_a} = 1$
ANGLES	$\frac{\theta_m}{\theta_a} = 1$
ANGULAR VELOCITIES	$\frac{\dot{\theta}_m}{\dot{\theta}_a} = \left( \frac{l_a}{l_m} \right)^{1/2}$
ANGULAR ACCELERATIONS	$\frac{\ddot{\theta}_m}{\ddot{\theta}_a} = \frac{l_a}{l_m}$

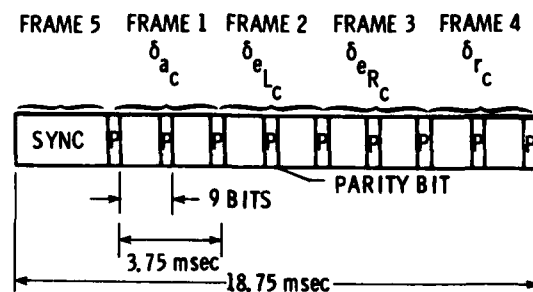


Figure 11.- Telemetry uplink time schedule.

Figure 8.- Model-scaling relationships.

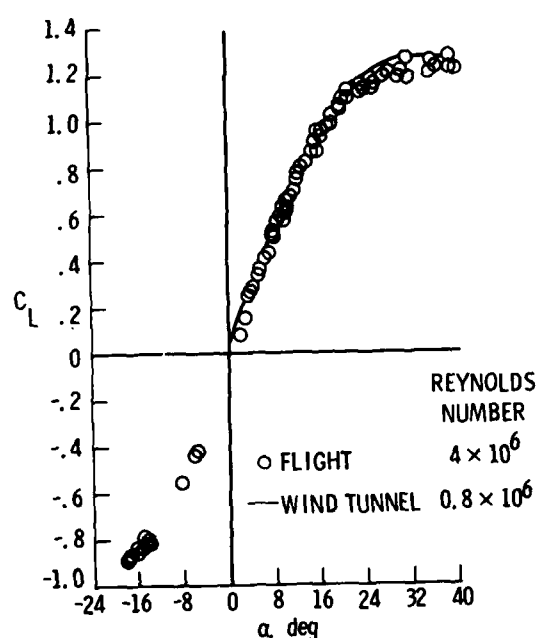


Figure 12.- Correlation of lift data.

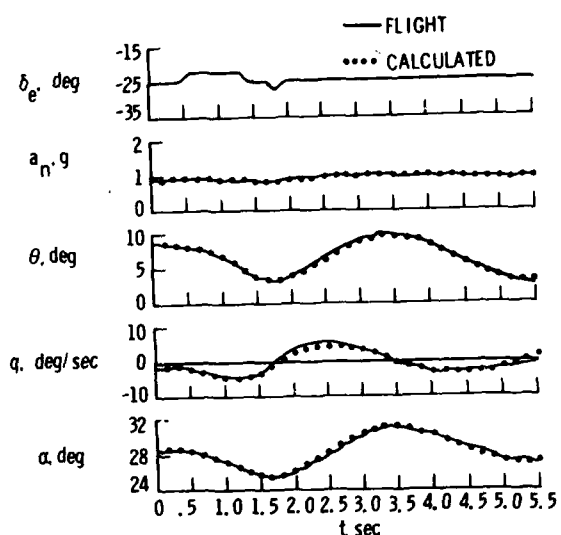


Figure 15.- Comparison of time histories for longitudinal maneuver.

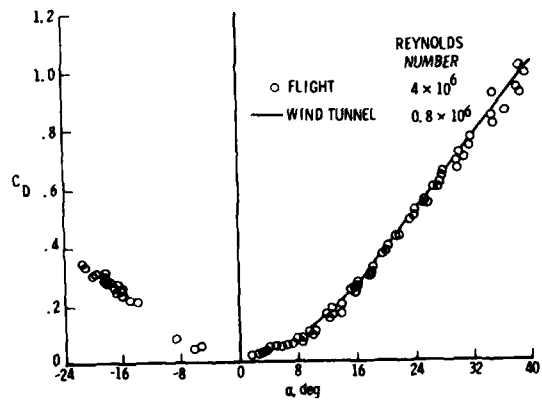


Figure 13.- Correlation of drag data.

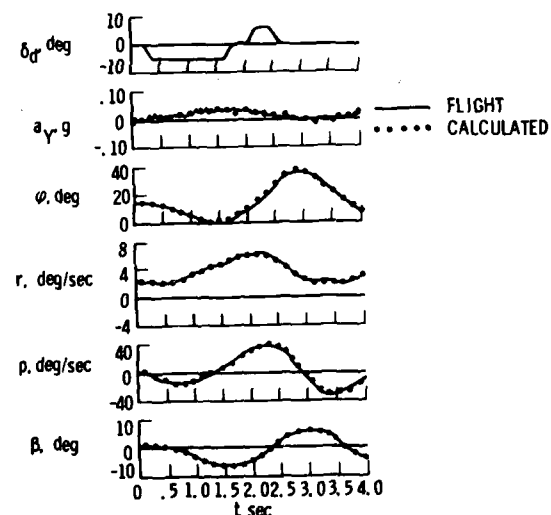
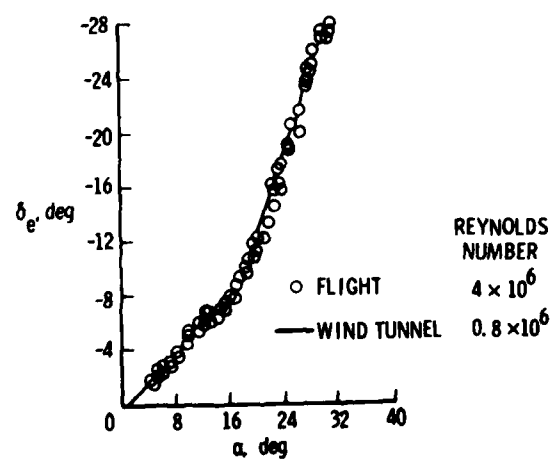
Figure 16.- Comparison of time histories for lateral-directional maneuver.  $\alpha = 23^\circ$ .

Figure 14.- Stabilator deflection required for trim.

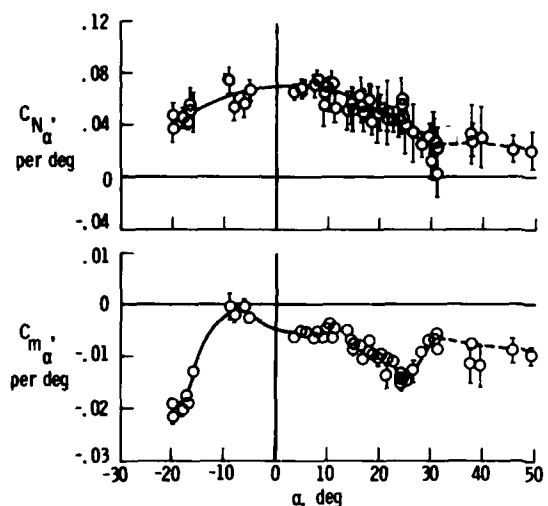


Figure 17.- Static longitudinal parameters extracted from flight.

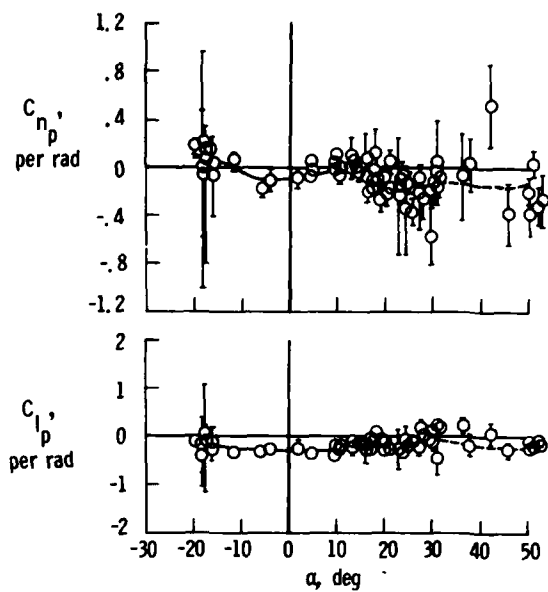


Figure 20.- Dynamic rolling parameters extracted from flight.

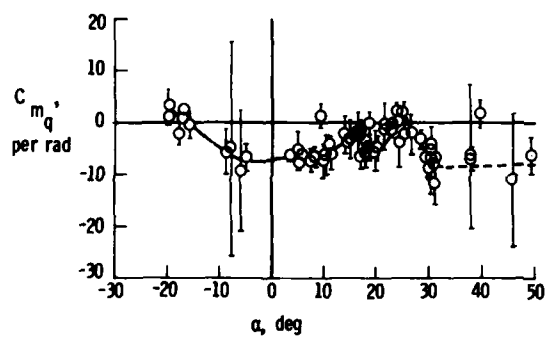


Figure 18.- Damping-in-pitch parameter extracted from flight.

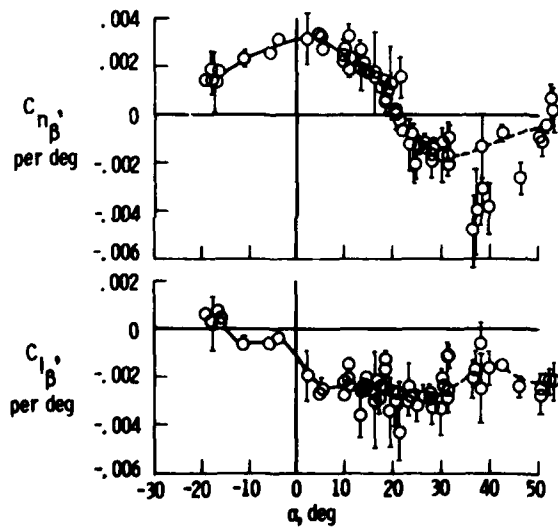


Figure 19.- Static lateral-directional parameters extracted from flight.

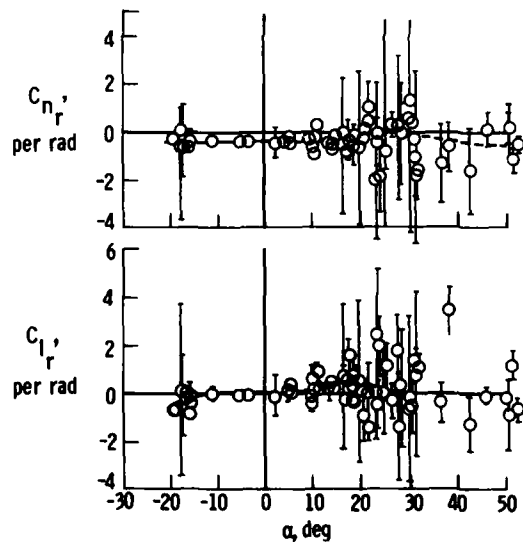


Figure 21.- Dynamic yawing parameters extracted from flight.



Figure 22.- Spin Research Vehicle with nose strakes.

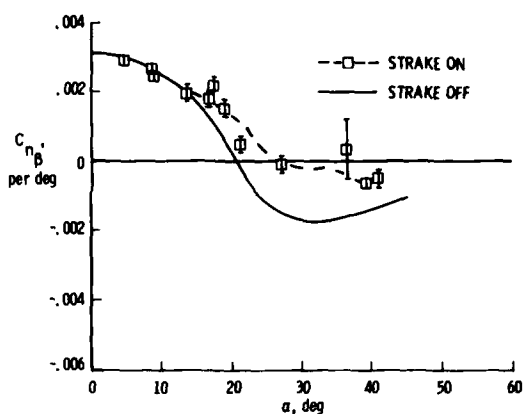


Figure 23.- Flight-determined effect of nose strakes on  $C_{n_B}$ .

## ANALYTICAL DETERMINATION OF DYNAMIC STABILITY PARAMETERS

by

C.P. Schneider

Messerschmitt-Bölkow-Blohm GmbH

Munich

## SUMMARY

This lecture on theoretical methods for the determination of stability derivatives is based on previous theoretical studies at MBB and on a literature survey presented at the AGARD Conference "Dynamic Stability Parameters" in Athens.

The design of modern missiles for military use is characterized by compromises between flight stability and high manoeuvrability. High manoeuvrability yet stable flight performance requires secure missile control at high angles-of-attack and yaw, with possibly rapid changes of these angles and of the roll angle and - not to forget - with coupled motions. From the theoretical viewpoint, this means that the aerodynamic derivatives - needed for performance predictions - result from complex solutions of non-linear and unsteady or quasisteady relations.

The prediction methods and results presented herein are grouped in those which lead to expressions of the derivatives in closed forms - such as slender body theory or those, which require numerical procedures. Only derivatives of longitudinal stability are discussed in detail. For subsonic flow condition, the derivatives of the missile components, i.e. wing and body and their interference - when arranged in configurations - are investigated at high angles-of-attack. With rigid missile components, unsteady flight conditions rarely occur. Therefore, most of the theoretical methods can be reduced to quasi-steady treatment, which simplifies the solution significantly. The scope of performances of modern missiles recently includes high angle-of-attack manoeuvrability in supersonic flight. For slender wings, a prediction method based on the theory of indicial functions, is outlined. Possibilities of obtaining the stability derivatives of bodies at high angle-of-attack in supersonic flight are discussed.

The application of solution methods using finite elements or panelling is presented on the basis of the above mentioned literature study and on a previous AGARD lecture series at the VKI.

## LIST OF SYMBOLS

$a$	speed of sound
$c, c_0, \bar{c}$	total body length, wing root chord and mean wing chord length
$f$	frequency
$f(T)$	indicial function, Fig. 2.4b
$f_0, f_1$	functions in eqs. 5-8, ref. 1
$k, k'$	reduced frequency: $k = qc_0/V$ or $qc/V$ , $k = kD_0/c$
$k^*$	vortex strength
$l_c, l_w$	length of body cylindrical section with constant radius, distance from body nose tip to wing, Fig. 5.4
$m$	parameter specified in ref. 1, $m = \beta + \tan\delta$
$p$	pressure (eq. 57)
$p, q, r$	angular velocities
$s$	half span
$t, T$	dimensionless time parameter, time
$u, v, w$	translational velocities
$\bar{v}$	term, specified in ref. 16, eq. 9
$x, y, z$	dimensionless coordinates
$A$	altitude
$AR$	aspect ratio
$C$	aerodynamic coefficient of forces and moments and their derivatives
$C_N$	normal force coefficient
$C_{Nq}, C_{N\delta}$	linear normal force slope, non-linear normal force coefficient, wing reference area $S$ , body reference area $S_0 = \pi D_0^2/4$ , eqs. 45, Figs. 3.26, 3.27
	normal force damping coefficient, wing reference length and area $\bar{c}$ , $S$ , body reference length and area $D_0$ , $S_0 = \pi D_0^2/4$

$C_{N_C}$	normal force correction, eq. 3
$C_1$	non-linear part of normal force coefficient, eq. 44, 48
$C_m$	pitching moment coefficient
$C_{m\alpha}, C_{mn}$	linear pitch stiffness, non-linear pitching moment coefficient; reference lengths and areas are the same as for $C_{Nq}, C_{Na}$ section 3.4.3, Figs. 3.26, 3.27
$C_{mq}, C_{ma}$	pitch damping coefficient, reference lengths and areas see $C_{Nq}, C_{Na}$
$(C_{mc})_0$	pitching moment correction, eq. 4
$C_2$	non-linear part of pitching moment coefficient, eqs. 50, 52
$C_p$	pressure coefficient
$CD_V$	viscous drag coefficient, section 4.1, eq. 65, Fig. 4.1
$C_{nr}, C_{n\beta}$	coefficients of yawing moments, section 4.2, Fig. 4.5
$D, D_0$	diameter, base diameter
$F$	function, eq. 66
$K$	interference factor, section 5
$K_M$	compressibility factor, section 3.5.1, eq. 53
$L$	lift, Fig. 2.1
$L_1, L_2$	linear operators, eqs. 24, 26
$M, M$	Mach number, pitching moment, section 5
$N, N(t)$	normal force, normal force response function, Fig. 2.4b
$N_\alpha$	normal force slope, Fig. 2.4b
$P_0, P_1$	dimensionless pressure distribution due to plunging (0) and due to pitching (1) respectively
$R$	radius
$S, S_r, S_0$	surface area, reference area, base area
$V$	resultant velocity
$V_c$	cross flow velocity, Fig. 55
$V_0$	body volume, section 4
$X, Y, Z$	coordinates
$X_c$	coordinate of wing camber, eq. 14
$X_N$	location of neutral point, eqs. 3, 4, Fig. 3.3
$X_v$	location of normal force vector induced by leading edge vortices
$X_p, X_1, X_2$	location of pitching axis, eq. 13
$X_1, Y_1, Z_1$	arbitrary location on the wing, Fig. 2.3
$\alpha, \alpha_s$	angle-of-attack, round leading edge correction
$\beta$	Prandtl-Glauert factor
$\gamma$	Euler constant $\gamma = 0.5772$ ; strength of circulation, Figs. 5.7, 5.8
$\delta$	leading edge sweep angle, between leading edge and root chord of the wing, section 3.2
$\phi$	dimensionless time variable, section 3.5.2
$\lambda$	wing taper ratio
$\xi, \eta, \zeta$	dimensionless coordinates, section 3.4.2, eq. 2.4
$\eta, \eta_R$	dimensionless coordinates, $\eta = Y/(R+s)$ ; $\eta_R = R/(R+s)$ , section 5
$\psi_l, \psi_{tr}$	wing leading and trailing edge sweep angle respectively $\psi = 90 - \delta$
$\Delta$	deviation, Fig. 3.24

## 1. INTRODUCTION

The need for extending the operational range and versatility of modern missiles continuously increases standards in performance and efforts in coordination of manoeuvrability and stability. These requirements can be approached to a satisfactory degree only if inputs of experiment and theory enable system-analysts and designers to apply fairly accurate data of aerodynamic forces and moments in the feasibility and development phases. Present and future missile development requires theoretical and experimental investigation of subsonic, transonic and supersonic missile behavior at extreme flight conditions involving mainly high angles of attack and/or fast angular and side motions.

The mathematical equations which are involved, either in prediction theories or for evaluation of experimental data contain non-linear quasisteady terms, rendering solutions extremely difficult, time- and cost-consuming. For a few special although often occurring flight conditions, the relations can be simplified without abandoning essential characteristics in physical interpretation. Herein, mathematical models for the theoretical prediction of unsteady and quasisteady aerodynamic forces and moments of missile components and configurations at moderate and high angle of attack are presented. Two commonly used models are outlined in section 2. They describe the unsteady vertical motions of missiles in a way which enables the reduction to aerodynamic problems associated with potential flow theory. These can be treated analytically on the concept of linearized small perturbation theory and on wave-potential solutions of the wave equation. In section 3, the stability derivatives connected with unsteady vertical motions of wings in the low and high angle-of-attack range are estimated with various theoretical and half-empirical procedures. Section 4 presents methods of determining the corresponding stability parameters of slender missile bodies. The wing-body interference in subsonic flow at high angle of attack is treated in section 5. Finally, section 6 presents a brief survey on the application of numerical solution procedures - such as the panel method for instance.

This lecture concentrates on the aerodynamic parameters of the longitudinal stability in quasisteady flight. Also, steady coefficients, needed in the "quasisteady" analysis, are presented. The simplification introduced to the prediction method by the assumption of quasisteadiness, is not a serious restriction, if rigid missile components are treated. Before confirming the latter statement, a definition of "unsteady" and "quasisteady" motion is given. In fluid dynamics, an arbitrary property of a flow with superimposed time dependent and time independent components is termed by the comprehensive designation "unsteady". The result of the superposition may be a flow whose properties change slowly with time. In this case, the reactions (forces and moments) of a body immersed in the flow may be considered as first order functions of the steady flow conditions. Of second order importance (also magnitude) are the reactions depending directly on the flow conditions changing slowly with time - providing, the deviation from a linear relationship between action and reactions is small. The reactions are quasisteady, i.e. there is no time lag between the flow conditions and the reactional forces and moments of the missile. In case of rapidly changing flow conditions the reactions are strongly dependent on the rates of the flow conditions. They are first order functions of the time dependent conditions. A time lag between action and reaction exists. In this case truly an "unsteady" situation prevails. There is a similarity to the frozen flow condition in chemical kinetics of fluids.

## 2. MATHEMATICAL MODELLING OF UNSTEADY VERTICAL MOTIONS

A measure for differentiation between steady, quasisteady and unsteady lateral motion with respect to the cruising (longitudinal) flight is the reduced frequency  $k$ . It compares lateral and longitudinal velocities. If we consider a missile with angular pitch velocity  $q$ , as shown in Fig. 2.1, the reduced frequency may be defined as  $k = q \cdot c/V$ , where  $V$  is the resultant velocity or cruising speed of the missile and "c" the total body length. A reduced frequency  $k < 0.1$  permits to assume a quasisteady flight condition, where the velocity and its change with time of vertical motions of a rigid missile (Fig. 2.2) is slow compared to the cruising velocity. As shown in Table 2.1, most of the missile types have reduced frequencies equal or smaller than 0.05. In this case, the pitching motion  $q$  can be represented mathematically with a constant velocity which adds a non-constant angle of attack distribution over the length of the missile (or missile component) to the constant angle of attack at cruise velocity. This is demonstrated on the model of a plane wing in Fig. 2.3. Here, the coordinates  $x_1, z_1$  determine an arbitrary location on the wing surface and  $x$  denotes the location of the pitching axis counted from the wing tip (or the origin of the fixed-body system).

The slow or quasisteady vertical motion may be considered a special case ( $k=0$ ) of harmonic pitching and plunging with small amplitude. The latter is the mathematical model most frequently used in numerical procedures for solution of the unsteady linear potential equation (refs. 1, 2).

Another model which is suited to describe linear and non-linear motions as well was proposed by Tobak (ref. 3) and Belotserkovskii (ref. 4). A discontinuous or step-like change of  $\alpha$  or  $q$  initiates the unsteady vertical motion. Fig. 2.4a indicates this step in case of an angle-of-attack change. Before this happens, the body had a steady flight phase, which results in steady-state reactions, such as a constant normal force  $N$ . After the step, the

steady state is approached or restored in a "transient phase", where the normal force changes slowly as seen in Fig. 2.4b. This change is denoted the "indicial function" or response to the step  $\Delta\alpha$ . A superposition of a sequence of equal differential steps  $\Delta\alpha$  can simulate a linear or non-linear motion (Fig. 2.5a). The resultant normal force (Fig. 2.5b) is the sum of like indicial functions  $N(T)$ , beginning subsequently at  $T_n$  of any new step  $\Delta\alpha$ .

The derivatives of the longitudinal stability follow from a Taylor expansion of the aerodynamic coefficients of the normal force and the pitching moment. The independent variables of pitching and plunging motions are  $\alpha$  and  $q$  and the time derivatives thereof are  $\dot{\alpha}$ ,  $\ddot{\alpha}$  ... and  $\dot{q}$ ,  $\ddot{q}$  ... . Retaining in the "expansion" of  $C_N$  and  $C_m$  zero'th and first order terms only, the coefficients  $C_N = C_{N_0}(\alpha, q, \dot{\alpha}, \ddot{\alpha}, \ldots)$  and  $C_m = C_{m_0}(\alpha, q, \dot{\alpha}, \ddot{\alpha}, \ldots)$  are given by the series

$$C_N = C_{N_0} + C_{N_\alpha} \cdot \alpha + C_{N_q} \cdot \frac{q}{V} + C_{N_{\dot{\alpha}}} \cdot \frac{\dot{\alpha}}{V} + \dots$$

and

$$C_m = C_{m_0} + C_{m_\alpha} \cdot \alpha + C_{m_q} \cdot \frac{q}{V} + C_{m_{\dot{\alpha}}} \cdot \frac{\dot{\alpha}}{V} + \dots$$

where we recognize the reduced frequency  $k$ . In the series,  $C_{N_q}$  and  $C_{m_q}$  are derivatives of steady longitudinal stability. They define the normal force slope with the angle-of-attack and the pitch stiffness respectively. The derivatives  $C_{N_\alpha}$ ,  $C_{m_\alpha}$  are quasisteady and defined as normal-force-and pitch-damping. The unsteady derivatives  $C_{N_{\dot{\alpha}}}$  and  $C_{m_{\dot{\alpha}}}$  are denoted the normal-force-and angle-of-attack-damping coefficients.

### 3. STABILITY DERIVATIVES OF WINGS WITH HARMONIC PITCHING AND PLUNGING AT LOW FREQUENCY

#### 3.1 Delta wing in subsonic flow and in the linear angle-of-attack range

The difficulty of solving an unsteady flow problem is greatly reduced if the unsteady motion occurs at low frequency  $k=0$ . All quadratic frequency terms in the unsteady equation and in the boundary condition become negligibly small. In the solution, only linear frequency terms are retained. In physical interpretation this means, that the pressure distribution oscillates with low frequency.

Thus, Garner (ref. 5) simplified his integral equation, which is based on Multhopp's subsonic lifting theory. Results of Garner's solution for delta wings are presented in a report by Goethert and Otto (ref. 6). There, they are compared to various other solutions to the quasisteady potential equation, leading to the determination of pitching derivatives of delta wings at low angle-of-attack ( $\alpha \leq 5^\circ$ ). The comparison covers the theories of Schlichting and Truckenbrodt (ref. 7), Garner (ref. 5), Tobak and Lessing (ref. 8) and Ribner (ref. 9).

The quasisteady method of ref. 7 for thin wings in subsonic flow makes use of a Prandtl-Glauert transformation reducing thereby the potential for compressible flow to one of incompressible flow. The upwash condition to the integral equation provides for two angle-of-attack distributions as shown in Fig. 2.3. Each distribution yields a pressure distribution of its own (ref. 10). Results of this procedure which are linear with the angle-of-attack are shown in Figs. 3.1 and 3.2, where they are compared to experimental data of Thompson and Fail (ref. 11). In addition, theoretical results of Acum and Garner (refs. 12 and 5) for the normal-force- and pitch-damping coefficient of delta wings in subsonic flow are displayed. The work of Tobak and Lessing (ref. 8) deals with damping coefficients of thin wings of arbitrary planform. The analysis of the pitch-damping coefficient  $C_{m_q}$  and the normal-force coefficient  $C_{N_q}$  correspond to those of Ribner (ref. 8). The subsonic coefficients  $C_{m_\alpha}$  and  $C_{N_\alpha}$  caused by a constant vertical acceleration can be estimated with a modification of the solution of the unsteady potential equation for supersonic speed, adding a potential term for adaptation to subsonic speed, where the Kutta-Joukowski condition is to be satisfied at the trailing edge. The solution for delta wings is obtained by use of the loadings of slender wing theory. These are multiplied with a chordwise correction factor accounting for the non-slenderness. Simple expressions are derived this way. The pitch damping is given by

$$(C_{m_q})_0 = \frac{9}{8} \left( \frac{c_o}{c} \right)^2 (C_{m_\alpha})_0 \cdot (C_{N_q})_0 / (C_{N_\alpha})_0 \quad (1)$$

where the subscript "0" indicates that the terms are evaluated for an axis located at the wing apex. In eq. 1, the normal force damping is

$$(C_{N_q})_0 = -\frac{3}{2} \left( \frac{c_o}{c} \right) (C_{m_\alpha})_0 \quad (2)$$

while the functions  $X_N/c_o = -(C_{m_\alpha})_0 (\frac{c_o}{c})/C_{N_\alpha}$  and  $C_{N_\alpha}$  needed in eqs. 1 and 2 are displayed in Fig. 3.3 as functions of the reduced aspect ratio  $\beta \cdot AR$ , where  $\beta = (1-M^2)^{1/2}$ . The unsteady damping coefficients are determined with the relations

$$(C_{N_d})_0 = \frac{1}{2} \left( \frac{c_o}{c} \right) \frac{X_N}{c_o} (C_{N_\alpha} + C_{m_\alpha}), \quad (3) \quad \text{and} \quad (C_{m_d})_0 = -\frac{9}{16} \left( \frac{c_o}{c} \right)^2 \left( \frac{X_N}{c_o} \right)^2 C_{N_\alpha} + (C_{m_\alpha})_0. \quad (4)$$

The correction terms  $C_{Nq}$  and  $(C_{Mq})_0$  in eqs. 3 and 4 are given as functions of  $\beta \cdot AR$  in Fig. 3.4. Results of  $C_{Mq} + C_{Md}$  for delta wings with  $AR = 1.45$ , 2 and 4 are plotted versus the Mach number in Figs. 3.5 - 3.7 respectively. They are compared to experimental and other theoretical data in subsonic flow by Brune and Dusto (ref. 13) and Ericsson and Reding (ref. 14). Although different approaches to the solution of the potential equations are chosen by Garner (ref. 5) and by Tobak and Lessing (ref. 8), the load distributions obtained either way are the same, as demonstrated in ref. 6. The two-dimensional method of Ribner (ref. 9) delivers unsatisfactory results for wings with  $AR > 0$ , as the Kutta-Joukowski condition in subsonic flow is not met without the above mentioned correction terms.

### 3.2 Delta wing in supersonic and transonic flow and in the linear angle of angle-of-attack-range

Several procedures reduce the boundary value problem associated with a given planform in unsteady supersonic flow to an equivalent problem in steady flow. One of them is developed by Miles (ref. 1) applying a frequency expansion to the solution of the Fourier transformed potential equation. At very low frequency, of the expanded terms only the ones of first order in frequency are retained. For a slender delta wing, Miles constructs a simple exact solution to the problem. The resulting relations for the steady and unsteady derivatives of longitudinal stability of delta wings with supersonic leading edges involve the functions  $f_0$  and  $f_1$  representing the zero'th and first order potentials, corresponding to a constant unit angle of attack and to the angle of attack distribution along the wing chord due to a constant rotational velocity about the pitch axis  $X_p$ . The functions  $f_0$  and  $f_1$  are dependent on  $m = \beta \tan \delta$  (see Fig. 3.8). The leading edge sweep angle  $\delta$  lies between leading edge and root chord of the wing. The parameter  $m < 1$  or  $m > 1$  designates a delta wing as one with subsonic or supersonic leading edge respectively. The derivatives of a delta wing with subsonic leading edge ( $m \leq 1$ ) are determined with a set of closed relations, which are used to calculate complimentary data in Figs. 3.1, 3.2, 3.9 and 3.10. The damping derivatives, presented as sums  $C_{Nq} + C_{Nd}$  and  $C_{Mq} + C_{Md}$  in ref. 1 are separated into their components for  $m \leq 1$  in eqs. 5-8, in order to show the influence of either  $C_{Nd}$  and  $C_{Nq}$  or  $C_{Md}$  and  $C_{Mq}$  on the wing stability, which may differ depending on the parameter  $m$ .

$$C_{Nq} = (4/\beta) (c_o/\bar{c}) \left( \frac{2}{3} f_1 - \frac{X_p}{c_o} f_0 \right), \quad (5)$$

$$C_{Nd} = (4/\beta) (c_o/\bar{c}) \left[ \frac{1}{3} f_0 - \frac{M^2}{\beta^2} (f_0 - \frac{2}{3} f_1) \right], \quad (6)$$

$$C_{Mq} = -(4/\beta) (c_o/\bar{c})^2 \left\{ \left[ \left( \frac{X_p}{c_o} - \frac{2}{3} \right)^2 + \frac{1}{18} \right] f_0 + \left( \frac{1}{2} - \frac{2}{3} \frac{X_p}{c_o} \right) (f_1 - f_0) \right\} \quad (7)$$

and

$$C_{Md} = (4/\beta) (c_o/\bar{c})^2 \left[ f_0 - \frac{3M^2}{\beta^2} (f_0 - \frac{2}{3} f_1) \right] \left( \frac{1}{3} \frac{X_p}{c_o} - \frac{1}{4} \right). \quad (8)$$

Setting  $f_0 = f_1 = 1$  in eqs. 5-8, yields the derivatives for delta wings with supersonic leading edge. The results obtained with eqs. (5-8) for a delta wing of  $AR=4$  are compared to experimental data for a cropped delta wing  $AR=3$ ,  $\lambda = 0.072$  by Orlik-Rückemann and Laberge (ref. 15) in Fig. 3.10. Also, in Fig. 3.2, theoretical results obtained with eqs. (5-8) are displayed.

Estimating pitching and plunging derivatives of wings in transonic flow, Landahl (ref. 16) uses a Fourier transformed differential equation, a slender wing potential as first order solution and higher order terms according to Adams and Sears (ref. 17), accounting for deviation from slenderness. The solution is simple if the requirements of a continuous leading edge slope and curvature of the wing is satisfied and if the angle of attack distribution and its first two derivatives with  $X$  have no discontinuities. The delta wing fulfills the requirements. For low frequency pitching and plunging oscillations, Landahl derives the stability derivatives from generalized force coefficients for low aspect ratio delta wings at transonic speed. The damping derivatives are

$$C_{Nq} = \frac{\pi AR}{2} (c_o/\bar{c}) \left[ 1 - \frac{X_p}{c_o} - \frac{\pi k AR^2}{64} \left( \frac{3}{2} - \frac{X_p}{c_o} \right) \right] + \frac{\pi AR}{2} \frac{c_o}{\bar{c}} \frac{\pi k AR^4}{4096} (6\bar{v} - \frac{15}{8}), \quad (9)$$

$$C_{Nd} = \frac{\pi AR}{2} (c_o/\bar{c}) \left[ \frac{1}{3} - \frac{AR^2}{64} (2\bar{v} + \frac{k\pi}{2}) \right], \quad (10)$$

$$C_{Mq} = -\frac{\pi AR}{2} (c_o/\bar{c})^2 \left\{ \frac{3}{4} - \frac{5}{3} \frac{X_p}{c_o} + \left( \frac{X_p}{c_o} \right)^2 - \frac{AR^2}{64} \left[ \frac{3}{8} + \pi k \left( \frac{6}{5} - \frac{9}{4} \frac{X_p}{c_o} + \left( \frac{X_p}{c_o} \right)^2 \right) \right] \right\}, \quad (11)$$

$$C_{m\dot{\alpha}} = -\frac{\pi AR}{2} (c_0/\bar{c})^2 \left\{ \frac{1}{3} \left( \frac{3}{4} - \frac{x_p}{c_0} \right) - \frac{AR^2}{64} \left[ 2\bar{v} \left( \frac{3}{4} - \frac{x_p}{c_0} \right) - \frac{1}{2} + \pi k \left( \frac{2}{5} - \frac{1}{2} \frac{x_p}{c_0} \right) \right] \right\}, \quad (12)$$

where  $\bar{v} = \ln \frac{128}{KAR^2} - \gamma$ , and  $\gamma = 0.5772$  denotes the Euler constant. Similar to eq. 9 for  $C_{Nq}$ , eq. 11 may contain higher order terms in the aspect ratio ( $AR^4$ ). They are not given here (following ref. 18), as an apparent misprint of the generalized force coefficients in ref. 16 cannot be eliminated without greater effort or consulting Landals original work (ref. 19). The results obtained for a delta wing with  $AR = 4$  at  $M = 1$  are meant as complementary data for Figs. 3.9 and 3.10. There, they are not plotted because of their relatively large amounts exceeding the scale of the ordinates. The normal force slope is  $C_{Nq} = 6$ , and for  $x_p/c_0 = 0$  the pitch stiffness is  $(C_{m\alpha}) = -6$  according to ref. 16. The second order terms containing  $AR^2$  reduce the absolute values of both derivatives by approximately 4% of the first order term, when a low frequency  $k = 0.05$  is assumed. The absolute value of  $C_{m\dot{\alpha}} = -8.6$  by eq. 11 is 20% lower than the value of the first order term by itself. The unsteady derivative  $C_{m\dot{\alpha}} = 18.7$  provides a "positive" damping coefficient  $C_{m\dot{\alpha}} + C_{m\ddot{\alpha}} = 11.1$  for a pitch axis at the apex. The normal force damping coefficient equals  $C_{Nq} = 8.9$  without and 11.2 with the third order term containing  $AR^4$ . This amounts to a 25% increase over the value obtained from the first and second term of eq. 9. Both, the unsteady damping coefficient  $C_{N\dot{\alpha}} = -18$  and the sum  $C_{Nq} + C_{N\dot{\alpha}} = -9.1$  are negative.

### 3.3 Accuracy of the delta wing derivatives, transformation of the pitch axis

For various pitch axis locations and aspect ratios, the derivatives of delta wings are displayed in Figs. 3.1, 3.2, 3.5 - 3.9 and 3.10. The results are either obtained from eqs. 1-12 (refs. 1, 8 and 16), or determined with relations from ref. 14, or taken from numerical calculations (refs. 5, 10, 13). They cover the Mach range  $0 < M < 3.5$ . All theoretical data and corresponding experimental results collected in a diagram for each derivative will provide a survey on the accuracy of derivatives of delta wings. The results of the survey may be generalized and transferred to other wing shapes. The transfer appears commonly accepted: For the confirmation of numerical data the delta wing is usually chosen as "testing" shape offering the possibility of comparison to exact solutions. The comparison of data in a single diagram for each derivative requires a transformation of  $C_{m\alpha}$ ,  $C_{Nq} + C_{N\dot{\alpha}}$  and  $C_{m\dot{\alpha}} + C_{m\ddot{\alpha}}$  to a common pitch axis. This is done with relations taken from refs. 10 and 15 which are adapted to the present notation of derivatives and to the coordinate system of Figs. 2.1 and 3.11. A common pitch axis location  $x/c_0 = 0.5$  is chosen. The shift of  $\Delta X/\bar{c} = (X_1 - X_2)/\bar{c}$  from  $X_1$  to the new axis  $X_2$  with  $|x_2| < |x_1|$  yields in case of the new damping moment

$$(C_{m\dot{q}} + C_{m\ddot{\alpha}})_2 = (C_{m\dot{q}} + C_{m\ddot{\alpha}})_1 + (\Delta X/\bar{c}) (C_{m\alpha})_1 - (\Delta X/\bar{c}) (C_{Nq} + C_{N\dot{\alpha}})_1 - (\Delta X/\bar{c})^2 \cdot C_{N\alpha}. \quad (13)$$

The efficiency of the transformation relations (refs. 10, 15) is demonstrated with Figs. 3.12 - 3.15, where the derivatives of delta wings in subsonic flow are shown as functions of the pitch axis location: The theoretical results match well with measured data. This is confirmed also in ref. 37. The theoretical data of Figs. 3.1, 3.2, 3.5 - 3.7, 3.9 and 3.10 complimented by the analytical results of Martin, Smith et al. (refs. 20 and 21), are collected in Figs. 3.16 - 3.19. The aspect ratio ( $AR = 0.9, 1.5, 2$  and  $4$ ) is chosen as parameter. The scattering of results provided by the various theories for a specific aspect ratio leads to data bandwidths, which - in the case of  $AR = 0.9, 1.5$  and  $2$  - are transferred to the diagrams (Figs. 3.20-3.23) with experimental results by refs. 15, 22-28. This enables one to determine the deviation from the mean values for each derivative. For delta wings with  $AR \leq 2$ , the average deviations of  $C_{Nq}$ ,  $C_{m\dot{q}}$ ,  $C_{Nq} + C_{N\dot{\alpha}}$  and  $C_{m\dot{q}} + C_{m\ddot{\alpha}}$  from the mean values are displayed in percentage as function of the Mach number  $0 \leq M \leq 3$  (see Fig. 3.24). Theoretical results alone would give narrower bands of data scattering. The derivatives of fig. 3.20 include experimental results. The relatively large deviation of  $C_{Nq} + C_{N\dot{\alpha}}$  is caused by the use of eq. 13 for the generation of additional values, which often are missing in theory or experiment. This procedure involves repeated transformation of the coefficients  $C_{m\dot{q}} + C_{m\ddot{\alpha}}$  introducing twice the inaccuracy of this derivative to  $C_{Nq} + C_{N\dot{\alpha}}$ . The overestimation of the deviation of  $C_{Nq} + C_{N\dot{\alpha}}$  is apparent in Fig. 3.24. Values in the order of the deviations of  $C_{m\dot{q}} + C_{m\ddot{\alpha}}$  appear more appropriate.

### 3.4 Wings of arbitrary planform in subsonic flow and in the non-linear angle-of-attack range

The non-linear angle-of-attack dependence of forces and moments of wings, oscillating about a mean incidence may be predicted using the free vortex model of Bollay (ref. 29). The model was successfully applied in subsonic steady wing aerodynamics in ref. 30 and 31: The free vortices of a horse shoe vortex distribution over the wing surface at the incidence  $\alpha$  separate at an angle  $\alpha/2$ , as shown in Fig. 3.25. The latter assumption is based on observations in experiments. In connection with a low frequency expansion, Garner and Lehrian (ref. 32) used the model assuming a small amplitude oscillation of the vortices about  $\alpha/2$ . Their analytic method is based on Multhopp's subsonic lifting surface theory (ref. 5) and is applied to a slender gothic wing. The damping coefficients  $C_{Nq} + C_{N\dot{\alpha}}$  and the non-linear steady stability coefficients  $C_{Nn}$ ,  $C_{mn}$  obtained in ref. 32 are shown in Fig. 3.26. Applying the approach of Schlichting and Truckenbrodt (ref. 7), which leads to two steady angle-of-attack distributions (Fig. 2.3), the free vortex model of Bollay may be used to derive the non-linear stability coefficients  $C_{Nq}$  and  $C_{mn}$ , and the damping derivatives  $C_{Nq}$  and  $C_{m\dot{q}}$  for arbitrary wing shapes. This procedure (ref. 10) will be presented subsequently in detail.

### 3.4.1 Downwash velocity in case of pitching

The angle-of-attack distribution due to a constant pitching velocity is similar to the one of a cambered wing. A wing with an angle-of-attack  $\alpha$  and with the camber  $\alpha_1(X)$  has the total angle of attack distribution  $\alpha(X) = \alpha + \alpha_1(X)$ . This results in a normal force coefficient

$$C_N = \alpha \frac{\partial C_N}{\partial \alpha} + \alpha_1(X_C) \left( \frac{\partial C_N}{\partial \alpha} \right)_C, \quad (14)$$

where  $\alpha_1(X_C)$  describes the wing camber, i.e. the deviation of the wing surface in Z-direction. In case of harmonic oscillatory pitching motion with the rotational speed  $q$  the deviation in Z-direction of the plane wing surface is a complex property, given by

$$\hat{z} = \hat{Z}(X, T) = Z(X) \exp(iqT) \quad (15)$$

Given a pitching axis  $x_p$  and an amplitude  $\alpha$ , we have

$$Z(X) = -\alpha(X_1 - x_p), \quad (16)$$

as shown before in Fig. 2.3. The downwash  $w$ , which is assumed to be positive in positive Z-direction (Fig. 2.1), is given by

$$\hat{w} = \frac{DZ}{DT} = \frac{\partial Z}{\partial T} + V \frac{\partial Z}{\partial X} = V \frac{\partial Z}{\partial X} + iqZ. \quad (17)$$

Introducing here eq. 16, dimensionless variables  $x = X/\bar{c}$ ,  $t = VT/\bar{c}$  and the reduced frequency  $k = qc/V$ , we obtain

$$\frac{\hat{w}(x,t)}{V} = -\alpha(1 + ik(x-x_p)) \exp(ikt)$$

or, using the relation  $\alpha(x,t) = -w(x,t)/V$

$$\hat{\alpha}(x,t) = \alpha(1 + ik(x-x_p)) \exp(ikt)$$

The expansion of the exponential frequency term  $\exp(ikt) = 1 + ikt + \dots$  may be reduced to the zeroth-order term (i.e. "1"), providing the reduced frequency is much smaller than "1", as defined in unison with the definition of quasisteadiness in section 2. We then get

$$\hat{\alpha}(x) = \alpha(1 + ik(x-x_p)). \quad (18)$$

An expansion of the downwash velocity in a Taylor Series with respect to the reduced frequency yields according to refs. 1 and 33:

$$\frac{\hat{w}}{V} = \frac{1}{V_0} k^{2n} (w_{2n} + ikw_{2n+1}).$$

Retaining the zeroth term only

$$\frac{\hat{w}}{V} = \frac{1}{V} (w_0 + ikw), \quad (19)$$

a comparison of eqs. 18 and 19 yields two downwash distributions, namely the real part

$$\frac{w_0}{V} = -\alpha \quad (20)$$

and the imaginary part

$$\frac{w_1}{V} = -\alpha(x-x_p). \quad (21)$$

In analogy to eq. 14, i.e. the normal force coefficient of a cambered wing, we achieve in case of a pitching motion

$$C_N = \alpha \frac{\partial C_N}{\partial \alpha} + ik\alpha(x-x_p) \frac{\partial C_N}{\partial \alpha}. \quad (22)$$

Comparing eq. 22 with the series expansion of  $C_N$  in section 2, disregarding the complex number  $i$ , we get

$$\hat{C}_N = \alpha C_{N_\alpha} + ikC_{N_q}$$

and correspondingly a normal force damping coefficient

$$C_{N_q} \equiv \alpha(x-x_p) C_{N_\alpha}. \quad (23)$$

### 3.4.2 Integral equations of non-linear lifting surface theory

With known angle-of-attack distribution we have a boundary condition on the wing surface, which enables the determination of the vortex strength distribution  $k^* = V\Delta C_D/2$  over the wing surface. The Kutta condition requires the resulting normal velocity to vanish on the wing surface. In linear theory, linear operators are used to form the surface condition

$$\alpha_i = L_1(k^*),$$

where  $\alpha_i$  is the induced angle of attack or the downwash angle  $\alpha_i = -w(x,y)/V$ . The linear operator

$$L_1(k^*) = \frac{1}{4\pi V} \int_{x_1}^{x_{tr}} \int_1^{\infty} \frac{\partial}{\partial n} \{ k^*(\xi, n) (1 + \frac{x-\xi}{\sqrt{(x-\xi)^2 + \beta^2(y-n)^2}}) \} \frac{dn d\xi}{y-n} \quad (24)$$

is given by the integral equation (eq. 24, refs. 5, 7, 31). It defines the induced downwash velocity  $-w(x,y)$  caused by  $k^*$ . The integral of eq. 24 extends over the wing surface from leading ( $x_1$ ) to trailing edge ( $x_{tr}$ ) and between the wing tips. In the high angle-of-attack range, the physical model of free vortices lying on the wing surface does not hold up to reality. The free vortex model of refs. 29 and 30 proposes the free vortices to emanate from the wing surface under an angle of  $\alpha/2$  (Fig. 3.25). For this situation one needs two linear operators to define the downwash velocity or the induced angle-of-attack

$$\alpha_i = L_1(k^*) + \frac{\alpha}{|\alpha|} \alpha_i L_2(k^*), \quad (25)$$

where the second operator is defined as

$$L_2(k^*) = \frac{1}{8V} \frac{\partial^2}{\partial y^2} \{ \int_{x_1}^{x_{tr}} (1 + \frac{x-\xi}{|x-\xi|}) k^*(\xi, n) (x-\xi) d\xi \}. \quad (26)$$

In eq. 26,  $\alpha_i$  is the local angle-of-attack induced at the surface location  $(x,y)$ . The angle  $\alpha$  represents the incidence of the wing with respect to the direction of the undisturbed flow.

Introducing a vortex distribution

$$k^* \equiv k_1^* \alpha + k_2^* \alpha^2 \quad (27)$$

to eq. 25, one gets the induced angle-of-attack

$$\alpha_i = L_1(k_1^*) \alpha + L_1(k_2^*) \alpha^2 + \frac{\alpha}{|\alpha|} \alpha_i L_2(k_1^*) \alpha + \frac{\alpha}{|\alpha|} \alpha_i L_2(k_2^*) \alpha^2. \quad (28)$$

Setting  $\alpha_i = \alpha$  for wings without camber, using the approximation  $\alpha_i = \alpha$  for cambered wings neglecting the fourth term (with  $\alpha^3$ ) on the right hand side of eq. 28, leaves us an equation which permits the separation into terms with same order potentials in  $\alpha$ :

$$\alpha_i = L_1(k_1^*) \alpha \quad \text{or} \quad 1 = L_1(k_1^*) \quad (29)$$

and

$$L_1(k_2^*) = -L_2(k_1^*). \quad (30)$$

Substituting eq. 29 in the integral equation (eq. 24), yields the relationship

$$1 = \frac{1}{4\pi V} \frac{x_{tr}}{x_1} \int_{-1}^{+1} \frac{\partial}{\partial n} \left\{ k_1^*(\xi, n) \left( 1 + \frac{(x - \xi)}{\sqrt{(x-\xi)^2 + \beta^2(y-n)^2}} \right) \right\} \frac{d\xi dn}{y-n},$$

which can be solved numerically with the method of Truckenbrodt (ref. 34). The mathematical statement for the determination of  $k_1^*(\xi, n)$  contains the normal distributions over subsonic wings according to Birnbaum and also the distributions of the circulation and pitching momentum of the linear theory. In order to solve the non-linear part of the integral equation,  $k_1^*$  is substituted in eq. 26. The integral of the operator  $L_2$  has a straight forward solution. With known  $L_2(k_1^*)$  follows from eq. 30, where  $k_1^*$  is also formed with the normal distributions of Birnbaum, adding terms with quadratic dependence on  $\alpha$ .

### 3.4.3 Estimation of $C_{Nq}$ and $C_{mq}$ with the non-linear theory

Following the formulation of  $\alpha(x)$  in eq. 19, a complex expression is developed for the vortex strength:

$$\hat{k}^* = k_R^* + ikk_I^* \quad (31)$$

where  $k_R^*$  and  $k_I^*$  define the real and imaginary part respectively. According to eq. 27 one gets

$$k_R^* = k_{1R}^* \alpha + k_{2R}^* \alpha^2 \quad (32)$$

and

$$k_I^* = k_{1I}^* \alpha + k_{2I}^* \alpha^2. \quad (33)$$

The linear operators  $L = L_1 + \alpha L_2$ , and the angle-of-attack distribution for pitching about a mean incidence  $\alpha$  are combined following eq. 25:

$$\alpha(1 + ik(x-x_p)) = L_1(k_R^* + ikk_I^*) + \alpha L_2(k_R^* + ikk_I^*). \quad (34)$$

The combination of eqs. 32, 33 and 34 yields as real part a constant angle-of-attack distribution

$$\alpha = L_1(k_{1R}^* \alpha + k_{2R}^* \alpha^2) + \alpha L_2(k_{1R}^* \alpha + k_{2R}^* \alpha^2), \quad (35)$$

and as imaginary part an angle-of-attack distribution due to pitch, which changes linearly with  $x$ :

$$\alpha(x-x_p) = L_1(k_{1I}^* \alpha + k_{2I}^* \alpha^2) + \alpha L_2(k_{1I}^* \alpha + k_{2I}^* \alpha^2). \quad (36)$$

Separating eqs. 35 and 36 by equal coefficients, the real system has a linear part in terms of  $\alpha$

$$1 = L_1(k_{1R}^*) \quad (37)$$

and a non-linear part

$$L_1(k_{2R}^*) = -L_2(k_{1R}^*). \quad (38)$$

The third order potential term in  $\alpha$  is neglected as before in eq. 28. The separation of the imaginary system accordingly yields

$$(x - x_p) = L_1 k_{1I}^* \quad (39)$$

and

$$L_1(k_{2I}^*) = -L_2(k_{1I}^*). \quad (40)$$

Thus, the mathematical statements needed for the solution of the integral equations in case of pitching motions are known. The vortex strengths  $k_R^*$  and  $k_I^*$ , the linear numerical procedure of ref. 34 and the non-linear method of refs. 30 and 31 allow to determine the non-linear normal force- and pitching moment coefficients. They are given by

$$\hat{C}_N = \frac{2}{S_r \cdot V} \int_S (k_R^* + ik_I^*) ds = \frac{2\alpha}{S_r \cdot V} \int_S (k_{1R}^* + \alpha k_{2R}^*) ds + i \frac{2\alpha k}{S_r \cdot V} \int_S (k_{1I}^* + \alpha k_{2I}^*) ds, \quad (41)$$

and

$$\begin{aligned} \hat{C}_m = - \frac{2}{S_r \cdot V \cdot C} \int_S (x - x_p) \cdot (k_R^* + ik_I^*) ds &= - \frac{2\alpha}{S_r \cdot V \cdot C} \int_S (x - x_p) \cdot (k_{1R}^* + \alpha k_{2R}^*) ds \\ &- i \frac{2\alpha k}{S_r \cdot V \cdot C} \int_S (x - x_p) \cdot (k_{1I}^* + \alpha k_{2I}^*) ds. \end{aligned} \quad (42)$$

With  $\hat{C}_N(x) = \alpha C_{N_\alpha} + ikC_{N_q}(x)$  one derives from eq. 41:

$$\hat{C}_N = \alpha \left( \frac{\partial C_N}{\partial \alpha} \right)_R + \alpha C_{1R} + ik \frac{x_{tr}}{x_1} (x - x_p) \cdot \left( \left( \frac{\partial C_N}{\partial \alpha} \right)_I + \alpha C_{1I} \right) dx,$$

where by comparison with eq. 41 a linear normal force derivative is given by

$$\left( \frac{\partial C_N}{\partial \alpha} \right)_R = \frac{2}{S_r \cdot V} \int_S k_{1R}^* ds \quad (43)$$

and a non-linear term by

$$C_{1R} = \frac{2}{S_r \cdot V} \int_S k_{2R}^* ds. \quad (44)$$

The addition of eqs. 43 and 44 yields a "non-linear" normal force coefficient

$$C_{N_n} = \frac{\partial C_N}{\partial \alpha} + \alpha C_{1R}. \quad (45)$$

The non-linear normal force damping coefficient

$$C_{N_q} = \frac{x_{tr}}{x_1} (x - x_p) \cdot \left( \frac{\partial C_N}{\partial \alpha} \right)_I + \alpha C_{1I} dx \quad (46)$$

separates into the linear term in  $\alpha$

$$\frac{x_{tr}}{x_1} (x - x_p) \cdot \left( \frac{\partial C_N}{\partial \alpha} \right)_I dx = \frac{2}{S_r \cdot V} \int_S k_{1I}^* ds \quad (47)$$

and the non-linear

$$\frac{x_{tr}}{x_1} (x - x_p) C_{1I} dx = \frac{2}{S_r \cdot V} \int_S k_{2I}^* ds. \quad (48)$$

Similarly, for the non-linear pitching moment coefficient  $C_{m_n} = \left( \frac{\partial C_m}{\partial \alpha} \right)_R + \alpha C_{2R}$  and the pitch damping coefficient  $C_{m_q} = \alpha \frac{x_{tr}}{x_1} (x - x_p) \cdot \left( \left( \frac{\partial C_m}{\partial \alpha} \right)_I + \alpha C_{2I} \right) dx$  one derives

by comparison with eq. 42:

$$\left( \frac{\partial C_m}{\partial \alpha} \right)_R = - \frac{2}{S_r \cdot V \cdot C} \int_S (x - x_p) k_{1R}^* ds, \quad (49)$$

$$C_{2R} = - \frac{2}{S_r \cdot V \cdot C} \int_S (x - x_p) k_{2R}^* ds, \quad (50)$$

$$\int_{x_1}^{x_{tr}} (x-x_p) \left( \frac{\partial C_m}{\partial \alpha} \right)_I dx = - \frac{2}{S_r V_c} \int_S (x-x_p) k_1^* I ds, \quad (51)$$

and finally

$$\int_{x_1}^{x_{tr}} (x-x_p) C_2 I dx = - \frac{2}{S_r V_c} \int_S (x-x_p) k_2^* I ds. \quad (52)$$

### 3.4.4 Results of non-linear theory in comparison to experimental and other analytical data

The non-linear static stability coefficients  $C_{Nn}$ ,  $C_{mn}$  and the damping derivatives  $C_{Ng}$  and  $C_{mg}$  were determined for delta wings with the method described in sections 3.4.1-3.4.3. The delta wing results obtained this way are compared in Figs. 3.26 and 3.27 to experimental results of Schmidt (ref. 24) and of Woodgate and Pugh (ref. 26). As already mentioned in section 3.4, the analytical data of Garner and Lehrman (ref. 32) are also shown in Fig. 3.26 in addition to those of Ericsson and Reding's theory (refs. 35, 36) in the diagrams of both figures. The agreement between experimental and analytical derivatives shown here as functions of the angle-of-attack is satisfactory. The quality of analytical results by the method in sections 3.4.1-3.4.3 was confirmed lately with new experimental results for arbitrary wing shapes (ref. 37).

In Figs. 3.26 and 3.27, the derivatives change linearly with  $\alpha$ . The non-linear character becomes noticeable when the total aerodynamic coefficients  $C_N$  and  $C_m$  are formed. From Figs. 3.26, 3.27 and other delta wing data (ref. 10) one may deduce, that the amount of the pitch damping coefficient  $C_{mg}$  decreases with increasing aspect ratio. According to the predictions of Tobak (ref. 3), this behavior is expected with delta wings between  $0.9 < AR < 1.6$ . For  $AR < 0.9$ , the coefficient  $C_{mg}$  has the same sign as  $C_{mg}$  and increases the stabilizing effect of the total damping coefficient  $C_{mg} + C_{m\alpha}$ . For larger aspect ratios  $AR > 1.6$  a change of the sign of  $C_{mg}$  decreases the amount of the total damping coefficient with a tendency to destabilization. The physics causing the changes of  $C_{mg}$  with  $AR$  can be explained with the changes of the pressure - or normal force distribution over the wing during the transient phase after a step  $\Delta\alpha$ , giving rise to the indicial function shown before in Fig. 2.4b. Further details will be given in section 3.5.2.

### 3.5 Slender wings in supersonic flow and in the non-linear angle-of-attack range

A semi-empirical method for the determination of unsteady aerodynamic coefficients of longitudinal stability of slender wings at high angle-of-attack in supersonic flow was developed by Ericsson and Reding (ref. 14). The non-linear steady coefficients ( $C_{Nn}$ ,  $C_{mn}$ ) of this method will be used in connection with Tobak's indicial function theory (ref. 3), in order to estimate non-linear unsteady derivatives. The combination of the two procedures was attempted in ref. 38 in order to derive aerodynamic coefficients of delta wings with subsonic and supersonic leading edges.

#### 3.5.1 Non-linear steady coefficients $C_{Nn}$ and $C_{mn}$ of delta wings

The semi-empirical method of ref. 14 superimposes an attached potential flow and a flow separating from the leading edge in modelling the conditions about delta wings at high incidence. As practiced in potential theory, deviations from the mean incidence must be small. The derivatives for attached flow are obtained with a modification of the slender body theory: It is assumed that the Kutta condition is valid for wings with sharp leading edges. In this case leading edge suction lowers the reactional forces of the wing. This behavior is taken into account by correction factors, covering the influence of the angle-of-attack and the compressibility effect. The latter influence was considered similarly in earlier work by Jones (ref. 39). For the purpose of discernibility, the non-linear force coefficient  $C_{Nn}$  for attached flow is given the index "1":

$$C_{Nn(1)} = \frac{\pi AR}{2} K_M (\cos^2 \alpha - \sin^2 \alpha), \quad (53)$$

where

$$K_M = \frac{2}{1 + \frac{8AR}{4} + \sqrt{1 + (\frac{8AR}{4})^2}}$$

is the compressibility factor and  $(\cos^2 \alpha - \sin^2 \alpha)$  the angle-of-attack factor. The non-linear pitching moment coefficient is given by

$$C_{mn(1)} = \frac{\pi AR}{2} K_M \frac{c_o}{c} \left( \frac{x_p}{c_o} - \frac{x_n}{c_o} \right) (\cos^2 \alpha - \sin^2 \alpha). \quad (54)$$

In subsonic flow the resultant normal force vector is located at  $x_n/c_o = 2/3$  of the wing root chord measured from the apex. In the supersonic flow range  $1 \leq M \leq \sqrt{1 + (4/AR)^2}$  the

vector is located at  $X_n/c_o = K_N + 2/3$ . Fig. 3.28 provides a diagram for the determination of  $C_{Nn}(1)$  as function of the angle-of-attack.

The aerodynamic coefficients for detached flow are given the index (2). These coefficients are estimated with a procedure based on Polhamus' leading edge suction theory (refs. 41, 41). In the supersonic range  $1 \leq M \leq \sqrt{1 + (4/AR)^2}$  the normal force coefficient

$$C_{Nn}(2) = \pi \sqrt{1 + (\frac{AR}{4})^2} K_M^2 \sqrt{1 - (\frac{AR}{4})^2} \sin 2(\alpha - \alpha_s) \quad (55)$$

contains an effective angle-of-attack ( $\alpha - \alpha_s$ ), which is corrected by  $\alpha_s \neq 0$  when round instead of sharp leading edges are present, i.e. for sharp leading edges  $\alpha_s = 0$ . The pitching moment coefficient is given by

$$C_{mn}(2) = \frac{c_o}{\bar{c}} \left[ -0.3 \left( \frac{x_p}{c_o} - \frac{x_n}{c_o} \right) + 0.7 \left( \frac{x_p}{c_o} - \frac{x_v}{c_o} \right) \right] C_{Nn}(2) \quad (56)$$

where  $x_v/c_o = 0.587$  within  $1 \leq M \leq \sqrt{1 + (4/AR)^2}$  is a parameter which defines the location of the normal force vector induced by separated leading edge vortices. For sharp leading-edged delta wings, the coefficient  $C_{Nn}(2)$  may be read off Fig. 3.29. The total non-linear coefficient are given by summing  $C_{Nn}(1) + C_{Nn}(2)$  and  $C_{mn}(1) + C_{mn}(2)$  from eqs. 53, 54 and eqs. 55, 56 respectively.

### 3.5.2 Indicial function method applied to delta wings with subsonic leading edge

In case of subsonic leading edges the indicial functions or response functions of the reactions on a step-like deviation from steady flight conditions (Fig. 2.4) are dependent on the wing geometry. The intersections and lines of interactions between Mach waves emanating from the apex and from wing edges define regions of differing pressure distribution. For simplicity, the change of pressure distribution with time is shown for a wing cord only (Fig. 3.30). As seen, sections of different pressure distributions are limited by the traces of Mach waves. The corresponding regions of the surface of a delta wing have the leading edge slope as additional limit. The integration of the pressure distribution over the various regions at a certain time after the step-like deviation yields a value of the indicial function or the response function at this time. The integration of the indicial function that follows a chosen deviation over a time period, beginning with the steps and ending when new steady state conditions are approached, provides the corresponding unsteady derivative. The procedure shall be demonstrated in the case of an angle-of-attack step  $\Delta\alpha$  (plunging) of a slender delta wing.

For a slender delta wing, the unsteady three dimensional flow problem can be simplified. With the assumption that flow velocity gradients in the X-direction are negligibly small, the slender wing surface can be divided into strips parallel to the Y coordinate. Each strip can be treated separately as a rectangular wing with an infinite aspect ratio. This way, the unsteady three dimensional problem is reduced to an unsteady two dimensional one. According to strip theory, a wing section A-A moving with V covers the area shown in the Y-t' diagram of Fig. 3.31a, where  $t' = t \cdot a$  has the dimension of a length. The waves beginning at the wing tips follow the projected paths. In the chosen coordinate system, where the speed of any disturbance is the same in the Y and t' direction, the shock waves and their reflexions always form angles of 45 degrees with the traces of the wing tips. The wave-path pattern of Fig. 3.31a suggests a coordinate transformation  $t' \rightarrow X$ . This converts the unsteady problem into a steady one as shown in Fig. 3.31b. Here, the former wave projections have become Mach cones of  $\tan \mu = 1/\beta = 1$ . Now, a rectangular wing of span  $2s$  and of an infinite chord length (no longer an infinite aspect ratio as in Fig. 3.31a) at a supersonic speed  $M = \sqrt{2}$  is to be investigated.

Plunging ( $\Delta\alpha$ ) and pitching ( $\Delta q$ ) motions are treated this way in ref. 3. The dimensionless pressure distribution for plunging is defined by

$$P_0 = \frac{M}{2sa} \int_{-s}^{+s} \frac{\Delta p}{\rho V^2/2} dy \quad (57)$$

and the one for pitching is given by

$$P_1 = \frac{(M \cdot V \cdot \tan \delta)}{2s^2 q} \int_{-s}^{+s} \frac{\Delta p}{\rho V^2/2} dy.$$

These distributions are defined as functions of time  $t$  beginning at the event of the disturbance ( $\Delta\alpha$  or  $\Delta q$ ). A dimensionless time parameter  $t'/s = t \cdot a/s$  is formed with the speed of sound ( $a$ ) and the half span ( $s$ ). The parameter  $t'$  already appeared in Fig. 3.31a. A factor  $M \cdot s / c_0$  converts  $t'/s$  in a new dimensionless variable  $\theta = Mt'/c_0$ , which enables a comparison of the variable  $X$  of the steady problem in Fig. 3.31b with the parameter  $t'/s$ . The independent variable  $\theta$  is used in ref. 3 for a display of the indicial functions. According to ref. 3, the solution of the steady problem is explicit for  $X > 2s$  (or  $t'/s > 2$ ). For values  $X < 2s$  (corresponding to  $t'/s < 2$ ), wave reflexions of higher order

require numerical solutions. After inverse transformation,  $P_0$  and  $P_1$  must be categorized in the "time"-periods  $0 \leq t'/s < 2$  and  $2 \leq t'/s < \infty$ . One gets for

$$0 \leq t'/s < 2 \text{ (or } 0 \leq \phi < 2 \text{ Ms}/c_0)$$

$$P_0 = 2(2 - t'/s) + 4 \tan\delta \cdot M \cdot t'/s$$

and

$$P_1 = 2(2 - t'/s) + 4 \tan\delta \cdot M \cdot t'/s - 1/2 \tan\delta \cdot M \cdot (t'/s)^2.$$

In period

$$2 \leq t'/s < \infty \text{ (or } 2 \text{ Ms}/c_0 \leq \phi < \infty)$$

we have

$$P_0 = \pi(1 - \tan\delta \cdot M \cdot (t'/s)) \cdot f(t'/s) + 2 \tan\delta \cdot M \cdot \pi \int_0^{t'/s} f(t'_1/s) d(t'_1/s), \quad (58)$$

and

$$P_1 = \pi(1 - \tan\delta \cdot M \cdot (t'/s)) \cdot f(t'/s) + 3 \tan\delta \cdot M \cdot \pi \int_0^{t'/s} f(t'_1/s) d(t'_1/s). \quad (59)$$

In Table 3.1, the numerical solutions of the function  $f(t'/s)$ , of the integral and of  $P_0$  and  $P_1$  of eqs. 58, 59 are listed for two delta wing geometries,  $M \tan\delta = 1/8$  and  $1/4$ . The pressure parameters are also displayed in figs. 3.32 and 3.33. Here, they are given for  $M \tan\delta = 1/8$  and  $1/4$  as functions of  $t'/s$ . In order to form the indicial functions, we need  $P_0$  and  $P_1$  as functions of  $\phi$ . For conversion, we have the equivalence of the independent dimensionless variables  $(t'/s \equiv \phi / (x M \tan\delta))$ , where  $x = X/c_0$ . In the transient phase between the step  $\Delta\alpha$  or  $\Delta q$  and the approach of a new steady state situation, we must consider  $P_0$  and  $P_1$  as functions of  $x$ . Then we are able to determine the derivatives by integration of functions such as  $x^n P_0(x)$  in  $x$ -direction from the apex to the wing trailing edge. In the following, the procedure of determining the deviations of longitudinal stability shall be shown on the example of the normal force coefficient for a step change  $\Delta\alpha$ . Generally, we have

$$C_N = \frac{1}{S} \int_0^{\infty} \int_{-s}^{+s} \frac{\Delta p}{\rho V^2 / 2} dy dx,$$

which becomes after substituting eq. 57

$$C_N = \frac{2 \tan\delta}{M \cdot S} \int_0^{\infty} x_0 P_0 dx = \frac{2 \alpha}{M} \int_0^1 x P_0 \left( \frac{\phi}{x M \tan\delta} \right) dx. \quad (60)$$

Accordingly, the derivatives are derived:

$$C_{N_\alpha} = \frac{2}{M} \int_0^1 x P_0 dx. \quad (61)$$

The following coefficients of the pitching moment, the normal-force- and pitch damping are given with reference to a pitch axis situated at the wing apex:

$$C_m = \frac{2}{M} \int_0^1 x^2 P_0 dx, \quad (62)$$

$$C_{N_q} = \frac{2}{M} \int_0^1 x^2 P_1 dx, \quad (63)$$

and

$$C_{m_q} = \frac{2}{M} \int_0^1 x^3 P_1 dx. \quad (64)$$

The function  $C_{N_\alpha}(\theta)$  derived from eq. 61 is shown in Fig. 3.34. The initial value  $C_{N_\alpha}|_{\theta=0} = 4/M$  and the initial slope  $M \cdot \partial C_{N_\alpha}/\partial \theta = 4 \cdot (2 - (M \tan \delta)^{-1})$  follow from eq. 58 and 61 for  $t'/s=0$ . The steady state value  $C_{N_\alpha} = 2\pi \tan \delta$  is obtained with  $t'/s \gg 2$ . In this case, the function  $f(t'/s)$  approaches zero, its integral (Table 3.1) approximates "1" and  $P_0 = 2\pi M \tan \delta$ . The hatched area in Fig. 3.34 represents the value of the unsteady coefficient  $M \cdot C_{N_\alpha}$  for the delta wing geometry  $M \cdot \tan \delta = 1/8$ . The difference of the areas above and below the steady state value,  $M \cdot 2\pi \tan \delta$ , yields a positive value of  $C_{N_\alpha}$ .

### 3.5.3 Angle-of-attack influence

The linear indicial function method applied in section 3.5.2 provides stability derivatives which are independent of the angle-of-attack. The combination of the indicial function method with semi-empirical procedures allows to estimate approximately the dependency on the mean incidence. With the assumption that the response - or indicial function on a small deviation from the mean incident does not vary appreciably with the changes of the mean incidence, the unsteady problem can be reduced to a steady one, namely to the estimation of the initial value of the indicial function and of the final steady value, now both at high angle-of-attack. The initial value of the linear indicial function is given in section 3.5.2 in case of  $C_{N_\alpha}|_{\theta=0}$ . This value will also be derived with the linear piston theory. Either a non-linear piston theory or an extension of the unsteady slender body theory to high angles-of-attack by application of the free vortex model of refs. 29,39 may be suited for the estimation of the initial value at high angle-of-attack. So far, neither of these methods has been developed as yet. Therefore we are restricted to introduce a final non-linear steady value. This we obtain from the theory of refs. 14, 36 described in section 3.5.1. As shown schematically in Fig. 3.35 for instance now the non-linear coefficient  $C_{N_\alpha}$  instead of the linear coefficient  $C_{N_\alpha}$  is approached by the indicial function near the end of the transient phase. This causes a larger negative area below the steady value which decreases slightly the value of  $C_{N_\alpha}$  at high incidence in comparison to that near  $\alpha=0$ , obtained with the linear theory in section 3.5.2. We should recall that this is true for a slender delta wing with  $M \cdot \tan \delta = 1/8$ .

In Figs. 3.36, 3.37, the normal force and pitching moment coefficients of a delta wing of  $AR=1$  at  $M=2$  are displayed as function of the mean angle-of-attack. They are found in good agreement with experimental values. For the same wing geometry and flow speed, the total normal force damping coefficient in Fig. 3.38 reveals an increase with the angle-of-attack due to the contribution of  $C_{m_\alpha}$ . Our semi-empirical theory predicts an increase with  $\alpha$  also for the pitch damping  $C_{m_q} + q C_{m_\alpha}$  (Fig. 3.39) while the theory of refs. 14,36 give an initially (at  $\alpha=0$ ) greater nearly constant value, but with increasing  $\alpha$ . No experimental results (except at  $\alpha=0$ ) were available to support either theory.

## 4. STEADY AND UNSTEADY DERIVATIVES OF LONGITUDINAL STABILITY OF BODIES OF REVOLUTION

Slender body theory provides simple expansions for the derivatives of longitudinal stability, as there are

$$C_{N_\alpha} = 2, \quad C_{m_\alpha} = - \int_0^1 (dC_{N_\alpha}/dx) \cdot (x - x_N) dx$$

and

$$C_{N_q} = 2(c/D_o) \sqrt{(1-x_p) + v_o/(cS_o)}, \quad C_{m_q} = - 2(c/D_o)^2 \cdot (1-x_p)^2.$$

The piston theory (ref. 42) introduces slight improvements to the damping coefficients with the allowance of substituting the normal force slope  $C_{N_\alpha}$  instead of the factor 2. Further improvements were introduced to the slender body theory of steady flow by corrections for thickness, compressibility and viscous effects. The angle-of-attack dependence of the derivatives was studied by Robinson (ref. 43), who utilized the viscous cross flow theory of Jorgensen (ref. 44).

### 4.1 Viscous cross flow theory, non-linearity with the incidence in subsonic flow

The flow about a body at an angle-of-attack  $\alpha \neq 0$  may be separated in a potential flow with a velocity component parallel to the body and a viscous flow with a velocity component normal to the longitudinal body axis. The latter causes a normal force due to the drag of the body in the viscous cross flow field. Usually, the drag is determined from experiments with an "infinitely" long cylinder in the flow field of a wind-tunnel, the longitudinal axis of which is arranged perpendicularly to the flow. Applying the experimentally found drag coefficient to a slender missile body, a correction factor  $n$  is needed to account for the final length of the body. According to the semi-empirical theories of

refs. 43, 44, the local normal force coefficient  $C_N(x)$  is linearly dependent on the local viscous drag force  $C_{D_V}$ :

$$C_N(x) = (4/\pi) \cdot n \cdot \sin^2 \alpha \cdot (D(x)/D_0) \cdot C_{D_V}(x, \alpha), \quad (65)$$

where  $C_{D_V}$  is determined by experiment and theory for an "infinite" cylinder in a flow suddenly set into motion. The results of  $C_{D_V}$  are shown in Fig. 4.1. Differentiating  $C_N(x)$  in eq. 65 with respect to  $\alpha_p = \alpha + \Delta\alpha(t)$ , where  $\Delta\alpha \approx q(x-x_p)/V \ll \alpha$ , the local normal force damping coefficient

$$C_{N_q}(x) = \partial C_N(x) / \partial (qD_0/V) = (4/\pi) \cdot \bar{\sin}^2 \alpha \cdot (x-x_p) \cdot (C_0/D_0) \frac{\partial}{\partial \alpha} (\eta(D(x)/D_0) C_{D_V}(x, \alpha)) + \mathcal{T}(x, \alpha), \quad (66)$$

where

$$\mathcal{T}(x, \alpha) = 2n \cdot \sin \alpha \cos \alpha (x-x_p) \cdot (C_0/D_0) \cdot (D(x)/D_0) C_{D_V}(x, \alpha).$$

The pitching moment derivatives follow from section 4:

$$C_{m_\alpha}(x) = -(\partial C_N(x) / \partial \alpha) \cdot (x-x_p) \cdot (C_0/D_0) \quad (67)$$

and

$$C_{m_q}(x) = -(\partial C_N(x) / \partial (qD_0/V)) \cdot (x-x_p) \cdot (C_0/D_0). \quad (68)$$

The integration of eqs. 65-68 with  $x$  requires the specification of a function  $C_{D_V}(x, \alpha)$ . The data of Sarpkaya (ref. 45) in Fig. 4.1 may be approximated by linear function  $C_{D_V} = \text{Const. } X \tan \alpha / D(X)$  in the range  $0 \leq X \tan \alpha / D(X) \leq 1.5$ . The required derivative in eq. 66 is

$$\frac{\partial}{\partial \alpha} C_{D_V} = \frac{C_{D_V}}{\tan \alpha} \cdot \frac{1}{\cos^2 \alpha}. \quad (69)$$

In the range  $X \tan \alpha / D(X) > 1.5$ ,  $C_{D_V}$  is approximated by a constant value, which gives here

$$\frac{\partial}{\partial \alpha} C_{D_V} = 0. \quad (70)$$

In laminar and turbulent flow,  $C_{D_V}$  takes on different maximum values, i.e.  $C_{D_V, \text{max}} = 1.5$  or 0.5 respectively.

Forming the normal-force and the pitching moment coefficient caused by the viscous cross flow, we get

$$(C_N)_V = \alpha (C_{N_n})_V + (qD_0/V) (C_{N_q})_V + \dots$$

and

$$(C_m)_V = \alpha (C_{m_n})_V + (qD_0/V) (C_{m_q})_V + \dots$$

where

$$(C_{N_n})_V = (\int (C_{N_\alpha})_V d\alpha) / \alpha \quad \text{and} \quad (C_{m_n})_V = (\int (C_{m_\alpha})_V d\alpha) / \alpha.$$

The total derivatives are obtained by additive superposition of the corresponding terms of slender body theory (section 4) and of the viscous flow method (section 4.1). For a body with an ogive-cylinder configuration, where the diameter  $D(X)$  is given in Fig. 4.2, we obtain the normal-force and pitch damping coefficients, plotted in the diagrams of Figs. 4.3 and 4.4 as functions of the angle-of-attack. The pitch axis is located at 5.67  $D_0$ , measured from the body nose tip. The viscous-flow-derivatives are calculated for a laminar boundary layer.

#### 4.2 Non-linearity with the incidence in supersonic flow

The derivatives  $C_{mg} + C_{ma}$  and  $C_{nr} - C_{ng}$  for a ten degree cone at  $M=2$  at high incidences in Fig. 4.5 are obtained with the Newtonian theory by Stone et al. (ref. 46). In this procedure, the authors utilize the flow model by Maple and Synge (ref. 47). Accordingly, forces and moments of the cone are considered functions of the instantaneous values of translational and rotational velocity components, which may be represented in a multi-dimensional Taylor series. The results of Stone et al. predict non-symmetrical damping moments at high angle-of-attack. The asymmetry in dynamic damping is assumed being caused by asymmetric vortex detachment and flow separation on the lee side of the body. The theoretical data of Stone et al. is confirmed by the mean values of experimental results.

In the low angle-of-attack range (Fig. 4.5), experimental data of Schiff and Tobak (ref. 48) and theoretical results of Tobak and Wehrend (ref. 49) are added for comparison. Van Dyke's concept of including the thickness effect in slender body theory (ref. 50) is extended in ref. 49 to account for unsteady flow about slender cones. For this purpose, a low frequency approximation is required. The body thickness is accounted for by maintaining the correct boundary conditions and pressure equation, thus avoiding the approximations inherent with the slender body theory. In addition, a second method, also proposed by Van Dyke is used in ref. 48. This combines the first order crossflow potential with an axial potential correct to second order. Applied to slender cones, both methods have closed-form solutions and yield the data of Fig. 4.5.

Presently at MBB, Revell's second-order slender body theory (ref. 51) for steady and unsteady supersonic flow past slender lifting bodies with finite thickness is used as a base for the development of a computing method applicable at high angles-of-attack. Revell estimates the corrections for thickness and compressibility from a second-order approximation to the non-linear time-dependent velocity potential. The crossflow theory from Miles and Munk (ref. 1, 52) predicting the stability derivatives as functions of the body shape only, and Adams-Sears axial flow theory (ref. 17) are the starting points to Revell's successive approximation scheme. Then the second-order slender body theory of Lighthill (ref. 53) applicable to steady flow past bodies of revolution is used to account for thickness effects. Essentially, the solution is obtained by approximating the non-linear terms in the second-order potential equation by their first order values. Then the resulting inhomogeneous partial differential equation is solved which now is subject to more refined boundary conditions. The isentropic pressure equation is likewise refined and integrated to give the second-order corrections to lift and pitching moment coefficients.

#### 5. NORMAL FORCE AND PITCHING MOMENT OF WING-BODY-COMBINATIONS IN THE NON-LINEAR ANGLE-OF-ATTACK RANGE AT SUBSONIC SPEEDS

The interference of wing and body of missiles with high maneuverability in the non-linear angle-of-attack range causes a non-negligible contribution to the forces and moments governing the longitudinal stability. This is shown in a recent coefficient synthesis (ref. 54) of quasisteady derivatives of missile configurations in subsonic flow: Figs. 5.1 and 5.2 display as function of the angle-of-attack the pitch damping coefficient of wing-body-combinations at  $M_\infty = 0.8$ . The pitch axis is located at the center of gravity of the body with a homogeneous mass distribution. The fractions 1 and 2 represent the contribution of the body, the boundary layer of which is assumed to be laminar. The fraction 3 is the pitch damping of the wing alone, and parts 4 and 5 caused by the interference between wing and body. With the wing position of Fig. 5.1, the fraction due to wing-body-interference is small, with the wing position of Fig. 5.2 however, this portion averages 17 % of the total pitch damping over the given angle-of-attack range. The semi-empirical methods of ref. 54 used for the prediction of the forces and moments due to the wing-body-interference yielded differences of the results as shown in Fig. 5.3, where the interference factors  $K_B(W)$  of the normal force slope, pitch stiffness, normal force damping and pitch damping of the configuration of Fig. 5.1 are plotted versus the incidence. These differences and the lack of comparable experimental data in the case of non-linear quasisteady factors called for additional theoretical methods in order to confirm the results of one or the other existing procedure.

##### 5.1 Wing-body interference factor

The dimensionless interference factors  $K$  according to ref. 55 are formed with the lift or normal force of the wing in the presence of a body or viceversa in relation to the lift or normal force of the wing alone. The normal force of a missile configuration  $N_C$  may be defined as the sum

$$N_C = N_B + N_W + N_{W(B)} + N_{B(W)}$$

of the normal force of the body alone  $N_B$ , of the wing alone  $N_W$ , of the fraction gained or lost by the wing due to the presence of a body  $N_{W(B)}$  and the part gained or lost by the body due to the interference of a wing. In the presence of a body the normal force of the wing is  $N_W + N_{W(B)}$ . This sum related to the normal force of an isolated wing  $N_W$  yields the factor

$$K_W = 1 + K_{W(B)}$$

where  $K_{W(B)} = N_{W(B)}/N_W$ . According to slender body theory (ref. 55), the factor  $K_W$  varies with the ratio  $r_R$  of the body radius  $R$  and the sum of wing half span and body radius ( $s+R$ ) from 1 for a wing without body ( $R=0$ ) up to 2 for a very wide body ( $R+\infty$ ) with a

wing of a small half span. In the high angle-of-attack range,  $K_W$  may accept smaller values for a given  $n_p$  than slender body theory predicts. This can be caused by body vortices changing the downwash distribution and hence the loading over the wing surface. Linear slender body theory predicts a body normal force consisting of the nose or contoured aft body contribution  $N_B$  and the part due to the lift carry-over from the wing  $N_B(W)$ . For a cylindrical body of constant radius, i.e. without a contoured nose or aft body section we get  $N_B = 0$ . Then the body normal force in the presence of a wing is given by  $N_B = N_W \cdot K_B(W)$ , where  $K_B(W) = N_B(W)/N_W$ . In the high angle-of-attack range, the body normal force will be changed by a cross-flow term. Also, the  $K_B(W)$  factor due to lift carry-over will change because of non-linear wing characteristics. The terminology of interference factors  $K$  as specified in ref. 55 for normal force  $N$  and moment  $M$  is extended here to account for the interference effects on pitch damping and normal force damping.

### 5.2 Non-linear steady interference factor $K_W$

The upwash distribution over the wing induced by symmetric body vortices and caused by the cross flow accelerating when passing around the body (ref. 56) can be fed into the relations of the non-linear lifting surface theory (ref. 10). This will provide the possibility of calculating non-linear steady and quasisteady interference factors  $K_W$  (ref. 54). In Fig. 5.4 the steady non-linear normal force factor  $K_W(N)$  obtained this way is compared to experimental results of ref. 57. The influence of different body lengths is noticeable with the experimental data: The normal force of the wing and hence the interference factor are lower with the longer fore body section. According to ref. 57 at low incidences this is due to change of the upwash velocity over the wing as consequence of the nose and body boundary layer influence. In the higher angle-of-attack range, the position and strength of the body vortices is changed which also may decrease the  $K_W$ -factor. Generally, the theory of ref. 54 determines higher  $K_W$  values than those obtained in the experiment. In particular a much weaker influence of the body vortices is predicted. As the present theory neglects the body boundary layer thickness which diminishes the effective wing area, the general differences between theory and experiment are understandable. A turbulent boundary layer can lower the interference factor by as much as 20 % (ref. 58). To some extent, the latter influence will also account for the lower  $K_W$  with the longer fore body section. The weak influence of body vortices on the wing normal force - predicted by theory - may be explained in Fig. 5.5. Here, the free body vortices and their images, the vortex induced velocity and the cross flow velocity distribution over the wing span are displayed. The cross flow plane of this diagramm lies at the wing trailing edge of the configuration of Fig. 5.4. At subsonic speeds, the vortex positions are close to the body surface and near the vertical body axis. The induced upwash velocity  $w$  of an individual vortex is quite large, but the resultant induced by the two vortex pairs of the present model becomes small due to partial compensation. Not even arbitrary changes up to 20 % of either the vortex position or the vortex strength do alter the induced upwash significantly to reproduce the experimentally determined  $K_W$  for a wing with long forebody. Again in Fig. 5.6 the present method overestimates  $K_W$  in comparison to the experimental data of ref. 59, but determines the correct slope of  $K_W$  with the incidence up to  $\alpha \leq 20^\circ$ , whereas the result of slender body theory matches the measured value of  $K_W$  at low incidences. If a correction for a body boundary layer were taken into account, a decrease of  $\Delta K_W/K_W$  from -10 % to -20 % would render the slender body value too low, the data of the present method however would compare well with the experimental result. In conclusion of this paragraph, the body boundary layer growth must be taken into account with the present theory, if both the value and slope of  $K_W$  with  $\alpha$  are to be simulated correctly.

### 5.3 Modified Lennartz interference factor $K_B(W)$

According to Lennartz' linear two-dimensional theory (ref. 60), the ratio of  $N_B(W)/N_W$  of a wing-body combination is given by a factor  $K_B(W) = n_R$ . It changes from zero at  $R = 0$ , i.e. without the presence of a body to 1 for  $R \rightarrow \infty$ , as shown in Fig. 5.7a. Here,  $K_B(W)$  is plotted versus  $n_R$  for combinations of body and rectangular wings of various aspect ratios  $0 < AR < \infty$ . The linear relation between  $K_B(W)$  and  $n_R$  holds for a wing with  $AR \rightarrow \infty$ . The corresponding normal force distribution over wing and body is shown in the diagram of Fig. 5.7b. The wing normal force is proportional to the area  $AR Y_0 \cdot (1-n_R)$ , the portion carried over to the body amounts to  $AR Y_0 \cdot n_R (1-n_R)$ . In the modified version of Lennartz' theory, the normal force of a rectangular wing with finite aspect ratio is represented by the area  $2AR Y^*(n=n_R) \cdot n_W$  according to ref. 7. The length

$$n_W = (1-n_R) \cdot C_{N_W} / (2AR Y^*(n=n_R)) \quad (71)$$

shown in Fig. 5.8 is folded about the wing root chord at  $n=n_R$  on the body coordinate according to conformal mapping. Now a rectangular area  $2n_W \cdot n_R AR Y^*(n=n_R) / (n_W + n_R)$  will represent the portion of the normal force of the body due to the wing interference. The ratio  $K_B(W) = N_B(W)/N_W$  combined with eq. 71 leads to the expression

$$K_B(W) = \frac{1}{1 + \frac{1-n_R}{n_R} \frac{C_{N_W}}{2AR Y^*(n=n_R)}} \quad . \quad (72)$$

The factor contains the ratio between the total normal force of the wing and the local normal force at the wing root. In the special case of  $AR \rightarrow \infty$ , the ratio  $C_{N_W}/AR Y^*(n=n_R)$  approaches 1, which reduces  $K_B(W)$  of eq. 72 to the one of Lennartz theory, shown in Fig. 5.7a together with results of eq. 72 for rectangular wings of finite aspect ratio at zero incidence. Through the normal force ratio, a non-linear dependence on the incidence enters eq. 72 when a non-linear lifting surface theory is applied. For a family of wings

characterized by straight trailing edges without sweep, of the normal force distribution over the span the local normal force at the wing root will be maximum. In this case, the product of two functions  $C_{N_W}/2AR^*(n=n_R)$  for  $\alpha=0$  and  $j(\alpha)$  match the result  $C_{N_W}/2AR^*(n=n_R)$  of the non-linear lifting surface theory for  $\alpha \neq 0$ . They relate the normal force ratio to the wing form, i.e. the leading edge sweep and the taper ratio (Fig. 5.9) and to the angle of attack (Fig. 5.10). Within the subsonic range, the Mach number dependence was found negligibly small. As a result, simple relations will provide an estimate of the dependence of the  $K_B(W)$  factor on the incidence and wing form. As seen from Fig. 5.10 delta wings reveal a stronger dependence on the incidence than rectangular or trapezoidal wings. The  $K_B(W)(N)$  of trapezoidal wings are added to the diagrams of Fig. 5.3 and 5.11. Only quantities of wing normal forces are used to obtain  $K_B(W)$  by means of eq. 72. Therefore, no other information but  $K_B(W)(N)$  can be given by the modification of the Lennertz theory.

#### 5.4 $K_B(W)$ by replacement of the body with a rectangular flat middle section

This procedure replaces the cylindrical body between the wing roots by a rectangular flat middle section. The non-linear lifting surface theory is applied twice in order to determine the normal forces and moments of the original wing and of the substitute wing consisting of the original one plus the rectangular middle section. The difference between forces (or moments) of the substitute and the original wing in relation to the corresponding force (or moment) of the original wing alone yields the interference factor  $K_B(W)$ . The normal force factor becomes

$$K_B(W)(N) = \frac{N_{SW} - N_W}{N_W} \quad (73)$$

where  $N_{SW}$  denotes the normal force of the substitute wing. Using dimensionless force or moment coefficients, the  $K_B(W)$  of the pitch stiffness, normal force damping and pitch damping are given by

$$K_B(W)(M_n) = \frac{(C_{m_n})_{SW} - (C_{m_n})_W}{(C_{m_n})_W} \equiv \frac{(C_{m_n})_B(W)}{(C_{m_n})_W}, \quad (74)$$

$$K_B(W)(N_q) = \frac{(C_{N_q})_{SW} - (C_{N_q})_W}{(C_{N_q})_W} \equiv \frac{(C_{N_q})_B(W)}{(C_{N_q})_W}, \quad (75)$$

$$K_B(W)(M_q) = \frac{(C_{m_q})_{SW} - (C_{m_q})_W}{(C_{m_q})_W} \equiv \frac{(C_{m_q})_B(W)}{(C_{m_q})_W}. \quad (76)$$

The coefficients of the derivatives in eqs. 74-76 have the wing root chord  $c_0$  rather than the aerodynamic mean chord  $\bar{c}$  for reference length, as  $\bar{c}$  may vary with  $n_R$ . As reference area of the coefficients of the substitute wing  $(C_N)_{SW}$  and  $(C_m)_{SW}$ , the planform of the original wing, i.e. the wetted wing area is chosen. Results of this procedure for the configurations of body and trapezoidal wings are displayed in Figs. 5.3 and 5.11. The computer program which is used repeatedly for determining  $K_B(W)$  is limited to wings with straight leading edges or leading edges with one bend only. With exception of  $\psi_l = 0$ , the latter shape always applies for the substitute wing. Hence, the computer program cannot handle those original wings which already have a leading edge bend and angles  $\psi_l \neq 0$ . In order to allow for this particular wing shape, eqs. 74-76 have been rederived in terms of the normal force factor  $K_B(W)(N)$ , the ratio of the pressure point of original and substitute wing  $X_{NW}/X_{NSW}$  and the ratio of the locations of vanishing normal force damping  $X_{OW}/X_{OSW}$ :

$$K_B(W)(M_n) = (K_B(W)(\alpha)+1) \frac{X_{NW}}{X_{NW}} - 1, \quad (77)$$

$$K_B(W)(N_q) = (K_B(W)(\alpha)+1) \frac{X_{OW}}{X_{OSW}} - 1 \quad (78)$$

and

$$K_B(W)(M_q) = (K_B(W)(\alpha)+1) \frac{(X_O^2 + X_N^2)_W}{(X_O^2 + X_N^2)_{NSW}}. \quad (79)$$

Now, the normal force  $K_B(W)$  of a wing (with leading edge bend for instance) may be taken from the modified Lennertz theory or from experiment. The ratios  $X_{NW}/X_{NSW}$  and  $X_{OW}/X_{OSW}$  still must be calculated for a wing which the "substitute wing"-method can handle and which approximates in shape the wing with leading edge bend. In ref. 54, empirical relations for  $X_{NW}/X_{NSW}$  and  $X_{OW}/X_{OSW}$  are fitted to the results of the non-linear lifting surface theory for a family of wings tabulated in Fig. 5.9. The empirical relations were used in eqs. 77-79 to obtain the  $K_B(W)$  by the dashed curve in Fig. 5.3. The differences of  $K_B(W)$  calculated with various procedures based on the non-linear lifting surface theory are noticeable in Figs. 5.3 and 5.11.

#### 5.5 Interference factors by the vortex tracing method

Without comparable experimental data, the results of one or the other preceding method can be confirmed only by a more refined analysis. The procedure proposed here for

this purpose links the non-linear three-dimensional lifting surface theory with the two-dimensional theory of slender wing-body configurations. This way, forces and moments non-linear with the angle-of-attack ( $\alpha \leq 25^\circ$ ) due to the interference of body and body vortices on the wing, and of the wing on the body can be determined step by step proceeding in the direction of the longitudinal (X) axis of the configuration (Fig. 5.12).

Two different wing vortex models convert the wing circulation into discrete free vortices whose paths are traced along the X-axis (Fig. 5.12). The wing-body section shown in Fig. 5.13 is supposed to oscillate harmonically about a specified incidence  $\alpha$  with low frequency and amplitude, i.e. with a quasisteady lateral pitching motion. The linear and non-linear parts of the circulation obtained with the lifting surface theory are integrated over the wing chord. These parts are converted separately into discrete vortices. The lateral position (Y) on the wing surface and strength of the vortices are estimated with the methods of Rossow and Williams (refs. 61, 62). Vortices with a core will result. Only the X-coordinate of the vortex origin must be suitably selected. One of the vortex models locates the origins or separation points of the vortices representing the non-linear part of the circulation on the leading edge. The "linear" vortices separate from the trailing edge as shown in Fig. 5.14. The other model provides for sectioning of the non-linear part of the pressure distribution according to the arrangement of panel elements on the wing planform. A discrete vortex is assigned to each pressure section using the method in ref. 63. Again, the origins of linear vortices are located on the trailing edge (Fig. 5.15). After shedding, each vortex is treated as a free viscous vortex (ref. 62). The subsequent positions will be computed step by step from the local induced velocity at the vortex. The induced velocity is obtained with conformal mapping of vortices in the cross flow plane. The relations for the vortex path tracing are available from refs. 64 or 68. The satisfaction of the Kutta condition at each step may require an additional vortex, the strength of which will be selected to yield zero induced normal velocity in the mean at the wing surface. The strength of the additional vortex relative to the strength of the vortices determined from the wing circulation, is a criterium for the quality of the assumed vortex model in simulating the wing circulation.

Slender body theory will be applied to determine force and moment distribution induced by the free vortices along the X-axis of the wing-body combination. The steady derivatives and corresponding K-factors follow from the vortices which are derived from the real part of the wing circulation as determined by the non-linear lifting surface theory. The quasisteady derivatives and corresponding K-factors are calculated by tracing the vortices obtained with the imaginary part of the wing circulation. The steady interference factor  $K_B(W)$  will be obtained when in the lifting surface theory, the linear upwash distribution over the wing is constant and proportional to the incidence  $\alpha$ . When the upwash distribution varies over X corresponding to the pitching velocity  $q \cdot X$ , the quasisteady factor  $K_B(W)$  will be determined. When in addition the velocities induced by the free body vortices and the cross flow velocity about the body are taken into account in the wing upwash distribution, the sum of the factors  $K_W + K_B(W)$  will result.

Results of steady aerodynamic coefficients determined with the procedure using the vortex model of Fig. 5.14 are shown in Figs. 5.3 and 5.17. The diagram of Fig. 5.17 displays the non-linear part of the normal force distribution along the wing-body longitudinal axis. The geometry and flight condition of the configuration is given in Fig. 5.3. Although a non-linear circulation increasing quadratically with the incidence is converted to yield the initial values of the discrete vortices emanating from the wing leading edge, the vortex lift induced on the wing-body combination has a higher than quadratic exponential dependence. This is seen by the distribution of Fig. 5.17 and also from Fig. 5.3 where the steady  $K_B(W)$ -factors of the vortex tracing procedure are added. In the low angle-of-attack range ( $\alpha < 10^\circ$ ), the normal force factor follows the results obtained with the "Substitute wing method", but deviates to larger values for  $\alpha > 10^\circ$ . The non-linear  $K_B(W)$  of the normal force by the vortex method is derived from Fig. 5.17 the following way: The total non-linear part of the vortex normal force is integrated from the distribution. The linear part of the wing-body configuration is determined with the linear wing normal force multiplied by the linear factor  $1+K_B(W)$  according to Lennertz. The sum of the non-linear and linear wing-body normal force is diminished by the non-linear normal force of the wing alone and then divided by the latter. Fig. 5.17 still needs experimental confirmation.

### 5.6 Proposal for improvement of analytical results

Critical examination of the interference factors  $K_W$  and  $K_B(W)$ , leads to the following proposal for the improvement of the analytical results. Including in the analysis of  $K_W$  the effect of boundary layer growth along the forebody section on the distribution of upwash velocity over the wing, will positively affect the  $K_W$  values in comparison to experimental results. This correction will be decisive on the improvement of the analytical results of  $K_W$ . The arbitrary change of body vortex strength and the vortex positions in the cross flow plane by as much as  $\pm 20\%$  had no noticeable effect on  $K_W$ . The substitution of the applied symmetrical vortex model of Jorgensen and Perkins (ref 56) by either of the asymmetric models of Wardlaw (ref. 66) or Deffenbaugh and Koerner (ref. 67) may not alter the present results appreciably in the range of incidence ( $\alpha < 20^\circ$ ) considered here. Thus, the additional effort encountered with the use of these models may not be rewarding. However, this will change at angles-of-attack  $\alpha > 20^\circ$ . Most critical in the analysis of  $K_B(W)$  (Figs. 5.3 and 5.11) is the assumption that the replacement of the cylindrical body between wing root chords by a rectangular middle section will provide the correct locations in X-direction of the pressure point and of the point of zero nor-

mal force damping. The proposed procedure based on vortex tracing which determines the normal force distribution along the longitudinal (X) axis of the wing-body combination will certainly yield more accurate results. Considering in Fig. 5.16 the dashed curves which represent the steady normal force and pitching moment of the wing-body combination treated throughout this report, one will anticipate, that at least the proposed corrections of  $K_w$  reflects favourably on the values of the normal force, as they will lower them to better agreement with experimental data.

## 6. BRIEF SURVEY ON NUMERICAL PROCEDURES

The state of art of stability-parameter-studies in 1961 and 1968 was discussed in the survey reports by Thomas (ref. 68) and Ellison and Hook (ref. 69). At this time, most analytical procedures were based on linear wave-potential theory. With this method the steady and quasi-steady derivatives of the following components were treated:

- o Wings of large aspect ratio (Multhopp's lifting line theory),
- o Wings of small aspect ratio with taper and sweep of the leading and/or trailing edge (Multhopp's and Garner's lifting surface theory, ref. 5),
- o Slender pointed wings (slender body theory by Martin, Cole, Margolis, Malvestuto et al. (ref. 20, 70, 71)),
- o Slender bodies (slender body theory).

The authors of refs. 68 and 69 suggested the development of half-empirical methods in order to predict non-linear and viscous flow effects and the influence of flow separation in unsteady body-flow-interaction, especially since at this time progress was made in non-linear steady wing theory (ref. 30). Particularly with missile components - slender wings, cones, ogive-cylinder configurations - the suggestions of Thomas, Ellison and Hook were realized in recent work (refs. 14, 43).

The problems and progress in numerical lifting-surface theory were discussed by Landahl and Stark in ref. 72. Herein, possible forms of the integral equation mainly for subsonic (see section 3.4.2) and transsonic wing application are investigated. Directions are given on the appropriate load function in the velocity potential: For wings of large aspect ratio for instance the load functions of surface elements can be composed of two load functions derived from the two dimensional lifting line theory. This procedure fails in the case of wings of small or medium aspect ratio, where the load variation near the wing root cannot be simulated accurately this way. Here, load functions of a closed form as for instance given with dipoles (ref. 73) are practicable. An example for application of this concept to the unsteady boundary value problem is the work of Laschka (ref. 2).

Reviews of Bland (ref. 74, 75) discuss linearization techniques of the unsteady potential equation and numerical procedures for its solution. Ref. 74 is mainly concerned with transonic flow problems, ref. 75 covers the entire velocity range. An abstract of linearization - and numerical procedures, partly taken from refs. 74, 75 is given in table 6.1. For the transsonic flow case, Bland describes means of separation of the general potential equation in steady and unsteady parts. This can be done for instance, with the introduction of velocity potentials containing a main steady term and a time-dependent "small perturbation" term simulating a harmonic motion. The boundary condition is given a similar treatment. The separation yields a non-linear potential equation for the steady flow and a linear one for the unsteady flow part. In the transsonic case, the linear unsteady potential equation contains variable coefficients, which depend on the solution of the steady flow problem. In sub- and supersonic flow, only terms with constant coefficients remain in the unsteady wave equation. Herein, the linearization is complete, provided the degree of unsteadiness satisfies the conditions of a "small disturbance".

Recent Russian investigations concerning the solution of unsteady lifting surface problems by means of numerical procedures are reviewed by Belotserkovskii (ref. 4). The schematization of an aircraft in steady and unsteady flow for the purpose of modelling it and its wake for description by linearized or non-linear boundary conditions, is one of the major concerns of this report. For example: The slender wing and the circular cylinder as simplest and oldest schemes of discretization are often employed also in modern approaches, such as those by Kalman, Rodden and Giesing (refs. 76 - 78). According to Belotserkovskii, the main deficiency of the simple schemes is that they provide only partial description of the actual configuration, which most times is much more complicated. For the complicated configurations a modelling with plane base elements (panels) is appropriate. They are the loci on the body surface where a distribution of mathematical singularities such as vortices, dipoles and sources satisfies the kinematic condition. In ref. 4, methods of solution such as the integral representation of the velocity potential and the panel method in subsonic and supersonic flow problems, the discrete vortex method in subsonic flow and the "direct" method in supersonic flow (where the conditions of a boundary value problem are satisfied directly) are interpreted with regard to steady and unsteady flow problems. Some of the solutions are characterized briefly in Table 6.1. For the time history of unsteady forces and moments, transient functions between an initial step deviation and the approximation of steadiness are proposed. The same approach of modelling unsteady events is suggested by Tobak (ref. 3, see also section 2, Fig. 2.4a). For the treatment of non-linear body-flow interaction, Belotserkovskii favors the discrete-vortex method as most effective among numerical approaches. He presents results on the formation of separated flow patterns, i.e. the development of vortex structures on rectangular and triangular wings at high angle-of-attack. Discrete vortices are constructed in section 5.5, Fig. 5.15. They are subject to vortex tracing in a study (ref. 79)

with the purpose of simulating the interference effect of the wing on the body at high angle-of-attack. This analysis involved a very cost- and time-consuming numerical solution, which still is to be extended to quasisteady flow conditions. New results of the discrete vortex method are presented in a recent report by Rehbach (ref. 80).

In an extensive review, McCroskey (ref. 81) lists several recent symposia and meetings on theoretical and experimental progress in unsteady aerodynamics. This survey should be complimented with the 99th VKI lectures, where Pörsching (ref. 82) and Labrujère, Roos and Erkelens (ref. 83) summarized numerical solutions to the unsteady potential theory.

## 7. CONCLUSION

Dynamic longitudinal stability problems in missile aerodynamics have the appearance of being easier to solve than problems in the same field encountered in airplane aerodynamics. This is true with respect to the frequency of vertical motions, superimposing to the steady flight motion. The frequency is low with the size and mass of missiles and projectiles encountered. Here the assumption of body rigidity is close to reality. The reduced frequency of pitching, plunging or yawing motion of missiles is of the order of  $k=0.1$ . This permits to treat vertical motion as nearly steady. Accordingly, the mathematical treatment with potential theory is essentially a steady one. This however involves a more complicated upwash field over the missile part which ever is considered. If a low frequency approximation should be necessary, the analytical procedure becomes quasisteady providing solutions, which depend linearly on the frequency. In literature, at times this kind of motion is termed "unsteady". The low frequency approach is satisfactory for most dynamic stability problems in missile aerodynamics. It is needed for instance, when analytical results are to be compared to experimental data which usually are obtained with small scale models oscillating at higher frequency than  $k=0.1$ .

While low frequencies simplify the estimation of stability derivatives, the amplitudes of oscillation can become large. Also, the mean angle-of-attack of steady flight can be large. Both flight conditions are not consistent with the usual assumption of small perturbations in potential theory. Thus, high angle-of-attack flight and large amplitudes of oscillatory lateral motion renders missile aerodynamics non-linear and difficult. Nevertheless, also for these conditions a very accurate prediction of stability parameters is required to guarantee stable flight even in the case of large shifts of the center of gravity due to mass reduction of a propelled missile. Some methods explained or mentioned in this report are considered to suit the above requirement. In conclusion, these methods again are called to attention.

For bodies of revolution, the theory of Revell (refs. 51, 84) and for wings, the theory of Brune and Dusto (ref. 13) appear appropriate for subsonic and supersonic flight speeds. The theories are suitable to determine the derivatives of longitudinal stability, provided these are linearly dependent on the state variables. In the case of non-linear problems, at present an analysis geared toward the treatment of missile components and a subsequent data synthesis including interference effects appears more promising with the usually simple missile configurations than a complete configuration analysis. The latter always requires models for configuration discretization and consequently time- and cost-consuming numerical solutions of the steady and unsteady potential equations (refs. 4, 74, 75). The configuration analyses are more appropriate for the investigation of dynamic problems of airplanes (refs. 82, 83). If separated into components, the analytical assessment of the aerodynamic properties of a missile in general requires the treatment of simple body and wing shapes and of interference effects. For immediate application or for extension to future problems, we have the method of indicial functions (ref. 3, 4). It can handle quasisteady motions of small or of larger amplitude of wings and bodies in subsonic and supersonic flow. For application to high angle-of-attack problems, the piston theory (ref. 1), which provides the reactional forces and moments immediately after a lateral step should be extended to high-incidence application. Subsonic and supersonic indicial functions should be available for more complicated wing forms than the delta and rectangle (ref. 89). For comparison and confirmation of results of the available method of indicial functions, an additional quasisteady method applicable to wings of arbitrary shape in the transonic range could be derived by combination of Brune's and Dusto's program with the vortex models by Bollay (ref. 29) or Gersten (ref. 30). In the extension of the steady vortex models of Wardlaw (ref. 66) or Deffenbaugh (ref. 71) for application in quasisteady aerodynamics should not be forgotten that, concerning quasisteadiness, the interference of the body on the wing and on the symmetric body nose vortex model of Mendenhall and Nielsen (ref. 72) and on the body and on the tail could be obtained with the pro-

"The theory of unsteady supersonic flow", Cambridge monograph, Cambridge University Press, Cambridge at the university press, 1959.

"Über den thermisch schwingenden Fläche bei Unter- und Überschallflug", Aeronautics Quarterly, Heft 7, Juli 1963, pp. 265 - 292.

"Indicial function concept in the analysis of unsteady flow", NACA TR 1188.

4. S.M. Belotserkovskii, "Study of the unsteady aerodynamics of lifting surfaces using the computer", Ann. Rev. Fluid Mech. 1977.9, pp. 469 - 494.
5. H.C. Garner, "Multhopp's subsonic lifting surface theory of wings in slow pitching oscillations", 1952, A.R.C., R.&M. 2885.
6. R. Göthert, H. Otto, "Berechnung der Stabilitätsderivativa für die Nickbewegung von Deltaflügeln im Unterschallbereich", Z. Flugwissenschaft, Vol. 15, Heft 10, 1967, pp. 363 - 368.
7. H. Schlichting, E. Truckenbrodt, "Aerodynamik des Flugzeuges", Vol. 2, Chapter 8.2, Springer-Verlag, Berlin, Heidelberg, New York, 1969.
8. M. Tobak, H.C. Lessing, "Estimation of rotary stability derivatives at subsonic and transonic speeds", 1961, AGARD Rep. 343.
9. H.S. Ribner, "The stability derivatives of low-aspect-ratio triangular wings at subsonic and supersonic speeds", 1947, NACA TN 1423.
10. C.P. Schneider, D. Nikolitsch, "Längsmomentederivative von Flügeln bei hohen Anstellwinkeln in Unterschallströmung", 1976, BMVg-FBWT 76-26.
11. J.S. Thompson, R.A. Fail, "Oscillatory-derivative measurements on sting-mounted wind-tunnel models: Method of test and results for pitch and yaw on a cambered ogee wing at Mach numbers up to 2.6", 1962, A.R.C. C.P. 3355.
12. W.E.A. Acum, H.C. Garner, "The estimation of oscillatory wing and control derivatives", 1964, A.R.C. C.P. No. 623.
13. G.W. Brune, A.R. Dusto, "Slowly oscillating lifting surfaces at subsonic and supersonic speeds", J. Aircraft, Vol. 9, No. 11, Nov. 1972, pp. 777 - 783.
14. L.E. Ericsson, J.P. Reding, "Effect of angle-of-attack and Mach number on slender wing aerodynamics", 1977, AIAA Paper No. 77-667.
15. K.J. Orlik-Rückemann, J.G. Laberge, "Static and dynamic longitudinal stability characteristics of a series of delta wings and sweptback wings at supersonic speeds", 1966, National Research Council of Canada, Aeron. Rep. LR-396.
16. M.T. Landahl, "Unsteady transonic flow", International Series of Monographs in Aeronautics and Astronautics Division II: Aerodynamics Vol. 2, Oxford, Pergamon Press, 1961.
17. M.C. Adams and W.R. Sears, "Slender-body theory-review and extension", J. Aero. Sci., Vol. 20, No. 2, pp. 85 - 98.
18. K. Orlik-Rückemann, C.O. Olsson, "A method for the determination of the damping-in-pitch of semi-span models in highspeed wind tunnels, and some results for a triangular wing", 1956, FFA Rep. 62, Stockholm.
19. M.T. Landahl, "The flow around oscillating low aspect ratio wings at transsonic speeds", 1954, KTH AERO TN 40, Stockholm.
20. J.C. Martin, K. Margolis, I. Jeffreys, "Calculation of lift and pitching moments due to the angle-of-attack and steady pitching velocity at supersonic speeds for thin sweptback tapered wings with streamwise tips and supersonic leading and trailing edges", 1952, NACA TN 2699.
21. J.H.B. Smith, J.A. Beasley, A. Stevens, "Calculation of the lift slope and aerodynamic centre of cropped delta wings at supersonic speeds", 1960, R.A.E. Techn. Note Aero. 2697, A.R.C. 22200, C.P. 562.
22. E. Khaski, "Transonic /supersonic longitudinal aerodynamic derivatives", 1977, v.K.I.F.D. Lecture Series 99: Aerodynamic input for problems in aircraft dynamics.
23. K.J. Turner, A.J. Ross, G. Early, "The dynamic stability derivatives of a slender wing, a comparison of theory with free-flight model test at near-zero lift, M=0.8 to 2.4", June 1966, R.A.E. T.R. No. 66170.
24. E. Schmidt, "Experimentelle und theoretische Untersuchungen über die instationären flugmechanischen Derivativa der Längsbewegung an schlanken Flugkörpern bei mäßiger Geschwindigkeit", 1971, Jahrbuch der DGLR, pp. 71 - 97.
25. I.C. Statler, "Dynamic wind-tunnel tests of a delta-wing model at transsonic speeds", 1970, AFFDL-TR-69-97, Air Force Flight Dynamics Lab., Wright-Patterson Air Force Base, Ohio.
26. L. Woodgate, P.G. Pugh, "Measurements of the pitching-moment derivatives on a sharp-edged delta wing in incompressible flow", 1963, A.R.C. R.&M. No. 3379.

27. N. Treinies, "Die Ermittlung aerodynamischer Derivativa mit Hilfe der diskreten Fourier-Transformation freier Schwingungen", 1974, DLR-FB 74-17.

28. H.F. Emerson, C.R. Robinson, "Experimental wind-tunnel investigation of the transonic damping-in-pitch characteristics of two wing-body combinations", 1958, NASA Memo 11-30-58A, Washington.

29. W. Bollay, Z. angew. Math. Mech. 19, 1939, p.21, and J. Aero. Sci. 4, 1937, p. 294.

30. K. Gersten, "Nichtlineare Tragflächentheorie insbesonders für Tragflächen mit kleinem Seitenverhältnis", Ing.-Archiv, Bd. 30, 1961, pp. 431 - 452.

31. D. Nikolitsch, "Über die nichtlineare Tragflügeltheorie von Gersten", 1967, Bölkow Bericht FM 370, 67.

32. H.C. Garner, Doris E. Lehrian, "Pitching derivatives for a gothic wing oscillating about a mean incidence", 1963, A.R.C. C.P. No. 695.

33. G.W. Brune, "Low-frequency approximation in unsteady aerodynamics", J. Aircraft, Vol. 6, No. 5, Sept.-Oct. 1969, pp. 478 - 480.

34. E. Truckenbrodt, "Tragflächentheorie bei inkompressibler Strömung", Jahrbuch 1953 der WGL, pp. 40 - 65.

35. L.E. Ericsson, J.P. Reding, "Unsteady aerodynamic analysis of space shuttle vehicles, Part II: Steady and unsteady aerodynamics of sharp-edged delta wings", 1973, Lockheed Missiles and Space Company, LMSC-D 352320.

36. L.E. Ericsson, J.P. Reding, "Approximate non-linear slender wing aerodynamics", J. Aircraft, Vol. 14, No. 12, December 1977, pp. 1197 - 1204.

37. H. Fuchs, "Dynamische Derivativa von Flugkörpern (Phase I), Auswertung der Windkanalmessungen und Vergleich mit theoretischen Ergebnissen", January 1979, Dornier Bericht Nr. 79 / 1B.

38. C.P. Schneider, "Instationäre Beiwerte von Flugkörpern, Teil III, Derivative der Längsstabilität von Flügeln bei hohen Anstellwinkeln in Überschallströmung", 1980, BMVg-FBWT 80-8.

39. R.T. Jones, "Properties of low-aspect-ratio pointed wings at speeds below and above the speed of sound", 1945, NACA Rep. 1105.

40. E.C. Polhamus, "A concept of the vortex lift of sharp-edged delta wings based on a leading-edge-suction analogy", 1966, NASA TN D-3767.

41. E.C. Polhamus, "Predictions of vortex-lift characteristics by leading-edge-suction analogy", J. Aircraft, Vol. 8, No. 4, April 1971, pp. 193 - 199.

42. R.L. Bisplinghoff, H. Ashley, R.L. Halfman, "Aeroelasticity", Addison-Wesley, Cambridge, Mass. 1955, pp. 418 - 419.

43. M.L. Robinson, "The estimation of pitch damping derivatives of missile configurations at subsonic speeds", 1970, AIAA Paper No. 70-537.

44. L.H. Jorgensen, "Prediction of static aerodynamic characteristics for space-shuttle like and other bodies at angle-of-attack from  $0^\circ$  to  $180^\circ$ ", January 1973, NASA TN D-6996.

45. T. Sarpkaya, "Separated flow about lifting bodies and impulsive flow about cylinders", AIAA J., Vol. 4, No. 3, March 1966, pp. 414 - 420.

46. G.W. Stone, E.L. Clark Jr., G.E. Burt, "An investigation of non-symmetrical aerodynamic damping moments", 1972, AIAA Paper No. 72 - 29.

47. C.G. Maple, J.L. Synge, "Aerodynamic symmetry of projectiles", Quarterly of Applied Mathematics, Vol. 6, No. 4, 1949, pp.345 - 366.

48. L.B. Schiff, M. Tobak, "Results from a new wind-tunnel apparatus for studying coning and spinning motions of bodies of revolution", AIAA Journal, Vol. 8, No. 11, 1970, pp. 1953 - 1957.

49. M. Tobak, W.R. Wehrend, "Stability derivatives of cones at supersonic speeds", 1956, NACA TN 3788.

50. M.D. Van Dyke, "First and second order theory of supersonic flow past bodies of revolution", J. Aero. Sci., Vol. 18, No. 3, 1951, pp. 161 - 178.

51. J.D. Revell, "Second-order theory for unsteady supersonic flow past slender, pointed bodies of revolution", J. Aerospace Sci., Vol. 27, Oct. 1960, pp. 730 - 740.

52. M. Munk, "The aerodynamic forces on airship hulls", 1923, NACA Rep. 184.

53. M.J. Lighthill, "Supersonic flow past slender pointed bodies of revolution at yaw", Quart. J. Mech. & Appl. Math., Vol. 1, 1948, pp. 76 - 89.

54. C.P. Schneider, "Instationäre Beiwerte von Flugkörpern, Teil II: Derivative der Längsstabilität von Flügel-Rumpf-Anordnungen mit hohen Anstellwinkeln in Unterschallströmung", BMVg-FBWT 78 - 19.

55. W.C. Pitts, J.N. Nielsen, G.E. Kaattari, "Lift and center of pressure of wing-body-tail combinations at subsonic, transonic, and supersonic speeds", 1957, NACA Rep. 1307.

56. L.H. Jorgensen, E.W. Perkins, "Investigation of some wake vortex characteristics of an inclined ogive-cylinder body at Mach number 2", 1959, NACA Rep. 1371.

57. H. Esch, "Windkanalmessungen zum Einfluß der Rollage auf die Normalkraft eines Flugkörperleitwerks", 1975, DFVLR-Bericht No. IB 351 - 75 / 7.

58. H. Mathauer, S. Schultz, "Die Berechnung aerodynamischer Daten von Artillerie-Rak. Konfigurationen mit Hilfe eines Digitalprogrammes..", 1972, BMVg-FBWT 72-28.

59. J.N. Nielsen, "Nonlinearities in missile aerodynamics", 1978, AIAA Paper 78-20.

60. J. Lennertz, "Beitrag zur theoretischen Behandlung des gegenseitigen Einflusses von Tragfläche und Rumpf", ZAMM, Bd. 7, Heft 4, 1927, pp. 249 - 276.

61. V.J. Rossow, "On the inviscid rolled-up structure of lift-generated vortices", J. Aircraft, Vol. 10, No. 11, 1973, pp. 647 - 650.

62. G.M. Williams, "Viscous modelling of wing-generated trailing vortices", Aerospace Quarterly, May 1974, pp. 143 - 153.

63. R.R. Clements, D.J. Maul, "The rolling up of a trailing vortex sheet", Aerospace J., January 1973, pp. 46 - 51.

64. A.H. Sacks, R.E. Lundberg, C.W. Hanson, "A theoretical investigation of the aerodynamics of slender wing-body combinations", 1975, NASA CR-2473.

65. M.R. Mendenhall, J.N. Nielsen, "Effect of symmetrical vortex shedding on the longitudinal aerodynamic characteristics of wing-body-tail combinations", 1975, NASA CR-2473.

66. A.G. Wardlaw, "Prediction of normal force, pitching moment, and yawing force on bodies of revolution on angles-of-attack up to 50 degrees using a concentrated vortex flow-field model", 1973, NOLTR 73-209.

67. F.D. Deffenbaugh, W.G. Koerner, "Asymmetric vortex wake development on missiles at high angles-of-attack", J. Spacecraft, Vol. 14, No. 3, March 1977, pp. 155 - 162.

68. H.H.B.M. Thomas, "State of the art of estimation of derivatives", 1961, AGARD Rep. 339.

69. D.E. Ellison, D.E. Hoak, "Stability derivative estimation at subsonic speeds", 1968, Annals New York Academy of Science, International Congress on Subsonic Aeronautics, pp. 367 - 396.

70. I.J. Cole, K. Margolis, "Lift and pitching moment at supersonic speed due to constant vertical acceleration for thin sweptback tapered wings with streamwise tips. Supersonic leading and trailing edges", 1954, NACA TN 3196.

71. F.S. Malvestuto, D.M. Hoover, "Lift and pitching derivatives of thin sweptback tapered wings with streamwise tips and subsonic leading edges at supersonic speeds", 1951, NACA TN 2994.

72. M.T. Landahl, V.J.E. Stark, "Numerical lifting-surface theory-problems and progress", AIAA Journal, Vol. 6, No. 11, Nov. 1968, pp. 2049 - 2060.

73. H.G. Küssner, "Allgemeine Tragflächentheorie", Luftfahrtforschung, Bd. 17, Lfg. 11/12, pp. 370 - 378.

74. S.R. Bland, "Comments on NASA Langley research on transonic unsteady aerodynamics", 1973, AGARD Rep. 619.

75. S.R. Bland, "Recent advances and concepts in unsteady aerodynamic theory", 1975, NASA SP-347, NASA conference on aerodynamic analysis requiring advanced computers.

76. T.P. Kalman, W.P. Rodden, J.P. Giesing, "Application of the doublet-lattice method to non-planar configurations in subsonic flow", 1970, AIAA Paper No. 70-539, AIAA Atmospheric Flight Mechanics Conference, Tullahoma, Tennessee.

77. W.P. Rodden, J.P. Giesing, T.P. Kalman, "New developments and applications of the subsonic doublet-lattice method for non-planar configurations", 1971, AGARD-CP-80-71, Part II.

78. J.P. Giesing, T.P. Kalman, W.P. Rodden, "Subsonic unsteady aerodynamics for general configurations", 1972, AIAA Paper No. 72-26.

79. C.P. Schneider, D. Nikoliczsch, "Normal force and pitching moment of wing-body-combinations in the non-linear angle-of-attack range at subsonic speeds", AGARD-CP-247-78.

80. C. Rehbach, "Numerical calculation of three-dimensional unsteady flows with the vortex sheets", 1978, AIAA Paper No. 78-111, AIAA 16th Aerospace Science Meeting, Huntsville, Alabama.

81. W.J. McCroskey, "Some current research in unsteady fluid dynamics", J. Fluid Engineering, Vol. 99, No. 1, March 1977.

82. H. Försching, "Prediction of unsteady aerodynamic forces in high frequency oscillatory flow", 1977, VKI LS 99 on "Aerodynamic impulse for problems in aircraft dynamics".

83. T.E. Labrujère, R. Roos, L.J.J. Erkelens, "The use of panel methods with a view to problems in aircraft dynamics", 1977, VKI LS 99 on "Aerodynamic impulse for problems in aircraft dynamics", and NRL MP 77009 U.

84. J.D. Revell, "Second-order theory for steady or unsteady subsonic flow past slender lifting bodies of finite thickness", AIAA J., Vol. 7, No. 6, June 1969, pp. 1070 - 1078.

85. M.A. Heaslet, H. Lomax, "Two-dimensional unsteady lift problems in supersonic flight", 1949, NACA Rep. 945.

86. H. Wagner, "Über die Entstehung des dynamischen Auftriebes von Tragflügeln", Z.f. a. MM., Bd. 5, Heft 1, Febr. 1925, pp. 17 - 25.

87. H. Lomax, M.A. Heaslet, F.B. Fuller, L. Sluder, "Two- and three-dimensional unsteady lift problems in high-speed flight", 1952, NACA Rep. 1077.

88. J.W. Miles, "Transient loading of wide delta airfoils at supersonic speeds", 1950, NAVORD Rep. 1235.

89. J.W. Miles, "Transient loading of supersonic rectangular airfoils", J.Aero. Sci., Vol. 17, No. 10, Oct. 1950, pp. 647 - 652.

90. G.Z. Harris, "The calculation of generalized forces on oscillating wings in supersonic flow by lifting surface theory", 1966, A.R.C. R.&M. 3453.

91. D.D. Liu, M.F. Platzer, S.Y. Ruo, "On the calculation of static and dynamic stability derivatives for bodies of revolution at subsonic and transonic speeds", 1970, AIAA Paper No. 70-190, AIAA 8th Aerospace Sciences Meeting, New York, N.Y..

92. S.Y. Ruo, E.C. Yates Jr., J.G. Theisen, "Calculation of unsteady transonic aerodynamics for oscillating wings with thickness", J. Aircraft, Vol. 11, No. 10, 1974, pp. 601 - 608.

93. L. Morino, "A general theory of unsteady compressible potential aerodynamics", 1974, NASA CR-2464.

94. E. Albano, W.P. Rodden, "A doublet-lattice method for calculating lift distributions on oscillating surfaces in subsonic flow", AIAA Journal, Vol. 7, No. 2, Feb. 1969, pp. 279 - 285.

95. W.P. Rodden, J.P. Giesing, "Application of oscillatory aerodynamic theory to estimation of dynamic stability derivatives", J. Aircraft, Vol. 7, No. 3, June 1970, pp. 272 - 275.

96. B. Bennekers, T.E. Labrujère, "Calculation of unsteady subsonic aerodynamic characteristics by means of the doublet-lattice method", 1972, NLR TR 73031 V.

97. R. Roos, B. Bennekers, R.J. Zwaan, "A calculation method for unsteady subsonic flow about harmonically oscillating wing-body configurations", 1975, AIAA Paper No. 75-864.

98. W. Geissler, "Ein numerisches Verfahren zur Berechnung der instationären aerodynamischen Druckverteilung der harmonisch schwingenden Tragfläche mit Ruder in Unterschallströmung, Teil I: Theorie und Ergebnisse für inkompressible Strömung", 1975, DLR-FB 75-37, "Teil II: Theorie und Ergebnisse für kompressible Strömung", 1977, DFVLR-AVA-Rep. IB 253 - 77J04.

99. D.E. Davies, "Calculation of unsteady generalized air forces on a thin wing oscillating harmonically in subsonic flow", 1963, A.R.C. R.&M., No. 3409

100. D.E. Lehrian, H.C. Garner, "Theoretical calculation of generalized forces and load distributions on wings oscillating at general frequency in a subsonic stream", 1971, A.R.C. R&M., No. 3710.

101. H. Ashley, S. Windall, M.T. Landahl, "New directions in lifting surface theory", AIAA Journal, Vol. 3, No. 1, January 1965, pp. 3 - 16.

102. P. Salaün, "Calcul précis des pression aérodynamiques instationnaires en subsonic", 1970, ONERA NT. No. 163.

103. J. Fromme, D. Halstead, "The use of local basis functions in unsteady aerodynamics", 1975, AIAA Paper No. 75-100, AIAA 13th Aerospace Sciences Meeting, Pasadena, Cal.

104. J. Becker, "Vergleich gemessener und berechneter instationärer Druckverteilungen für den hohen Unterschall an einem elastischen gepfeilten Flügel", 1969, MBB, EWR-Rep. Nr. 403-69.

105. Appa Kari, G.C.C. Smith, "Further developments in consistent supersonic aero-dynamic coefficients", 1971, AIAA Paper No. 71-177, 9th Aerospace Sciences Meeting, New York, N.Y.

## TABLES

Table 2.1: Reduced frequency of various MBB missiles at cruise-speed and -altitude

missile (No.)	cruise Mach number M	flight altitude $A \text{ km}^{-1}$	body length $c \text{ m}^{-1}$	natural pitch frequency $f \text{ s}^{-1}$	reduced frequency $k = \frac{2\pi f c}{a M} = \frac{q c}{V}$
1	0.7	<1	0.5	3.6	~0.05
2	3.3	20	3.3	0.45	0.02
3	1.8	10	3.3	1.15	0.06
4	0.97	<1	4.4	0.04	0.04
5	2.5	<1	3.6	1.6	0.043

Table 3.1: Indicial function theory:  $f(t'/s)$  and pressure distributions  $P_0$  and  $P_1$  for delta wings with subsonic leading edge, plunging and pitching about apex in supersonic flow ( $M \tan \delta = 1/8, 1/4$ )

$t'/s$	$f(t'/s)$	$t'/s$ $f$ $\frac{t'}{s}$	$P_0 \text{ (M tan} \delta \text{=1/8)}$		$P_0 \text{ (M tan} \delta \text{=1/4)}$		$P_1 \text{ (M tan} \delta \text{=1/8)}$		$P_1 \text{ (M tan} \delta \text{=1/4)}$	
			$t'/s < 2$	$t'/s > 2$						
0			4		4		4		4	
0,5			3,25		3,5		3,47		3,938	
1,0	0,734	0,9122	2,5	2,734	3,0	3,162	2,88	3,092	3,75	3,878
1,5	0,39	1,195	1,75	1,934	2,5	2,643	2,22	2,403	3,44	3,581
1,8	0,188	1,2807	1,3	1,464	2,2	2,337	1,8	1,967	3,19	3,342
2,0	0,0724	1,3067	1,0	1,197	2,0	2,166	1,5	1,71	3,0	3,192
2,2	-0,0245	1,3115	0,7	0,942	1,8	2,025	1,2	1,489	2,79	3,055
2,4	-0,1008	1,299	0,4	0,7986	1,6	1,914	0,88	1,309	2,56	2,934
2,667	-0,16	1,25	0	0,64		1,81		1,12		2,825
2,8	-0,1919	1,2385		0,5808		1,765		1,067		2,737
3,0	-0,2098	1,1983		0,5292	1,0	1,718		0,999		2,658
3,2	-0,2126	1,1561		0,5073		1,682		0,961		2,59
3,4	-0,2031	1,1145		0,5084		1,655		0,946		2,53
3,6	-0,1843	1,0758		0,5265		1,632		0,949		2,477
3,8	-0,1593	1,0414		0,5552		1,611		0,964		2,429
4,0	-0,1307	1,0124		0,5898	0	1,59		0,987	0	2,385
4,4	-0,0716	0,972		0,6622		1,549		1,044		2,31
4,8	-0,0207	0,9539		0,7232		1,511		1,098		2,26
5,0	-0,0008	0,9517		0,7465		1,495		1,12		2,243
5,4	0,0265	0,9573		0,7789		1,475		1,155		2,226
5,8	0,0379	0,9705		0,7950		1,471		1,176		2,233
6,0	0,0388	0,9782		0,7987		1,476		1,183		2,244
6,4	0,0338	0,9929		0,8011		1,496		1,191		2,265
6,8	0,0237	1,0045		0,8001		1,526		1,195		2,314
7,0	0,018	1,0087		0,8039		1,542		1,195		2,334
7,6	0,0026	1,0146		0,7973		1,586		1,196		2,383
8,0	-0,005	1,015		0,7972		1,61		1,196		2,407
10,0	0	1,0		0,7854		1,571		1,178		2,356

Table 6.1: Linearization of the unsteady potential equation and some numerical procedures of solution to the potential theory for the estimation of aerodynamic loads on lifting-surfaces and bodies in subsonic, transonic and supersonic flow

	Soliton Flow	Transonic Flow	Supersonic Flow
An unsteady time history with few exceptions (ref. 4) harmonic oscillations of small amplitude in the potential and boundary condition are assumed.			
Laminarization of the unsteady potential equation	<p>In laminar flow, steady and unsteady effects decouple. The potential equation is linear in terms of the unsteady potential.</p> <p><b>High frequency:</b> A linearization is possible at high unsteady frequency, <math>\delta = [M-1]</math>. In this case, variable coefficients of the unsteady linear potential equation can be removed only with some difficulty in the nonlinear steady equation. Literature: S.R. Brand, ref. 16.</p> <p><b>Low frequency:</b> Using a steady-state linearization technique by Chorlton and Kamm, Mander and Thompson, a general solution of the unsteady potential equation can be obtained. For M=1, the general solution is expanded in a Fourier series. At low frequency, terms of higher order can be eliminated. <b>Assumptions:</b> blades of semi-infinite delta wings with thickness. Literature: D.D. Liu, M.F. Pelesov, S.Y. Lin, ref. 21.</p> <p><b>Arbitrary frequency:</b> A local linearization method is applicable to profiles of wings of finite thickness i.e., two-dimensional flow problems or in three-dimensional flow only in connection with some other methods. Literature: S.R. Brand, ref. 16; S.Y. Lin, E.C. Yih Jr., J.G. Thomsen, ref. 22.</p>	<p>In transonic flow, variable coefficients of the unsteady linear potential equation can be removed only with some difficulty in the nonlinear steady equation. This becomes linear in terms of the unsteady potential.</p>	
Mathematical side	<p>In all numerical methods the unsteady unsteady potential equation is satisfied exactly.</p> <ol style="list-style-type: none"> <li><b>Integral equation method:</b> A solution is arrived by application of Green's theorem, which lead to an integral representation of the velocity potential in terms of the values of the potential on the boundary.</li> <li><b>Finite difference method:</b> This is a direct approach to solve the governing equation by replacing derivatives by finite differences and some or all of the continuous variables by discreteordinates. Finite differences is hard to use with irregular geometries or complicated boundary conditions.</li> <li><b>Finite element method:</b> In this method nodal equations are derived by a suitable averaging process over finite subregions in which a piecewise smooth approximation of the solution has been previously carried out. The techniques used to derive the set of nodal equations are variational and weighted residual techniques.</li> </ol>		
In connection with the mathematical side, within the velocity ranges of laminar, transonic and supersonic flow, the following physical models are commonly used.			
Physical models	<p><b>Doublet-Liftline / Discrete Vortex Model:</b></p> <p><b>Application:</b> Thin wings of arbitrary planform, three-dimensional configurations, finite aspect ratios.</p> <p><b>Literature:</b> T.P. Kallman, W.P. Barden, J.P. Cossling (ref. 23); W.P. Barden, T.P. Kallman (ref. 24); T.P. Kallman, W.P. Barden, J.P. Cossling (ref. 25); R. Remond, T.E. Lakshminarayana (ref. 26); T.E. Lakshminarayana, R. Remond, L.J.L. Franssen (ref. 27); S.M. Dehghani-Heravi (ref. 28); C. Rohrbach (ref. 29); R. Remond, A. Remond, R.J. Zonneveld (ref. 30).</p> <p><b>Panel Method:</b></p> <p><b>Application:</b> Wings, bodies, interference</p> <p><b>Literature:</b> H. Hirschberg (ref. 32); M. Goldstein (ref. 33).</p> <p><b>Kutta-Joukowski Method:</b></p> <p><b>Application:</b> Thin wings of arbitrary planform; in connection with local distribution of load functions also complicated three-dimensional configurations.</p> <p><b>Literature:</b> D.E. Davies (ref. 35); D.E. Davies, G.C.C. Smith (ref. 36); G.C. Carter (ref. 37); R.H. Atkins (ref. 38); R.H. Atkins, S. Venkateswaran (ref. 39); P. Sato (ref. 40); J. Fornstam, D. Ljungqvist (ref. 41); G.M. Brune, A.R. Darin (ref. 42).</p>	<p><b>Lifted Medium Analysis:</b></p> <p><b>Application:</b> Pointed profiles and three-dimensional wings about M=1</p> <p><b>Literature:</b> S.R. Brand (ref. 14).</p> <p><b>Modified Source Line Method:</b></p> <p><b>Application:</b> Pointed wings with finite thickness at M=1</p> <p><b>Literature:</b> S.Y. Lin, E.C. Yih Jr., J.G. Thomsen (ref. 23).</p> <p><b>Mixed Flow Analysis:</b></p> <p><b>Application:</b> Wings of arbitrary planform, Porter analysis</p> <p><b>Literature:</b> J. Becker (ref. 34); S.R. Brand (ref. 14).</p>	<p><b>Kutta Function Method:</b></p> <p><b>Application:</b> Thin wings of simple planform in connection with local distribution of load functions also complicated three-dimensional configurations.</p> <p><b>Literature:</b> G.W. Jones, A.R. Darin (ref. 31).</p> <p><b>Match Line Method:</b></p> <p><b>Application:</b> Thin slender pointed wings with sub- and supersonic flow fields.</p> <p><b>Literature:</b> H. Hirschberg (ref. 32); S.R. Brand (ref. 14).</p> <p><b>Direct Method:</b></p> <p><b>Application:</b> Pointed delta wing</p> <p><b>Literature:</b> Karlofka, G.C.C. Smith (ref. 35); L. Martin (ref. 33); E.M. Riedel-Grothe (ref. 43).</p>

## FIGURES

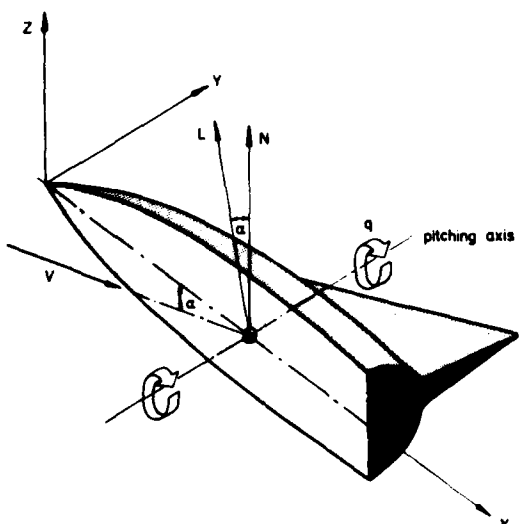


Fig. 2.1: Body-fixed coordinate system for the determination of pitching derivatives (theoretical aerodynamics)

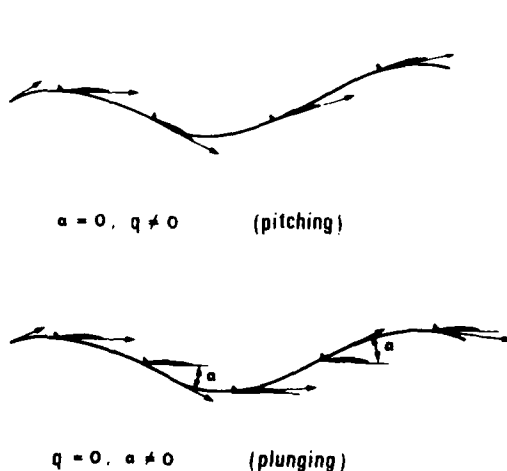


Fig. 2.2: Pitching and plunging motion of a missile

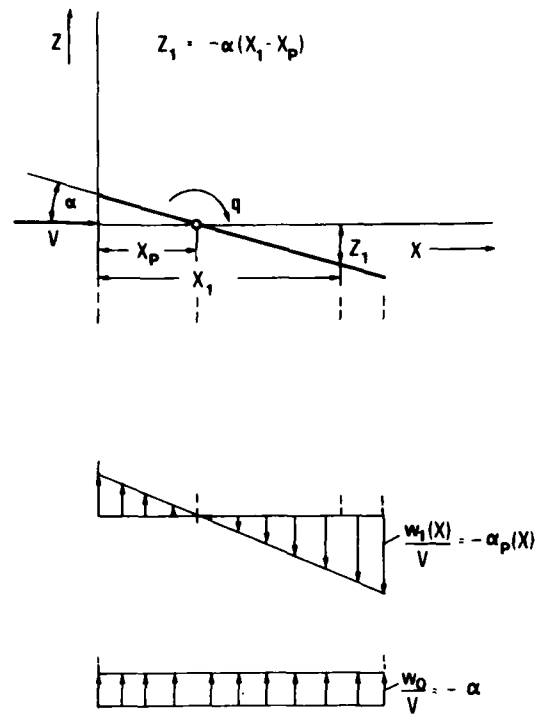


Fig. 2.3: Angle-of-attack distributions over a wing at angle-of-attack  $\alpha$  and pitching velocity  $q$  about  $X_p$

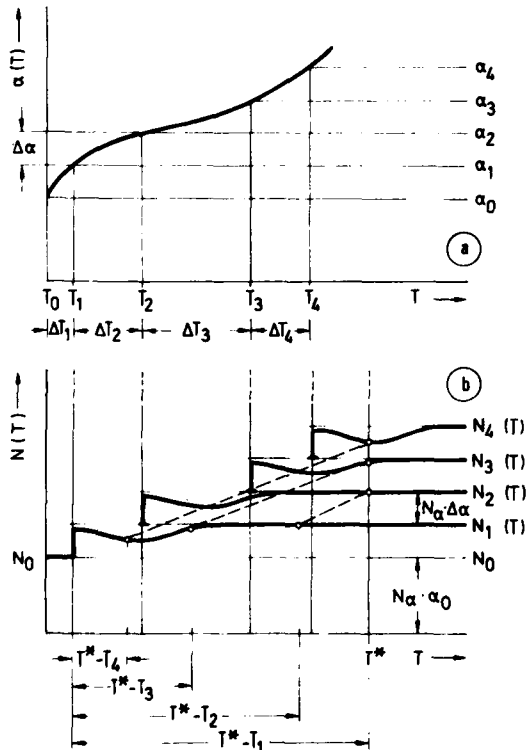


Fig. 2.5: Linear addition of response functions  
a) Sequence of differential steps  $\Delta \alpha$  as discretization of a linear or non-linear angle-of-attack with time  
b) Sum of response functions  $N(T)$

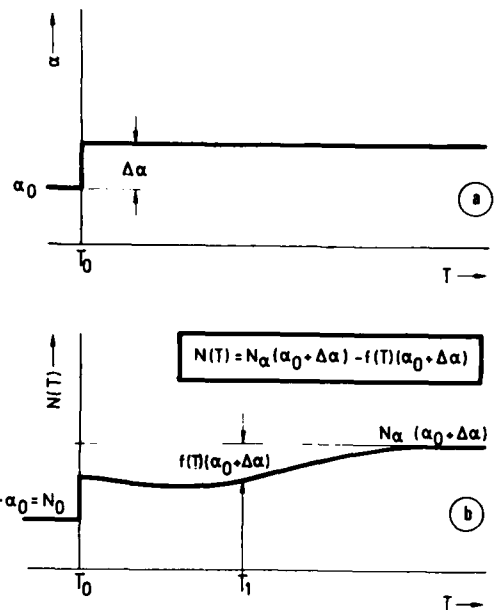


Fig. 2.4: Indicial function method  
a) Steplike change  $\Delta \alpha$  of the angle-of-attack from  $\alpha_0$  to  $\alpha$   
b) Response of the normal force  $N(T)$  to  $\Delta \alpha$ , indicial function  $f(T)$  according to M. Tobak

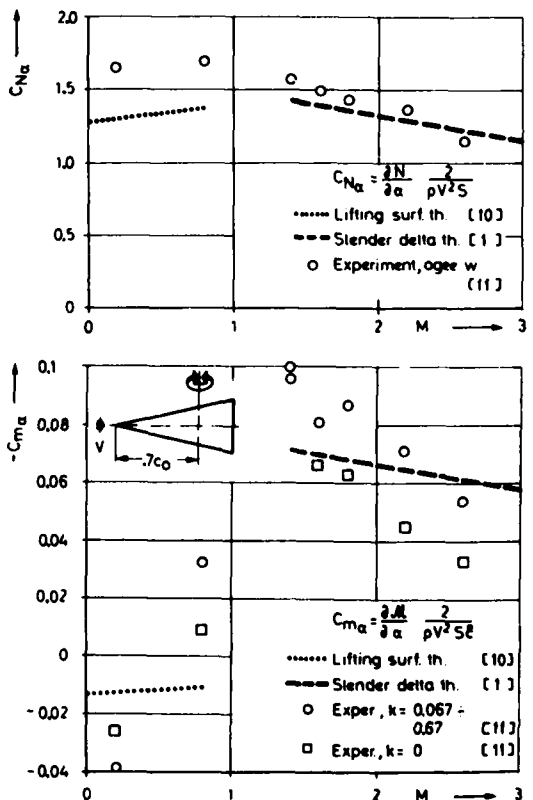


Fig. 3.1: Normal force slope and pitch stiffness of low aspect-ratio delta and ogee wings,  $AR = 0.924$

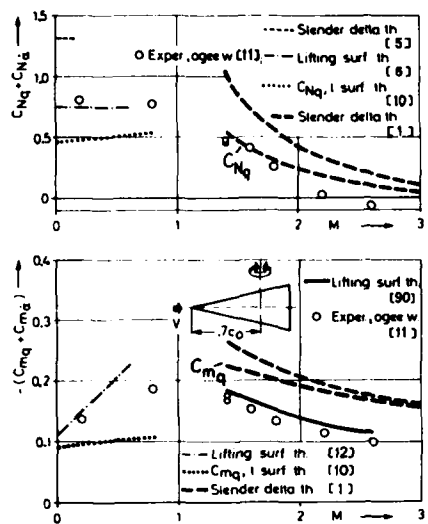


Fig. 3.2: Normal-force and pitching moment damping of low aspect-ratio delta- and ogee-wings  $AR=0.924$ , comparison of theoretical and experimental results, pitch frequency of experiment  $k = q \cdot \bar{c} / V = 0.067 \pm 0.067$

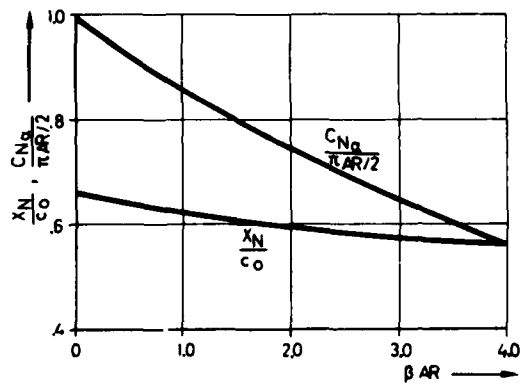


Fig. 3.3: Variation of  $C_{Nq} / (\frac{1}{2} \pi AR / 2)$  and  $X_N / c_0$  with reduced aspect ratio,  $\beta AR$

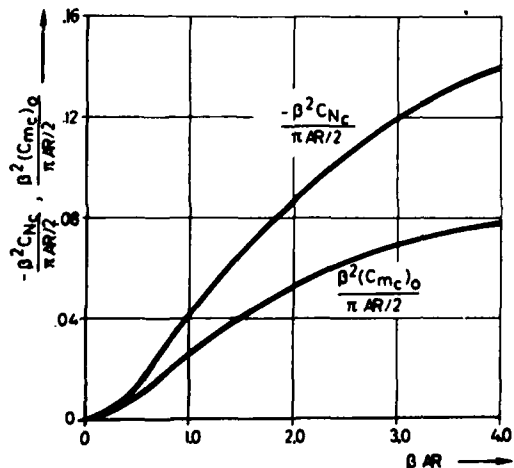


Fig. 3.4: Variation of lift- and moment-coefficient correction terms with reduced aspect ratio,  $\beta AR$

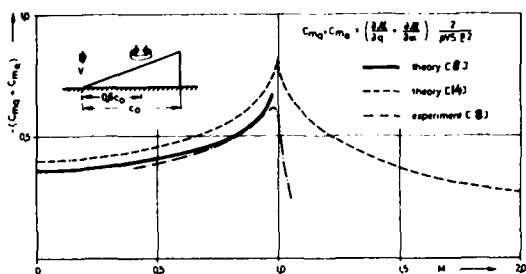


Fig. 3.5: Pitch damping of a delta wing  $AR=1.45$  in subsonic and supersonic flow, comparison of theoretical and experimental results

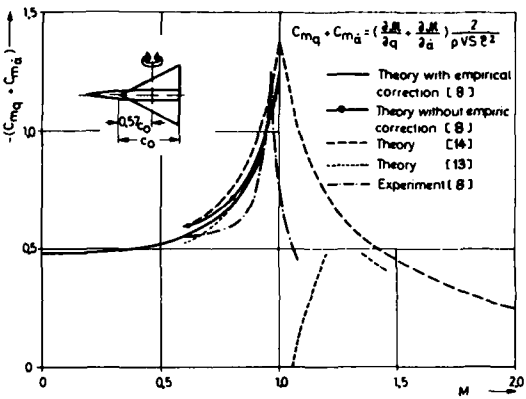


Fig. 3.6: Pitch damping of a delta wing  $AR=2$  in subsonic and supersonic flow, comparison of theoretical and experimental results

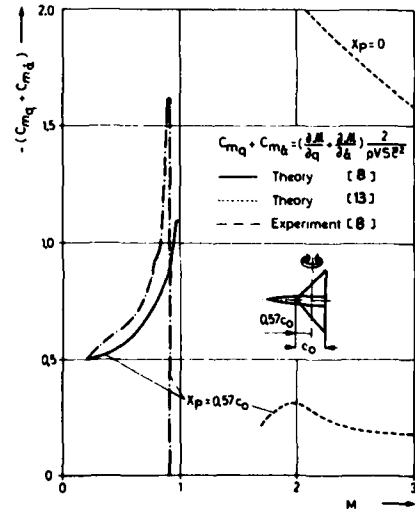


Fig. 3.7: Pitch damping of a delta wing  $AR=4$  in subsonic and supersonic flow, comparison of theoretical and experimental results

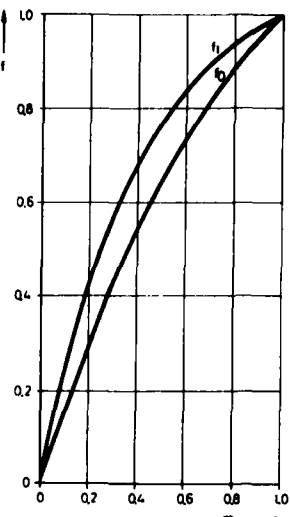


Fig. 3.8:

The functions  $f_0(m)$  and  $f_1(m)$  of Miles' supersonic theory of slender delta wings (ref. 1)

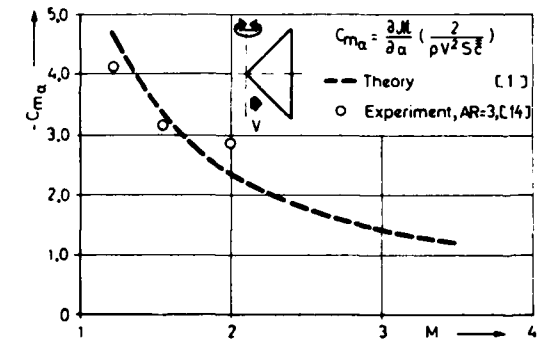
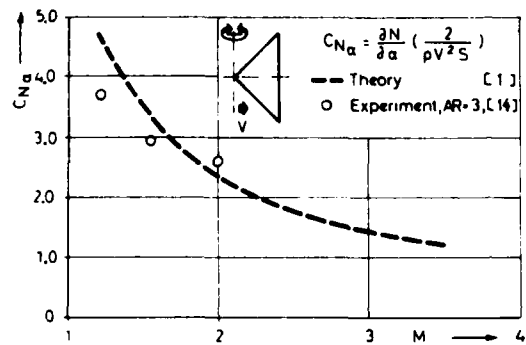
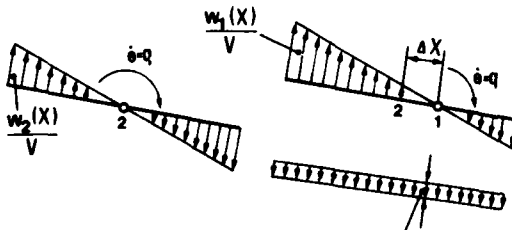


Fig. 3.9: Normal force slope and pitch stiffness of a delta wing  $AR=4$  in supersonic flow, comparison of theoretical and experimental results



$$\frac{\Delta W}{V} = -\Delta X \cdot \frac{c}{V}$$

Fig. 3.11: Change of the angle-of-attack distribution due to a shift of the pitch axis  $\Delta x$

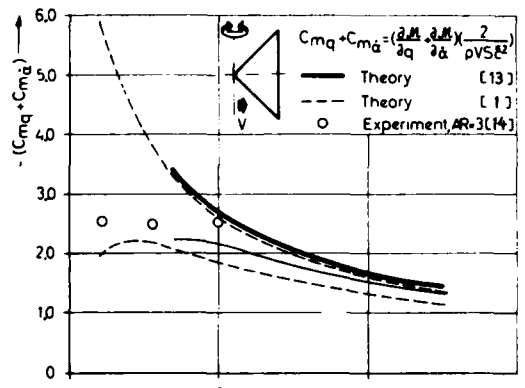
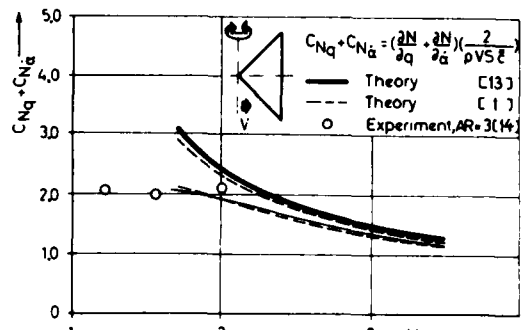


Fig. 3.10: Normal-force- and pitch-damping of a delta wing  $AR=4$  in supersonic flow, comparison of theoretical and experimental results

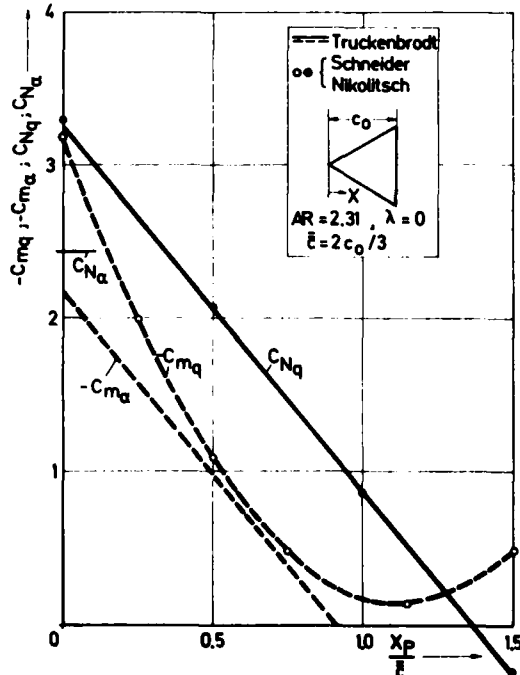


Fig. 3.12: Normal force slope, pitch stiffness, normal-force-and-pitch-damping of a delta wing in subsonic flow ( $M=0.2$ ), influence of the location of the pitching axis, comparison of theoretical data

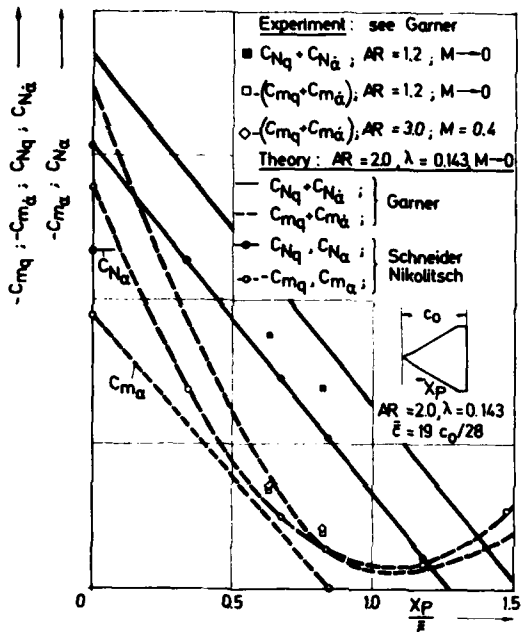


Fig. 3.13: Normal-force- and pitch-damping of delta wings in subsonic flow as function of the location of the pitching axis, comparison of theory and experiment

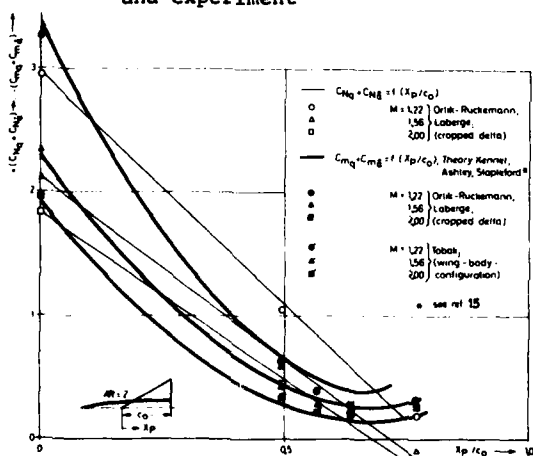


Fig. 3.15: Normal-force- and pitch-damping of a cropped delta wing ( $AR = 2, \lambda = 0.072$ ) and a delta wing-body-configuration ( $AR = 2$ ) in supersonic flow, influence of the location of the pitching axis, comp. theory, experiment

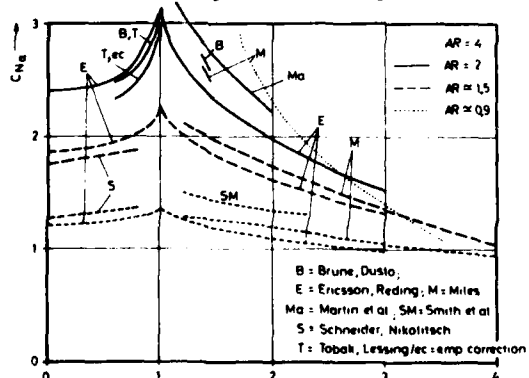


Fig. 3.16: Theoretical data of the normal force slope of delta wings at zero angle of attack

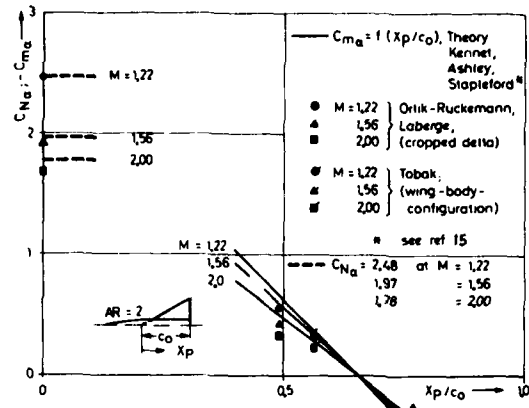


Fig. 3.14: Normal force slope and pitch stiffness of a cropped delta wing ( $AR = 2, \lambda = 0.072$ ) and a delta wing-body-configuration ( $AR = 2$ ) in supersonic flow, influence of the location of the pitching axis on the pitch stiffness, comparison of theory and experiment

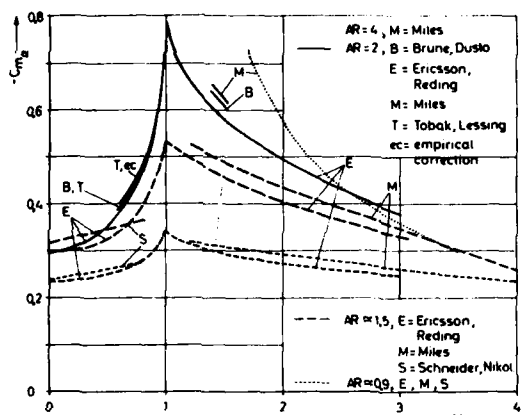


Fig. 3.17: Theoretical data of the pitching moment slope of delta wings at zero angle of attack, location of pitch-ing axis at  $X_p/c_0 = 0.5$

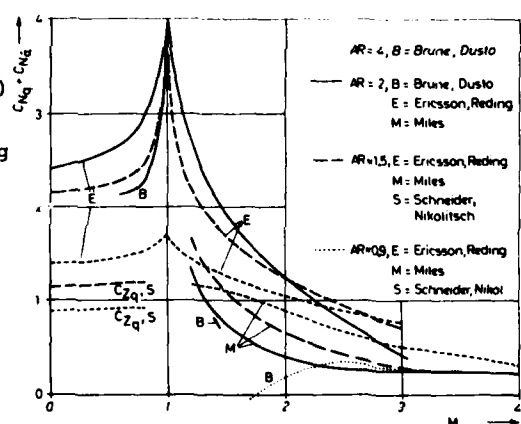


Fig. 3.18: Theoretical data of normal force damping of delta wings at zero angle of attack, location of pitch-ing axis at  $X_p/c_0 = 0.5$

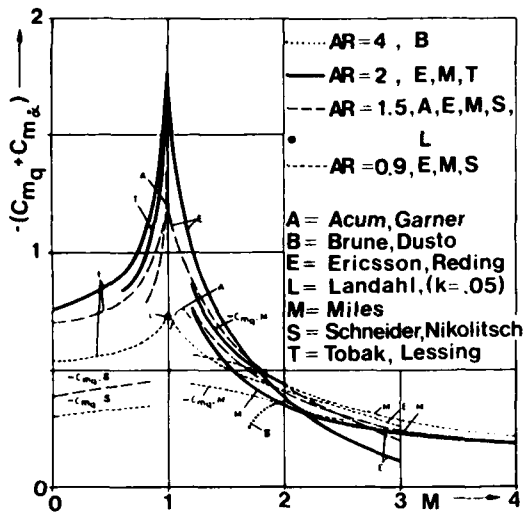


Fig. 3.19: Theoretical data of pitch damping of delta wings at zero angle of attack, location of pitching axis at  $X_p/c_0=0.5$

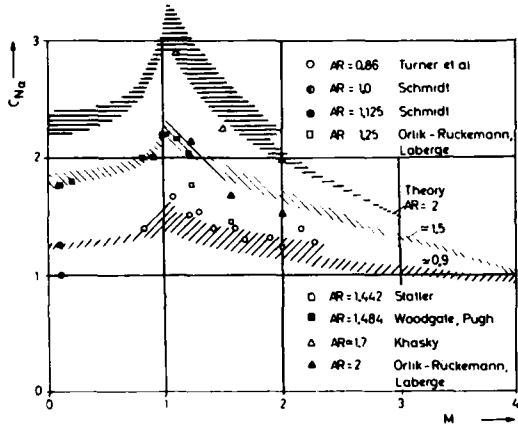


Fig. 3.20: Experimental results of the normal force slope of delta wings compared to the bandwidth of theoretical data of fig. 3.16

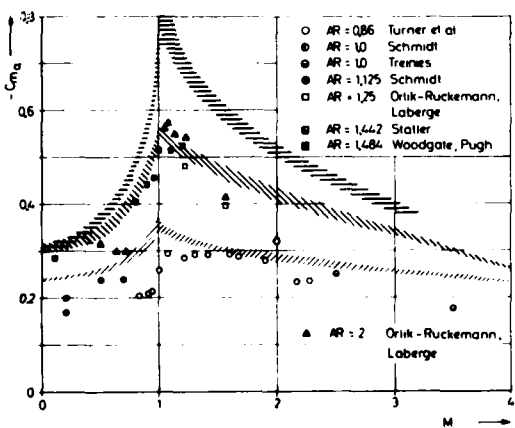


Fig. 3.21: Experimental data of the pitch stiffness of delta wings compared to the bandwidth of theoretical data of fig. 3.17, location of pitching axis  $X_p/c_0=0.5$

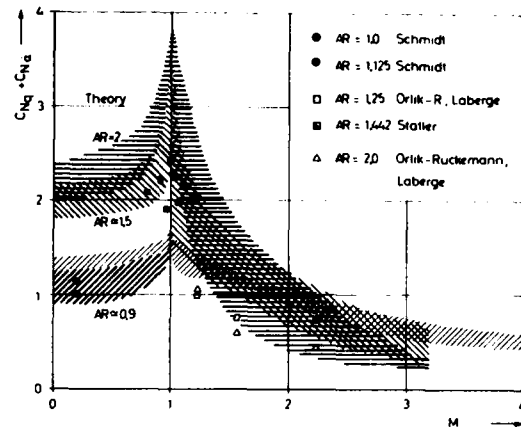


Fig. 3.22: Experimental data of the normal force damping of delta wings compared to the bandwidth of theoretical data of fig. 3.18, location of pitching axis  $X_p/c_0=0.5$

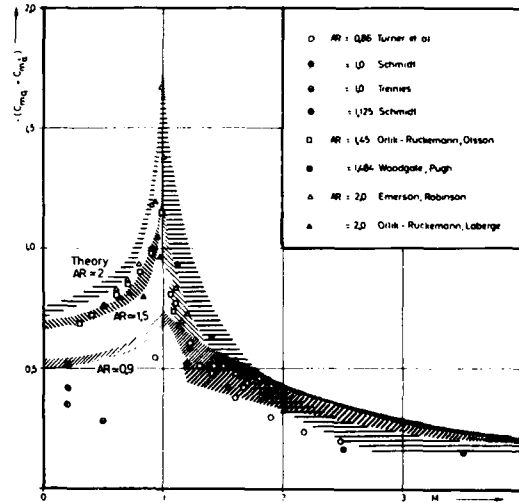


Fig. 3.23: Experimental data of pitch damping of delta wings compared to the bandwidth of theoretical data of fig. 3.19, location of pitching axis  $X_p/c_0=0.5$

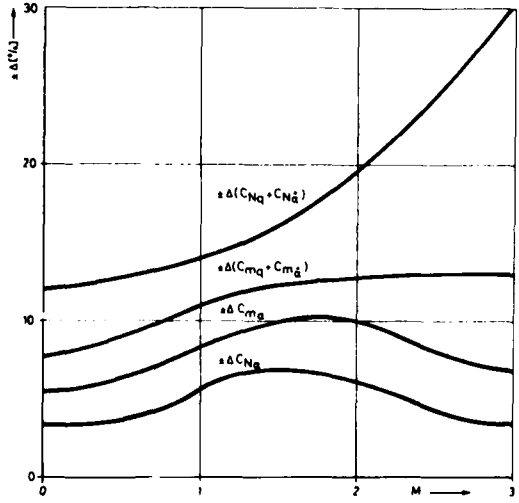


Fig. 3.24: Percentage of the deviation from the mean values of  $C_{N_a}$ ,  $C_{m_q}$ ,  $C_{N_q}+C_{N_d}$ ,  $C_{m_q}+C_{m_d}$  of slender delta wings ( $AR \leq 2$ )

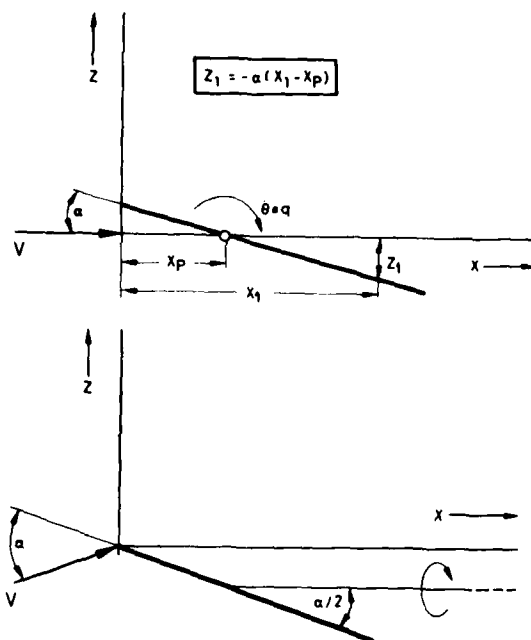


Fig. 3.25: Wing displacement due to the pitching velocity  $q$  and model of free vortex separation according to Bollay

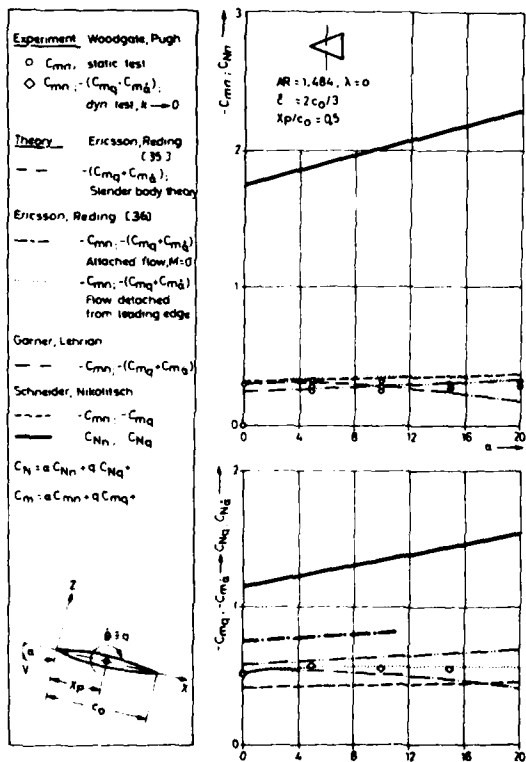


Fig. 3.26: Nonlinear normal force and pitching moment coefficients  $C_N$ ,  $C_m$ , normal-force- and pitch-damping of a delta wing in subsonic flow ( $M=0.2$ ) as functions of the angle of attack, comparison of theory and experiment

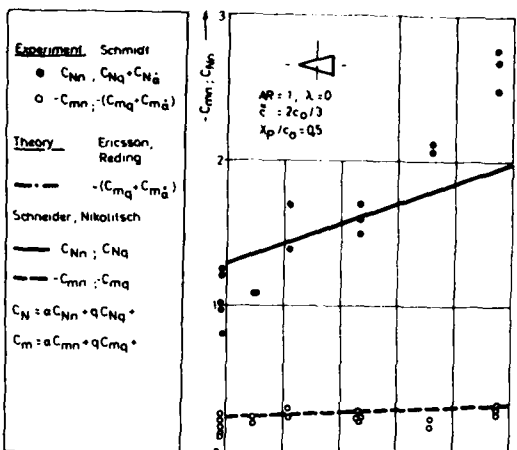


Fig. 3.27: Nonlinear normal force and pitching moment coefficients  $C_Nn$ ,  $C_mn$ , normal-force- and pitch-damping of a delta wing in subsonic flow ( $M=0.2$ ) as functions of the angle of attack, comparison of theory and experiment

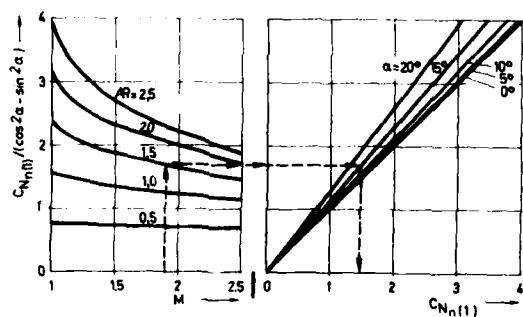


Fig. 3.28: Normal force coefficient  $C_Nn(1)$  of delta wings ( $0.5 \leq AR \leq 2.5$ ) at angle-of-attack ( $0^\circ \leq \alpha \leq 20^\circ$ ) in attached supersonic flow ( $1 \leq M \leq 2.5$ )

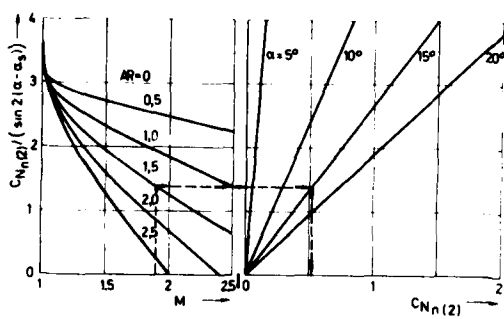


Fig. 3.29: Normal force coefficient  $C_{N_n}(2)$  of delta wings ( $0.5 \leq AR \leq 2.5$ ) at angle-of-attack ( $0^\circ \leq \alpha \leq 20^\circ$ ) in detached supersonic flow ( $1 \leq M \leq 2.5$ )

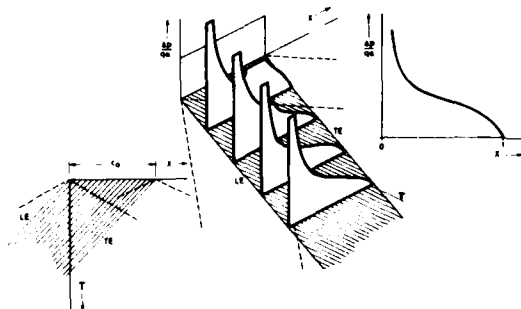


Fig. 3.30: Transient values of the pressure distribution on a two-dimensional wing at subsonic speed (LE=leading edge, TE=trailing edge)

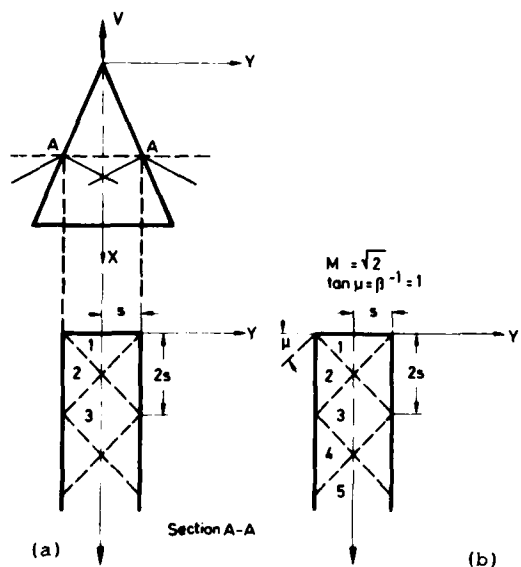


Fig. 3.31: Strip theory, slender delta wing  
a) Traces of wing section A-A,  $Y-t'$  diagram  
b) Equivalent steady problem,  $Y-X$  diagram

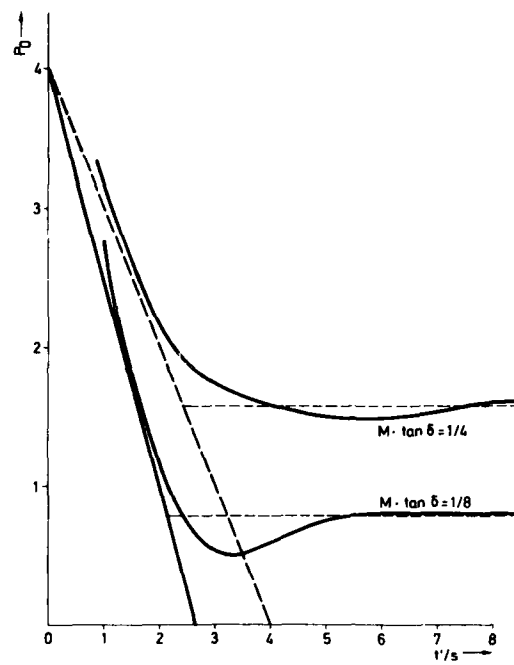


Fig. 3.32: Pressure parameter  $P_0$  as function of dimensionless time  $t'/s$ , delta wing ( $M \tan \delta = 1/4, 1/8$ ) plunging motion in supersonic flow, subsonic leading edge

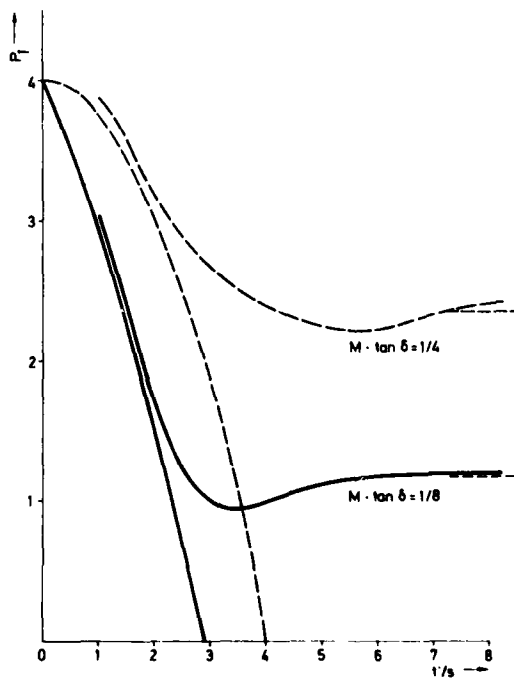


Fig. 3.33: Pressure parameter  $P_1$  as function of dimensionless time  $t'/s$ , delta wing ( $M \tan \delta = 1/4, 1/8$ ) pitching motion about apex in supersonic flow, subsonic leading edge

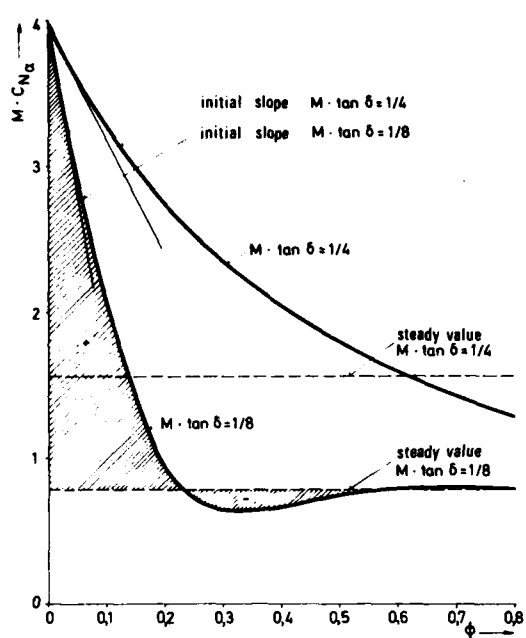


Fig. 3.34: Response function  $M \cdot C_{N_0}(\phi)$  of delta wings ( $M \tan \delta = 1/4, 1/8$ ) in supersonic flow, subsonic leading edge

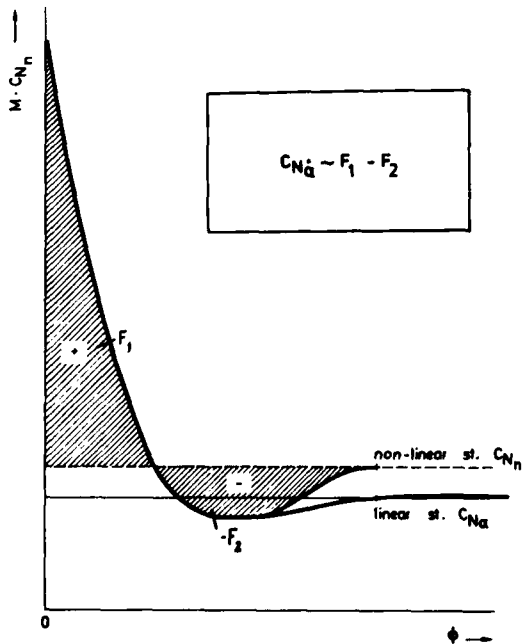


Fig. 3.35: Schematic diagram of  $C_{N_0}$  in the non-linear angle-of-attack range

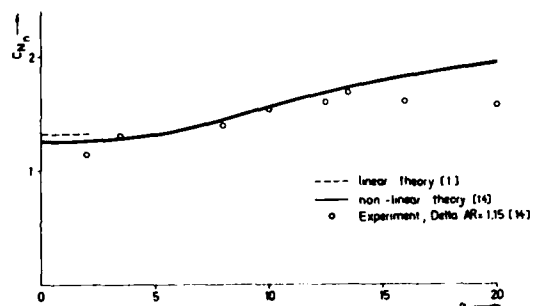


Fig. 3.36: Non-linear normal force slope  $C_{Nn}(\alpha)$  of a delta wing with  $AR=1$  at  $M=2$

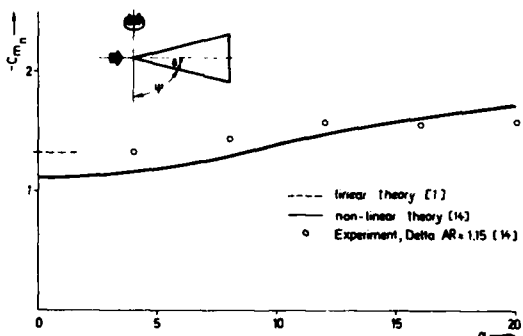


Fig. 3.37 Non-linear pitch stiffness  $C_{mn}(\alpha)$  of a delta wing with  $AR=1$  at  $M=2$

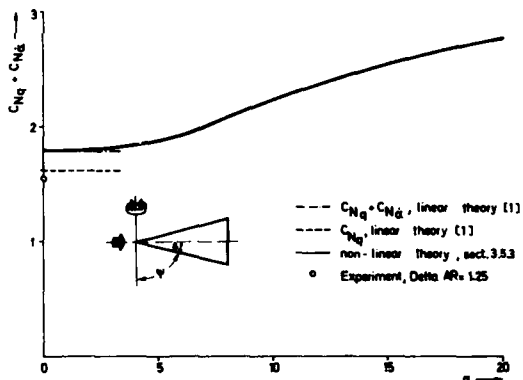


Fig. 3.38: Normal-force-damping of a delta wing with  $AR=1$  at  $M=2$ , as function of angle-of-attack

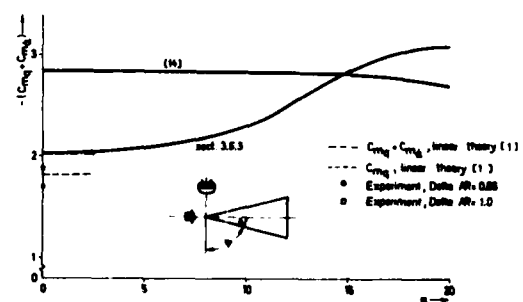
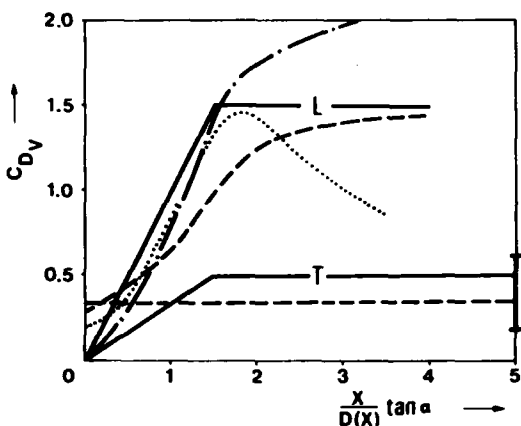


Fig. 3.39: Pitch damping of a delta wing with  $AR=1$  at  $M=2$ , as function of angle-of-attack

Jorgensen  
 Jones et al. } steady flow  
 s. [44]  
 Schwabe  
 Saripaya } impulsively  
 started flow  
 Bryson } s. [43, 44]  
**Approximations [43]**  
 — L — laminar cross-flow  
 — T — turbulent cross-flow



$$\frac{dC_D}{dx} = \sqrt{C_D \left( \frac{D_0}{c_0} + \frac{1}{x} \right)^2 + 2 c_{\infty} x - x^2} - C_D \left( \frac{D_0}{c_0} + \frac{1}{x} \right)$$

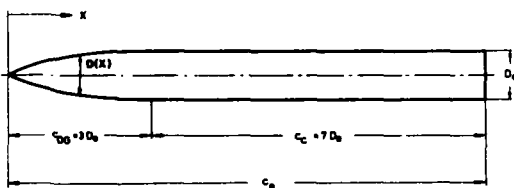


Fig. 4.2: Ogive-cylinder-configuration (COG=length of ogive,  $C_C$ =length of cylinder,  $D(x)$ =diameter of ogive)

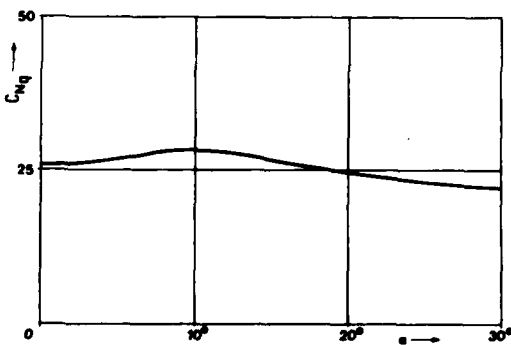


Fig. 4.3: Normal-force-damping  $C_{Nq}(\alpha)$  of an ogive-cylinder-configuration of Fig. 4.2 at  $M=0.8$ , laminar cross-flow boundary layer, location of pitching axis  $X_p/D_0 = 5.67$

Fig. 4.1: Local viscous cross flow drag  $C_D v$  of a cylindrical body at angle-of-attack  $\alpha$ , cross flow velocity  $V \sin \alpha$  ( $L$ =laminar boundary layer,  $T$ =turbulent boundary layer)



Fig. 4.4: Pitch damping  $C_{Mq}(\alpha)$  of an ogive-cylinder-configuration of Fig. 4.2 at  $M=0.8$ , laminar cross-flow boundary layer, location of pitching axis  $X_p/D_0 = 5.67$

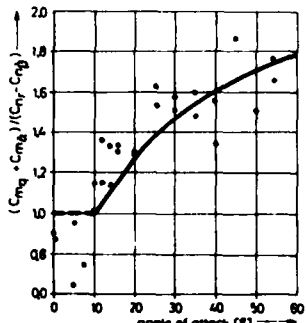
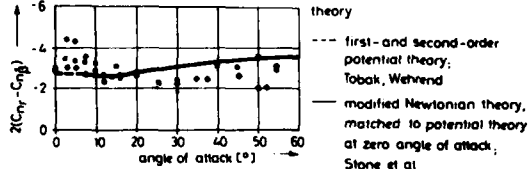
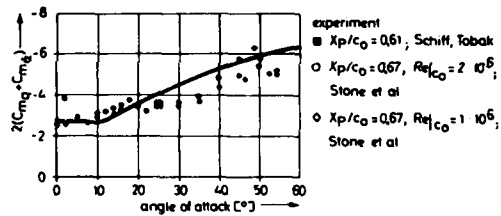


Fig. 4.5: High angle-of-attack effect on the damping moments of a cone of  $10^\circ$  half angle at  $M=2$ , comparison of experimental data with Newtonian and potential theory

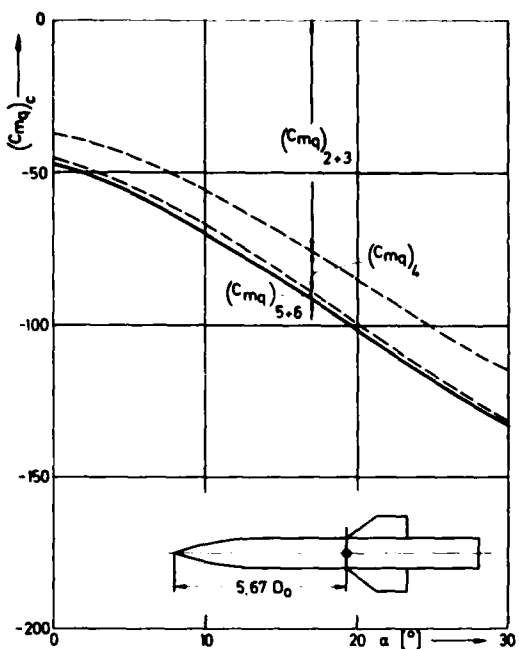


Fig. 5.1: Pitch damping of a missile configuration with the fin tip and pitch axis at  $X_p = 5.67 D_0$ ,  $M = 0.8$ ; indices:  $2+3 \equiv$  body,  $4 \equiv$  wing,  $5+6 \equiv$  wing/body interference

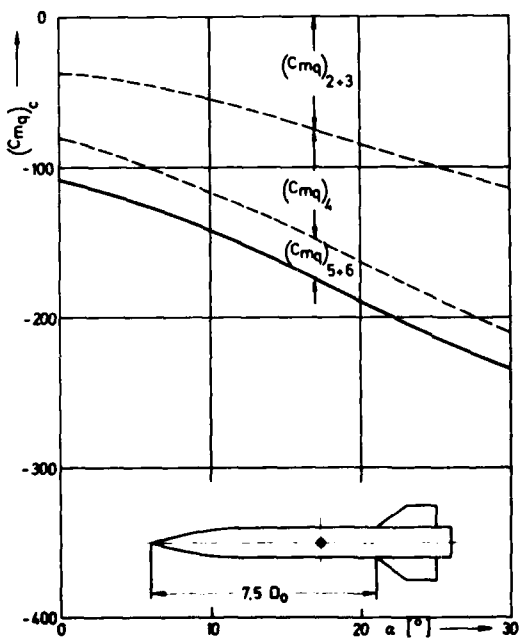


Fig. 5.2: Pitch damping of a missile configuration with the fin tip at  $7.5 D_0$  and the pitch axis at  $X_p = 5.67 D_0$ ,  $M = 0.8$ ; indices see fig. 5.1

- (1)  $\cdots - K_{B(W)}(N_n)$ , modified Lennartz theory
- (2)  $\cdots$  cylindrical body replaced by rectangular wing section
- (3)  $\cdots$  empirical relations simulating (2)
- (4)  $\cdots$  vortex separation, model fig. 5.14

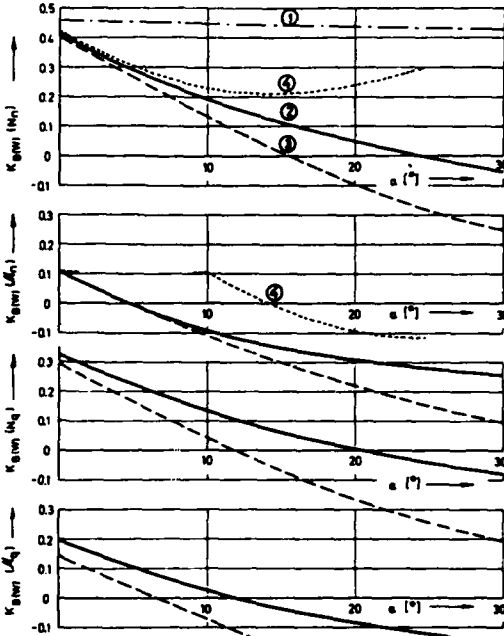


Fig. 5.3: Interference factors  $K_B(W)$  of the normal force slope  $N_n$ , pitch stiffness  $M_n$ , normal force damping  $N_g$  and pitch damping  $M_g$  of the wing-body configuration of Fig. 5.1:  $M = 0.8$ ,  $n_R = 0.4$ ,  $AR = 1$ ,  $\lambda = 0.5$ ,  $\psi_L = 53.13^\circ$

Experiment  $M = 0.5$ , Esch

config	$c_c/D$	$c_w/D$	$\psi_L$	$\lambda$	$AR$	$\eta_R$
A	4.8	6.63	63.4°	0.4	0.8575	0.5
B	9.8	11.63	63.4°	0.4	0.8575	0.5

Slender body theory ; Pitts, Nielsen, Kaattari

$\eta_R = 0.5$

Non-linear lifting surface + symmetrical body vortices

— configuration A

- - - configuration B

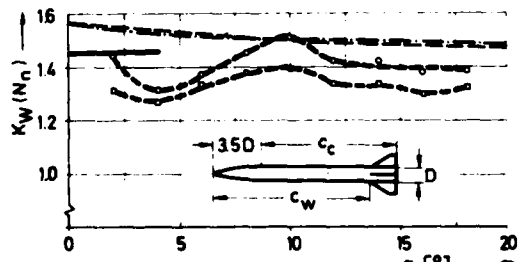


Fig. 5.4: Steady normal force interference factor  $K_W(N_n)$  of a missile with cruciform fins in plus-position and with different body length. Comparison of theoretical and experimental results

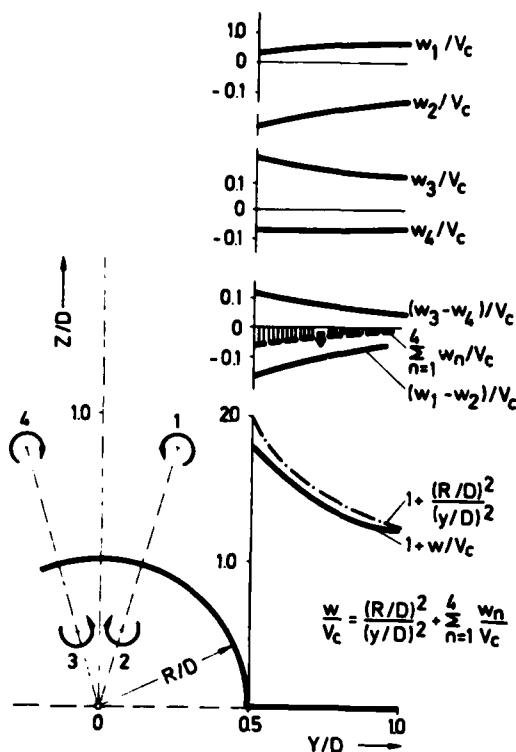


Fig. 5.5: Vortices and upwash velocity distribution in the cross-flow plane at the fin trailing edge of the configuration of Fig. 5.4 at  $\alpha=25^\circ$

Experiment  $M=0.8$ ; Nielsen

$\cdots \circ \cdots \psi_1 = 76^\circ, \lambda=0, AR=1, n_R=0.5$

Slender body theory; Pitts, Nielsen, Kaattari

$n_R = 0.5$

Non-linear lifting surface theory + body interference

$M=0.8$

$\cdots \circ \cdots \psi_1 = 76^\circ, \lambda=0, AR=1, n_R=0.5$

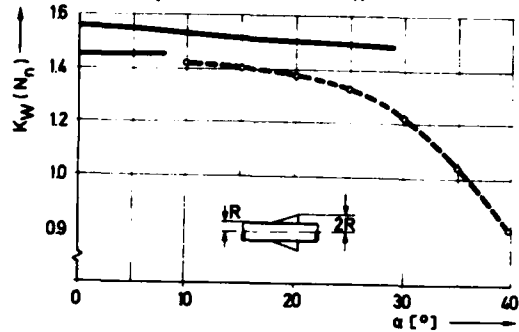


Fig. 5.7: Interference factor  $K_B(W)$   
a)  $K_B(W)$  for various wing aspect ratios as function of  $n_R$  (modified Lennartz theory)  
b) Normal force distribution of a rectangular wing-body with  $AR \rightarrow \infty$  and  $n_R=0.4$  (lin. Lennartz theory)

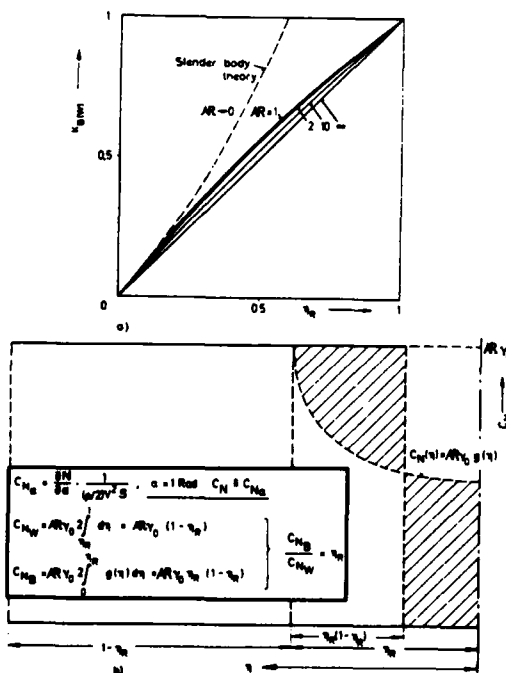


Fig. 5.6: Steady normal force interference factor  $K_W(N_n)$  of a wing-body combination without nose, comparison of theoretical and experimental results

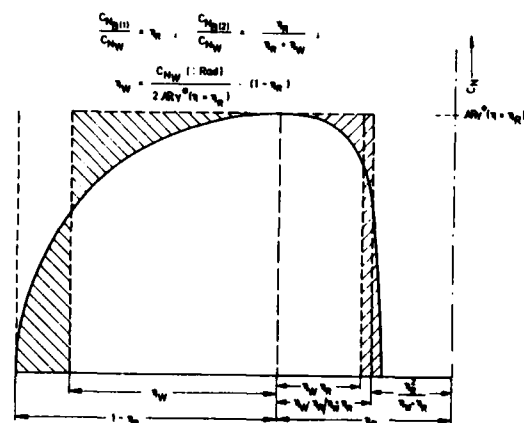


Fig. 5.8: Representation of the wing normal force  $C_{N_W}/2$  by the area  $n_W \cdot AR \cdot Y^* (n=n_R)$  and the body normal force  $C_{N_B}/2$  by the area  $n_W n_R \cdot AR \cdot Y^* (n=n_R)$  or by  $((n_W n_R)/(n_W + n_R)) \cdot AR \cdot Y^* (n=n_R)$ . Rectangular wing-body configuration  $n_R=0.4, AR=2$

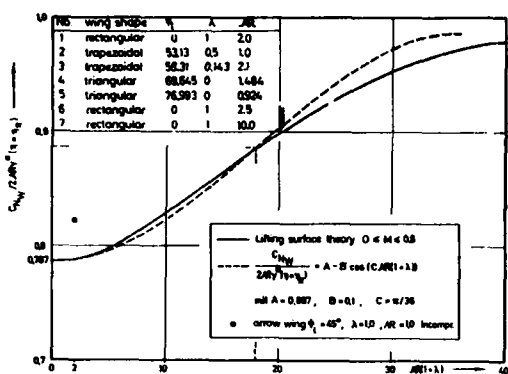


Fig. 5.9: Ratio of  $C_{Nw}/(2AR\gamma^*(n=n_R))$  at  $\alpha=0^\circ$  for the tabulated wing shapes, influence of the taper ratio and the leading edge sweep

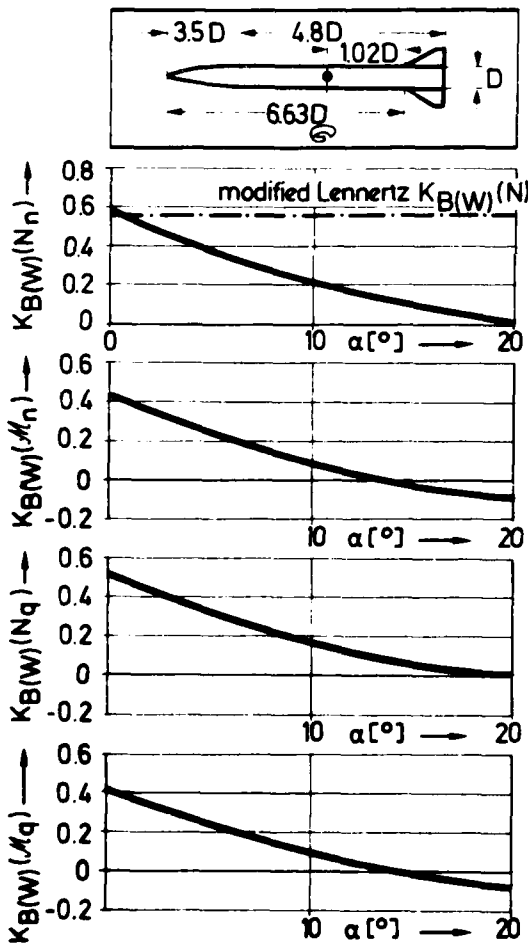


Fig. 5.11: Non-linear interference factor of a wing-body configuration at  $M=0.5$  with  $\psi_l=63.4^\circ$ ,  $AR=0.8575$  and  $n_R=0.5$

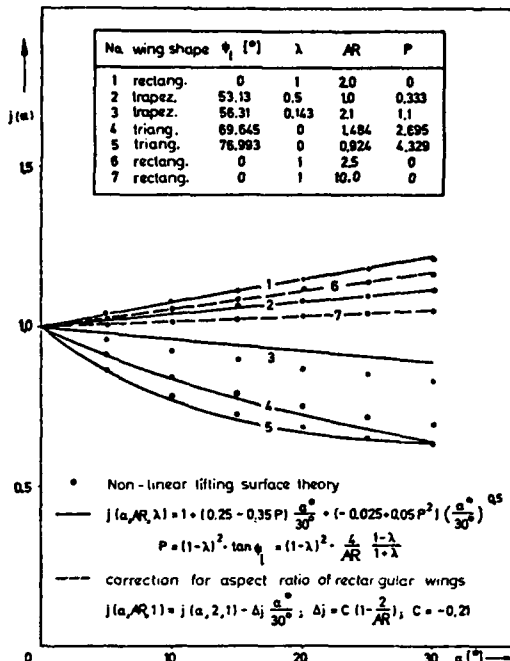


Fig. 5.10: Influence of the angle-of-attack on the ratio  $C_{Nw}/(2AR\gamma^*(n=n_R))$  for the tabulated wing shapes

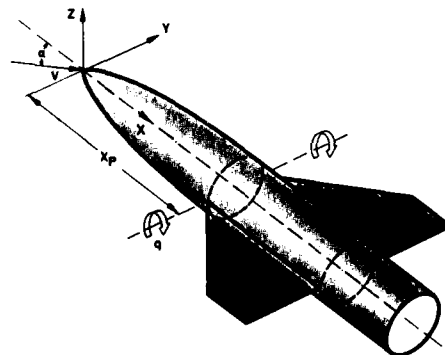


Fig. 5.12: Body fixed coordinate system for the determination of pitching derivatives

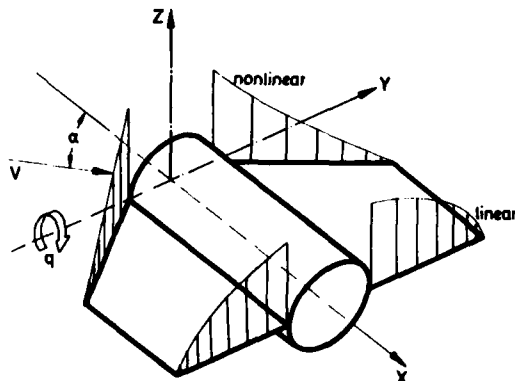


Fig. 5.13: Linear and non-linear circulation over the wing span

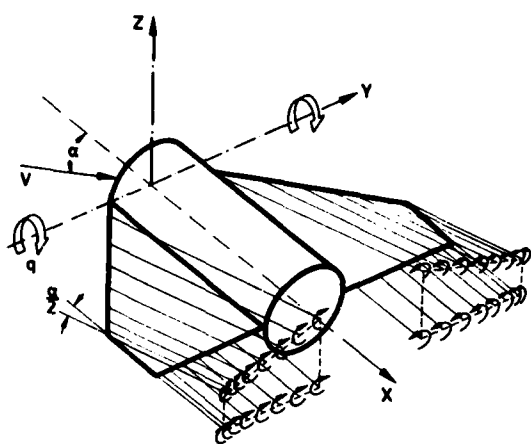


Fig. 5.14: Model of vortex separation from the wing leading and trailing edges

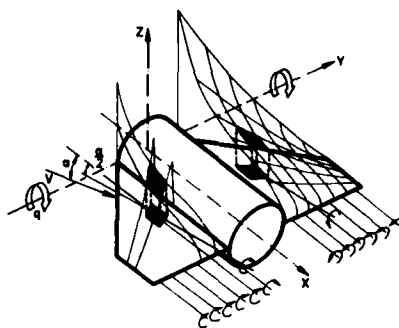


Fig. 5.15: Model of vortex separation from the wing surface and trailing edges

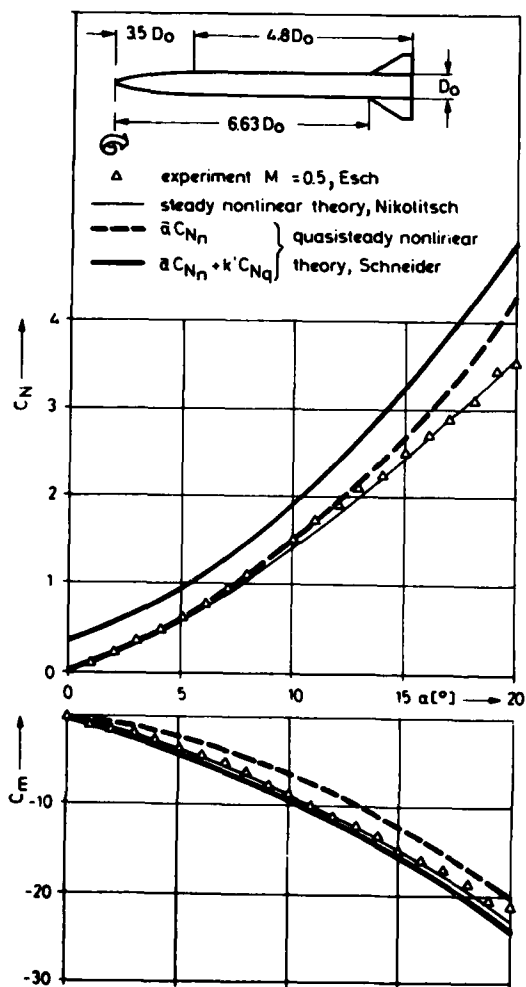


Fig. 5.16: Normal force and moment coefficients of a missile configuration with laminar body boundary layer, comparison of theoretical and experimental results, reduced frequency  $k' = kD_0/c$  with  $k = qc/V = 0.05$

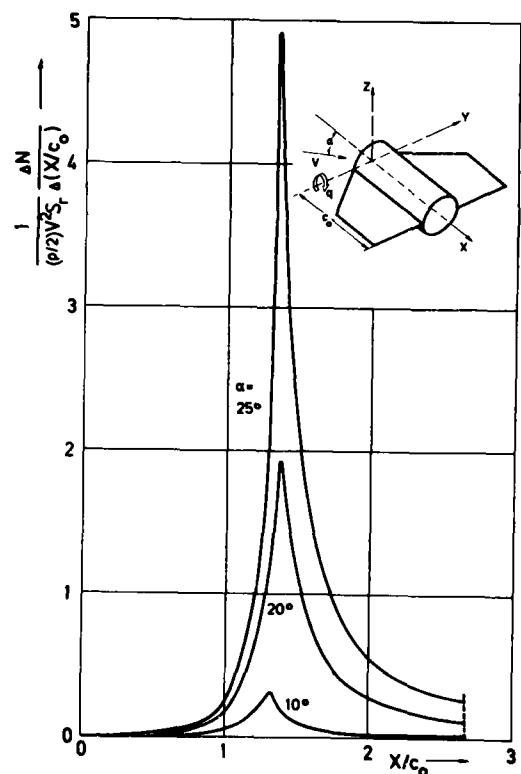


Fig. 5.17: Non-linear part of the local lift along the wing longitudinal axis

AEROELASTICITY, INCLUDING DYNAMIC  
EFFECTS OF SEPARATED FLOW

L. E. Ericsson  
Lockheed Missiles & Space Co., Inc.  
Sunnyvale, California, USA

**SUMMARY**

No purely theoretical means exist whereby the aeroelastic effects of separated flow can be computed. The static aeroelastic response, the structural divergence, can be determined using experimental results directly. This is, however, not the case in regard to the dynamic response of the structure. It is rare that applicable dynamic experimental results are available. The present paper describes how static experimental data can be used to define the unsteady aerodynamics of separated flow, and how these in turn are used to define the dynamic structural response.

**NOMENCLATURE**

A	axial force, coefficient $C_A = A/(\rho U^2/2)S$
d	body diameter
$D_{ref}$	reference length
D	aerodynamic damping derivative
$f(t)$	driving function
i	imaginary number, $i = (-1)^{1/2}$
K	aerodynamic stiffness derivative
L	longitudinal distance
M	Mach number
M	moment, coefficient $C_m = M/(\rho U^2/2)S D_{ref}$
m	generalized mass
N	normal force, coefficient $C_N = N/(\rho U^2/2)S$
P(t)	generalized force
P	static pressure, coefficient $C_p = (p-p_\infty)/(\rho U^2/2)$
q	pitch rate
q(t)	normalized coordinate
S	reference area
t	time
U	velocity
$\bar{U}$	convection velocity
X	horizontal coordinate (Fig. 21)
Z	vertical coordinate (Fig. 21)
z	relative deflection
$\alpha$	angle-of-attack
$\tilde{\alpha}$	generalized angle of attack, e.g. $\tilde{\alpha} = \theta + \dot{Z}/U$
$\beta$	equivalent spike deflection angle
$\delta$	boundary layer thickness
$\Delta$	difference
$\rho$	air density
$\omega$	free-free bending frequency
$\zeta$	structural damping, fraction of critical
$\zeta_s, \zeta_a$	aerodynamic damping, fraction of critical
$\theta$	rotation angle (Fig. 21)

$\nu$	Prandtl-Meyer expansion angle
$\nu_{\max}$	maximum number of sinusoidal gusts (Fig. 32)
$\phi$	normalized modal deflection
$\phi'$	normalized modal slope

Subscripts

A	axial force contribution
a	attached flow
b	base, also buffeting
c	cylinder
e	edge of boundary layer
ps	pseudo-static
s	separated flow
t	total
$\infty$	undisturbed flow
o	at $\alpha = 0$

Superscripts

i induced, e.g.  $\Delta^i C_N$  = separation-induced normal force

Derivative Symbols

$$\varphi' = \partial \varphi / \partial X$$

$$\dot{\alpha} = \partial \alpha / \partial t : \ddot{\alpha} = \partial^2 \alpha / \partial t^2$$

$$C_{m\alpha} = \partial C_m / \partial \alpha$$

$$C_{mq} + C_{m\dot{\alpha}} = C_{m\dot{\theta}} = \partial C_m / \partial (c\dot{\theta}/U)$$

## 1. INTRODUCTION

When the aerodynamic loads are generated by attached flow there are time-proven theoretical methods<sup>1,2</sup> by which the aeroelastic response of aircraft, missiles, and space vehicles can be determined. However, in many cases, especially in regard to missiles and aerospace launch vehicles, aerodynamic considerations rarely have any decisive impact on the design. As a result these vehicles often have large regions of separated flow, as is exemplified by the Saturn-Apollo rocket (Fig. 1), and the aerodynamic loads are dominated by separated flow (Fig. 2). In spite of all the progress that is constantly being made no satisfactory theoretical method is yet available whereby these separated flow effects can be predicted. Thus, they have to be determined experimentally, as in the case shown in Fig. 2.

The experimental static load distribution can be used directly in an aeroelastic analysis to compute the static divergence characteristics of the structure. However, to determine the dynamic structural response requires knowledge of the unsteady aerodynamic loads. For an elastic vehicle, such as the Saturn-Apollo launch vehicle, these loads can only be obtained through tests in which the elastic vehicle dynamics are fully simulated<sup>3</sup>. Because of the complexity of such tests the model design has to be "frozen" 6 months or more before the test. During this time period the full scale vehicle design rarely remains "frozen". In the case of the Saturn-Apollo booster, its structure, geometry, and design trajectory had all changed significantly when the dynamic test data<sup>3</sup> finally became available. Without an analytic method, in which the effects of these changes could be accounted for, the test data could not be used to determine the dynamic response of the full scale vehicle.

The main theme of the present paper is to describe how such analytic means can be developed, which use static experimental data to compute dynamic aeroelastic characteristics. A step-by-step description will be given first, using the Saturn-Apollo launch vehicle as an example. After that, various other examples will be discussed briefly to demonstrate the versatility of the method, while at the same time illustrating how almost every new design brings new flow mechanisms into the aeroelastic picture, preventing the analysis from ever becoming routine.

## 2. ANALYTIC APPROACH

A key feature in the analytic approach is the use of static experimental data to obtain the unsteady aerodynamic loads. My colleague Peter Reding and I have used the terminology "quasi-steady" to signify this feature in our analyses. Unfortunately, the term has been used extensively in the literature to designate loads determined only by the instantaneous, local flow conditions. In order to separate the two concepts the term "pseudo-static" will be used in this paper to indicate that the dynamic loads are derived from static data.

A complete understanding of the static separated flow effects and the dependence of the various separation-induced loads on the attitude and relative location of the forebody are necessary prerequisites for the "pseudo-static" dynamic load analysis. Since nearly every type of flow separation is present on the Saturn-Apollo booster, it is a good example to use for demonstration of how various types of flow separation alone and in combination can affect elastic vehicle dynamics.

The loads occurring in a separated flow region fall generally in two categories: 1) the classical "quasi-steady" load which only depends upon the instantaneous local flow conditions. 2) the separation-induced load which is dependent upon the effect of forebody attitude and relative displacement on the flow separation. In the latter case there is a time lag before a body perturbation has altered the load on the body element submerged in separated flow. The determination of this time lag and the differentiation between local and separation-induced loads are the critical elements in the pseudo-static loads analysis.

### 3. ANALYSIS

The analysis in Ref. 4 of the Saturn-Apollo booster will be used to illustrate the pseudo-static analytic method.

#### 3.1 Steady Aerodynamics

Figure 3a is a shadowgraph of the flow field in the vicinity of the Apollo escape rocket and command module, showing the large region of flow separation produced by the escape-rocket wake. Figure 4a illustrates the occurrence at the command module shoulder of extensive flow separation caused by the blunt (33 deg) conical command module at subsonic Mach number,  $M = 0.9$ . These two types of flow separation drastically alter the static force loadings over the submerged afterbodies, as is illustrated in the accompanying normal force distributions (Figs. 3b and 4b). Furthermore, the steep interstage flares produce their own regions of flow separation, both subsonically and supersonically.

The impingement of the escape-rocket wake on the command module produces the most severe separated-flow effect. The tower-mounted escape rocket creates a flow field that is very similar to that obtained with a flow separation spike.

##### 3.1.1 Spike-Induced Separation

The similarity between spike-induced separation<sup>5</sup> and the separation caused by the escape rocket may be seen by comparing Figs. 5 and 6. Figure 5 shows that a flow separation spike produces a reduced axial force at  $\alpha = 0$  while increasing the normal force derivative and producing a more stable pitching moment. Figure 4 shows that similar changes in the Apollo command module characteristics are produced by adding the escape rocket and tower.

These force variations are the result of the velocity deficit and the large velocity gradients which occur within the separated region. (See flow sketch in Fig. 5). The axial force reduction is caused by the reduced average velocity in the wake. The increased normal force derivative and the stabilizing axial force moment result from translating the wake over the submerged body, thus exposing the windward side to rapidly increasing velocities while the leeward side is exposed to reduced velocities. The wake translating effects of angle of attack and of spike deflection then should be the same for a thin spike. The aerodynamic forces produced by the traversing wake are solely a function of the lateral position  $z$  of the spike tip relative to the windshield. Figure 7 shows that the effects of  $\alpha$  and the effective spike deflection angle  $\beta$  are similar but not equivalent. Since  $z = \beta L = \alpha l$  for small angles the difference between  $\alpha$  and  $\beta$  characteristics in Fig. 7 are due to rotating the windshield through the angle  $\alpha$ . Thus, two force derivatives are generated with angle of attack; an induced force,  $\Delta C_{N\beta}$ , proportional to the effective spike deflection angle  $\beta$ , and a local rotational force,  $C_{N\alpha_s}$ , due to the attitude  $\alpha_s$  of the windshield.

The effect of the Apollo escape rocket then may be analyzed similarly to the spiked-body effect, the escape-rocket disk acting as the spike tip. The effect of local attitude of the command module may be assessed by considering the command module pitched in the reduced dynamic-pressure field of the wake. The reduced axial force on the command module is a direct measure of the dynamic-pressure deficit. Thus,

$$\frac{q_s}{q_\infty} = \frac{\left( C_{A0} \right)_s}{\left( C_{A0} \right)_a} \quad (1)$$

where  $a$  refers to attached flow (measured with tower off) and  $s$  refers to separated flow (measured with tower on).

The command module force dependent upon local attitude is then

$$C_{N\alpha_s} = \frac{\left( C_{A0} \right)_s}{\left( C_{A0} \right)_a} C_{N\alpha_a} \quad (2)$$

and the induced derivative due to wake source translation is,

$$\Delta^i C_{N\alpha_s} = \Delta^i C_{N\beta} = C_{N\alpha_{total}} - C_{N\alpha_s} \quad (3)$$

Figure 8 shows how these command module forces vary with Mach number.

When the escape-rocket disk is removed, a further complication is introduced, viz., the wake-directing capability of the escape rocket flare. Figure 9 shows that the wake of a directing spike tip is moved downward an amount  $\Delta z$  which is proportional to the wake source attitude  $\theta_s$ . The total induced derivative is then

$$\Delta^i C_{N_{\alpha_s}} = \Delta^i C_{N_\beta} + \Delta^i C_{N_{\theta_s}} \quad (4)$$

where  $\Delta^i C_{N_{\theta_s}} < 0$

The disk-off relative displacement effect may be evaluated from the disk-on data by adjusting for wake size effects<sup>5</sup>. Since the  $\alpha = 0$  axial force reduction is indicative of wake size, the disk-off relative displacement derivative may be computed as follows

$$\begin{aligned} \frac{\left(\Delta^i C_{N_\beta}\right)_{\text{disk on}}}{\left(\Delta^i C_{N_\beta}\right)_{\text{disk off}}} &= \frac{\left(\Delta^i C_{A_0}\right)_{\text{disk on}}}{\left(\Delta^i C_{A_0}\right)_{\text{disk off}}} , \text{ where } \Delta^i C_{A_0} = \left(C_{A_0}\right)_a - \left(C_{A_0}\right)_s . \text{ Therefore,} \\ \left(\Delta^i C_{N_\beta}\right)_{\text{disk off}} &= \frac{\left(\Delta^i C_{A_0}\right)_{\text{disk off}}}{\left(\Delta^i C_{A_0}\right)_{\text{disk on}}} \left(\Delta^i C_{N_\beta}\right)_{\text{disk on}} \end{aligned} \quad (5)$$

The remaining portion of the induced derivative is  $\Delta^i C_{N_{\theta_s}} = \Delta^i C_{N_{\alpha_s}} - \Delta^i C_{N_\beta}$

Figure 10 shows the Mach number dependence of these local and induced derivatives. The local and induced command-module axial-force moments are obtained by the same considerations.

The wake from the escape rocket, after impinging on the command module, reattaches on the service module aft of the shoulder. The pressure distributions of Fig. 11 indicate that a negative shoulder loading is generated by the reattaching wake, the main contribution coming from the leeward side through greatly reduced negative pressures. The negative normal force region is mainly due to the upstream effects of the pressure rise at reattachment. At angle of attack the leeward separation is increased as more of the escape rocket wake is translated over to the leeward side allowing more of the recompression pressure rise to be propagated upstream. The opposite effect occurs on the windward side. The distortion of the leeward pressure distribution reflects this upstream pressure propagation. The loading so generated is always negative, and is induced by the wake-source translation. The local load may be either positive or negative depending on the initial ( $\alpha = 0$ ) wake configuration. At transonic speeds the tower wake initially passes over the shoulder and a contracting flow field exists aft of the shoulder, similar to that of a boattail. Thus, local rotation produces negative lift, as with a boattail. Supersonically, the wake attaches on the command module and the local rotation gives a positive normal force derivative. The magnitude of the local loading may be assessed by eliminating the reattachment shock distortions from the pressure distribution, as is indicated in Fig. 11. The difference between this local load and the total load is of course the negative, induced loading, which has the same forebody dependence as the induced command module force. The Mach number dependence of this negative shoulder load, with its local and induced components, is shown in Fig. 12 for the disk-on configuration. In comparing these loadings with the command module loadings in Fig. 8, it can be seen that the negative shoulder load will dominate at subsonic and sonic speeds, whereas at supersonic speeds the positive command-module load is dominant.

### 3.1.2 Nose-Induced Separation

When the escape system is removed, the blunt command module causes the flow to separate off its shoulder at subsonic Mach numbers. This nose-induced separation, shown in Fig. 4, results from the steep, adverse pressure gradient over the forward service module, which the boundary layer cannot negotiate without separating. This separation is akin to the thin airfoil leading-edge separation with its so-called long bubble<sup>6</sup>. The pressure distribution in Fig. 13 shows that at  $\alpha = 0$  the pressure is constant in the separated flow region which extends to the aft service module and flare, where the reattachment process occurs. The negative and positive pressure peaks in the separated region are substantially less than for attached flow. At angle of attack the windward boundary layer on the command module is strengthened and made thinner; hence, it can withstand a greater adverse pressure gradient. This thinner boundary layer and the added constraint of the external flow bring the windward side pressures closer to attached flow values, and the command module shoulder pressure becomes more negative. On the leeward side the effect is opposite but less drastic, giving slightly reduced negative shoulder pressures. The resulting negative shoulder load is proportional to the forebody crossflow, which in lumped form can be represented by the crossflow at the shoulder. On the aft service module and flare the increased velocities in the windward side of the wake produce increased pressures that approach attached flow values. On the leeward side, the decreased velocities in the wake produce the opposite effect. The positive aft-body forces, induced by these changes in the wake are determined by the crossflow at the command module shoulder. The effect of local attitude on the flare force may be determined in the usual way by the drag reduction, i.e.,

$$C_{N_{\alpha_s}} = \frac{\left(C_{A_0}\right)_s}{\left(C_{A_0}\right)_a} C_{N_{\alpha_a}} \quad (6)$$

The remainder of the flare force is induced by the wake changes

$$\Delta^i C_{N_{\alpha_s}} = C_{N_{\alpha_{total}}} - C_{N_{\alpha_s}} \quad (7)$$

The same ratio between local and induced loads is used for the service module loading. In Fig. 14 these cylinder and flare forces are shown as a function of Mach number, demonstrating the large effect of the nose-induced separation at subsonic speeds. At supersonic speeds the nose-induced separation disappears. Instead, a small separated flow region caused by the flare shocks appears. This supersonic shock-induced separation is discussed in the next section.

The pressure distribution in Fig. 13 also shows the existence of a negative shoulder load aft of the flare. This loading is similar to the negative shoulder load aft of the command module obtained in presence of the escape system. Thus the partitioning into local and induced force components is done in the same manner as was discussed in the previous section.

### 3.1.3 Shock-Induced Separation

The existence of separated regions over the various interstage flares has been indicated by the force distributions of Figs. 3 and 4 and by the Mach number variations of the flare force in Fig. 14. The pressure distributions in Fig. 15 for tower-on and Fig. 16 for tower-off indicate that a region of shock-induced separation occurs forward of the interstage flare joining the service module with the S-IV stage. The separation induces a negative cylinder load at the start of separation due to the differential windward and leeward shock position. The positive loads induced on the cylinder and flare immediately aft of the shocks result not only from the differential shock position but also from the difference in windward and leeward side shock strength, as is evidenced by the higher windward pressures in Fig. 15.

The effect of the differential shock position may be visualized by studying Fig. 17. The extent of the separation forward of the flare is proportional to the boundary layer thickness  $\delta$  immediately ahead of the separation<sup>7</sup>. The effect of angle of attack is to increase the leeward boundary layer thickness and decrease that of the windward side. Thus, on the leeward side the extent of the separation is increased and on the windward side it is decreased. The result is a negative cylinder load, due to differential shock positions, and a positive flare load, due to the changed separated flow extent. The effect of the differential shock angles is sketched in Fig. 18. At angle of attack the windward shock gives a higher pressure rise than the leeward shock, i.e.,  $P_{SW} > P_{SL}$ . The boundary conditions for the separated region is  $P_1 = P_S$ , and the separated-flow static pressure is therefore higher on the windward side than on the leeward side,  $P_{SW} > P_{SL}$ . This is possible because of three-dimensionality, which allows crossflow from windward to leeward side in the separated flow region. Thus, the differential shock angle, which is due to local crossflow, induces positive aft-body loads on the cylinder and flare.

The separation of the effects of differential shock position and local shock angle is a much simplified representation, since coupling exists between the two phenomena. However, by considering these effects as two separate entities, it is possible to ascertain the primary dependence of the induced derivatives on the forebody crossflow ahead of the shock and the local crossflow at the shock location.

The negative cylinder load is induced and dependent upon the forebody influence on the boundary layer at separation. (See Fig. 19). The effect of local flare attitude,  $\alpha_s$ , can again be assessed by considering the dynamic pressure deficit in the separated flow region, as manifested by the reduced drag. The remainder of the flare force,  $\Delta^i C_{N_{\alpha_s}}$ , is induced by the separation and is forebody-dependent. One part,  $\Delta^i C_{N_{\alpha_s1}}$ , is determined by the forebody crossflow ahead of the separation, and the other part,  $\Delta^i C_{N_{\alpha_s2}}$ , is dependent upon the local crossflow at the shock location. The same partition of loads is used for the positive service-module loading. The resultant positive cylinder-flare load, with its local and induced components, is shown in Fig. 17. The figure indicates that a subsonic flare-induced separation exists. It is the tower-wake reattachment shocks that produce this reseparated flow region over the aft cylinder and flare. When the separated flow reattaches on the cylinder aft of the flare a negative load is obtained. This load is similar to the flare shoulder load caused by the nose-induced separation, or the command-module shoulder load, caused by the escape-rocket wake, and the loading is treated in the same way.

## 3.2 Unsteady Aerodynamics

The unsteady aerodynamic characteristics are obtained using pseudo-static analytic methods. Pseudo-static forces are essentially static forces that are modified to account for slow perturbations from the steady-state condition. In what follows it will be shown how the static experimental data is modified to give the pseudo-static forces induced by the various types of separation.

### 3.2.1 Spike-Induced Separation

The spike-induced pseudo-static force can be derived in a straightforward manner by use of Fig. 20. As the thin spike does not have any effect on the wake, only the location of the spike tip is important. The spike is describing translatory oscillations relative to the conical windshield, the relative displacement  $z$  being a function of time. At time  $t$  the spike tip has the lateral displacement  $z(t)$ . The tip is, however, moving with a certain velocity  $z'(t)$ , and the wake impinging upon the windshield at time  $t$  was generated a time increment  $\Delta t$  earlier, when the spike tip had the relative displacement  $z(t - \Delta t)$ . This is the pseudo-static spike position, i.e., the equivalent static spike position for which the wake will impinge at the same location on the windshield as in the nonstationary case. The time increment  $\Delta t$  is the time required for the wake impinging upon the windshield to respond to the change in spike tip position. If the velocity  $U$  in the wake were constant,  $\Delta t$  would be  $\Delta t = L/U$  i.e., the time required for the wake to travel from the spike tip to the windshield. A representative average velocity  $\bar{U}$  can be derived from the dynamic pressure deficit manifested by the reduced drag of the windshield.

$$\frac{\bar{U}}{U} = \sqrt{\frac{q_s}{q_\infty}} = \sqrt{\frac{(C_{A_0})_s}{(C_{A_0})_a}} \quad (8)$$

where  $(C_{A_0})_s$  is the zero-angle-of-attack drag in the wake and  $(C_{A_0})_a$  is the drag obtained with attached flow, i.e., without the spike.

Since the attitude of the spike tip has no effect on the lateral position of the wake impinging upon the windshield, the (pseudo-static) force induced by lateral wake movement is

$$\Delta^i C_{PS} = \frac{\partial C_{N_s}}{\partial z} z(t - \Delta t) \quad (9)$$

$$\text{where } \frac{\partial C_{N_s}}{\partial z} = \frac{1}{L} \Delta^i C_{N_\beta}; \Delta t = \frac{L}{\bar{U}}$$

The remaining pseudo-static force on the windshield is dependent upon the local instantaneous angle of attack by the relationship

$$C_{PS} = \frac{\partial C_{N_s}}{\partial \alpha_s} \left[ \theta(t) + \frac{\dot{z}(t)}{\bar{U}} \right] \quad (10)$$

where  $\theta$  and  $\dot{z}$  are the local attitude and translatory velocity of the windshield

In studying Fig. 20 it is apparent that the non-steady wake is inclined an angle  $\epsilon$  relative to the pseudo-static wake. However, the unsteady wake also has a translatory velocity  $\dot{z}(t - \Delta t) \approx \dot{z}(t)$  relative to the pseudo-static wake, negating the effect of the inclined wake axis. That is,

$$\epsilon = \frac{z(t) - z(t - \Delta t)}{L} \approx \frac{\dot{z}(t)\Delta t}{L}$$

$$\text{But } \Delta t = \frac{L}{\bar{U}}$$

$$\text{Thus } \epsilon \approx \frac{\dot{z}(t)}{\bar{U}}$$

On the Saturn I-Apollo configuration, the escape rocket disk corresponds directly to the spike tip. There is some influence of the escape rocket on the leeward portion of the disk wake at angle of attack. However, this effect is small<sup>14</sup>. Equation (9) sufficiently describes the disk-wake-induced pseudo-static forces on the command module and forward service module. When the disk is removed, the escape rocket flare attitude has a directing influence on the wake. Thus Eq. (9) is modified as follows:

$$\Delta^i C_{PS} = \frac{\partial C_{N_s}}{\partial z} z(t - \Delta t) + \frac{\partial C_{N_s}}{\partial \theta_s} \theta_s(t - \Delta t) \quad (11)$$

where  $\theta_s$  is the attitude of the rocket flare and  $\partial C_{N_s}/\partial \alpha_s < 0$  is the directing effect of the rocket flare, shown earlier for the static aerodynamics.

### 3.2.2 Nose-Induced Separation

The forces  $\Delta^i C_{N_s}$ , induced in the separated flow from the blunt command module, are determined by the crossflow at the command module shoulder. In the pseudo-static case a time lag  $\Delta t$  occurs before this crossflow has affected the separated flow region aft of the shoulder, i.e.,

$$\Delta^i C_{PS} = \Delta^i C_{N_{\alpha_s}} \left[ \theta_N(t - \Delta t) + \frac{\dot{z}_N(t - \Delta t)}{\bar{U}} \right] \quad (12)$$

where  $\theta_N$  and  $\dot{z}_N$  are the local attitude and translatory velocity of the command module shoulder.

The time lag  $\Delta t$  is again assessed by accounting for the velocity deficit in the wake, evidenced by the flare drag reduction

$$\Delta t = \frac{L}{\bar{U}} : \frac{\bar{U}}{U} = \sqrt{\frac{(C_{A_0})_a}{(C_{A_0})_a}} \quad (13)$$

The quantity L is the distance between the command module shoulder and the location of the induced force.

The local force components have the same composition as before (See Eq. 10).

### 3.2.3 Shock-Induced Separation

It was shown earlier, in the discussion of static characteristics, that the extent of the separation, induced by the flare shock, was mainly determined by the boundary-layer thickness at the onset of separation. It was demonstrated that the variation in extent of separation between the windward side and leeward side is caused by the effect that local crossflow over the forebody ahead of the separation has on boundary-layer thickness at the point of separation. The pseudo-static boundary layer thickness at the separation point at time t is dependent upon local crossflow upstream at earlier time instants  $t - \Delta t$ , where  $\Delta t$  is the time required for the boundary layer at the separation point to respond to the upstream crossflow change. The forebody normal force distribution is a measure of the local crossflow effects. Therefore, the forebody crossflow can be represented in lumped form by the crossflow at the aerodynamic center,  $X_{AC}$ , of the forebody attached-flow loading. Thus, the pseudo-static boundary-layer thickness at the separation point at time t is determined by the local crossflow at  $X_{AC}$  at time  $t - \Delta t$ , where  $\Delta t = L/\bar{U}$  is the time required for the crossflow effect to be transmitted through the boundary layer the distance  $L = X_{AC} - X_s$  down to the separation point  $X_s$ . For the velocity  $\bar{U}$  a value  $\bar{U} = 0.8U$  is used. This is the convection speed in a turbulent boundary layer at transonic and low supersonic speeds.<sup>8</sup>

The pseudo-static separation-induced negative cylinder force at  $X_C$  can now be expressed as

$$(\Delta^l C_{PS})_C = \Delta^l C_{N_{\alpha_{AC}}} \tilde{\alpha}_{AC}(t - \Delta t) \quad (14)$$

$$\text{where } \tilde{\alpha}_{AC} = \theta_{AC} + \frac{\dot{z}_{AC}}{\bar{U}}$$

The term  $\tilde{\alpha}_{AC}$  is the crossflow angle at  $X_{AC}$  defined by the local attitude  $\theta_{AC}$  and translatory velocity  $\dot{z}_{AC}$ .

Likewise, the pseudo-static flare force at  $X_S$ , induced by the shock movement, is

$$(\Delta^l C_{PS})_1 = \Delta^l C_{N_{\alpha_{S_1}}} \tilde{\alpha}_{AC}(t - \Delta t - \Delta t_1) \quad (15)$$

$$\text{where } \Delta t_1 = \frac{X_C - X_S}{\bar{U}_1}$$

is the additional time lag through the separated region,  $(X_C - X_S)$ . The velocity  $\bar{U}_1$  is the average wake velocity, as defined in Eq. (13).

The pseudo-static force corresponding to the static force component induced by the shock-angle change is

$$(\Delta^l C_{PS})_2 = \Delta^l C_{N_{\alpha_{S_2}}} \tilde{\alpha}_C(t - \Delta t_1) \quad (16)$$

where

$$\tilde{\alpha}_C = \theta_C + \frac{\dot{z}_C}{U}$$

is the crossflow angle at the shock location,  $x_C$ .

Static force data give only the sum of these two force components,

$$\Delta^i C_{N\alpha_s} = \Delta^i C_{N\alpha_{s_1}} + \Delta^i C_{N\alpha_{s_2}} \quad (17)$$

Until more information becomes available these two components are weighted as the lengths of the approaching attached flow region and the separated flow region, respectively. This weighting makes the induced flare force dependent upon the crossflow at two upstream stations and, therefore, tends to moderate the effect of lumping the forebody crossflow effects for a long upstream cylinder, that in higher bending modes may have both positive and negative mode slopes.

The pseudo-static separation-induced negative load on the flare shoulder is treated the same way as the positive flare load, the only difference being the additional time lag required to cover the distance from flare to shoulder load.

Of the separation-induced forces discussed here, the shock induced pseudo-static force is by far the most difficult to assess. It is, therefore, fortunate that the shock-induced forces always appear in pairs, a negative cylinder load followed by a positive flare load. Thus, the net effect on both static and dynamic loads is moderate. This is also true, to a certain degree, when the positive flare load is followed by a negative shoulder load.

### 3.3 Vehicle Dynamics

The dynamics of the elastic vehicle are analyzed for single-degree-of-freedom oscillations in one bending mode.

#### 3.3.1 Equation of Motion

The equation of motion can be written in the following form using standard notations:

$$\tilde{m} [q(t) + 2\zeta\omega\dot{q}(t) + \omega^2 q(t)] = P(t) \quad (18)$$

where

$\tilde{m}$  = generalized mass

$\zeta$  = structural damping coefficient (as a fraction of critical damping)

$\omega$  = natural free-free bending frequency

$q$  = normalized coordinate (dots denoting time derivatives in the usual way)

$P(t)$  = generalized force

The generalized force  $P(t)$  is given by the virtual work done by the aerodynamic forces on the vehicle\*.

$$P(t) = \int \frac{dF}{dX} \varphi(X) dX + \int \frac{dM_A}{dX} \varphi'(X) dX \quad (19)$$

where

$dF/dX$  = normal force per unit length

$dM_A/dX$  = axial force moment per unit length

$\varphi(X)$  = normal mode

$\varphi'(X)$  = normal mode slope

There are three different types of generalized force

$$P(t) = P_s(t) + P_a(t) + P_b(t) \quad (20)$$

\* If  $W$  is the work done,  $P = \partial W / \partial q$

where

$P_s(t)$  = generalized force in separated flow

$P_a(t)$  = generalized force in attached flow

$P_b(t)$  = generalized force independent of vehicle motion, e.g., due to buffeting forces

Both  $P_b(t)$  and  $P_a(t)$  can be defined by well established methods.  $P_b(t)$  is a forcing function, a random function for the case of buffeting forces.  $P_a(t)$  is obtained by use of first-order theory.  $P_b(t)$  is, however, more difficult to determine, and the main effort here is devoted to describing how this force can be estimated by the use of static experimental data. In Fig. 21 it is assumed that the flow is attached aft of body station  $X_s$ . The forces in the separated flow forward of  $X_s$  are represented in lumped form. In general, the force  $C_N$  and the axial force moment  $C_m$ , generated on the conical frustum in the separated flow field from the nose, will be dependent not only upon the local angle of attack  $\alpha_s$  but also upon the angle of attack  $\alpha_N$  at the nose and the relative displacement,  $z = -(Z_N - Z_s)$ , between nose and frustum. For small deflections one may write  $F_s$  in the following form: (A similar expression is obtained for  $M_s$ ).

$$F_s = \frac{\rho U^2}{2} S \left\{ \frac{\partial C_N}{\partial \alpha_N} \tilde{\alpha}_N + \frac{\partial C_N}{\partial z} z + \frac{\partial C_m}{\partial \alpha_s} \tilde{\alpha}_s \right\} \quad (21)$$

In the nonstationary case  $\tilde{\alpha}_N$  and  $Z_N$  in  $z = -(Z_N - Z_s)$  will be the values at a time  $\Delta t$  earlier than the instantaneous value for  $\tilde{\alpha}_s$ , i.e.,

$$\begin{aligned} F_s(t) = & \frac{\rho U^2}{2} S \left\{ \frac{\partial C_{N_s}}{\partial \alpha_s} \tilde{\alpha}_s(t) + \frac{\partial C_{N_s}}{\partial \alpha_N} \tilde{\alpha}_N(t - \Delta t) \right. \\ & \left. - \frac{\partial C_{N_s}}{\partial z} [Z_N(t - \Delta t) - Z_s(t)] \right\} \end{aligned} \quad (22)$$

$\Delta t$  is the time required for the force  $F_s$  to respond to changes in  $\tilde{\alpha}_N$  and  $Z_N$ .

For the elastic vehicle in Fig. 21

$$\tilde{\alpha} = \theta + \frac{Z}{U}$$

where  $\theta = \varphi'(X) q(t)$ ,  $Z = -\varphi(X) q(t)$

The contribution to the generalized force  $P_s(t)$  from the force  $F_s$  and moment  $M_s$  of the frustum in the separated flow can then be expressed as follows, using the lumped version of Eq. (19).

$$\begin{aligned} P_s(t) = & \frac{\rho U^2}{2} S \varphi(X_s) \left\{ \frac{\partial C_{N_s}}{\partial \alpha_s} \left[ \varphi'(X_s) q(t) - \varphi(X_s) \frac{\dot{q}(t)}{U} \right] \right. \\ & + \frac{\partial C_{N_s}}{\partial \theta_N} \varphi'(X_N) q(t - \Delta t) - \frac{\partial C_{N_s}}{\partial \left( \frac{Z_N}{U} \right)} \varphi(X_N) \frac{\dot{q}(t - \Delta t)}{U} \\ & \left. + \frac{\partial C_{N_s}}{\partial z} \left[ \varphi(X_N) q(t - \Delta t) - \varphi(X_s) q(t) \right] \right\} \\ & + \frac{\rho U^2}{2} S D_{Ref} \varphi'(X_s) \left\{ \frac{\partial C_{m_s}}{\partial \alpha_s} \left[ \varphi'(X_s) q(t) - \varphi(X_s) \frac{\dot{q}(t)}{U} \right] \right. \\ & + \frac{\partial C_{m_s}}{\partial \theta_N} \varphi'(X_N) q(t - \Delta t) - \frac{\partial C_{m_s}}{\partial \left( \frac{Z_N}{U} \right)} \varphi(X_N) \frac{\dot{q}(t - \Delta t)}{U} \\ & \left. + \frac{\partial C_{m_s}}{\partial z} \left[ \varphi(X_N) q(t - \Delta t) - \varphi(X_s) q(t) \right] \right\} \end{aligned} \quad (23)$$

The force on the nose is dependent only on the local angle of attack. The force on the shoulder aft of the frustum, where the separated flow reattaches on the cylinder, will be composed the same way as the force on the frustum. How the time lag  $\Delta t$  is evaluated has been discussed earlier. The term  $P_s(t)$  in this form, Eq. (23), together with Eqs.(18) and (20), can be used in a real-time analytical simulation of the vehicle ascent. Equation (23) can, however, be simplified further. In general, the structural stiffness will be an order of magnitude larger than the aerodynamic stiffness, i.e., the effect of aerodynamic forces on the bending frequency is small. As the structural and aerodynamic damping are two orders of magnitude less than critical, the vehicle may be assumed to oscillate with the natural free-free bending frequency  $\omega$ . Thus,  $q(t)$  can be expressed as follows

$$q(t - \Delta t) \approx e^{-i\omega\Delta t} q(t) = \cos(\omega\Delta t) q(t) - \sin(\omega\Delta t) [iq(t)] \quad (24)$$

where  $q(t) \approx \omega [iq(t)]^*$

Equation (23) can, therefore, be written

$$P_s(t) = \frac{\rho U^2}{2} S \left[ K_s q(t) + D_s \frac{\dot{q}(t)}{U} \right] \quad (25a)$$

$$\begin{aligned} K_s &= \varphi(X_s) \left\{ \frac{\partial C_{N_s}}{\partial \alpha_s} \varphi'(X_s) + \frac{\partial C_{N_s}}{\partial \theta_N} \varphi'(X_N) \cos(\omega\Delta t) \right. \\ &\quad \left. - \frac{\partial C_{N_s}}{\partial \left( \frac{Z_N}{U} \right)} \varphi(X_N) \frac{\omega}{U} \sin(\omega\Delta t) + \frac{\partial C_{N_s}}{\partial z} \left[ \varphi(X_N) \cos(\omega\Delta t) - \varphi(X_s) \right] \right\} \\ &\quad + D_{Ref} \varphi'(X_s) \left\{ \frac{\partial C_{m_s}}{\partial \alpha_s} \varphi'(X_s) + \frac{\partial C_{m_s}}{\partial \theta_N} \varphi'(X_N) \cos(\omega\Delta t) \right. \\ &\quad \left. - \frac{\partial C_{m_s}}{\partial \left( \frac{Z_N}{U} \right)} \varphi(X_N) \frac{\omega}{U} \sin(\omega\Delta t) + \frac{\partial C_{m_s}}{\partial z} \left[ \varphi(X_N) \cos(\omega\Delta t) - \varphi(X_s) \right] \right\} \end{aligned} \quad (25b)$$

$$\begin{aligned} D_s &= -\varphi(X_s) \left\{ \frac{\partial C_{N_s}}{\partial \alpha_s} \varphi(X_s) + \left[ \frac{\partial C_{N_s}}{\partial \theta_N} \varphi'(X_N) + \frac{\partial C_{N_s}}{\partial z} \varphi(X_N) \right] \frac{U}{\omega} \sin(\omega\Delta t) \right. \\ &\quad \left. + \frac{\partial C_{N_s}}{\partial \left( \frac{Z_N}{U} \right)} \varphi(X_N) \cos(\omega\Delta t) \right\} - D_{Ref} \varphi'(X_s) \left\{ \frac{\partial C_{m_s}}{\partial \alpha_s} \varphi(X_s) \right. \\ &\quad \left. + \left[ \frac{\partial C_{m_s}}{\partial \theta_N} \varphi'(X_N) + \frac{\partial C_{m_s}}{\partial z} \varphi(X_N) \right] \frac{U}{\omega} \sin(\omega\Delta t) \right. \\ &\quad \left. + \frac{\partial C_{m_s}}{\partial \left( \frac{Z_N}{U} \right)} \varphi(X_N) \cos(\omega\Delta t) \right\} \end{aligned} \quad (25c)$$

\* This assumption also makes  $2\zeta\ddot{q}(t)$  equivalent to  $i\omega^2q(t)$  in Eq. (18) where  $2\zeta = g$ .

Similarly,  $P_a(t)$  may be expressed as

$$P_a(t) = \frac{\rho U^2}{2} S \left[ K_a q(t) + D_a \frac{q(t)}{U} \right] \quad (26)$$

Combining Eqs. (18), (20), (25), and (26) gives

$$\ddot{q}(t) + 2\omega \left[ \zeta - \frac{B}{2\omega U} (D_s + D_a) \right] \dot{q}(t) + \omega^2 \left[ 1 - \frac{B}{\omega^2} (K_s + K_a) \right] q(t) = f(t) \quad (27)$$

where

$$B = \frac{\rho U^2 S}{m}; \quad f(t) = \frac{P_b(t)}{m}$$

### 3.3.2 Aerodynamic Damping

As the aerodynamic stiffness is small compared to the structural stiffness, and the damping is much less than critical, the solution  $q(t)$  of Eq. (27) will be oscillatory. One requirement for stability is then that the amplitude  $|q(t)|$  is bounded, i.e., does not increase with time without limit. This implies that the coefficient for  $q(t)$  in Eq. (27) cannot be negative, i.e.,

$$\zeta - \frac{B}{2\omega U} (D_s + D_a) \geq 0 \quad (28)$$

In the presence of the driving function  $f(t)$ , the requirement of an amplitude below a certain limiting value gives a more severe criterion for stability:

$$\zeta - \frac{B}{2\omega U} (D_s + D_a) \geq \zeta_{min} \quad (29)$$

$D_s$  and  $D_a$  are the aerodynamic damping contributions from regions with separated and attached flow, respectively. They correspond to the damping derivative for a rigid body, a negative value indicating damped oscillation. The multiplication factor  $-B/2\omega U$  brings the aerodynamic damping into the same form as the structural damping,  $\zeta$ . Thus, the damping contributions from the separated and attached flow regions have the following ratios to the critical damping:

$$\zeta_s = -\frac{\rho US}{4\omega m} D_s \quad \text{and} \quad \zeta_a = -\frac{\rho US}{4\omega m} D_a \quad (30)$$

$D_s$  is obtained from first order theory<sup>1</sup>, and  $D_a$  is obtained from Eq. (25c). For the lower frequency bending modes the expression for  $D_s$  can be simplified further by approximating  $\cos(\omega\Delta t) = 1$  and  $\sin(\omega\Delta t) = \omega\Delta t$ . In discussing the spiked body aerodynamics it was shown that

$$\frac{\partial C_s}{\partial z} = \frac{1}{L} \frac{\partial C_s}{\partial \beta}$$

where  $L = X_N - X_s$  and  $\beta = (Z_N - Z_s)/L$  ( $\beta$  is the angular relative deflection). The time lag  $\Delta t$  is determined as  $\Delta t = L/\bar{U}$ , where the average velocity  $\bar{U}$  is determined by the velocity deficit in the wake as was discussed earlier. Using these simplifications and definitions in Eq. (25) gives the expression shown in Eq. (31) for  $\zeta_s$  of Eq. (30).

$$\begin{aligned} \zeta_s = & \frac{\rho US}{4\omega m} \left\{ \varphi(X_s) \left( \frac{\partial C_{N_s}}{\partial \alpha_s} \varphi(X_s) + \frac{U}{\bar{U}} \left[ \frac{\partial C_{N_s}}{\partial \theta_N} \varphi'(X_N)(X_N - X_s) + \frac{\partial C_{N_s}}{\partial \beta} \varphi(X_N) \right] \right. \right. \\ & \left. \left. + \frac{\partial C_{N_s}}{\partial \left( \frac{Z_N}{U} \right)} \varphi(X_N) \right) + D_{Ref} \varphi'(X_s) \left( \frac{\partial C_{m_s}}{\partial \alpha_s} \varphi(X_s) \right. \right. \\ & \left. \left. + \frac{U}{\bar{U}} \left[ \frac{\partial C_{m_s}}{\partial \theta_N} \varphi'(X_N)(X_N - X_s) + \frac{\partial C_{m_s}}{\partial \beta} \varphi(X_N) \right] + \frac{\partial C_{m_s}}{\partial \left( \frac{Z_N}{U} \right)} \varphi(X_N) \right) \right\} \end{aligned} \quad (31)$$

In the discussion of the pseudo-static aerodynamics earlier it was outlined how the information necessary for formulating  $D_s$  in Eq. (31) is obtained for the various types of separation. The derivation of  $D_a$  is given in Ref.<sup>1</sup>

The total aerodynamic damping  $\zeta_s + \zeta_a$  for the elastic vehicle in single-degree-of-freedom bending oscillations is obtained by summing the contributions to  $\zeta_s$  and  $\zeta_a$  from all the lumped forces over the vehicle.

### 3.3.2.1 Launch Vehicle Damping Distribution

The static load distribution at  $M = 1.2$  on the Saturn I-Apollo launch vehicle with escape rocket and disk (Fig. 3) demonstrates the drastic effects caused by separated flow. The single-degree-of-freedom damping distribution for the second bending mode at  $M = 1.1$  is shown in Fig. 22. The static load distribution is also shown for reference and the interplay between the static loads and the mode shape is clearly illustrated. In general, positive static loads contribute positive damping and negative loads give negative damping. The exception is the separation-induced loading for the case that there is a nodal point between the separation source and the location of the separation-induced force. Then there is a sign reversal, and positive static loads contribute undamping, negative loads contribute damping. The disk-wake-induced forces on the command module and forward service module show this sign reversal. The damping distribution, as illustrated in Fig. 22, tells the designer which characteristics in the vehicle geometry adversely affect the vehicle damping.

### 3.3.2.2 Comparison With Experimental Results

At the NASA Langley Research Center, the difficult task of simulating elastic vehicle dynamics in a wind tunnel test was successfully undertaken<sup>3</sup>. An 8-percent dynamically scaled model of the Saturn I-Apollo vehicle was excited by an electromagnetic shaker in each of its first three bending modes, one at a time, and the aerodynamic damping was measured. In general, the pseudo-static predictions agree reasonably well with the measured damping for the three configurations tested, Figs. 23, 24 and 25. The configuration with escape rocket and disk was tested extensively using dual force balances, and has, therefore, the best-defined static load input of the three configurations. The agreement between pseudo-static predictions and measured damping is good for the first and second bending mode, Fig. 23. Treating the measured static loads as if they all were dependent only on local crossflow, as in the classic quasi-steady theory, gives obviously the wrong damping values. This is especially true for the second bending mode, where the trend with Mach number then becomes opposite to the measured trend. For the configuration without disk (Fig. 24), the agreement is acceptable, considering the scatter in the experimental data. The static load input for this configuration is based largely on pressure distribution data and, to a lesser degree than for disk-on, is determined by measured component forces. This is also true for the tower-off configuration in Fig. 25. In addition, the separation of the forebody caused by the blunt command module is very sensitive to both Reynolds number and surface roughness. The static force data used in Fig. 25 were obtained with a transition strip of No. 70 roughness on the 33-deg. conical command module. The Langley dynamic model had no artificial roughness, but the test Reynolds number was compatible with that of the static test. Considering the "touchiness" of the nose-induced separation, the agreement between quasi-steady predictions and measured damping is not bad. The deviations suggest that the Langley model may have had nose-induced separation up to  $M = 1.1$ . In the static test that supplied the input for the pseudo-static predictions, the model had no nose-induced separation at  $M > 1.0$ .

At the NASA Ames Research Center, Mr. Henry Cole, Jr., in his "partial-mode" testing technique, dynamically simulated the forward portion of the Saturn I-Apollo configuration in its second bending mode. In Fig. 26 the pseudo-static prediction of the forebody damping for the second bending mode of the Langley configuration is shown for disk on and disk-off. The predictions agree generally with the trends measured by Cole<sup>4</sup>. The damping is positive for both configurations at subsonic speeds, whereas at supersonic speed the disk gives a large negative damping contribution.

In Fig. 27 the computed forebody damping for the tower-off configuration is shown for the second bending mode. When the loads aft of the flare are neglected, the results are comparable with the pitch damping measured on rigid bodies of similar geometry, i.e., flare-stabilized blunt-nosed cylinders. Large subsonic undamping and moderate supersonic damping are typical for these bodies. Furthermore, the alleviating effect on the undamping of an added cylindrical skirt is verified by experimental results for rigid bodies.

That the pseudo-static analytic method can provide reasonable prediction of the aeroelastic characteristics of various Saturn-I Apollo launch configurations has been demonstrated by the above examples. The method was judged to be accurate enough to provide the full scale aeroelastic characteristics of all the other Apollo-Saturn boosters following the Saturn I-Apollo launch vehicle<sup>10</sup>.

### 3.4 Relative Magnitude of Dynamic Loads

The vehicle designer needs to know how important the dynamic loads will be for a particular vehicle. In this respect, it is helpful to relate the aeroelastic response to the static, aerodynamic loads. This has been done for the Saturn-Apollo booster<sup>11</sup> (Fig. 28). It can be seen that oscillations in the first bending mode with an amplitude of  $|\theta_{N1}| = 10^\circ$  at the nose produces the same maximum bending moment as the static loads at an angle of attack of  $10^\circ$  degrees,  $\alpha = 10^\circ$ . The dynamic moment reaches its maximum at the first antinode, the point of maximum modal curvature. This one order of magnitude relationship,  $|\theta_{N1}| = 10^\circ$  roughly equivalent to  $\alpha = 10^\circ$ , has also been found for other aerospace launch vehicles.

### 3.5 Sinusoidal Gusts

The size of the Saturn-Apollo launch vehicle made it sensitive to so called sinusoidal gusts<sup>12-14</sup> (Fig. 29). Neglecting the velocity deficit in the separated flow region ( $\kappa = 1$  implying  $\bar{U} = U$ ) had little effect for the relatively mild flow separations on the Saturn V configuration (Figs. 29 and 30),

\* Note that in the figures the old "Quasi-Steady" nomenclature is used instead of the suggested "Pseudo-Static" designation.

but significantly affected the gust-induced loads on the disk-on Saturn I launch vehicle (Fig. 31). The computed sinusoidal gust response<sup>14</sup> (Fig. 32) shows that for the number of sinusoidal gust waves available<sup>12</sup> ( $N_{MAX}$ ), the elastic vehicle damping has little effect on the maximum attained response amplitude,  $\Delta\theta_N^{MAX}$ . This explains why the elastic vehicle response computed using attached flow loads<sup>15</sup> deviates so little from the one obtained including separated flow effects<sup>14</sup> (Fig. 33), in spite of the large differences in aerodynamic damping<sup>4</sup> (Fig. 23).

#### 4. ANALYTIC COMPLICATIONS

In the analysis discussed so far the only modification of the static loads was the inclusion of the time lag occurring between a perturbation of the separated flow generator and the resulting change of the separation-induced load. That is, flow separation was assumed to occur at exactly the same local flow inclination in both the static and dynamic case. This is not true in general, although it is a good approximation for the Saturn-Apollo geometry just discussed. Due to accelerated flow effects the vehicle can in the dynamic case attain a larger local flow inclination than in the static case before flow separation occurs<sup>16</sup>.

##### 4.1 Accelerated Flow Effects

The pressure gradient of the external flow at the edge of the boundary layer is given by the complete Bernoulli equation

$$-\frac{1}{\rho_e} \frac{\partial p_e}{\partial X} = \frac{\partial U_e}{\partial t} + U_e \frac{\partial U_e}{\partial X} \quad (32)$$

For constant velocity,  $U_e$  changes only through body pitching or bending. Thus, with  $\xi = X/c$ , where  $c = D_{ref}$ :

$$\frac{\partial p_e}{\partial \xi} = -\rho_e U_e \left[ \frac{\partial U_e}{\partial \alpha} \frac{c\dot{\alpha}}{U_e} + \frac{\partial U_e}{\partial \xi} \right] \quad (33)$$

That is

$$\frac{\partial C_{p_e}}{\partial \xi} = \left( \frac{\partial C_{p_e}}{\partial \xi} \right)_{\dot{\alpha}=0} + \frac{\partial C_{p_e}}{\partial \alpha} \cdot \frac{c\dot{\alpha}}{U_e} \quad (34)$$

For Prandtl-Meyer expansion,  $\partial C_{p_e}/\partial \alpha$  is obtained as

$$\frac{\partial C_{p_e}}{\partial \alpha} = -\frac{1}{\frac{\gamma M_\infty^2}{2}} \frac{\partial}{\partial \nu} \left( \frac{p_e}{p_\infty} \right) = -2 \left( \frac{M_e}{M_\infty} \right)^2 \left( M_e^2 - 1 \right)^{-1/2} \quad (35)$$

Thus, the body pitching (or bending) motion  $\dot{\alpha}_{ref}/U > 0$  decreases the pressure gradient  $\partial C_{p_e}/\partial \xi$  and will, therefore, delay the boundary-layer separation. That is, in the unsteady case the separation will lag behind its static or steady state position. This lag is to be added to the convective time lag effects discussed earlier.

It is shown in Ref. 16 how this accelerated flow effect can become the dominant time lag effect for the shock-induced separation occurring aft of the slender nose of an axisymmetric vehicle, such as a cone-cylinder. When a critical angle of attack is exceeded the shock and associated flow separation jumps to the cone-cylinder shoulder. This causes a highly nonlinear aerelastic response, as is illustrated by the analytic results in Fig. 34. Using static experimental data for cone-cylinders<sup>17,18</sup> and the structural characteristics for a Saturn booster, the analysis predicts as much as 1% of critical negative damping for a nose amplitude of  $\Delta\theta_N = 0.250$ . Experimental results obtained at this amplitude for an elastic model of the Saturn I booster with a Jupiter nose shroud<sup>19</sup> show such a loss of damping when the angle of attack is increased to 2 degrees or more (Fig. 35).

##### 4.2 Wake Recirculation Effects

When the submerged body (e.g. the Apollo command module on the Saturn booster) is located in the wake throat, (or wake neck), strong communication occurs from the submerged body up through the wake. This changes the flow conditions at the wake-generator (the escape rocket), thereby changing the wake geometry as well as the loads on the wake generator<sup>20</sup>. This is the most prominent flow mechanism in dynamic support interference<sup>21-23</sup>. It is usually not a problem of concern for launch vehicles, but could have been in the case of the Saturn-Apollo booster if the length of the escape rocket tower had been different<sup>20</sup> (Fig. 36). For the actual geometry the upstream communication effects from the Apollo command module were negligible ( $L_T/c = 0.5$  in Fig. 36).

#### 5. OTHER EXAMPLES

The early straight wing space shuttle booster presented a situation analogous to that for the Apollo escape system. The booster vertical tail is located in the wake from the orbiter and experiences loads dependent upon the orbiter motion<sup>24</sup> (Fig. 37). The second yaw mode is undamped, as  $U/U \leq 0.8$  for wake-submerged bodies. A simple means of eliminating the negative aerodynamic damping is to use a double-tail arrangement, which gives the positive damping shown in the figure.

The current delta wing orbiter on top of the HO tank with its strapped-on solid rocket boosters (SRB's) creates an inlet-like flow. It was shown in Ref. 25 that even this very complicated flow could be analyzed by pseudo-static means to provide the elastic and rigid body dynamics. The orbiter shock causes flow separation on the HO tank. Pressure distribution data<sup>26</sup> show how this separation responds to angle of attack changes (Fig. 38). Forebody crossflow on the HO tank thickens the leeside boundary layer, causing a forward movement of the orbiter bow shock and the associated flow separation. The static pressures on the HO tank top and orbiter bottom exhibit nonlinearities that correlate with the orbiter shock movement, indicating that the entire flow field is coupled, having inlet-like characteristics<sup>27</sup>.

It is impossible to determine the time lag of this inlet flow by purely theoretical means. Through iterations<sup>25</sup> it was found that using an effective dimensionless time lag of  $\Delta\tau = 26$  (the vehicle travels 26 reference chords during the time lag  $\Delta t$  seconds) together with static experimental data in a pseudo-static analysis produced predictions that were in good agreement with the measured rigid body damping<sup>28</sup> (Fig. 39). The "plateau" between  $\alpha = -2^\circ$  and  $\alpha = 1^\circ$  is the effect of continuous movement of the orbiter bow shock (Fig. 39), whereas the peak at  $\alpha = 20^\circ$  is the effect of a discontinuous jump of the shock forward to the HO nose shoulder. At  $M = 0.9$  this orbiter shock-discontinuity is not present, but instead there is a discontinuous change of the shock-induced separation on the orbiter wing (Fig. 40). With the good agreement between predictions and experimental rigid body dynamics (Figs. 39 and 40) the task of predicting the aeroelastic characteristics could be undertaken with confidence. Figure 41 shows the predicted effects of the orbiter wing shock jump.

The first of the shuttle configurations to fly, the 747/Orbiter, presented problems similar to the ones for the straight-wing orbiter discussed earlier (Fig. 37). Because of the 747's lesser stiffness and associated large tail deflection (Fig. 42), the potential dynamic instability did not materialize (Fig. 43). It can be seen that the local, classical, quasi-steady damping,  $D_{vw}$ , completely overpowers the separation-induced negative damping,  $\Delta D_{vw}$ .

## 6. SCALING PROBLEMS

The extrapolation from subscale wind tunnel data to full scale flight is a well-recognized problem, which becomes especially difficult when flow separation is involved. The problem is compounded when flow separation is preceded by boundary layer transition, which usually is the case in the full scale flight cases of interest. The root of this dilemma is the strong sensitivity of boundary layer transition to vehicle attitude and body motion, which makes it impossible to simulate the dynamic effects of separated flow at subscale Reynolds number<sup>30,31</sup>. Although ground testing facilities are now becoming available, which can achieve full scale test Reynolds number<sup>32</sup>, they will all be very busy. Even if time were made available, it is not certain that elastic vehicle dynamic simulation would be possible<sup>33</sup>.

It appears then that the pseudo-static analytic methods discussed here will have to be extended to provide the capability to extrapolate analytically to full scale Reynolds numbers<sup>34</sup>. How this may be done will be illustrated for the rigid body dynamics of a slender cone. Experimental results show that transition effects can increase the pitch damping of a  $10^\circ$  sharp cone by as much as 30 percent<sup>35</sup> (Fig. 44). It is shown in Ref. 36 how these dynamic effects of transition can be predicted if the static effects are known. Of course, as the mean transition front moves forward of C.G. the static effects reverse from statically destabilizing to stabilizing, and the dynamic effects from damping to dynamically destabilizing. That is, it is possible that the transition effects are damping in the subscale test and undamping in full scale. How can one include this in the analytic extrapolation?

It is shown in Ref. 37 how the effect of angle of attack on the transition front can be related to the transition location at  $\alpha = 0$ . There are means available for prediction of the effect of Reynolds number alone on boundary layer transition location for sharp cones<sup>38</sup>, and Ref. 39 shows how to account for nose bluntness effects. Using the results in Refs. 36-39 as a starting point analytic means can be developed that will predict the effect of boundary layer transition on slender cone dynamics. Once the rigid body dynamics can be predicted, the analytic tools are at hand for prediction of the transition effects on a conic frustum of an elastic vehicle. The same procedure can be followed in regard to the observed effects of transition on ogive cylinder bodies<sup>40</sup> (Fig. 45).

When transition is followed by flow separation the mathematics become slightly more complicated, but the same procedure can be followed. The established analytical relationships between dynamic and static characteristics are first proven out by static and dynamic tests at (the same) subscale Reynolds numbers. Then the effect of Reynolds number on static aerodynamics is determined up to and including full scale Reynolds number. In some cases it may be possible to check out the analytic extrapolation by performing rigid body dynamic tests at full scale Reynolds numbers. The rigid body degree of freedom can be selected such that it will simulate a critical part of the elastic body motion.

## 7. CONCLUSIONS

By using static experimental data in a pseudo-static analytic theory one can compute the aerodynamic damping of an elastic vehicle including the often dominating effects of separated flow. The method has been applied successfully to predict the aeroelastic characteristics of the Saturn-Apollo and Space Shuttle launch vehicles. The method needs to be extended to handle analytic extrapolation from subscale dynamic test data to full scale elastic vehicle dynamics, as it appears to be the only means short of full scale flight to determine the aeroelastic stability characteristics of the flight hardware.

## 8. REFERENCES

1. Bisplinghoff, R. L., Ashley, H., and Halfman, R. L., "Aeroelasticity" Addison-Wesley Publishing Co., Inc., Cambridge, Mass., 1955.
2. Bisplinghoff, R. L. and Ashley, H., "Principles of Aeroelasticity", John Wiley and Sons, Inc. New York, 1962.
3. Hanson, P. W. and Doggett, R. V., Jr., "Aerodynamic Damping and Buffet Response of an Elastic Model of the Saturn I Block II Launch Vehicle", NASA TN-D-2713.
4. Ericsson, L. E. and Reding, J. P., "Analysis of Flow Separation Effects on the Dynamics of a Large Space Booster", J. Spacecraft and Rockets, Vol. 2, 1965, pp. 481-490.
5. Harman, R. W. and Boatright, W. B., "Investigation of the Aerodynamic Characteristics of a Re-Entry Capsule with Various Nose Shapes at a Mach Number of 2.91, Including Studies of Nose Spikes as a Means of Control", NASA TM X-426, Jan. 1961.
6. Norburg, J. F. and Crabtree, L. F., "A Simplified Model of the Incompressible Flow Past Two-Dimensional Airfoils With a Long Bubble Type of Flow Separation", Royal Aircraft Establishment, RAE TN-Aero 2352 (June 1955).
7. Kuehn, D. M., "Turbulent Boundary-Layer Separation Induced by Flares on Cylinders at Zero Angle of Attack", NASA TR R-117(1961).
8. Kistler, A. L. and Chen, W. S., "The Fluctuating Pressure Field in a Supersonic Turbulent Boundary Layer", Jet Prop. Lab., CALTECH, TR 32-277 (August 1962).
9. Cole, H. Jr., Robinson, R. and Gambucci, B., "Buffeting Response of the Apollo Partial Mode Model at Subsonic and Supersonic Mach Numbers" NASA TN-D 2689 (Feb. 1965).
10. Rainey, G., "Progress on the Launch Vehicle Buffeting Problem", J. Spacecraft and Rockets, Vol 2, 1965, pp. 289-299.
11. Ericsson, L. E., Reding, J. P. and Guenther, R. A., "Relative Magnitude of Stresses Caused by Static and Dynamic Launch Vehicle Loads", J. Spacecraft and Rockets, Vol. 10, 1973, p. 276.
12. Vaughn, W. W., "Sinusoidal Gust Criteria Guideline for Apollo Emergency Detection System Angular Rate Studies", NASA MSFC Memo R-AERO-Y-31-64, June 1964.
13. Ericsson, L. E., Reding, J. P. and Guenther, R. A., "Launch Vehicle Gust Penetration Loads", J. Spacecraft and Rockets, Vol. 9, 1972, pp. 19-25.
14. Ericsson, L. E., Reding, J. P. and Guenther, R. A., "Elastic Launch Vehicle Response to Sinusoidal Gusts", J. Spacecraft and Rockets, Vol. 10, 1973, pp. 244-252.
15. Papadopoulos, J. G., "Wind Penetration Effects on Flight Simulation", AIAA Paper 67-609, 1967.
16. Ericsson, L. E., "Aeroelastic Instability Caused by Slender Payloads" J. Spacecraft and Rockets, Vol. 4, 1967, pp. 65-73.
17. Robertson, J. E. and Chevalier, H. L., "Characteristics of Steady-State Pressures on the Cylindrical Portion, of Cone-Cylinder Bodies at Transonic Speeds", AEDC TDR-63-104, Aug. 1963.
18. Ericsson, L. E., "Loads Induced by Terminal-Shock Boundary Layer Interaction on Cone-Cylinder Bodies", J. Spacecraft and Rockets, Vol. 7, 1970, pp. 1006-1112.
19. Hanson, P. W. and Doggett, R. V., Jr., "Aerodynamic Damping and Buffet Response of an Aeroelastic Model of the Saturn I Block II Launch Vehicle", NASA TN D-2713, March 1965.
20. Ericsson, L. E., Reding, J. P. and Guenther, R. A., "Analytic Difficulties in Predicting Dynamic Effects of Separated Flow", J. Spacecraft and Rockets, Vol. 8, 1971, pp. 872-878.
21. Reding, J. P. and Ericsson, L. E., "Dynamic Support Interference", J. Spacecraft and Rockets, Vol. 9, 1972, pp. 547-553.
22. Ericsson, L. E. and Reding, J. P., "Viscous Interaction or Support Interference-The Dynamicist's Dilemma", AIAA Journal, Vol. 16, 1978, pp. 363-368.
23. Ericsson, L. E., "Support Interference" Paper No. 8, AGARD LS-114, 1981.
24. Reding, J. P. and Ericsson, L. E., "Unsteady Aerodynamics Could Dominate the Space Shuttle Booster Aeroelastic Stability", AIAA Paper 74-362, April 1974.
25. Reding, J. P. and Ericsson, L. E., "Effects of Flow Separation on Shuttle Longitudinal Dynamics and Aeroelastic Stability", J. Spacecraft and Rockets, Vol. 14, 1977, pp. 711-718.
26. Gilling, R. L., "Airloads Investigation of a 0.03-Scale Model of the Space Shuttle Launch Vehicle 140 AIB Launch Configuration (Model 47-OTS) in the ARC 11-Foot Unitary Plan Wind Tunnel for Mach Number Range 0.6 to 1.4 (1A14A)" NASA CR 134-445, March 1975.

27. Dailey, C. E., "Supersonic Diffuser Stability", J. Aer. Sci., Vol. 22, 1955, pp. 733-749.
28. Freeman, D. C. Jr. , Boyden, R. P., and Davenport, E. E., "Subsonic and Transonic Dynamic-Stability Characteristics of the Space Shuttle Launch Vehicle", NASA TM X-336, March 1976.
29. Reding, J. P. and Ericsson, L. E., "Aeroelastic Stability of the 747/Orbiter", J. Spacecraft and Rockets, Vol. 14, 1977, pp. 988-993.
30. Ericsson, L. E. and Reding, J. P., "Scaling Problems in Dynamic Tests of Aircraft-Like Configurations", Paper 25, AGARD CP-227, Feb. 1978.
31. Ericsson, L. E. and Reding, J. P., "Reynolds Number Criticality in Dynamic Tests", AIAA Paper No. 78-166, Jan 1978.
32. Howell, R. R. and McKinney, L. W., "The US 2.5 Meter Cryogenic High Reynolds Number Tunnel", 10th ICAS Congress, Ottawa, Canada , Oct. 3-9, 1976.
33. Workshop on High Reynolds Number Research, NASA SP-2009, Oct. 27-28, 1976.
34. Ericsson, L. E. and Reding, J. P., "Dynamic Simulation Through Analytic Extrapolation", AIAA Paper No. 81-0399 , Jan. 1981.
35. Ward, L. K., "Influence of Boundary-Layer Transition on Dynamic Stability at Hypersonic Speeds", Paper 8, Vol. II, Transactions of the Second Technical Workshop on Dynamic Stability Testing, AEDC, Arnold Air Force Station, Tennessee, April 20-22, 1965.
36. Ericsson, L. E., "Transition Effects on Slender Vehicle Stability and Trim Characteristics", J. Spacecraft and Rockets, Vol. 11, 1974, pp. 3-11.
37. Ericsson, L. E., "Correlations of Attitude Effects on Slender Vehicle Transition", AIAA Journal Vol. 12, 1974, pp. 523-529.
38. Donaldson, C. P., Sullivan, R. D., and Yates, J. E., "An Attempt to Construct an Analytical Model of the Start of Compressible Transition", AFFDL-TR-70-153, Jan. 1971.
39. Ericsson, L. E. "Entropy Gradient Effects on Blunted Cone Transition", AIAA Paper No. 75-195, Jan. 1975.
40. Ward, L. K., Private Communication of Unpublished Experimental Results, Feb. 1972.

#### 8. ACKNOWLEDGEMENTS

The author wants to acknowledge the contributions by J. Peter Reding, not only through all the referenced material but also through our continuing dialogue. The author is also indebted to Nancy Lipsanopoulos, without whose ability to transform a stack of handscrubbed notes into readable material the present paper is not likely to have appeared in AGARD LS-114.



Figure 1. Shadowgraph of Flow over the Saturn-V Launch Vehicle at  $M = 1.46$ .

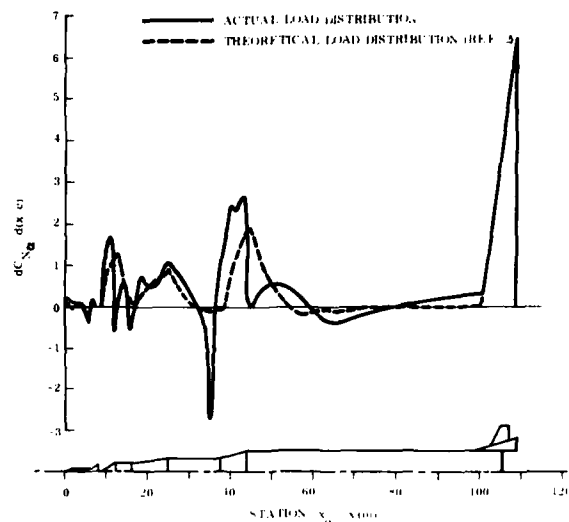


Figure 2. Static Load Distribution on the Saturn-V Launch Vehicle at  $M = 1.3$ .

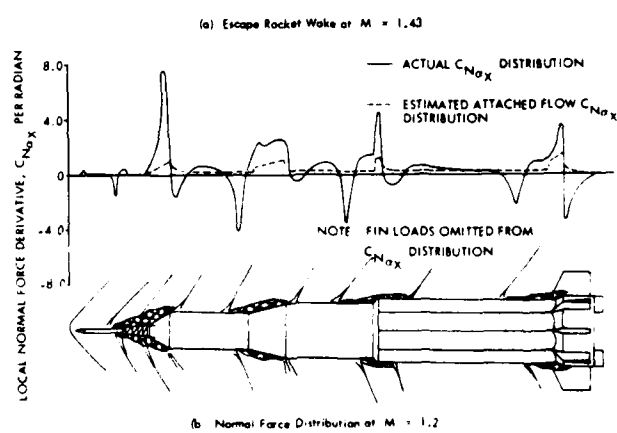


Figure 3. Aerodynamic Characteristics of Saturn I Apollo Tower on Configuration.

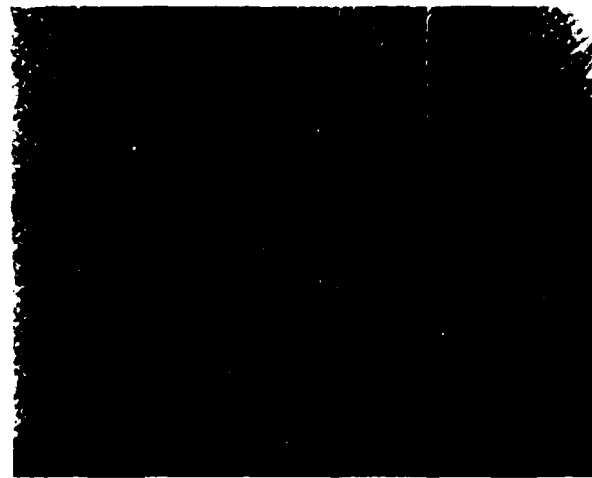
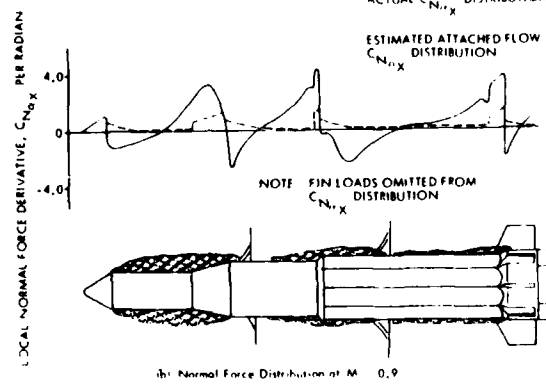
(a) Nose Induced Separation at  $M = 0.9$ 

Figure 4. Aerodynamic Characteristics of Saturn I Apollo Tower of Configuration.

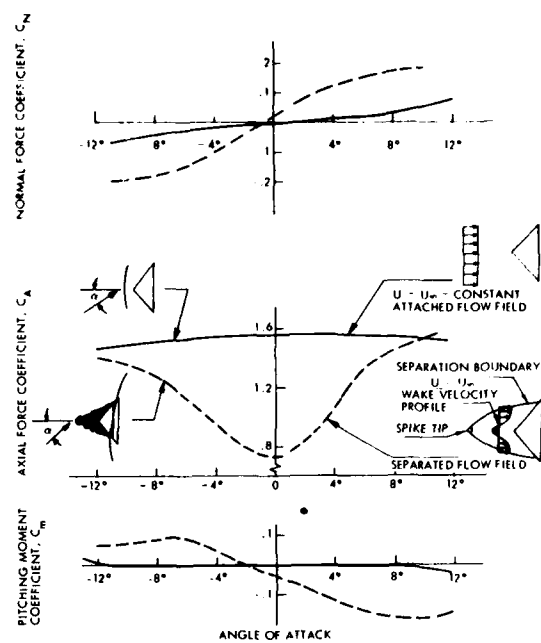
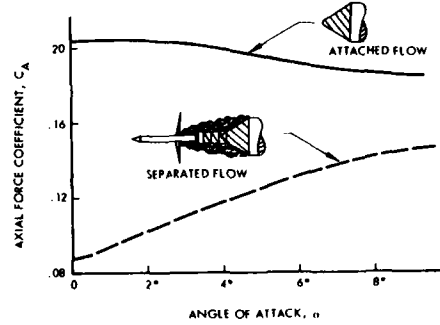
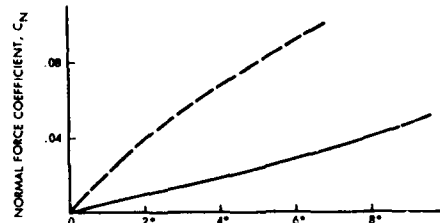
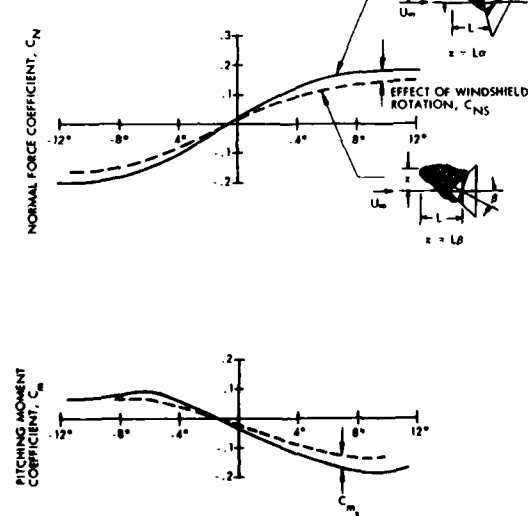
Figure 5. Effect of a Flow Separation Spike on the Aerodynamic Characteristics of a Conical Windshield ( $M = 2.91$ )Figure 6. Effect of Escape Rocket on Command Module Forces ( $M = 1.0$ ).

Figure 7. Comparison of Angle of Attack and Spike Deflection Effects.

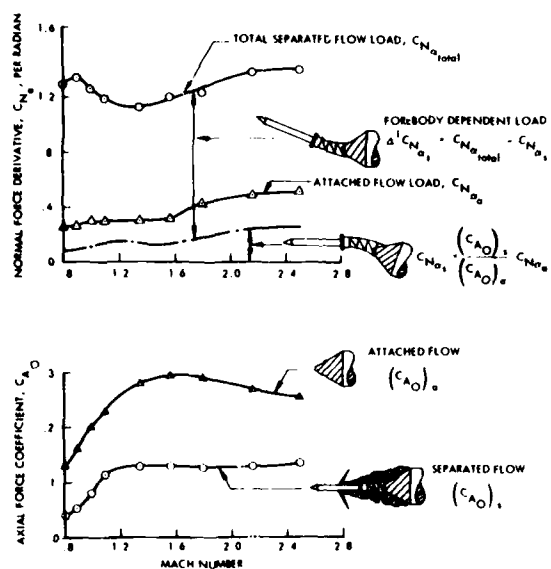


Figure 8. Disk-On Command Module Forebody Dependent and Local Loads ( $\alpha = 0$ ).

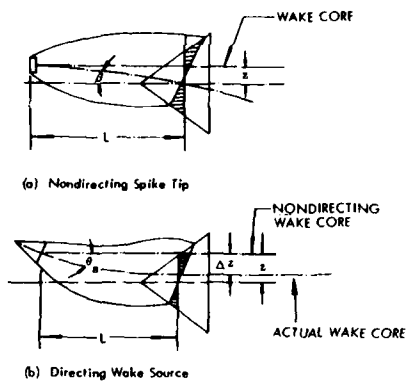


Figure 9. Directing and Non-Directing Spike Wakes.

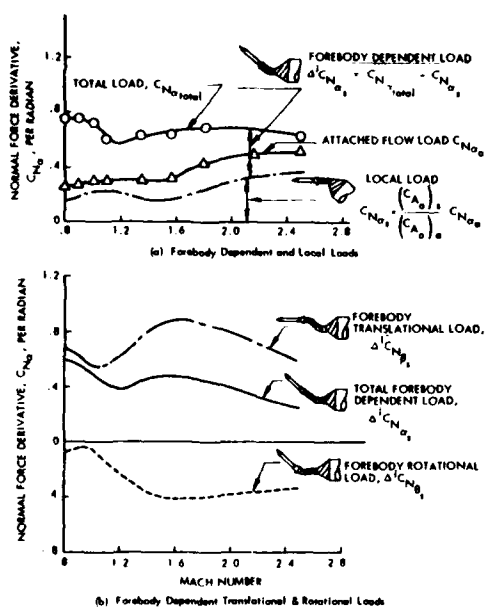


Figure 10. Disk-Off Command-Module Forebody Dependent and Local Loads ( $\alpha = 0$ ).

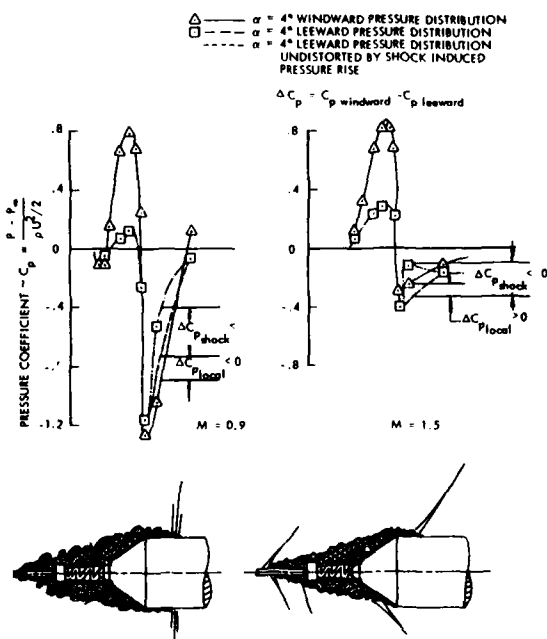


Figure 11. Command Module Shoulder Pressure Distribution at  $\alpha = 40^\circ$ .

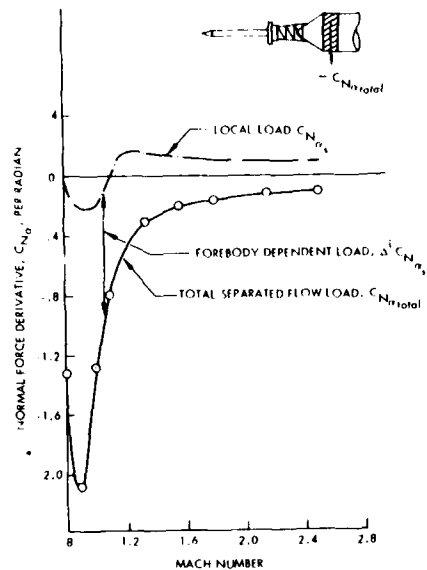


Figure 12. Local and Forebody-Dependent Negative Command Module Shoulder Loading at  $\alpha = 0$  (Tower and Disk On)

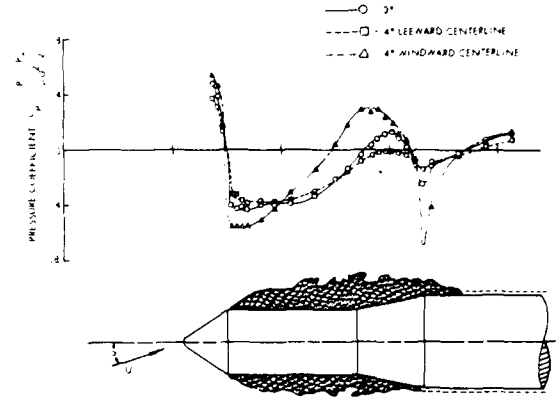
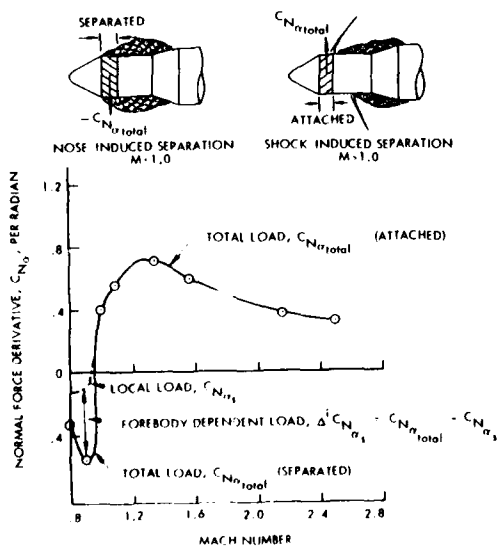
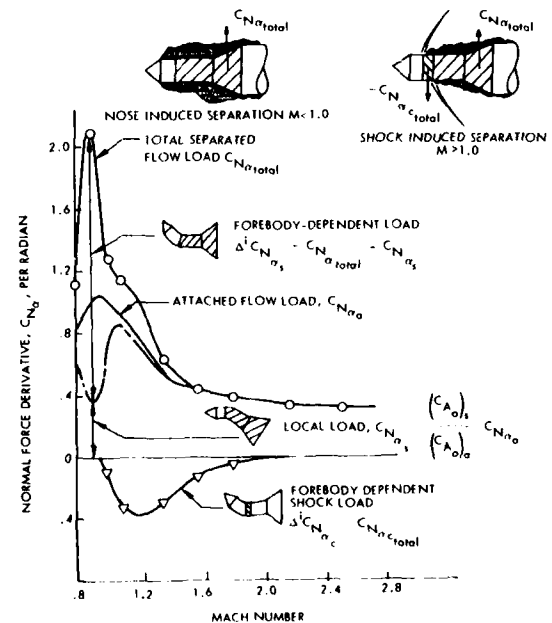


Figure 13. Forebody Pressure Distribution at  $M = 0.9$  (Tower Off)



a. Command Module Shoulder Loads



b. Cylinder and Flare Loads

Figure 14. Local and Forebody-Dependent Loads at  $\alpha = 0$  on the Tower-Off Configuration

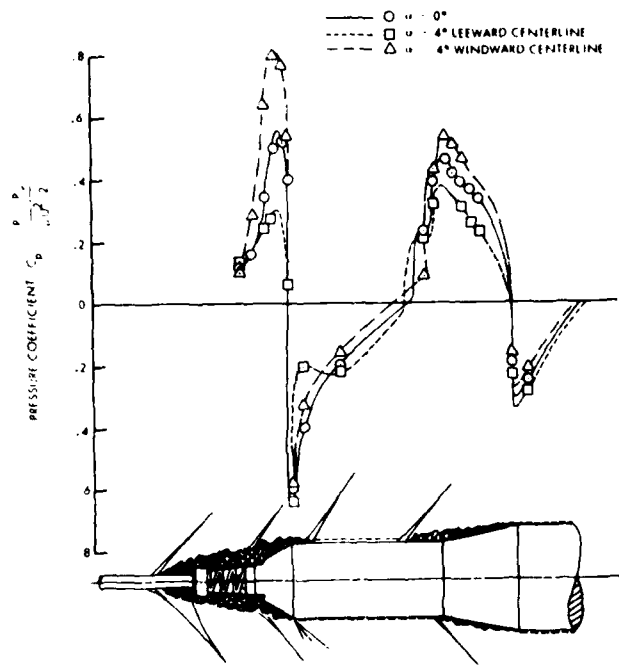


Figure 15. Forebody Supersonic Pressure Distribution, Tower On,  $M = 1.2$ .

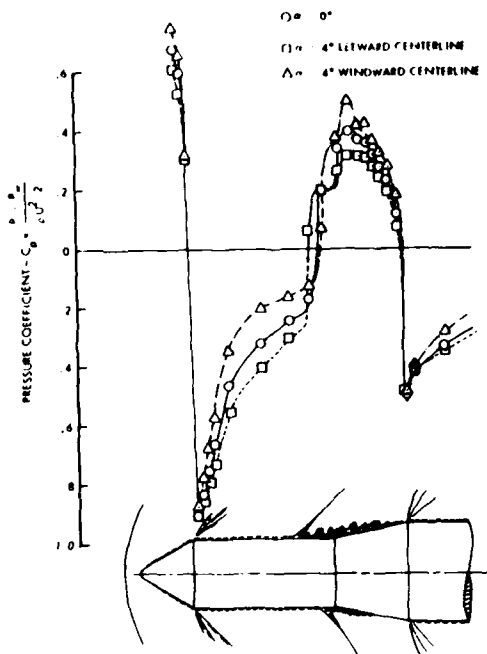


Figure 16. Forebody Supersonic Pressure Distribution, Tower Off,  $M = 1.1$ .

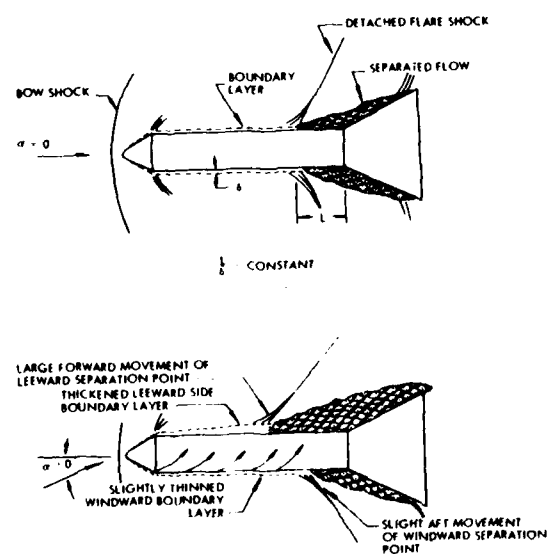


Figure 17. Effect of Boundary Layer Thickness On Shock Induced Separation.

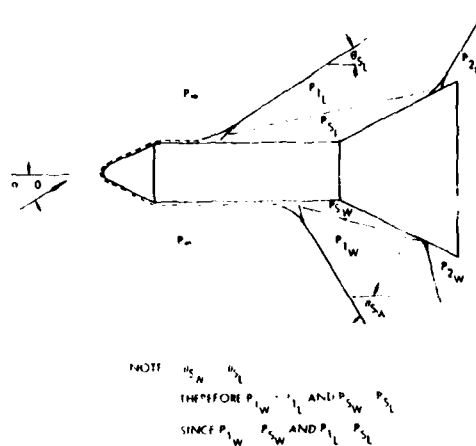


Figure 18. Effect of Detached-Shock Angle On Shock Induced Separation.

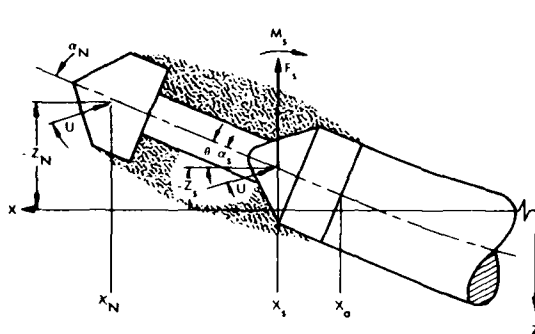
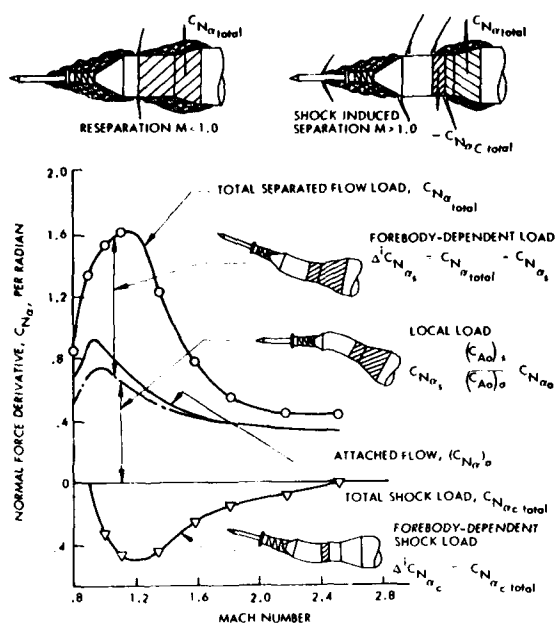


Figure 21. Coordinate System For The Elastic Vehicle.

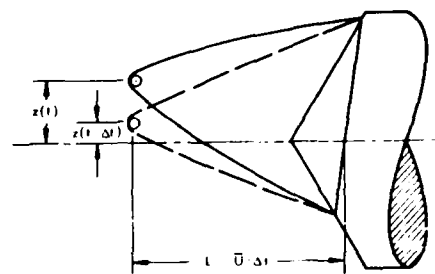
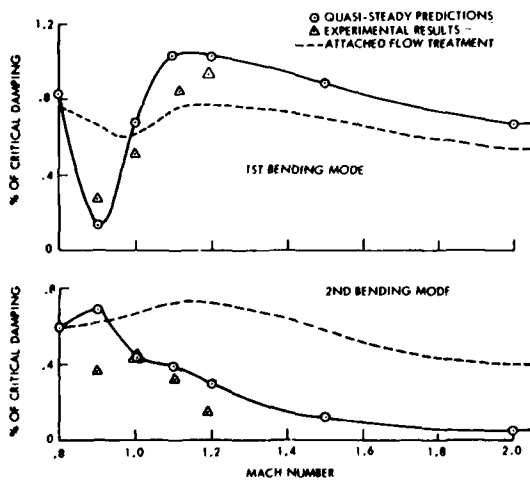


Figure 20. Sketch of Pseudo-Static Spike Wake

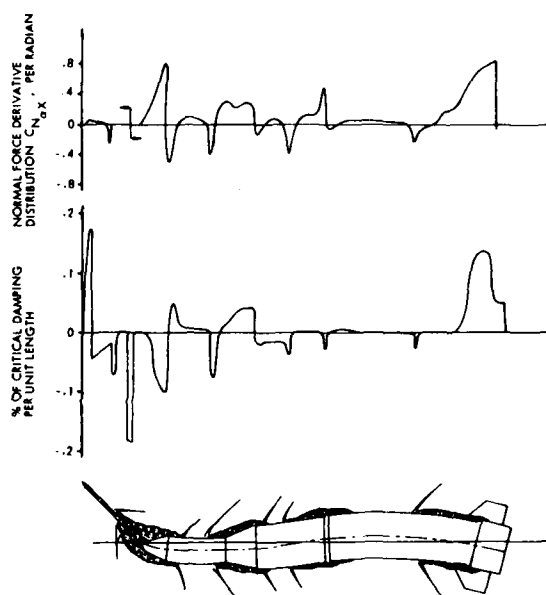
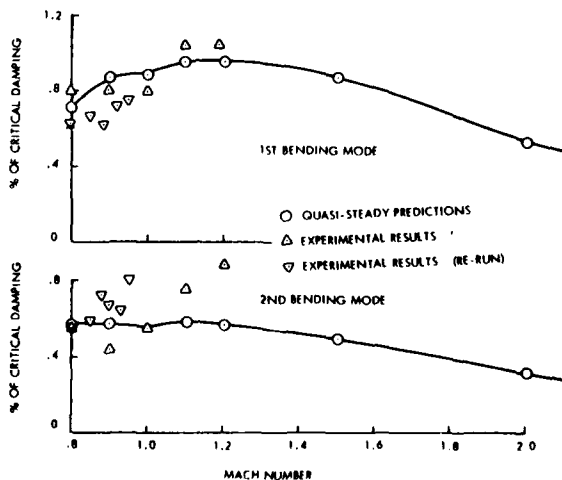


Figure 22. Correlation of Static and Dynamic Load Distributions at  $M = 1.1$  for the Second Bending Mode of the Saturn I-Apollo With Escape Rocket, Disk On.



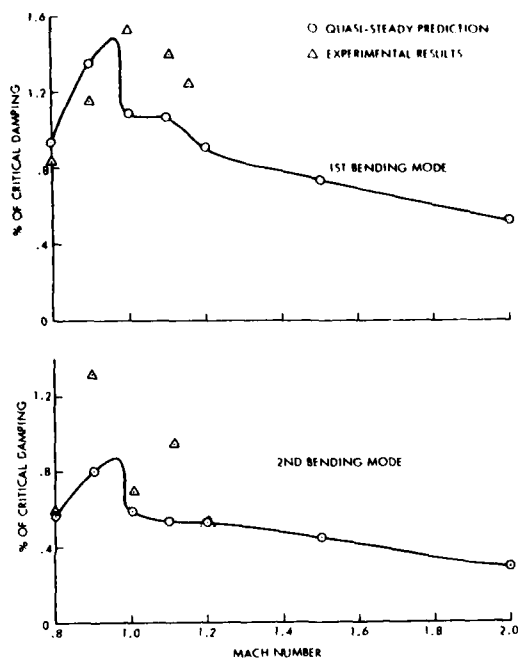


Figure 25. Aerodynamic Damping at  $\alpha = 0$  of the Saturn I-Apollo Vehicle Without Escape Rocket.

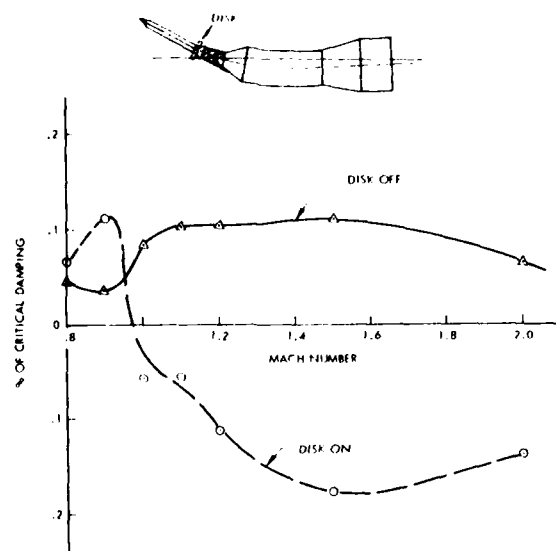


Figure 26. Forebody Damping at  $\alpha = 0$  for the 2nd B.M. of the Saturn I-Apollo with Escape Rocket, Disk On and Off.

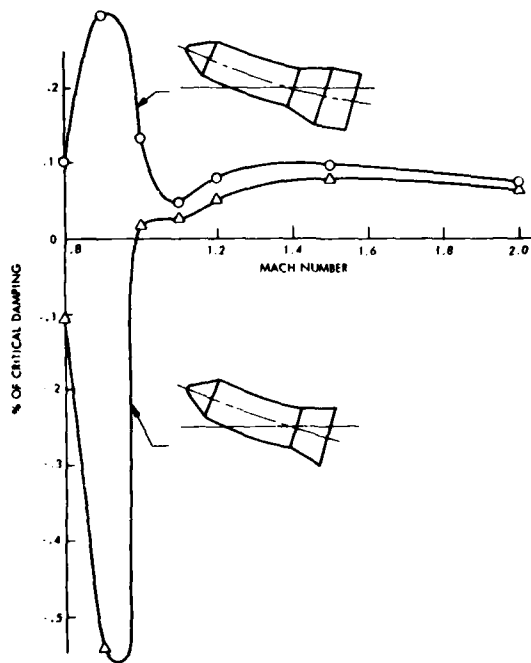


Figure 27. Forebody Damping at  $\alpha = 0$  for the 2nd B.M. of the Saturn I-Apollo Without Escape Rocket.

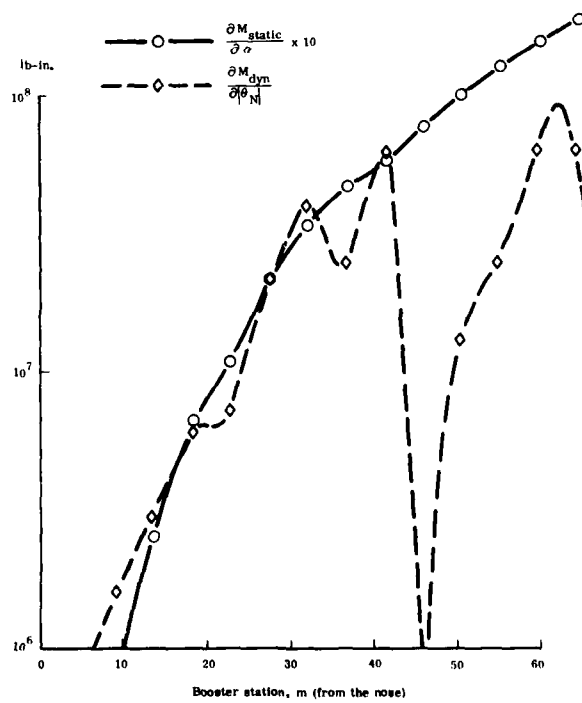


Figure 28. Comparison of Dynamic and Static Bending Moments on Saturn-V at  $M = 1.6$ , 1st B.M.

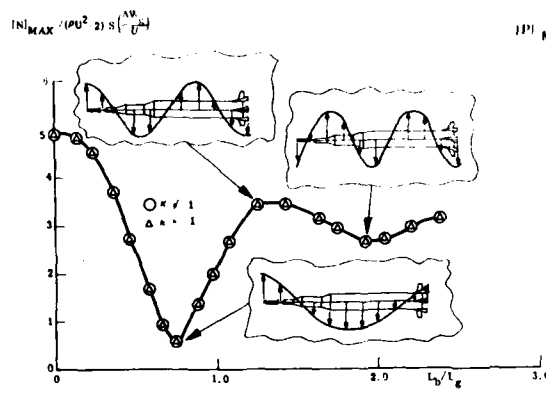


Figure 29. Saturn-V Maximum Gust-Induced Normal Force at  $M = 1.6$  as a Fraction of Sinusoidal Gust Wave Length.

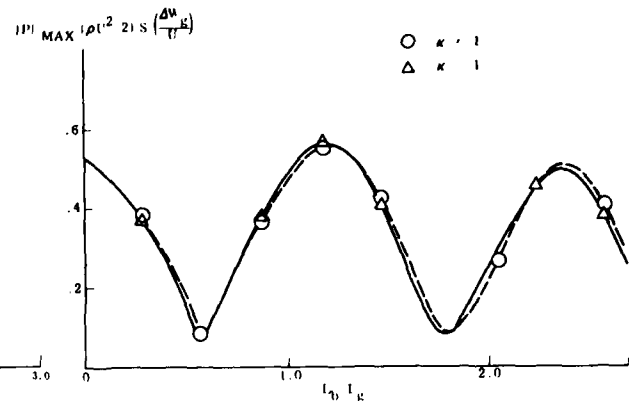


Figure 30. Maximum Elastic Body Gust-Induced Bending Loads on the Saturn-V Vehicle at  $M = 0.9$  (1st B.M.)

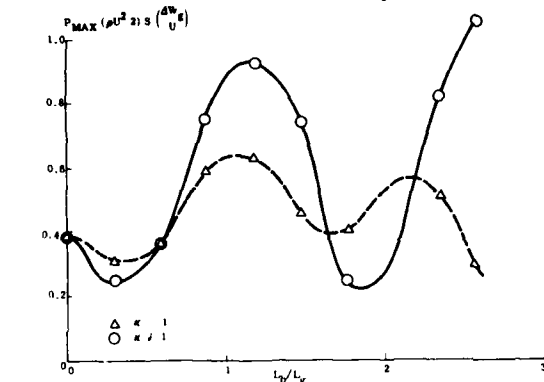


Figure 31. Maximum Elastic Body Gust-Induced Bending Loads on the Saturn-I Launch Vehicle with Disk-On Escape Rocket at  $M = 0.9$  (1st B.M.).

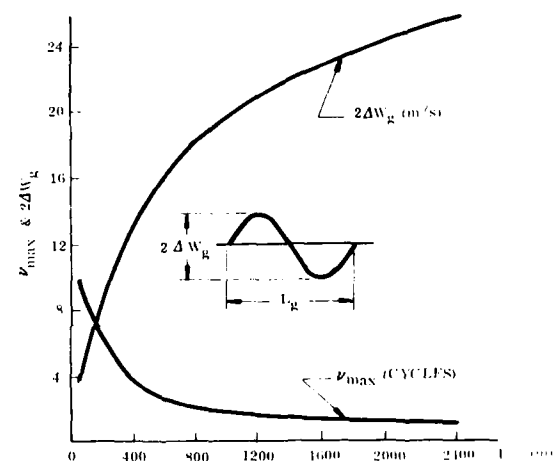


Figure 32. Atmospheric Gust Amplitude and Frequency Data for Sinusoidal Gusts.

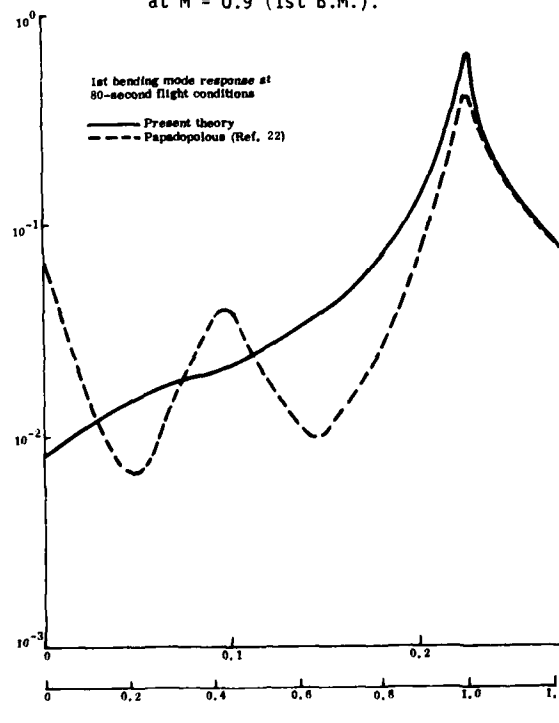


Figure 33. Saturn-I (AS-9) Elastic Vehicle Response to Sinusoidal Gusts as Determined by Different Theories (Ref. 14).

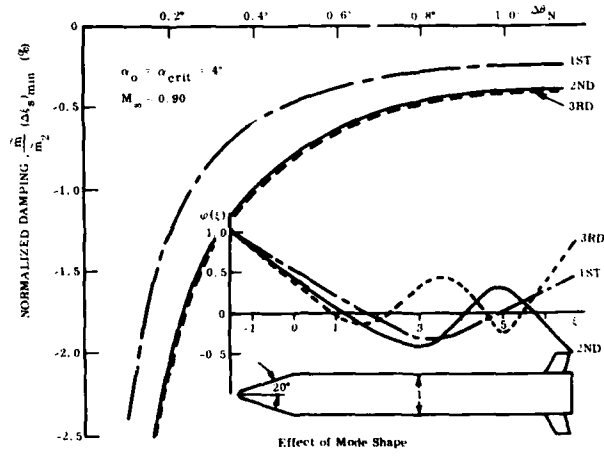


Figure 34. Separation-Induced Elastic Vehicle Damping (Ref. 16).

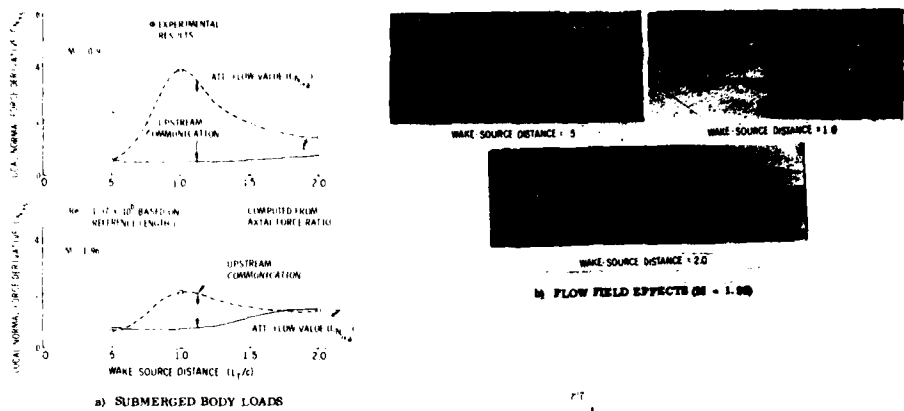


Figure 36. Aerodynamic Characteristics of Bodies in Wakes (Ref. 20)

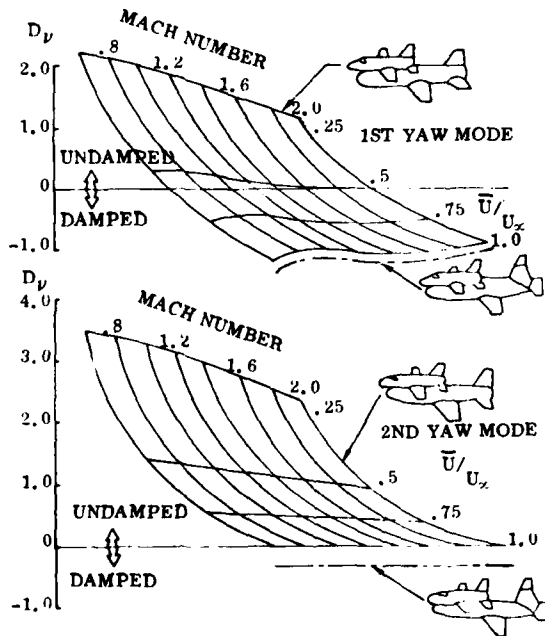


Figure 37. Yaw Damping for Straight Wing Space Shuttle Booster (Ref. 24).

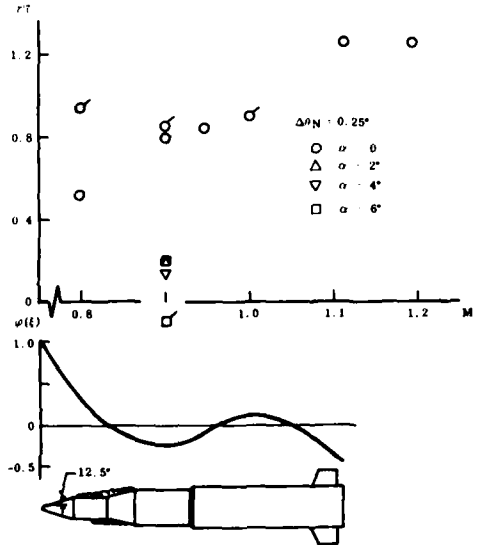


Figure 35. Aerodynamic Damping Measured on an 8 Percent Elastic Model of the Saturn I, Block II Vehicle With a Jupiter Nose Shroud (Ref. 19)

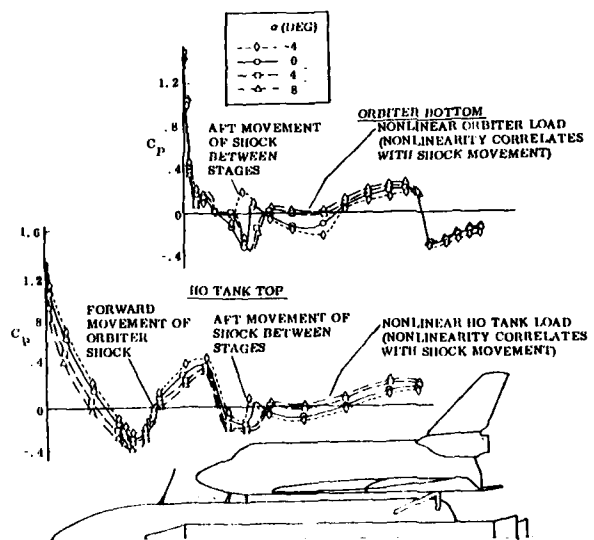


Figure 38. Pressure Distributions Between Stages of Space Shuttle Launch Configuration at  $M = 1.2$  (Ref. 25).

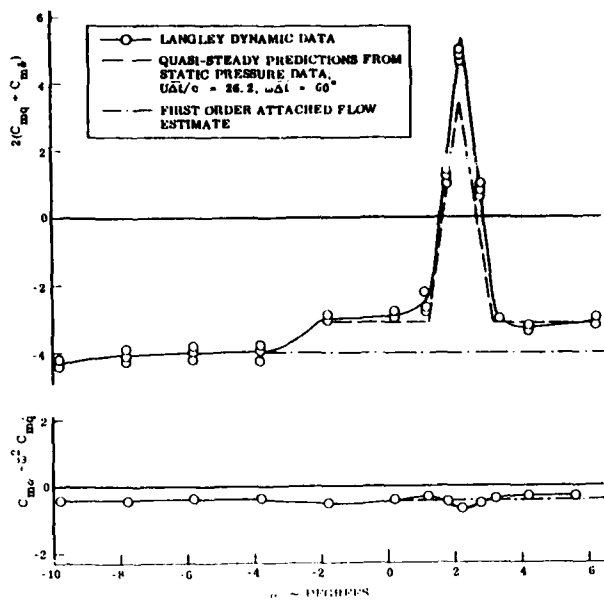


Figure 39. Comparison Between Predicted and Experimental Rigid Body Damping of the Space Shuttle Launch Configuration at  $M = 1.2$  (Ref. 25).

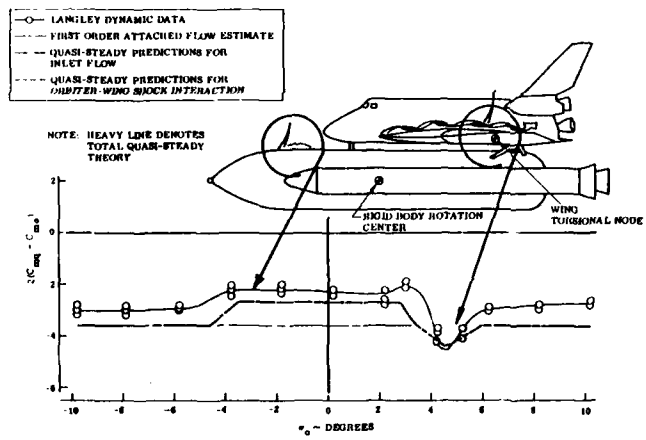


Figure 40. Effect of H0 Tank Flow Separation and Wing Shock Interaction on Launch Configuration Rigid Body Damping at  $M = 0.9$  (Ref. 25)

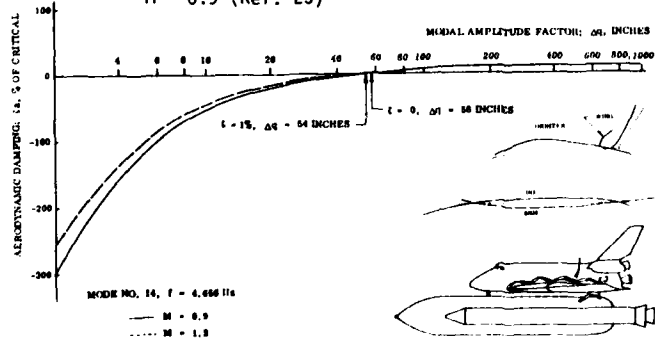


Figure 41. Effect of Orbiter Wing Shock Jump on the Elastic Body Damping of the Space Shuttle Launch Vehicle, Mode 14 (Ref. 25).

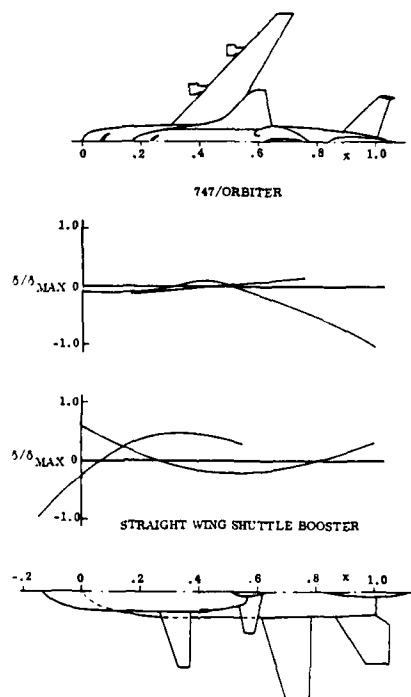


Figure 42. Comparison of Critical Modes (Ref. 29).

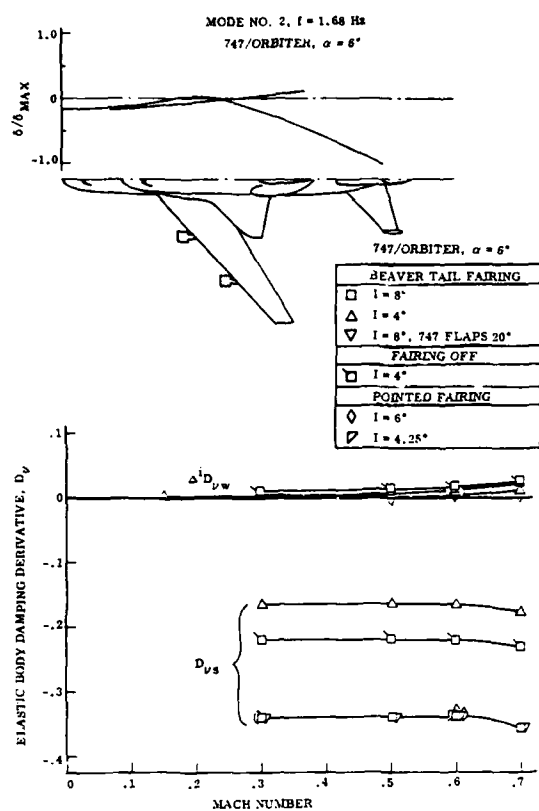


Figure 43. Elastic Body Damping Derivatives of 747 Tail for the Critical Antisymmetric Mode (Ref. 29).

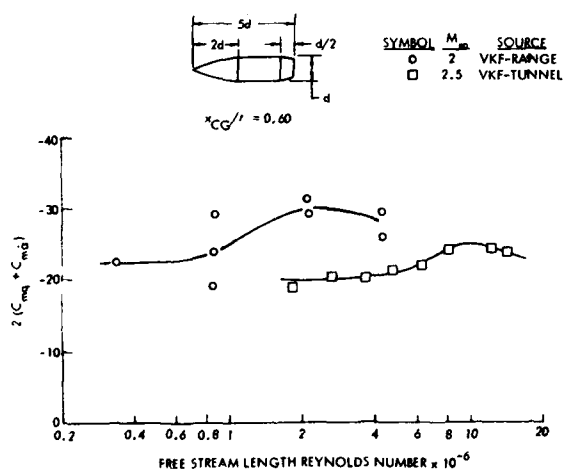
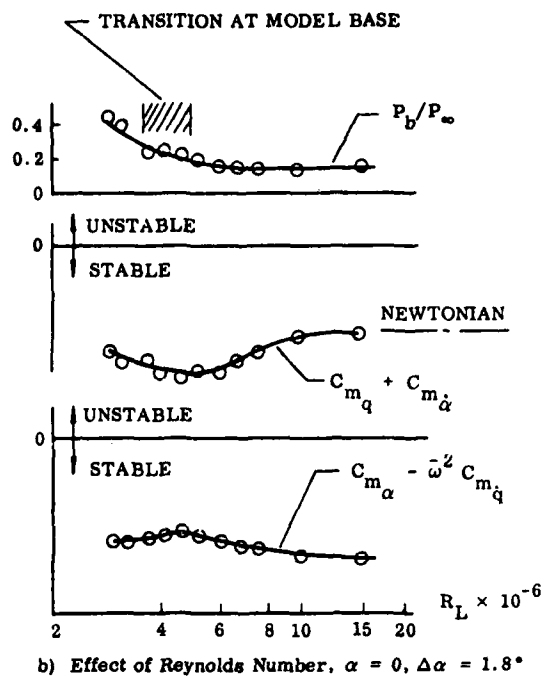


Figure 45. Effect of Reynolds Number on the Damping of an  $1/d = 5$  Ogive-Cylinder (Ref. 40).



b) Effect of Reynolds Number,  $\alpha = 0$ ,  $\Delta\alpha = 1.8^\circ$

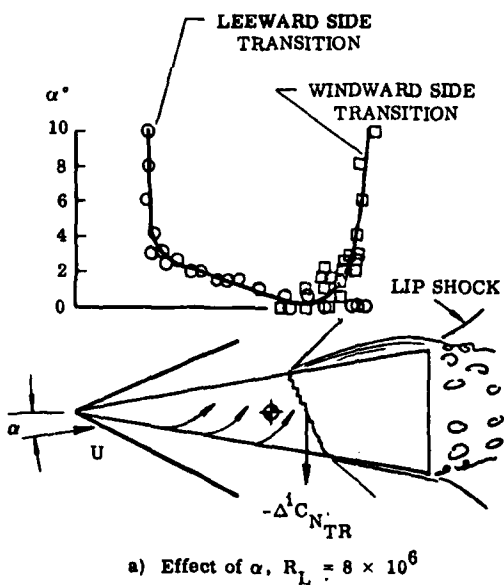


Figure 44. Boundary Layer Transition and its Effects on Sharp Cone Aerodynamics at  $M = 5$  (Ref. 35).

## CONTROL DERIVATIVES

A. Jean Ross  
 Royal Aircraft Establishment  
 Farnborough, Hampshire, GU14 6TD, UK

## SUMMARY

Two distinct groups of dynamic parameters associated with control surfaces are discussed. The first group consists of the hinge moments which determine the dynamic response of the control surface to the control demand. There has been a resurgence of interest recently, due to the possible repercussions on the performance of active control systems, and some of the results presented at a recent AGARD Conference on "Aerodynamic characteristics of controls" are described briefly.

More attention is paid to the second group, the control derivatives which influence the dynamic response of the aircraft. The design of the control surfaces and other motivators is, of course, governed primarily by the requirements for the manoeuvrability of the aircraft, but the control forces and moments generated are becoming of increasing importance in the design of the control systems used to improve the flying qualities. Thus the dynamic stability parameters of the aircraft with control system are dependent on the control characteristics, and examples are given to illustrate both this dependence and the typical variations of control derivatives with angle of attack and Mach number. Selected results for conventional control surfaces (such as flaps, elevator, aileron and rudder) and for other controls of current interest (such as horizontal and vertical canards and vectored thrust) are included.

## LIST OF SYMBOLS

The coefficient form of derivatives are used, but with control deflections denoted by symbols used in the UK, and expressed in radians, i.e

$\xi$	roll motivators
$\eta$	pitch motivators
$\zeta$	yaw motivators
$\delta$	lift, sideforce motivators.

Suffices are used to denote a particular type of motivator.

A	aileron
D	differential tail
HC	horizontal canard
LEF	leading edge flap
S	spoiler
TEF	trailing edge flap
V	vectored thrust
VC	vertical canard

## 1 INTRODUCTION

The aerodynamic characteristics of the control surfaces have always been of major importance in the design of an aircraft, and the 'stability' and 'control' aspects have been considered as complementary, together determining the flying (handling) qualities. As the control systems which use feedback signals to improve the basic flying qualities have become more sophisticated and more powerful, so have the stability and control aspects become more inter-related, and nowadays it is of paramount importance to have reliable data on both the inherent dynamic stability parameters, and the control parameters, in order to integrate successfully the designs of the airframe and the control system. Thus it is right and proper that a Lecture Series on Dynamic Stability Parameters include the topic of control derivatives. A recent AGARD Conference on 'Aerodynamic characteristics of controls' drew some 30 papers covering theoretical and experimental (from wind tunnel and flight) results for a variety of controls, and some of these results are reproduced here to illustrate the characteristics of control surfaces which impinge on the dynamic stability characteristics of aircraft. It is impossible to include more than a sample, but a selection has been made to cover most of the features of interest.

The dynamic stability characteristics of control surfaces themselves are discussed first, in section 2. These are probably of growing importance for the design of active control systems which alleviate loads and aircraft response to atmospheric gusts, and so have to be quick-acting. Some basic data on flap-type controls are described, and show the current inability to predict the forces and moments due to an oscillatory control at transonic speeds. The possibility of using spoilers as quick-acting control surfaces is also discussed briefly.

Examples of the ways in which control characteristics affect the dynamic response of the aircraft form the main part of the lecture, and are described in section 3. The motivators which produce principally moments (i.e. the primary control surfaces) are grouped

according to the axis of rotation, *i.e.* pitch, roll and yaw, and some characteristics of each of the conventional control surfaces used as primary controls are discussed. These include symmetric and differential deflections of tailplanes, ailerons, spoilers and rudder, with brief mention of vectored thrust and canard controls. The development of active control systems to provide the pilot with direct lift or direct sideforce control means that symmetric and differential deflections of canards are being used in more designs, and that flaps (which are usually classified as secondary controls when only used at specific discrete flap settings) at leading and/or trailing edges of wings are being used as part of the primary control system. The concept of using scheduled control deflections to enhance performance as well as stability of aircraft is introduced, with examples from the development of the CCV YF-16.

The effects of control deflections on the dynamic stability parameters discussed earlier in this Lecture Series have not been studied extensively, and only a few results are published. For most flight conditions, the effects are assumed to be negligible, but the use of scheduled leading edge flaps or other devices on the wings to maintain lift to higher angles of attack could be expected to influence some of the stability derivatives. Some results for the YF-16 aircraft are discussed briefly in section 4 to illustrate the trends.

## 2 DYNAMIC CHARACTERISTICS OF CONTROL SURFACES

Although the main theme of this Lecture Series is the dynamic stability of a complete aircraft, in the context of the parameters associated with controls it is necessary to consider also the dynamic stability of the control surface itself. The transient response of a control surface to the demanded input is determined by the hinge moment characteristics, both the hinge moment due to control deflection and that due to rate of change of control deflection. (There is also a hinge moment due to the angle of attack of the main wing, or fin, surface, but this does not affect the dynamic response and will not be discussed here.)

Some results for a full-span rudder on a fin<sup>2</sup> illustrate one of the basic difficulties for transonic flight regimes. The plain rudder, configuration (b) in Fig 1, is mass-balanced and shows typical instability for  $M > 0.975$  with positive damping derivative. This instability can be avoided either by using a set-back hinge to give aerodynamic balance, configuration (c), or by adding small spoilers to the plain rudder (configuration (a)). The stiffness hinge moments are reduced, but that of the aerodynamically balanced rudder changes sign at subsonic speeds, as might be expected with the degree of aerodynamic balance used. Although the rudder with spoilers gives the most acceptable hinge moments, the control effectiveness, *i.e.* the yawing moment due to rudder, is reduced drastically by 40%.

The hinge moment derivatives also depend on the geometry of the control, *e.g.* trailing edge thickness and shape, and on the oscillatory motion being experienced, particularly the amplitude and frequency. Most of the experimental results available were obtained over 20 years ago, although some checks have continued to give data for flutter investigations. There has been renewed interest recently, largely due to the possibility of using active control systems to alleviate gust loads, when the control surface would be required to respond at high rates. Of current concern is the inability of theoretical methods to predict the hinge moments, or the pressure distributions giving rise to the hinge moments, and some recent results were presented in Papers 19 and 20 of Ref 1. The hinge moments for an outboard trailing edge flap on a swept wing are shown in Fig 2 for subsonic Mach number, and it may be seen that linearised inviscid theory does not give the correct magnitude for either stiffness or damping, nor even the correct trend with Mach number for the stiffness derivative. If the effect of the boundary layer is taken into account in the theoretical estimates, then better agreement is obtained, but more information is needed to define these aspects. Paper 20 (by D.G. Mabey, D.M. McOwat and B.L. Welsh of RAE, Bedford) describes some experiments made to investigate the effects of boundary layer thickness on the oscillatory pressure distributions, and these were found to be very important, even at zero lift. An example of the comparison of theoretical estimates of the pressure distribution with measured values is taken from some work at ONERA (Paper 20 of Ref 1), to illustrate the difficulties, in Fig 3. The 25% chord flap on a two-dimensional model was oscillated through an amplitude of  $10^\circ$  about a mean deflection of  $-0.47^\circ$ , with the main surface at zero angle of attack. The results for  $M = 0.73$  and reduced frequency of 0.23 are typical of those presented in the original paper, the magnitude of the measured chordwise pressure distribution (upper figure) indicating a peak at a different chordwise position to that predicted by inviscid theory and of different magnitude to that obtained theoretically with boundary layer effects included. For the hinge moments, the measured pressure distribution over the flap would give very different results to those predicted, as both the magnitude and phase (lower figure) show large discrepancies. Work is continuing in these areas to develop experimental techniques and theoretical methods.

Spoilers are an alternative control surface for gust and load alleviation systems, since the actuation forces and moments are smaller than those for flaps, but it is now the lag in the transient change in pressure distribution which is of concern. Some interesting results are given in Papers 18 (by R. Destuynder of ONERA) and 21 (by S.R. Siddalingappa and G.J. Hancock of Queen Mary College, UK) of Ref 1. The records, given in the latter paper, of the transient pressures at four stations on a symmetric two-dimensional aerofoil are reproduced in Fig 4. The effects of opening the spoiler through  $45^\circ$  in the time taken for the free stream to travel one aerofoil chord length is shown in Fig 4a, and those due to closing in Fig 4b. The pressures in the trailing edge region (stations 2,3,4) due to opening the spoiler settle to their final values within the time taken for the free stream

to travel about four chord lengths. This is significantly smaller than theory indicates, where a sudden change in angle of attack is predicted to give 85% of the final lift in about six chord lengths, and it is suggested that tunnel-wall interference may affect the results. The transient pressures due to closing the spoiler have smaller fluctuations, and take less time to reach the steady values. Such experiments are contributing to the extra knowledge needed, now that control surfaces are being used in novel ways, with different types of demand coming from the control systems.

### 3 CONTROL EFFECTIVENESS

#### 3.1 Pitching moment

The conventional aircraft layout is fuselage, wing, tail and fin, with the tailplane often incorporating an elevator as the primary pitch control. The aerodynamic characteristics of elevators and all-moving tailplanes are well documented, and various estimation methods<sup>3,4</sup> are available for calculating the effects of angle of attack and Mach number. However, aircraft layouts are changing as active control technology is applied to its full potential. The once-basic requirement for inherent static stability\* may be waived, and the aircraft designer is free to optimise the overall performance without this constraint. There are many aspects of using this relaxed static stability to be considered, but the first example chosen to illustrate control characteristics which influence dynamic behaviour of aircraft emphasises two particular important points, that the maximum control power available can be more significant than the control derivative, and that off-design flight conditions may be crucial to the success of the aircraft design.

Two fighter configurations using relaxed static stability, one with tail and one with canard, have been investigated by NASA (Langley) (Paper 11 of Ref 1), with particular reference to their behaviour at high angles of attack. The aircraft with tail is slightly unstable for  $\alpha < 20^\circ$ , near neutrally stable for  $20^\circ < \alpha < 40^\circ$ , but at  $\alpha = 62^\circ$  it is trimmed and statically stable with zero tailplane deflection (Fig 5). This type of pitching moment variation with angle of attack has been encountered previously for aircraft which are statically stable at low angles of attack, but usually only for T-tails, where the high tail loses effectiveness when it is immersed in the wake of the wing. For statically unstable aircraft, the  $C_m - \alpha$  variation is highly likely to exhibit such a stable trim angle of attack within the easily-attainable range. It may be seen from Fig 5 that the aircraft is also trimmed at  $\alpha = 58^\circ$  with full nose-down tailplane deflection, and still statically stable, and there is insufficient control power to recover to lower angles of attack by straight application to full nose-down pitch control, *i.e.* a deep stall or super stall is encountered. A dynamic technique was developed on a piloted simulator which usually led to recovery, by moving the control stick in phase with the aircraft response, to cause an oscillatory build-up so that angles of attack below  $50^\circ$  would be encountered.

The configuration with canard exhibits a much more stable deep-stall condition, and again the control moments available for recovery are small at such high angles of attack. A possible means of overcoming the deficiencies in pitch control is to use vectored thrust, and two-dimensional nozzles, (*i.e.* a control surface with a thin rectangular nozzle at its trailing edge), appear to be an attractive form of this type of control. A study of comparative layouts for a supersonic fighter (Paper 5 of Ref 1) included a tailless configuration, which was 13% unstable at subsonic speeds to give near-neutral stability supersonically. The pitching moment increment required to control and limit angle of attack is shown in Fig 6, together with the moment available. Even with  $90^\circ$  deflection, there is insufficient control available between  $M = 0.6$  and  $0.9$ , and the conclusion was drawn that further research and development is needed before the concept can be used in this way. However, the results do illustrate the variation with Mach number of the maximum pitching moment from two-dimensional nozzle controls.

The control derivatives due to all-moving canards and tail show similar losses with increasing Mach number, as shown in Fig 7. For these comparative tests<sup>5</sup>, the same wing was used, and the same surface was tested at either a canard or tail position. The slightly larger numerical value of  $dC_m/d\alpha$  for the aft tail is accounted for by the 10% longer tail-arm, but the large difference in numerical values transonically, where the aft tail is 65% more effective at  $M = 0.9$ , indicate appreciable adverse interference effects with the canard. Such interference effects become dominant at high angles of attack/low speed, where the canard stalls and the downwash on the wing can produce zero or negative increments in pitching moment due to positive canard deflection. Even so, canard controls can be used successfully, and other results are quoted later.

#### 3.2 Rolling moment

A variety of control surfaces is used to generate rolling moments, the most common being ailerons. However, they do not retain their effectiveness over the flight envelope usually needed for combat aircraft, and so spoilers and differential tailplanes (taileron) are also used. A possible alleviation or postponement of the loss in aileron power at high angles of attack can be achieved by leading edge slats, flaps or other devices to maintain attached flow. The experimental results in Fig 8 show such effects for a model of the F-4<sup>6</sup> (Phantom) at  $M = 0.6$ , and at  $M = 0.9$  where the slat is not so successful. Also shown is the combined rolling moment due to aileron and spoiler, which again is reduced drastically at wing stall, and is improved by using slats. Alternatively, aileron

\*  $dC_m/d\alpha < 0$ , so that an increase in angle of attack is stabilised by nose-down pitching moment.

and differential tail may be combined, as for the YF-16<sup>7</sup>, and Fig 9a illustrates one of the reasons for using the latter, which retains effectiveness up to high angles of attack, while the ailerons (actually flaperons) lose effectiveness.

From the dynamic response point of view, the yawing moment produced by the roll control surfaces (due to the changes in lift-dependent drag caused by the deflection) is almost as important as the rolling moment. For ailerons (Fig 9b) the yawing moment is small at low angles of attack, but then changes sign and becomes of opposite sign to the rolling moment\*. This means that, if the pilot uses the aileron to roll the aircraft, the induced yaw has an adverse effect on the manoeuvre, tending to oppose the turn. This effect has been quantified in various parameters, such as adverse aileron yaw,  $w^2$  and currently LCDP (Lateral Control Departure Parameter) =  $C_{n\beta} - C_{n\xi}C_{\ell\beta}/C_{\ell\xi}$ . Zero values of LCDP can occur for sufficiently large  $C_{n\xi}$ , and indicate the probability of departure to uncontrolled flight if the pilot uses roll control. Alleviation can be achieved by introducing an aileron-rudder interconnect scheduled via the gearing  $K_{\xi\zeta}$  with angle of attack (and probably  $M$ ). In terms of derivatives, the yawing moment due to control deflections,  $C_{n\xi} + C_{n\zeta}\xi$  becomes  $(C_{n\xi} + K_{\xi\zeta}C_{n\zeta})\xi_p + C_{n\zeta}\zeta_p$  \*\*, with  $K_{\xi\zeta}(a,M)$  chosen to give  $C_{n\xi} + K_{\xi\zeta}C_{n\zeta}$  zero. Thus the adverse yawing moment due to aileron is counteracted by the yawing moment due to rudder. The yawing moment due to spoilers tends to remain proverse, but the rolling moment is small at high angles of attack, and so spoilers do not solve the problem. Differential tail deflections also tend to give proverse yawing moments (Fig 9b), but cannot usually be made powerful enough to provide sufficient roll control at low speed, low to moderate angle of attack. Hence, most modern combat aircraft have two types of roll control motivators, and the search continues for other sources of rolling moment. Flaperons, tiperons, spoiler/slot combinations, differential blowing, and introduction of asymmetries via strakes, canards, etc have been tested in wind tunnels, and some results are given in Papers 4, 6, 7 and 9 of Ref 1.

However, it is not possible to maintain positive values of LCDP to very high angles of attack (Fig 9c) even if  $C_{n\xi}$  is well behaved or counteracted, because of the variation of the static stability derivatives,  $C_{n\beta}$  and  $C_{\ell\beta}$ , in particular, the tendency of  $C_{n\beta}$  to become zero and then negative. Fig 9c shows the variation of LCDP with angle of attack for the YF-16, for the basic aircraft and with the aileron/rudder interconnect. LCDP tends to zero at about  $\alpha > 32^\circ$ , and so a departure prevention system has also to be designed, in this case by limiting the maximum angle of attack which the pilot can demand, and below which flying qualities are good.

The loss of rolling moment due to aileron as Mach number becomes supersonic is another factor which must be borne in mind, although the roll power is usually sufficient for the manoeuvring required, due to the high dynamic pressure. Typical variation of  $C_{\ell\xi}$  is shown in Fig 10 for the Viggen aircraft, and these results also show the importance of aeroelastic effects, which can cause the outer wing to deform under the load due to aileron deflection, reducing the expected rolling moment. Wind tunnel results measured using a rigid model have to be corrected by static aeroelastic factors obtained theoretically, or elastic models have to be manufactured for wind tunnel experiments. Both techniques have been applied successfully to the Viggen, to give comparison (Fig 10a) between theoretical and aeroelastic factors (obtained from tests on both rigid and elastic models), and the comparison (Fig 10b) between results from flight and wind tunnel experiments. The latter results were corrected by a factor appropriate to the structural properties of the full-scale Viggen, and the agreement obtained is excellent.

### 3.3 Yawing moment

The usual yaw control, the rudder, has well-behaved characteristics, giving near-constant yawing moments up to angles of attack near or even beyond the stall, but losing effectiveness as Mach number is increased supersonically. The associated rolling moment is small, due to the small moment arm, and does not have large effects on the response of an aircraft. The sideforce does have some influence, but not of great significance. Rudders have been incorporated in augmentation systems for many aircraft, particularly to augment damping-in-yaw, and also to compensate for adverse aileron yaw, as described above. In order to augment damping, the yaw rate has to be measured by a rate gyro onboard the aircraft, and a proportion of its signal is fed back to the rudder. Thus, in the combined yawing moment,  $C_{n_r}(\frac{rb}{2V}) + C_{n\xi}\xi$ , the rudder deflection now consists of two components, the pilot input,  $\zeta_p$  and from the augmentation system,  $K_{\zeta rr}$ , so that the expression becomes

$$(C_{n_r} + K_{\zeta r} \frac{2V}{b})(\frac{rb}{2V}) + C_{n\xi}\zeta_p .$$

As required, the direct aerodynamic damping,  $C_{n_r}$ , can be augmented substantially with

\* Note that American and British definitions of positive aileron deflection can differ, so the derivatives in the two systems are then of opposite sign, with  $C_{n\xi}$  positive and  $C_{n\zeta}$  negative.

\*\* Suffix P denotes pilot input.

relatively small rudder inputs. However, the maximum rate of yaw fed back to the rudder is usually limited, in order to prevent large rudder deflections due to system failure, and so the damping cannot be augmented beyond the corresponding level.

To illustrate the typical characteristics of rudders, some results for the twin-finned F-15 are shown in Fig 11a, taken from Paper 3 of Ref 1. The curves obtained from full-scale flight tests are shown, and these agree remarkably well with results from wind tunnel tests. As stated above, the yawing moment derivative is near constant up to  $\alpha \approx 17^\circ$ , but then reduces to about 20% of this level for  $\alpha > 40^\circ$ . It is also near constant for  $M < 1.0$ , showing a typical slight increase in effectiveness in the high subsonic region, and then reducing as  $M$  is increased supersonically. Corrections to wind tunnel values have usually to be made for aeroelastic effects, and for the effects of engine thrust, particularly for large transport aircraft. Such corrections appear to be small for the combat aircraft, F-15, although there is a significant 20% difference between rudder effectiveness obtained from free-flight tests<sup>9</sup> of a 3/8-scale model of the F-15 at low speeds and from earlier full-scale tests (Fig 11b). This did not appear to be due to thrust level, as results from the full-scale tests showed no consistent trend with variation of engine mass flow, and so it is suggested that the difference may be due to scale effects.

The development of controls for yawing is being influenced by the possibility of using relaxed lateral static stability systems, which enable smaller fin area to be envisaged, but also entail increased demand on the yaw control. The possibilities are to develop more efficient rudders (eg blown flaps, slotted rudders) or to use all-moving fins and vertical canards.

### 3.4 Sideforce

The application of sideforce to manoeuvre combat aircraft has only recently been made possible, using active systems to combine deflections of rudder and canard to give the required response. At first sight, vertical canards (chin fins) would appear to be the most useful source of sideforce, but wind tunnel tests show that asymmetric deflection of horizontal canards often gives better characteristics. Various canard configurations were tested during the development of the CCV YF-16, and some results are shown in Fig 12. The vertical canard quickly loses effectiveness as angle of attack increases (Fig 12a) and  $25^\circ$  deflection gives only small increments in  $C_y$  at manoeuvring angles of attack (say  $10^\circ$  to  $20^\circ$ ). In contrast, differential deflection of horizontal canards appear to have remarkably linear characteristics, even though the sideforce and yawing moment are generated by interference effects (Fig 12b&c). If the yawing moment is automatically trimmed by the rudder, then the sideforce is augmented (Fig 12b) to useful levels, for  $40^\circ$  differential deflection. The sideforce is also near linear with differential deflection (Fig 12c) and almost independent of Mach number (Fig 12d). Similar results have been obtained on other models, so the linearity is not particular to the YF-16 configuration. The canards actually installed on the CCV YF-16 are canted at  $45^\circ$ , and so are less effective than the results above indicate. Other possible sideforce generators tested include split flaps on pylons (on the CCV Alpha-Jet), and differential spanwise blowing.

One of the implications of the use of sideforce controls on the dynamic response of aircraft is that the effective spiral mode becomes dominant, and so some of the approximations used in assessing dynamic response are no longer valid. In particular, the 'combined' derivatives measured on oscillatory rigs in the wind tunnel, such as  $C_{n_r} - C_{n_\beta} \cos \alpha$  and  $C_{l_p} + C_{l_\beta} \sin \alpha$  are usually used with the assumption that the derivatives due to  $\dot{\beta}$  are small. It can be shown (Appendix C of Ref 10), that the combined derivatives give very good approximations to the characteristics of the Dutch roll and roll subsidence modes, even if the  $\dot{\beta}$  derivatives are significant, but that the characteristics of the spiral mode depend mainly on the 'separated' derivatives due to rate of yaw,  $r$ . Thus there is need to gain some knowledge of the dynamic derivatives due to 'pure' roll, 'pure' yaw, and rate of change of sideslip, as described in earlier lectures, especially at high angles of attack, where the  $\dot{\beta}$  derivatives can be expected to be comparable in magnitude to the other derivatives.

### 3.5 Lift

The examples given in the previous sub-sections mostly illustrate the interdependence of the dynamic response of an aircraft and the aerodynamic characteristics of control surfaces, but attention is now focussed on the growing interdependence of the performance of an aircraft and its control system. Landing flaps, manoeuvre flaps, leading edge flaps and slats have all been used on transport and combat aircraft to increase the lifting capability for particular flight conditions, and the pilot selected an appropriate constant control setting which had been chosen to give optimum performance at one design flight condition, or mean 'best' performance over a range of flight conditions. With an active control system, it is possible to design continuous control settings, which vary with the flight condition (particularly angle of attack and Mach number), so that optimum performance is achieved throughout the flight envelope. Results for trimmed lift and drag from wind tunnel tests are used to design the flap schedules required to give minimum drag for maximum lift; for example, the results for the F-18 aircraft<sup>11</sup> at  $M = 0.8$  are shown in Fig 13. The control system uses both leading and trailing edge flaps, and it may be seen that it is possible to define a minimum drag envelope (for each Mach number), and so define the separate schedules for deflections of the flaps with angle of attack and Mach number, which will yield minimum drag throughout the transonic flight envelope.

However, it may not be possible for the pilot to use the maximum lift indicated by static wind tunnel tests, due to adverse flying qualities<sup>12</sup>, such as buffet, pitch-up, nose slice, wing drop, wing rock, etc. These are dynamic phenomena, and so it seems appropriate to describe the effects of controls on their onset. Many of the phenomena (which define the manoeuvre boundary of combat aircraft) occur below wing stall, but are associated with the type and development of flow separation on the wings, and so the leading edge devices developed to maintain lift also usually delay the onset of adverse flying qualities. The development of the YF-16 was used as an example in Paper 2 of Ref 1, and the collected results are reproduced here to demonstrate the close interdependence of performance, static stability and dynamic stability parameters for today's aircraft with active control systems. Ref 13 describes the 'aerodynamic design evolution of the YF-16', and particularly emphasises the improvements due to the strake and the scheduled leading edge flap deflection. First, the trimmed lift vs drag is shown in Fig 14, where the variable leading edge flap deflection has been determined in the same way as the F-18 schedules described above. The basic variations of  $C_L$  and  $C_m$  with angle of attack are also shown in Fig 14, and it may be seen that the increased lift is obtained with reduced pitching moment at high  $C_L$ 's, which leads to the improvements in both trimmed  $C_L$  and  $C_D$ . The active control system is required to schedule the leading edge flap deflection, and also to overcome the near-neutral static stability, but there could still be dynamic phenomena preventing this lift being achieved in flight. The first concern is the buffet characteristics, which are given in Ref 13. Unfortunately, the effects of strake and leading edge flap deflection are given at different Mach numbers, so that direct comparisons of each contribution cannot be made, but the improvements in buffet intensity are striking enough to warrant reproduction here, in Fig 15. Next<sup>14</sup>, several of the possible adverse flying qualities are associated with loss of directional stability, expressed as either  $C_{n\beta}$  or 'dynamic  $C_{n\beta}$ ' =  $C_{n\beta} - i_z C_{l\beta} \sin \alpha / i_x$ . The presence of the strake and leading edge flap deflection each improve sideslip characteristics at high angle of attack, i.e.  $C_{n\beta}$  more positive and  $C_{l\beta}$  more negative, as shown in Fig 16a for the effect of flap deflection at low speed. The resulting dynamic  $C_{n\beta}$  becomes zero at  $\alpha = 28^\circ$ , although at  $M = 0.9$ , it remains positive up to  $\alpha \approx 40^\circ$ , as shown in Fig 16b. The lateral departure control parameter also becomes negative at similar angles of attack, as discussed earlier in section 3.2.

More wind tunnel tests<sup>15</sup> had to be done for the development of the CCV YF-16, and the results for the sideforce have been described in section 3.4. Although horizontal canards would have given substantial direct lift, the configuration flown has to rely on trailing edge flap and tail deflections. The buffet characteristics are affected adversely (Fig 17) by the trailing edge flap deflection<sup>16</sup>, and the direct lift control command had to be limited to flap deflections of  $15^\circ$  to avoid this moderate buffet, and to prevent penetration to strong buffet at the higher angles of attack. The presence of the canted canards also changes the directional stability. The flight results show that  $C_{n\beta}$  is halved at low angles of attack by the presence of the canards, but that directional stability is increased as angle of attack increases to  $20^\circ$ . The dihedral of the canted vertical canards also increases the magnitude of  $C_{l\beta}$ , so that 'dynamic  $C_{n\beta}$ ' has better characteristics at high angles of attack if the canards are on (Fig 17). Data on roll control are not available, to evaluate LDCP, but it is stated in Ref 16 that canard interference reduces the rolling effectiveness of the differential tail, and also has a smaller reducing effect on the ailerons. Of course, the dynamic stability parameters are another vital data set required before the behaviour of aircraft can be predicted, particularly at high angles of attack, but the effects of canards have not been published. Some results for the effects of leading edge flap deflections are discussed in section 4.

The use of direct lift control, on the CCV YF-16 and other aircraft, has similar implications on the determination of dynamic stability parameters as mentioned in section 3.4 for the use of direct sideforce. Oscillatory rig tests yield measurements of the combined derivative,  $C_{m\dot{q}} + C_{m\dot{\alpha}}$ , which can be used directly to estimate the damping of the longitudinal short period mode. It is also often possible to estimate  $C_{m\dot{\alpha}}$  with sufficient accuracy (based on downwash delay for tailed aircraft) so that  $C_{m\dot{q}}$  can be derived to give the contribution to the frequency of the short period oscillation, which is approximately proportional to  $\nu C_{m\dot{\alpha}} + C_{m\dot{q}} C_{z\dot{\alpha}}$ , where  $\nu$  is the relative density. The modes experienced by aircraft with direct lift control are, by definition, due to significant normal force, so that the difference between  $\dot{\alpha}$  and  $\dot{q}$  is not negligible, as is usually assumed in the short period mode, since  $\dot{\alpha} - \dot{q} = \frac{\Delta Z}{mV} - \frac{g}{V} \theta$ . Techniques have been described in earlier lectures for measuring derivatives due to  $\dot{q}$  and  $\dot{\alpha}$  separately in order to check the importance of the  $\dot{\alpha}$  terms particularly. Some amelioration of the difficulty usually comes from the active control system, where the relaxed static stability has to be regained using various feedback loops, so that the values of the 'effective' derivatives are largely due to the control system (and so the control derivatives) rather than to the aerodynamic dampings.

#### 4 EFFECT OF CONTROL DEFLECTION ON DYNAMIC STABILITY PARAMETERS

As stated in the Introduction, control deflections are usually assumed to have negligible effect on the dynamic derivatives, and so the experimental data are sparse. In fact, some of the oscillatory rigs used in wind tunnels require the model to be at or near trim conditions, in order to keep the loads to a minimum, and so the opportunities for gathering data are few. For most primary control surfaces it would seem that the assumption is justified, except possibly at extreme flight conditions, but the use of

(scheduled) leading edge devices to maintain attached flow on the wings to higher angle of attack can be expected to lead to changes in the stability derivatives. The development of such devices to the variable camber concept also means that the basic shape to be tested dynamically is not well defined, but tests need to be made to investigate the significance of such changes to wing shape. Some results for the leading edge flap on the YF-16 have been quoted in Ref 7, and these show the changes in the dynamic stability derivatives, as measured using a forced oscillation technique, due to 2° deflection at low speeds. The rolling and yawing moment derivatives are changed significantly for  $\alpha > 30^\circ$  (Fig 18), which is beyond the range of interest for the actual aircraft, but there are also some changes to the derivatives due to roll rate for  $\alpha < 20^\circ$  which are of importance.

For example, at  $\alpha = 15^\circ$  the scheduled leading edge flap<sup>7</sup> deflection is 20°, so that the increment in  $C_{\ell p}^*$  is -0.08 and in  $C_{n p}$  is -0.05. At the flight condition considered in Ref 7, ie level flight at 20000 feet, the damping of the Dutch roll mode is given as  $1/t_1 = 0.5 \text{ s}^{-1}$  for the aircraft without yaw damper, and  $0.85 \text{ s}^{-1}$  with the yaw damper operative, both with scheduled leading edge flap. The approximate contribution to the Dutch roll damping due to the flap deflection is found to be  $0.08 \text{ s}^{-1}$  due to  $\Delta C_{\ell p}$ , and  $-0.035 \text{ s}^{-1}$  due to  $\Delta C_{n p}$ , ie  $0.055 \text{ s}^{-1}$ , which is 11% of the damping for the aircraft without yaw damper. The approximate contributions for the derivatives due to yaw rate are much smaller ( $0.01 \text{ s}^{-1}$ ), partly because the Dutch roll damping is less sensitive to those derivatives at moderate to high angles of attack for aircraft with large yaw/roll inertia ratio, and partly because the changes in the values of the derivatives are smaller. Thus the use of scheduled leading edge flap does influence the levels of damping of the Dutch roll mode, as well as delaying the onset of departure as discussed earlier, in section 3.5. It will be interesting to see, in the future, whether scheduled control deflections or other in-flight changes of wing profile will have significant contributions to the dynamic stability derivatives for other configurations, but it is probable that schedules chosen to optimise performance will tend to be beneficial also for dynamic stability.

## 5 CONCLUDING REMARKS

This lecture has aimed to present a short survey of the aerodynamic characteristics which are particularly relevant to the dynamic stability parameters associated with actively-controlled aircraft. It is hoped that some of the concepts introduced will also act as a bridge between the previous lectures in this series, on the determination of the dynamic stability parameters, and those following, which discuss the application of the parameters to determine the flight dynamic characteristics of aircraft.

---

\* The derivatives obtained from the oscillatory rig are written here as  $C_{\ell p}$  etc, rather than  $C_{\ell p} + C_{\ell \beta} \sin \alpha$ , following Ref 7.

## REFERENCES

- 1 Aerodynamic characteristics of controls. May 1979, AGARD CP262 (Naples)
- 2 F.W. Gibson, R.W. Herr, R.S. Osborne, Some effects of flow spoilers and of aerodynamic balance on the oscillating hinge moments for a swept fin-rudder combination in a transonic wind tunnel. 1958, NACA RM L58C28
- 3 Stability and Control Handbook of the United States Airforce
- 4 Aerodynamic Sub Series, Engineering Sciences Data, Engineering Sciences Data Unit, London
- 5 R.B. Eberle, R.T. Stancil, W.C. Fowler, A critical review of canard relative to aft horizontal tail based on low and high speed tunnel tests of a fighter/attack configuration. 1971, AIAA 71-8
- 6 E.T. Ray, E.G. Hollingsworth, Subsonic characteristics of a twin-jet swept-wing fighter model with manoeuvring devices. 1973, NASA TN-D-6921
- 7 W.P. Gilbert, L.T. Nguyen, R.W. Van Gunst, Simulator study of the effectiveness of an automatic control system designed to improve the high angle of attack characteristics of a fighter airplane. 1976, NASA TN-D-8176
- 8 J. Kloos, L. Elmeland, Static aeroelastic effects on the aerodynamics of the SAAB 37 Viggen aircraft, a comparison between calculations, wind tunnel tests and flight tests. 1974, ICAS 74-55
- 9 K. Iliffe, Estimation of aerodynamic characteristics from dynamic flight test data. 1978, Paper 15 of AGARD CP 235
- 10 A. Jean Ross, G.W. Foster, T. Turvey, An investigation of Dutch roll and wing rock oscillations of a Gnat Trainer aircraft: flight test and linear analysis. 1978, RAE Technical Report 78032
- 11 R.F. Stewart, R.E. Whitehead, Analysis of advanced variable camber concepts. 1977, Paper 14 of AGARD CP 241
- 12 Manoeuvre limitations of combat aircraft. 1979, AGARD AR 155A
- 13 J.K. Buckner, P.W. Hill, D. Benepe, Aerodynamic design evolution of the YF-16. 1974, AIAA 74-935
- 14 J.P. Lamars, Design for departure prevention in the YF-16. 1974, AIAA 74-794
- 15 S.C. Stumpf, R.A. Whitmoyer, Horizontal canards for two-axis CCV fighter control. 1974, Paper 6 of AGARD CP 157
- 16 R.A. Whitmoyer, Aerodynamic interactions on the fighter CCV test aircraft. 1978, Paper 16 of AGARD CP 235

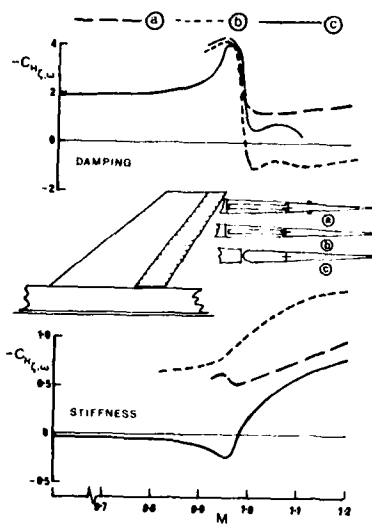


Fig 1 Hinge moments on three rudder configurations

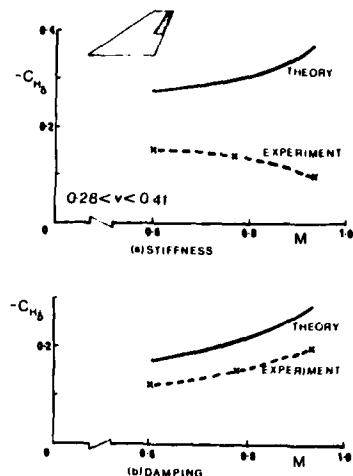


Fig 2 Comparison of experimental results and inviscid theory for hinge moments

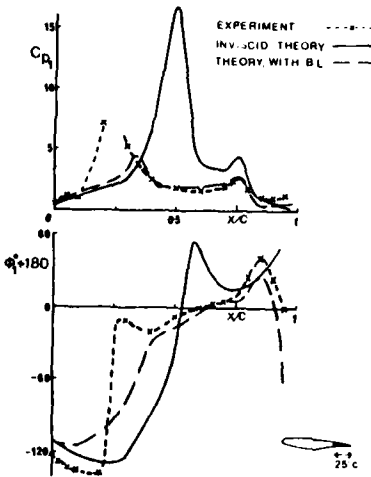


Fig 3 Comparison of experimental and theoretical results for oscillatory pressure distribution due to oscillating two-dimensional flap

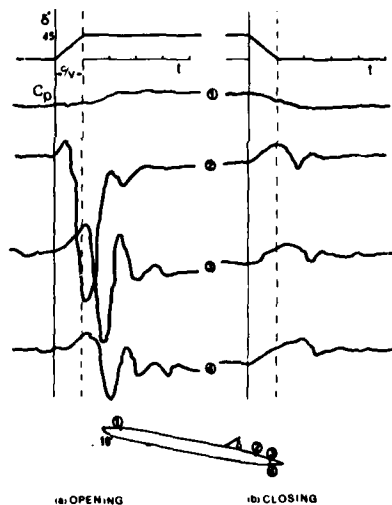


Fig 4 Transient pressures due to opening and closing a spoiler on a two-dimensional aerofoil

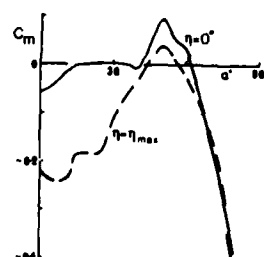


Fig 5 Pitching moment at angle of attack for swept-wing/tail configuration using relaxed static stability

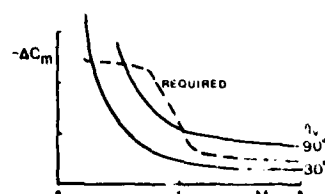


Fig 6 Available pitching moment from vectored thrust control on a tailless configuration, and level required for pitch control

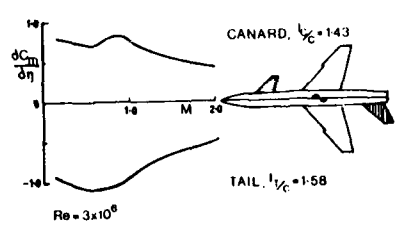


Fig 7 Pitching moment derivative due to canard or tail deflection

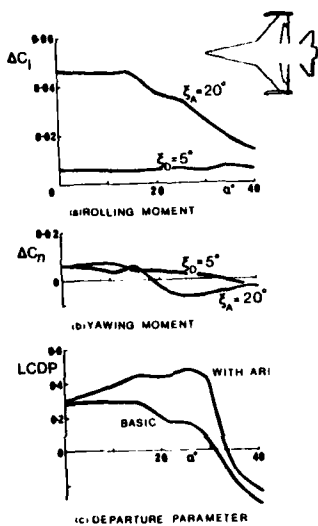


Fig 9 Roll control characteristics for YF-16

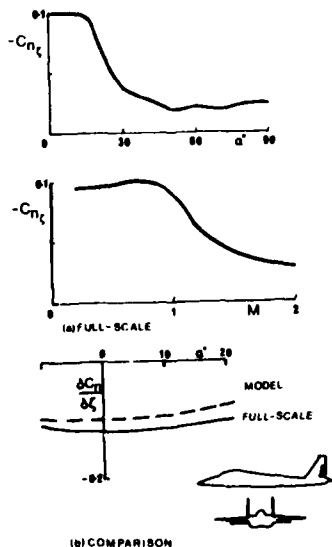


Fig 11 Yawing moment due to rudder, F-15 aircraft

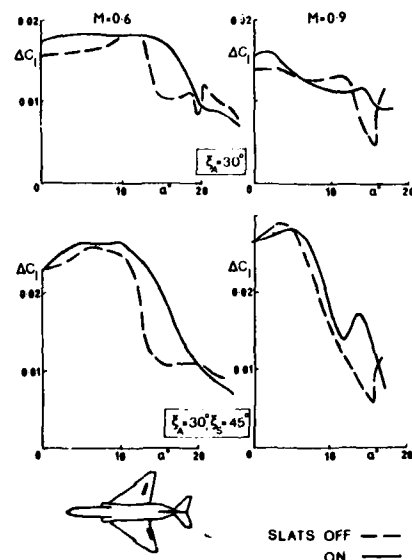


Fig 8 Rolling moment due to aileron and spoiler, F-4 configuration

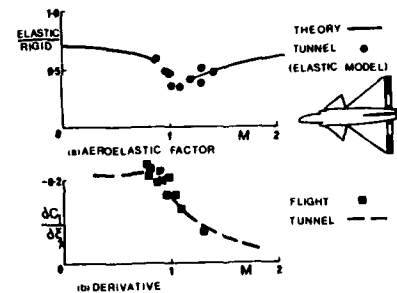


Fig 10 Effect of aeroelasticity on rolling moment due to elevator, Viggen aircraft

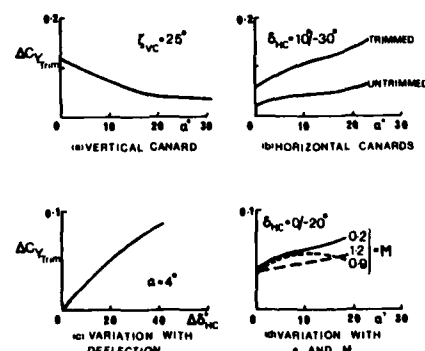


Fig 12 Trimmed sideforce characteristics for canard controls on CCV YF-16 configuration

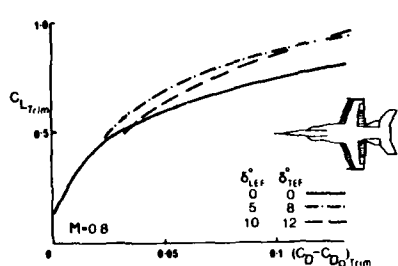


Fig 13 Lift-v-drag envelope for F-18 flap schedule

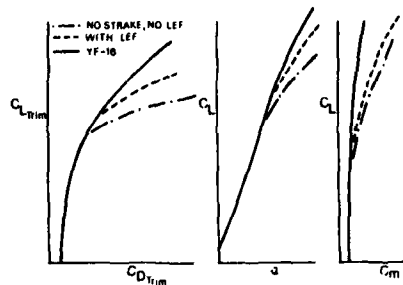


Fig 14 Effects of strake and leading edge flap on trim, YF-16

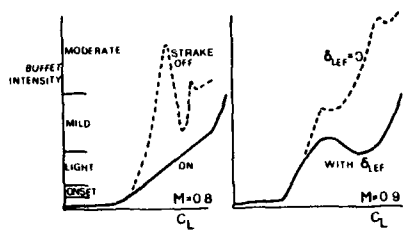


Fig 15 Effects of strake and leading edge flap on buffet, YF-16

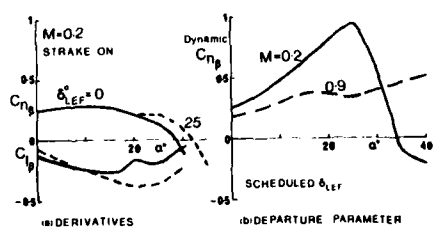


Fig 16 Effect of leading edge flap on sideslip characteristics

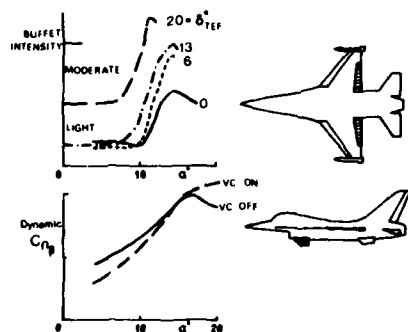


Fig 17 Effects of control systems on handling parameters, CCV YF-16

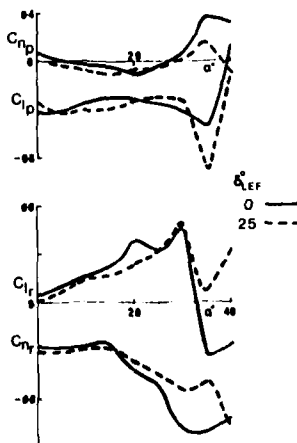


Fig 18 Effect of leading edge flap on dynamic stability derivatives, YF-16

**SENSITIVITY OF AIRCRAFT MOTION TO CROSS-COUPING AND  
ACCELERATION DERIVATIVES**

by

K. J. Orlik-Rückemann

Unsteady Aerodynamics Laboratory  
National Aeronautical Establishment  
National Research Council of Canada  
Ottawa, Ontario, Canada

**1. INTRODUCTION**

Modern military aircraft are often designed to maneuver at relatively high angles of attack and therefore are subjected to conditions where the flow becomes highly asymmetric. They are sometimes equipped with direct-lift or direct-sideforce controls and therefore able to perform translational as well as the traditional rotational maneuvers. Under such flight conditions and maneuvers, certain derivatives that are negligible under symmetric, low-angle-of-attack flight conditions, may become large enough to be significant. Here belong certain static and dynamic cross-coupling derivatives and derivatives due to translational acceleration. In addition, most derivatives, including the categories just mentioned, usually display strong non-linearities at high angles of attack. It is the purpose of this lecture to describe some recent studies of the sensitivity of the predicted aircraft and missile motion to the inclusion of the cross-coupling and acceleration derivatives and of the taking into account the various non-linear effects.

**2. SENSITIVITY STUDIES**

Sensitivity studies are usually carried out by programming, on a computer, as complete a set as possible of equations of motion pertinent to a particular configuration and particular flight condition, by inserting a set of stability parameters, including - if required - some non-linear effects, by varying those parameters in a predetermined manner, and by observing the responses of the variables of motion to some form of disturbance applied to the set of equations. The stability parameters are usually varied individually, but may also be studied in combinations. The difference between responses obtained for two different values of a parameter or for two different combinations determines the sensitivity of the aircraft behaviour to the variation of that particular stability parameter or that particular combination of parameters.

The system of equations required to perform a sensitivity study encompasses (a) the proper equations of motion, or *inertial equations*, (b) the equations defining the external forces and moments, or *loading equations*, and (c) the equations describing the required coordinate transformations and relations between some of the variables, or *auxiliary equations*. A derivation of the necessary equations from the basic principles is outside the scope of this lecture but can be found in numerous books on flight dynamics (such as Ref. 1). An example of a complete set of equations needed for a sensitivity study (or generally for a simulation on a computer of flight dynamics of a symmetric aircraft) is given below:

**(a) Equations of Motion\***

$$\begin{aligned}\dot{u} &= \sum F_x/m = qw + rv \\ \dot{v} &= \sum F_y/m = ru + pw \\ \dot{w} &= \sum F_z/m = -pv + qu \\ \dot{p} &= [\Sigma L - (I_z - I_y)qr + I_{x_z}(r + pq)]/I_x \\ \dot{q} &= [\Sigma M - (I_x - I_z)rp + I_{x_z}(r^2 - p^2)]/I_y \\ \dot{r} &= [\Sigma N - (I_y - I_x)pq + I_{x_z}(p - qr)]/I_z\end{aligned}$$

**(b) Loading Equations**

$$\begin{aligned}\sum F_x &= T - mg \sin \theta + C_x \bar{q}s \\ \sum F_y &= mg \cos \theta \sin \phi + C_y \beta \bar{q}s \\ \sum F_z &= mg \cos \theta \cos \phi + [C_{z_T} + C_{z_\alpha}(\alpha - \alpha_T) + C_{z_q}(q\bar{c}/2V) + C_{z_\alpha}(\dot{\alpha}\bar{c}/2V)]\bar{q}s\end{aligned}$$

\* All symbols are defined in the Appendix.

$$\Sigma L = [C_{L_T} + C_{L_\alpha}(\alpha - \alpha_T) + C_{L_\beta}\beta + C_{L_p}(pb/2V) + C_{L_q}(q\bar{c}/2V) + C_{L_\alpha}(\dot{\alpha}\bar{c}/2V) + C_{L_r}(rb/2V) + C_{L_\beta}(\dot{\beta}b/2V)]\bar{q}Sb$$

$$\Sigma M = [C_{m_T} + C_{m_\alpha}(\alpha - \alpha_T) + C_{m_\beta}\beta + C_{m_p}(pb/2V) + C_{m_q}(q\bar{c}/2V) + C_{m_\alpha}(\dot{\alpha}\bar{c}/2V) + C_{m_r}(rb/2V) + C_{m_\beta}(\dot{\beta}b/2V)]\bar{q}Sc$$

$$\Sigma N = [C_{n_T} + C_{n_\beta}\beta + C_{n_\alpha}(\alpha - \alpha_T) + C_{n_p}(pb/2V) + C_{n_r}(rb/2V) + C_{n_\beta}(\dot{\beta}b/2V) + C_{n_q}(q\bar{c}/2V) + C_{n_\alpha}(\dot{\alpha}\bar{c}/2V)]\bar{q}Sb$$

## (c) Auxiliary Equations

$$\dot{X} = u \cos \psi \cos \theta + v(\cos \psi \sin \theta \sin \phi - \sin \psi \cos \phi) + w(\cos \psi \sin \theta \cos \phi + \sin \psi \sin \phi)$$

$$\dot{Y} = u \sin \psi \cos \theta + v(\sin \psi \sin \theta \sin \phi + \cos \psi \cos \phi) + w(\sin \psi \sin \theta \cos \phi - \cos \psi \sin \phi)$$

$$\dot{Z} = -u \sin \theta + v \cos \theta \sin \phi + w \cos \theta \cos \phi$$

$$\alpha = \arctan(w/u)$$

$$\beta = \arctan(v/u)$$

$$\dot{\alpha} = (u\dot{w} - \dot{u}w)/(u^2 + w^2)$$

$$\dot{\beta} = (u\dot{v} - \dot{u}v)/(u^2 + v^2)$$

$$\Phi_A = \arctan(v/w)$$

$$\gamma_H = \arctan(\dot{Y}/\dot{X})$$

$$\gamma_V = \arctan[-\dot{Z}/(\dot{X}^2 + \dot{Y}^2)^{1/2}]$$

$$V = (u^2 + v^2 + w^2)^{1/2}$$

The auxiliary equations can have various alternative forms. For instance, the relations between  $\dot{X}$ ,  $\dot{Y}$  and  $\dot{Z}$  and  $u$ ,  $v$ ,  $w$  are often replaced by relations between  $\phi$ ,  $\theta$ ,  $\psi$  and  $p, q, r$ .

In addition to the above equations, a sensitivity study requires the use of suitable initial conditions. For a flight condition that is more general than a straight level flight and that may require aerodynamic trimming around several axes, the number of parameters that must be included in such initial conditions is quite substantial. For instance, for a steady turning flight at a constant load factor, the initial conditions have to be determined from the following expressions:

$$\bar{q}_o = nm\bar{g}/[-C_z(\sin \alpha_o \tan \alpha_o + \cos \alpha_o)S]$$

$$T = (-C_z \tan \alpha_o - C_x)\bar{q}_o S$$

$$-(h_o/33300)$$

$$\rho_o = 0.002377e$$

$$V_o = (2\bar{q}_o/\rho_o)^{1/2}$$

$$\Phi_o = \text{arc cos } (1/n)$$

$$\Theta_o = \text{arc sin } (\sin \Phi_o \sin \beta_o + \cos \Phi_o \sin \delta \cos \beta_o)$$

$$\Psi_o = \text{arc sin } [(\sin \Phi_o \sin \delta \cos \beta_o - \cos \Phi_o \sin \delta \sin \beta_o)/\cos \theta_o]$$

$$\Phi_o = \text{arc sin } [(\sin \Phi_o \cos \beta_o - \cos \Phi_o \sin \delta \sin \beta_o)/\cos \theta_o]$$

$$\dot{\Psi}_o = g \sin \Phi_o / [(cos \Phi_o \cos \alpha_o + \tan \theta_o \sin \alpha_o)V_o]$$

$$P_o = -\dot{\Psi}_o \sin \theta_o$$

$$Q_o = \dot{\Psi}_o \cos \theta_o \sin \Phi_o$$

$$R_o = \dot{\Psi}_o \cos \theta_o \cos \Phi_o$$

$$C_{z_T} = C_z - C_{z_q} (q_0 \bar{c} / 2V_0)$$

$$C_{l_T} = -C_{l_p} \frac{b}{2V_0} - C_{l_q} \frac{c}{2V_0} - C_{l_r} \frac{b}{2V_0} + ((I_z - I_y) q_0 r_0 - I_{xz} p_0 q_0) / \bar{q} s b$$

$$C_{m_T} = -C_{m_q} \frac{\bar{c}}{2V_0} - C_{m_r} \frac{b}{2V_0} + ((I_x - I_z) r_0 p_0 - I_{xz} (r_0^2 - p_0^2)) / \bar{q} s c$$

$$C_{n_T} = -C_{n_p} \frac{b}{2V_0} - C_{n_r} \frac{b}{2V_0} - C_{n_q} \frac{\bar{c}}{2V_0} + ((I_y - I_x) p_0 q_0 + I_{xz} q_0 r_0) \bar{q} s b$$

Digital or hybrid computers are normally used for this kind of studies. When employing a hybrid computer, some of the aforementioned groups of equations are solved on the analogue computer and the rest on the digital computer. The choice of computers is often based on practical considerations, such as the existence of suitable programmes or the desire to have a short turn-around time between successive simulations. In hybrid operations, analogue samples may have to be corrected for error introduced by digital lag (Ref. 2). The simulation is often run in real time, with a typical run duration of 8-20 seconds and a few minutes usually required between runs to change parameters and reinitialize.

The aerodynamic information employed in the loading equations consists predominantly of the static and dynamic moment derivatives, and includes only the most important static force derivatives, such as  $C_y \beta$  or  $C_z \alpha$ . Only in exceptional cases are any dynamic force derivatives, such as  $C_{z_q}$  or  $C_{z_a}$ , taken into account in the analysis. This stems from the fact that the dynamic force derivatives are generally considered to be of less significance than the corresponding moment derivatives and therefore are also less known.

All the static derivatives and the dynamic direct derivatives (damping derivatives) and dynamic cross derivatives are usually available, for the configuration of interest, from low-speed wind tunnel experiments. The oscillatory wind tunnel data are in the form of composite derivatives, such as  $C_{m_q} + C_{m_a}$ .

Since usually no sufficient information is available to separate the two parts of composite derivatives, the sum is often used in place of the rotary derivative ( $C_{m_q}$ ) alone, or else the composite derivative is divided into its two parts in an arbitrary fashion. The direct and cross derivatives are often provided in the form of look-up tables and may be available as functions of  $\alpha$ ,  $\beta$  and of various control surface deflections.

The situation is rather different for the dynamic cross-coupling derivatives. At the present time the only set of such derivatives available (Refs. 3 and 4) is for an "aircraft-like" configuration which has been tested at  $M = 0.7$  in the angle of attack range of up to  $40^\circ$  and for angles of sideslip of  $0^\circ$  and  $5^\circ$ . Until more data become available, this set has to be used, regardless of the configuration or speed range investigated.

Although apparatuses for translational oscillation experiments are now becoming available, most of the information on acceleration derivatives (especially  $\beta$  derivatives) that is available at the present time has been inferred from the subtraction of purely rotary derivatives, obtained in a low-speed curved-flow or rolling-flow wind tunnel, from the composite derivatives, obtained from angular oscillation experiments. Such information can be found in Refs. 5-7 for a few configurations of interest, for angles of attack up to  $50^\circ$ .

Both the cross-coupling and the acceleration derivatives, and in fact most of the other derivatives as well, display significant non-linear effects at higher angles of attack. Although the look-up tables provide an excellent means of identifying the correct value of a given derivative for the constant equilibrium value of the angle of attack, they are not as convenient for introducing into the equations of motion the variation of the derivative with a varying angle of attack as the aircraft performs an oscillatory motion in pitch. For that purpose an analytical description of the variation of the derivative with angle of attack is more suitable. Since such an analytical description in a large range of angles of attack would in most cases be rather complex, it may be more practical to limit the range of angle of attack for which an analytical description is made to the immediate vicinity of the equilibrium angle of attack, corresponding to the range covered by the amplitude of oscillation. It may also be possible to further simplify the procedure by assuming that the derivative varies linearly with  $\alpha$  in that narrow range of angle of attack. Such a locally linearized derivative (Ref. 8) can then be written as  $a + b(\alpha - \alpha_T)$ , where  $\alpha_T$  is the trim (or equilibrium) angle of attack.

Dynamic derivatives that are subject to the sensitivity study are often varied in a relatively wide range, such as from zero to perhaps twice the nominal value including, in some cases, also a change of sign. It is important that during such a variation the remaining derivatives be kept at their nominal values rather than zero, otherwise gross misrepresentation and, in some cases, even an erroneous elimination of the effect of a given derivative may result (Ref. 9). Sometimes there may be some interest in investigat-

ing the effect of a whole group of derivatives such as cross-coupling derivatives, by including or excluding the entire group all at once. In cases involving composite derivatives it is often of interest to divide the total value between the two component parts in different proportions and to insert the resulting two derivatives at their proper place in the equations of motion, as purely rotary and purely time-rate-of-change or acceleration effects.

The sensitivity of the flight behaviour of an aircraft to a given derivative (and therefore the importance of determining that derivative and including it in the equations of motion) is obtained by comparing the responses in various degrees of freedom to a given disturbance for two or more values of the derivative. The disturbance often involves a simulated sudden application of a control deflection, e.g. by applying an elevator or rudder "doublet", i.e. moving the control surface quickly all the way up, then all the way down and then back to zero. If control deflections are not included (explicitly or implicitly, through a suitable variation of some aerodynamic coefficients) in the equations of motion, an even simpler (and in fact probably more general) initial disturbance may consist of perturbing the nominally steady flight condition by starting the simulation with a variable (such as angle of attack or angle of sideslip) set at a value different from the trimmed value.

The response of the aircraft to a disturbance can be described, for various derivative combinations, by the time history of the variation of various motion variables or their rates, by the value of the damping ratio in one or more modes of motion (such as short period, phugoid, dutch roll, spiral or roll) or by the root locus method of presentation. In the latter method the roots (eigenvalues) of the characteristic equation are plotted in the root locus format, with the real part of the root representing the damping ratio and the imaginary part representing the frequency of oscillation. The damping ratio is inversely related to the time required for a given mode to damp to one half amplitude (if the real part is negative) or to increase to double amplitude (if the real part is positive) and the frequency is, of course, inversely related to the period of the oscillation. If the imaginary part is zero the motion is aperiodic.

### 3. A "QUICK-LOOK" SENSITIVITY ASSESSMENT

Rather than conducting a complete sensitivity analysis as described in the previous section, some appreciation of the significance of a given cross-coupling derivative can be obtained by comparing the magnitude of the term (in an appropriate equation of motion) that includes such a derivative with the magnitude of another term (in the same equation) that contains one of the traditional derivatives whose significance is well established. Such an approach was suggested in Ref. 10. For example, in a rolling-moment equation for a captive aircraft model (oscillating around a fixed axis), the two terms representing the rolling moment due to the rate of yaw and the rate of pitch can be written:

$$\frac{q_{SB}}{2V} [(C_{l_r} - C_{l_\beta} \cos \alpha) br + (C_{l_q} + C_{l_\alpha}) \bar{c}q]$$

Therefore the ratio of the dynamic cross-coupling term to the "traditional" term (in this case a cross derivative term) is

$$\frac{\bar{c}q}{br} \cdot \frac{C_{l_q} + C_{l_\alpha}}{C_{l_r} - C_{l_\beta} \cos \alpha}$$

Similarly, the dynamic cross-coupling terms in other moment equations can be compared to the traditional terms (such as damping terms) in those equations, yielding ratios such as

$$\frac{br}{\bar{c}q} \frac{C_{m_r} - C_{m_\beta} \cos \alpha}{C_{m_q} + C_{m_\alpha}} \quad \text{or} \quad \frac{\bar{c}q}{br} \frac{C_{n_q} + C_{n_\alpha}}{C_{n_r} - C_{n_\beta} \cos \alpha}$$

Using  $b/\bar{c} = 2.77$  (from Ref. 10), assuming  $q = r$ , and inserting the values of various dynamic derivatives as reported in Refs. 3 and 10, it can be shown that the above ratios may attain values as high as 2 to 4, indicating that the dynamic cross-coupling derivatives due to pitch and yaw may in some instances be of comparable significance to the well established damping and cross derivatives. If  $r \neq q$ , it follows from the above ratios that the significance of some cross-coupling derivatives will be decreased while that of some others will actually be increased. Thus, no matter what  $r/q$  is, there should always be at least one dynamic cross-coupling derivative that at a certain angle of attack may be of fairly high significance.

This reasoning is based on the equations and data obtained for an aircraft (model) performing oscillations around a fixed axis. Although the present lack of suitable data prevents us from separating out  $\alpha$ - and  $\beta$  effects, there is no reason to expect that the application of a similar reasoning to an unrestricted aircraft would yield significantly different results. However, any "quick-look" sensitivity assessment such as the one described here remains somewhat speculative and should usually be confirmed by a more rigid sensitivity analysis using a full set of equations of motion.

(a)  $\alpha = 20^\circ$ 

Case	k (a)	Aerodynamic derivatives												Results					
		$C_{Y\beta}$	$C_{n\beta}$	$C_{l\beta}$	$C_{Y\dot{\beta}}$	$C_{n\dot{\beta}}$	$C_{l\dot{\beta}}$	$C_{Y_p}$	$C_{n_p}$	$C_{l_p}$	$C_{Y_r}$	$C_{n_r}$	$C_{l_r}$	Dutch roll mode	Roll mode	Spiral mode	Aperiodic modes		
1	---	-0.510	0.135	-0.155	0	0	0	0.239	-0.062	-0.168	0.513	-0.332	0.023	11.90	0.086	1.79	16.03	---	
2	0.066							-0.130	-0.357						4.35	0.086	1.79	16.10	---
3	.109							-0.239	-0.306						5.63	0.086	1.79	16.10	---
4	.132							-0.280	-0.258						6.97	0.086	1.79	16.11	---
b <sub>5</sub>	.066							0	0						.358	4.42	0.085	1.48	-19.63
b <sub>6</sub>	.109							0	0						.107	.311	5.70	0.086	1.46
b <sub>7</sub>	.132							0	0						.158	.256	.265	7.02	0.086
																		1.60	-15.49

<sup>a</sup>Reduced frequency at which  $\dot{\beta}$  derivatives were measured.<sup>b</sup> $\dot{\beta}$  derivatives combined with pure angular-rate derivatives.(b)  $\alpha = 28^\circ$ 

Case	k (a)	Aerodynamic derivatives												Results					
		$C_{Y\beta}$	$C_{n\beta}$	$C_{l\beta}$	$C_{Y\dot{\beta}}$	$C_{n\dot{\beta}}$	$C_{l\dot{\beta}}$	$C_{Y_p}$	$C_{n_p}$	$C_{l_p}$	$C_{Y_r}$	$C_{n_r}$	$C_{l_r}$	Dutch roll mode	Roll mode	Spiral mode	Aperiodic modes		
1	----	-0.196	-0.121	-0.015	0	0	0	0.155	-0.011	-0.214	0.400	-0.260	-0.171	1.27	0.014	51.14	-1.15	---	
2	0.066							.452	-1.940							46.21	-2.85	1.72	0.34
3	.109							.387	-.998							48.52	-2.00	1.48	.54
4	.132							.336	-.858							48.88	-1.87	1.43	.60
b <sub>5</sub>	.066							0	0						.201	-1.125	-.659	1.542	-2.44
b <sub>6</sub>	.109							0	0						.171	-.683	-.802	.710	-2.36
b <sub>7</sub>	.132							0	0						.147	-.817	-.557	.586	-2.33
																.013	.58	1.02	---

<sup>a</sup>Reduced frequency at which  $\dot{\beta}$  derivatives were measured.<sup>b</sup> $\dot{\beta}$  derivatives combined with pure angular-rate derivatives.TABLE 1 EFFECT OF  $\dot{\beta}$  DERIVATIVES ON CALCULATED DYNAMIC STABILITY CHARACTERISTICS (FROM REF. 6)

## 4. RESULTS OF SOME SENSITIVITY STUDIES

As already shown many years ago (Ref. 11), the inclusion or omission of the  $\dot{\beta}$  derivatives in theoretical equations of motion can produce large differences in the calculated dynamic stability characteristics. In particular, it was shown that when composite derivatives obtained from oscillation experiments around a fixed axis were used in place of the pure angular-rate derivatives and when the  $\dot{\beta}$  derivatives were assumed to be zero, the results varied significantly from the results obtained when all pure derivatives (both angular-rate and lateral-acceleration derivatives) were used at their proper place in the equations of motion. A further illustration of these results was provided in Ref. 6, where calculations - using three-degree-of-freedom linearized equations - were made for a hypothetical delta-wing fighter configuration in trimmed flight at  $\alpha = 20^\circ$  and  $\alpha = 28^\circ$ . The purely rotary derivatives used were obtained by the curved-flow and rolling-flow test techniques, and the lateral acceleration derivatives by a lateral oscillation test technique.

The results are shown in Table 1. In Case 1 the true values of the purely rotary derivatives were used and the  $\dot{\beta}$  derivatives were omitted. In Cases 2 to 4, both the purely rotary and the  $\dot{\beta}$  derivatives were correctly included. In Cases 5 to 7 the  $\dot{\beta}$  derivatives were added to the purely rotary ones to form composite derivatives, similar to those that would result from oscillation around a fixed axis. These composite derivatives were then used in place of the purely rotary derivatives and the  $\dot{\beta}$  terms in the equations were set equal to zero.

It can be seen from Table 1 that the inclusion and the proper use of the  $\dot{\beta}$  derivatives, although of only minor significance at  $\alpha = 20^\circ$  where the  $\dot{\beta}$  derivatives were rather small, had a very pronounced effect at  $\alpha = 28^\circ$ , where these derivatives were relatively large. In particular, when the derivatives were used properly (Cases 2 to 4), the Dutch roll mode was absent, the roll mode was virtually neutrally stable, the spiral mode was very unstable and two additional aperiodic modes were indicated. This should be compared with Cases 5 to 7, where the improper use of the derivatives resulted in an erroneous indication of a highly unstable Dutch roll mode, highly stable roll and spiral modes, and no aperiodic modes.

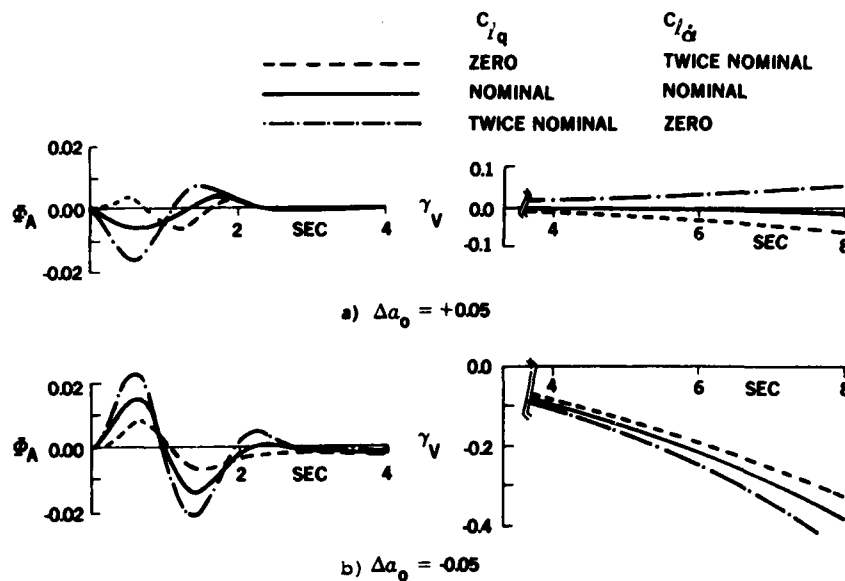
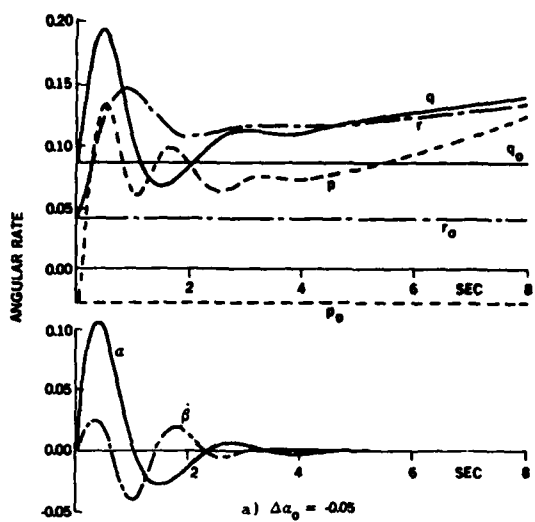


FIG. 1 EFFECT OF DISTRIBUTION OF DERIVATIVE  $C_{l_q} + C_{l_\alpha}$  INTO ITS TWO COMPONENT PARTS ON THE CALCULATED AERODYNAMIC ROLL ANGLE ( $\Phi_A$ ) AND THE VERTICAL FLIGHT PATH ANGLE ( $\gamma_V$ ) (FROM REF. 8)

An example of the effect of an  $\dot{\alpha}$  derivative is shown in Fig. 1. Significantly different roll angles and flight path angles are indicated depending on whether the measured value of derivative  $C_{l_q} + C_{l_\alpha}$  is used entirely as  $C_{l_q}$ , entirely as  $C_{l_\alpha}$ , or equally divided between  $C_{l_q}$  and  $C_{l_\alpha}$  (Ref. 8). The effect is particularly large on the calculated roll angle which in one case is shown to even change sign depending on the distribution chosen. This example involves a 2g turning flight and the calculations were made with locally linearized derivatives, which causes the results to also be a function of the direction of the initial disturbance ( $\Delta\alpha_0$ ).

The significance of cross-coupling moment derivatives was studied in Ref. 8 and is illustrated in Fig. 2. The measured values of composite derivatives were equally distributed between their rotary and acceleration parts. The non-linear effects were taken into account by local linearization. The cross-coupling derivatives due to oscillation in roll were unknown at the time of the analysis and therefore set equal to zero. The various angular rates ( $p$ ,  $q$ ,  $r$ ,  $\dot{\alpha}$  and  $\dot{\beta}$ ) are shown as functions of time after an initial disturbance in the angle of attack (Fig. 2a) and angle of sideslip (Fig. 2b). The constant angular rates for the unperturbed case ( $p_0$ ,  $q_0$ ,  $r_0$ ) are also shown. Had the cross-coupling derivatives not been included, the rates  $p$ ,  $q$  and  $r$  in Fig. 2a and the rates  $q$  and  $\dot{\alpha}$  in Fig. 2b would have remained essentially constant. It can be seen that the departures of  $p$ ,  $r$  and  $\dot{\beta}$  in Fig. 2a from their constant values is much larger than the corresponding departures of  $q$  and  $\dot{\alpha}$  in Fig. 2b, indicating a much larger effect of the cross-coupling derivatives of the rolling and yawing moments due to pitching than of the cross-coupling derivative of the pitching moment due to yawing. Figure 2 pertains to a 2g turning flight at  $\alpha = 33^\circ$ .

Studies of the sensitivity of the aircraft behaviour to variation of an individual cross-coupling or acceleration derivative were carried out both in Ref. 8 and Ref. 12. Although the two studies were performed using two significantly different approaches, the results were quite similar. Some examples of the results obtained in Ref. 12 for a fighter/bomber configuration in a 3g turning flight are shown in Figs. 3 - 5. In the study, the variations in each successive derivative were performed with all the other derivatives fixed at their nominal values. The cross-coupling derivatives were again based on the results of Ref. 3 but were treated as purely rotary derivatives in the equations of motion. The acceleration derivatives were based on data in Ref. 6. The nominal values used represented extreme values that had actually been measured in the wind tunnel experiments. The initial disturbance was introduced as an elevator or a rudder doublet. The resulting time histories of  $\alpha$ ,  $\beta$  and some angular rates are shown in Figs. 3 - 4 for the cross-coupling derivative variations and in Fig. 5 for the acceleration derivative variation.



NOTE 1: ANGULAR RATES FOR THE UNPERTURBED CASE REMAIN CONSTANT AND ARE DENOTED BY  $p_0$ ,  $q_0$ ,  $r_0$ .

NOTE 2: WITH ALL AERODYNAMIC CROSS COUPLING DERIVATIVES EQUAL TO ZERO, THE RATES  $p$ ,  $r$ , AND  $\dot{\beta}$  REMAIN ESSENTIALLY CONSTANT WHEN PERTURBED IN  $\alpha$ ; SIMILARLY THE RATES  $q$  AND  $\dot{\alpha}$  REMAIN ESSENTIALLY CONSTANT WHEN PERTURBED IN  $\beta$ .

FIG. 2 EFFECT OF INCLUDING CROSS-COUPLED DERIVATIVES DUE TO PITCHING AND YAWING ON THE ANGULAR RATES FOR 2g TURNING FLIGHT (FROM REF. 8)

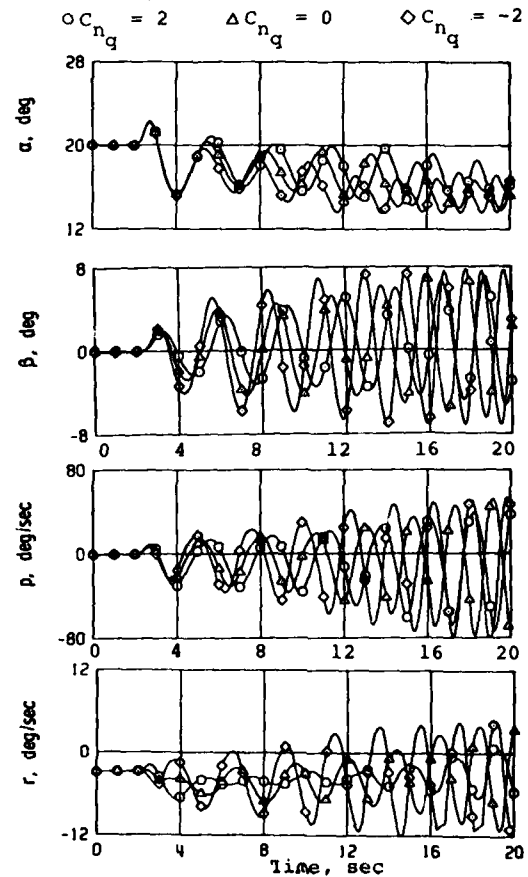
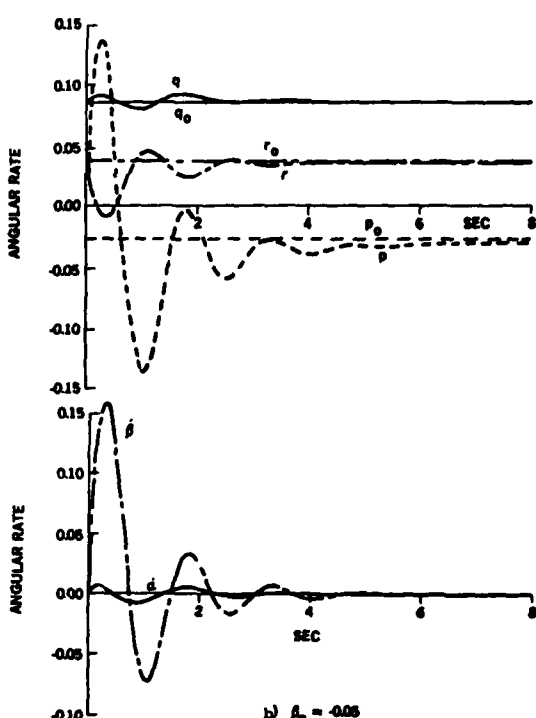
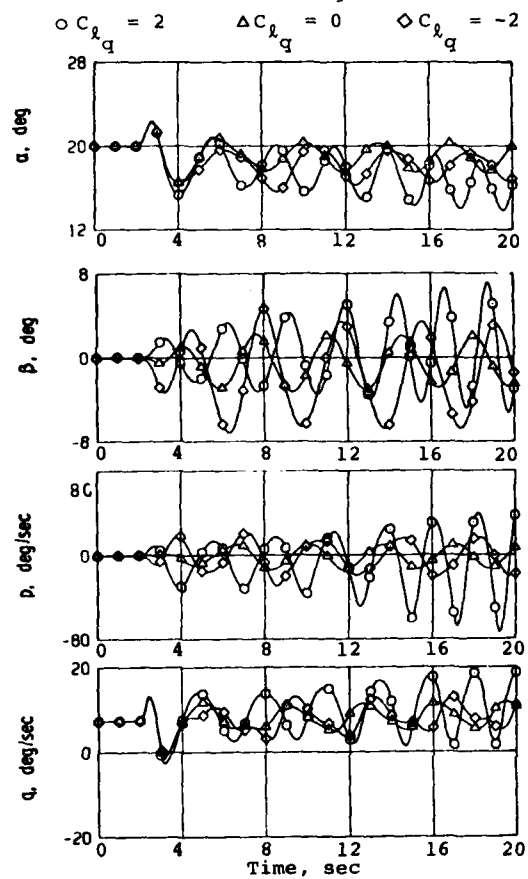


FIG. 3 EFFECT OF VARIATION OF  $C_{l_q}$  AND  $C_{n_q}$  DERIVATIVES. FIGHTER/BOMBER IN 3g TURNING FLIGHT. NOMINAL CROSS-COUPLED DERIVATIVES.  $\dot{\beta}$  DERIVATIVES ZERO. ELEVATOR DOUBLET. (FROM REF. 12)

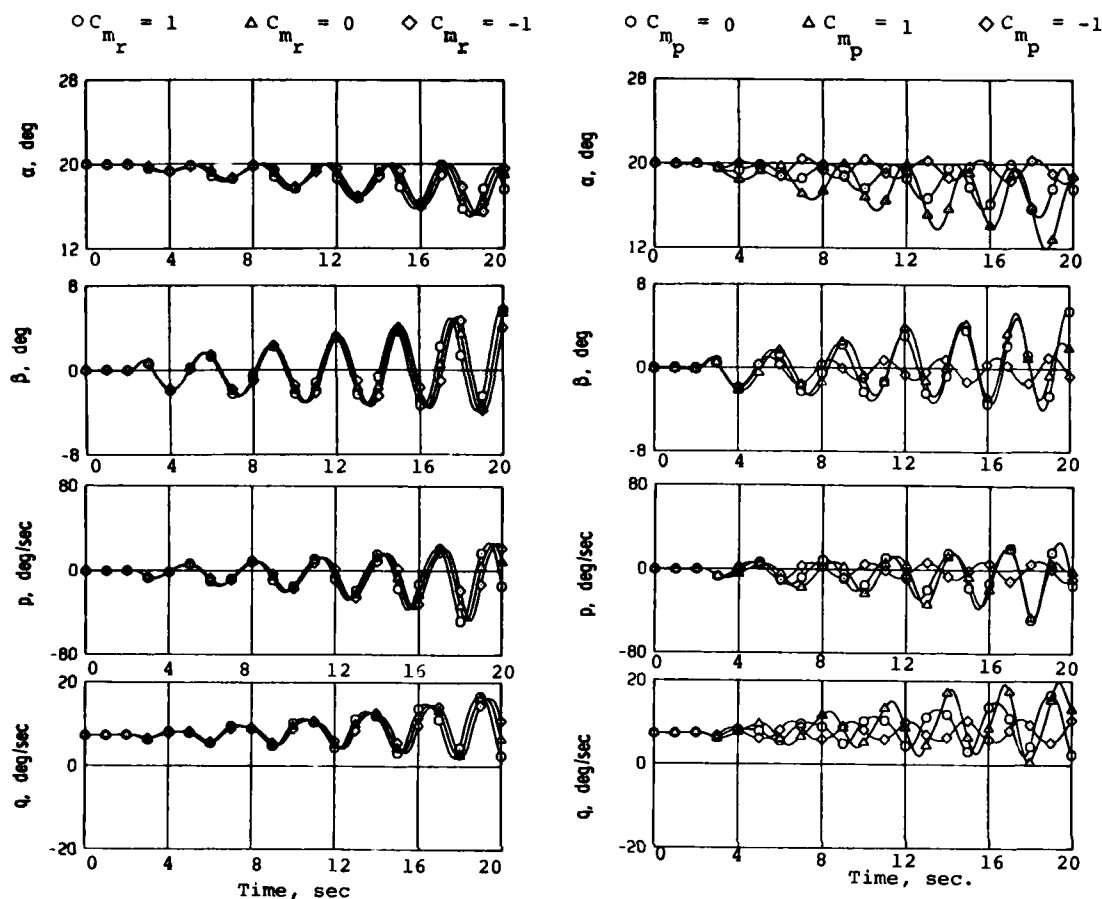


FIG. 4 EFFECT OF VARIATION OF  $C_{m_r}$  AND  $C_{m_p}$  DERIVATIVES. FIGHTER/BOMBER IN 3g TURNING FLIGHT. NOMINAL CROSS-COUPLING DERIVATIVES.  $\dot{\beta}$  DERIVATIVES ZERO. RUDDER DOUBLET. (FROM REF. 12)

Large effects of variations of both  $C_{l_q}$  and  $C_{n_q}$  can be seen in  $\beta$ ,  $p$  and  $r$  motions (Fig. 3). These motions display almost a mirror image for the positive and negative values of the pertinent derivatives. The inclusion of  $C_{l_q}$  derivatives causes instability in the  $\beta$  and  $p$  motions. However, it should be noted that this effect is strongly dependent on the values of the remaining dynamic rolling moment derivatives, such as  $C_{l_p}$  and  $C_{l_\beta}$ , which, in this particular example, were very small or zero, respectively.

By comparison, the effects of varying the cross-coupling derivatives of the pitching moment,  $C_{m_r}$  and  $C_{m_p}$ , were much smaller (Fig. 4). The effect of  $C_{m_r}$  was insignificant, which agrees well with the findings of Ref. 8. The effects of  $C_{m_p}$  were somewhat larger, but it should be remembered that this derivative was varied in the range of +1 to -1, while the highest value actually measured in a subsequent wind tunnel experiment (Ref. 4) was 0.2.

The motion sensitivity to variations of  $C_{l_\beta}$  derivative (Fig. 5) is quite significant. In particular, it should be noted, that for  $C_{l_\beta}$  values of 0.2 and greater, the  $\alpha$ ,  $\beta$ ,  $\dot{\beta}$  and  $p$  motions show strong oscillatory divergence. Conversely, the negative value of -1 of  $C_{l_\beta}$  derivative has a strong damping effect on all these motions. By comparison, the motion sensitivity to variations in  $C_{n_\beta}$  derivative is less significant.

Additional results, not shown here, indicate that most of the abovementioned effects are quite dependent on the remaining stability characteristics of the aircraft. The smaller the static margin and the lower the aerodynamic damping, such as represented by  $C_{l_p}$ ,  $C_{l_\beta}$  or  $C_{n_\beta}$  derivatives, the more sensitive the aircraft motion to the variations in cross-coupling derivatives and vice versa. The sensitivity of the flight behaviour during a turning maneuver is in general larger than in a straight flight.

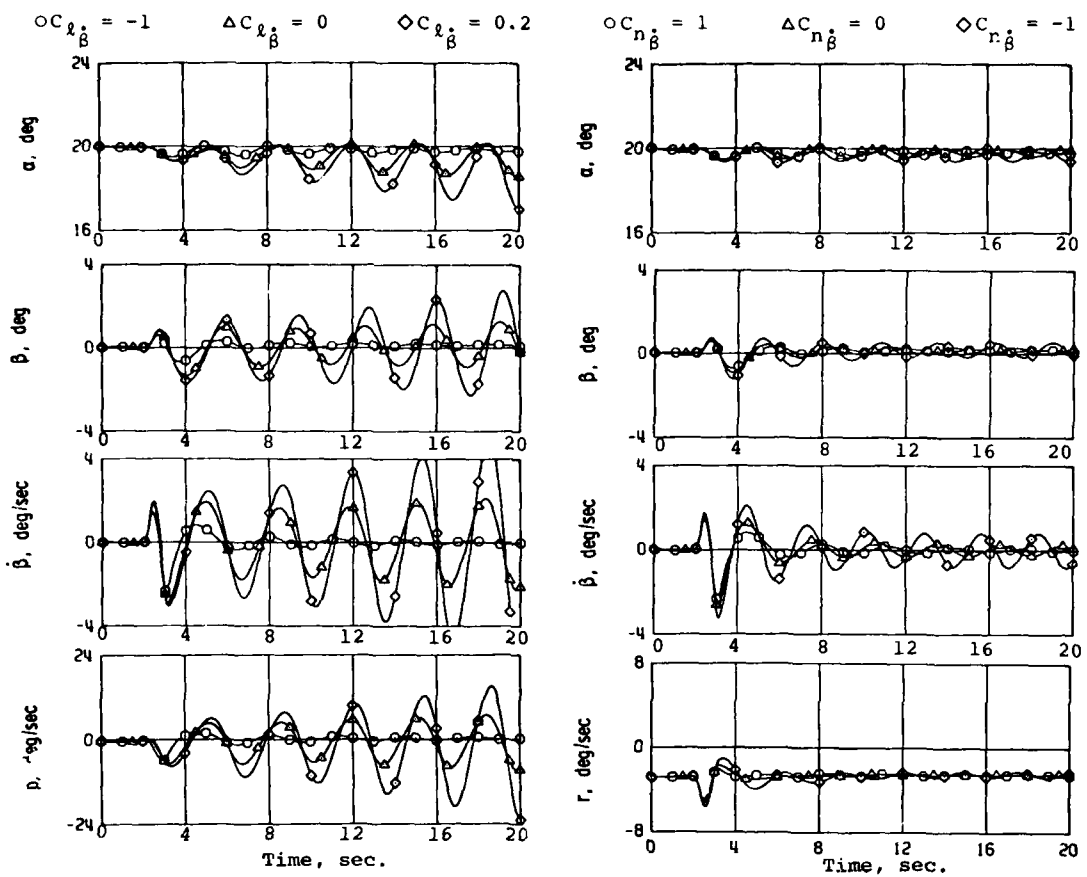


FIG. 5 EFFECT OF VARIATION OF  $C_{l\beta}$  AND  $C_{n\beta}$  DERIVATIVES. FIGHTER/BOMBER IN 3g TURNING FLIGHT. NOMINAL CROSS-COUPLING AND  $\dot{\beta}$  DERIVATIVES. RUDDER DOUBLET (FROM REF. 12)

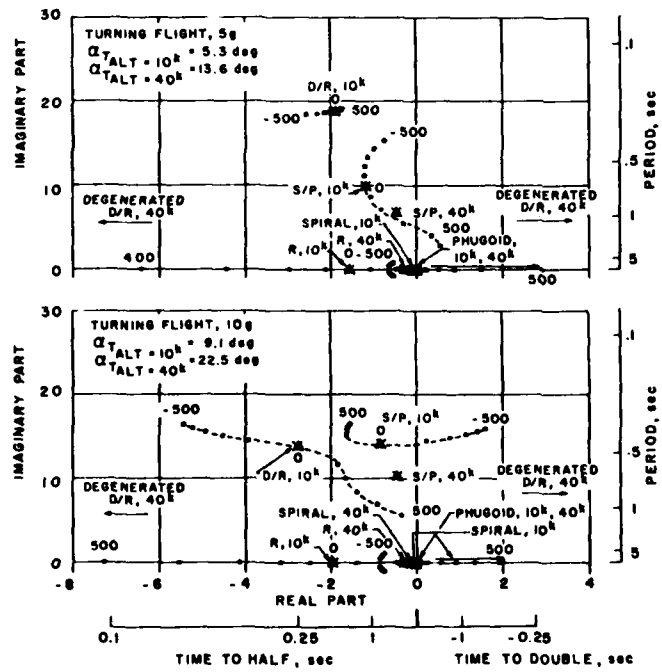


FIG. 6 EFFECT OF VARIATION OF  $C_{lq}$  DERIVATIVE. YAW-TO-TURN MISSILE IN 10g TURNING FLIGHT AT  $M = 3$ . ROOT LOCUS (FROM REF. 13)

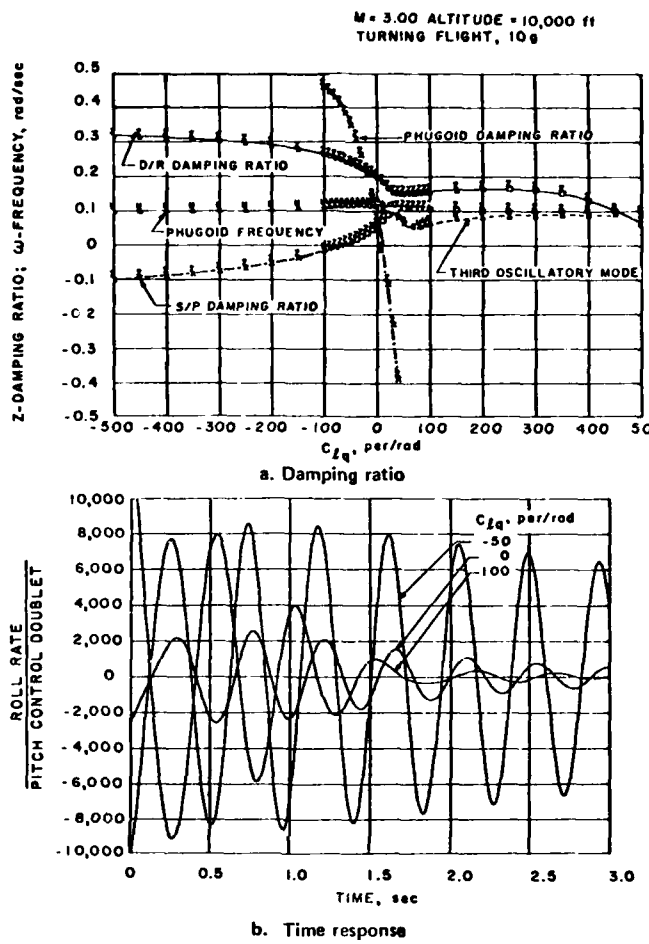


FIG. 7 EFFECT OF VARIATION OF  $C_{lq}$  DERIVATIVE. YAW-TO-TURN MISSILE IN 10 g TURNING FLIGHT AT  $M = 3$ . DAMPING RATIOS AND ROLL RATE TIME HISTORY (FROM REF. 13)

Although this lecture is mainly concerned with stability and motion of aircraft, a brief mention has to be included about the corresponding studies related to the motion of missiles. A comprehensive investigation of missile motion sensitivity to dynamic stability derivatives has recently been completed (Ref. 13). In that investigation, which to some extent may be considered as a companion study to that of Ref. 12, the importance of dynamic stability derivatives for the simulation of motion of both bank-to-turn and yaw-to-turn missile configurations was examined, using a six-degree-of-freedom linearized stability programme.

Among the most pronounced effects due to the variation of a dynamic cross-coupling derivative was that due to the variation of  $C_{lq}$  at high Mach number, high load factor

and relatively low altitude. Sample results showing the influence of that derivative on the simulated motion of the yaw-to-turn missile are shown in Figs. 6 and 7. It can be seen that the short period (S/P), dutch roll (D/R) and roll (R) modes are quite sensitive to the variation of  $C_{lq}$  over the range  $\pm 500$  (per radian) and that the dutch

roll sensitivity increases with an increasing load factor (Fig. 6). The S/P and D/R damping ratios as well as the phugoid damping ratio are also strongly affected (Fig. 7a). Even a variation of  $C_{lq}$  within a much more narrow range (0 to -50) results in a large

effect on the roll rate time history (four times higher roll rates at  $C_{lq} = -50$  than at  $C_{lq} = 0$ ), as shown in Fig. 7b.

## 5. CONCLUDING REMARKS

The following conclusions can be derived from the sensitivity studies discussed in this lecture.

- (a) The cross-coupling derivatives  $C_{l_q}$  and, to a lesser extent,  $C_{n_q}$ , are considered important for both aircraft and missile motion simulation.
- (b) The cross-coupling derivative  $C_{m_p}$  is relatively important for missiles but is less significant for aircraft.
- (c) The cross-coupling derivative  $C_{m_r}$  appears to be insignificant for both aircraft and missiles.
- (d) The acceleration derivative  $C_{l_\beta}$  has a strong effect on aircraft; its significance for missiles is not known.
- (e) The acceleration derivative  $C_{n_\beta}$  appears to be much less significant than  $C_{l_\beta}$  for aircraft; its significance for missiles is not known.
- (f) The acceleration derivative  $C_{m_a}$  is important for both aircraft and missiles.
- (g) In both the longitudinal and the lateral cases it is important to separate the purely rotary and the acceleration derivatives and use them in their proper place in the equations of motion. The importance of this has been demonstrated for aircraft, but not yet for missiles.

The above conclusions apply to flight at high angles of attack or at any other asymmetric flow conditions. They are based on the assumption that the investigated ranges of the various derivatives are representative of the aerodynamic characteristics of the aircraft or missile considered.

In addition, the following conclusions may be included, regarding the direct and cross moment derivatives and certain force derivatives of missiles:

- (h) The moment derivatives  $C_{m_q}$ ,  $C_{m_a}$ ,  $C_{n_r}$ ,  $C_{l_p}$ ,  $C_{l_r}$  and  $C_{n_p}$  are all important, particularly at higher Mach numbers and higher load factors.
- (i) The force derivatives  $C_{L_q}$ ,  $C_{L_a}$ ,  $C_{Y_p}$  and  $C_{Y_r}$  appear to be insignificant.

## 6. REFERENCES

1. Perkins, C. D.  
Hage, R. E. *Airplane Performance, Stability and Control*. John Wiley and Sons, Ltd., New York, 1949.
2. Curry, W. H. *An Evaluation of a Correction Method for Digital Computer Lag in Hybrid Systems*. Proceedings of the Summer Computer Simulation Conference, Chicago, 1977.
3. Orlik-Rückemann, K. J.  
Hanff, E. S.  
LaBerge, J. G. *Direct and Cross-Coupling Subsonic Moment Derivatives due to Oscillatory Pitching and Yawing of an Aircraft-Like Model at Angles of Attack up to 40° in Ames 6' x 6' Wind Tunnel*. NRC NAE LTR-UA-38, November 1976.
4. Hanff, E. S.  
Orlik-Rückemann, K. J.  
Kapoor, K. B.  
Moulton, B. E.  
LaBerge, J. G. *New Oscillatory Roll Apparatus and Results on Direct, Cross and Cross-Coupling Subsonic Moment Derivatives for an Aircraft-Like Model*. NRC NAE LTR-UA-50, Sept. 1979.
5. Coe, P. L., Jr.  
Newson, W. A., Jr. *Wind Tunnel Investigation to Determine the Low-Speed Yawing Stability Derivatives of a Twin-Jet Fighter Model at High Angles of Attack*. NASA TN D-7721, 1974.
6. Coe, P. L., Jr.  
Graham, B. H.  
Chambers, J. R. *Summary of Information on Low-Speed Lateral-Direction Derivatives due to Rate of Change of Sideslip,  $\beta$* . NASA TN D-7972, 1975.
7. Skow, A. M.  
Titiriga, A., Jr. *A Survey of Analytical and Experimental Techniques to Predict Aircraft Dynamic Characteristics at High Angles of Attack*. AGARD CP 235, Paper 19, 1978.
8. Curry, W. H.  
Orlik-Rückemann, K. J. *Sensitivity of Aircraft Motion to Aerodynamic Cross-Coupling at High Angles of Attack*. AGARD CP 235, Paper 34, 1978.

9. Butler, R. W.  
Langham, T. F. Aircraft Motion Sensitivity to Variations in Dynamic Stability Parameters. AGARD CP 235, Paper 35, 1978.

10. Orlik-Rückemann, K. J. Aerodynamic Coupling between Lateral and Longitudinal Degrees of Freedom. AIAA Journal, vol. 15, no. 12, pp 1792 - 1799, December 1977.

11. Campbell, J. P.  
Woodling, C. H. Calculated Effects of the Lateral Acceleration Derivatives on the Dynamic Lateral Stability of a Delta-Wing Airplane. NACA RM L54K26, 1955.

12. Langham, T. F. Aircraft Motion Sensitivity to Dynamic Stability Derivatives. AEDC-TR-79-11, 1980.

13. Langham, T. F. Missile Motion Sensitivity to Dynamic Stability Derivatives. AEDC-TR-80-11, 1980. Also AIAA-81-0400, 1981.

## APPENDIX - SYMBOLS

$\underline{b}$	wing span
$\underline{c}$	wing mean aerodynamic chord
$C_L$	$L/(\bar{q}Sb)$
$C_m$	$M/(\bar{q}Sc)$
$C_n$	$N/(\bar{q}Sb)$
$C_x, C_y, C_z$	(aerodynamic force components)/ $\bar{q}S$
F	force
g	acceleration of gravity
h	altitude
I	moment or product of inertia
L	aerodynamic rolling moment; also aerodynamic lift force
m	mass
M	aerodynamic pitching moment
N	aerodynamic yawing moment
n	aircraft load factor
p	angular velocity about roll axis
q	angular velocity about pitch axis
q	dynamic pressure
r	angular velocity about yaw axis
S	gross wing area
T	thrust
t	time
u, v, w	velocity components in x, y and z directions, respectively
V	freestream velocity
X, Y, Z	earth fixed orthogonal axes with origin at origin of flight and with Z-axis pointing down
x, y, z	orthogonal system of body axes with origin at the aircraft CG and with x-axis pointing forward
$\alpha$	angle of attack
$\Delta\alpha$	difference between $\alpha$ and $\alpha_T$
$\beta$	angle of sideslip
$\phi$	aircraft bank angle
$\phi_A$	aerodynamic roll angle
$\gamma_H, \gamma_V$	horizontal and vertical flight path angles, respectively
$\delta$	$\arctan (\tan \alpha_0 \cos \beta_0)$
$\psi, \theta, \phi$	Euler angular rotations in yaw, pitch, and roll, respectively

Subscripts:

$_0$	refers to value at time zero
T	refers to trimmed flight condition
x, y, z	refer to x, y or z body axis
$\alpha, \beta, \dot{\alpha}, \dot{\beta}, p, q, r$	denote derivative (of a moment) with respect to $\alpha, \beta$ , etc.

Superscripts:

A dot indicates time derivative

Traditional Moment Derivatives:

$$C_{\dot{\ell}}_{\beta} = \partial C_{\dot{\ell}} / \partial \beta$$

$$C_{m_{\alpha}} = \partial C_m / \partial \alpha$$

$$C_{n_{\beta}} = \partial C_n / \partial \beta$$

$$C_{\dot{\ell}}_{\dot{\beta}} = \partial C_{\dot{\ell}} / \partial (\dot{\beta}b/2V)$$

$$C_{m_{\dot{\alpha}}} = \partial C_m / \partial (\dot{\alpha}\bar{c}/2V)$$

$$C_{n_{\dot{\beta}}} = \partial C_n / \partial (\dot{\beta}b/2V)$$

$$C_{\dot{\ell}}_p = \partial C_{\dot{\ell}} / \partial (pb/2V)$$

$$C_{m_q} = \partial C_m / \partial (qc\bar{c}/2V)$$

$$C_{n_p} = \partial C_n / \partial (pb/2V)$$

$$C_{\dot{\ell}}_r = \partial C_{\dot{\ell}} / \partial (rb/2V)$$

$$C_{n_r} = \partial C_n / \partial (rb/2V)$$

Cross-Coupling Moment Derivatives:

$$C_{\dot{\ell}}_{\alpha} = \partial C_{\dot{\ell}} / \partial \alpha$$

$$C_{m_{\beta}} = \partial C_m / \partial \beta$$

$$C_{n_{\alpha}} = \partial C_n / \partial \alpha$$

$$C_{\dot{\ell}}_{\dot{\alpha}} = \partial C_{\dot{\ell}} / \partial (\dot{\alpha}\bar{c}/2V)$$

$$C_{m_{\dot{\beta}}} = \partial C_m / \partial (\dot{\beta}b/2V)$$

$$C_{n_{\dot{\alpha}}} = \partial C_n / \partial (\dot{\alpha}\bar{c}/2V)$$

$$C_{\dot{\ell}}_q = \partial C_{\dot{\ell}} / \partial (qc\bar{c}/2V)$$

$$C_{m_p} = \partial C_m / \partial (pb/2V)$$

$$C_{n_q} = \partial C_n / \partial (qc\bar{c}/2V)$$

$$C_{m_r} = \partial C_m / \partial (rb/2V)$$

Corresponding force derivatives are defined in a similar fashion. All derivatives are referenced to a system of body axes. The "rotary" derivatives are those with respect to p,q,r; and the "acceleration" derivatives are those with respect to  $\alpha$  and  $\beta$ .

**SOME APPLICATIONS OF AERODYNAMIC FORMULATIONS TO PROBLEMS  
IN AIRCRAFT DYNAMICS**

Lewis B. Schiff and Murray Tobak  
Ames Research Center, NASA  
Moffett Field, California 94035, U.S.A.

**SUMMARY**

Two applications of the concepts of mathematical modeling to aerodynamic problems of current interest are discussed. The first application is an investigation of the capacity of a nonlinear aerodynamic mathematical model to describe the aerodynamic reactions on an airfoil with a deflecting flap in transonic flow. Flow-field computational methods are used to evaluate the nonlinear, unsteady aerodynamic data in terms of characteristic motions called for by the model. Histories of unconstrained motions of the flap are generated from the flap equations of motion, with the aerodynamic reactions specified by the mathematical model. These motion histories are compared with analogous motion histories, obtained from simultaneous, coupled solutions of the flap equations of motion and the flow-field equations, to assess the regime of validity of the aerodynamic mathematical model. In the second application the phenomenon of wing rock is investigated. Our most recent model is shown to accommodate experimental results describing wing rock by admitting the existence of aerodynamic hysteresis in the variation of the steady-state rolling-moment coefficient with roll angle. Interpretation of the experimental results in terms of bifurcation theory reveals the general conditions under which aerodynamic hysteresis must exist.

**1. INTRODUCTION**

In Lecture 1 (Ref. 1) we reviewed the basic concepts involved in the mathematical modeling of an aircraft's aerodynamic response to arbitrary flight maneuvers. Concepts from nonlinear functional analysis were adopted to derive a hierarchy of aerodynamic mathematical models, with successive levels of the hierarchy accommodating increasingly complex aerodynamic phenomena. In this lecture we discuss two recent applications of our mathematical models to aerodynamic problems of current interest. In the first application we show how computational methods have been used by Chyu and Schiff (Ref. 2) to investigate whether a mathematical model at the second level of the hierarchy adequately describes the aerodynamic reactions caused by arbitrary motions of a flap on an airfoil in transonic flow. Secondly, via Ref. 3, we investigate the phenomenon of wing rock to determine whether results from experiments involving wing rock can be accommodated within our most recent mathematical model, which accounts for aerodynamic hysteresis.

**2. APPLICATION TO FLAP MOTIONS**

Recent papers (Refs. 4-12) have reported the results of computations for the time-dependent flow fields surrounding two-dimensional airfoils undergoing specified harmonic oscillations in transonic flow. Such computations yield the unsteady airloads on the airfoil resulting from the specified motion. Although this information is very valuable, it does not entirely respond to the principal concern of a designer, which is to know the nature of the airloads for unspecified motions, that is, the aerodynamic response to the motions that may actually occur in flight. It is now possible to think of responding directly to this concern by solving the flow-field equations simultaneously with the vehicle's inertial equations of motion, for specified initial conditions. Results from these coupled computations would be complete time-histories of the aerodynamic responses and body motion, in which the motion would be specified in advance only through the choice of initial conditions. Indeed, computations undertaken to attain this goal have already been carried out for several cases of two-dimensional flow (Refs. 13-15).

Although direct coupling of the flow-field equations and the vehicle's equations of motion represents, in principle, an exact approach to the problem of arbitrary maneuvers, one which automatically accounts for all time-history effects within the flow field, it will inevitably be a very costly approach. This will be especially true when the aerodynamic loads are nonlinearly dependent on the motion variables. Under such conditions the vehicle can experience widely differing motion histories, even if the initial conditions are close. Thus, to completely evaluate the vehicle's performance envelope, a large number of coupled computations will be required, one for each change in initial conditions. Further, with the coupled-equations approach there can be no reutilization of the previously obtained aerodynamic results.

An alternative approach (Fig. 1), in which a principal goal is to avoid the need for lengthy coupled computations, is to rely on mathematical "modeling" to describe the nonlinear aerodynamic terms (both steady and unsteady) in the vehicle's equations of motion. In formulating a model, one tries to specify a form for the aerodynamic response that underlies the response to all motions of interest. In Ref. 1 we have reviewed the development of hierarchy of mathematical models that suggests that the aerodynamic response to a general motion of a body can be modeled from the known aerodynamic responses to a limited number of characteristic motions. In principle the aerodynamic responses to the characteristic motions can be determined once and for all, and then be applicable (i.e., reusable) over a range of motion variables and flight conditions. Flight motions can then be determined by solving the equations of motion independently of the flow-field equations, at much less cost.

The utility of the modeling approach depends on the adequacy with which the mathematical model describes the aerodynamic response to an arbitrary aircraft motion. One approach (Fig. 1) to validating a candidate mathematical model would require (1) evaluating the aerodynamic data in terms of the characteristic motions called for by the model, (2) predicting motion histories of the aircraft from equations of motion incorporating the aerodynamic reactions specified by the model, and (3) comparing the predicted motion histories with actual motion histories having identical initial conditions. The validity of the candidate model would be demonstrated by a close agreement between the predicted and actual motion histories.

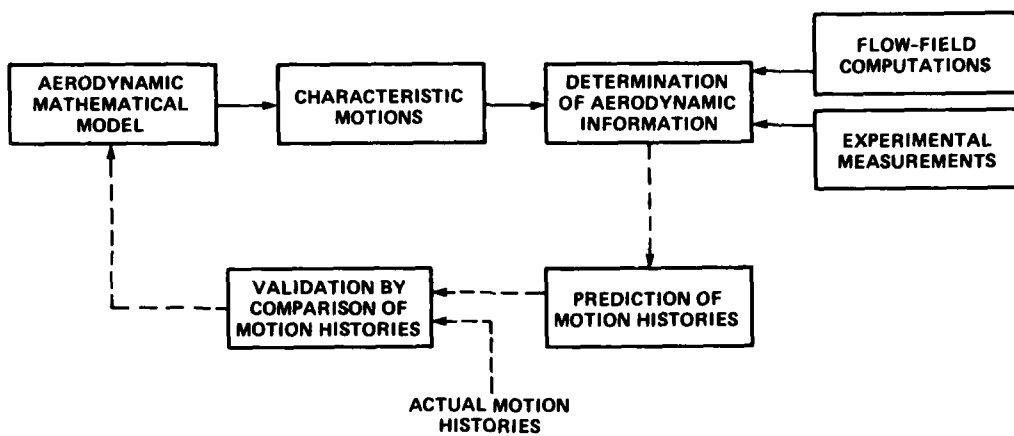
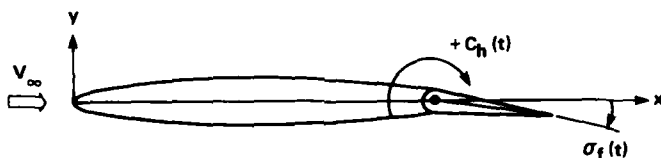


Figure 1. Aerodynamic mathematical modeling and validation procedure.

In a recent study, Chyu and Schiff (Ref. 2) carried out the procedure outlined above, using flow-field computations, to investigate the regime of validity of a mathematical model describing the aerodynamic response to motions of a flap on an airfoil in transonic flow. Finite-difference flow-field computations were used to evaluate the aerodynamic responses to the characteristic motions. Histories of the flap motion obtained from the flap equations of motion with aerodynamic terms given by the model were compared with motion histories that are, in principle, exact; namely, those obtained from simultaneous solutions of the flow-field equations and the flap equations of motion. In the following sections we discuss the procedures and results of Ref. 2, focusing in particular on the validation of the mathematical model and on the costs of the modeling approach relative to those of the coupled-equations approach.

### 2.1 Aerodynamic Modeling of Flap Motions

The two-dimensional airfoil and flap considered in Ref. 2 is a NACA 64A010 section hinged at the 75%-chord point (Fig. 2). An  $x, y$  coordinate system is fixed to the airfoil with  $x$  aligned with the chord line. The forward portion of the airfoil is held fixed, parallel to the free stream. The flap, on the other hand, is free to execute a single-degree-of-freedom motion about its pivot point. Flow properties such as dynamic pressure and Mach number are considered to remain constant throughout the maneuver. The flap deflection angle,  $\sigma_f$ , is measured from the chord line and is defined positive for a downward displacement of the flap trailing edge. The hinge-moment coefficient  $C_h$  is the nondimensional aerodynamic hinge moment acting on the flap, measured about the hinge point. As shown in Fig. 2, a positive hinge-moment coefficient would tend to increase the flap deflection angle.



NACA 64A010 AIRFOIL

Figure 2. Coordinates and notation for flap motions.

The inertial equation governing mechanically unconstrained motions of the flap is

$$I\ddot{\sigma}_f(t) = qS\bar{z}C_h(t) \quad (1)$$

where  $C_h(t)$  is the instantaneous hinge-moment coefficient. In Eq. (1),  $I$  is the moment of inertia of the flap about its hinge point,  $q$  is the dynamic pressure, and  $S$  and  $\bar{z}$  are the reference area and length, respectively. The reference length  $\bar{z}$  is chosen as the chord length of the undeflected airfoil and flap.

Development of a mathematical model of the aerodynamic response to flap motions parallels the development discussed in Ref. 1. In general, the models are derived by (1) identifying the motion variables describing the motion under consideration, (2) defining the aerodynamic indicial responses to independent step changes in each of the motion variables, and (3) showing how the aerodynamic response to an arbitrary motion is obtained from a summation of the indicial responses. As discussed at length in Ref. 1, the level of complexity of the mathematical model is directly linked to the extent to which the indicial response is said to depend on the past history of the motion. The assumption that the aerodynamic indicial response is independent of the motion occurring prior to the step leads to the classical linear mathematical model. At the second level of approximation the indicial response is assumed to depend only on the state of the motion existent when the step occurs. Mathematical models at this level of approximation are particularly suited to slowly varying motions and allow a rational introduction of nonlinear effects into the aerodynamic force and moment system. The assumption of slowly varying motions also allows one to reduce the formulation to a form correct to the first order in frequency. Applied to the single-degree-of-freedom flap motion, the resulting nonlinear model, analogous to Eq. (31) of Ref. 1, is

$$C_h(t) = C_h(\omega; \alpha_f(t)) + \dot{\alpha}_f(t) \frac{2}{V} C_{h_{\dot{\alpha}_f}}(\alpha_f(t)) \quad (2)$$

Consistent with the approximations made in its development, the model is applicable to slowly varying flap motions, although the flap deflection angle can be large. Each of the terms in Eq. (2) is associated with a characteristic motion from which it can be evaluated. Thus the term  $C_h(\omega; \alpha_f(t))$  is the hinge-moment coefficient that would be determined in a steady motion with the flap deflection angle held fixed at  $\alpha_f(t)$ . The remaining term  $C_{h_{\dot{\alpha}_f}}(\alpha_f(t))$  is the flap hinge-moment damping coefficient that would be evaluated from a characteristic motion in which the flap performs small-amplitude harmonic oscillations in  $\alpha_f$  about a mean value of  $\alpha_f$  held fixed at the instantaneous value of  $\alpha_f(t)$ . From the computational standpoint, evaluation of  $C_{h_{\dot{\alpha}_f}}(\alpha_f)$  would require the solution of a time-dependent, two-dimensional flow-field problem. Computational evaluation of  $C_h(\omega; \alpha_f)$ , on the other hand, would require the solution of a steady two-dimensional flow-field problem. Generally, however, the availability of a method for the solution of the time-dependent flow-field problem defining  $C_{h_{\dot{\alpha}_f}}$  should suffice for the evaluation of the steady flow-field problem defining  $C_h(\omega; \alpha_f)$ .

In the study reported in Ref. 2, numerical solutions were obtained for the flow fields from which  $C_h(\omega; \alpha_f)$  and  $C_{h_{\dot{\alpha}_f}}(\alpha_f)$  could be evaluated. The flow fields were assumed to be governed by the time-dependent inviscid Euler equations, and numerical methods were applied to solve these equations. The computer code for the solution of the flow field was also modified to permit its use in generating simultaneous solutions of the flow-field equations and the flap equation of motion, Eq. (1). The use of identical numerical methods to evaluate the aerodynamic coefficients in terms of the characteristic motions called for by the modeling approach, and also to generate motion histories using the coupled-equations approach, ensured that the unsteady aerodynamic responses in both approaches were treated consistently. In this manner questions concerning the applicability of the inviscid gas-dynamic equations to describe the flow, and questions concerning the accuracy of the numerical method could be circumvented.

The time-dependent Euler flow-field equations were solved using an implicit finite-difference technique on a computational grid which conformed to the deforming airfoil. Grids similar to those used in the computations are shown in Fig. 3 for extreme positive and negative values of the flap deflection angle,  $\alpha_f = \pm 20^\circ$ . Computational grids required at intermediate values of the flap deflection angle were obtained from those at the extreme values by interpolation. The grids have a common outer boundary located 8 chord lengths above and below the airfoil, and 8 chord lengths upstream and downstream from the airfoil leading edge. Consequently, the outer boundary of the computational grid remains fixed in space as the flap moves.

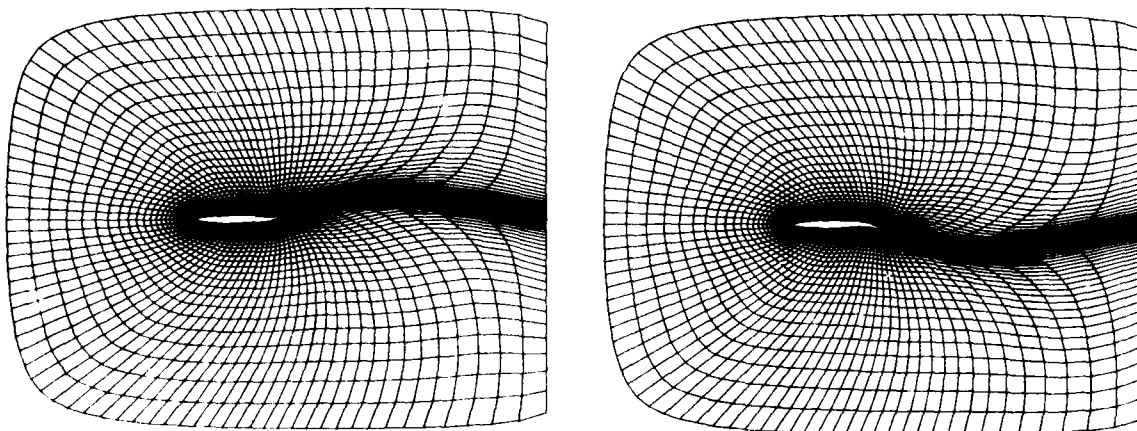


Figure 3. Typical grids with flap at extreme deflection angles.

The flow-field equations are advanced in time, subject to appropriate surface and far-field boundary conditions, to obtain the desired solutions. At the airfoil surface, the flow is maintained tangent to the moving surface. Further, a Kutta condition is enforced at the flap trailing edge. Free-stream conditions are maintained along the outermost top, bottom, and upstream boundaries of the computational grid to enforce a far-field boundary condition. A simple extrapolation exit boundary condition is applied at the downstream boundary.

At each time-step during the course of the flow-field computation, the instantaneous positions and velocities of the computational grid points must be supplied. In computations that determine the unsteady aerodynamic response to a specified motion (for example, the response to the characteristic motions) the grid positions and velocities are known, in advance, for all times during the interval of the computation. In contrast, in the coupled-equations approach, these quantities are determined during the course of the computation, as discussed below.

#### 2.2.1 Computations for characteristic motions

To evaluate the steady flow field that defines  $C_h(\omega; \alpha_f)$  a time-invariant computational grid was used. Flow-field variables were set to free-stream values at all grid points, and the flow-field equations were advanced in time until a steady flow-field solution was obtained.

To evaluate the unsteady flow field that defined  $C_{h\delta_f}(\alpha_f)$ , the computations were initiated using previously obtained steady solutions. The flap was specified to move sinusoidally with an instantaneous deflection angle

$$\alpha_f(t) = \alpha_{f_m} + \alpha_{f_1} \sin \omega t \quad (3)$$

where  $\alpha_{f_m}$  ranged from  $0^\circ$  to  $20^\circ$ , and  $\alpha_{f_1}$  was small, usually equal to  $0.5^\circ$ . The reduced frequency of the motion,  $k = \omega t/V$ , was held fixed at 0.15 for all cases. A test computation, carried out at a lower reduced frequency, confirmed that the unsteady aerodynamic responses varied linearly with  $k$ , consistent with the form of the mathematical model, Eq. (2). A steady solution, obtained for  $\alpha_f = \alpha_{f_m}$  was imposed as an initial solution, and computations were carried out for three cycles of flap motion,  $0 \leq \omega t \leq 6\pi$ , to ensure that successive cycles of the response to the motion had become sufficiently close to be called periodic. Typically, the solution obtained for the third cycle of oscillation was identical with that obtained in response to the second cycle.

### 2.2.2 Coupled-equation computations

Histories of the flap motion were generated by solving the equation of flap motion, Eq. (1), simultaneously with the flow-field equations. Coupling of the inertial equation with the flow-field equations is conceptually a straightforward numerical procedure. At each time-step in the solution of the flow-field equations the instantaneous positions and velocities of the grid points are required. In the coupled-equations approach, the flap (and thus the grid) position and flap velocity are known at an initial time, together with the initial state of the flow field, and in consequence, the initial value of the hinge-moment coefficient. In the study reported in Ref. 2, the flap was released from rest with an initial deflection angle. Thus the initial flow-field condition is that of a steady flow obtained with  $\alpha_f$  held fixed at the initial flap deflection angle. To advance the solution to the next time-level Eq. (1) is used to predict the new flap velocity and position, thus determining new positions and velocities of the computational grid points. The new grid point velocities and positions, together with the flow-field initial conditions, are entered into the flow-field computation, and the instantaneous state of the flow field (and thus the instantaneous hinge-moment coefficient) is determined at the new time level. With both the flap position and the hinge-moment coefficient known at the new time level, this procedure is repeated to generate both the history of the flap motion and the time-history of the aerodynamic response. Coupling of the flow-field and inertial equations in this manner automatically includes, in principle, proper consideration of all nonsteady and nonlinear aerodynamic effects.

### 2.3 Results of Computations for Characteristic Motions

#### 2.3.1 Steady flow

Surface-pressure coefficient distributions on the airfoil, obtained from the computations of Ref. 2 for steady flow at  $M_\infty = 0.8$ , are shown in Fig. 4 for flap deflection angles ranging from  $0^\circ$  to  $20^\circ$ . At  $\alpha_f = 0^\circ$

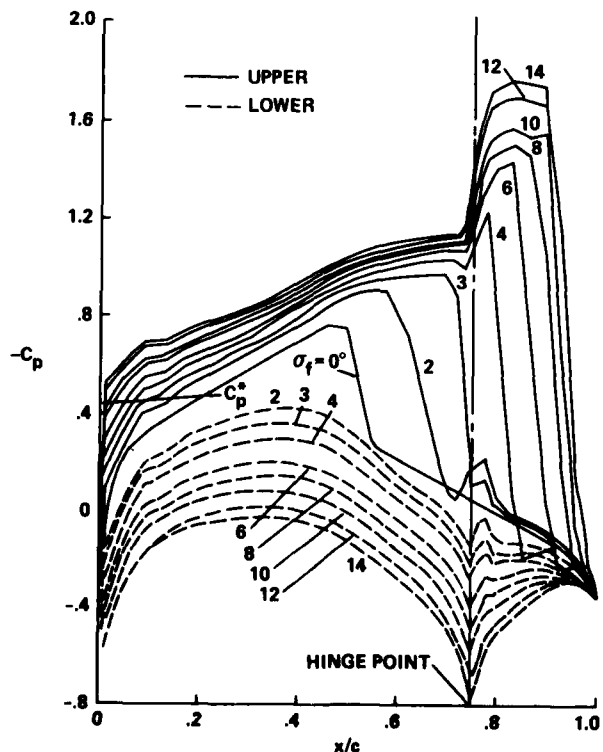


Figure 4. Static surface-pressure coefficient distributions;  $M_\infty = 0.8$  (Ref. 2).

a shock wave can be seen at  $x/c = 0.5$  on both the upper and lower surfaces of the airfoil. As the flap deflection angle increases, the shock wave on the upper surface becomes stronger and is located farther aft along the airfoil. At  $\alpha_f = 3^\circ$  the upper surface shock wave is located at the flap hinge point. Further increases in the flap deflection angle cause the shock wave to move aft along the flap surface, and for  $\alpha_f \approx 10^\circ$  the shock wave is located essentially at the flap trailing edge.

The surface-pressure distributions were spatially integrated to obtain the static hinge-moment coefficient  $C_h(\infty; \alpha_f)$ . These results are presented in Fig. 5 as a function of the flap deflection angle. The hinge-moment coefficient is a linear function of  $\alpha_f$  for  $|\alpha_f| < 3^\circ$ , and is statically stabilizing, tending to oppose the flap deflection. For flap deflection angles greater than  $3^\circ$ , where the upper surface shock is located on the flap, the hinge-moment coefficient is a nonlinear function of  $\alpha_f$ .

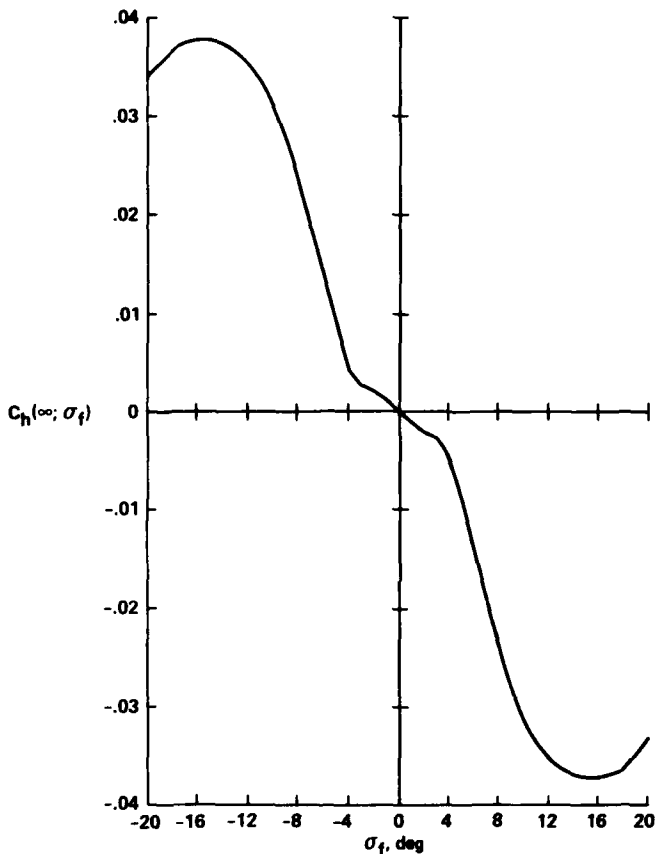


Figure 5. Static hinge-moment coefficient;  $M_\infty = 0.8$  (Ref. 2).

### 2.3.2 Nonsteady flow

Time histories of the hinge-moment coefficient, obtained for small-amplitude harmonic oscillations of the flap about fixed mean values of  $\alpha_f$ , are shown in Fig. 6. The results demonstrate a mild time-variation of the moment coefficient for those cases in which the shock wave lies forward of the hinge point ( $\alpha_{f_m} < 3^\circ$ ) and also for those cases in which the shock is essentially fixed at the flap trailing edge ( $\alpha_{f_m} > 10^\circ$ ). For those cases in which the shock wave moves along the flap as the deflection angle varies, the hinge-moment coefficient exhibits a greater sensitivity to the flap movement.

The flap hinge-moment damping coefficient  $C_{h_f}(\alpha_f)$  is evaluated from the component of the time history of the hinge-moment response that is  $90^\circ$  out-of-phase with the time history of the flap deflection angle. These results are shown in Fig. 7 as a function of the mean flap deflection angle. At the flow conditions investigated in Ref. 2, the flap hinge-moment damping coefficient is a highly nonlinear function of the flap attitude. For values of  $|\alpha_{f_m}| < 3^\circ$  the damping coefficient is negative (dynamically stabilizing) and would tend to damp an unconstrained oscillation of the flap. For values of  $\alpha_{f_m}$  ranging between  $3^\circ$  and  $17^\circ$ , however, the flap damping coefficient is positive (dynamically destabilizing) and would cause an unconstrained oscillation of the flap to grow in amplitude.

The nonlinear variation of the hinge-moment damping coefficient with the flap deflection angle is qualitatively linked to the behavior of the slope of the static hinge-moment coefficient curve. To demonstrate this linkage let us first consider the analogous behavior of the damping-in-pitch coefficient  $[C_{m_q}(-\delta) + \gamma C_{m_q}(\delta)]$  that would be evaluated for an airfoil performing small-amplitude pitch oscillations about a fixed pivot point. It is known that the contribution of  $C_{m_q}(\delta)$  to the airfoil damping is always stabilizing, whereas the

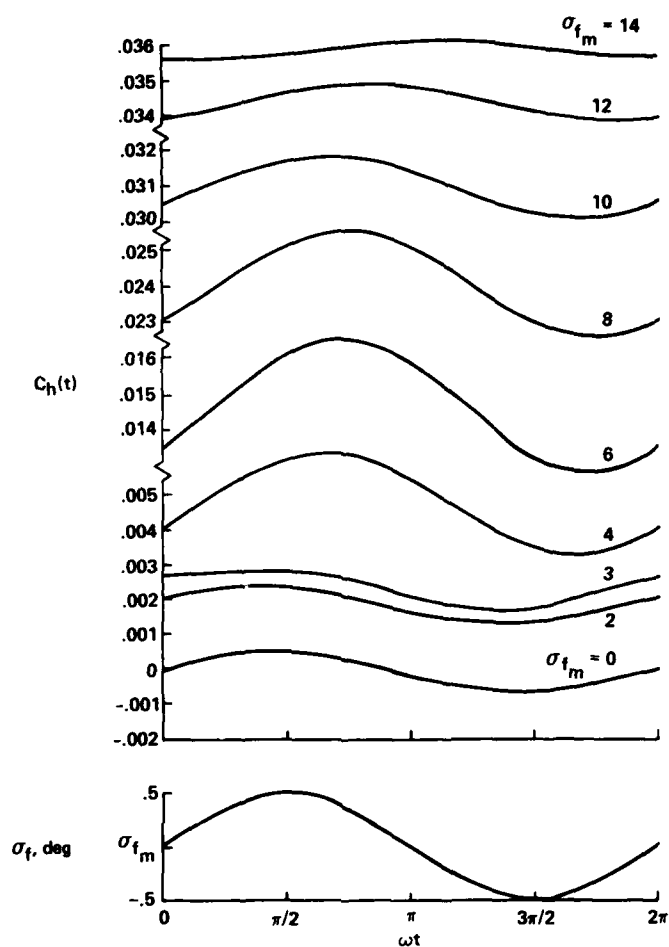


Figure 6. Time histories of hinge-moment coefficient response to specified oscillations;  
 $\sigma_f(t) = \sigma_{f_m} + \sigma_{f_1} \sin \omega t$ ,  $\sigma_{f_1} = 0.5^\circ$ ,  $M_\infty = 0.8$  (Ref. 2).

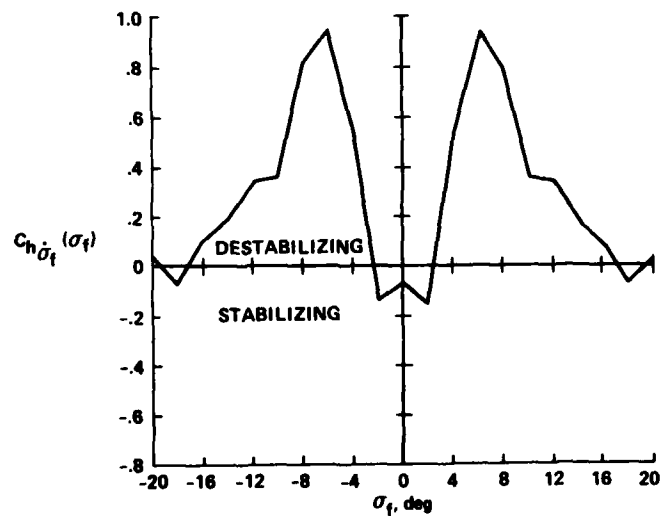


Figure 7. Hinge-moment damping coefficient;  $M_\infty = 0.8$  (Ref. 2).

contribution of  $C_{m\delta}(\delta)$  can be destabilizing. Further, it has been shown (cf. Eq. (35) of Ref. 1) that a qualitative relationship exists between  $C_{m\delta}$  and the static aerodynamic pitching-moment coefficient, namely

$$C_{m\delta}(\delta) = A + BC_{m_0}(\infty; \delta) \quad (4)$$

where  $A$  and  $B$  are constants, with  $B < 0$ , and  $C_{m_0}(\infty; \delta)$  is the local slope of the static pitching-moment curve. Thus, at angles of attack where  $C_{m\delta}$  is large and negative (statically stabilizing),  $C_{m\delta}$  will be correspondingly large and positive and will tend to make  $[C_{m_0}(\infty; \delta) + \gamma C_{m\delta}(\delta)]$  dynamically destabilizing. Analogous trends are obtained for the case of the oscillating flap. At flap deflection angles for which the local slope of the static hinge-moment coefficient curve is large and negative, that is, for  $3^\circ < \sigma_{f_0} < 9^\circ$ ,  $C_{h\delta_f}(\sigma_{f_0})$  is dynamically destabilizing. In contrast, at flap deflection angles for which the local slope of the static curve is either small or positive,  $C_{h\delta_f}(\sigma_{f_0})$  is negative, that is, dynamically stabilizing.

#### 2.4 Results of Computations for Motion Histories

Oscillatory time histories of the flap motion were generated using the coupled-equations approach. In these computations, the flap moment of inertia was chosen to give a value of reduced frequency close to the one specified for the characteristic-motion computations. Corresponding histories of the flap motion were also predicted using the flap equation of motion, Eq. (1), with the instantaneous hinge-moment coefficient specified by the nonlinear aerodynamic mathematical model. After initial values of the flap deflection angle and velocity were specified, the equation of motion was solved numerically to obtain the motion histories. In the modeling approach, the instantaneous hinge-moment coefficient was given by Eq. (2) where the terms  $C_h(\infty; f(t))$  and  $C_{h\delta_f}(\sigma_f(t))$  were obtained from table look-ups in Figs. 5 and 7, respectively.

Oscillatory motion histories of the flap, generated with both the coupled-equations approach and the mathematical modeling approach for a case in which the flap was released with an initial deflection angle  $\sigma_{f_0} = 4.0^\circ$  are shown in Fig. 8. The dynamically stabilizing portion of the hinge-moment damping curve (Fig. 7) governed the motion, and the amplitude of oscillation was found to decay smoothly. However, when the flap was released from a slightly larger initial deflection angle,  $\sigma_{f_0} = 4.5^\circ$ , the dynamically destabilizing region of the damping curve caused the amplitude of the oscillatory motion to grow rapidly (Fig. 9). In both

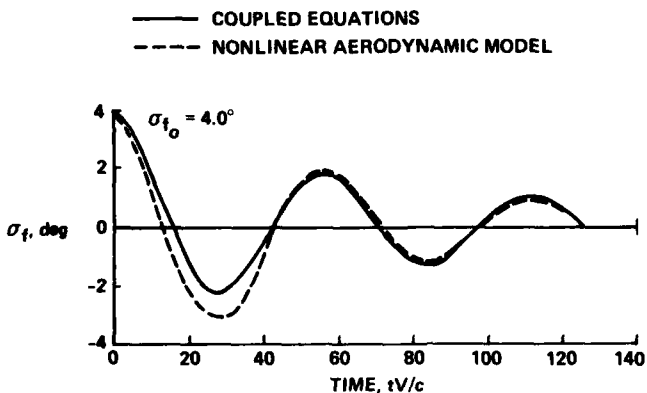


Figure 8. Time history of flap deflection;  $\sigma_{f_0} = 4.0^\circ$  (Ref. 2).

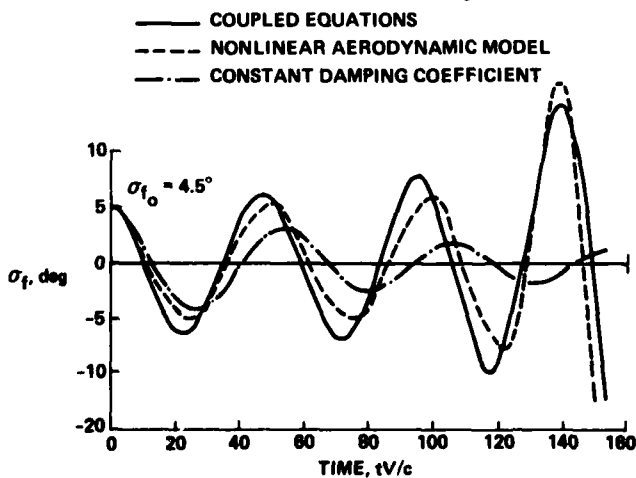


Figure 9. Time history of flap deflection;  $\sigma_{f_0} = 4.5^\circ$  (Ref. 2).

the damped and undamped cases, the motion histories generated using the nonlinear mathematical model were in close agreement with the motion histories obtained from the coupled-equations computations. This confirmed the validity of the mathematical model. In contrast, a motion history generated for the undamped case ( $\alpha_{f_0} = 4.5^\circ$ ) with an aerodynamic mathematical model that does not account for nonlinear unsteady aerodynamic contributions (i.e., Eq. (2) with the nonlinear variation of the static hinge-moment coefficient given by Fig. 5, and with the value of the damping term  $C_{h_{pf}}$  held fixed for all  $\alpha_f$  at the value obtained at  $\alpha_f = 0^\circ$ ) failed to predict the undamped growth of the motion (Fig. 9).

## 2.5 Discussion

The close agreement between the flap motion histories obtained with the coupled-equations approach and those generated with the modeling approach confirmed the capacity of the nonlinear aerodynamic mathematical model to adequately describe the aerodynamic response to arbitrary flap motions. The success of the modeling approach in this case has significant implications for the approach to future problems involving nonsteady motions. In our view, for those cases in which nonlinear aerodynamic mathematical models analogous to Eq. (2) are valid, and large numbers of motion histories are to be determined, the modeling approach will be less costly and more versatile than the coupled-equations approach. Further, use of the modeling approach will give better insight into the physics governing the flow than will use of the coupled-equations approach.

First, regarding costs, we note that computation of motion histories from the vehicle equations of motion requires negligible computational effort in comparison with that needed for time-dependent flow-field computations. Consequently, with the modeling approach, once the initial effort of evaluating the aerodynamic responses to the characteristic motions is expended, computation of motion histories would be relatively inexpensive. In the transonic flow case reported in Ref. 2, 11 flow-field computations of the small-amplitude oscillatory characteristic motions were carried out, for mean flap deflections spaced every  $2^\circ$  between  $0^\circ$  and  $20^\circ$ . On the other hand, each one of the coupled-equations computations of flap motion histories required computer costs equivalent to one of the characteristic-motion computations. Thus, in a similar case, if more than 11 flap motion histories needed to be evaluated, the modeling approach would be less costly. Further, in the modeling approach, methods are known for extending the utility of a given numerical solution by making it applicable over a range of parameters (cf. in particular Ref. 16, where it is shown how the method of strained coordinates could be applied to extend a given numerical solution for transonic flow over a range of airfoil thicknesses and Mach numbers). Thus, when such methods can be utilized, a significant reduction in the number of required flow-field computations of characteristic motions can be realized. Additionally, regarding versatility, the modeling approach makes it easy to introduce changes into the equations of motion — for example, changes in the flap moment of inertia or mass center location, addition of a mechanical restoring force or mechanical damping, or inclusion of a model of a control system — and to evaluate their effects at low cost, since the aerodynamic data within the mathematical model would remain unchanged. In contrast, with the coupled-equations approach the simplest change in any of the equations would require a complete reevaluation of the flow field and flap response.

Second, the modeling approach would appear to give better insight into the physics governing the unsteady flow than does the coupled-equations approach. If an undamped or divergent motion results from coupled-equation computations, it would be difficult to identify the aerodynamic phenomenon causing the instability. On the other hand, computations carried out in terms of the characteristic motions permit an investigation of the underlying aerodynamic mechanisms. For the transonic flap motions considered in Ref. 2, the computations indicated that it was the rearward movement of the upper-surface shock wave onto the flap that caused the large change in the slope of the static hinge-moment curve. It was also possible to show how the change in static hinge-moment coefficient was related to the destabilizing behavior of the hinge-moment damping coefficient. Further, the modeling approach is compatible with the established methods for determining the stability of motions. Thus, for the case of flap motions, knowledge of the behavior of the damping coefficient with increasing deflection angle allowed a qualitative prediction of the types of motion histories that were observed.

The demonstrated success of the modeling approach for the motions of the flap in transonic flow supports our belief that analogous mathematical models (cf. Ref. 1) will be applicable in more general cases and, in particular, that the models will be adequate to describe the nonlinear aerodynamic response of an aircraft to arbitrary flight maneuvers. This is fortunate, for in the case of aircraft motions computational resources are currently inadequate to permit either the computational evaluation of the aerodynamic responses to the characteristic motions or the use of the coupled-equations approach. Consequently, in the case of aircraft maneuvers, mathematical modeling, with the aerodynamic responses to the characteristic motions evaluated from wind-tunnel measurements, is the only approach currently available.

## 3. APPLICATION TO WING ROCK

A current problem in flight dynamics is the wing-rock phenomenon, which is observed on several types of fighter aircraft at angles of attack near stall. Possible aerodynamic causes of wing-rock are discussed in a recent paper by Chambers et al. (Ref. 17). In that paper, the authors present some experimental results taken from Ref. 18 in which a wind-tunnel model of a fighter-type aircraft was made to undergo roll oscillations at various amplitudes and frequencies at high, fixed angles of attack. The results indicate that the damping-in-roll coefficient is destabilizing at small amplitudes of oscillation and is a strongly nonlinear function of both oscillation amplitude and frequency. The authors of Ref. 17 indicate further that they have found it necessary to fully incorporate this nonlinear behavior of the damping-in-roll coefficient within the equations of motion used in their simulator studies in order to achieve a satisfactory match with the wing-rock motions observed in full-scale flight experiments. This raises the question whether our aerodynamic formulation as presently constituted (i.e., Eq. (65) of Ref. 1) is of sufficient scope to accommodate the data presented in Ref. 17 or whether a further generalization will be required. We investigate this question in the following sections.

### 3.1 Formulation

The problem in question involves a single-degree-of-freedom rolling maneuver at fixed resultant angle of attack. In Ref. 1, we used this maneuver as an example in demonstrating how our formulation could be modified to accommodate hysteresis in the steady-state aerodynamic response, that is, a double-valued, discontinuous behavior in the steady-state aerodynamic response. For convenience, the main result is repeated here.

$$C_z(t) = C_z(\infty; \psi(t), h(t), \sigma_0) - \sum_{\text{intervals}} \int_t^{\tau} F(t - \tau; \psi(\tau), \dot{\psi}(\tau), h(\tau), \sigma_0) \frac{d\psi}{d\tau} d\tau - \sum_{i=1}^N \Delta F(t - \bar{\tau}_i; \psi(\bar{\tau}_i), \dot{\psi}(\bar{\tau}_i), h(\bar{\tau}_i), \sigma_0) \quad (5)$$

In Eq. (5), the first term  $C_z(\infty; \psi(t), h(t), \sigma_0)$  is the rolling moment coefficient that would be measured in a steady flow with roll angle  $\psi$  fixed at  $\psi(t)$  and resultant angle of attack  $\sigma$  fixed at  $\sigma_0$ . The parameter  $h(t)$  can take one of two possible values depending on the type of flow regime existent in the recent past relative to  $t$ . Thus, it is possible for the steady-state rolling-moment coefficient to be a double-valued function of  $\psi$ . The type of variation envisaged for  $C_z$  is illustrated in Fig. 10. Note further that the deficiency function  $F$  within the integral term in Eq. (5) depends on both  $\psi(t)$  and  $\dot{\psi}(t)$ . Retention in the deficiency function of a dependence on the time-rate-of-change of the variable prior to the origin of a step may be necessary to properly model aerodynamic phenomena involving dynamic hysteresis as well as hysteresis in the steady-state aerodynamic response. The final terms in Eq. (5), namely, the transient terms  $\Delta F(t - \bar{\tau}_i; \dots)$ , arise as a result of the change in flow regime that is signaled by  $h(t)$  changing from one value to the other whenever  $\psi$  passes through a critical point in the proper direction. It is required to determine whether Eq. (5) is of sufficient scope to accommodate the experimental results reported in Ref. 17. Before we undertake to answer this question, however, we must briefly review the method by which the data were acquired and reduced, since this plays a significant role in the interpretation of the results.

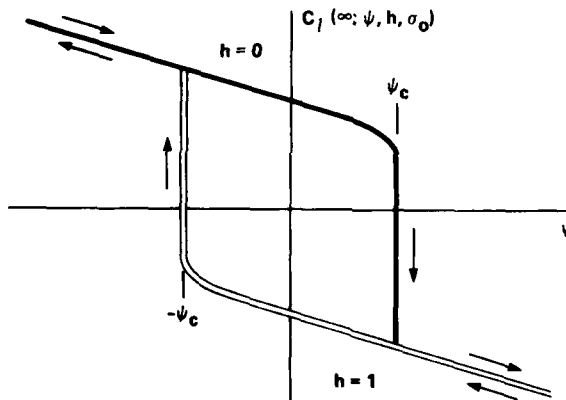


Figure 10. Schematic representation of aerodynamic hysteresis in steady-state rolling-moment coefficient.

### 3.2 Experiments

The apparatus used in the forced oscillations-in-roll experiments of Ref. 18 is illustrated in Fig. 11. Rotating the turntable to the desired position fixes the angle of attack of the model. Other than the angle of attack, the only motion variables in the experiment are the frequency and amplitude of the oscillation. The roll oscillation is imparted to the model by means of an electric drive motor and push-rod mechanism. Controlling the offset of the push rod determines the amplitude of the oscillation, while the oscillation frequency is determined by the rotational speed of the drive motor. A strain-gage balance contained within the model measures the instantaneous forces acting on the model. In addition, the apparatus generates signals proportional to  $\psi$ , the roll angle, and to  $\dot{\psi}$ , the angular roll velocity.

It is important to note that the values of damping-in-roll coefficient  $C_{z\dot{\psi}}$  reported in Ref. 17 (labeled  $C_{z_p} + C_{z_B} \sin \alpha$  in Refs. 17 and 18) were actually effective, that is, average values of the coefficient. This is so because the coefficients were evaluated from energy considerations for large-amplitude oscillations in  $\psi$ . The effective damping-in-roll coefficient is proportional to the energy per cycle imparted to the model during an oscillation in roll of constant amplitude and frequency about  $\psi = 0$ , with  $\sigma$  held fixed. The energy is determined experimentally by multiplying the signal proportional to the instantaneous rolling moment by the roll velocity signal and averaging the product over a cycle of oscillation. With the roll angle  $\psi$  and roll velocity  $\dot{\psi}$  being harmonic functions of time,  $\psi(t) = \psi_0 \sin \omega t$ ,  $\dot{\psi}(t) = \psi_0 \omega \cos \omega t$  the effective damping-in-roll coefficient can be shown, by comparison with the energy per cycle absorbed by a linear constant coefficient aerodynamic system, to be

$$(C_{z\dot{\psi}})_{\text{eff}} = \frac{1}{\omega \psi_0^2 \pi} \frac{V}{2} \int_0^T C_z(t) \dot{\psi}(t) dt \quad (6)$$

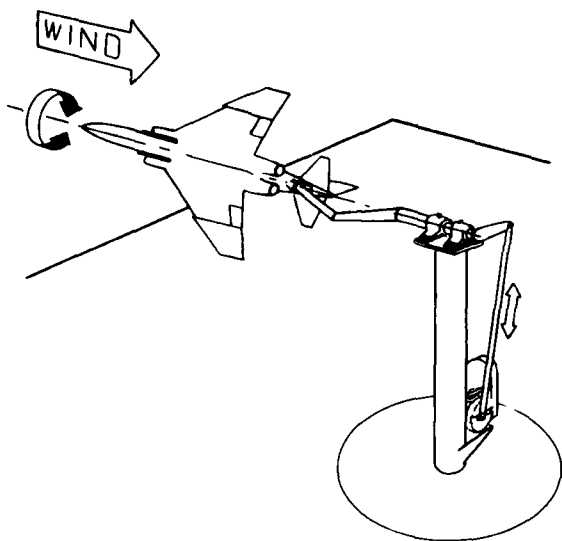


Figure 11. Langley large-scale forced-oscillations-in-roll apparatus (Ref. 18).

where  $T$  is the period of oscillation ( $T = 2\pi/\omega$ ) and  $z$ , the reference length, is specified to be the wing semispan. Values of  $(C_{I\psi})_{\text{eff}}$ , evaluated from experimental measurements according to Eq. (6), are taken from Ref. 18 and presented in Fig. 12. The highly nonlinear dependence on both oscillation amplitude and frequency should be noted.

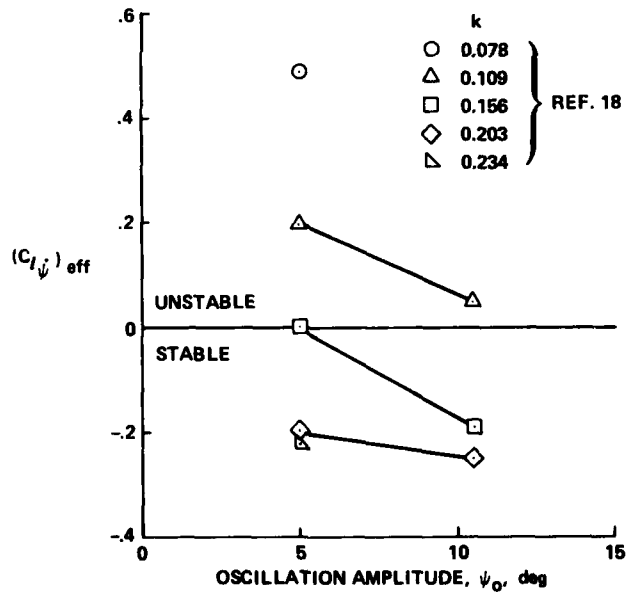


Figure 12. Variation of the effective damping-in-roll coefficient with amplitude of oscillation;  $\sigma_0 = 20^\circ$  (Ref. 18).

### 3.3 Recasting of Formulation

To determine whether the general aerodynamic moment formulation as currently constituted (Eq. (5)) can accommodate the experimental results illustrated in Fig. 12, we must determine what happens to the formulation when it is recast to yield an effective damping-in-roll coefficient for large-amplitude oscillations just as were the experimental data by means of Eq. (6).

To this end, after specifying that the arbitrary rolling maneuver in Eq. (5) be a harmonic oscillation  $\psi(t) = \psi_0 \sin \omega t$  and substituting Eq. (5) for  $C_l(t)$  within the integral in Eq. (6), we get

$$\begin{aligned}
 (C_{L\psi})_{\text{eff}} &= \frac{1}{\psi_0 \pi} \frac{V}{Z} \int_0^T C_L(\omega; \psi(t), h(t), \sigma_0) \cos \omega t dt \\
 &\quad - \frac{\omega V}{\pi Z} \sum_{\text{intervals}} \left\{ \int_0^t \left\{ \int_0^t F(t - \tau; \psi(\tau), \dot{\psi}(\tau), h(\tau), \sigma_0) \cos \omega \tau d\tau \right\} \cos \omega t dt \right\} \\
 &\quad - \frac{1}{\psi_0 \pi} \frac{V}{Z} \sum_{i=1}^N \int_0^T \Delta F(t - \bar{\tau}_i; \psi(\bar{\tau}_i), \dot{\psi}(\bar{\tau}_i), h(\bar{\tau}_i), \sigma_0) \cos \omega t dt
 \end{aligned} \tag{7}$$

If  $C_L(\omega; \psi(t), h(t), \sigma_0)$  is a continuous, single-valued function of  $\psi$  (meaning that there is only one possible flow regime and consequently only one possible value for  $h$ ), it is easy to show that the first integral in Eq. (7) will vanish. Likewise, with  $C_L(\omega; \psi(t), \dots)$  single-valued, the transient terms  $\Delta F(t - \bar{\tau}_i; \dots)$  in Eq. (5) will be identically zero and so will make no contribution in Eq. (7). Let us assume for the time being that this is the case, so that the effective damping-in-roll coefficient is determined solely by the second integral term in Eq. (7).

To evaluate the second integral, we expand the deficiency function  $F$  in a Taylor series about  $\psi(\tau) = 0$ ,  $\dot{\psi}(\tau) \approx 0$ . Thus,

$$\begin{aligned}
 F(t - \tau; \psi(\tau), \dot{\psi}(\tau), h(\tau), \sigma_0) &= \sum_{n=0} f_n \left( \frac{V}{Z} (t - \tau); \sigma_0 \right) \left( \frac{\omega Z}{V} \right)^n \psi_0^n \cos^n \omega \tau + \sum_{n=1} g_n \left( \frac{V}{Z} (t - \tau); \sigma_0 \right) \psi_0^n \sin^n \omega \tau \\
 &\quad + \sum_{n=1} \sum_{m=1} k_{nm} \left( \frac{V}{Z} (t - \tau); \sigma_0 \right) \psi_0^{n+m} \left( \frac{\omega Z}{V} \right)^m \sin^n \omega \tau \cos^m \omega \tau
 \end{aligned} \tag{8}$$

Let

$$\begin{aligned}
 s &= \frac{tV}{Z}, \text{ characteristic lengths traveled in time } t, \\
 \xi &= \frac{\tau V}{Z}, \text{ characteristic lengths traveled in time } \tau, \\
 k &= \frac{\omega Z}{V}, \text{ reduced frequency}
 \end{aligned} \tag{9}$$

and

$$s - \xi = u; \quad 0 \leq u \leq s_a$$

where  $s_a$  represents the number of characteristic lengths required for the deficiency function to die out essentially to zero. When Eqs. (8) and (9) are substituted in Eq. (7) and the variables of integration are interchanged, the integrations over  $s$  can be carried out. Retaining terms up to the second power in  $\psi_0$  and reduced frequency  $k$ , we obtain

$$\begin{aligned}
 (C_{L\psi})_{\text{eff}} &= - \left\{ \int_0^{s_a} f_0(u; \sigma_0) \cos ku du + \frac{\psi_0^2}{4} \int_0^{s_a} g_2(u; \sigma_0) \cos ku du \right. \\
 &\quad \left. - \frac{k\psi_0^2}{4} \int_0^{s_a} k_{11}(u; \sigma_0) \sin ku du + \frac{3}{4} k^2 \psi_0^2 \int_0^{s_a} f_2(u; \sigma_0) \cos ku du \right\}
 \end{aligned} \tag{10}$$

Finally, after expanding the trigonometric terms within the integrals in powers of  $ku$ , we see that, according to our formulation, to within terms of  $O(k^2)$  the effective damping-in-roll coefficient must have the form

$$(C_{L\psi})_{\text{eff}} = A(\sigma_0) + \psi_0^2 B(\sigma_0) + O(k^2) \tag{11}$$

If the effective damping-in-roll coefficient actually has the characteristics assigned to it by our formulation, it follows from Eq. (11) that all of the following conditions must be satisfied: (1) for oscillations of small amplitude and low reduced frequency, the damping-in-roll coefficient should be independent of both oscillation amplitude and frequency; (2) at fixed reduced frequency, the damping-in-roll coefficient should vary quadratically with amplitude of oscillation; and (3) at fixed amplitude of oscillation, the damping-in-roll coefficient should vary quadratically with reduced frequency. Examination of the experimental results (Fig. 12) reveals that not all of these conditions are satisfied. Indeed, at fixed amplitude of oscillation, the damping-in-roll coefficient would appear to vary inversely, rather than quadratically, with reduced frequency.

On the basis of Fig. 12, it would appear that the aerodynamic formulation given in Eq. (5) is incapable of accounting for the form that the experimental results display, and that a further extension of the formulation will be required. Let us recall, however, that we began by assuming that the steady-state rolling-moment coefficient in Eq. (5) was a single-valued function of  $\psi$ , on which basis the first and third terms in Eq. (7) vanished identically. We now withdraw this assumption and admit the possibility that  $C_l(\omega; \psi(t), \dots)$  may be a double-valued function of  $\psi$  for some range of  $\psi$  about  $\psi = 0$ ; we assume, in other words, that  $h(t)$  may have two possible values (cf., e.g., Fig. 10). Under this condition the first integral term in Eq. (7) does not vanish if the oscillation amplitude  $\psi_0$  exceeds the range of  $\psi$ ,  $-\psi_c < \psi < \psi_c$ , over which  $C_l(\omega; \psi, \dots)$  is double-valued. Further, again provided  $\psi_0 > \psi_c$ , there are two points within a cycle of oscillation at which  $h$  changes value, and the transient term  $\Delta F(t - \tau_i; \dots)$  corresponding to each of these points contributes to the energy absorbed over the cycle. When account is taken of these additional contributions in Eq. (7) it can be shown that the effective damping-in-roll coefficient takes the form

$$\left( C_{l\psi} \right)_{\text{eff}} = A(\sigma_0) + \psi_0^2 B(\sigma_0) + \frac{1}{\psi_0^2 k} C(\psi_0/\psi_c; \sigma_0) + \frac{1}{\psi_0} D(\psi_0/\psi_c; \sigma_0) + O(k^2) \quad (12)$$

where both  $C$  and  $D$  are zero if  $\psi_0/\psi_c < 1$  and finite when  $\psi_0/\psi_c > 1$ . The term involving  $C$  is proportional to the area enclosed by the hysteresis loop in  $C_l(\omega; \psi(t), \dots)$ , while each of the transients contributes a term to  $D$  of the order of

$$\sqrt{1 - (\psi_0/\psi_c)^2} \int_0^{S_a} \Delta F(u; \sigma_0) du .$$

If Eq. (12) is multiplied by  $\psi_0^2 k$ , we see that the quantity  $\psi_0^2 k (C_{l\psi})_{\text{eff}}$  has the form

$$\psi_0^2 k (C_{l\psi})_{\text{eff}} = C(\sigma_0) + k E(\psi_0; \sigma_0) + O(k^3 \psi_0^2) \quad (13)$$

We note that with  $\psi_0/\psi_c > 1$  satisfied, the parameter  $C$  in Eq. (13), being proportional to the area enclosed by the hysteresis loop, is not dependent on the magnitude of  $\psi_0$ . On the basis of this form, therefore, we expect that all of the experimental results for  $\psi_0^2 k (C_{l\psi})_{\text{eff}}$  for a given value of  $\psi_0$  should fall on a single straight line when plotted against  $k$ . Further, all such straight lines should originate from the same point at  $k = 0$ , namely  $C$ . It will be seen in Fig. 13, where the measured values  $\psi_0^2 k (C_{l\psi})_{\text{eff}}$  are presented as functions of  $k$  for the two experimental values of  $\psi_0$ , 5° and 10.5°, that these conditions are essentially satisfied. The fact that  $C$  is nonzero again implies the existence of a hysteresis loop in the rolling-moment coefficient curve. Although experimental measurements of the static rolling-moment coefficient for this aircraft model (Ref. 18) were not conducted in such a way as to confirm the existence of a hysteresis loop, the

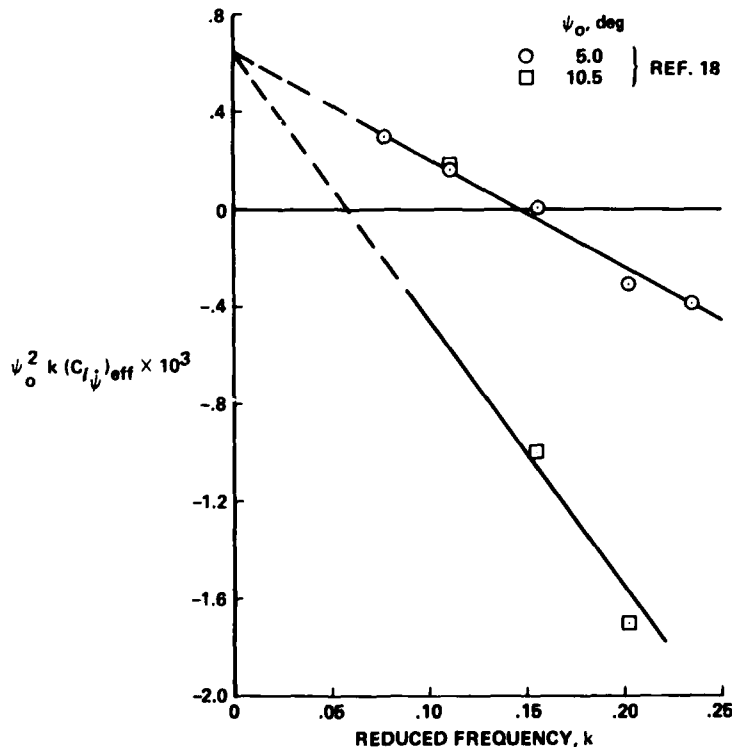


Figure 13. Variation of the damping-in-roll parameter  $\psi_0^2 k (C_{l\psi})_{\text{eff}}$  with reduced frequency;  $\sigma_0 = 20^\circ$ .

results do suggest the presence of such a loop, whose area is consistent with that implied by the value of  $C_z$ . Thus, the seemingly anomalous dependence of the effective damping-in-roll coefficient on oscillation frequency and amplitude can be satisfactorily explained within the framework of the present mathematical model by admitting the existence of a hysteresis loop in the steady-state rolling-moment coefficient curve. In fact, it seems reasonable to suggest the following as a general rule: Whenever an average aerodynamic damping coefficient is determined from large-amplitude oscillatory measurements and the coefficient turns out to have an inverse dependence on reduced frequency, this should be taken as an indicator that the oscillation has encompassed a hysteresis loop in the steady-state component of the aerodynamic moment being measured.

### 3.4 Formulation for Arbitrary Rolling Maneuvers

Aside from the inverse dependence on  $k$ , Eq. (12) indicates that oscillation frequency plays no other significant role in the determination of  $C_{z\psi_{eff}}$ ; moreover, Fig. 13 shows experimental confirmation of this indication. In the application of Eq. (5) to arbitrary maneuvers, this result suggests that it should be permissible to reduce the form to the level of complexity in which the indicial response depends only on the magnitude of  $\psi$  just prior to the origin of the step. It is then a consistent approximation to further reduce the integral term in Eq. (5) to a form that is correct to the first order in frequency. The reduction procedure, explained in detail in Ref. 1, leads to the following result:

$$C_z(t) = C_z(\infty; \psi(t), h(t), \sigma_0) + \frac{\dot{\psi}(t)\lambda}{V} C_{z\dot{\psi}}(\psi(t), h(t), \sigma_0) \quad (14)$$

Equation (14) should apply for all values of  $t$  except possibly those immediately subsequent to any time at which  $h$  has changed value where the corresponding transient term in Eq. (5) may still be large. It will be noted that Eq. (14) is consistent with Eq. (40) of Ref. 1 (with  $\sigma$  held fixed at  $\sigma_0$  and  $\lambda$  held fixed at zero), except that we now admit double-valued behavior in  $C_z(t)$  by allowing  $h(t)$  to have two possible values. The term  $C_{z\dot{\psi}}$  in Eq. (14) must be determined from small-amplitude oscillations in  $\psi$  about a fixed value of  $\psi$  equal to the instantaneous value, while  $\sigma$  is held fixed at  $\sigma_0$ . The oscillation amplitude must be small enough to ensure that the oscillation remains on one branch of the hysteresis loop in  $C_z(\cdot; \psi(t), h(t), \sigma_0)$ ; otherwise, as we have seen, there will be unwanted additional contributions when the energy is measured.

### 3.5 Experimental Evidence of Aerodynamic Hysteresis

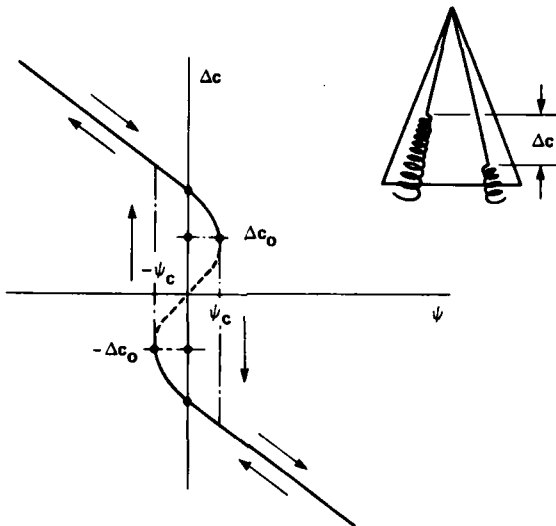
Results from several experimental investigations can be cited to lend support to our finding that the results reported by Chambers et al. (Ref. 17) are explainable by admitting the existence of aerodynamic hysteresis in the curves of steady-state rolling-moment coefficient. In particular, Schmidt (Ref. 20), hypothesizing aerodynamic hysteresis as the source of wing rock, refers to wind-tunnel tests of a fighter-aircraft model (Ref. 21) in which the angle of sideslip was varied slowly through a cycle about zero while the angle of attack was held fixed. At angles of attack near stall, the rolling-moment coefficient, plotted against the sideslip angle, gave clear evidence of hysteresis. Similar results exhibiting aerodynamic hysteresis have recently been obtained in wind-tunnel tests (Ref. 22) of a fighter-type model in transonic flow.

A possible source of aerodynamic hysteresis may be the asymmetric breakdown of the lee-side vortices that occurs on slender wings and bodies at high angles of attack. In a study of the vortices on the leeward side of a slender delta wing, Elle (Ref. 23) observed that at high angle of attack, the more-or-less symmetric breakdown of the pair of lee-side vortices that occurs downstream of the trailing edge is not stable to small perturbations in sideslip. When perturbed, the pattern of breakdown becomes asymmetric, with breakdown of one vortex occurring closer to the apex of the wing than the other. Once the asymmetric flow pattern is established, it appears to be stable since opposite sideslip of some degrees could be applied without appreciably altering the relative positions of breakdown of the two vortices. Such an asymmetric pattern of breakdown would, of course, induce a rolling moment, even at zero sideslip angle. In a related study, Lowson (Ref. 24) noted the existence of hysteresis and asymmetry in the vortex breakdown patterns when a delta wing was slowly pitched to large angle of attack with sideslip angle held fixed at zero. Which of the two possible asymmetric patterns was observed after any single pitch-up was probabilistic, but, once established, the relative position of the two vortex breakdowns would persist over the wing, even as the angle of attack was reduced to values where the breakdown had occurred initially downstream of the wing trailing edge. Finally, we are indebted to W. A. Moore and D. J. Lorincz of the Northrop Corporation for the loan of a very revealing film that clearly shows, by means of visualization of the vortex cores in a water tunnel, the close relationship between asymmetric vortex breakdown on a slender delta wing at high angle of attack and self-induced roll oscillations.

### 3.6 Conjectures on Origin of Aerodynamic Hysteresis

We intend to show that the essential observations on vortex breakdown, as they pertain to wing-rock, can be placed within the framework of ideas common to a host of physical phenomena in a wide variety of fields that has come to be known as "bifurcation theory" (cf. Ref. 23). (We gratefully acknowledge the assistance of G. T. Chapman of Ames Research Center, whose contributions were instrumental in our framing an understanding of aerodynamic hysteresis in terms of bifurcation theory.) Let us note, to begin with, that the critical observation is that of Lowson (Ref. 24): for slender wings at sufficiently high angles of attack, the pattern of vortex breakdowns becomes asymmetric at zero roll angle. This is to say that the vortex-breakdown pattern at  $\psi = 0$  is bimodal; two stable states are possible under the same boundary conditions. As we shall see, everything follows from this one observation.

Let us denote by  $\Delta c$  the difference between the chordwise positions of the left-hand and right-hand vortex breakdowns, and let  $\Delta c$  be positive when the left-hand breakdown position is the closer of the two to the wing apex. Let us call the curve of  $\Delta c$  versus  $\psi$  the curve of equilibrium states, reflecting all of the possible equilibrium positions of the vortex breakdowns for a fixed value of  $\sigma$ . From symmetry considerations, we know that  $\Delta c$  must be an odd function of the roll angle  $\psi$ . From Lowson's observation (Ref. 24), we know that there must be two possible nonzero values of  $\Delta c$  at  $\psi = 0$ . It follows that the curve relating  $\Delta c$  and  $\psi$  must be at least a cubic function. A typical variation of  $\Delta c$  versus  $\psi$  is shown schematically in Fig. 14. Following the curve of equilibrium states from left to right, we see that as  $\psi$  goes from large negative values toward zero,  $\Delta c$  diminishes, but retains a finite positive value as  $\psi$  passes through zero. The equilibrium state  $\Delta c$

Figure 14. Curve of equilibrium states for fixed  $\sigma$ .

continues to diminish toward a limit value  $\Delta c_0$  at  $\psi = \psi_c$  as  $\psi$  increases through positive values beyond zero. As  $\psi$  increases beyond  $\psi_c$ , there are no further positive equilibrium states, so that, at  $\psi = \psi_c$ ,  $\Delta c$  must jump to the negative branch of the curve and remain on it for all subsequent larger values of  $\psi$ ,  $\psi > \psi_c$ . Thus, as  $\psi$  diminishes toward zero from large positive values,  $\Delta c$  retains a finite negative value at  $\psi = 0$ , and jumps to the positive branch of the curve as  $\psi$  passes through  $-\psi_c$ . We see that the part of the curve of equilibrium states for which  $|\Delta c| < |\Delta c_0|$  (shown dotted in Fig. 14) is inaccessible, in that equilibrium states in this interval are never attained. They are, in fact, unstable equilibrium states, reflecting the physical observation that at a large enough value of  $\sigma$ , when the positions of left-hand-vortex and right-hand-vortex breakdowns are too close together, the breakdowns cannot sustain themselves at those positions. Thus, we find, in view of the antisymmetric nature of the curve of  $\Delta c$  versus  $\psi$ , that hysteresis is a necessary consequence of the existence of bimodal stable states at  $\psi = 0$ .

Finally, it is important to note that since  $\Delta c$  should be directly proportional to  $C_l$ , the rolling-moment coefficient, we could have used  $C_l$  as the ordinate in all of the preceding discussion in place of  $\Delta c$ . This means that any physical phenomenon giving rise to bimodal behavior in  $C_l$  at  $\psi = 0$  will necessarily bring with it aerodynamic hysteresis behavior of the type we have just observed in the variation of  $\Delta c$  with  $\psi$ .

#### 4. CONCLUDING REMARKS

Two applications of the concepts of mathematical modeling to aerodynamic problems of current interest have been discussed. In the first application, the regime of validity of an aerodynamic mathematical model, applicable to the nonlinear aerodynamic reactions on a transonic airfoil with a deflecting flap, was investigated. A time-dependent finite-difference technique was used to compute the nonsteady flow fields and thus to determine the nonlinear, unsteady aerodynamic data in terms of the characteristic motions called for by the model. Histories of unconstrained flap motions were generated from the flap equations of motion with the aerodynamic reactions specified by the mathematical model. These motion histories were compared with analogous motion histories obtained from simultaneous, coupled solutions of the flap equations of motion and the flow-field equations. The histories of the flap motion generated with the aerodynamic mathematical model approach agreed well with those obtained from the coupled-equations approach, even for a case in which the flap exhibited an undamped oscillatory behavior.

In the second application, experimental results describing the wing-rock phenomenon were accommodated within our most recent mathematical model by admitting the existence of aerodynamic hysteresis in the variation of the rolling-moment coefficient with roll angle. We have shown how the links between vortex breakdown, hysteresis, and wing rock can be understood when they are placed within the framework of bifurcation theory. The analysis leads to a general conclusion that any physical phenomenon giving rise to bimodal stable behavior of the rolling-moment coefficient at zero roll angle will cause aerodynamic hysteresis behavior, and thus can be a possible source of wing rock.

#### 5. REFERENCES

1. Tobak, M. and Schiff, L. B., "Aerodynamic Mathematical Modeling - Basic Concepts." AGARD Lecture Series No. 114 on Dynamic Stability Parameters, Lecture No. 1, Mar. 1981.
2. Chyu, W. J. and Schiff, L. B., "Nonlinear Aerodynamic Modeling of Flap Oscillations in Transonic Flow - A Numerical Validation." AIAA Paper 81-0073, St. Louis, Mo., Jan. 1981.
3. Schiff, L. B., Tobak, M., and Malcolm, G. N., "Mathematical Modeling of the Aerodynamics of High-Angle-of-Attack Maneuvers." AIAA Paper 80-1583-CP, Danvers, Mass., Aug. 1980.
4. Magnus, R. and Yoshihara, H., "Unsteady Flows Over an Airfoil." AIAA Journal, Vol. 13, No. 12, Dec. 1975, pp. 1622-1628.

5. Steger, J. L., "Implicit Finite-Difference Simulation of Flow About Arbitrary Two-Dimensional Geometries." AIAA Journal, Vol. 16, No. 7, July 1978, pp. 679-686.
6. Lerat, A. and Sides, J., "Numerical Calculations of Unsteady Transonic Flows." AGARD Meeting of Unsteady Airloads in Separated and Transonic Flow, Lisbon, Portugal, Apr. 17-22, 1977.
7. Chyu, W. J. and Davis, S. S., "Calculation of Unsteady Transonic Flow Over an Arbitrary Airfoil." AIAA Paper 79-1554, Williamsburg, Va., July 1979 (also AIAA Journal, in print).
8. Ballhaus, W. F. and Goorjian, P. M., "Implicit Finite Difference Computations of Unsteady Transonic Flows About Airfoils." AIAA Journal, Vol. 15, No. 12, Dec. 1977.
9. Rizzetta, D. P. and Chin, W. C., "Effect of Frequency in Unsteady Transonic Flow." AIAA Journal, Vol. 17, No. 7, July 1979, pp. 779-781.
10. Rizzetta, D. P. and Yoshihara, H., "Computation of the Pitching Oscillation of an NACA 64A010 Airfoil in the Small Disturbance Limit." AIAA Paper 80-0128, Pasadena, Calif., Jan. 1980.
11. Isogai, K., "Calculation of Unsteady Transonic Flow Using the Full Potential Equation." AIAA Paper 77-448, San Diego, Calif., Mar. 1977.
12. Goorjian, P. M., "Implicit Computation of Unsteady Transonic Flow Governed by the Full Potential Equation in Conservation Form." AIAA Paper 80-150, Pasadena, Calif., Jan. 1980.
13. Steger, J. L. and Bailey, H. E., "Calculation of Transonic Aileron Buzz." AIAA Journal, Vol. 18, No. 3, Mar. 1980, pp. 249-255.
14. Ballhaus, W. F. and Goorjian, P. M., "Computation of Unsteady Transonic Flows by the Indicial Method." AIAA Journal, Vol. 16, No. 2, Feb. 1978, pp. 117-124.
15. Rizzetta, D. P., "Time-Dependent Response of a Two-Dimensional Airfoil in Transonic Flow." AIAA Journal, Vol. 17, No. 1, Jan. 1979, pp. 26-32.
16. Nixon, D. L., "On the Derivation of Universal Indicial Functions." AIAA Paper 81-0328, St. Louis, Mo., Jan. 1981.
17. Chambers, J. R., Gilbert, W. P., and Nguyen, L. T., "Results of Piloted Simulator Studies of Fighter Aircraft at High Angles of Attack." AGARD CP-235, Dynamic Stability Parameters, Paper No. 33, May 1978.
18. Grafton, S. B. and Libbey, C. E., "Dynamic Stability Derivatives of a Twin-Jet Fighter Model at Angles of Attack from  $-10^\circ$  to  $110^\circ$ ." NASA TN D-6091, Jan. 1971.
19. Anglin, E. L., "Static Force Tests of a Model of a Twin-Jet Fighter Airplane for Angles of Attack From  $-10^\circ$  to  $110^\circ$  and Sideslip Angles from  $-40^\circ$  to  $40^\circ$ ." NASA TN D-6425, Aug. 1971.
20. Schmidt, L. V., "Wing Rock Due to Aerodynamic Hysteresis." Journal of Aircraft, Vol. 16, No. 3, Mar. 1979, pp. 129-133.
21. Ottensoser, J., "High Angle of Attack Aerodynamic Data for a 0.10 Scale A-7 Model Evaluated in the 7- by 10-Foot Transonic Wind Tunnel for Investigating the Stall Departure Phenomena, Phase 1." NSRDC TM-16-76-16, Oct. 1975.
22. Herman, J. F. and Washington, E. S., "Wind Tunnel Investigation of the Aerodynamic Hysteresis Phenomenon on the F-4 Aircraft and its Effects on Aircraft Motion." AEDC-80-10, Sept. 1980.
23. Elie, B. J., "An Investigation at Low Speed of the Flow Near the Apex of Thin Delta Wings With Sharp Leading Edges." British R&M 3176, ARC 19 780, 1961.
24. Lowson, M. V., "Some Experiments with Vortex Breakdown." Journal of the Royal Aeronautical Society, Vol. 68, No. 641, May 1964, pp. 343-346.
25. Thompson, J. M. T. and Hunt, G. W., "Towards a Unified Bifurcation Theory." ZAMP, Vol. 26, Fasc. 5, 1975, pp. 581-604.

**APPLICATIONS OF DYNAMIC STABILITY PARAMETERS  
TO PROBLEMS IN AIRCRAFT DYNAMICS**

By

Joseph R. Chambers, Daniel J. DiCarlo, and Joseph L. Johnson, Jr.  
NASA Langley Research Center  
Hampton, Virginia 23665  
U.S.A.

**SUMMARY**

Current interest in flight at high angles of attack has resulted in a renewed interest in the basic nature and application of dynamic stability parameters to problems in aircraft flight dynamics. Procedures for estimating aerodynamic characteristics and the mathematical modeling of such phenomena are urgently needed, particularly for advanced airplane configurations.

The paper presents highlights of a recent study which illustrates the application and analysis of dynamic stability parameters. More specifically, the investigation consisted of an evaluation of the effects of wing leading-edge modifications on the stalling and spinning characteristics of a single-engine general aviation research airplane. The results of the investigation illustrate how dynamic stability parameters measured in wind-tunnel tests are used to predict the spin resistance of this class of aircraft; and that autorotation criteria can be derived from the relationships which exist between static and dynamic aerodynamic characteristics.

Recommendations for research areas for dynamic stability parameters are indicative of the relatively poor understanding of the effects of separated flow conditions at high angles of attack.

**SYMBOLS**

b	wing span, m (ft)
$C_D$	drag coefficient, Drag/ $\rho_\infty$
$C_L$	lift coefficient, Lift/ $\rho_\infty$
$C_L^{\max}$	maximum lift coefficient
$C_R$	resultant aerodynamic coefficient, $\sqrt{C_L^2 + C_D^2}$
$C_x$	rolling moment coefficient, $\left(\frac{M_x}{\rho_\infty S b}\right)$
$C_{x_p} + C_{x_B} \sin \alpha$	angular rate damping in roll, per rad
$\alpha$	free-stream dynamic pressure, N/m <sup>2</sup> (lb/ft <sup>2</sup> )
RN	Reynolds number
S	wing area, m <sup>2</sup> , (ft <sup>2</sup> )
V	velocity, m/sec (ft/sec)
$\alpha$	angle of attack, deg or rad
$\beta$	angle of sideslip, deg
$\Omega$	total angular velocity in spin, rad/sec (deg/sec)

**INTRODUCTION**

From a historical perspective, the technology associated with the use of dynamic stability parameters for the analysis of aircraft flight dynamic problems has rapidly matured and reached a high level of sophistication for a wide variety of applications. The continual refinement of analytical and experimental methods has included studies of open-loop dynamic stability and control, aircraft response to external disturbances and turbulence, development of handling-quality criteria, and sophisticated closed-loop simulations of pilot/control/display integration. The current status of interest in dynamic stability parameters is indicated in figure 1. As a result of concentrated efforts in the area during the 1940's and 1950's, much of the technology required for analysis of conventional flight has become well-known text-book material; and the estimation procedures for dynamic derivatives, equations of motion used in the analysis, and handling-quality criteria used for correlation with predicted results have all become rather mundane, unexciting computerized operations which require only milliseconds of computer time.

In the 1980's, however, the changing interests of the aircraft designer have directed attention to radically new, advanced airplane configurations which dramatically extend the operational ranges of angle of attack, angle of sideslip, and Mach number to such an extent that many of the previously-developed methods and concepts can no longer be applied. For example, the renewed military interest in flight at high angles of attack with its complex aerodynamic flows, and the usage of close-coupled designs which are subject to large component interference effects require a reevaluation of the past methods and the development of new capabilities, ranging from basic understandings of fluid-flow phenomena to the use of non-linear analytical methods in early stages of design. The purpose of this paper is to briefly review the importance and applications of dynamic stability parameters within the area of high angle of attack flight conditions. An example of a recent application of such concepts to stall / spin studies of general aviation research airplane will be presented, and an overview of recommended research requirements for dynamic stability parameters in general is given.

### ROLE OF DYNAMIC PARAMETERS IN HIGH- $\alpha$ ANALYSIS

As a result of the extremely complex, configuration-dependent aerodynamics associated with stalled flow phenomena, it has been difficult or impossible to arrive at simple criteria which generalize data, or to develop rapid back-of-the-envelope high angle-of-attack prediction procedures using 3-view drawings of airplane designs. However, as a result of numerous airplane development programs for general aviation and military airplanes, a highly-recommended method of approach for designers has evolved which has resulted in many successful designs (see references 1 and 2, for example). As indicated in figure 2, the approach utilizes several methods in an integrated fashion to obtain the maximum amount of information and confidence as the design progresses from the preliminary stage to production.

Each test or analysis technique is conducted at a logical time, when necessary preliminary analyses have been completed. Although the approach is time consuming and much cut and try work is required, it has proven to be extremely successful in providing accurate predictions of the characteristics of specific airplane designs. As shown in figure 2, the analysis techniques can be grouped into: wind-tunnel tests, dynamic model flight tests, analytical studies and piloted simulation, and airplane flight tests. Dynamic aerodynamic tests are involved in each of the analysis techniques to some extent. For example, conduct of piloted simulator studies cannot be accomplished without dynamic stability parameters; and the interpretation and analysis of dynamic model flight tests and airplane flight tests may be subject to considerable question without dynamic data.

The dynamic tests are usually delayed to an appropriate point in an aircraft program. That is, before any dynamic aerodynamic measurements are made, comprehensive static stability and control measurements and analysis are in order; and due to the strong nonlinearities and rapid variations encountered in certain angle of attack and sideslip ranges the tests must be carried out with small increments of  $\alpha$  and  $\beta$ .

In the detailed design stage, the static wind-tunnel tests will be supplemented by dynamic tests and the complete set of data will be used as input to a six degree of freedom motion analysis. The nature of the dynamic tests depends on the extent of the analytical objectives, which can be limited to a study of the airplane behavior for angles of attack below the potential high- $\alpha$  problems, or it can also include the analysis of stall, departure, incipient spin, developed spin, and the corresponding recovery procedures. The dynamic wind-tunnel tests are also needed to validate the static criteria and to define maneuver limits when the static criteria are not sufficient--for example, loss of tracking capability due to "wing rock".

The most commonly used dynamic wind-tunnel testing procedure is the forced-oscillation method where the model is sting mounted on an oscillating internal balance. This type of data is used in small-perturbation stability analysis, and it is in widespread use today. For example, experience has shown that the damping in roll of current fighters at high- $\alpha$  is usually a function of the amplitude and frequency of the motion, and any valid mathematical representation of lateral response at high- $\alpha$  absolutely requires the use of forced oscillation data.

To continue the stall/spin analysis to the spin area, the high angle of attack static and forced-oscillation test results must be combined with rotary-balance test data (references 3, 4, and 5). Rotary-balance tests determine the important nonlinear effects of angular rates on aerodynamic data during the spin. The aircraft response, based on six degree of freedom nonlinear analysis using these data, will provide the best analytical information on the developed spin characteristics of the airplane. In this technique, six-component measurements are made of the aerodynamic forces and moments acting on a wind-tunnel model during continuous 360° spinning motions at a constant angle of attack. Such tests were initially conducted many years ago, and the past studies identified some of the major factors which influenced spin characteristics for configurations at that time, such as the autorotative tendencies of unswept wings and certain fuselage cross-sectional shapes. The use of the technique in the United States however, was discontinued because of the laborious, time-consuming manual methods of data acquisition in use at that time. In recent years, the advent of high-speed data acquisition systems has permitted more productive operation of such test rigs, and there are currently numerous rotary-balance installations in operation in the United States and Europe.

The dynamic test tools available to the current-day designer have been used in numerous applications for both civil and military aircraft designs for high angle-of-attack conditions. These studies have included determinations of open-loop stability; the effects of various airframe components at high  $\alpha$ ; autorotative tendencies of wings and fuselages during spins; dynamic cross-coupling derivatives; inputs for piloted simulator studies; and control system development. A complete review of each type of application is beyond the intended scope of this paper; instead, an overview is presented of a recent stall/spin study for a general aviation research airplane. The study is particularly interesting to review, in that dynamic parameters were dominant in the analysis and conclusions reached. In addition, it was possible to relate trends of certain important dynamic parameters to trends displayed by conventional static test results.

### REPRESENTATIVE APPLICATION OF DYNAMIC PARAMETERS

#### Scope of Project

A broad research program is underway at the NASA Langley Research Center to develop the technology required to improve the stall departure and spin resistance characteristics of light general aviation airplanes. This research is of interest because stall/spin is the major causal factor in general aviation accidents. Examination of the circumstances involved in a large number of fatal accidents indicates that the pilot may have lost lateral-directional control at the stall, and that ground impact occurred either before a spin developed (if loss of control experienced at low altitude) or following a spin with no apparent recovery. In view of the well-known fact that the wing employed by general aviation airplanes significantly influences lateral stability at the stall, recent attention within the NASA program has focused on studies of the possibilities of improving stall/spin resistance through wing design.

Wing leading-edge modifications such as slats have long been recognized as an approach to improve the aerodynamic damping in roll of wings near the stall; however, many of the past concepts proved unfeasible for applications to general aviation airplanes because of degradation in aerodynamic performance, complexity and cost. In addition, experience has shown that although certain types of leading-edge modifications may improve maximum lift and result in more gentle stall characteristics, such modifications may aggravate or severely degrade the resistance of the airplane to spin and may result in more critical spin and spin recovery characteristics.

Recently, the potential benefits of leading-edge modifications on lateral stability at the stall were reexamined by the University of Michigan and the NASA Ames Research Center (reference 6). The results of that program, which consisted of static wind-tunnel tests and theoretical aerodynamic studies, indicated the possibility of achieving a flat-top lift curve for a wing with segmented leading-edge airfoil modifications. Such a characteristic would be expected to result in improved lateral stability at stall. These results encouraged further exploratory studies by the NASA Langley Research Center, which employs a wide variety of unique test technique to study the stalling and spinning motions of airplanes.

The present paper discusses the results of an exploratory study of the effects of leading-edge modifications on the stalling and spinning characteristics of a low-wing general aviation research airplane configuration. The study included static wind-tunnel tests, dynamic wind-tunnel tests, radio-controlled model tests, and airplane flight tests (references 7, 8, and 9).

#### Airplane Configuration

The basic airplane configuration used for the wind tunnel and flight tests is shown in figure 3. The wing airfoil of the basic airplane was a NACA 642-415 section with under-surface modifications near the trailing edge. This airfoil is characterized by a near-symmetric leading edge with a small leading-edge radius.

As shown in figure 4, the leading-edge modification studied consisted of a "drooped" nose section which employed a larger leading-edge radius and introduced additional nose camber to the airfoil. The airfoil modification was tested for several spanwise segments, with and without discontinuities.

#### Static Force Tests

The objective of the research project was to arrive at suitable wing leading-edge modifications which promised to eliminate or delay autorotation in roll without incurring severe penalties in aerodynamic drag or mechanical complexity. As a first step toward the accomplishment of this objective, low-speed ( $RN = 0.3 \times 10^6$ ) tests were conducted with the 1/5-scale model shown in figure 5 and the lift characteristics were analyzed using the well-known correlation of autorotation and negative lift curve slope.

Typical longitudinal results from the static tests are given in figure 6. The data show the variation of  $C_L$  with  $\alpha$  for the basic model, the model with full-span droop, and for a segmented leading-edge droop configuration. For the basic wing, the data indicate a stall angle of attack of about  $10^\circ$  followed by a large negative lift-curve slope from  $\alpha = 10^\circ$  to  $\alpha = 150^\circ$ . Such a negative slope is indicative of an autorotative tendency or unstable roll damping. With the addition of full-span droop, the stall angle of attack and  $C_{L_{max}}$  were increased, as expected. Again at the stall, a negative lift-curve slope was

exhibited with a potential for autorotation in the range  $\alpha = 120^\circ$  to  $\alpha = 170^\circ$ . When a portion of the leading-edge droop was removed, the data obtained for the resulting segmented configuration indicated a primary and secondary stall, or a "double-peaked" lift-curve. The primary stall occurred near a lift coefficient of 1.1, followed by a positive lift-curve slope to a secondary stall at  $\alpha = 300^\circ$ .

The significance of the results obtained with the segmented leading-edge configuration is that the data suggested a delay of any significant autorotational tendency to an angle of attack of  $300^\circ$ , which is approximately  $20^\circ$  higher than that for either the basic or full-span droop wings. Thus, roll instability could possibly be removed from the trimmable flight envelope of the airplane. With the double-peaked lift curve, the initial stall buffet might serve as a stall warning. If sufficient control is available to trim the airplane to higher angles of attack, the positive lift-curve slope that follows the initial stall indicates the aerodynamic damping in roll would remain stable and maintain lateral stability, thereby preventing autorotation which might cause an inadvertent spin entry.

#### Forced Oscillation Tests

Although the static tests strongly suggested beneficial effects of wing modifications on autorotational tendencies, dynamic force tests were required to verify the hypothesis. An assessment of the potential autorotational tendencies for several of the configurations was afforded by forced-oscillation tests using a 1/3-scale model, shown in figure 7, in the 9-by-18m (30-by-60 ft.) test section of the Langley Full Scale Wind Tunnel. These tests, designed to measure aerodynamic damping in roll were conducted using the test set-up illustrated in figure 8. The oscillatory output signals of an internal strain-gage balance were used to compute the damping and cross derivatives due to rolling for the angles of attack, oscillation frequencies, and roll amplitudes tested. Additional information regarding this dynamic testing technique is presented in reference 10. The Reynolds number based on the mean aerodynamic chord of the wing was  $0.55 \times 10^6$ .

The results of forced-oscillation tests for the model in the basic and segmented-wing configurations are shown in figure 9. The aerodynamic damping in roll  $C_{x_p} + C_{x_B} \sin \alpha$  for the basic model became positive (unstable) at and beyond the stall angle of attack, indicative of the onset of autorotation.

When the segmented leading-edge modification was added to the model, the roll damping was maintained to almost  $\alpha = 30^\circ$ , as would be expected based on the preceding static-force data. The correlation between the dynamic measurements and the trends expected from the static data is extremely good. For example, with the segmented leading-edge, the damping in roll decreases near the primary stall, then increased as the lift-curve slope increases toward the secondary stall at  $\alpha = 30^\circ$ . Finally, after the secondary stall, the roll damping becomes positive (unstable), as expected from the negative lift-curve slope. Based on the results, the model with segmented leading-edge flaps would not be expected to autorotate for angles of attack up to about  $\alpha = 30^\circ$ , in contrast to the basic configuration, which should enter autorotation near  $\alpha = 14^\circ$ , where the roll damping becomes positive.

#### Rotary-Spin Balance Tests

The small perturbation derivatives measured in the forced-oscillation tests are useful in analyzing autorotational tendencies; however, a valid representation of the autorotative moments acting on an airplane during spin entry requires special analysis because of extensive nonlinear variations of rolling moments with rate of roll at post-stall angles of attack. In order to obtain such data for the modified wing, rotary-balance tests were conducted using the method described in reference 4. In these tests the model was mounted as shown in figure 10 on a rotating sting in the vertically-rising airstream of the Langley Spin Tunnel. The model's attitude and rotation rate were varied to permit an evaluation of the damping or autorotative nature of the aerodynamic moments for angles of attack from  $80^\circ$  to  $35^\circ$  at a Reynolds number of  $0.13 \times 10^6$  based on the mean aerodynamic chord of the wing.

Earlier static-force tests had indicated that several leading-edge modifications should be included in these tests because of beneficial (or degrading) effects expected on autorotational stability. The primary configurations of interest, which were then subjected to rotary-spin balance tests and flight tests, are shown in figure 11.

The pertinent results of the rotary tests are shown in figure 12 in terms of the variations of rolling moment  $C_g$  with nondimensional rate of rotation  $\frac{\Omega b}{2V}$  for the various wing configurations. Positive values of  $C_g$

produced by positive  $\frac{\Omega b}{2V}$  are propelling, hence, unstable, while negative values are stable. At  $\alpha = 80^\circ$ ,

the data show that all the wing configurations produced stable variations of  $C_g$  with  $\frac{\Omega b}{2V}$ . At  $\alpha = 16^\circ$ ,

however, the basic wing has stalled and autorotative moments are produced. The wing with full-span droop also exhibits autorotative properties, but to an even greater degree than the basic wing. In contrast to the basic and full-span droop wing, the wing with the outboard droop exhibits favorable aerodynamic damping. Of particular interest is the data for the outer droop with fairing, which indicates that the fairing eliminated the beneficial effect of the outer droop. With the fairing, the variation in  $C_g$  with  $\frac{\Omega b}{2V}$  was similar to that for the full-span droop configuration. Thus, the abrupt discontinuity at the inboard end of the outer droop panel appeared to be critical to the autorotative resistance of the modified wing.

#### Radio Controlled Model Tests

Aerodynamic damping in roll is, of course, only one parameter affecting the spinning characteristics of airplanes. Therefore, in order to evaluate the significance of the wind-tunnel studies stalling and spinning tests were conducted with a powered 1/5-scale radio-controlled model to determine the effects of various full-span, partial-span, and segmented leading-edge configurations. The model was geometrically similar to the model used for the static force tests, and dynamically similar to a full-scale airplane weighing 6672 N (1500 lbs.) flying at an altitude of 1980 m (6500 ft.). A photograph of the model and test crew is shown in figure 13. The model was equipped with a 1.5 horsepower engine, an emergency spin-recovery parachute, and a seven channel proportional control system.

The results obtained for the radio-controlled model with the various wing leading-edge modifications may be summarized as follows: When a 1-g wings-level stall (neutral ailerons and rudder) was attempted for the basic configuration, the model would roll abruptly to the right or left at the stall and enter a steep spin. On some occasions the model exhibited several cycles of "wing rock" (lateral oscillations) at the stall. The roll-off encountered at stall always occurred before full trailing-edge up travel was reached on the elevator. The rudder was maintained neutral during the steep spin which ensued following the roll off, and recovery was quickly effected by neutralizing the elevator.

When six-turn spins were attempted with neutral ailerons, a moderately flat spin was always obtained regardless of entry technique. Recovery was obtained in about one turn by simultaneously reversing the rudder to against the spin and neutralizing the elevator. However, using a unique control technique developed during subsequent airplane flight tests, the spin was aggravated and the model driven into an unrecoverable flat spin mode requiring the use of the emergency spin recovery parachute. This technique was as follows: Three turns with normal prospin controls (allowing the steeper spin to become fairly well stabilized), two turns with full forward stick, maintaining prospin rudder (almost doubling the turn rate because of gyroscopic precession moments created by the elevator input), stick aft for one turn (flattening the spin and converting roll to yaw), then neutral elevator.

The most impressive results were obtained for the configuration whereby the outboard section of the basic wing was changed to a modified outboard leading-edge (MOLE) configuration. When a 1-g wings-level stall was attempted with idle power, this configuration generally exhibited a slight amount of wing rock upon reaching what appeared to be the primary stall discussed in the wind-tunnel section of this paper. This stall was reached with less than full-up elevator. When the elevator was moved to the full-up position, the model exhibited no tendency to roll off, and it could be flown for extended periods of time with the elevators held full-up. The model was observed to be quite stable laterally, and flying at an extremely high angle of attack.

When spins were attempted for this configuration, with the ailerons neutral, the model did not enter the moderately flat spin as was the case for the basic configuration. Instead, the model entered what appeared to be a steep spiral or extremely steep spin with a rotation rate of about 90 degrees per second (4 seconds per turn). Rapid recoveries were obtained from such motions by neutralizing either rudder or elevator. Spins attempted with ailerons held against the spin produced similar results, with the model always entering the steep, slow rotating motion and immediate recoveries upon neutralization of either rudder or elevators.

The foregoing results obtained with this modified outboard leading-edge configuration were considered to be extremely significant in that the overall resistance of the model to spin--either moderately flat or flat--was markedly improved, as was suggested by the previously discussed wind-tunnel results. Subsequent flights with the model indicated that numerous aerobatic maneuvers, aggravated control inputs at stall, and aborted maneuvers could be flown without roll-off or inadvertent spins.

Additional tests were conducted to determine the sensitivity of the foregoing results to the geometry of the outer wing droop modification. As part of the study, the notch generated at the inner edge of the MOLE was eliminated by a modification which faired it into the leading edge of the basic wing (figure 11). Results obtained during stalls and spins with neutral ailerons for this modification were similar to those obtained with the MOLE, including stable stalls with full-up elevators and spiral motion obtained during deliberate spins. However, when spins were attempted with ailerons against the spin, the spin resistance was extremely poor. During a right spin attempt, a moderately flat spin was obtained. Recovery was obtained in 4 turns by full rudder reversal, movement of the elevators to neutral, and the ailerons to neutral. For left spin attempts, the model went flat and the recovery controls were ineffective. The spin was terminated by the emergency recovery parachute. The spin entry and spin resistance characteristics with MOLE-F were obviously degraded from the MOLE configuration. These results are in agreement with trends indicated by the rotary balance data presented in figure 12..

The results of the tests conducted with full-span leading-edge droop indicated that the stalling characteristics of the model were somewhat enhanced, but the resistance of the model to enter the flat spin was significantly degraded. During 1-g and accelerated stalls, the model exhibited similar characteristics to the basic configuration; that is, a tendency to roll off before full trailing-edge up elevator deflection was obtained. However, the model could be flown to noticeably higher angles of attack and lower speeds, as would be expected.

When spins were attempted with neutral ailerons, the model entered a moderately flat spin which appeared to be flatter than the moderate spin exhibited by the basic configuration; however, the model did not enter the flat spin, as was also the case for the basic configuration.

When spins were attempted with the ailerons deflected against the spin, the resistance of the model to enter the flat spin was obviously degraded. The model could be flown into the flat spin within three turns following application of prospin controls (back stick, rudder with the spin, ailerons against the spin). Thus, the resistance of the model to enter the flat spin was significantly less than that for the basic model, and the flat spin could be obtained on virtually every flight if such prospin controls were maintained beyond three turns after stall.

#### Airplane Flight Tests

With the promising wind-tunnel data verified by sub-scale flight tests, the study proceeded to full-scale flight tests to address questions regarding scale effects. Full-scale flight tests were conducted with the airplane shown in figure 14. The tests included powered and unpowered stalls, and spins which were entered by slowly decelerating, at idle power, to a 1-g wings level stall at which time prospin controls were abruptly applied. A variety of prospin controls were investigated, both to the right and left for 1-, 3-, and 6-turn spins. Various recovery control techniques were also employed.

#### Stalls

The basic aircraft had a roll-off tendency beyond the stall, with partial or full-up elevator control input. The full-up elevator could not be held for more than a few seconds without experiencing a roll-off that would, in most cases, lead to an incipient spin. The motion was apparently the result of the unstable roll damping associated with angles of attack above that for maximum lift. Pilot commentary indicated that a wings level condition could be maintained providing sufficient control power (moment) was available and the pilot kept ahead or at least stayed with the aircraft motions. Control could be maintained with the use of rudders; however, due to dihedral effect, a pilot-induced oscillation often resulted, causing the aircraft behavior to be marginal at best. The airplane's stall behavior with the full-span drooped wing was comparable to that with the basic wing.

The aircraft's stall characteristics with the modified outboard wing panel were greatly improved. No roll-off tendency was noted throughout the period that the elevator control was held fullup. A slight wing rock developed, but the bank angle never exceeded 30°. Pilot commentary was highly favorable regarding the aircraft's behavior with the wing modification versus the basic configuration. Though no performance tests were conducted, a qualitative assessment of the climb time, operating speeds, along with pilot commentary, indicated no degradation in performance. Also, for the limited number of flight tests conducted with the fairing added at the juncture of the modified and basic airfoils, stall characteristics were the same as those with the MOLE having the sharp discontinuity.

#### Spins

The moderately flat spin mode of the basic configuration was characterized by an angle of attack of 50° to 52°, a slow rate of descent 32 to 38 m/sec (105 to 125 ft./sec.) and a turn rate of 150 to 157 degrees

per second (2.3 to 2.4 seconds per turn). The airplane also exhibited a flat spin mode, characterized by an angle of attack of  $70^\circ$ , a rate of descent of about  $27 \text{ m/sec}$  ( $90 \text{ ft/sec}$ ), and a turn rate of 200 degrees per second (1.8 seconds per turn).

The spin with the MOLE wing was characterized by an angle of attack of approximately  $28^\circ$ , a turn rate of about 100 degrees per second (3.5 seconds per turn) and a high rate of descent. This motion was the same regardless of the type of spin entry attempted and required about 2 or 3 turns to achieve steady state conditions. The airplane also displayed a tendency to slice through or a hesitancy to enter the first turn, and exhibited a quick recovery tendency regardless of the recovery control technique employed. In fact, pilot observations indicated that simply relaxing pressure on any control effected recovery immediately.

The spin characteristics associated with the full-span droop leading-edge wing were severely degraded. Regardless of the prospin controls employed, the only result was a flat spin which necessitated, at times, the use of the spin recovery parachute. This flat spin mode was characterized by an angle of attack of  $60^\circ$  to  $70^\circ$  and a turn rate of 164 to 200 degrees per second (1.8 to 2.2 seconds per turn), which are comparable to the flat spin results achieved with the basic wing.

The addition of the leading-edge fairing degraded the spin behavior. Specifically, for the entry condition employing ailerons against the spin, a flat ( $\alpha = 74^\circ$ ) spin developed which could not be arrested with the use of normal recovery controls. The spin-recovery parachute was deployed to recover the aircraft from the flat-spin. The pilot did indicate that this particular flat spin was quite powerful, and was worse than the flat spin associated with the basic configuration. It should be noted that for the modified configuration with the fairing, the spin was going flat after one turn, whereas the basic aircraft configuration had to be driven into a flat spin. Eliminating the abrupt airfoil discontinuity as characterized with the modified outboard panel, also eliminated the attendant spin resistance, as predicted by the rotary balance results and radio-controlled model results.

#### Correlation With Model Results

An important area of interest is the comparison of the airplane flight results to those data obtained with wind-tunnel and radio-controlled models. The marked improvement in the aircraft stall and spin behavior with the modified wing agrees well with the model results. Also, the flight data has substantiated the flight characteristics predicted by the radio-controlled model tests conducted with corresponding configurations. In fact, the stall and spin characteristics of the radio-controlled model for the full-span droop and the modified outboard leading ledge (with and without the tapered fairing at the inboard juncture) were practically identical to the full-scale results. Furthermore, though it is recognized that Reynolds number greatly affects the values of maximum lift coefficient and the shape of the lift curve at and beyond stall, it is significant that all analyses leading up to the full-scale airplane flight testing were accomplished with data based on low Reynolds number.

#### Full-Scale Model Tests

Subsequent to the airplane flight tests, a full-scale model of the airplane configuration was tested to obtain detailed aerodynamic information at full-scale values of Reynolds number. A photograph of the model mounted in the Langley Full-Scale Tunnel is shown in figure 15 and the location of unique instrumentation used in the study is shown in figure 16. In addition to recording the overall aerodynamic forces and moments of the aircraft on the full-scale tunnel balance system, the aircraft was modified to include a wing balance to record the forces and moment on the outer-wing panel independent of the tunnel scale system. The model was provided with several spanwise rows of wing pressure ports to provide chord-wise pressure measurements for most of the tests. Also, the investigation included flow surveys, and flow-visualization studies utilizing surface tufts, a tuft grid, and smoke. In addition, oil flow studies were conducted on a 1/3-scale model at the University of Maryland's Glenn L. Martin Wind Tunnel to supplement the flow-visualization studies in the Langley Full-Scale Wind Tunnel.

Presented in figure 17 are the aerodynamic characteristics of the airplane for the four leading-edge configurations illustrated in figure 11. Lift and drag coefficient data are presented as a function of angle of attack for the complete airplane on the left side of the figure. On the right side of the figure, the resultant-force coefficient,  $C_R$ , for the outer-wing panel is presented as a function of angle of attack. The wing-tip balance data are included in the data plots because the wing tip aerodynamics on unswept wings are believed to be closely related to the damping or autorotation tendencies exhibited by the wing. Previous research has indicated that autorotation is encountered when the variation of the resultant-force coefficient of the wing with angle of attack becomes negative; that is when  $\partial C_R / \partial \alpha < 0$ . In the case of the subject configurations, the slope of the resultant-force coefficient with  $\alpha$  of the wing tip provided good predictions of autorotation tendencies.

The data of figure 17 show that the aerodynamic characteristics of the complete airplane configuration at high angles of attack were generally determined by the aerodynamics of the outer-wing panels. This result is not surprising since unswept, untapered wings tend to stall first on the inboard portion of the wing while the tips maintain lift up to the main stall angle of attack. The data show that the basic wing tip stalled abruptly at an angle of attack of about  $200^\circ$ , and the lift dropped rapidly at higher angles of attack. The addition of the outboard droop is shown to eliminate the abrupt stall of the wing tip and to maintain or increase lift up to  $\alpha = 40^\circ$ . This change in slope of the resultant-force coefficient with  $\alpha$  from negative to positive values at the higher angles of attack is believed to be important for eliminating autorotation and for providing spin resistance. It is interesting to note that the addition of the fairing to the outboard droop, or the addition of full-span leading-edge droop reintroduced abrupt stall and caused the slope of the resultant-force coefficient curve with  $\alpha$  to become very negative at high angles of attack.

As noted in flight tests, the outboard-droop arrangement was very spin resistant, whereas the basic configurations showed a flat-spin mode. The airplane with the fairing added to the outboard-droop

configuration or with the full-span droop arrangement also exhibited a flat-spin mode. Correlation of the values of  $\partial C_R / \partial \alpha$  for the four basic test configurations with the airplane flight-test results can be made on the basis of the data of figure 18. The data of figure 18 show values of  $\partial C_R / \partial \alpha$  plotted against angle of attack which predict autorotation for all configurations except the outboard-droop configuration. It is interesting to note that all the leading-edge modifications extended the angle of attack at which  $\partial C_R / \partial \alpha$  became zero, but apparently the longitudinal-control effectiveness was great enough to drive the airplane to angles of attack where only the outboard-droop arrangement could provide attached flow on the wing tips in flight.

A plot showing the autorotational stability derivative  $\partial C_R / \partial \alpha$  plotted against the semi-span location of the inboard discontinuity of various partial span arrangements is shown in figure 19. The values of  $\partial C_R / \partial \alpha$  in figure 19 are presented for angles of attack of  $20^\circ$  to  $40^\circ$  together with results of flight tests which define boundaries of spanwise effectiveness of the outboard leading-edge droop for preventing the airplane from entering the moderately flat or flat spin modes. The flight data show that the outboard leading-edge droop was effective for providing resistance to spinning when the inboard discontinuity was located between the semi-span stations of 35- and 67-percent. The force-test data indicate fairly good qualitative agreement with the flight data, based on the autorotation stability criterion that autorotation is encountered when  $\partial C_R / \partial \alpha < 0$ . The original outboard droop arrangement (discontinuity at 57-percent semi-span) is seen to provide stabilizing tendencies over the test angle-of-attack range; but shortening the droop is seen to produce unstable values of  $\partial C_R / \partial \alpha$  at semi-span stations corresponding very closely to those identified in flight tests for loss of droop effectiveness. At the inboard flight-test boundary for droop effectiveness, the wind-tunnel data show that large negative values of  $\partial C_R / \partial \alpha$  can be encountered for angles of attack above  $30^\circ$ . Apparently, angles of attack of  $30^\circ$  or above can be induced at the wing tips under rotational conditions.

Photographs of oil-flow studies of the model as a function of angle of attack for the basic and outboard-droop configurations showed a classical trailing-edge root stall which progressed forward and outward to form a large flow-separation region as the angle of attack was increased. The photographs also showed that the outboard-droop configuration tended to keep the outer-wing panel flow attached to very high angles of attack by stabilizing the separated flow region inboard to prevent flow separation from progressing to the outer-wing panel. Photographs at  $\alpha = 20^\circ$  are presented for both configurations in figure 20. From the photograph at the top of figure 20 it is clearly evident that the separated flow over the wing has an outward flow direction toward the wing tips—a result which appears very similar to that for swept wings at high angles of attack. A close examination of the flow pattern for the modified wing at the bottom of figure 20 shows vortex flow emanating from the inboard edge of the droop in a direction to oppose the outward progression of the separated flow region. The nature of the flow at the inboard edge of the droop indicates that the effectiveness of the outboard leading-edge droop in maintaining attached flow at the wing tips was the result of the vortex flow. The vortex flow apparently acted as an aerodynamic fence to turn the outward spanwise flow in a rearward direction and effectively block the progression of the separated flow region toward the outer-wing panel. The attached flow at the outer wing panels was maintained to a very high angle of attack, in a manner generally similar to that of a low-aspect ratio wing.

#### SUMMARY

In summary, this study of wing leading-edge effects on stalling and spinning characteristics serves to illustrate an important area of application of dynamic stability parameters within high- $\alpha$  technology. The guidance provided by forced-oscillation and rotary-spin balance tests was invaluable, providing a significant insight as to configurational effects and physical phenomena. Particularly valuable was the success of relating static aerodynamic characteristics to dynamic stability parameters and spin resistance.

Many other examples of applications of dynamic parameters can be cited; particularly with regard to "wing rock" studies and control system design for military aircraft. The reader is referred to the literature for a review of current technology, which impresses one with the vast knowledge to be gained in this technical field.

#### RESEARCH REQUIREMENTS

It is the opinion of the authors that the current renewal of interest in dynamic stability parameters at high angles of attack has highlighted our lack of knowledge and understanding of many important aspects of dynamic parameters. Throughout the present lecture series, various presentations have been made illustrating the progress underway in many areas; however, a considerable amount of fundamental research is still required in order to advance the state of the art. Some of the most urgent research requirements are listed in figure 21.

From an aircraft designer's point of view, one of the most serious deficiencies in the existing technology is the lack of rapid, valid estimation methods for predicting dynamic stability parameters at high angles of attack for current configurations. As a result of this shortcoming, many airplane development programs encounter problems related to dynamic parameters extremely late in the development cycle, when airframe modifications or control system "fixes" are difficult to incorporate into the design. The research required to develop such methods will involve extensive wind-tunnel studies of the effects of configuration variables and aerodynamic phenomena. Hopefully, the experimental data base could be coupled with theoretical or semi-empirical methods and perhaps related to variations of static aerodynamic characteristics.

Currently, our understanding of the effects of Mach and Reynolds number on dynamic stability parameters at high angles of attack is extremely limited due to the lack of adequate wind-tunnel test capabilities. For example, at the present time, most transonic and supersonic wind tunnels are not equipped to permit tests over the large ranges of  $\alpha$  and  $\beta$  required for high  $\alpha$  analysis. As a result, many fighter development programs are conducted with insufficient information on the potential effects of Mach number

on stability derivatives, departure characteristics, or gain-scheduling requirements for automatic control systems. Flight experience at high angles of attack has continually shown significant variations with Mach number of the onset angle of attack for many important aerodynamic and motion phenomena. Future efforts should be directed at increasing static and dynamic wind-tunnel test capability (particularly at transonic speeds), including basic research involving airframe component build-up tests to accumulate fundamental information on Mach effects for current fighters.

As pointed out in this lecture series, the measurement and evaluation of  $\beta$  and cross-coupling derivatives for current aircraft configurations are of particular significance. Research required in this area includes measurement of  $\beta$  derivatives for current fighters which employ vortex lift at high  $\alpha$ ; measurement of cross-coupling derivatives during oscillating and steady rolling motions; and piloted simulator studies of the effects of these derivatives on handling qualities and departure prevention.

More effort is needed in the important area of wind-tunnel/flight correlation in order to ensure the adequacy of predictive methods and ground-based facilities. Particular attention is required in the areas of flight test instrumentation and maneuvers; and the continued refinement of parameter extraction techniques for the complex environment of flight at high angles of attack.

In general, experience has shown that mathematical methods for predicting aircraft motions at or near stall departure and in the fully-developed spin are in a satisfactory status. However, calculations of aircraft motions from departure through spin entry to the fully developed spin are questionable due to the combined large-amplitude oscillatory and rotary motions experienced. Mathematical models of the aerodynamic phenomena encountered during such motions do not exist, and combined rotary and forced oscillation wind-tunnel test methods could provide a better understanding of these modeling problems.

Finally, as discussed in another lecture of this series, wind-tunnel facilities must be developed to permit interference-free measurements of dynamic stability parameters over a large range of angle of attack and sideslip. Current experimental test rigs tend to be massive, with large flow obstructions near or above the model. These obstructions cause artificial pressure fields resulting in premature vortex bursting and erroneous measurements. The development of support-free magnetic suspension techniques for high- $\alpha$  dynamic testing is therefore of particular interest.

#### CONCLUDING REMARKS

The high level of international interest in dynamic stability parameters has stimulated many new and exciting research activities. Much information is now being generated for civil and military airplane configurations, and the potential for significant advances in the technology exists. It is imperative that such efforts continue if design and analysis methods are to keep up with the rapid advances in overall design technology.

#### REFERENCES

1. Skow, A. M.; and Titiriga, A., Jr.: A Survey of Analytical and Experimental Techniques to Predict Aircraft Dynamic Characteristics at High Angles of Attack. AGARD CP-235, Dynamic Stability Parameters, pp 19-1 to 19-37, May 1978.
2. AGARD Advisory Report No. 155A: Manoeuvre Limitations of Combat Aircraft. Papers prepared by a Working Group Sponsored by the Flight Mechanics Panel of AGARD, August 1979.
3. Bazzocchi, Dr. Ing. Ermanno: Stall Behavior and Spin Estimation Methods by Use of Rotating Balance Measurements. AGARD CP-199, Stall/Spin Problems of Military Aircraft, pp 8-1 to 8-16, November 1975.
4. Bahrle, William Jr.; and Bowman, James S., Jr.: The Influence of Wing Fuselage and Tail Design on Rotational Flow Aerodynamic Data Obtained Beyond Maximum Lift with General Aviation Configurations. AIAA Paper 80-0455, March 1980.
5. Malcolm, G. N.; and Davis, S. S.: New NASA-Ames Wind-Tunnel Techniques for Studying Airplane Spin and Two-Dimensional Unsteady Aerodynamics. AGARD CP-235, Dynamic Stability Parameters, pp 3-1 to 3-12, May 1978.
6. Feistel, T. W.; Anderson, S. B.; and Kroeger, R. A.: A Method for Localizing Wing Flow Separation at Stall to Alleviate Spin Entry Tendencies. AIAA Paper 78-1476, August 1978.
7. Staff of Langley Research Center: Exploratory Study of the Effects of Wing Leading-Edge Modifications on the Stall/Spin Behavior of a Light General Aviation Airplane. NASA TP-1589, December 1979.
8. DiCarlo, D. J.; Stough, H. P.; and Patton, J. M., Jr.: Effects of Spanwise Location of a Discontinuous Drooped Wing Leading-edge Modifications on the Spinning Characteristics of a Low-Wing General Aviation Airplane. AIAA Paper 80-1843, August 1980.
9. Johnson, J. L., Jr.; Newsam, W. A.; and Satran, D. R.: Full-Scale Wind-Tunnel Investigation of the Effects of Wing Leading-Edge Modifications on the High Angle-of-Attack Aerodynamic Characteristics of a Low-Wing General Aviation Airplane. AIAA Paper 80-1844, August 1980.
10. Orlitz-Ruckemann, K. J.: Techniques for Dynamic Stability Testing in Wind Tunnels. AGARD CR-235, Dynamic Stability Parameters, pp 1-1 to 1-24, May 1978.

- EXTENSIVELY RESEARCHED FIELD, PARTICULARLY DURING 1940's AND 50's
- ESTIMATION METHODS AND STABILITY ANALYSIS OF CONVENTIONAL DESIGNS NOW TEXT-BOOK MATERIAL
- WIDE SELECTION OF COMPUTER CODES AVAILABLE FOR ATTACHED-FLOW CONDITIONS
- RENEWED INTEREST IN HIGH- $\alpha$  FLIGHT, SEPARATED FLOWS, AND CLOSE-COUPLED DESIGNS REQUIRES NEW METHODS

Figure 1.- Current status of technology in application of dynamic-stability parameters to aircraft problems.

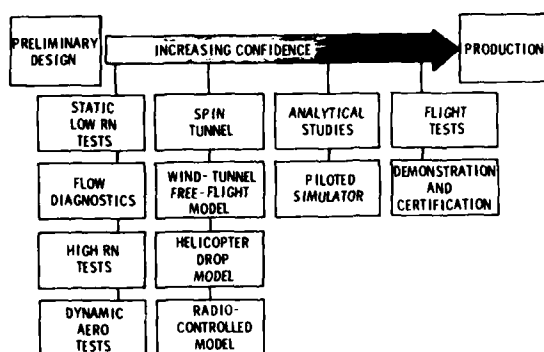


Figure 2.- Method of approach for the prediction and analysis of high- $\alpha$  characteristics.

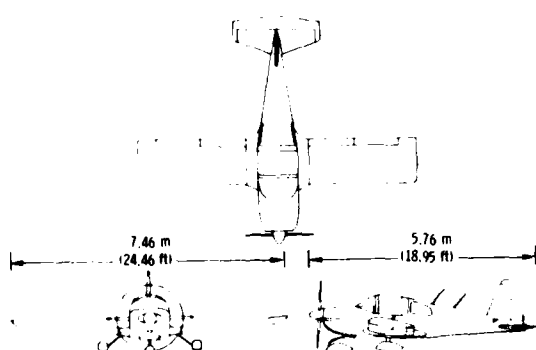


Figure 3.- Three-view drawing of research airplane configuration.

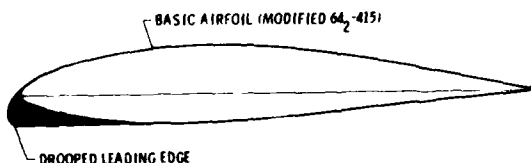


Figure 4.- Wing leading-edge droop modification used in the investigations.

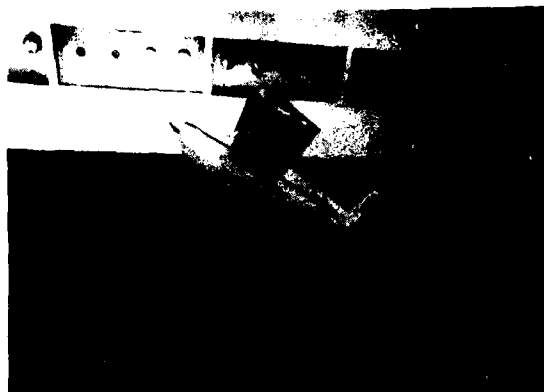


Figure 5.- Photograph of 1/5-scale model used in exploratory static force tests.

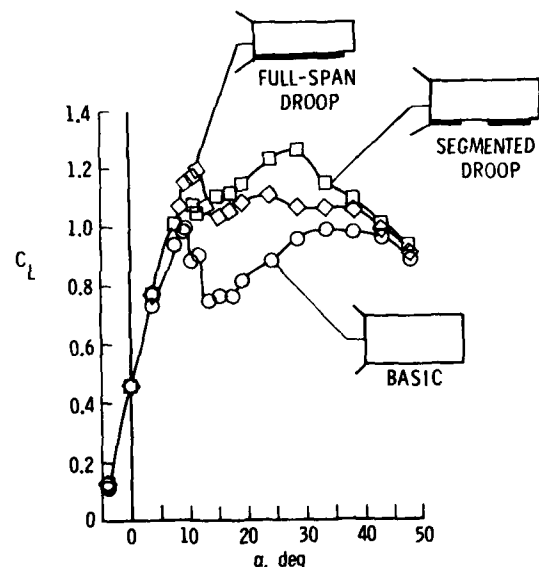


Figure 6.- Effects of wing modifications on lift.

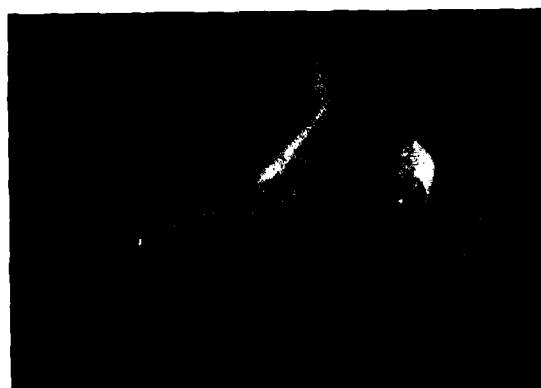


Figure 7.- Photograph of 1/3-scale model used in forced oscillation tests.

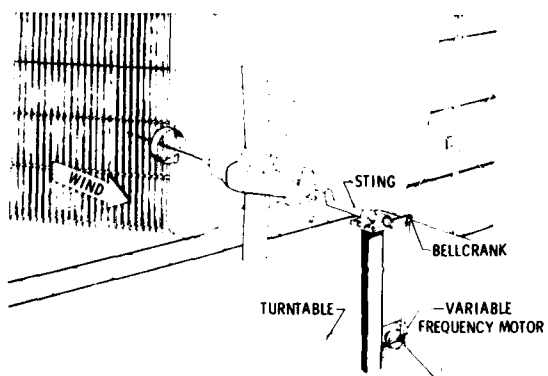


Figure 8.- Test setup for forced oscillation tests.

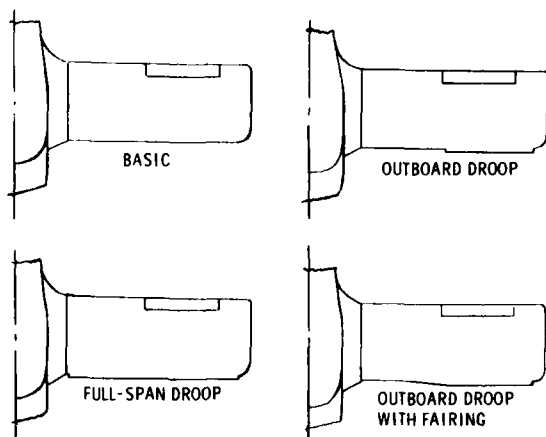


Figure 11.- Wing configurations investigated in wind-tunnel and flight.

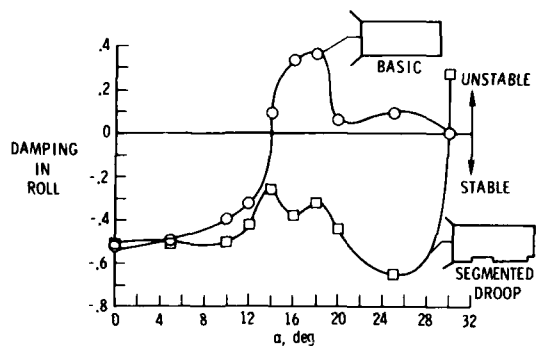


Figure 9.- Effect of wing modification on damping in roll.

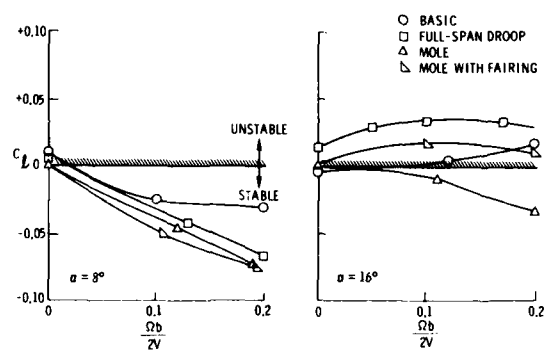


Figure 12.- Effect of wing modifications on rotary-spin balance data.

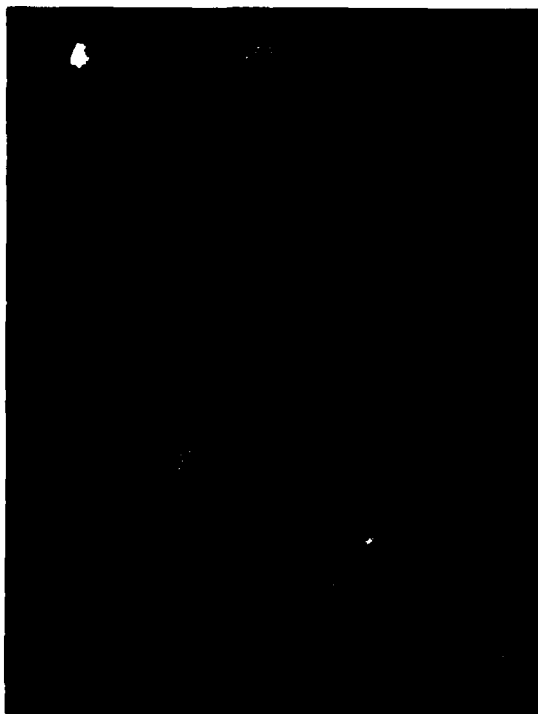


Figure 10.- Photograph of 1/5-scale model installed on rotary balance apparatus.



Figure 13.- Radio-controlled model and test crew.



Figure 14.- Spin research airplane.

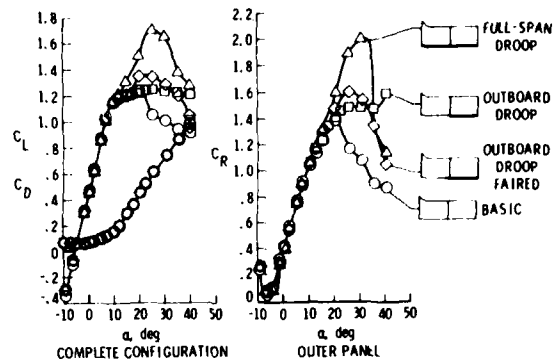


Figure 17.- Aerodynamic characteristics of the model with several leading-edge modifications.

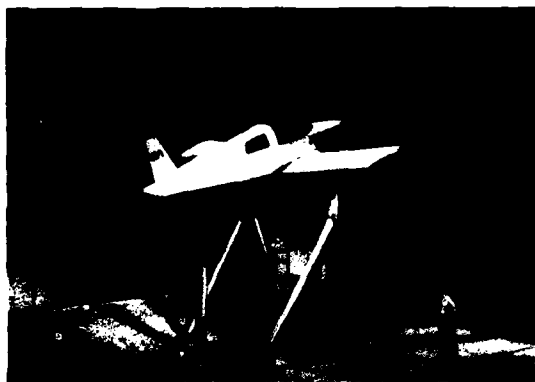


Figure 15.- Full-scale model mounted in the Langley 30-by 60-Foot Wind Tunnel.

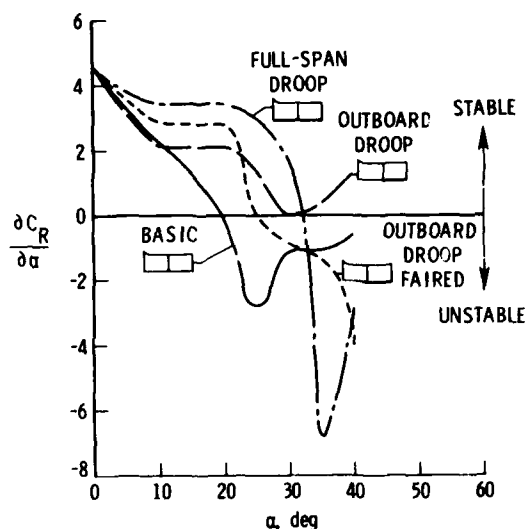


Figure 18.- Effect of wing modifications on auto-rotational stability parameter.

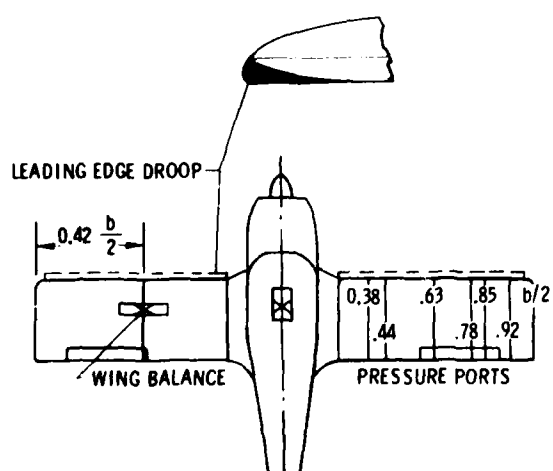


Figure 16.- Wing balance and pressure port locations used in full-scale force test investigation.

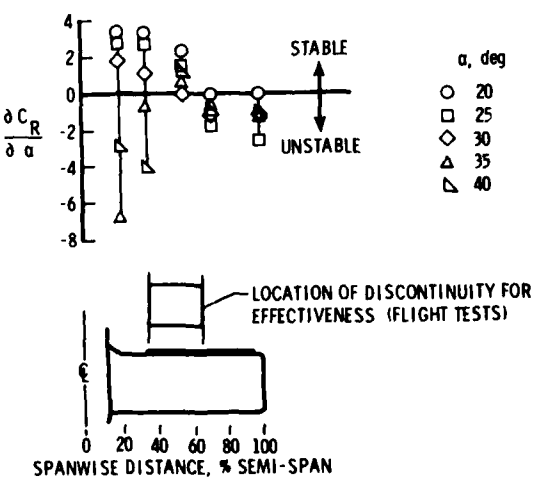


Figure 19.- Effect of spanwise location of leading-edge droop discontinuity on auto-rotational stability parameter.

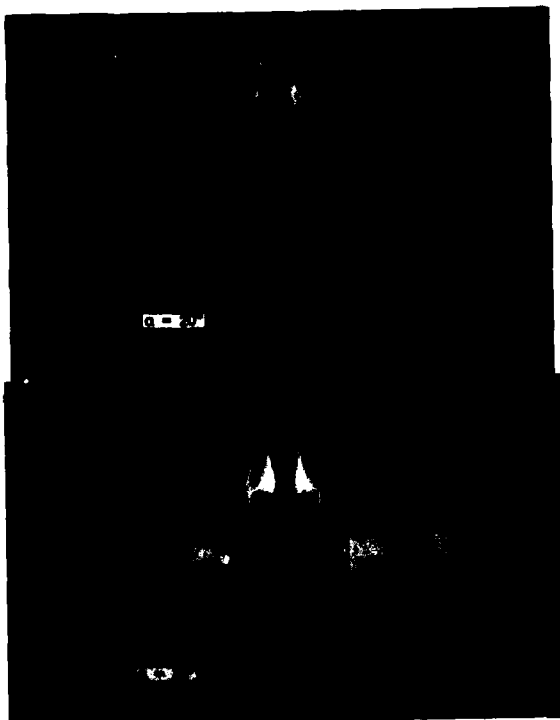


Figure 20.- Photographs of oil-flow studies of basic and modified leading-edge configurations.  
 $\alpha = 20^\circ$ .

- ESTIMATION METHODS FOR CURRENT CONFIGURATIONS
- EFFECTS OF MACH AND RN
- MEASUREMENT AND EVALUATION OF  $\delta$  AND CROSS-COUPLING DERIVATIVES
- WIND-TUNNEL/FLIGHT CORRELATION
- COMBINED ROTARY AND OSCILLATORY DATA
- INTERFERENCE-FREE TESTS (MAGNETIC SUSPENSION)

Figure 21.- Current research needs for dynamic stability parameters.

## APPLICATION TO MISSILE DYNAMICS

by

C.P. Schneider

Messerschmitt-Bölkow-Blohm GmbH

Munich

## SUMMARY

Generally, in theoretical dynamics, the missile motion is described in six degrees of freedom. The corresponding system of equations of motion contains as external forces lift, drag and side force besides motor thrust and gravity, and as external moments the moments of pitch, yaw and roll. Forces and moments - which are dependent on flight conditions such as angles of attack, yaw, and roll, flight speed, acceleration and the angular velocities of pitch, yaw and roll - may be given as partial derivatives of these variables. In case of non-linearity, higher order terms - and in case of unsteady flight conditions, time derivatives must be included.

In this lecture, the connexion between aerodynamic modelling and the equation of motions is explained. Simple missile motions are chosen to explain steady and dynamic stability. The influence of steady and dynamic (quasisteady) derivatives is estimated. From literature, examples for the simulation of complicated flight motions caused by non-linear unsteady forces and moments are selected and shown in diagrams.

## LIST OF SYMBOLS

$d, d_E$	distance between center of gravity of a gyroscope and the supporting point (section 3.2), distance between the nozzle exit area and the center of gravity of a missile (section 2.2)
$f_R, f_C$	resonance frequency, characteristic frequency (section 3)
$g$	gravitational constant
$h_{xg}, h_{yg}, h_{zg}$	components of the angular momentum in the direction of the geodetic axes (section 2.2)
$\hat{i}, \hat{j}, \hat{k}$	unit vectors of Q in the direction of the fixed-body axes (section 2.1)
$k, k'$	reduced frequency (Fig. 3.3)
$k_1, k_2, k_3$	auxiliary axes (Fig. 2.3)
$m$	mass
$n, n_\delta$	load factor, additional load factor due to flap deflection (section 3.1)
$p, q, r$	angular velocity components about the body-fixed axes x,y,z respectively (Fig. 2.2c)
$P_g, q_g, r_g$	angular velocity components about the earth-fixed or geodetic axes $x_g, y_g, z_g$ respectively
$s, s_w, \dot{s}$	roll stability condition of a ballistic missile, stability condition of a gravitational gyroscope, auxiliary parameter in the roll stability criterion (section 3.2, ref. 11)
$t, t_{1/2}$	time, half life time
$u, v, w$	translational velocity components in the direction of the body-fixed axes x,y,z respectively (Fig. 2.2a)
$u_g, v_g, w_g$	translational velocity components in the direction of the earth-fixed or geodetic axes $x_g, y_g, z_g$ respectively
$x, y, z$	axes in the body-fixed coordinate system (Fig. 2.2)
$x_a, y_a, z_a$	axes in the aerodynamic coordinate system (Fig. 2.4)
$x_g, y_g, z_g$	axes in the earth-fixed or geodetic coordinate system (Fig. 2.1)
$x_\delta$	distance between the center of flap lift force and center of gravity of the missile
$A, B$	damping constant, spring constant (section 3)
$A^*, B^*$	dimensionless damping constant and spring constant respectively
$A_z$	altitude
$C_0, C_1, C_2$	constants in the solution of equation of motion of a spring-mass-damper system
$C_D, C_L, C_N$	coefficients of drag, lift and normal force (Fig. 2.2a)
$C_x, C_y, C_z$	axial force coefficients in the body-fixed coordinate system (Figs. 2.2b, 2.4)
$C_{xa}, C_{ya}, C_{za}$	axial force coefficients in the aerodynamic coordinate system (Fig. 2.4)

$C_{Xg}$ , $C_{Yg}$ , $C_{Zg}$	axial force coefficients in the earth-fixed or geodetic coordinate system (Fig. 2.3)
$C_{Nn}$	non-linear normal force coefficient (section 2.3, Fig. 3.3)
$C_{1R}$	non-linear part of $C_{Nn}$
$C_{mn}$	non-linear pitching moment coefficient (Fig. 3.4)
$C_{mp\beta}$	derivative coefficient of Magnus moment
$C_{lp}$	derivative coefficient of the roll moment
$D$	diameter
$D_A$	damping factor
$I_{xg}$ , $I_{yg}$ , $I_{zg}$	moments of inertia in the direction of the geodetic axes (section 2.2)
$I_{xyg}$ , $I_{xzg}$ ....	products of inertia with respect to the geodetic coordinate system (section 2.2)
$K$	constant in the linear relationship between line of sight and yaw angle (Fig. 1.2)
$L$ , $M$ , $N$	moment components in the direction of the body-fixed axes
$L_g$ , $M_g$ , $N_g$	(fictitious) moment components in the direction of the earth-fixed or geodetic coordinate system (section 2.2)
$L_\alpha$ , $L_\delta$	lift force slope with $\alpha$ and with flap deflection $\delta$ respectively (section 3.1)
$M_\delta$	pitch stiffness with flap deflection $\delta$ (section 3.1)
$M_a$	Mach number
$P$	period of resonance cycle
$Q$ , $\tilde{Q}$	quaternion, complex conjugate of $\tilde{Q}$ (section 2.1, Fig. 2.5)
$S$	reference surface area
$V$	flight velocity
$W$	weight
$X$ , $Y$ , $Z$	force components in direction of the body-fixed axes, subscript a <sup>a</sup> aerodynamic, subscript g <sup>g</sup> geodetic, (Figs. 2.2b, 2.3, 2.4)
$\alpha$ , $\beta$	angles of attack with respect to the body-fixed axes (Fig. 2.2a)
$\gamma$	flight wind angle (Fig. 3.1)
$\delta$	individual control deflection (Fig. 2.2b)
$\xi_s$ , $\xi_i$	control signal, flap deflection angle (Fig. 1.2)
$n$ , $\xi$ , $\xi$	flap deflections (Fig. 2.2b)
$\lambda_0$	scalar of $Q$ (section 2.1)
$\lambda_1$ , $\lambda_2$ , $\lambda_3$	vector components of $Q$
$\lambda_I$ , $\lambda_{II}$	roots of the solution of the Laplace transformation of a spring-mass-damper eq. of motion (section 3)
$\lambda$ , $\sigma$	polar angles-of-attack (Fig. 2.2b)
$\rho$ , $\rho_M$	density, relative density $\rho_M = 2m / (\rho DS)$ , (section 3)
$\sigma_l$	line of sight angle (Fig. 1.1)
$\sigma_r$	auxiliary parameter in roll stability criterion (Fig. 3.8)
$\psi$	phase shift
$X$	azimuth or yaw angle between aerodynamic and geodetic coordinate system (Fig. 1.1)
$\omega$ , $\omega_R$ , $\omega_C$	rotational frequency, rotational resonance frequency, rotational characteristic frequency of undamped spring-mass-system (section 3)
$\psi$ , $\theta$ , $\phi$	Euler angles between body-fixed and earth-fixed or geodetic axes (Fig. 2.3)

## 1. INTRODUCTION

Mathematically, the dynamics of a missile are described by the equations of motion. They are briefly presented in section 2 of this lecture. The aerodynamic parameters of steady, quasi-steady, unsteady nature are linked to the equations of motion in the aerodynamic model of flight motion. This also is described in section 2. Section 3 covers simple case studies of missile static and dynamic stability. Aerodynamic means which influence the stability behavior are demonstrated on various missile configurations. From literature, cases are selected, showing linear and non-linear missile motion and the resultant stability behavior.

The following context, which is based on ref. 1, is intended to integrate "missile dynamics" in a general concept of missile function: Supposing, a guided missile with an

active homing head is launched against a ship target and cruises at low altitude above sea level. Its motion in the plane of yaw - parallel to the water surface - is considered in connexion with the interaction of seeker, control system and aerodynamic steering. The angles  $\sigma$ ,  $x$ ,  $\psi$  in the plane of yaw (Fig. 1.1) respectively represent the line-of-sight angle, determined by the positions of the target and the missile in a geodetic coordinate system, the azimuth or yaw angle between aerodynamic and geodetic coordinate system and the yaw angle between body-fixed and geodetic coordinate system. We are interested in the role of missile dynamics in the control procedure which links the line-of-sight angle  $\sigma$  to a change of the flight path azimuth angle  $x$ , with the purpose that both angles are equal at the end of the procedure. Upon target recognition, the seeker measures the position of the target with respect to instantaneous missile position. The line-of-sight angle is determined and, assuming a linear dependency between rotational velocities  $\dot{x} = K \cdot \delta$ , the seeker signal is converted and fed into the control system. This generates a control signal  $\zeta_s$  which activates the flap regulator. A flap angle  $\zeta_1$  results. The change of the aerodynamic moment initiates a lateral acceleration which leads to the angular velocity  $x$ . The latter continuously changes by the new inputs from the homing system, until the line-of-sight angle coincides with  $x$ . Inertia effects cause perturbations in missile motion, which superimpose on the yaw velocity  $\dot{x}$ . This results in an overshoot  $x \neq \sigma$  or deviation from the intended flight path. The yaw control circuit is supposed to minimize these perturbations, which can be measured by means of accelerometers, position or velocity gyros. The output signals of the measurement instruments are fed into the flap control circuit. This feedback and the flap activation  $\zeta$  determines the lateral missile dynamics, i.e. the turning manoeuvre directing the missile flight path towards the target. The rotational yawing motion is regulated with a minimum of disturbance. In the above mentioned case of a guided missile function, the missile dynamics are integrated in the control circuit shown in Fig. 1.2. In the following section, the mathematical modelling reduces the missile dynamics to the motion of a point mass under external influences. This general description can be applied to any specific mission pattern.

## 2. DESCRIPTION OF MISSILE MOTION AND FLIGHT PATH

Missile dynamics require a description of the missile motion in six degrees of freedom in a three-dimensional coordinate system. In the aerodynamic model, the direction of the motion and the vectors of the forces and moments acting on the missile are defined with respect to the axes of the chosen coordinate system. There are three commonly accepted coordinate systems, the geodetic, the body-fixed and the aerodynamic system. For differentiation, the geodetic and aerodynamic systems are given the subscripts g and a respectively. All systems are orthogonal and right-hand turning coordinate systems. The latter specification requires the vector of rotation to coincide with the third axis, when in the cycle  $x, y, z, x, \dots$  one axis is turned into the subsequent one.

### 2.1 Coordinate systems and coordinate transformations

The geodetic system (Fig. 2.1) permits the definition of the position of a missile in space. The curvature of the earth surface usually is neglected and as origin of the axes, often the location of the missile launcher is chosen. The  $x_g$  axis is situated in the plane of the earth surface and points in the direction of the missile launch. Also, the  $y_g$  axis is positioned in the plane of the earth surface. The  $z_g$  axis points in the direction of the earth center. In the body-fixed coordinate system, the angles-of-attack, the axial velocity components  $u, v, w$  and the aerodynamic forces  $D, Y, L$  and  $N$  are shown in Fig. 2.2a. The polar angles-of-attack  $\sigma, \lambda$  and the control deflection angles are defined in Fig. 2.2b (ref. 2). The angular velocity components are given in Fig. 2.2c. Here, a coincidence of body-fixed and geodetic axis is assumed. Generally, the transformation between the latter two systems requires auxiliary axes ( $k_1, k_2, k_3$ ) as shown in Fig. 2.3. The origin of the body-fixed system may be placed at any position along the body longitudinal axis. Most times, the center of gravity is chosen. We differ rolling and non-rolling fixed-body systems. The rolling system rotates with the angular velocity  $p$  about the longitudinal axis. In a non-rolling system, the  $y$ -axis remains horizontal in case of  $q=r=0$ . A rolling missile in a non-rolling coordinate system causes the  $y$ -axis to lag behind the missile by the angle  $\phi_t = \int^t \omega dt$ . Again, the  $y$ -axis remains horizontal, provided  $q=r=0$ . Fig. 2.4 finally, presents the relationship between body-fixed and aerodynamic coordinate systems (ref. 3).

The application of the equations of motion to a specific missile mission requires the comparison of the vector components of velocities, forces and moments in different coordinate systems: One has to convert the vector components in the body-fixed coordinate system (Fig. 2.2) for application in the geodetic system (Fig. 2.1) in order to simulate the flight path. The conversion is possible with Euler-angle-trigonometry, see Fig. 2.3. As alternative, quaternions can be used. Both, the system of Euler angles and the quaternions require the definition of a coordinate system and a reference system. The application of quaternions has the advantage of avoiding mathematical singularities in the transformation of the angular velocities, which appear in the trigonometric conversion relations for  $\theta=90^\circ$ . The cause of this advantage has been given in literature, for instance in refs. 1, 4, 5, 6. It is repeated briefly in the following context: The quaternion consists of a scalar- and of a vector-part, which are additive, i.e.

$$Q = \lambda_0 + \hat{i}\lambda_1 + \hat{j}\lambda_2 + \hat{k}\lambda_3 = \lambda_0 + |\lambda|\hat{\lambda},$$

where " $i$ ",  $\hat{i}$ ,  $j$  and  $\hat{j}$  are the basic units ( $\hat{i}, \hat{j}, \hat{k}$  representing unit vectors) and where  $\lambda_0, \lambda_1, \lambda_2$  and  $\lambda_3$  are the scaling numbers. The vector amount  $|\lambda|$  equals  $\sqrt{\lambda_1^2 + \lambda_2^2 + \lambda_3^2}$ .

The vector part has the character of a complex number. Thus, the complex conjugate of the quaternion is given by

$$\bar{Q} = \lambda_0 - i\lambda_1 - j\lambda_2 - k\lambda_3 = \lambda_0 - |\lambda|\hat{\lambda} .$$

Both properties  $Q$ ,  $\bar{Q}$  with the amount of  $|Q| = \sqrt{Q \cdot \bar{Q}} = \sqrt{\lambda_0^2 + \lambda_1^2 + \lambda_2^2 + \lambda_3^2}$  are shown in Fig. 2.5, consisting of a vector axis  $\hat{\lambda}$  and a unit axis. From the diagram of Fig. 2.5, one may derive the quaternion in trigonometric form

$$Q = |Q| (1 \cdot \cos \alpha + \hat{\lambda} \sin \alpha) ,$$

from which the reciprocal value  $Q^{-1}$  easily follows: Since  $Q \cdot Q^{-1} = 1$ , we obtain

$$Q^{-1} = \frac{1}{|Q|} (1 \cdot \cos \alpha - \hat{\lambda} \sin \alpha) .$$

The fact that the quaternion has a non-zero reciprocal value, is sufficient for the avoidance of mathematical singularities in the transformation. A detailed presentation of the transformation relations either derived with quaternions or with the trigonometric function of Euler's angles can be found in the literature (see for instance refs. 1, 4, 7).

## 2.2 Equations of Motion

With respect to geodetic coordinates or to the inertial system the equations of motion of a body with mass  $m$  and six degrees of freedom follow from the translational and angular momentum equations. The time derivative of the translational momentum yields for the forces in the inertial system

$$\frac{d}{dt}(mu_g) = \Sigma X_g, \quad \frac{d}{dt}(mv_g) = \Sigma Y_g, \quad \text{and} \quad \frac{d}{dt}(mw_g) = \Sigma Z_g ,$$

where  $u_g$ ,  $v_g$  and  $w_g$  are the components of the flight velocity vector  $\vec{v}_g$  in  $x_g$ ,  $y_g$  and  $z_g$  direction. The gravity influence is included in  $\Sigma Z_g$ . With the notation

$$h_{x_g} = I_{x_g} p_g - I_{xy_g} q_g - I_{xz_g} r_g$$

for the  $x_g$ -component of the angular momentum (where  $p_g$ ,  $q_g$  and  $r_g$  are the angular velocities about the  $x_g$ ,  $y_g$  and  $z_g$  axis, and  $I_{x_g}$ ,  $I_{xy_g}$ ,  $I_{xz_g}$  the moment or the products of inertia), we obtain the relation of the yaw moment pointing in the direction of the  $x_g$  axis:

$$\frac{d}{dt}(h_{x_g}) \equiv L_g$$

and accordingly (ref. 1, 7, 8) for the other axis of the inertia (geodetic) system

$$\frac{d}{dt}(h_{y_g}) \equiv M_g \quad \text{and} \quad \frac{d}{dt}(h_{z_g}) \equiv N_g .$$

Since the axes  $x_g$ ,  $y_g$  and  $z_g$  are fixed in space, any arbitrary rotational motion of the missile will change the moments and products of inertia. Therefore it is more convenient to define the equations of motion, i.e. the force and moment equations, in body axes (Euler's equations). Then by transformation, the translational and rotational velocities in the inertial system may be derived, in order to determine the position of the missile in space. In general, this requires a rotation of the time derivative  $d\vec{v}/dt|_g = d\vec{v}/dt + \vec{\omega} \times \vec{v}$ , where  $d\vec{v}/dt|_g$  is the derivative in the geodetic system. In body axes,  $d\vec{v}/dt$  rotates with  $\vec{\omega}$  and must be complimented by  $\vec{\omega} \times \vec{v}$ . To the component  $du/dt$ , the products  $qxw$  and  $rxv$  are to be added, which yields  $du_g/dt = du/dt + qw - rv$ . Correspondingly, the forces read in body-axes

$$m(\dot{u} + qw - rv) = \Sigma X, \quad m(\dot{v} + ru - pw) = \Sigma Y \quad \text{and} \quad m(\dot{w} + pv - qu) = \Sigma Z ,$$

where gravity forces may be contained in all force components  $\Sigma X$ ,  $\Sigma Y$  and  $\Sigma Z$ . The general moment equations may be found in refs. 1, 7, 8. In the special case of a missile of rotational symmetry, when the products of inertia  $I_{xy}$ ,  $I_{yz}$  .... are zero, these equations are reduced to

$$I_x(d\dot{p}/dt) = L, \quad I_y(d\dot{q}/dt) + (I_x - I_z)p_r = M \quad \text{and} \quad I_z(d\dot{r}/dt) + (I_y - I_x)p_q = N .$$

For certain applications, non-rolling axes where the  $x$  axis only coincides with a major body axis (the missile longitudinal axis), are preferable to the completely body-fixed system. As mentioned before, then the  $y$  and  $z$  axes lag behind the rolling missile, which requires a further transformation between the rolling and non-rolling systems.

Besides the aerodynamic forces and moments and the gravitational force, the motor thrust must be regarded as external force. We have  $d(mu)/dt = \dot{m}u + \dot{m}\vec{u}$  in case of a thrust vector in  $x$ -direction. This relation takes into account the change of the missile mass due to the reduction of the propellant mass during the burning time and the external force  $\dot{m}\vec{u} = \dot{m}u_a$ , which is found from the conservation law of the total impulse. Here,  $u_a$  denotes the velocity of the propellant gas at nozzle exit in relation to the missile velocity. Generally, thrust vectors will also cause external moments in the equations of motion. In connection with the mass reduction ( $\dot{m}u$ ) jet damping is noticeable when the mass flow  $\dot{m}$  is large and when it travels a long distance inside the missile body. These conditions give

rise to a reactional force similar to a Coriolis force, when angular velocities  $\dot{\alpha}$  or  $\dot{\beta}$  normal to the propellant flow direction exist. For a missile pitching with  $\dot{\alpha}$ , the change of angular momentum due to the propellant flux  $\dot{m}$  is given by  $\dot{m}d\dot{\alpha}$ , provided the main moment of inertia axes of the missile coincide with the body axes. As can be seen, the distance  $d$  between the nozzle exit area and the center of gravity of the rocket (ref. 1) is an important parameter in jet damping.

With fast rolling missiles the Magnus-force and -moment must be included in the equations of motion. They are dependent on the angular velocity  $\dot{\rho}$  and on the polar angle of attack  $\sigma = \arcsin(\sqrt{v^2+w^2}/V)$ . In summary, the force and moment equations contain the aerodynamic forces  $X$ ,  $Y$ ,  $Z$  and moments  $L$ ,  $M$ ,  $N$ , the thrust force and -moment and the gravity force.

### 2.3 Aerodynamic model

The aerodynamic models provide means to present the aerodynamic forces and moments as functions of the flight parameters which possibly are given during the missile mission. In the following, these external forces and moment shall be considered in detail. They are largely proportional to the dynamic pressure  $(\rho/2)V^2$  and therefore most times conveniently described by dimensionless aerodynamic coefficients. In the aerodynamic or flight wind coordinate system of Fig. 2.4 the coefficients are given by the drag coefficient  $C_D$ , the lift coefficient  $C_L$  and the side force coefficient  $C_Y$ . We have  $C_X$ ,  $C_Y$  and  $C_Z = C_N$  in the body-fixed system (Fig. 2.2). By application of trigonometric functions of the angles-of-attack  $\alpha$ ,  $\beta$ , the coefficients of the aerodynamic system may be converted to  $C_X$ ,  $C_Y$  and  $C_Z$  by the relations

$$\begin{aligned} C_X &= -C_D \cos \alpha \cos \beta - C_Y \cos \alpha \sin \beta + C_L \sin \alpha \\ C_Y &= -C_D \sin \beta + C_Y \cos \beta \\ C_Z &= -C_D \sin \alpha \cos \beta - C_Y \sin \alpha \cos \beta - C_L \cos \alpha \end{aligned}$$

The moment coefficients are directly defined in the body-fixed system (s. Fig. 4b). Since all coefficients are dependent on the flight conditions, such as

$$C_Z = C_Z (\alpha, \beta, M, q, \dots)$$

for instance, they may be given in terms of partial derivatives:

$$\begin{aligned} dC_Z &= \frac{\partial C_Z}{\partial \alpha} d\alpha + \frac{\partial C_Z}{\partial \beta} d\beta + \frac{\partial C_Z}{\partial M} dM + \frac{\partial C_Z}{\partial q} dq + \dots \\ &= C_{Z_\alpha} d\alpha + C_{Z_\beta} d\beta + C_{Z_M} dM + C_{Z_q} d\left(\frac{qC}{V}\right) + \dots \end{aligned}$$

Here, we have linear derivatives only, but also higher order terms are necessary, when a non-linear dependency on a flight condition must be described. We recall the non-linear dependency of the normal force coefficient on the angle-of-attack, given in the AGARD lecture 114/12, namely  $C_N = C_{N_0} + C_{N_1} \alpha + C_{N_2} \alpha^2$  with  $C_{N_0} = C_{N_0}(\alpha) + \alpha C_{N_1}$ . Numerous derivatives result, when force and moment coefficients are developed in series as functions of the independent variables. Only few however are significant for the flight stability (refs. 3, 9, 10). In case of linear dependence on the state variables ( $\alpha, q$ ), some terms of the coefficient derivative series of the normal force and pitching moment are listed in Table 2.1. The second order derivatives, dependent on  $\dot{\alpha}$  and  $\ddot{\alpha}$ , most times can be neglected.

For aerodynamic models in missile design at MBB, among other versions the following coefficient patterns are in use, as demonstrated on the force coefficient  $C_X$ :

#### Missile 1

$$C_X = C_{X_1} + C_{X_2} (\alpha^2 + \beta^2) + C_{X_3} (\alpha^2 + \beta^2)^{3/2} + C_{X_4} (\alpha^2 + \zeta^2 + 2\beta\zeta) ,$$

where  $\alpha$ ,  $\beta$  and  $\zeta$  denote the flap deflection angles (see Fig. 4b).

#### Missile 2

$$C_X = C_{X_0} (\alpha=0, \beta=0) + C_{X_1} (\alpha^2) + C_{X_2} (\beta^2) + C_{X_3} \alpha + C_{X_4} \beta + C_{X_5} \beta .$$

#### Missile 3

$$C_X = C_{X_0} + C_{X_1} \sin^3 \alpha + C_{X_2} \sin^4 \alpha + C_{X_3} (\alpha^2 + \zeta^2 + 2\beta\zeta - \alpha\beta - \alpha\zeta) .$$

The polar angles  $\sigma$  and  $\lambda$  with  $\lambda = \arctan(v/w)$  may be introduced in case of rotationally symmetric missiles. The replacement of the two angles  $\alpha$  and  $\beta$  by the single angle  $\sigma$  simplifies the force and moment relations of the aerodynamic model. The use of trigonometric functions, as practiced in case of missile 3, enables the determination of flight

path also at very large angles-of-attack. The use of  $\alpha$  and  $\beta$  in case of missiles 1 and 2 involves the restriction to small incidences. The drag terms in the previous relations, which do not depend on angles-of-attack or of flap deflection may include the wave drag, the friction drag and base drag. In the computer programs, which calculate the flight paths, the coefficients usually are defined as functions of the Mach number. For  $C_{X_0}$  and  $C_{X_1}$ , the following data list may be given:

Ma	0.6	0.9	1.1	1.5	2.0
$C_{X_0}$	-0.31	-0.34	-0.58	-0.58	-0.5
$C_{X_1}$	-16.1	etc.			

Most times, the coefficients  $C_{X_0}$ ,  $C_{X_1}$  and others are derived from data of wind-tunnel experiments or flight tests. In the advanced stages of missile design, rarely coefficients from theoretical prediction only are used.

The general notation of

$$C_X = C_{X_a} + C_{X_b} (\underline{\alpha}, \underline{\beta}) + C_{X_c} (\underline{n}, \underline{\xi}, \underline{\xi})$$

or

$$C_m = C_{m_a} (\underline{\alpha}, \underline{\beta}) + C_{m_b} (\underline{n}, \underline{\beta}) + C_{m_c} (\underline{q}, \underline{\alpha}, \Delta x) + C_{m_d} (\underline{z}, \Delta x)$$

$$+ C_{m_e} (\underline{\xi}, \underline{\alpha}, \underline{\beta}) + C_{m_f} (\underline{\xi}, \underline{\alpha}, \underline{\beta})$$

for instance, where  $(\underline{\alpha}, \underline{\beta})$  may be replaced by  $\sigma$  aids an easier analysis. In these general relations, the underlined properties in parenthesis define the main influence parameters.

### 3. STABILITY OF AN UNGUIDED MISSILE

For simplification, a two-dimensional motion of an unguided missile in the  $x$ - $z$  plane will be considered. The missile is assumed to have a constant flight velocity  $V$  and two degrees of freedom only, which permits motions of the center of gravity in  $z$ -direction and a rotational motion about the pitch axis, which points in direction of the  $y$ -axis. We have plunging, which changes the angle-of-attack  $\alpha = w/u$  and pitching with  $q$  (see Fig. 3.1). The missile motion is easily described with Euler's force and moment equations, where  $Z$  and  $M$  are supposed to represent aerodynamic forces only, which requires the drag to be compensated by the thrust and the missile weight to be equal to a constant force in  $z$ -direction. Then

$$Z = m(\dot{w} - qu) \quad \text{and} \quad M = q I_y .$$

With angular velocities  $\dot{w} = \dot{\alpha} u$ ,  $\theta = \alpha + \gamma$  and  $\ddot{\theta} = q$ , where in the present two-dimensional case,  $\gamma$  is the angle between flight velocity vector  $V$  (or the aerodynamic axis  $x_a$ ) and the  $x_g$  axis. Using the angular relations we get

$$\dot{\gamma} = \frac{Z}{mu} = \frac{L}{mV} \quad \text{and} \quad \ddot{\theta} = M/I_y$$

We may approximate  $Z$  and  $M$  by linear expansions:

$$Z = Z_\alpha \cdot \alpha + \dots \quad \text{and} \quad M = M_\alpha \alpha + M_q \cdot \dot{\theta} + M_{\dot{\alpha}} \ddot{\alpha} + \dots$$

Substituting  $\dot{\theta} = (1/I_y) (M_\alpha \cdot \alpha + M_q (\dot{\alpha} - Z/(mu)) + M_{\dot{\alpha}} \ddot{\alpha})$  in  $\theta - \ddot{\alpha} = -\dot{\alpha} Z_\alpha/(mu)$  we obtain the relation

$$\frac{1}{I_y} (M_\alpha \cdot \alpha + M_q (\dot{\alpha} - \frac{Z_\alpha}{mu}) + M_{\dot{\alpha}} \ddot{\alpha}) - \ddot{\alpha} = -\frac{Z_\alpha}{mu} \alpha .$$

Regrouping coefficients according to the variables  $\alpha$ ,  $\dot{\alpha}$  and  $\ddot{\alpha}$ , we get the differential equation describing the motion of a spring-mass-damper after excitation.

$$\ddot{\alpha} + A\dot{\alpha} + B\alpha = 0$$

with

$$A [s^{-1}] = -\frac{M_q + M_{\dot{\alpha}} + I_y Z_\alpha / (mu)}{I_y} \quad \text{and} \quad B [s^{-2}] = -\frac{M_\alpha - M_q Z_\alpha / (mu)}{I_y} ,$$

which are equivalent to a damping- and a spring-constant respectively. The solution of the differential equation can be obtained with Laplace-transformations, which yield the characteristic (quadratic) equation

$$\lambda^2 + A\lambda + B = 0 ,$$

with the solutions  $\lambda_{I,II} = (-A \pm \sqrt{A^2 - 4B}) / 2$ . The roots  $\lambda_{I,II}$  characterize the dynamic behavior of the missile. Both roots are real, when  $A^2 \geq 4B$ ; or complex conjugates, when  $A^2 < 4B$ . Real roots provide an aperiodic solution

$$\alpha = C_1 \exp(\lambda_I t) + C_2 \exp(\lambda_{II} t),$$

where  $C_1$  and  $C_2$  follow from the initial condition. If one of the roots is positive, the system is unstable, as  $\alpha$  diverges with time. Negative roots yield a stable system, as the amplitude  $\alpha$  is diminished with time. An aperiodic solution never occurs with an unguided weapon. Once excited, undamped or damped lateral motions never increase or decrease monotonically. Always oscillations occur. Conjugate complex roots provide a periodic solution

$$\alpha = C_0 \exp(-At/2) \cos(\omega t - \psi),$$

where  $C_0$  and the phase shift  $\psi$  are determined from the initial conditions. A resonance frequency is given with  $\omega_R = (\sqrt{4B - A^2}) / 2$ . The spring constant  $B$  determines the characteristic frequency of the undamped system  $\omega_c = \sqrt{B}$ . The damping factor is given by  $D_A = A / (2\sqrt{B})$ .

The characteristic frequency  $\omega_c = \sqrt{(M_q z_y / (I_y \mu)) - M_a / I_y}$  is controlled by the (negative) normal force slope  $-N_a = z_y$ , by the pitch stiffness  $M_q$  and the pitch damping derivative  $M_a$ . Substituting these properties and  $(m, u, I_y)$  of a ballistic missile into  $\omega_c$ , one can show that the pitch stiffness is the dominant control parameter of the characteristic frequency. For demonstration, firstly a dimensionless spring constant should be formed:

$$B^* \equiv \frac{4I_y}{m(\rho DS)^2} B = - \left( \frac{2m}{\rho DS} C_{m_\alpha} + C_{m_q} C_{L_\alpha} \right).$$

Herein, the factor  $\rho_M = 2m / (\rho DS)$  can be denoted a relative density. With

$m = 220 \text{ kg}$	$v = 1.2 \cdot 10^3 \text{ m/s}$	$(M=3.7)$	$C_{z_\alpha} = -CL_\alpha (V/u) = -4.95$
$D = 0.275 \text{ m}$	$A_z = 3.5 \cdot 10^3 \text{ m}$		$= -5.2$
$S = 0.0595 \text{ m}^2$	$\rho = 0.86 \text{ kg/m}^3$	$C_{m_\alpha}$	$= -25.0$
$I_y = 375 \text{ kg m}^2$	$\rho_M = 3.1 \cdot 10^5$	$C_{m_q}$	$= -210.0$

we find  $(2m / (\rho DS)) \cdot C_{m_\alpha} \gg C_{m_q} \cdot C_{L_\alpha}$ , which clearly defines the pitch stiffness as  $f_c$ -controlling property. We get  $\omega_c = \sqrt{141 + 0.915} = 11.92 \text{ s}^{-1}$  and the characteristic frequency  $f_c = \omega_c / (2\pi) \approx (1/2\pi) \cdot \sqrt{-(M_a/I_y)} = 1.9 \text{ s}^{-1}$ .

For the determination of the resonance frequency  $\omega_R = \sqrt{|B - A^2/4|}$  we also define a dimensionless parameter

$$A^* \equiv \frac{2m}{\rho VS} A = - \left[ \frac{mD^2}{I_y} (C_{m_q} + C_{m_\alpha}) - C_{L_\alpha} \right],$$

which yields after applying the missile data

$$0 \left[ \frac{mD^2}{I_y} (C_{m_q} + C_{m_\alpha}) \right] \geq 0 \left[ C_{L_\alpha} \right]$$

in our case an insignificantly greater product of the damping coefficients times  $(mD^2/I_y)$  than the lift curve slope, and hence an approximation between  $\omega_R$  and  $\omega_c$ . Still, because of  $\sqrt{|B-A^2/4|} < \sqrt{|B|}$ , the resonance frequency is slightly smaller ( $f_c = 1.89 \text{ s}^{-1}$ ) than  $f_c$  and in addition, weakly influenced by the pitch damping coefficient. The damping  $D_A = A / (2\sqrt{B}) = 0.09$  is smaller than unity. The unguided missile is slightly damped and any lateral deviation - after a number of oscillations within a certain time - is set back to zero. With the duration of a period  $P = 2\pi/\omega_R = 0.555 \text{ s}$  and the half life time  $t_{1/2} = 0.64 \text{ s}$ , where the initial amplitude  $\alpha_i$  is reduced to its half value, the time history  $\alpha(t)$  is easily presented (Fig. 3.2).

### 3.1 Static and dynamic longitudinal stability

The criterion for the longitudinal stability is (ref. 7)

$$(dC_m/dC_L)|_{L=W} < 0,$$

where the lift force  $L$  is supposed to complement weight  $W$ . At higher angles-of-attack we may replace  $C_{L_\alpha}$  by  $C_L \cos \alpha$ . Then we have the possibility of applying the data of the diagrams of Fig. 3.3, 3.4, in order to show longitudinal stability characteristics on the example of the missile configurations A and B, which have different wing positions. The configurations have a common pitch axis position and pitch frequency ( $k=q_c/V=0.05$ ), both cruise at  $M=0.8$ . The normal force and moment coefficients of the configurations are presented with and without the contributions of pitching, as indicated by solid and dashed curves respectively. The configuration A with its wing attached near the end of

the body has larger values of  $(-C_m)$  than configuration B, while the normal force coefficients of both missile version differ only slightly. Plotting schematically the moment coefficient  $C_m$  versus  $C_N$ , as shown in Fig. 3.5, we derive  $(dC_m/dC_N) < 0$  for both configurations. The static stability of missile A exceeds the one of B. The difference between the solid and dashed curve for A shows that the contribution of the pitch damping coefficient  $C_{Nq}$  and  $C_{Mq}$  slightly increases the stability, since from Fig. 3.3, 3.4  $|\alpha(C_{Mq}) + k' C_{Nq}| > |\alpha(C_{Nq}) + k' C_{Nq}|$ . The dash-dotted curve in Fig. 3.5 presents the characteristics of a statically unstable missile.

In this connexion a note on the relationship between stability and the load factor, i.e. the measure of the manoeuvrability of a guided missile should be in place (ref. 3). The value of the load factor  $n = \alpha L / W$  measures the ability of changing the direction of the flight path  $\dot{\gamma} = \alpha L / (m \cdot V)$ . In order to alter  $\dot{\gamma}$ , an additional lift force  $L_\delta$  due to flap deflection  $\delta$  is needed. This changes the load factor of a missile with wings and flaps near the body-end by an additional amount  $n_\delta$

$$n + n_\delta = \frac{\alpha L_\alpha + \delta (L_\delta - \frac{X_\delta}{D})}{W}$$

From this relationship one sees that the load factor is diminished when - at constant flap angle  $\delta$ -the stability increases. The latter occurs, when the distance  $x_\delta/D$  between the center of the flap lift force and the center of gravity becomes more negative.

The dynamic longitudinal stability is determined by the spring constant B in the differential equation  $\ddot{\alpha} + A\dot{\alpha} + B\alpha = 0$ , which describes the lateral motions of the missile in the x-z plane after an excitation or a disturbance of plunge ( $\Delta\alpha$ ) or ( $\Delta q$ ). The dimensionless spring constant  $B^* = -(2m/\rho DS) C_{Mq} + C_{Lq} C_{Mq}$  contains the static stability criterion given by the negative slope of the static pitching moment (pitch stiffness), and the dynamic criterion as well. This is given by the product of the pitch damping coefficient and the lift force slope. Pure dynamic stability we have with  $C_{Mq}=0$ , such that  $B^*=-C_{Lq} C_{Mq}$ . This case rarely exists in practice. Usually, the dynamic stability increases the static stability, as shown in Fig. 3.5. Thus, a statically weakly unstable missile may exhibit dynamic stability. Generally, however, the dynamic stability contribution is small in comparison to the static. This, we have seen on the numerical example of the unguided missile.

An unguided missile usually shows equal dynamic behavior in the horizontal and the vertical planes. Therefore, the stability criteria for an unguided missile with side motions in the x-y plane do not differ from those given above for the motion in the x-z plane.

In conclusion of this section, the significance of longitudinal stability derivatives may be demonstrated on the example of the "evolution" of a ballistic projectile. In the initial concept, shown in Fig. 3.6, a non-rolling projectile with a very simple shape was designed in order to minimize production cost. Wind-tunnel experiments with a static model at incidences up to  $10^\circ$  confirmed the effectiveness of the design. Free flight experiments and dynamic measurements showed a susceptibility to initial perturbation and revealed the alternating appearance of flow separation bubbles on top and bottom of the shoulder of the inclined body, leading to instability and - in the case of free flight - to deviations from the anticipated flight path. In the flight path prediction, the initial disturbance was simulated with the assumption of an initial low pitching frequency  $\omega_1$ . A positive value of the pitch damping derivative  $C_{Mq}$  was chosen for the representation of the combined action of a time varying pitch stiffness non-linear with the angle-of-attack and of the unsteady coefficients  $C_{Mq} + C_{Mq}$ . In the final design, lifting surfaces distributed over the length of the projectile including fixed fins and a flare at the end, turned the intended simple form in a more complicated one, but provided longitudinal stability over the angle-of-attack range of the mission (Fig. 3.7).

### 3.2 Roll stability of ballistic missiles

Missiles with their aerodynamic center upstream of the center of gravity are unstable. Their directional stability can be influenced by an angular velocity about the longitudinal axis. This rolling velocity is transferred to the missile during the launch phase or can be produced during the flight by canted fins. In flight the high angular momentum or torque withstands angular perturbations which may be induced by side winds. A roll stabilized missile obeys the gyroscopic laws and reacts on a perturbing angular moment with a rotation of its longitudinal axis in direction of the vector of the perturbing momentum. In case of side wind, the missile longitudinal axis changes its direction in the vertical plane. This causes a change of the flight distance.

The roll stability characteristic is derived with the physical model of a gyroscope being influenced by gravitational forces only. A symmetric gyroscope supported below its center of gravity will not tip as long the condition

$$\frac{I_x^2 p^2}{4I_y m g d} > 1$$

is satisfied (refs. 1, 11), where  $d$  marks the distance between the center of gravity and the location of the gyro-supporting point. In ballistics, the pitching moment  $M_\alpha$  replaces the moment  $mgd$ , which yields

$$s \equiv \frac{I_x^2 p^2}{4 I_y M_\alpha} > 1 .$$

In ref. 11, a roll stability criterion  $s > (4s(1-s))^{-1}$ , where

$$s = \frac{C_{z_\alpha} + (mD^2/I_x) C_m p \beta}{C_{z_\alpha} + (mD^2/I_y) (C_{m_q} + C_{m_\alpha}) + (mD^2/I_x) C_l p}$$

contains the roll moment and the derivative of the Magnus moment  $C_{mpg}$  besides the normal force slope and pitch damping. In terms of  $s$  a graphical sketch indicates the stability range at aerodynamic and roll stabilized conditions as well (Fig. 3.8). An auxiliary parameter  $\sigma_r = \sqrt{1 - s^{-1}}$  must satisfy the stability condition  $\sigma_r > |2s - 1|$ .

Roll stabilization introduces the coupling of rolling and side motions. Especially when we are involved with abnormal stability behavior, which cannot be described with linear theories, the analytical treatment becomes extremely difficult (refs. 12 - 20). This shall be described on the example of a phenomenon, termed "Catastrophic Yaw" by Nicolaides (ref. 19). This non-linear missile motion, a coupling of roll, pitch and yaw, may cause missile crash. According to ref. 19, this dynamic instability is characterized by the failure of the missile to pick up its full steady rolling velocity. Then, a growth of the pitching and yawing motion is observed. The first observation of the so-called roll-lock-in could be demonstrated in the wind tunnel tests and subsequently explained analytically. Roll-lock-in is possibly caused by the competition between the roll moment due to the fin cant and the roll moment induced by the change of missile roll orientation with angle-of-attack. The effect of change of the missile roll orientation with changing angle-of-attack is similar to the one described before, when side winds strike a rolling missile. In ref. 19, a reason for an initiation of the catastrophic growth of pitch and yaw could only be presumed. Wind tunnel tests do reveal that the roll orientation modifies the normal force and the pitching moment as well as the side force and the yawing moment, i.e. they become functions of the angles-of-attack and of the orientation angle. In order to determine the contributions of these non-linear forces and moments to the flight performance of missiles and specifically to the dynamic stability of the special pitching and yawing motions, it is necessary to add them to the aerodynamic model and to investigate the modified equations of motion. The general solution may still be extremely difficult, but approximate solutions to special cases such as the Catastrophic Yaw are possible. In fact, it is noted in ref. 19, that the addition of side moment may indeed have a catastrophic effect on the dynamic stability of lunar motion, which is a special form of the combined pitching and yawing.

#### 4. CONCLUSION

As demonstrated in the previous sections, flight path prediction and qualitative predictions of missile dynamic stability - even in case of abnormal missile behavior - nowadays is possible by means of computer programs, which contain linear and non-linear equations of missile motion in all six degrees of freedom. The introduction of mathematical aids such as as quaternions and the replacement of the linear dependency of forces on the independent variables by non-linear functions is necessary in order to simulate missile behavior of the type of catastrophic yaw - for instance. The precise or qualitative prediction or the analysis of experimentally observed missile reactions is still time- and cost-consuming, yet of importance in missile design, if unfavourable aerodynamic features or thrust characteristics are to be avoided. Besides the non-linear system of motions, the quality of the aerodynamic coefficients and derivatives for the aerodynamic modelling of the missile dynamics, is of great significance. Some of the aerodynamic coefficients can be provided by well established theories. Mostly the latter are linear theories. The non-linear coefficients are available from experiment or - at times - from empirical prediction methods. If the latter type of aerodynamic data prevails in the aerodynamic model, the model is good for a specific missile, but possibly fails for design purposes. This may be the reason that once in a while a newly designed missile fails to complete its mission according to the planned program. Then, an immense rise of development cost is caused. This cost exceeds the expense for an appropriate aerodynamic model and its application in the equations of motion by orders of magnitude. Analytical procedures for precise or merely qualitative prediction of missile flight performances provide means of early elimination of unpromising missiles in the research and development programs.

#### ACKNOWLEDGEMENT

The author thanks Mr. Stiklorus of MBB/AE123 for his advice and valuable information on this topic. Many thanks also to Mrs. Schad (BC) and my wife who helped to complete this lecture and lecture 12 in due time.

## REFERENCES

1. L. Stiklorus, "Das dynamische Verhalten von Flugkörpern, Teil 1", Lehrgangsreihe Flugtechnik der Carl-Cranz-Gesellschaft e.V., Lehrgang F3.04 Lenkung und Regelung von Flugkörpern, May 1979.
2. H. Gaidosch, "FMS (MSAMS), Launch Phase and Short Range Studies, Part I: Solid Rocket", 1980, MBB TN-AE12-8/80.
3. H. Barth, "Einführung in die Flugkörper-Aerodynamik, Teil 1" und "Allgemeine Flugkörper-Aerodynamik, Teil 2", Lehrgangsreihe Flugkörper-Aerodynamik der Carl-Cranz-Gesellschaft e.V., October 1977.
4. H. Gaidosch, "Koordinatentransformation in der Flugmechanik mit Hilfe der Quaternionenrechnung", Bölkow-Entwicklungen KG, October 1963, Mitteilung WM3-108/63.
5. D. Weißenbach, "Regeln für Rechnungen mit Quaternionen", Bölkow GmbH, July 1967, TN-W42-47/67.
6. M. Lagally, "Vorlesungen über Vektor-Rechnung", Akademische Verlagsanstalt Geest & Portig KG, Leipzig, 1949.
7. B. Etkin, "Dynamics of Atmospheric Flight", John Wiley & Sons, New York, Sidney, London, 1972.
8. S.S. Chin, "Missile Configuration Design", McGraw-Hill Book Co., New York, Toronto, London, 1961.
9. H.M.B.M. Thomas, "State of the Art of Estimation of Derivatives", 1961, AGARD Rep. 339.
10. D.E. Ellison, D.E. Hoak, "Stability Derivative Estimation at Subsonic Speeds", 1968, Annals New York Academy of Sciences, International Congress on Subsonic Aeronautics, New York, N.Y., Academy of Sciences, pp. 367-396.
11. H. Molitz, R. Strobel, "Außere Ballistik", Springer Verlag, Berlin, Göttingen, Heidelberg, 1963.
12. C.H. Murphy, "The Measurement of Non-Linear Forces and Moments by Means of Free Flight Tests", 1956, Ballistic Research Laboratories, Aberdeen Proving Ground, Maryland, BRL Rep. No. 974.
13. C.H. Murphy, "The Prediction of Non-Linear Pitching and Yawing Motion of Symmetric Missiles", J.Aero.Sci., Vol. 24, No. 7, July 1957, pp. 473-479.
14. C.H. Murphy, "Non-Linear Motion of a Symmetric Missile Acted on by a Double Valued Static Moment", AIAA Journal, Vol. 6, No. 4, April 1968, pp. 713-717.
15. C.H. Murphy, "Non-Linear Motion of a Missile with Slight Configurational Asymmetries", 1970, AIAA Paper No. 70-534, AIAA Atmospheric Flight Mechanics Conference, Tulsa, Okla., Tenn..
16. C.H. Murphy, "Gravity-Induced Angular Motion of a Spinning Missile", 1971, BRL Rep. No. 1546.
17. J.D. Nicolaides, "Basic Aerodynamics of Rockets", Jan. 1968, White Sand Missile Range Reprints of the Conference on Unguided Rocket Ballistics & Meteorology, N-68-27127.
18. J.D. Nicolaides, "On the Free Flight Motion of Missiles Having Slight Configurational Asymmetries", 1953, Institute of the Aeronautical Sciences 21st Annual Meeting, Reprint No. 395.
19. J.D. Nicolaides, "Two Non-Linear Problems in the Flight Dynamics of Modern Ballistic Missiles", Jan. 1959, IAS Rep. No. 59-17.
20. E.L. Clark, Jr., A.E. Hodapp, Jr., "An Improved Technique for Determining Missile Roll Rate with Epicyclic Theory", 1970, AIAA Paper No. 70-536.

## TABLES

Table 2.1: Coefficients of the normal force, the pitching moment and their derivatives. Reference lengths and surfaces of wing, body and their combination		
Normal force and pitching moment coefficient		
$C_N = N / (\frac{1}{2} \rho V^2 S)$	;	$C_m = M / (\frac{1}{2} \rho V^2 S l)$
Reference lengths, reference surfaces for $C_N$ and $C_m$		
Wing	Body	Wing-Body-Combinations
$l = c_o$ or $\bar{c}$	$l = D_o$ or $c$	$l = D_o$ or $c$
$S = S_{(W)}$	$S = S_o$	$S = S_o$
Coefficient derivative series, linear dependence on the variables of the flight condition		
$C_N = \alpha C_{N\alpha} + q(\frac{1}{V}) C_{Nq} + \dot{\alpha}(\frac{1}{V}) C_{N\dot{\alpha}} + \dot{q}(\frac{1}{V})^2 C_{N\dot{q}} + \ddot{\alpha}(\frac{1}{V})^2 C_{N\ddot{\alpha}} + \dots$ $= \alpha \frac{\partial N}{\partial \alpha} (\frac{2}{\rho V^2 S}) + \frac{q}{V} \frac{\partial N}{\partial q} (\frac{2}{\rho V S l}) + \frac{\dot{\alpha}}{V} \frac{\partial N}{\partial \dot{\alpha}} (\frac{2}{\rho V S l}) + \frac{q^2}{V^2} \frac{\partial N}{\partial \dot{q}} (\frac{2}{\rho S l^2}) + \frac{\dot{\alpha}^2}{V^2} \frac{\partial N}{\partial \ddot{\alpha}} (\frac{2}{\rho S l^2}) + \dots$		
$C_m = \alpha C_{m\alpha} + q(\frac{1}{V}) C_{mq} + \dot{\alpha}(\frac{1}{V}) C_{m\dot{\alpha}} + \dot{q}(\frac{1}{V})^2 C_{m\dot{q}} + \ddot{\alpha}(\frac{1}{V})^2 C_{m\ddot{\alpha}} + \dots$ $= \alpha \frac{\partial M}{\partial \alpha} (\frac{2}{\rho V^2 S l}) + \frac{q}{V} \frac{\partial M}{\partial q} (\frac{2}{\rho V S l^2}) + \frac{\dot{\alpha}}{V} \frac{\partial M}{\partial \dot{\alpha}} (\frac{2}{\rho V S l^2}) + \frac{q^2}{V^2} \frac{\partial M}{\partial \dot{q}} (\frac{2}{\rho S l^3}) + \frac{\dot{\alpha}^2}{V^2} \frac{\partial M}{\partial \ddot{\alpha}} (\frac{2}{\rho S l^3}) + \dots$		

## FIGURES

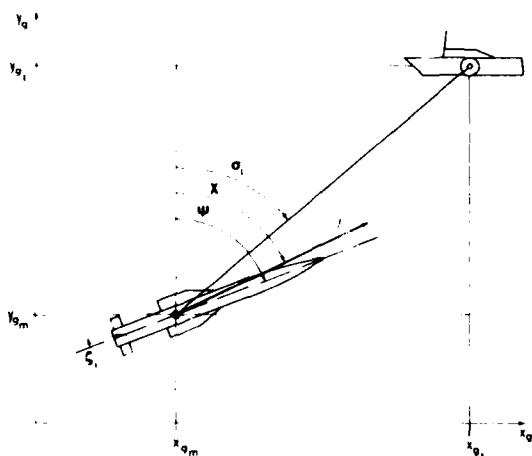


Fig. 1.1: Missile and ship-target positions in the plane of yaw of earth-fixed coordinates

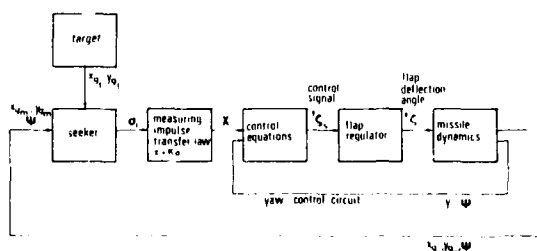


Fig. 1.2: Missile dynamics in the guidance control circuit

## Appendix A

LIST OF PARTICIPANTS – NASA AMES RESEARCH CENTER  
MOFFETT-FIELD, CALIFORNIA 94035, USA

2–5 March 1981

AGNEW, J.W. Mr	McDonnel Douglas Corp., St.Louis, MO, USA
ANDERSON, S. Mr	NASA, Ames Research Center, CA, USA
BACHI, R. Mr	NASA, Ames Research Center, CA, USA
BORGEAUD, C.E. M.	AGARD, Neuilly-sur-Seine, France
BROWER, D. Mr	General Dynamics, Convair Chula Vista, CA, USA
BUTTON, G. Mr	Northrop Corp., Hawthorne, CA, USA
CAHN, M.S. Mr	Northrop Corp., Hawthorne, CA, USA
CHAMBERS, J.R. Mr	NASA, Langley Research Center, Hampton, VA, USA
CHEN, R.T.N. Mr	NASA, Ames Research Center, Moffett-Field, CA, USA
CHOO, D. Mr	Northrop Corp., Hawthorne, CA, USA
CHRUSCIEL, G. Mr	Lockheed Missiles and Space Co., Sunnyvalle, CA, USA
CHYU WEI J. (Gil) Mr	NASA, Ames Research Center, Moffett-Field, CA, USA
CREER, B.Y. Mr	NASA, Ames Research Center, Moffett-Field, CA, USA
CUNNINGHAM, G. Mr	McDonnel Douglas Corp., Long Beach, CA, USA
CURRY, B. Mr	NASA, Dryden Flight Research Center, Edwards, CA, USA
DILLENIUS, M.F.E. Mr	Nielsen Engineering and Research Inc., Mountain View, CA, USA
DUPUIS, A. Mr	Defense Research Establishment, Valcartier PQ, Canada
ENEVOLDSON, E. Mr	NASA, Dryden Flight Research Center, Edwards, CA, USA
ERICSSON, L.E. Mr	Lockheed Missiles and Space Co., Sunnyvalle, CA, USA
FARRIS, G. Mr	NASA, Ames Research Center, Moffett-Field, CA, USA
FRANKLIN, J. Mr	NASA, Ames Research Center, Moffett-Field, CA, USA
FRY, E.B. Mr	NASA, Ames Research Center, Moffett-Field, CA, USA
GOORJIAN, P. Mr	NASA, Ames Research Center, Moffett-Field, CA, USA
GREGORY, T. Mr	NASA, Ames Research Center, Moffett-Field, CA, USA
GURUSWAMY, P. Mr	Informatics Inc., Moffett-Field, CA, USA
HABERMAN, D. Mr	CALSPAN/AEDC Division, Arnold AFS, TN, USA
HAMEL, P.G. Mr	Institut fur Flugmechanik, Braunschweig, Germany
HAMMETT, L. Mr	General Dynamics, Fort Worth, TX, USA
HANFF, E.S. Mr	National Aeronautical Est., Ottawa, Ontario, Canada
HANLEY, R.J. Mr	Naval Air Systems Command, Washington, DC, USA
HANSEN, R. Mr	NASA, Ames Research Center, Moffett-Field, USA
HEADLEY, J. Mr	Northrop Corp., Hawthorne, CA, USA
HEFFLEY, R.K. Mr	Systems Technology, Inc., Mountain View, CA, USA
HEINLEIN, W.H. Lt.Col.	USAF, Ames Research Center, Moffett-Field, CA, USA
HYNES, C.S. Mr	NASA, Ames Research Center, Moffett-Field, CA, USA
ILIFF, K.W. Mr	NASA, Dryden Flight Research Center, Edwards, CA, USA
ISHMAEL, S. Mr	NASA, Dryden Flight Research Center, Edwards, CA, USA

KALVISTE, J. Mr	Northrop Corp., Hawthorne, CA, USA
KARGER, W. Mr	Rockwell International, Los Angeles, CA, USA
KEHOE, E.R. Mr	General Dynamics, Fort Worth, TX, USA
KIRK, D.B. Mr	NASA, Ames Research Center, Moffett-Field, CA, USA
KOENIG, D.G. Mr	NASA, Ames Research Center, Moffett-Field, CA, USA
KOSEWICZ, R.K. Mr	McDonnell Douglas Corp., St.Louis, MO, USA
LACEY, D.W. Mr	Naval Ship R. and D. Center, Bethesda, MD, USA
LANGHAM, F. Mr	CALSPAN/AEDC Div., Arnold AFS, TN, USA
LEVIN, D. Mr	NASA, Ames Research Center, Moffett-Field, CA, USA
LOTTATI, I. Mr	NASA, Ames Research Center, Moffett-Field, CA, USA
MAINE, R. Mr	NASA, Dryden Flight Research Center, Edwards, CA, USA
MALCOLM, G.N. Mr	NASA, Ames Research Center, Moffett-Field, CA, USA
McNEILL, W.E. Mr	NASA, Ames Research Center, Moffett-Field, CA, USA
MENDENHALL, M.R. Mr	Nielsen Engineering and Research Inc., Mountain View, CA, USA
MERRICK, V.K. Mr	NASA, Ames Research Center, Moffett-Field, CA, USA
MEYER, R.T. Mr	Lockheed-Georgia, Co., Marietta, GA, USA
MILLARD, W. Mr	Sandia Laboratories, Albuquerque, NM, USA
NELSON, R.C. Mr	University of Notre Dame, Notre Dame, IN, USA
NIXON, D. Mr	Nielsen Engineering and Research Inc., Mountain View, CA, USA
OBAL, A. Capt.	AEDC, Arnold AFS, TN, USA
OBERKAMPF, W.L. Mr	Sandia Nat'l Labs., Albuquerque, NM, USA
OBI, W. Mr	Naval Air Development Center, Warminster, PA, USA
O'LEARY, C.O. Mr	Royal Aircraft Establishment, Bedford, UK
OTTENSOSER, J. Mr	Naval Air Systems Command, Washington, D.C., USA
ORLIK-RUCKEMANN, K.J. Mr	National Aeronautical Establishment, Ottawa, Ontario, Canada
OWEN, K. Mr	COMPLERE, Inc., Moffett-Field, CA, USA
PARKS, E.K. Mr	NASA, Ames Research Center, Moffett-Field, CA, USA
PEAKE, D.J. Mr	NASA, Ames Research Center, Moffett-Field, CA, USA
QUAM, D. Mr	USAF Academy, Colorado Springs, CO, USA
REDING, P. Mr	Lockheed Missiles and Space Co., Sunnyvale, CA, USA
RILEY, D.R. Mr	McDonnell Douglas Corp., St.Louis, MO, USA
RISING, J. Mr	Lockheed-California Co., Burbank, CA, USA
ROBERTS, L. Mr	NASA, Ames Research Center, Moffett-Field, CA, USA
RONCACE, R.A. Mr	NASA, Ames Research Center, Moffett-Field, CA, USA
ROSS, A.J. Mrs	Royal Aircraft Establishment, Farnborough, Hampshire, UK
SAUNDERS, G.H. Mr	CALSPAN/AEDC Division, Arnold AFS, TN, USA
SCHIFF, L.B. Mr	NASA, Ames Research Center, Moffett-Field, CA, USA
SCHNEIDER, C.P. Mr	Bayern Chemie GmbH, Ottobrunn, Germany
SHAFER, M.F. Ms	NASA, Dryden Flight Research Center, Edwards, CA, USA
SIM, A. Mr	NASA, Dryden Flight Research Center, Edwards, CA, USA
SNYDER, C.T. Mr	NASA, Ames Research Center, Moffett-Field, CA, USA
SPANGLER, S.B. Mr	Nielsen Engineering and Research Inc., Mountain View, CA, USA
STAHLARA, S. Mr	Nielsen Engineering and Research Inc., Mountain View, CA, USA
STATLER, I.C. Mr	U.S. Army Aeromechanics Lab., Moffett-Field, CA, USA
STEPHENSON, J.D. Mr	NASA, Ames Research Center, Moffett-Field, CA, USA
SULLY, P.R. Mr	Canadian Dept. of National Defence, Ottawa, Ontario, Canada
SWANN, M. Mr	NASA, Dryden Flight Research Center, Edwards, CA, USA

TANNER, C.E. Mr	Canadair Ltd., Montreal, Canada
TOBAK, M. Mr	NASA, Ames Research Center, Moffett-Field, CA, USA
TU, Y. Mr	U.S. Air Force Armament Lab., Eglin AFB, USA
TUSCH, C. Mr	U.S.A.F., Moffett-Field, CA, USA
USELTON, B.L. Mr	CALSPAN/AEDC Div., Arnold AFS, TN, USA
VAN LEYNSEELE, F. Mr	Boeing Aircraft Co., Edmonds, WA, USA
WINGROVE, R. Mr	NASA, Ames Research Center, Moffett-Field, CA, USA

**Appendix B****LIST OF PARTICIPANTS – VON KARMAN INSTITUTE  
RHODE ST. GENESE – BELGIUM****16–19 March 1981**

ALTENKIRCH, D. Mr	D.F.V.L.R., Braunschweig, Germany
BALANCA, J. M.	O.N.E.R.A., Châtillon, France
BOOKER, D. Mr	British Aerospace PLC, Preston, UK
BRADLEY, J.D. Mr	British Aerospace Ltd., Brough, North Humberside, UK
BRANNSTROM, E.B.H. Mr	The Aeronautical Research Institute, FFA, Bromma, Sweden
BREINBAUER, K. Mr	MBB – Messerschmitt Bölkow Blohm, München, Germany
BUCHACKER, E. Mr	AFB LGIV an der E 61 der Bundeswehr, Flugplatz, Marching, Germany
CALDARELLI, G. Mr	Aeritalia Pomigliano (Na), Italy
CALDWELL, A.E. Mr	University of Glasgow, Glasgow, UK
CHARON, W. Mr	Dornier GmbH, Friedrichshafen, Germany
CHRISTOPHE, J. M.	O.N.E.R.A., Châtillon, France
COSTA, G.C. Mr	Aermacchi SpA, Varese, Italy
COTON, P. Mme	Institut de Mécanique des Fluides, Lille, France
CUMMINGS, T.J. Mr	Short Brothers Limited, Belfast, UK
DARSES, Mr	Institut de Mécanique des Fluides, Lille, France
DAS, A. Mr	D.F.V.L.R., Braunschweig, Germany
DEPPE, D. Mr	MBB, Ottobrunn/München, Germany
DESGARDIN, A. M.	Laboratoire de Recherche, Balistiques et Aérodynamiques, Vernon, France
DESOPPER, A. M.	O.N.E.R.A., Châtillon, France
DOHERR, K.F. Mr	D.F.V.L.R., Braunschweig, Germany
DOUP, P.W. Mr	Prins Maurits Laboratory TNO, AA Rijswijk, Netherlands
DUJARRIC, C. M.	STPA, Paris 15°, France
FRISTEDT, K.A. Mr	The Aeronautical Research Institute, Bromma II, Sweden
FUCHS, H. Mr	Dornier GmbH, Friedrichshafen I, Germany
HARRISON, N. Mr	British Aerospace, Warton, Aerodrome, Lancaster, UK
HICKS, J.W. Mr	D.F.V.L.R., Wessling/OBB., Germany
HUYNH-HUU-THANH, M.	O.N.E.R.A., Châtillon, France
IANNARELLI, F. M.	S.N.I.A.S., Toulouse, France
JANSSON, S.E.T. Mr	The Royal Institute of Technology, Stockholm, Sweden
KARLSSON, I.K. Mr	The Aeronautical Research Institute, Bromma, Sweden
KOEHLER, R. Mr	D.F.V.L.R., Braunschweig, Germany
KRAG, B. Mr	D.F.V.L.R., Braunschweig, Germany
MACKIE, D.B. Mr	D.F.V.L.R., Braunschweig, Germany
MANCO, M. Mr	Aeritalia, Pomigliano, Italy
MORATILLA, D. Mr	Instituto Nacional de Técnica Aeroespacial, Torrejón de Ardoz/Madrid, Spain

**B-2**

NIEZGODKA, F.-J.	D.F.V.L.R., Köln, Germany
PAPWORTH, C.D. Mr	Baj Vickers Ltd., Avon, UK
RABACHINO, B. Mr	Aeritalia, Torino, Italy
RAFEL, G.G. Mr	Nationaal Lucht – en Ruimtevaart Lab., NLR, AD Emmeloord, Netherlands
REQUARDT, G. Mr	D.F.V.L.R., Köln, Germany
SACCO, G. Mr	I.A.M. Rinaldo Piaggio SpA, Finale Ligure, Italy
SCHMIDT, E. Mr	D.F.V.L.R., Göttingen, Germany
SETHNA, C.M. Mr	Science Research Council, Ditton Park, Slough, UK
THORNE, R. Mr	Cranfield Institute of Technology, Cranfield, Bedford, UK
TJOA, H.G. Mr	Fokker B.V., Schiphol-Oost, Netherlands
TOIA, P. Mr	Aeronautica Macchi, Varese, Italy
TRISTANT, D. M.	Institut de Mécanique des Fluides, Lille, France
UBEZIO, L. Mr	SIAI – Marchetti SpA, Sesto Calende (Varese), Italy
VAL TORTA, E. Mr	Aermacchi, Varese, Italy
VAN DEN HEILIGENBERG, Mr	Min. van Def., Den Haag, The Netherlands
VAN MANSART, M.G. Mr	Institut de Mécanique des Fluides, Lille, France
VANNUCI, M. Mr	Aeritalia, Torino, Italy
VERBRUGGE, R. M.	Institut de Mécanique des Fluides, Lille, France
VERGNE, M. M.	Direction des Recherches, Etudes et Techniques SDR/GGI, Paris, France
VERHAAGEN, N.G. Mr	Delft University of Technology, Kluyverweg, 1, Delft, Netherlands
WEBER, G. M.	Société Nationale Industrielle, Aérospatiale, Châtillon, France
WILHELM, K. Mr	D.F.V.L.R., Braunschweig, Germany
WOLFFELT, K.W. Mr	SAAB-SCANIA AB, Linköping, Sweden
<i>Lecture Series Director</i>	
ORLIK-RUCKEMANN, K. Dr	National Aeronautical Laboratory, Ottawa, Ontario, Canada
<i>Lecture Series Coordinator</i>	
SANDFORD, J. Prof.	Von Kármán Institute, Rhode St.Genèse, Belgium
<i>Lecturers</i>	
CHAMBERS, J.R. Mr	NASA Langley Research Center, Hampton, Virginia, USA
ERICSSON, L.E. Dr	Lockheed Missiles and Space Co., Sunnyvale, California, USA
HAMEL, P. Dr	D.F.V.L.R., Braunschweig, Germany
HANFF, E.S. Dr	National Aeronautical Establishment, Ottawa, Ontario, Canada
MALCOLM, G.N. Mr	NASA Ames Research Center, Moffett-Field, California, USA
O'LEARY, C. Mr	Royal Aircraft Establishment, Bedford, UK
ROSS, A.J. Dr	MoD(PE) Royal Aircraft Establishment, Farnborough, Hants, UK
SCHIFF, L. Dr	NASA Ames Research Center, Moffett-Field, California, USA
SCHNEIDER, C.P. Dr	Bayern-Chemie GmbH, Ottobrunn, Germany
<i>AGARD Staff</i>	
de CHASSEY, J.C. Col.	(FAF.) AGARD, Neuilly-sur-Seine, France
ROLLINS, B. Mr	(NASA,) AGARD, Neuilly-sur-Seine, France

REPORT DOCUMENTATION PAGE											
<b>1. Recipient's Reference</b>	<b>2. Originator's Reference</b>	<b>3. Further Reference</b>	<b>4. Security Classification of Document</b>								
	AGARD-LS-114	ISBN 92-835-1385-1	UNCLASSIFIED								
<b>5. Originator</b>	Advisory Group for Aerospace Research and Development North Atlantic Treaty Organization 7 rue Ancelle, 92200 Neuilly sur Seine, France										
<b>6. Title</b>	DYNAMIC STABILITY PARAMETERS										
<b>7. Presented at</b>	on 2-5 March 1981 at NASA Ames Research Center, Moffett Field, California, USA and 16-19 March 1981 at the von Kármán Institute, Rhode-Saint-Genèse, Belgium.										
<b>8. Author(s)/Editor(s)</b>	Various		<b>9. Date</b> May 1981								
<b>10. Author's/Editor's Address</b>	Various		<b>11. Pages</b> 400								
<b>12. Distribution Statement</b>	This document is distributed in accordance with AGARD policies and regulations, which are outlined on the Outside Back Covers of all AGARD publications.										
<b>13. Keywords/Descriptors</b>	<table> <tbody> <tr> <td>Aircraft</td> <td>Angle of attack</td> </tr> <tr> <td>Missiles</td> <td>Mathematical models</td> </tr> <tr> <td>Aerospaceplanes</td> <td>Windtunnel tests</td> </tr> <tr> <td>Aerodynamic stability</td> <td>Flight tests</td> </tr> </tbody> </table>			Aircraft	Angle of attack	Missiles	Mathematical models	Aerospaceplanes	Windtunnel tests	Aerodynamic stability	Flight tests
Aircraft	Angle of attack										
Missiles	Mathematical models										
Aerospaceplanes	Windtunnel tests										
Aerodynamic stability	Flight tests										
<b>14. Abstract</b>	<p>The advent of flight at high angles of attack has revived our interest in the dynamic stability of aircraft and missiles. This Lecture Series provides a review of the impact of high-<math>\alpha</math> aerodynamics on dynamic stability characteristics of aerospace vehicles and presents a state-of-the-art survey of the analytical, wind-tunnel and flight-test techniques used for dynamic stability work. The programme also features a discussion of the various mathematical models used for the analysis of flight behaviour of aircraft at high angles of attack including the non-linear and time dependent formulations as well as a review of some pertinent sensitivity and simulator studies. The material presented by the Lecture Series covers not less than four distinct disciplines: theoretical aerodynamics, wind-tunnel experiments, flight testing and flight mechanics. It is, of course, only through simultaneous use of all of these disciplines that a better understanding of the flight dynamics of a modern aerospace vehicle can be achieved.</p> <p>The material in this publication was assembled to support a Lecture Series under the sponsorship of the Fluid Dynamics Panel, the Consultant and Exchange Programme of AGARD and the von Kármán Institute for Fluid Dynamics.</p>										

<p><b>AGARD Lecture Series No.114</b> Advisory Group for Aerospace Research and Development, NATO <b>DYNAMIC STABILITY PARAMETERS</b> Published May 1981 400 pages</p> <p>The advent of flight at high angles of attack has revived our interest in the dynamic stability of aircraft and missiles. This Lecture Series provides a review of the impact of high-<math>\alpha</math> aerodynamics on dynamic stability characteristics of aerospace vehicles and presents a state-of-the-art survey of the analytical, wind-tunnel and flight-test techniques used for dynamic stability work. The programme also features a discussion of the various mathematical models used for the analysis of flight</p> <p>P.T.O.</p>	<p><b>AGARD-LS-114</b></p> <p>Aircraft Missiles Aerospaceplanes</p> <p>Aerodynamic stability Angle of attack Mathematical models Windtunnel tests Flight tests</p>	<p><b>AGARD Lecture Series No.114</b> Advisory Group for Aerospace Research and Development, NATO <b>DYNAMIC STABILITY PARAMETERS</b> Published May 1981 400 pages</p> <p>The advent of flight at high angles of attack has revived our interest in the dynamic stability of aircraft and missiles. This Lecture Series provides a review of the impact of high-<math>\alpha</math> aerodynamics on dynamic stability characteristics of aerospace vehicles and presents a state-of-the-art survey of the analytical, wind-tunnel and flight-test techniques used for dynamic stability work. The programme also features a discussion of the various mathematical models used for the analysis of flight</p> <p>P.T.O.</p>	<p><b>AGARD-LS-114</b></p> <p>Aircraft Missiles Aerospaceplanes</p> <p>Aerodynamic stability Angle of attack Mathematical models Windtunnel tests Flight tests</p>
	<p><b>AGARD-LS-114</b></p> <p>Aircraft Missiles Aerospaceplanes</p> <p>Aerodynamic stability Angle of attack Mathematical models Windtunnel tests Flight tests</p>	<p><b>AGARD Lecture Series No.114</b> Advisory Group for Aerospace Research and Development, NATO <b>DYNAMIC STABILITY PARAMETERS</b> Published May 1981 400 pages</p> <p>The advent of flight at high angles of attack has revived our interest in the dynamic stability of aircraft and missiles. This Lecture Series provides a review of the impact of high-<math>\alpha</math> aerodynamics on dynamic stability characteristics of aerospace vehicles and presents a state-of-the-art survey of the analytical, wind-tunnel and flight-test techniques used for dynamic stability work. The programme also features a discussion of the various mathematical models used for the analysis of flight</p> <p>P.T.O.</p>	<p><b>AGARD-LS-114</b></p> <p>Aircraft Missiles Aerospaceplanes</p> <p>Aerodynamic stability Angle of attack Mathematical models Windtunnel tests Flight tests</p>

<p>behaviour of aircraft at high angles of attack including the non-linear and time dependent formulations as well as a review of some pertinent sensitivity and simulator studies. The material presented by the Lecture Series covers not less than four distinct disciplines: theoretical aerodynamics, wind-tunnel experiments, flight testing and flight mechanics. It is, of course, only through simultaneous use of all of these disciplines that a better understanding of the flight dynamics of a modern aerospace vehicle can be achieved.</p> <p>The material in this publication was assembled to support a Lecture Series under the sponsorship of the Fluid Dynamics Panel, the Consultant and Exchange Programme of AGARD and the von Kármán Institute for Fluid Dynamics presented on: 2-5 March 1981 at NASA Ames Research Center, Moffett Field, California, USA and 16-19 March 1981 at the von Kármán Institute, Rhode-Saint-Genèse, Belgium.</p>	<p><b>ISBN 92-835-1385-1</b></p>	<p>The material in this publication was assembled to support a Lecture Series under the sponsorship of the Fluid Dynamics Panel, the Consultant and Exchange Programme of AGARD and the von Kármán Institute for Fluid Dynamics presented on: 2-5 March 1981 at NASA Ames Research Center, Moffett Field, California, USA and 16-19 March 1981 at the von Kármán Institute, Rhode-Saint-Genèse, Belgium.</p>
<p>behaviour of aircraft at high angles of attack including the non-linear and time dependent formulations as well as a review of some pertinent sensitivity and simulator studies. The material presented by the Lecture Series covers not less than four distinct disciplines: theoretical aerodynamics, wind-tunnel experiments, flight testing and flight mechanics. It is, of course, only through simultaneous use of all of these disciplines that a better understanding of the flight dynamics of a modern aerospace vehicle can be achieved.</p> <p>The material in this publication was assembled to support a Lecture Series under the sponsorship of the Fluid Dynamics Panel, the Consultant and Exchange Programme of AGARD and the von Kármán Institute for Fluid Dynamics presented on: 2-5 March 1981 at NASA Ames Research Center, Moffett Field, California, USA and 16-19 March 1981 at the von Kármán Institute, Rhode-Saint-Genèse, Belgium.</p>	<p><b>ISBN 92-835-1385-1</b></p>	<p>The material in this publication was assembled to support a Lecture Series under the sponsorship of the Fluid Dynamics Panel, the Consultant and Exchange Programme of AGARD and the von Kármán Institute for Fluid Dynamics presented on: 2-5 March 1981 at NASA Ames Research Center, Moffett Field, California, USA and 16-19 March 1981 at the von Kármán Institute, Rhode-Saint-Genèse, Belgium.</p>